Transactions of the ASME, Journal of Applied Mechanics (ISSN 0021-8936) is published bimonthly (Jan., Mar., May, July, Sept., Nov.) The American Society of Mechanical Engineers, Three Park Avenue, New York, NY 10016. Periodicals postage paid at New York, NY and additional mailing office. POSTMASTER: Send address changes to Transactions of the ASME, Journal of Applied Mechanics, c/o THE AMERICAN SOCIETY OF MECHANICAL ENGINEERS, 22 Law Drive, Box 2300, Fairfield, NJ 07007-2300. **CHANGES OF ADDRESS** must be received at Society headquarters seven weeks before they are to be effective. Please send old label and new address. **STATEMENT from By-Laws.** The Society shall not be responsible for statements or opinions advanced in papers or . . . printed in its publications (B7.1, Para. 3).

Journal of Applied Mechanics

Published Bimonthly by ASME

VOLUME 71 • NUMBER 3 • MAY 2004

TECHNICAL PAPERS

BRIEF NOTES

(**Contents continued on inside back cover**)

This journal is printed on acid-free paper, which exceeds the ANSI Z39.48-1992 specification for permanence of paper and library materials. ♾™
♻ 85% recycled content, including 10% post-consumer fibers.

ANNOUNCEMENTS AND SPECIAL NOTES

The ASME Journal of Applied Mechanics is abstracted and indexed in the following:

Alloys Index, Aluminum Industry Abstracts, Applied Science & Technology Index, AMR Abstracts Database, Ceramic Abstracts, Chemical Abstracts, Civil Engineering Abstracts, Compendex (The electronic equivalent of Engineering Index), Computer & Information Systems Abstracts, Corrosion Abstracts, Current Contents, EEA (Earthquake Engineering Abstracts Database), Electronics & Communications Abstracts Journal, Engineered Materials Abstracts, Engineering Index, Environmental Engineering Abstracts, Environmental Science and Pollution Management, Fluidex, Fuel & Energy Abstracts, GeoRef, Geotechnical Abstracts, INSPEC, International Aerospace Abstracts, Journal of Ferrocement, Materials Science Citation Index, Mechanical Engineering Abstracts, METADEX (The electronic equivalent of Metals Abstracts and Alloys Index), Metals Abstracts, Nonferrous Metals Alert, Polymers Ceramics Composites Alert, Referativnyi Zhurnal, Science Citation Index, SciSearch (Electronic equivalent of Science Citation Index), Shock and Vibration Digest, Solid State and Superconductivity Abstracts, Steels Alert, Zentralblatt MATH

On the Nearly Viscometric Torsional Motion of Viscoelastic Liquids Between Shrouded Rotating Disks

Dennis A. Siginer
Professor,
Department of Mechanical Engineering,
College of Engineering,
Wichita State University,
Wichita, KS 67260-0133
e-mail: dennis.siginer@wichita.edu
Fellow ASME

Flow of a viscoelastic liquid in a cylindrical cavity, driven by rotating finite disks is investigated. The cylindrical sidewall is fixed and the covers rotate with different angular velocities either in the same or in opposite directions. A regular perturbation in terms of the angular velocity of the caps is used. The flow field is resolved into a primary azimuthal stratified viscometric field and a weaker secondary meridional field. Results are presented for a range of cylinder aspect and cap rotation ratios and viscoelastic parameters. Interesting instabilities of the fluid of second grade are discussed. The controversy surrounding the sign of the first Rivlin-Ericksen constant is completely irrelevant to the discussion. It is shown qualitatively that loss of stability occurs repeatedly and bifurcating flows exist for critical values of an elasticity parameter at fixed aspect and cap rotation ratio. Branching flows also occur at a fixed value of the elasticity parameter for critical values of the cap rotation ratio, when the aspect ratio is fixed. [DOI: 10.1115/1.1651538]

1 Introduction

Flow in a cylindrical cavity driven by rotating finite shrouded disks is interesting both from theoretical and technological points of view. Theoretically it provides a good test to pass for constitutive equations simulating the class of nearly viscometric flows when angular velocities of the end caps are small. It may also find a host of applications in the industry when the working fluid is either Newtonian or non-Newtonian. This type of flow is relevant to gas centrifuges, computer disc drives, rotating machinery, viscometry, etc. In particular, geometries with large aspect ratios may find applications in chemical mixers and rotating heat exchangers.

The Newtonian problem has been rather extensively investigated starting with Dorfman and Romanenko [1], and Pao [2,3]. Later contributions include those of Dijkstra and Van Heijst [4] and Duck [5]. The first publications in this area concerning viscoelastic flows, to our knowledge, are by Kramer and Johnson [6] and Hill [7]. A new constitutive equation for slow, nearly viscometric motions of viscoelastic liquids is derived in the former, and applied to the motion of a viscoelastic liquid driven by the rotating top cap of a cylindrical cavity of aspect ratio one. The latter provides experimental validation of the theory developed by Kramer and Johnson [6]. The swirling flow of viscoinelastic and viscoelastic fluids driven by therotation of a disk in a cylindrical casing has been investigated recently by Escudier and Cullen [8], Itoh et al. [9,10], Moroi et al. [11,12], and Stokes et al. [13,14]. Neither of the early papers, [6,7], considers the effect of the aspect ratio and the effect of the differentially rotating end caps, either in the same sense or in opposite directions, and none of the recent investigations explores the effect of the differentially rotating disks. In addition to both of these effects we consider the influence on the flow field of the varying elasticity of the fluid and provide a detailed description of the flow field including interesting bifurcating flows which may happen for either critical values of the elasticity at fixed cap rotation ratio or critical values of the cap rotation ratio at fixed elasticity when the structure of the working fluid is that of the fluid of second grade. The fluid of order two or equivalently the fluid of second grade is widely used to describe qualitatively the behavior of slightly viscoelastic fluids in steady nearly viscometric motions. The present study is important to point out the limitations of the fluid of second grade.

Our analysis is set in the context of the fluids of grade N,

$$\mathbf{S}=\sum_{1}^{N}\mathbf{S}_i,\quad \mathbf{S}_1=\mu\mathbf{A}_1,\quad \mathbf{S}_2=\alpha_1\mathbf{A}_2+\alpha_2\mathbf{A}_1^2$$
$$\mathbf{S}_3=\beta_1\mathbf{A}_3+\beta_2(\mathbf{A}_2\mathbf{A}_1+\mathbf{A}_1\mathbf{A}_2)+\beta_3(tr\mathbf{A}_2)\mathbf{A}_1,\ \ldots \tag{1}$$

where μ, α_i, and β_i are the constitutive constants of the fluid of grade one (Newtonian) two and three, respectively. $\mathbf{A}_n$ is the Rivlin-Eriksen tensor of order n which can be obtained from the recursion formula,

$$\mathbf{L}=\text{grad}\,\mathbf{u},\quad 2\mathbf{D}=\mathbf{L}+\mathbf{L}^T,\quad \mathbf{A}_1=2\mathbf{D},$$
$$\mathbf{A}_{n+1}=\mathbf{A}_n+\mathbf{L}^T\mathbf{A}_n+\mathbf{A}_n\mathbf{L}.$$

We use a perturbation algorithm in terms of the angular velocity of the end caps to resolve the field into a primary, azimuthal, vertically stratified viscometric field and a weaker secondary field in the meridional plane. The former and the latter are first and second-order effects, respectively, in Ω, the common denominator of the angular velocity of the caps. The ongoing controversy about the sign associated with the first Rivlin-Ericksen constant α_1 is completely irrelevant to our analysis. That is because the elasticity parameter which governs the meridional field at the second order is defined in terms of the sum $\alpha_1+\alpha_2>0$ and α_1 does not appear anywhere by itself. Also, the instabilities we discuss occur for rather small values of the elasticity parameter in question. Therefore any objection to the use of the fluid of second grade on the grounds that it may be good enough only for slightly viscoelastic liquids does not have any support.

The analysis could be easily extended to the third and fourth orders to provide further corrections to the primary azimuthal and secondary meridional fields, respectively. But these corrections do not change the qualitative description of the field. On the other

Contributed by the Applied Mechanics Division of THE AMERICAN SOCIETY OF MECHANICAL ENGINEERS for publication in the ASME JOURNAL OF APPLIED MECHANICS. Manuscript received by the ASME Applied Mechanics Division, Jan. 2, 2001; final revision, Sept. 19, 2003. Associate Editor: L. T. Wheeler. Discussion on the paper should be addressed to the Editor, Prof. Robert M. McMeeking, Journal of Applied Mechanics, Department of Mechanical and Environmental Engineering University of California–Santa Barbara, Santa Barbara, CA 93106-5070, and will be accepted until four months after final publication of the paper itself in the ASME JOURNAL OF APPLIED MECHANICS.

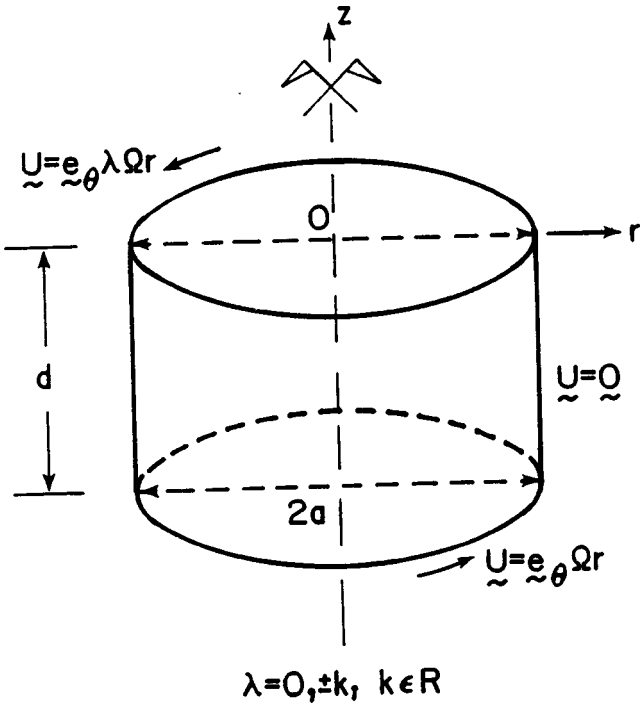

Fig. 1 Flow configuration

hand, if the liquid is strongly shear-thinning, the azimuthal viscometric field will be noticeably affected. A correction to the first order may have to be made by extending the analysis to the third order in the algorithm where the parameter $(\beta_2+\beta_3)$ defining the shear dependent viscosity behavior of the liquid appears for the first time. $(\beta_2+\beta_3)$ is negative and positive, respectively, for shear-thinning and shear-thickening liquids. Our analysis therefore takes into account only the elasticity of the liquid and works better for liquids with rather large second order range. For instance, polyacrylamide solutions of any concentration have a rather small second-order range whereas solutions of methacrylate copolymer in oil have considerably larger second order range.

We present a complete discussion of the change in the flow field with changing aspect ratio and rotation ratio of the caps for a range of elasticity parameters. In particular, we show numerically that repeated loss of stability and subsequent bifurcations occur in the flow field of the fluid of second grade for both counter and same sense rotation of the caps at almost any aspect ratio for critical values of the elasticity parameter and cap rotation ratio.

2 Mathematical Analysis

The flow configuration is shown in Fig. 1. The relevant field equations and boundary conditions read

$$\rho\frac{D\mathbf{u}}{Dt}=-\nabla\Phi+\nabla\cdot\mathbf{S},\quad \nabla\cdot\mathbf{u}=0, \tag{2}$$

$$\mathbf{u}(r,0)=\lambda r\Omega\mathbf{e}_\theta,\quad \mathbf{u}(r,-d)=r\Omega\mathbf{e}_\theta,\quad \mathbf{u}(a,z)=0, \tag{3}$$

where $\mathbf{S}$ is the extra stress given by $(1)_1$ and Φ is the modified pressure field which includes gravitational effects. We note that

$$\mathbf{u}=U\mathbf{e}_r+V\mathbf{e}_\theta+W\mathbf{e}_z,\quad U(\Omega)=U(-\Omega),$$
$$V(\Omega)=-V(-\Omega),\quad W(\Omega)=W(-\Omega), \tag{4}$$

and expand (U,W) and (V) in power series even and odd in Ω, respectively, with the coefficient of the nth-order term in the series the nth-order partial derivative evaluated at $\Omega=0$. The extra stress $\mathbf{S}$ is expanded in a Fréchet series around the base state, the state of rest.

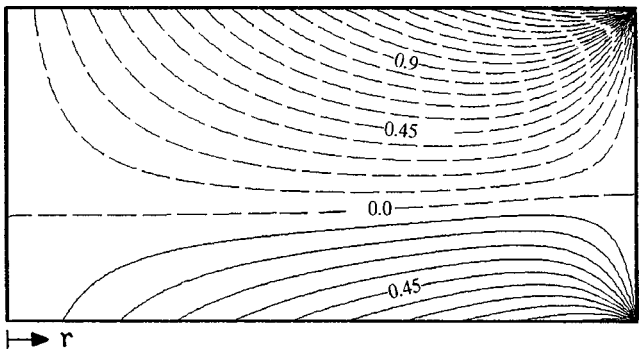

Fig. 2 Level lines of azimuthal velocity: δ=0.5; caps counter-rotating with the top cap twice as fast as the bottom, $\lambda=-2$

2.1 First-Order Solution. The first order problem is obtained from Eqs. (1)–(4)

$$\Delta\mathbf{u}^{(1)}=0,\quad \nabla\cdot\mathbf{u}^{(1)}=0,\quad u^{(1)}=V^{(1)}\mathbf{e}_\theta, \tag{5}$$

$$\mathbf{u}^{(1)}(r,0)=\lambda r\mathbf{e}_\theta,\quad \mathbf{u}^{(1)}(r,-d)=r\mathbf{e}_\theta, \tag{6}$$

$$\mathbf{u}(a,z)=0,\quad \mathbf{u}(0,z)<+\infty. \tag{7}$$

The problem defined by Eqs. (5)–(7) is reformulated in terms of dimensionless (ξ,η)-coordinates and a dimensionless azimuthal velocity ν obtained from the corresponding dimensional variables by dividing with the disk radius a.

$$\frac{1}{\xi}(\xi\nu_{,\xi})_{,\xi}-\frac{\nu}{\xi^2}+\nu_{,\eta\eta}=0,$$
$$\nu(\xi,0)=\lambda\xi,\quad \nu(\xi,-\delta)=\xi,\quad \nu(1,\eta)=0,\quad \nu(0,\eta)<\infty, \tag{8}$$
$$\xi=\frac{r}{a},\quad \eta=\frac{z}{a},\quad \delta=\frac{d}{a},\quad \nu=\frac{V^{(1)}}{a}.$$

The solution reads

$$\nu(\xi,\eta)=\sum_k B_kJ_1(A_k\xi)[\lambda Ch(A_k\eta)+C_kSh(A_k\eta)], \tag{9}$$
$$B_k=\frac{2}{A_kJ_2(A_k)},\quad C_k=\frac{1-\lambda Ch(-A_k\delta)}{Sh(-A_k\delta)},\quad J_1(A_k)=0,$$

where J_1 and J_2 are the Bessel functions of the first kind and first and second orders, respectively. The convergence of (9) to the

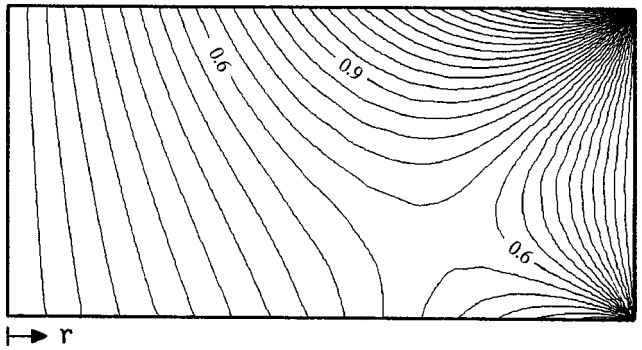

Fig. 3 Level lines of azimuthal velocity: δ=0.5; same sense rotation with the top cap rotating twice as fast as the bottom, $\lambda=2$

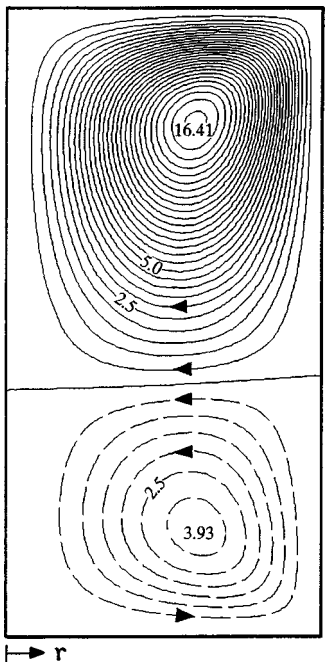

Fig. 4 Contour lines of the dimensionless Newtonian second-order stream function $\delta=2$, $\lambda=-2$

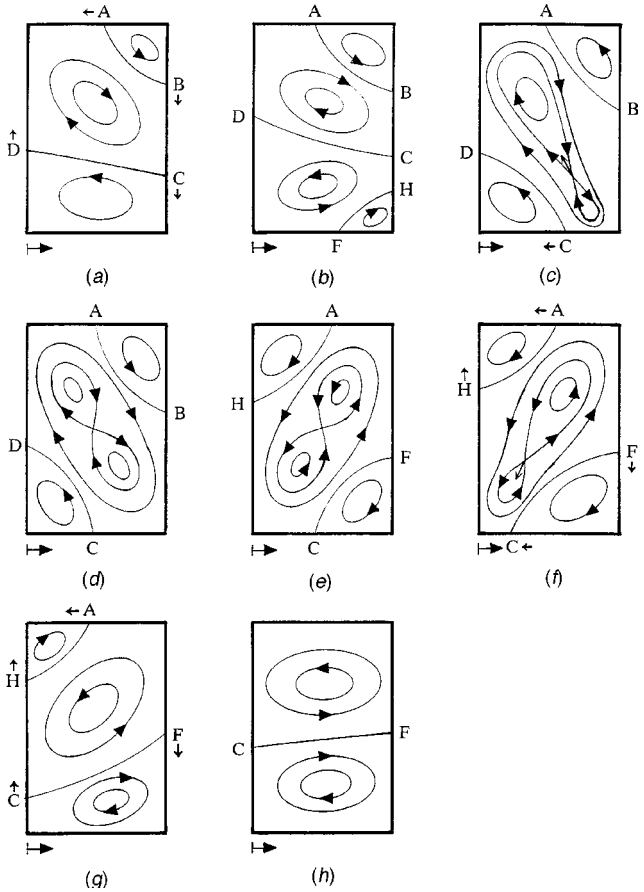

Fig. 5 Meridional flow configurations in a tall cylinder, $\delta=2$, at fixed cap rotation ratio $|\lambda|=2$, with varying dimensionless elasticity parameter β. (*a*) $\beta<0.01$; (*b*) $\beta<\beta_{cr}$; (*c*) $\beta=\beta_{cr}+\varepsilon$; (*d*) $\beta=\beta_{cr}-\varepsilon$; (*e*) $\beta=\hat{\beta}_{cr}+\varepsilon$; (*f*) $\beta>\hat{\beta}_{cr}$; (*g*) $\beta\gg\hat{\beta}_{cr}$; (*h*) $\beta=0.1$.

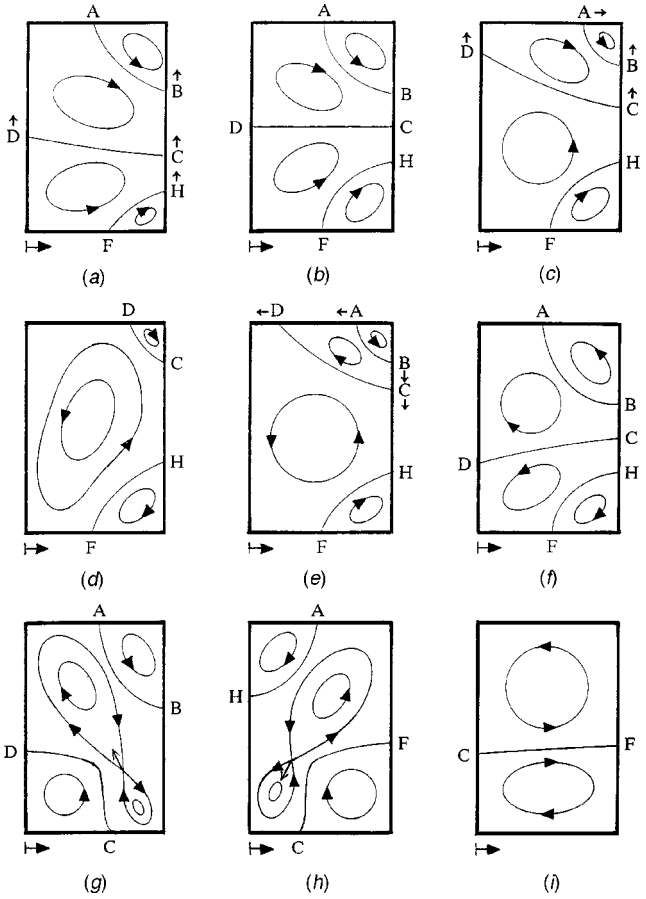

Fig. 6 Meridional flow configurations in a tall cylinder, $\delta=2$, at a fixed value of the elasticity parameter β such that $\beta<\hat{\beta}_{cr}$, with varying cap ratio λ. (*a*) $-2<\lambda<-1$; $\lambda\to-1$; (*b*) $\lambda=\pm1$; (*c*) $-1<\lambda<0$; $\lambda\to0$; (*d*) $\lambda=0$ (*e*) $0<\lambda<1$; $\lambda\to1$; (*f*) $1<\lambda<2$; $\lambda\to2$; (*g*) $\lambda=\lambda_{cr}+\varepsilon$ (*h*) $\lambda>\lambda_{cr}$ (*i*) $\lambda\gg\lambda_{cr}$.

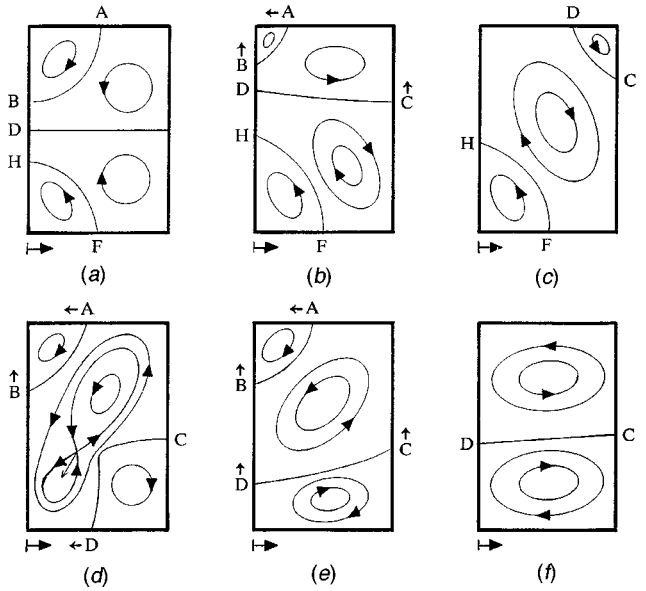

Fig. 7 Same as Fig. 6 except for $\beta>\hat{\beta}_{cr}$. (*a*) $\lambda=\pm1$; (*b*) $-1<\lambda<0$; $\lambda\to0$; (*c*) $\lambda=0$; (*d*) $\lambda=\lambda_{cr}+\varepsilon$ (*e*) $\lambda>\lambda_{cr}$; (*f*) $\lambda\gg\lambda_{cr}$.

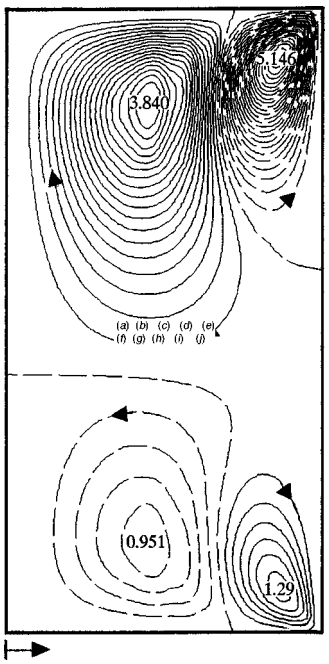

Fig. 8 Bifurcated flow field configuration in the meridional plane. β is slightly larger than β_{cr}. β=0.03, δ=2, λ=−2.

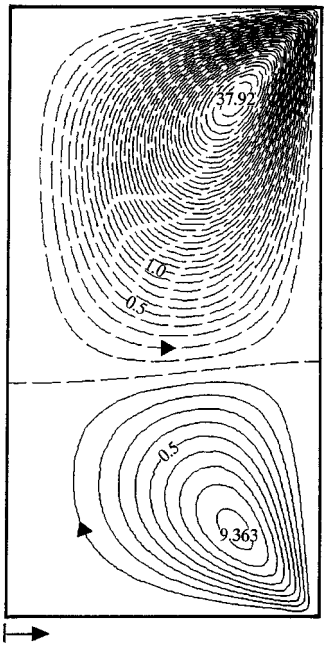

Fig. 10 Dimensionless meridional stream function contours. β=0.1, δ=2, λ=−2.

ramp functions on the top and bottom caps is quite good, especially when Cesaro sums are used. For instance, in the case of the top cap, we compute the Cesaro sum $\overline{\nu}_N(\xi,0)$ as

$$\overline{\nu}_N(\xi,0)=\frac{1}{N+1}\sum_{1}^{N}\nu_m(\xi,0),\quad \nu_m(\xi,0)=2\lambda\sum_{1}^{m}\frac{J_1(A_n\xi)}{A_nJ_2(A_n)}.$$

Representative level lines of this primary, azimuthal field are given in Figs. 2–3 for one aspect ratio δ=0.5 and cap rotation ratios $\lambda=-2$, 2. We note that Newtonian solutions of the type (9) were given first by Hort [15]. Figures for the level lines of the primary, azimuthal field for other cap rotation ratios $\lambda=-1$, 0, 1 investigated in this paper are not included here in the interest of space. Level lines for $\lambda=-1$, 1 look very much like level line patterns for $\lambda=-2$, 2 in Figs. 2 and 3, respectively, except that there is now symmetry with respect to the midline (plane) in the radial direction. And the level lines for the case of top cap at rest (λ=0) show an almost rigid body rotation close to r∼0, that is fluid rotation is very much like in concentric annuli close to the axis of rotation of the finite bottom disk.

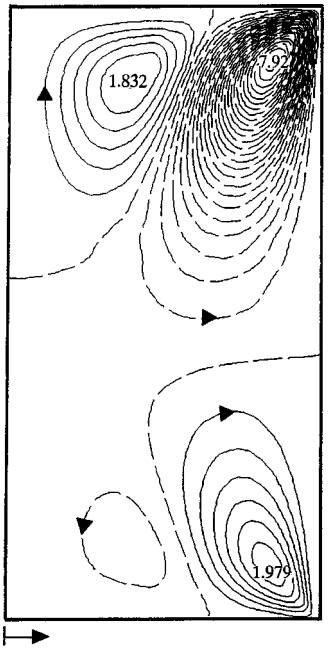

Fig. 9 Bifurcated flow field configuration in the meridional plane. β is slightly larger than $\hat{\beta}_{cr}$. β=0.0375, δ=2, λ=−2.

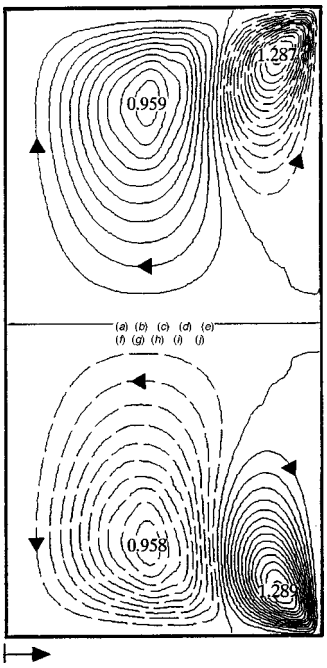

Fig. 11 Dimensionless meridional stream function contours. β=0.03, δ=2, λ=−1.

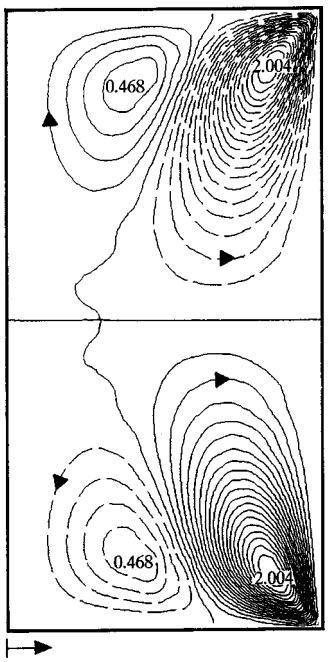

Fig. 12 Same as Fig. 11 except for β=0.0375

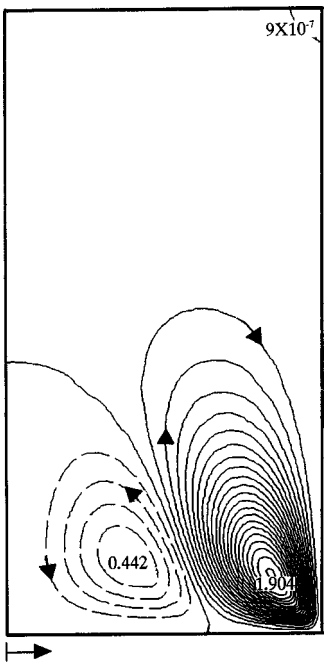

Fig. 14 Same as Fig. 13 except for β=0.0375

2.2 Second-Order Solution. At the second order the Stokes problem obtained from Eqs. (1)–(4) reads

$$2\rho\mathbf{u}^{(1)}\cdot\nabla\mathbf{u}^{(1)}=-\nabla\Phi^{(2)}+\nabla\cdot\mathbf{S}^{(2)},\quad \nabla\cdot\mathbf{u}^{(2)}=0, \tag{10}$$

$$\mathbf{u}^{(2)}(r,0)=\mathbf{u}^{(2)}(r,-d)=\mathbf{u}^{(2)}(a,z)=\mathbf{u}^{(2)}(0,z)=0. \tag{11}$$

The extra stress $\mathbf{S}^{(2)}$ is obtained from (1). We introduce dimensionless velocity and pressure fields $\mathbf{U}$ and P and dimensionless parameters β and β^* defined as

$$\mathbf{U}=\frac{\mathbf{u}^{(2)}\mu}{\rho a^3},\quad P=\frac{\Phi^{(2)}}{\rho a^2},\quad \beta=\frac{\alpha_1+\alpha_2}{\rho a^2},\quad \beta^*=\frac{2\alpha_1+\alpha_2}{\rho a^2},$$

and express $(10)_1$ in terms of dimensionless coordinates (ξ,η) defined in (8),

$$\Delta\mathbf{U}=\nabla P+\frac{2}{\xi}[2\beta(b^2+c^2)-\nu^2]\mathbf{e}_\xi-\beta^*\nabla(b^2+c^2). \tag{12}$$

The variables (b,c) in (12) are defined in terms of the dimensionless first-order azimuthal velocity ν,

$$b=\nu_{,\xi}-\frac{\nu}{\xi},\quad c=\nu_{,\eta},\quad \nu=\frac{V^{(1)}}{a}.$$

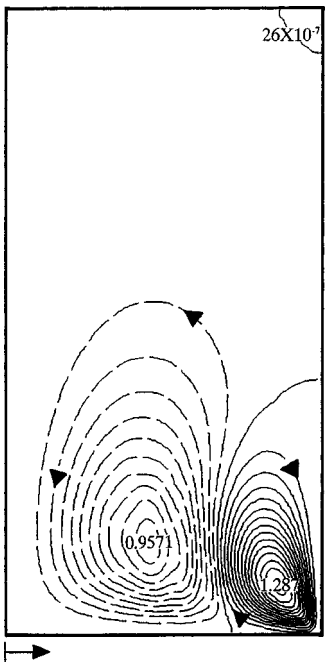

Fig. 13 Same as Fig. 11 except for λ=0

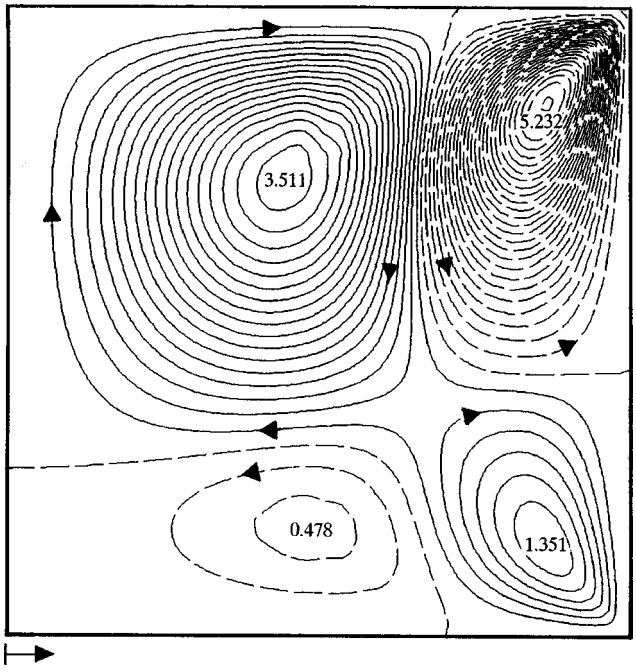

Fig. 15 Bifurcated meridional flow field configuration. β is slightly larger than β_{cr}; β=0.03, δ=1, λ=−2.

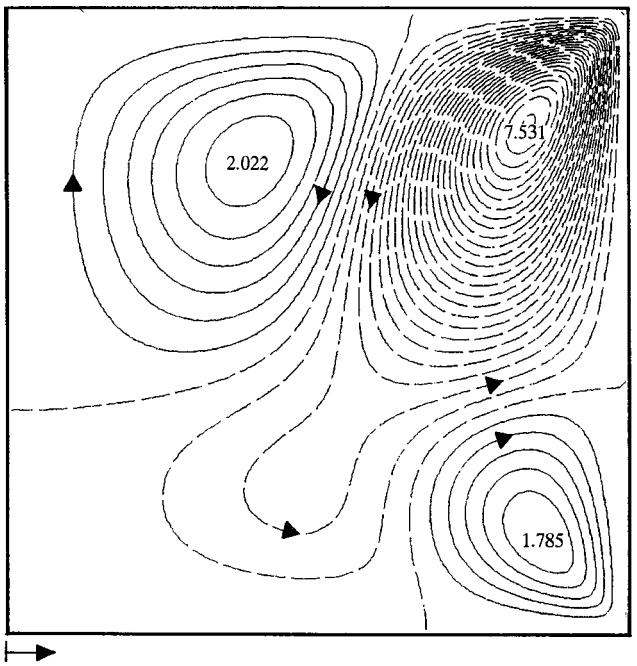

Fig. 16 Bifurcated meridional flow field configuration. β is slightly larger than $\hat{\beta}_{cr}$; β=0.0375, δ=1, λ=−2.

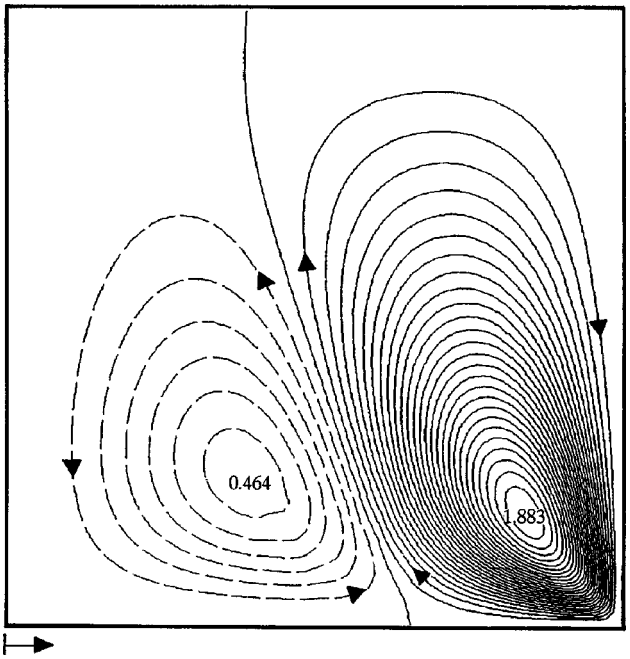

Fig. 18 Dimensionless meridional stream function contours. β=0.0375, δ=1, λ=0.

We note that the combinations of the Rivlin-Ericksen constants α_1 and α_2 which appear in (12) are related to the first and second normal stress differences $N_1(\kappa)$ and $N_2(\kappa)$, respectively, in the following way:

$$\alpha_1+\alpha_2=\lim_{\kappa\to 0}\left(\frac{N_1+2N_2}{2\kappa^2}\right),\quad 2\alpha_1+\alpha_2=\lim_{\kappa\to 0}\frac{N_2}{\kappa^2},$$

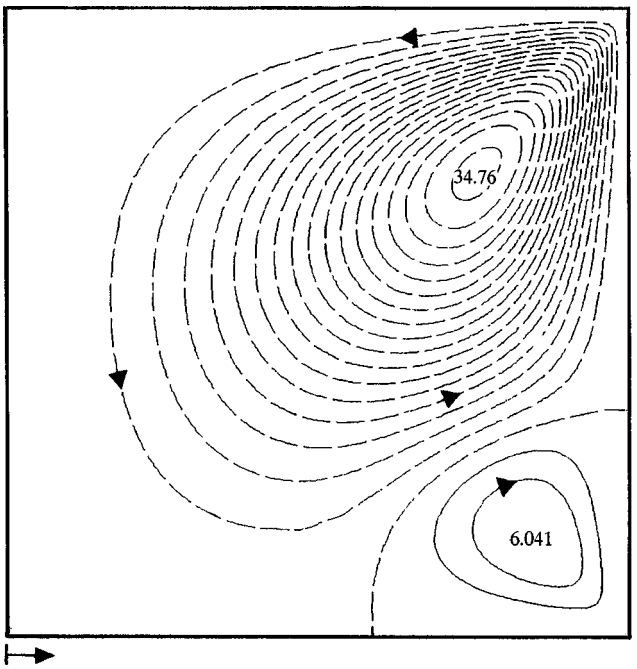

Fig. 17 Dimensionless meridional stream function contours. β=0.1, δ=1, λ=−2.

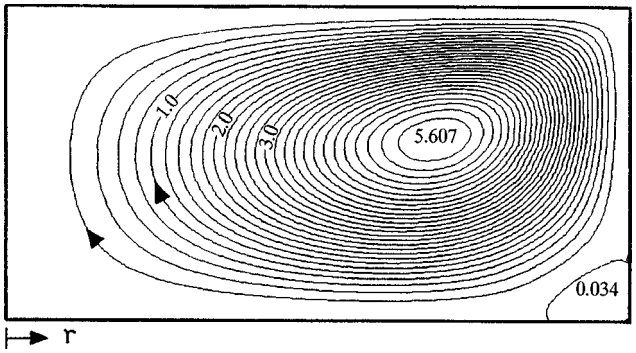

Fig. 19 Contour lines of the dimensionless Newtonian second-order stream function; δ=0.5, λ=2. If λ=−2, the field is qualitatively the same with a stronger and weaker corner and central eddy, respectively.

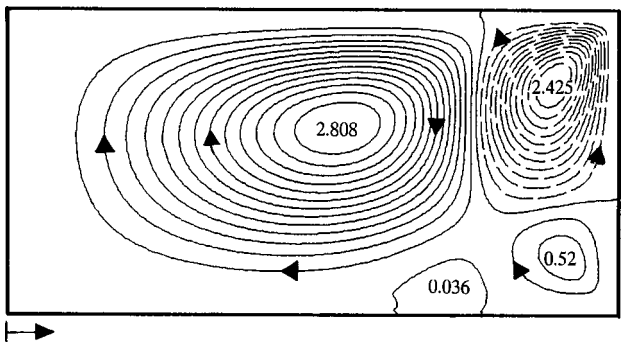

Fig. 20 Bifurcated meridional flow field configuration. β is slightly larger than β_{cr}. β=0.02, δ=0.5, λ=−2.

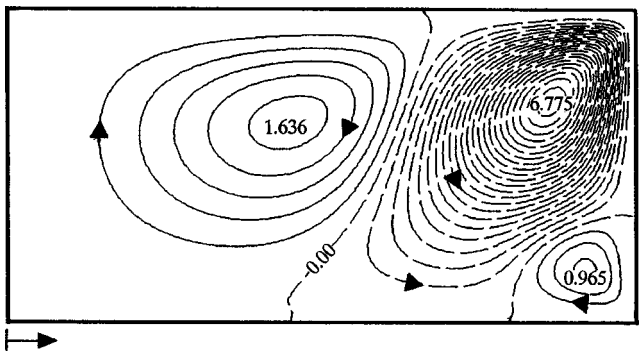

Fig. 21 Bifurcated meridional flow field configuration. β is somewhat larger than β_{cr}. β=0.0375, δ=0.5, λ=−2.

where κ is the shear rate. Introducing a dimensionless stream function Ψ and taking the curl of (12) twice, the momentum balance at the second order can be rewritten as

$$L^2\Psi = 2\nu_{,\eta}^2 - 4\beta(b^2+c^2)_{,\eta}, \quad \Psi = \frac{\mu\psi}{\rho a^5},$$

$$L = (\cdot)_{,\xi\xi} - \frac{1}{\xi}(\cdot)_{,\xi} + (\cdot)_{,\eta\eta}, \tag{13}$$

to be solved subject to the boundary conditions obtained from (11),

$$\Psi(\xi,0) = \Psi_{,\eta}(\xi,0) = \Psi(\xi,-\delta) = \Psi_{,\eta}(\xi,-\delta) = 0, \tag{14}$$

$$\Psi(1,\eta) = \Psi_{,\xi}(1,\eta) = \Psi(0,\eta) = \Psi_{,\xi}(0,\eta) = 0. \tag{15}$$

It is worthwhile to note that the dimensionless parameter β^* which represents second normal stresses does not play a role in shaping the flow field but enters the determination of the pressure field. The modified second-order momentum balance $(13)_1$ subject to (14), (15), is solved using a novel numerical technique appropriate for fourth-order operators generated by operators of the Stokes-Beltrami type given in $(13)_3$, Siginer and Knight [16]. In this paper we adopt the aspect and rotation ratios δ=0.25, 0.5, 1, 2 and λ=−2, −1, 0, 1, 2 and investigate the effect of the increasing elasticity of the liquid on the flow field at fixed cap rotation ratio together with the effect of the varying cap rotation ratio at fixed elasticity. Results are presented in Figs. 4–22. To save as much space as possible results for δ=0.25 which bear striking similarities to δ=0.5 are not included.

A comment concerning the torque on the covers is in order. The torque T depends on the first-order velocity to the second order in the analysis, and thus is determined entirely by the Newtonian stress field up to this order,

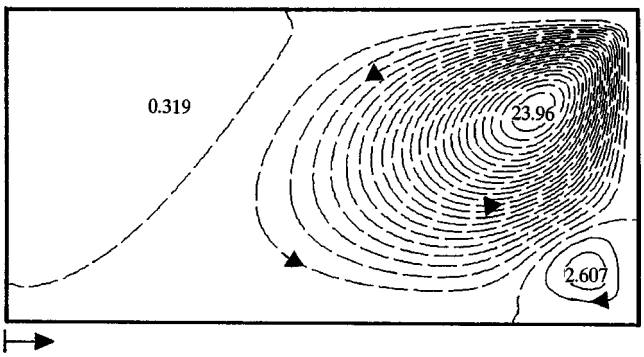

Fig. 22 Dimensionless meridional stream function contours. β=0.1, δ=0.5, λ=−2.

$$T = 2\pi\int_0^a r^2 S_{Z\theta}\,dr = \pi\mu\Omega a^3\int_0^1 \xi^2\nu_{,\eta}\,d\xi,$$

$$C_M = \frac{T}{\frac{1}{2}\rho\Omega^2 a^5} = \frac{2\pi}{\mathrm{Re}}\int_0^1 \xi^2\nu_{,\eta}\,d\xi, \quad \mathrm{Re} = \frac{\Omega a^2}{\nu}. \tag{16}$$

Equation (16) can be computed using (9). C_M and Re are the torque coefficient and the disk Reynolds number, respectively. We already commented in Sec. (2.1) that the convergence of (9) to the ramp function on the covers is quite good when Cesaro sums are used. Nevertheless the series converge to zero at both (1,0) and $(1,-\delta)$ and consequently in a small neighborhood of either rim fail to represent the ramp function. As a consequence, (16) underestimates the torque. A better approximation can be obtained if one assumes that the boundary layer thickness near the tip stays constant,

$$T = \pi\mu\Omega a^3\left(\int_0^{1-\varepsilon}\xi^2\nu_{,\eta}\,d\xi + \nu_{,\eta}\Big|_{\eta=1-\varepsilon}\frac{(1-\varepsilon)^3}{3}\right) \quad \varepsilon \ll 1.$$

In practice, there is always a small gap between the disks and the side wall and the singularity is avoided. That the torque increases very fast as this gap gets smaller has been shown by Schmieden [17]. The singularity is of the form $(1-\varepsilon)^{-1}$ and has almost no consequence in computing the flow field since its effect is confined to the immediate neighborhood of the rims. An excellent study of singularities of this type is given by Van Heijst [18].

3 Discussion

Close to the rotating covers of the cavity the primary surfaces of shear are concentric cylinders. Normal stresses acting in the radial direction are generated which compete with centrifugal forces. If there is a balance, stagnation rings may result on the covers.

For relatively high aspect ratios, say two for instance, the shear layer separating the top and bottom CW and CCW cells, respectively, joins a stagnation line on the side wall to a stagnation point on the axis of rotation both for strong counter and same sense rotation when the liquid is Newtonian (β=0=β^*), Fig. 4. When the fluid is only very slightly viscoelastic, strong enough normal stresses are developed in the neighborhood of the corner of the faster rotating disk and the side wall to overcome centrifugal forces there and make the particles stall in the Ekman and Stewartson layers on the cap and side wall, respectively, with the formation of two stagnation points and a CCW rotating cell around that corner, Fig. 5(*a*).

As the elasticity of the fluid is on the rise, the stagnation points A and B move towards the center on the cap and down the side wall, respectively, pushing C down and D up. At the same time increased elasticity generates strong enough normal stresses in the neighborhood of the corner of the slower rotating disk and the wall to result in the inception of a CW cell, around that corner, Fig. 5(*b*). With further increase in the value of β, stagnation point C is pushed further down by the faster growing primary non-Newtonian cell around the corner of the faster rotating top disk and the wall. But it cannot come close to the lower corner $(1,-\delta)$, because the weaker, non-Newtonian corner eddy there is also growing, although at a slower rate than the eddy around the upper corner (1,0).

Depending on the aspect ratio, when $\delta \geqslant 1$, for a critical value β_{cr} of the elastic parameter β between 0.02 and 0.03, there is a loss of stability and the stagnation point C suddenly moves onto the slower bottom cap, Fig. 5(*c*). The stagnation points H and F move into the flow field, join up and form a saddle point, Figs. 5(*d*), 8, and 15. The bifurcated field is made up of CCW upper right and lower left corner eddies together with CW upper left and lower right eddies separated by the saddle point (H,F), Figs. 5(*d*), 8, and 15. If the aspect ratio is below one, $\delta < 1$, this bifurcation

occurs for a critical value of $\beta=\beta_{cr}$ smaller than 0.02. For instance in Fig. 20 where $\delta=0.5$ and $\beta=0.02$ it has already occurred. Furthermore, stagnation point D which was on the bottom cap to start with in the Newtonian case, $\beta=0$, Fig. 19, stays on the bottom cap when C jumps from the side wall onto the slower bottom cap. They are joined by a shear layer starting and ending on the bottom cap, encapsulating a CCW eddy, Fig. 20. This is the Newtonian lower corner eddy of Fig. 19, now pushed towards the midspan of the bottom cap.

The saddle point (H,F) moves upwards, towards the faster disk with further increase in β, Fig. 5(*c*,*d*). The stagnation ring C is pushed further towards $(0,-\delta)$ squeezing the lower left eddy into smaller and smaller areas. But C can never make it to $(0,-\delta)$. When β reaches a second critical value $\beta=\hat{\beta}_{cr}$, stability is lost again and a second bifurcation occurs for $0.03<\hat{\beta}_{cr}<0.0375$, Fig. 9. The top right corner, normal stress effects dominated eddy, and the lower left centrifugal forces dominated eddy become part of a larger cell, separated by a new saddle point (B,D), Figs. 5(*e*) and 9. The stagnation points H and F, which formed the former saddle point (H,F), now may be conceived of as having moved onto the centerline and side wall, respectively, to form two CW rotating eddies, a centrifugal forces dominated eddy in the upper left and a normal stress effects dominated eddy in the lower right corners, Figs. 5(*e*), 9, and 16. For aspect ratios below one, $\delta<1$, this second bifurcation occurs for values of the elasticity parameter smaller than $\hat{\beta}_{cr}<0.03$, depending on the aspect ratio, with the additional change that there is a three-cell structure in the meridional plane and no saddle point, Fig. 21. The smaller the aspect ratio the smaller becomes the critical value of β at fixed cap rotation ratio.

Increasing further the elasticity of the liquid results in the migration of the saddle point (B,D) towards the slower rotating bottom disk, Fig. 5(*f*). At the same time the bottom right and the top left corner eddies grow and decrease in size, respectively. But this time, the stagnation point C does not show a sudden jump onto the centerline as it did when it moved from the side wall onto the bottom cap as shown in Fig. 5(*c*). Instead it moves continuously, first coinciding with $(0,-\delta)$ and then starting to climb toward the top (0,0) on the centerline. By the time it moves onto the centerline the lower left CCW cell, below the saddle point, is almost gone. As it keeps moving up, this cell completely disappears, the top left Newtonian cell becomes smaller and smaller, Fig. 5(*g*). Eventually, for values of $\beta>0.08$ the stagnation points A and H collapse onto(0,0) and the field is made up of two normal-stress effects dominated CCW and CW rotating cells on top and bottom, respectively, Figs. 5(*h*) and 10.

The above chain of events is somewhat different when $\delta\leqslant 1$. If $\delta=1$, increasing the elasticity again leads to the annihilation of the top left Newtonian cell and the disappearance of the saddle point (B,D), but now the stagnation point C although it moves towards $(0,-\delta)$ on the bottom somewhat, stays on the bottom cap, not even reaching midspan, even for quite high values of β, Fig. 17. When $\delta<1$, of the two stagnation points on the bottom cap in Fig. 21 right after the second bifurcation, the one on the right is almost stationary as β grows, and the one on the left, which defines the boundary of the only Newtonian cell among the three in Fig. 21, moves briskly, reaches $(0,-\delta)$ and is already on the centerline for the same value of $\beta=0.1$ as in Fig. 17 when $\delta=1$, Fig. 22.

Next we offer a qualitative analysis of the flow structure in the meridional plane and of the migration patterns of the stagnation points (rings) at a fixed value of the elasticity parameter β when the cap rotation ratio varies from strong counter rotation to strong same sense rotation. We observe that for any aspect ratio, when $|\lambda|\geqslant 2$ and growing at a fixed value of β, flow and stagnation point migration patterns similar to those depicted in Fig. 5, for fixed cap rotation ratio and varying elasticity parameter, are found to occur in the same order as shown in Fig. 5 when $\beta<\hat{\beta}_{cr}$ with two successive bifurcations when the cap rotation ratio reaches two critical values. The order of events is almost the same when $\beta>\hat{\beta}_{cr}$ with the exception that now there is only one bifurcating flow. Thus $\beta<\hat{\beta}_{cr}$ and $\beta>\hat{\beta}_{cr}$ define two definitely different classes of flow structure development and they are analyzed separately in Figs. 6 and 7, respectively.

For relatively tall cylinders, say $\delta=2$, there exists a four cell configuration in the meridional plane, when $-1>\lambda>-2$, Fig. 6(*a*), with the shear layer D-C below the mid plane but moving up with decreasing cap rotation ratio, $\lambda\rightarrow -1$, and coinciding with the mid-plane for $|\lambda|=1$. Depending on the value of β, the stagnation points on the side wall may or may not have relocated on the dividing shear layer when $|\lambda|=1$ is reached. For instance in Fig. 11 they are still on the side wall for $\beta=0.03$, but they have been on the shear layer already for quite a while in Fig. 12 for $\beta=0.0375$. For larger values of β they would be located on the centerline. In Fig. 6 we consider the case of the stagnation points B and H still on the side wall when $|\lambda|=1$, $\beta<\hat{\beta}_{cr}$ and in Fig. 7 we look at the case of the stagnation points B and H located on the centerline when $|\lambda|=1$, $\beta>\hat{\beta}_{cr}$.

As the rotation ratio $\lambda\rightarrow 0$, curiously enough, the stagnation point F on the slower bottom cap remains almost stationary in either case, Figs. 6(*c*) and 7(*b*), as the other stagnation points move and alter the flow structure. When $\beta<\hat{\beta}_{cr}$, stagnation points D and C move up and converge to the upper right corner (1,0) gradually squeezing out the CCW, normal stress dominated cell, around that corner. Ultimately A and B collapse onto the upper right corner (1,0) with D and C quite close to the corner (1,0), thereby forming a three cell structure in the meridional plane, Figs. 6(*d*) and 13, with a small CW cell in the upper right corner. On the other hand when $\beta>\hat{\beta}_{cr}$, although stagnation points D and C still converge to (1,0) as $\lambda\rightarrow 0$, A and B collapse onto (0,0) instead of (1,0) as was the case previously when $\beta<\hat{\beta}_{cr}$, squeezing out the Newtonian centrifugal force dominated left upper cell, Figs. 7(*b*,*c*) and 14, and thereby forming a CCW cell around the upper right corner.

As $\lambda\rightarrow 1$, the flow structure development shown in Figs. 6 and 7 for $\lambda\rightarrow 0$, $0>\lambda>-1$, is repeated in reverse order. As λ increases further, the shear layer D-C is pushed further and further down, Fig. 6(*f*). For a critical value of $\lambda=\lambda_{cr}$ a loss of stability and branching occur, the stagnation points H and F move into the flow to form a saddle point with upper right normal stress and lower left centrifugal force dominated cells, when $\beta<\hat{\beta}_{cr}$, Fig. 6(*g*). For instance, if β is close to $\hat{\beta}_{cr}$ from below, $\beta<\hat{\beta}_{cr}$, λ_{cr} is close to $\lambda=2$ from above, $\lambda_{cr}>2$. On the other hand when $\beta>\hat{\beta}_{cr}$ as $\lambda\rightarrow 1$, a flow structure similar to the one shown in Fig. 7(*b*) exists. As a result the shear layer D-C, as it moves down with increasing λ, squeezes the left bottom CCW eddy. When λ reaches a critical value $\hat{\lambda}_{cr}$ different from the previous λ_{cr} a branching occurs, the stagnation points F and H move into the flow field to form a saddle point, Fig. 7(*d*). For instance, if β is close to $\hat{\beta}_{cr}$ from above, $\beta>\hat{\beta}_{cr}$, $\hat{\lambda}_{cr}$ is close to $\lambda=2$ from below, $\hat{\lambda}_{cr}<2$. With further increases in λ the saddle point (H,F) moves towards the slower bottom cap in either case, $\beta\gtrless\hat{\beta}_{cr}$, and a smooth and continuous transition to a two cell structure occurs as shown in Figs. 6(*h*,*i*) and 7(*d-f*).

When aspect ratio δ is smaller than one, the same chain of events occurs with some variations. For instance when $|\lambda|=1$ the stagnation points H and B can never be located on the centerline, no matter how high the value of β is.

References

[1] Dorfman, L. A., and Romanenko, Yu. B., 1966, "Flow of a Viscous Fluid in a Cylindrical Vessel With a Rotating Cover," Izv. Akad. Nauk SSSR, Mekh. Zhidk. Gaza, **1**, pp. 63–69.

[2] Pao, H., 1970, "A Numerical Computation of the Confined Rotating Flow," ASME J. Appl. Mech., **37**, pp. 480–487.

[3] Pao, H., 1972, "Numerical Solution of the Navier-Stokes Equations for Flows in the Disk-Cylinder System," Phys. Fluids, **15**, pp. 4–11.

[4] Dijkstra, D., and Van Heijst, G. J. F., 1983, ''The Flow Between Finite Rotating Disks Enclosed by a Cylinder,'' J. Fluid Mech., **128**, pp. 123–154.
[5] Duck, P. W., 1986, ''On the Flow Between Two Rotating Shrouded Disks,'' Comput. Fluids, **14**, pp. 183–196.
[6] Kramer, J. M., and Johnson, M. W., 1972, ''Nearly Viscometric Flow in the Disk and Cylinder System. I: Theoretical,'' Trans. Soc. Rheol., **16**, pp. 197–212.
[7] Hill, C. T., 1972, ''Nearly Viscometric Flow of Viscoelastic Fluids in the Disk and Cylinder System II: Experimental,'' Trans. Soc. Rheol., **16**, pp. 213–245.
[8] Escudier, M. P., and Cullen, L. M., 1996, ''Flow of a Shear-Thinning Liquid in a Container With a Rotating End Well,'' Exp. Therm. Fluid Sci., **12**, pp. 381–387.
[9] Itoh, M., Moroi, T., and Toda, H., 1998, ''Viscoelastic Flow due to a Rotating Disc Enclosed in a Cylindrical Casing,'' Trans. Jpn. Soc. Mech. Eng., **64**, (621), pp. 1351–1358.
[10] Itoh, M., Suzuki, M., and Moroi, T., 2003, ''Swirling Flow of Viscoelastic Fluids in a Cylindrical Casing,'' *Proceedings of the 4th ASME-JSME Joint Fluids Engineering Conference*, Honolulu, HI, July 6–10, ASME, New York.
[11] Moroi, T., Itoh, M., and Fujita, K., 1999, ''Viscoelastic Flow due to a Rotating Disc in a Cylindrical Casing (Numerical Simulation and Experiment),'' Trans. Jpn. Soc. Mech. Eng., **65** (639), pp. 3361–3568 (in Japanese).
[12] Moroi, T., Itoh, M., Fujita, K., and Hamasaki, H., 2001, ''Viscoelastic Flow due to Rotating Disc Enclosed in a Cylindrical Casing (Influence of Aspect Ratio),'' JSME Int. J. Ser. B: Fluids Therm. Eng., **44** (3), pp. 465–475.
[13] Stokes, J. R., Graham, L. J. W., Lawson, N. J., and Boger, D. V., 2001, ''Swirling Flow of Viscoelastic Fluids, Part I: Interaction Between Inertia and Elasticity,'' J. of Fluid Mech., **429**, pp. 67–115.
[14] Stokes, J. R., Graham, L. J. W. Lawson, N. J., and Boger, D. V., 2001, ''Swirling Flow of Viscoelastic Fluids, Part II: Elastic Effects,'' J. Fluid Mech., **429**, pp. 117–153.
[15] Hort, W., 1920, ''Die Geschwindigkeitsverteilung im Inneren rotierender zäher Flüssigkeiten,'' Z. Tech. Phys. (Leipzig), **1**, pp. 213–221.
[16] Siginer, D. A., and Knight, R., 1993, ''Swirling Free Surface Flow in Cylindrical Containers,'' J. Eng. Math., **27**, pp. 245–264.
[17] Schmieden, C., 1928, ''Uber den Widerstand einer in einer Flussigkeit rotierenden Scheibe,'' Z. Angew. Math. Mech., **8**, pp. 460–466.
[18] Van Heijst, G. J. F., 1983, ''The Shear-Layer Structure in a Rotating Fluid Near a Differentially Rotating Sidewall,'' J. Fluid Mech., **130**, pp. 1–12.

Lateral Deflections of Webs in Air-Flotation Ovens

Peter M. Moretti
School of Mechanical and Aerospace Engineering,
Oklahoma State University,
Stillwater, OK 74078-5016
e-mail: moretti@ceat.okstate.edu

A long web span supported by many, regularly spaced, alternating air-bars is studied. The focus is on the lateral forces on the web due to the interaction of lateral curvature with out-of-plane deflections. The effect of stretching of the elastic web material is included, and the effect of high web speed is handled by distinguishing between the tension in the material T_{mat} and the apparent tension $T_{app}=T_{mat}-\mu v^2$. The governing partial differential equations for a continuous representation of the web's lateral deflection, stability, and control is developed for both straight and cambered webs. The dimensionless parameters for web-tension effect, web-camber effect, and stretching effect are identified. The influence of tilted air-bars is studied, towards developing a control mechanism to compensate for camber. [DOI: 10.1115/1.1756922]

Introduction

In the operation of flotation ovens, lateral deflections have been observed. This is an important problem, because there is a need for longer air-support ovens to accomplish drying of water-based coatings, yet the length of the ovens is limited by our ability to control lateral excursions of the web. For the purpose of analytical study of an oven containing many similar elements (i.e., regular undulations between bottom air-bars alternating with top air-bars), the entire length of the web within the oven may be represented as a single continuum element with continuous-beam properties. These averaged properties depend on the engagement geometry of the alternating air-bars, the air-cushion characteristics of each bar, the web tension, and the web elasticity. (See Fig. 1.)

Background

The systematic treatment of the lateral deflections of webs in paper machines, printing presses, and plastic-film manufacturing and coating, is approached by treating the web as a very deep, very narrow rectangular beam under tension, [1]. If the bending moment exceeds a critical value, putting one edge of the web under compression which the web cannot sustain without buckling, nonlinear effects are introduced, [2], and the web loses some lateral stiffness; in web-line operation, there is incentive for maintaining tension and avoiding a slack edge.

When there is good traction at the rollers, the end conditions of the web-as-a-beam are fixed lateral position and slope at the upstream end, and right-angle entry onto the roller at the downstream end, [1]; this latter condition is frequently employed for lateral guiding of webs, [3,4]. The remaining steady-state end condition, for the case of full-width traction, is zero lateral curvature while entering the cylindrical exit roller, since both edges must feed through at the same rate. However, tests indicate that, even when traction is sufficient to assure right-angle entry into a roller, there may be partial slip, allowing the fourth end condition to approach zero-moment instead, [5]. This has implications for cambered (laterally curving) webs and also for moment transfer across rollers, between spans, [6].

In flotation ovens, the air-supported web undulates up and down over alternating air-bars; as a result, the extensional stiffness of the web is reduced, [7]. Where there are many repeated support elements, we will treat the web as a periodic structure, obtaining equivalent continuous-beam properties. The contribution of each element to these properties will be obtained from the geometrical relationships between out-of-plane deflections and lateral curvature, [8].

The resulting analysis must explain the observations made in tests on lateral deflection in air-support conveyance by Ron Swanson [5], and further tests on extensional resilience of an air-floated web by Ron Swanson, Young-Bae Chang, and Peter Moretti [7]:

- lateral forces required to deflect the web are small.
- webs in air-suspension ovens tend to diverge to one side or the other.
- web camber aggravates the lateral divergence.
- correction/control by tilting air-flotation bars yields small improvement.

Mid span Behavior

As we pointed out in an exploratory paper, [8], there are several different factors at play in the lateral deflection of a web in an air-flotation oven:

- A web on air-support bars is supported by the air cushions in a ''springy'' fashion, permitting deflections in the out-of-plane (usually vertical) direction. Because of the accordion-like undulations of the web, these potential deflections cause it to be less stiff with respect to longitudinal (MD) extension as well, which in turn yields less beam stiffness in the lateral direction (CMD), so that small lateral forces can result in significant deflection to one side or the other. Lateral stiffness can be improved by using low-flying-height airfoil bars giving ''stiff'' support, or by using high tension, or by using shallow undulations.
- When a perturbation causes the mid-span of the web to deflect to one side, and that side of the web curves outward, the inside of the curve floats higher off the air supports, and the outside cinches down tighter on the supports, so that the web tilts over each pad. As a result the normal (lift) vector of the pressure force over each pad acquires a lateral force component towards the outside of the curve, tending to increase the lateral curvature further—a destabilizing effect inherent in this geometry. (A secondary effect is a small cross-flow drag force in the opposite direction.)
- Web camber is one of the perturbations which initiates web divergence. Furthermore, when a web has camber, the longer edge of the web will tend to float higher off the air supports, so that the normal vector of the pressure force will tend to push the web towards the side with the shorter edge.

Contributed by the Applied Mechanics Division of THE AMERICAN SOCIETY OF MECHANICAL ENGINEERS for publication in the ASME JOURNAL OF APPLIED MECHANICS. Manuscript received by the Applied Mechanics Division, March 12, 2001; final revision, November 3, 2003. Associate Editor: W. S. Saric. Discussion on the paper should be addressed to the Editor, Prof. Robert M. McMeeking, Journal of Applied Mechanics, Department of Mechanical and Environmental Engineering, University of California–Santa Barbara, Santa Barbara, CA 93106-5070, and will be accepted until four months after final publication in the paper itself in the ASME JOURNAL OF APPLIED MECHANICS.

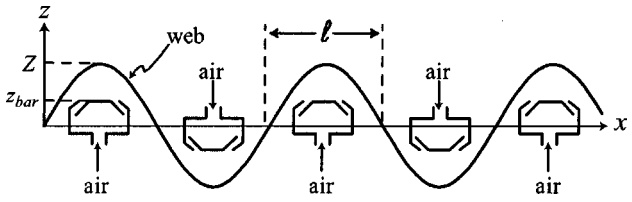

Fig. 1 Nomenclature; the sine wave is drawn with exaggerated amplitude—actual amplitudes are small, and z_{bar} may be negative

- Since the tilt of the web, not of the air-bar, determines the lateral component of the lift vector, tilting air-bars has only a modest effect on lateral dynamics—but it does introduce a secondary effect of biased lateral pressure distribution, with consequences for both the tension profile and the lateral drag forces.

In subsequent sections we will quantify these effects.

Extensional Stiffness

Sinusoidal Geometry. We will approximate the web path (Fig. 1) by the first term of a Fourier series representation

$$z_{(x)} = Z_1 \sin\frac{\pi x}{\ell} - Z_3 \sin\frac{3\pi x}{\ell} + \ldots \cong Z \sin\frac{\pi x}{\ell} \tag{1}$$

where ℓ is the spacing between (alternating) air-bars and Z is the half-amplitude of the undulation. The equilibrium relationship between apparent tension-per-unit-width $T_{\text{app}} \triangleq (T_{\text{mat}} - \mu v^2)$ and the gage pressure p acting on the flexible web, as shown in Fig. 2, is

$$p_{(x)} = -T_{app} \cdot \frac{\partial^2 z}{\partial x^2} = T_{app} \cdot Z\left(\frac{\pi}{\ell}\right)^2 \sin\frac{\pi x}{\ell} = P \sin\frac{\pi x}{\ell} \tag{2}$$

where

$$P = T_{app} \cdot Z\left(\frac{\pi}{\ell}\right)^2$$

for an average pressure of $2P/\pi$, and a total lift of $2Pb\ell/\pi = 2bT_{app}Z\pi/\ell$, over each half-sine-wave opposing an air-bar. The constant difference μv^2 between the *apparent* tension T_{app} measured from roller reaction forces, and the *material* tension T_{mat} observed in the stretching of the web material, is small in most plastic-coating applications; but we will maintain the distinction in order to make our equations applicable to high-speed webs as well.

This gives us one relationship between air-pad pressure, deflection-amplitude, and tension; we need a second relationship to get useful stiffness results.

Pad Pressure Versus Flying Height. In a long series of experiments carried out in the Web Handling Research Center at Oklahoma State University by Pinnamaraju [9], Perdue [10], and Nisankararao [11], the pressure field between an air-bar and a flat plate was measured, and integrated to obtain the total lift generated by an air-bar. The lift was shown to be a function of the spacing between air-bar and plate (flying height). The shape of the plotted function, shown in an earlier paper, [8], depends on the design of the air bar. A theoretical analysis based on ground-effect hovercraft theory was developed by Y. B. Chang et al. [12–14] for symmetrical ''pressure-pad'' bars, matching the experimental results. Some asymmetrical designs, notably ''airfoil'' or ''Coanda'' bars, give ''stiffer'' support to the plate, showing more rapid increase of lift with decrease in flying height.

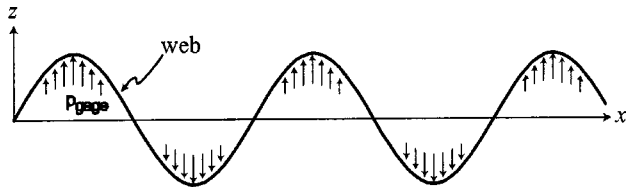

Fig. 2 Relationship between web curvature y'' and pressure distribution p, both shown as functions of x

Although our flexing web differs somewhat from the flat plate, and the simple pressure distribution assumed for this analysis is also different, we can at least conclude that the nominal pad-pressure P is a somewhat similar function of the flying height. The *nominal* flying height is $(Z - z_{\text{bar}})$, where Z is the sinusoidal amplitude of the web, and z_{bar} is the distance by which each air-bar intrudes past a straight line through the oven—a positive number if the alternating air-bars overlap, negative if they do not cross the central plane. We can generically represent this functional relationship as

$$P = \mathcal{F}(Z, z_{\text{bar}}) \cong \mathcal{F}(Z - z_{\text{bar}}) \tag{3}$$

For small deflections, it may be convenient to linearize this relationship near the design point with an air-cushion ''spring-constant'' $\kappa \triangleq -dP/dZ$, so that the pressure is

$$\mathcal{F} \approx P_{\text{design}} - \kappa(Z - Z_{\text{design}})$$

$$\frac{d\mathcal{F}}{dZ} \approx -\kappa \tag{4}$$

where κ is typically positive for stable air-bars (i.e., the pressure drops when the flying height increases). Alternatively, for larger deflections, it may be better to fit a hyperbola to the function, leading to the expression

$$\mathcal{F} \cong P_{\text{design}} \times \frac{(Z_{\text{design}} - z_{\text{bar}})}{(Z - z_{\text{bar}})}$$

$$\frac{d\mathcal{F}}{dZ} = -P_{\text{design}} \times \frac{(Z_{\text{design}} - z_{\text{bar}})}{(Z - z_{\text{bar}})^2}. \tag{5}$$

If the relationship between pressure and flying height has not been measured for a particular air-bar, it may be calculated on the basis of hovercraft theory. The applicable ground-effect analyses, [12,13], generally lead to a basic form

$$\mathcal{F} = P_o(1 - e^{-\text{constant}/Z - z_{\text{bar}}}) \tag{6}$$

plus some added complexity relating to the difference between the nominal flying height and the actual distance from the edge of the slot to the corresponding location on the web.

Any of these representations of $\mathcal{F}(Z - z_{\text{bar}})$ can be inserted into Eq. (2), solved for tension

$$T_{\text{app}} = \left(\frac{\ell}{\pi}\right)^2 \frac{\mathcal{F}}{Z} \tag{7}$$

and differentiated to obtain

$$\frac{dT}{dZ} = \frac{-1}{Z}\left[T_{\text{app}} - \left(\frac{\ell}{\pi}\right)^2 \frac{d\mathcal{F}}{dZ}\right]. \tag{8}$$

This gives us a second relationship between tension, deflection-amplitude, and the pressure function.

Extensibility. The path length s of the web for each machine-length ℓ (and the overall web path length S for the overall machine length L) is

$$s = \int_0^{\ell} \sqrt{1 + a^2 \cos^2\frac{\pi x}{\ell}}\, dx \tag{9}$$

where $a \triangleq \pi Z/\ell$. For $a < 1$, we can use the series solution

$$\frac{S}{L}=\frac{s}{\ell}=1+\frac{1}{4}a^2-\frac{3}{64}a^4+\frac{5}{256}a^6-\ldots \tag{10}$$

which shows that, when $a^2 \ll 1$,

$$\frac{s}{\ell}\cong 1+\frac{1}{4}a^2=1+\frac{\pi^2 Z^2}{4\ell^2}$$

$$ds\cong\frac{\pi^2 Z}{2\ell}dZ$$

$$dS\cong\frac{\pi^2 Z}{2L}dZ \tag{11}$$

Inverting the $T-Z$ Eq. (8) above,

$$\frac{dZ}{dT}=\frac{-Z}{T_{\text{app}}-\left(\frac{\ell}{\pi}\right)^2\frac{d\mathcal{F}}{dZ}} \tag{12}$$

we combine it with Eq. (11) to eliminate dZ in the equation for dS, and obtain

$$k_{\text{air}}\triangleq\frac{-dT}{dS}\cong\frac{2L}{\pi^2 Z^2}\left[T_{\text{app}}-\left(\frac{\ell}{\pi}\right)^2\frac{d\mathcal{F}}{dZ}\right]. \tag{13}$$

Since a *lengthened* path dS shows up as an apparent *shortening* of the web as seen from the ends of the oven, dT/dS is the *negative* of k_{air}, the extensional spring constant per-unit-width of the web in extension, due to the air-cushioning.

In general, observations, [7], confirm that extensional stiffness increases if tension is increased; in one test, when the weight attached to the end of a stationary web in an air-support oven was doubled and tripled, the natural frequency of extensional oscillations changed only slightly, indicating that the spring constant approximately doubled and tripled as well.

The extensional spring constant k_{air} obtained in Eq. (13) accounts only for air-cushioned out-of-plane deflection; the deflection due to the material's elastic stretching

$$k_{\text{mat}}=\frac{E_{\text{mat}}A}{Lb} \tag{14}$$

must be added to that, so that the total effective spring constant is

$$\frac{1}{k_{\text{eff}}}=\frac{1}{k_{\text{air}}}+\frac{1}{k_{\text{mat}}}. \tag{15}$$

In the vicinity of any particular operation point, the total extension due to an additional increment of tension is composed of both an air-cushion-geometry component and an elastic-stretching component. The fraction of the additional extension due to the *web material's* elastic stretching, ξ, is

$$\text{stretch-ratio:}\quad \xi\triangleq\frac{1/k_{\text{mat}}}{1/k_{\text{eff}}}=\frac{k_{\text{air}}}{k_{\text{mat}}+k_{\text{air}}} \tag{16}$$

and its complement $(1-\xi)$ is the fraction due to the air-cushion effects:

$$(1-\xi)=\frac{1/k_{\text{air}}}{1/k_{\text{eff}}}=\frac{k_{\text{mat}}}{k_{\text{mat}}+k_{\text{air}}}. \tag{17}$$

If the air-bar characteristics are not available, these extensional spring constants can be obtained experimentally. The k_{mat} can be measured by pulling on the end of the stationary web when the air is turned off, and observing the displacement. The k_{eff} can be obtained the same way, but while the air is on, and ξ determined from Eq. (16). Then k_{air} can be computed by solving for it in the Eq. (15) and the effective air-cushion constant $\kappa\triangleq -d\mathcal{F}/dZ$ of the air-support bars backed out from Eq. (13).

Lateral Effects

Lateral Bending Stiffness. J. J. Shelton [1] treated a web as a flat beam, resisting lateral curvature with a lateral bending moment $EI\cdot y''$. The effective value of Young's modulus for a web of width b and cross-sectional area A is obtained from

$$E_{\text{eff}}A=Lbk_{\text{eff}} \tag{18}$$

and

$$I=A\cdot b^2/12 \tag{19}$$

so that

$$E_{\text{eff}}I=\frac{Lb^3}{12}k_{\text{eff}} \tag{20}$$

where k_{eff} may be obtained from Eqs. (13), (14), and (15), or directly from an extensional test with the air supply turned on.

Thus we can obtain the effective bending stiffness from operating parameters and material properties.

Lateral Moments. The complementary way of viewing the lateral bending stiffness is to consider lateral curvature. Like extension, bending has both an elastic material and an air cushion component: The total lateral curvature is the sum of two components, the apparent curvature (as seen from a top view) due to the geometric coupling of out-of-plane deflections with the projected path, y''_{air}, plus the curvature due to differential stretching of the web material by the lateral bending moment, y''_{mat}:

$$y''_{\text{total}}=y''_{\text{mat}}+y''_{\text{air}}$$

$$y''_{\text{mat}}=\xi\cdot y''_{\text{total}}=\frac{12\times\text{Moment}}{Lb^3k_{\text{mat}}}$$

$$y''_{\text{air}}=(1-\xi)\cdot y''_{\text{total}}=\frac{12\times\text{Moment}}{Lb^3k_{\text{air}}}$$

$$y''_{\text{total}}=\frac{12\times\text{Moment}}{Lb^3k_{\text{eff}}} \tag{21}$$

The apparent lateral bending component y''_{air}, averaged over multiple elements of air support, requires the path of one edge of the web to become longer relative to the other edge, by an amount $b\ell\cdot y''_{\text{air}}$, where b is the width of the web and ℓ is the length under consideration. A change in length implies a change in the out-of-plane amplitude Z, as derived in Eq. (11) above:

$$\frac{ds}{dy}\cong\frac{\pi^2 Z}{2\ell}\cdot\frac{dZ}{dy}$$

$$\frac{dZ}{dy}\cong\frac{2\ell}{\pi^2 Z}\cdot\frac{ds}{dy}\cong\frac{2\ell^2}{\pi^2 Z}\cdot y''_{\text{air}} \tag{22}$$

showing the tilting of the maximum amplitude Z resulting from the apparent lateral bending y''_{air}. Combining this with the $T-Z$ relationship of Eq. (8), we find that the tension profile's dT/dy is a function of the nominal tilt dZ/dy.

$$y''_{\text{air}}=\frac{-\pi^2 Z^2}{2\ell^2\left[T_{\text{app}}-\left(\frac{\ell}{\pi}\right)^2\frac{d\mathcal{F}}{dZ}\right]}\cdot\frac{dT}{dy}$$

$$\text{Moment}=\frac{b^3}{12}\cdot\frac{dT}{dy}=\left[\frac{b^3}{6}\left(\frac{\ell}{\pi Z}\right)^2\left[T_{\text{app}}-\left(\frac{\ell}{\pi}\right)^2\frac{d\mathcal{F}}{dZ}\right]\right]\cdot y''_{\text{air}} \tag{23}$$

so that the lateral bending moment is governed by the tilt over the air-bars.

Lateral Forces. The lateral curvature component y''_{air} due to the geometric effects of the web undulating over and under air-support bars has been described in an earlier paper, [8], and results in Eq. (22) which shows the relationship between y''_{air} and tilting of the maximum amplitude Z. Along the length of the web, the tilt of z is

$$\frac{\partial z}{\partial y}=\frac{dZ}{dy}\sin\left(\frac{\pi x}{\ell}\right)=\frac{2\ell^2}{\pi^2 Z}\sin\left(\frac{\pi x}{\ell}\right)\cdot y''_{\text{air}}. \tag{24}$$

Combining this with the pressure obtained in Eq. (2), the lateral component of the pressure force on the sinusoidal web is, on the average,

$$\left|\frac{F_y}{\ell}\right|=\frac{b}{\ell}\int_0^\ell p\cdot\frac{\partial z}{\partial y}\cdot dx=\frac{b}{\ell}\int_0^\ell P\sin\frac{\pi x}{\ell}\cdot\frac{2\ell^2}{\pi^2 Z}\sin\left(\frac{\pi x}{\ell}\right)\cdot y''_{\text{air}}\cdot dx$$
$$=bT_{app}\cdot y''_{air}. \tag{25}$$

This establishes that the air supports produce a lateral force, proportional to that portion of the total lateral curvature y'' which is due to geometric effects: $y''_{\text{air}}=(1-\xi)y''_{\text{total}}$.

Continuum P.D.E.

Straight Webs. Introducing this lateral force $F_y=-bT\cdot y''$ into the partial differential equation for purely lateral motion we obtain for the total deflection y

$$\mu\ddot{y}+2\mu v\dot{y}'-bT_{\text{app}}\cdot y''+E_{\text{eff}}Iy''''$$
$$=-bT_{\text{app}}\cdot y''_{\text{air}}$$
$$=-bT_{\text{app}}\cdot(1-\xi)y''$$
$$\mu\ddot{y}+2\mu v\dot{y}'-bT_{\text{app}}\cdot\xi\cdot y''+E_{\text{eff}}Iy''''=0 \tag{26}$$

observing that the lateral force from tilting tends to cancel the straightening effect of tension, leaving only the fraction ξ of the hoped-for benefit. Note that this cancellation is independent of the form of the function $\mathcal{F}$, whether it is linear, or hyperbolic, or based on the ground-effect model.

For the equilibrium solution we can leave out the first two terms, which contain time derivatives, and rearrange the remaining terms to obtain the equilibrium equation

$$E_{\text{eff}}Iy''''-\xi bT_{\text{app}}y''=0 \tag{27}$$

where $E_{\text{eff}}I$ is the much-reduced value obtained in Eq. (20) above, $T_{\text{app}}\triangleq(T_{\text{mat}}-\mu v^2)$, and ξ is the fraction of the web flexibility due to material elasticity. The apparent lateral stiffness is small if ξ is small; ξ will have a larger value if the web flexibility due to the air cushioning can be kept small by means of small amplitudes Z and high stiffness $d\mathcal{F}/dZ$. However, the equation is basically stable if T_{app} is positive (it goes unstable for negative values exceeding Euler's buckling load).

If we normalize the dimensions x and y by dividing them by the span-length L, the dimensionless form of the equilibrium equation yields the independent parameter

$$\text{stretch-parameter:}\quad \Pi_\xi\triangleq\xi bT_{\text{app}}L^2/E_{\text{eff}}I \tag{28}$$

to govern the solutions.

Cambered Webs. When the web is cambered with an inherent lateral curvature Y''_o, two terms in our equations are modified: the beam stiffness term becomes zero when the web follows its natural camber, and the lateral force is zero when the web is level:

$$\mu\ddot{y}+2\mu v_{\text{web}}\dot{y}'-bT_{\text{app}}y''+\frac{\partial^2}{\partial x^2}E_{\text{eff}}I(y''-Y''_o)$$
$$=bT_{\text{app}}\cdot(Y''_o-y''_{\text{air}})$$
$$=bT_{\text{app}}Y''_o-bT_{\text{app}}(1-\xi)y''$$
$$\ddot{y}+2\mu v_{\text{web}}\dot{y}'-bT_{\text{app}}\cdot\xi\cdot y''+\frac{\partial^2}{\partial x^2}E_{\text{eff}}I(y''-Y''_o)=bT_{\text{app}}\cdot Y''_o \tag{29}$$

If the camber is constant along the length of the web, this simplifies to

$$\mu\ddot{y}+2\mu v_{\text{web}}\dot{y}'-bT_{\text{app}}\cdot\xi\cdot y''+E_{\text{eff}}Iy''''=bT_{\text{app}}Y''_o \tag{30}$$

so that our governing equation has acquired a constant lateral force-per-unit-length $f_y=bTY''_o$, acting towards the concave side of the web camber. The equilibrium equation is

$$E_{\text{eff}}Iy''''-bT_{\text{app}}\cdot\xi\cdot y''=bT_{\text{app}}Y''_o. \tag{31}$$

Because of the reduced effective beam stiffness $E_{\text{eff}}I$ and the considerable length of most air-flotation ovens, the effect of any lateral load f_y is considerable.

If we normalize the dimensions x and y by dividing them by the span-length L, the dimensionless form of the equilibrium equation yields the additional independent parameter

$$\text{camber-parameter:}\quad \Pi_f\triangleq bT_{\text{app}}Y''_oL^3/E_{\text{eff}}I. \tag{32}$$

Boundary Conditions. At the entry to the span, the displacement $y_{(x=0)}$ and the slope $y'_{(x=0)}$ are given; we establish the origin and alignment of the coordinates to make both of them zero:

$$y_{(x=0)}=0$$
$$y'_{(x=0)}=0. \tag{33}$$

In practice, the exit roller will be guided to maintain the exit displacement at

$$y_{(x=L)}=0 \tag{34}$$

by slanting the roller within the plane of the web, so that there will be an exit angle $y'_{(x=L)}=\theta_{ex}$. The fourth boundary condition is more difficult, especially in the presence of web camber, as discussed by Ron Swanson [5].

If roller traction is good and moments are moderate, equilibrium also requires that there must be a sufficient moment at the exit to insure that the both sides of the web have the same length as they feed through the roller, so that we have Swanson's moderate-span *full-width-traction* boundary condition

$$y''_{(x=L)}=0. \tag{35}$$

This condition would break down in the presence of large moments at the exit if the tension were not sufficient to maintain traction across the entire width of the roller, and we would end up with Swanson's long-span *partial-slip* boundary condition $y''_{(x=L)}\approx Y''_o$, indicating that the unequal-length edges would manage to slip through.

Equilibrium Solution. In terms of the parameters from Eqs. (28) and (32), our governing Eq. (31) is

$$y''''-\frac{\Pi_\xi}{L^2}y''=\frac{\Pi_f}{L^3}. \tag{36}$$

If we apply Swanson's *full-width-traction* exit boundary condition $y''_{(x=L)}=0$, so that both sides of the web feed through the roller evenly, the solution is

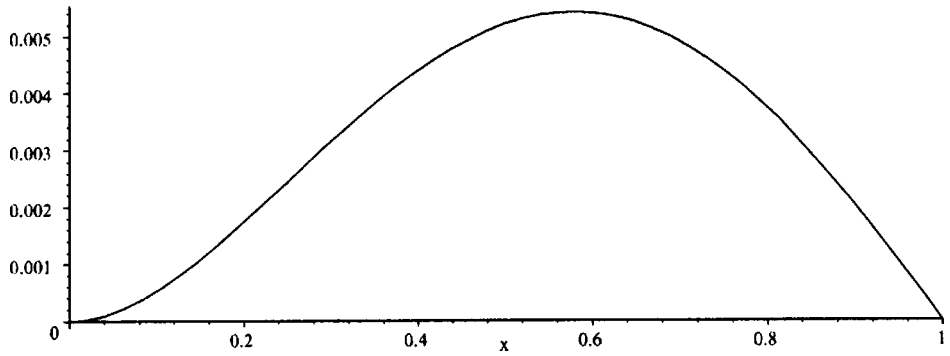

Fig. 3 Deflection shape, y/L versus x/L, from Eq. (39), the low-elasticity equilibrium solution for a cambered web, for *full-width-traction* at the exit, with unit camber parameter (Eq. (32))

$$\frac{y}{L}=C_o+C_1\left(\frac{x}{L}\right)+A\sin\left(\sqrt{\Pi_\xi}\frac{x}{L}\right)+B\cos\left(\sqrt{\Pi_\xi}\frac{x}{L}\right)+\frac{\Pi_f}{2\Pi_\xi}\left(\frac{x}{L}\right)^2 \tag{37}$$

where the coefficients (derived by *Maple* computer algebra incorporated in *Scientific WorkPlace* from http://www.mackichan.com/) are

$$C_o=\frac{\frac{\Pi_f}{2\Pi_\xi}\sin\sqrt{\Pi_\xi}-\frac{\Pi_f}{\Pi_\xi}(\sqrt{\Pi_\xi}-\sin\sqrt{\Pi_\xi})}{\sqrt{\Pi_\xi}\cos\sqrt{\Pi_\xi}-\sin\sqrt{\Pi_\xi}}$$

$$C_1=\frac{\frac{-\Pi_f}{2\sqrt{\Pi_\xi}}\cos\sqrt{\Pi_\xi}-\frac{\Pi_f}{\Pi_\xi\sqrt{\Pi_\xi}}(\cos\sqrt{\Pi_\xi}-1)}{\sqrt{\Pi_\xi}\cos\sqrt{\Pi_\xi}-\sin\sqrt{\Pi_\xi}}$$

$$A=\frac{\frac{\Pi_f}{2\Pi_\xi}\cos\sqrt{\Pi_\xi}-\frac{\Pi_f}{\Pi_\xi}(1-\cos\sqrt{\Pi_\xi})}{\sqrt{\Pi_\xi}\cos\sqrt{\Pi_\xi}-\sin\sqrt{\Pi_\xi}}$$

$$B=\frac{\frac{-\Pi_f}{2\Pi_\xi}\sin\sqrt{\Pi_\xi}-\frac{\Pi_f}{\Pi_\xi}(\sin\sqrt{\Pi_\xi}-\sqrt{\Pi_\xi})}{\sqrt{\Pi_\xi}\cos\sqrt{\Pi_\xi}-\sin\sqrt{\Pi_\xi}}.$$

On the other hand, if we apply Swanson's *partial-slip* exit boundary conditions $y''_{(x=L)}\approx Y''_o$, so that the moment at the exit roller is negligible, the solution coefficients change to

$$C_o=\frac{\frac{\Pi_f}{2\Pi_\xi}\sin\sqrt{\Pi_\xi}+\left(Y''_oL-\frac{\Pi_f}{\Pi_\xi}\right)\left(\frac{\sqrt{\Pi_\xi}-\sin\sqrt{\Pi_\xi}}{\sqrt{\Pi_\xi}}\right)}{\sqrt{\Pi_\xi}\cos\sqrt{\Pi_\xi}-\sin\sqrt{\Pi_\xi}L}$$

$$C_1=\frac{\frac{-\Pi_f}{2\sqrt{\Pi_\xi}}\cos\sqrt{\Pi_\xi}+\left(Y''_oL-\frac{\Pi_f}{\Pi_\xi}\right)\left(\frac{\cos\sqrt{\Pi_\xi}-1}{\sqrt{\Pi_\xi}}\right)}{\sqrt{\Pi_\xi}\cos\sqrt{\Pi_\xi}-\sin\sqrt{\Pi_\xi}L}$$

$$A=\frac{\frac{\Pi_f}{2\Pi_\xi}\cos\sqrt{\Pi_\xi}+\left(Y''_oL-\frac{\Pi_f}{\Pi_\xi}\right)\left(\frac{1-\cos\sqrt{\Pi_\xi}}{\Pi_\xi}\right)}{\sqrt{\Pi_\xi}\cos\sqrt{\Pi_\xi}-\sin\sqrt{\Pi_\xi}L}$$

$$B=\frac{\frac{-\Pi_f}{2\Pi_\xi}\sin\sqrt{\Pi_\xi}+\left(Y''_oL-\frac{\Pi_f}{\Pi_\xi}\right)\left(\frac{\sin\sqrt{\Pi_\xi}-\sqrt{\Pi_\xi}}{\Pi_\xi}\right)}{\sqrt{\Pi_\xi}\cos\sqrt{\Pi_\xi}-\sin\sqrt{\Pi_\xi}L}.$$

While these are closed-form solutions, they are difficult to visualize; neglecting material stretching leads to conservative solutions which are much simpler.

Low-Elasticity Equilibrium Solution. If the elastic-stretching parameter Π_ξ is very small, the governing Eq. (36) can be reduced to

$$y''''\cong\frac{\Pi_f}{L^3}. \tag{38}$$

If we apply Swanson's *full-width-traction* exit boundary condition $y''_{(x=L)}=0$, so that both sides of the web feed through the roller evenly, the solution is

$$\frac{y}{L}=\Pi_f\left[\frac{1}{16}\left(\frac{x}{L}\right)^2-\frac{5}{48}\left(\frac{x}{L}\right)^3+\frac{1}{24}\left(\frac{x}{L}\right)^4\right] \tag{39}$$

with an exit guiding angle

$$\theta_{ex}=y'_{(x=L)}=\frac{-\Pi_f}{48} \tag{40}$$

and the lateral deflection profile shown in Fig. 3. The maximum excursion of $y_{\max}/L=0.00542\Pi_f$ occurs at $x/L=58\%$.

On the other hand, if we apply Swanson's *partial-slip* exit boundary condition $y''_{(x=L)}\approx Y''_o$, so that the moment at the exit roller is negligible, the solution is

$$\frac{y}{L}=\Pi_f\left[\frac{1}{16}\left(\frac{x}{L}\right)^2-\frac{5}{48}\left(\frac{x}{L}\right)^3+\frac{1}{24}\left(\frac{x}{L}\right)^4\right]+Y''_oL\left[-\frac{1}{4}\left(\frac{x}{L}\right)^2+\frac{1}{4}\left(\frac{x}{L}\right)^3\right] \tag{41}$$

which gives us an exit guiding angle

$$\theta_{ex}=y'_{(x=L)}=\frac{1}{4}Y''_oL-\frac{1}{48}\Pi_f. \tag{42}$$

Evidently, the tension/stiffness ratio

$$\text{tension/beam-parameter:}\quad \Pi_{t/b}\triangleq\Pi_f/Y''_oL=bT_{\text{app}}L^2/E_{\text{eff}}I \tag{43}$$

determines the relative effect that any partial slip can have on the nature of the solution. When the value is $\Pi_{t/b}=8$, the deflection profile acquires an S-shape, the maximum amplitude is reduced, and the exit angle reversed, as shown by the dotted line in Fig. 4, indicating that a *partial-slip* condition at the exit can be beneficial. However, for smaller values of $\Pi_{t/b}$, *partial-slip* can reduce lat-

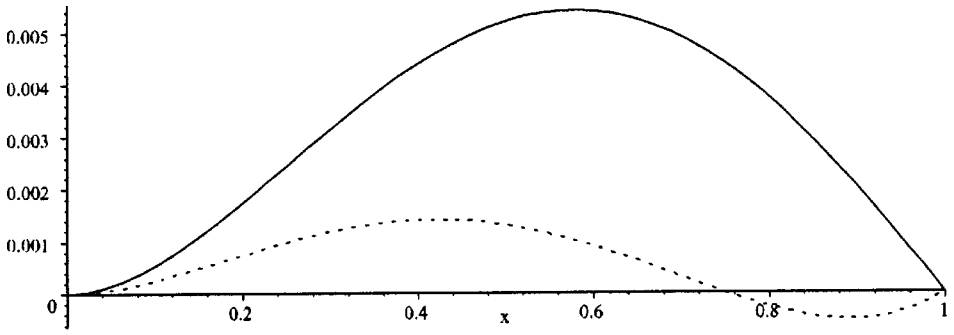

Fig. 4 Deflection shape from Eq. (41), the low-elasticity equilibrium solution for a cambered web, for *partial-slip* at the exit roller *(dotted line)* for a *high* value of 8 for the tension/beam-parameter (Eq. (43)), compared with full-width-traction at the exit (solid line)

eral control: the dotted line in the Fig. 5 shows the lateral excursions with partial slippage when $\Pi_{t/b}=3.7$; it shows that *partial-slip* can be detrimental when $\Pi_{t/b}<3.7$

Lateral Control

One of the suggestions for control of the curvature within an air-flotation oven is to tilt every other air-bar—either the top set of bars, or else the bottom set of bars, or else both sets in opposite directions—in order to introduce a compensating curvature. However, we have noted that the lateral force due to the primary effect of normal pressure forces on the web depends only on the tilt of the web relative to our global co-ordinate system, not the tilt of the bars. On the other hand, we see that the web material's tension profile depends on the flying height $(Z-z_{\text{bar}})$. Therefore, if there is a significant contribution of web elasticity to the curvature, we can achieve some control by tilting air-bars.

Let us look at the case where all the top air-bars are tilted by an angle $\pm\alpha$ radians, and all the bottom air-bars are tilted by the same amount in the *opposite* direction, for a relative angle of $\pm 2\alpha$. (The same result can be achieved by tilting only the top or only the bottom air-bars by 2α.) The lateral forces on the web are unaffected, because they depend only on the tilt of the web itself; but the tension profile of the web depends on the relative tilt of web and air-bar, and therefore the moments in the web change. Revising Eq. (23) accordingly,

$$\text{Moment}=\frac{b^3}{12}\left[\frac{2\ell^2}{\pi^2 Z}\cdot y''_{\text{air}}\pm\alpha\right]\left[\frac{T_{\text{app}}-\left(\frac{\ell}{\pi}\right)^2\frac{d\mathcal{F}}{dZ}}{Z}\right] \tag{44}$$

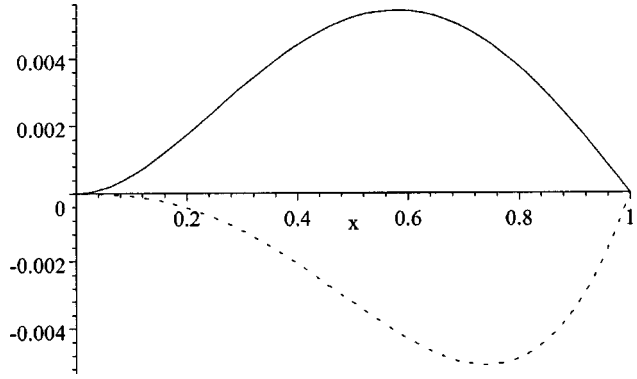

Fig. 5 Deflection shape from Eq. (41), the low-elasticity equilibrium solution for a cambered web, for *partial-slip* at the exit roller *(dotted line)* for a *low* value of 3.7 for the tension/beam-parameter (Eq. (43)), compared with full-width-traction at the exit (solid line)

we see that the effect of air-bar tilt is similar to the effect of the camber on moments. A tilt α with the proper sign can produce moments which assist in keeping the web straight.

Let us explore what this means for an inelastic, uncambered (straight) web, for which $y''=y''_{\text{air}}$: The lateral deflections will tend towards

$$\left[\frac{2\ell^2}{\pi^2 Z}\cdot y''_{\text{air}}\pm\alpha\right]=0$$

$$y''\ell=\mp\alpha\cdot\frac{\pi^2 Z}{2\ell} \tag{45}$$

giving us a quantitative indication of the nominal magnitude of steering effects from air-bar tilts. For the small values of Z/ℓ that we desire for robustness, only small control effects $y''\ell$ are possible. Conversely, if other considerations lead us to large web-amplitudes, tilt control on some or all bars might be promising.

Conclusion

1. The main effect of the sinusoidal shape of the web in an air-flotation oven is to reduce lateral bending stiffness. This reduction is directly proportional to the reduction of the extensional stiffness, insofar as the same ''effective Young's modulus'' enters into both MD extension and lateral bending. This makes extensional tests useful for judging lateral rigidity.
2. The same measures which raise extensional stiffness will improve lateral rigidity:

a. Choice of air-bars: bars which have been identified in our past experiments as having good flying-height ''stiffness'' will also improve extensional and lateral rigidity.
b. Tension: increased tension will increase the flying-height ''stiffness'' as well as reduce sinusoidal amplitude.
c. Air pressure, if it is matched by increased tension to maintain low flying height.
d. Air-bar engagement: less engagement means a flatter web, with a moderate improvement in stiffness.

These four measures can be useful for controlling lateral-excursion troubles in ovens.

3. The lateral forces generated by the tilting of the web oppose the straightening effect of tension, indicating that air support is inherently destabilizing with respect to lateral position. In the broader field of fluid/structure interactions, this is in the category of divergent response (rather than the category of oscillatory response like web flutter).
4. A remaining effect of tension is to increase the likelihood of good traction at the exit roller, and therefore a greater likelihood that the moderate-span *full-width-traction* boundary

conditions apply, rather than *partial-slip*. As a result, increased tension can be counter-productive for straightening the web. The criterion for whether partial slip at the exit roller increases or decreases maximum lateral excursion is a critical value of the tension/beam parameter, Eq. (43).

5. The main effect of air support is to reduce lateral moments and tension variation in the web, eliminating slack regions and making longitudinal wrinkles less likely.

Acknowledgments

This work was supported by the Web Handling Research Center at Oklahoma State University in Stillwater.

Nomenclature

A = cross-sectional area of web (thickness×width b)
b = width of web
EA = extensional stiffness of web undulating over air supports
EI = lateral bending stiffness of air-supported web
$\mathcal{F}$ = functional dependence of pad pressure P on flying height $(Z-z_{\text{bar}})$
k = extensional spring constant of web span, per unit width
L = Length of entire web-span within air-flotation oven
ℓ = spacing of air-support bars, half-wavelength of sinusoidal shape
p = local gage pressure between air-support bar and web
P = maximum gage pressure between air-support bar and web
S = length of web path in air-flotation oven, $>L$ because of waviness
s = length of one-half wave of web, $>\ell$
T_{app} = apparent web tension per unit width, e.g., from dancer-roller forces
T_{mat} = actual tension in the web material, per unit width
v = machine-direction velocity of web
x = machine-direction (MD) coordinate, Fig. 1
y = cross-machine-direction (CMD) coordinate
Y_o'' = inherent lateral curvature $(1/R)$ of a cambered web
z = out-of-plane deflection coordinate, Fig. 1
Z = maximum out-of-plane deflection (half-amplitude) of web
z_{bar} = half of engagement (vertical overlap) of bars–often negative
α = lateral tilt angle of air-bar, in radians
κ = spring constant of air cushion supporting web over bar
μ = web mass per unit area, $\div g_c$ (32.174 lbm-ft/lbf-sec^2 or 1 kg-m/N-s^2)
ξ = fraction of total deflection due to elastic material stretching, Eq. (16)
Π_ξ = parameter for relative flexibility, $\xi\Pi_{t/b}$, Eq. (28)
Π_f = parameter for lateral force due to web camber, $Y_o''L\Pi_{t/b}$, Eq. (32)
$\Pi_{t/b}$ = normalized ratio of app. tension to eff. beam stiffness, Eq. (43)

References

[1] Shelton, John J., 1968, ''Lateral Dynamics of a Moving Web,'' Ph.D. thesis, MAE Department, Oklahoma State University, Stillwater, OK, July.
[2] Shelton, J. J., 1992, ''Initially Straight Moving Web With a Slack Edge: Steady State Behavior Caused by Roller Nonparallelism Greater Than Critical,'' *Web Handling–1992*, ASME, New York, **AMD-Vol. 149**, pp. 51–65.
[3] Young, G. E., Shelton, J. J., and Kardamilas, C., 1989, ''Modeling and Control of Multiple Web Spans Using State Estimation,'' ASME J. Dyn. Syst., Meas., Control, **111**, pp. 505–510.
[4] Shelton, J. J., 1985, ''Stability and Control of a Center or End Pivoted Web Guide,'' *Proc. 4th American Control Engineering Conf.*, American Automatic Control Council, Green Valley, AZ, pp. 385–387.
[5] Swanson, R. P., 1993, ''Air-Support Conveyance of Uniform and Non-Uniform Webs,'' *Proc. Second International Conference on Web Handling*, Stillwater, OK, June 6–9, Oklahoma State University, Stillwater, OK, pp. 1–21.
[6] Young, G. E., Shelton, J. J., and Fang, B., 1989, ''Interaction of Web Spans, Parts I and II,'' ASME J. Dyn. Syst., Meas., Control, **111**, pp. 490–504.
[7] Chang, Y. B., Swanson, R. P., and Moretti, P. M., 1999, ''Resiliency of an Air-Floated Web,'' *Proc. Fifth International Conference on Web Handling*, Stillwater, OK, June 6–9, Oklahoma State University, Stillwater, OK, pp. 543–559.
[8] Moretti, P. M., and Chang, Y. B., 1995, ''Coupling Between Out-of-Plane Displacements and Lateral Stability of Webs in Air-Support Ovens,'' *Proc. Third International Conference on Web Handling*, Stillwater, OK, June 18–21, Oklahoma State University, Stillwater, OK, pp. 338–347.
[9] Pinnamaraju, R., 1992, ''Measurement on Air-Bar/Web Interaction for the Determination of Lateral Stability of a Web in Flotation Ovens,'' MS thesis, MAE Department, Oklahoma State University, Stillwater, OK, Dec.
[10] Perdue, D. M., 1993, ''Lateral Stability Investigation of Air-Bar and Web Interaction for Use in Flotation Ovens,'' MS thesis, MAE Department, Oklahoma State University, Stillwater, OK, Dec.
[11] Nisankararao, S. K. V., 1994, ''An Experimental Study of Aerodynamic Forces of Air Bars,'' M.S. thesis, MAE Department, Oklahoma State University, Stillwater, OK, May.
[12] Chang, Y. B., and Moretti, P. M., 1995, ''Ground-Effect Theory and Its Application to Air-Flotation Devices,'' *Proc. Third International Conference on Web Handling*, Stillwater, OK, June 18–21, Oklahoma State University, Stillwater, OK, pp. 348–365.
[13] Chang, Y. B., and Moretti, P. M., 1997, ''Aerodynamic Characteristics of Pressure-Pad Air Bars,'' ASME International Mechanical Engineering Congress and Exposition, AD-Vol. 53-2 *4th International Symposium on Fluid-Structure Interactions, Aeroelasticity, Flow-Induced Vibration and Noise*, ASME, New York, **AD-Vol. 53-2**, pp. 3–9.
[14] Chang, Y. B., Swanson, R. P., and Moretti, P. M., 1999, ''Longitudinal and Out-of-Plane Stiffness of a Web in an Air-Flotation Oven,'' *Proc. ASME, Noise Control and Acoustics Division–1999*, ASME, New York, **NCA-Vol. 26**, pp. 435–443.

Finite Element Analysis of Pulsed Laser Bending: The Effect of Melting and Solidification

X. Richard Zhang

Xianfan Xu[1]
e-mail: xxu@ecn.purdue.edu

School of Mechanical Engineering,
Purdue University,
West Lafayette, IN 47907-1288

This work developes a finite element model to compute thermal and thermomechanical phenomena during pulsed laser induced melting and solidification. The essential elements of the model are handling of stress and strain release during melting and their retrieval during solidification, and the use of a second reference temperature, which is the melting point of the target material for computing the thermal stress of the resolidified material. This finite element model is used to simulate a pulsed laser bending process, during which the curvature of a thin stainless steel plate is altered by laser pulses. The bending angle and the distribution of stress and strain are obtained and compared with those when melting does not occur. It is found that the bending angle increases continulously as the laser energy is increased over the melting threshold value. [DOI: 10.1115/1.1753268]

1 Introduction

Laser bending (or laser forming) is a non-contact technique capable of achieving very high precision. The schematic of a laser bending process is illustrated in Fig. 1. A target is irradiated by a focused laser beam passing across the target surface. Heating and cooling cause plastic deformation in the laser-heated area, thus change the curvature of the target permanently. The mechanism of laser bending has been explained by the thermo-elasto-plastic theory, [1–3]. Three laser bending mechanisms, i.e., the temperature gradient mechanism, the buckling mechanism, and the upsetting mechanism have been discussed in the literature, [4,5]. For the temperature gradient mechanism, a sharp temperature gradient is generated by laser irradiation and the residual compressive strain causes permanent bending deformation toward the direction of the incoming laser beam. Most of the pulsed laser bending processes are attributed to the temperature gradient mechanism since the short pulse heating duration induces a very sharp temperature gradient near the target surface.

Using a pulsed laser for bending is of particular interest in the micro-electronics industry, where high precision bending, curvature adjustment, and alignment are often required. Chen et al. [6] achieved bending precision on the order of sub-microradian on stainless steel and ceramics targets, which is higher than any other bending techniques. The relations between the bending angle and laser processing parameters were studied with the use of a two-dimensional finite element method, [7]. In that study, the laser energy was controlled so that no melting and solidification happened during the bending process. However, in some laser bending processes where larger bending angles are needed, the laser energy used could be high enough to cause melting, [8].

The finite element method is a general and powerful tool for investigating the complex thermal and thermomechanical problems involved in laser bending, [9–12]. When an unconstrained material melts, its stress and strain will be completely released, and then begin to retrieve when solidification starts. In this respect, the main challenge of simulations is the handling of the stress and strain release and retrieval during melting and solidification. The stress release is usually approximated by specifying the temperature dependent material properties, for example, decreasing Young modulus and yield strength significantly near the melting point, [9–12]. On the other hand, the strain release is hardly being considered due to the difficulty involved in the numerical simulation.

In this paper, a finite element model for simulating pulsed laser bending involving melting and solidification is developed using the uncoupled thermal and thermomechanical theory. It is assumed that the pulsed laser beam is uniform across the width of the specimen (the *x*-direction in Fig. 1). Thus, a two-dimensional thermal-stress model can be applied, which greatly reduces the computational time. In order to release and retrieve the stress and strain during melting and solidification, the element removal and reactivation method is applied to each melted element. In addition, in order to compute the stress of the solidified element correctly, a second reference temperature for the thermal stress calculation is used. The bending angle, residual stress, and residual strain are obtained and compared with the results of pulsed laser bending without melting.

2 Simulation Procedure

In order to calculate laser bending, a thermal analysis and a stress and strain analysis are needed, which are considered as uncoupled since the heat dissipation due to plastic deformation is negligible compared with the heat provided by laser irradiation. In an uncoupled thermomechanical model, a transient temperature field is obtained first in the thermal analysis, and is then used as a thermal loading in the subsequent stress and strain analysis to obtain the transient stress, strain, and displacement distributions. The finite element code, ABAQUS (HKS, Inc., Pawtucket, RI) is used. As shown in Fig. 2, a dense mesh is generated around the laser path and then stretched away in the length and thickness directions (the *y* and *z*-directions). The domain size and laser parameters used in the simulations are given in Table 1. The same mesh is used for both the thermal and stress analyses. A total of 1200 elements are used in the mesh. Mesh tests are conducted by increasing the number of elements until the calculation result is independent of the mesh density.

2.1 Thermal Analysis. The thermal analysis is based on solving the two-dimensional heat conduction equation:

$$\rho\tilde{c}\frac{\partial T}{\partial t}=\nabla\cdot(k\nabla T)+\dot{Q}_{ab} \tag{1}$$

[1]To whom correspondence should be addressed.

Contributed by the Applied Mechanics Division of THE AMERICAN SOCIETY OF MECHANICAL ENGINEERS for publication in the ASME JOURNAL OF APPLIED MECHANICS. Manuscript received by the ASME Applied Mechanics Division, Aug. 29, 2001; final revision, June 30, 2003. Associate Editor: B. M. Moran. Discussion on the paper should be addressed to the Editor, Prof. Robert M. McMeeking, Journal of Applied Mechanics, Department of Mechanical and Environmental Engineering University of California–Santa Barbara, Santa Barbara, CA 93106-5070, and will be accepted until four months after final publication of the paper itself in the ASME JOURNAL OF APPLIED MECHANICS.

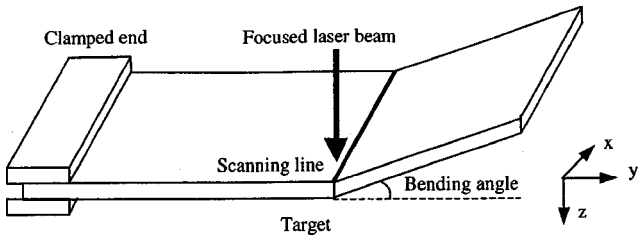

Fig. 1 Schematic of the laser bending process

where k is the thermal conductivity, ρ is the density of the stainless steel, $\tilde{c}$ is the derivative of the enthalpy with respect to temperature, and $\dot{Q}_{ab}$ is the volumetric heat source term resulted from irradiation of a laser pulse. The temperature-dependent properties of stainless steel 301, [13], are used in the calculation.

The parameter $\tilde{c}$ is equal to the specific heat c_p in solid and liquid regions. When an impure metal, like stainless steel, is heated from a solid state, it begins to melt at the solidus temperature T_s and melts completely at the liquidus temperature T_l. In the mushy zone, i.e., the region where the temperature is between T_s and T_l, $\tilde{c}$ is defined by

$$\tilde{c}=c_p+\frac{L}{T_l-T_s} \tag{2}$$

where L is the latent heat. Values of T_s, T_l, and L of stainless steel 301 are listed in Table 2, [13]. By using $\tilde{c}$, the effective specific heat, the phase change problem can be solved within a single domain. Solid and liquid material are treated as one continuous region and the phase boundary does not need to be calculated explicitly, [10].

The laser intensity is uniform in the x-direction and has a Gaussian distribution in the y-direction, expressed as

$$I_s(y,t)=I_0(t)e^{-8y^2/w^2} \tag{3}$$

where $I_0(t)$ is the time-dependent laser intensity at the center of the laser beam and w is the laser beam width at the target surface. The temporal profile of the laser intensity is treated as increasing linearly from zero to the maximum at 60 ns, then decreasing linearly to zero at the end of the pulse at 120 ns. Therefore, the volumetric heat source $\dot{Q}_{ab}$ in Eq. (1) can be expressed as

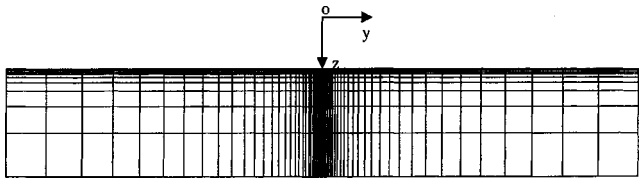

Fig. 2 Computational mesh

Table 1 Domain size and pulsed laser parameters

Specimen length (y)	600 μm
Specimen thickness (z)	100 μm
Laser wavelength	1.064 μm
Laser pulse full width	120 ns
Laser pulse energy	200–300 μJ
Laser line width	30 μm
Laser line length	1.3 mm

Table 2 Thermal properties of stainless steel 301

Solidus temperature, T_s	1673 K
Liquidus temperature, T_l	1693 K
Latent heat, L	265 J/g

$$\dot{Q}_{ab}=(1-R_f)\alpha I_0(t)e^{-8y^2/w^2}e^{-\alpha z} \tag{4}$$

where R_f is the optical reflectivity measured to be 0.66 for the stainless steel specimens. α is the absorption coefficient given by $\alpha=4\pi\kappa/\lambda$. The imaginary part of the refractive index κ of stainless steel 301 at the laser wavelength 1.064 μm is unknown, and $\kappa=4.5$ of iron is used. The initial condition is that the whole specimen is at the room temperature (300 K). Since the left and right boundaries as well as the bottom surface are far away from the laser irradiated area, the boundary conditions at these boundaries are prescribed as the room temperature. Convection and radiation with the surrounding are neglected.

Analyses are carried out with the laser pulse energy of 260 μJ, 270 μJ, 280 μJ, and 300 μJ, respectively. The peak temperature obtained by a 270 μJ pulse is 1703 K, higher than the liquidus temperature T_l (1693 K). For comparison, thermal analyses of three cases without melting are also performed; the laser pulse energies are 200 μJ, 230 μJ, and 250 μJ, respectively. The peak temperature obtained by a 250 μJ pulse is 1649 K, lower than the solidus temperature T_s (1673 K).

2.2 Stress and Strain Analyses. In the stress and strain analysis, the material is assumed to be linearly elastic-perfectly plastic. The Von Mises yield criterion is used to model the onset of plasticity. The left edge is completely constrained, and all other boundaries are force-free. Eight-node biquadratic plane-strain elements are employed.

As in the thermal analysis, the temperature dependent material properties are used, [13]. Poisson's ratio of stainless steel AISI 304, [14], is used. Considering the incompressibility in the liquid phase, the Poisson ratio of 0.4999 is used when the temperature is higher than T_s. The strain rate enhancement effect is neglected since temperature dependent data are unavailable. Sensitivity of unknown material properties on the computational results has been discussed by Chen et al. [7].

2.3 The Method of Element Removal and Reactivation In order to model the phenomena of melting and solidification, the element removal and reactivation method, [15], is applied. An element will be excluded from the stress and strain analysis when its temperature is higher than T_s, i.e., the element is removed from the domain after being melted and its stress and strain are released to zero. During cooling, the removed elements are reactivated in the calculation when their temperatures are lower than T_s and the stress and strain start to retrieve.

For the elements starting to solidify, the initial temperature for the thermal stress calculation T_i is replaced with a new initial temperature equal to the temperature at the moment when it is reactivated, i.e., T_s. This procedure is carried out for each element experiencing melting and solidification with the aid of the temperature history data obtained from the thermal analysis.

The reason for using a new initial temperature for a reactivated element is explained as follows. As mentioned before, the thermal stain of an unconstrained element is totally released after it melts. During solidification, the thermal strain will change gradually only if T_s is used as the initial temperature. Otherwise, if the room temperature T_i is still used as the initial temperature, the thermal strain will experience a sharp jump from zero to a high value, which is physically incorrect. Therefore, two initial temperatures should be used for each element involving melting and solidification.

The element removal and reactivation would not affect the thermal analysis since the thermal and the stress analysis are not coupled, and the thermal analysis is performed before the stress analysis. The forces in the element reaching the melting point are reduced to zero gradually before the element is removed, which is determined by the temperature-dependent stress-strain relations. Therefore, there is no sudden change of stress in elements involved in phase change. On the other hand, when the element is reactivated with zero stress, it exerts no nodal forces on the sur-

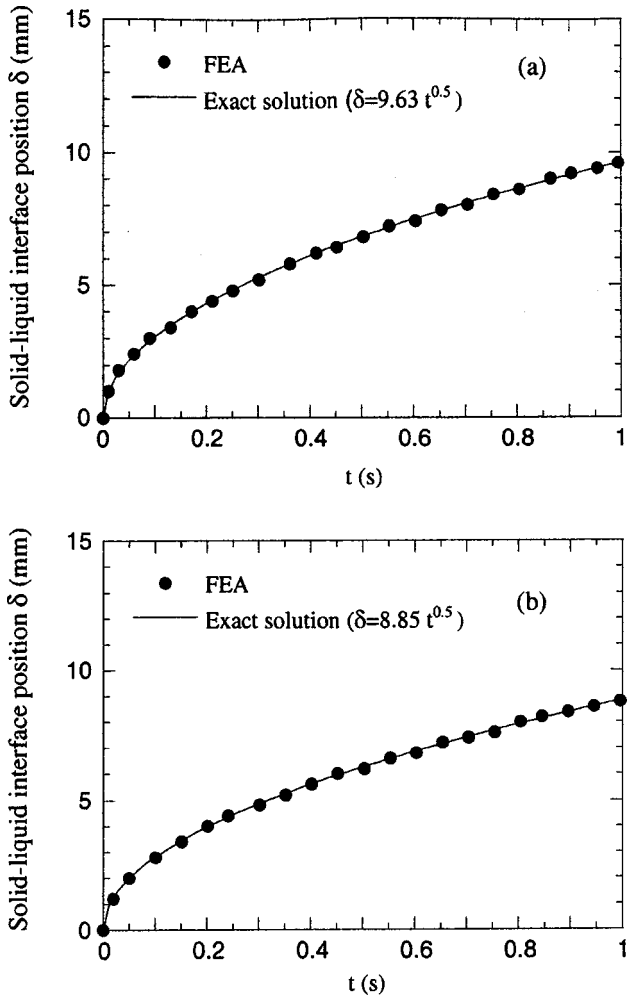

Fig. 3 Comparison between the results of FEA and an exact solution for (*a*) solidification, (*b*) melting

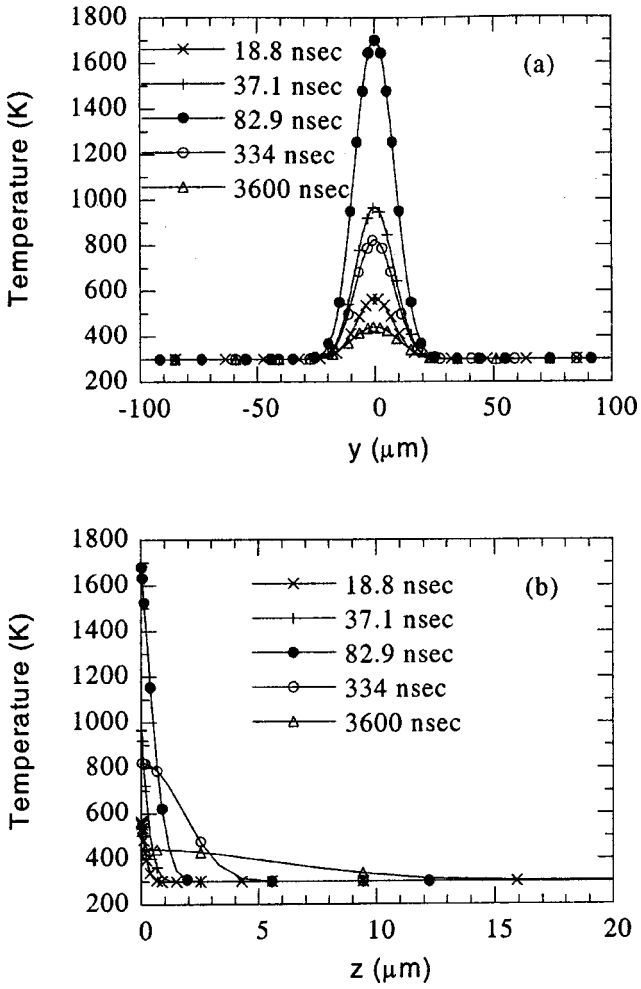

Fig. 4 Temperature distributions at different moments ($E = 270\ \mu J$) (*a*) along the *y*-direction on the top surface, (*b*) along the *z*-direction (at $y = 0$)

rounding elements. Thus the element removal and reactivation do not have any adverse effect on the thermal and stress calculation.

Based on the above description, the stress and strain for the elements involved in phase change are computed by the method of element removal and reactivation and the use of a new initial temperature at T_s to calculate the stress/strain of the solidified elements. During the calculation, element removal and reactivation are tracked for each element since each melted element begins to melt and solidify at different times. Hence, the computation is intensive even for the two-dimensional problem considered in this work.

3 Results and Discussion

Calculations are first conducted to verify the finite element analysis of melting and solidification. Results of finite element analysis are compared with exact solutions of solidification and melting problems given by Carslaw and Jaeger [16]. For the solidification case, the target is initially at the liquid state with a uniform temperature. At $t = 0$, the temperature at the surface ($x = 0$) is changed and held at a temperature lower than the melting point. Freezing thus starts and proceeds into the material. The position of the solid-liquid interface δ can be calculated with known material properties, and its expression is given in the insert of Fig. 3(*a*). Figure 3(*a*) shows the comparison of the results. It can be seen that the result of the finite element analysis matches exactly with the analytical solution. Similarly, results of the melting case are also compared. In this case, the target is initially at the solid state at the melting point. At $t = 0$, the surface temperature is increased to and kept at a constant temperature higher than the melting point. Again, exact match between the finite element result and the analytical solution is obtained, as shown in Fig. 3(*b*).

The above calculations are the only ones relevant to the problem studied here which have analytical solutions. There are no analytical solutions for thermomechanical problems with solid/liquid phase change since these problems are highly nonlinear. The rest of this work is focused computing the laser bending problem involving melting and solidification. We first present detailed temperature and residual stress distributions induced by a laser pulse at a fixed energy (270 μJ). Then, the laser pulse energy is varied, and bending with and without melting is compared in terms of the thermal strain, plastic strain, total strain, and stress. The dependence of the bending angle on the laser energy is also presented.

3.1 Results of Laser Bending With a Pulse Energy of 270 μJ. The transient temperature distribution in the target in first calculated. Figure 4 shows temperature distributions along the *x* and *z*-directions at different times. It can be seen that the maximum temperature, T_{max}, is obtained at the pulse center and reaches its peak value of 1703 K at 82.9 ns, and then drops slowly to 446 K at 3.6 μs. It can be estimated that the heat affected zone (HAZ) is around 40 μm wide (the laser beam is 30 μm wide). Figure 4(*b*) is the temperature distribution along the *z*-direction,

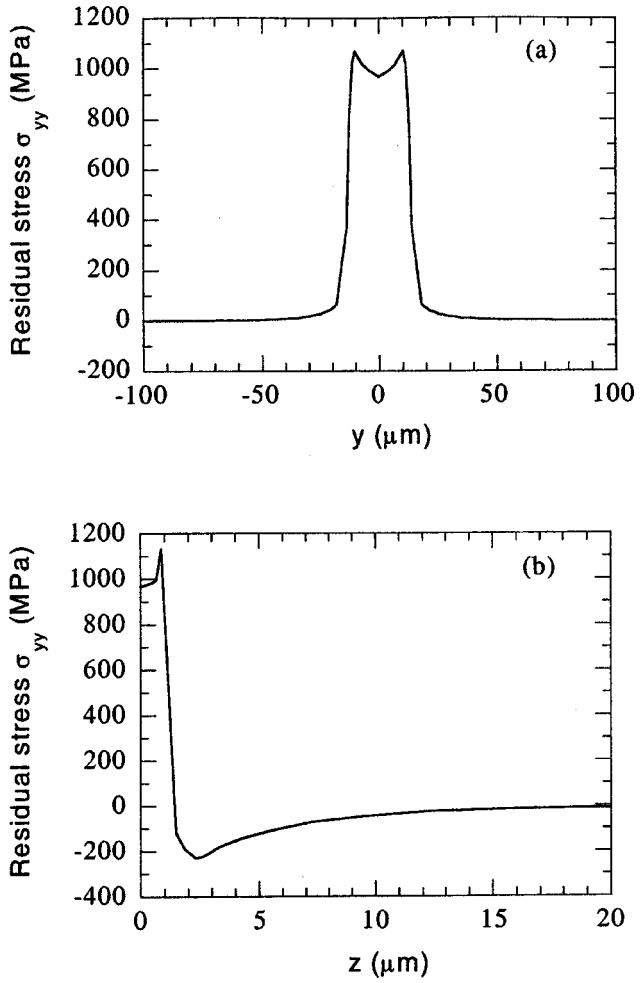

Fig. 5 Residual stress σ_{yy} distributions ($E=270\ \mu J$) (*a*) along the *y*-direction on the top surface, (*b*) along the *z*-direction (at $y=0$)

beginning from the upper surface of the target. It can be seen that the temperature gradient during heating period is higher than 500 K/μm.

Distributions of the transverse residual stress σ_{yy} along the *y* and *z*-directions are shown in Fig. 5. It can be seen from Fig. 5(*a*) that σ_{yy} is tensile, and has a value larger than 1.0 GPa. The stress-affected zone in the *y*-direction is about 30 μm. In the *z*-direction, σ_{yy} is more than 1.0 GPa within 1.0 μm from the surface. It becomes compressive at a depth of 1.5 μm from the surface. The maximum value of the compressive stress is about 250 MPa at $z=2.5\ \mu$m, and it gradually reduces to zero in the deeper region.

Figure 6 shows the deformation distribution along the *y*-direction. It can be seen that the permanent bending deformation is in the direction toward the incoming laser beam and the deflection is 42 nm at the free edge ($y=300\ \mu$m). There is a "Λ" shape surface deformation around $y=0\ \mu$m, the center of the laser beam. This is produced by thermal expansion along the negative *z*-direction because the surface is not constrained.

Detailed information about the thermal strain, the total strain, and the stress for the elements involved in melting and solidification and computed using the element removal and retrieval method is presented next, together with the case without melting for comparing their values.

3.2 Comparison Between Laser Bending With and Without Melting. Strain and stress histories during laser bending with melting (270 μJ) are compared with those without melting

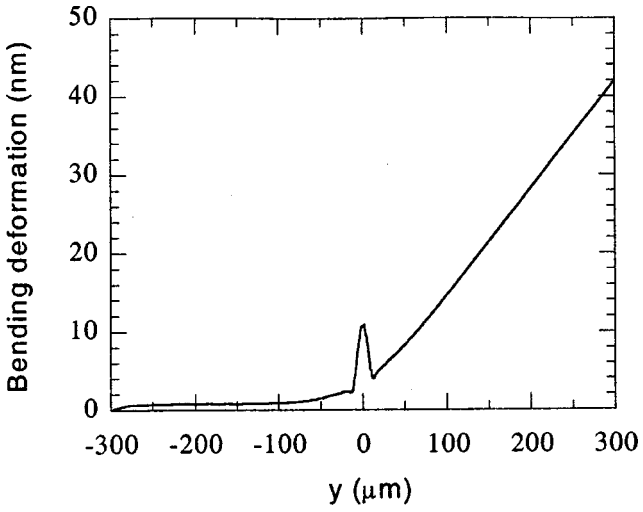

Fig. 6 Bending deformation along the *y*-direction ($E=270\ \mu J$)

(250 μJ). With the pulse laser energy of 270 μJ, the target begins to melt at about 70 ns and is completely solidified after 200 ns. Results of the center element on the top surface are compared.

Figure 7 shows histories of the thermal strain. For laser bending without melting, the thermal strain first increases as the temperature rises due to laser irradiation, and reaches a maximum value of 0.0228 at 82.03 ns. It then reduces to zero as the target cools to the room temperature. However, for bending involving melting, there are three periods in the thermal strain development: heating, melting and solidification, and cooling. The thermal strain reaches the peak value of 0.0232 at 69.52 ns. At this time, the corresponding average temperature of the element is 1673 K, which equals the solidus temperature. The element is excluded from the stress and strain analyses when it melts, which lasts for more than 28 ns. When it starts to solidify at 97.52 ns, the initial temperature of the element is replaced by the solidus temperature T_s, and then the thermal strain starts from zero to retrieve a negative value, which decreases continuously and reaches a residual value of -0.0229. The final thermal strain is very different from that of the nonmelting case because of the use of a second initial temperature.

Transverse plastic strains with and without melting are shown in Fig. 8. The compressive plastic strains are created during the

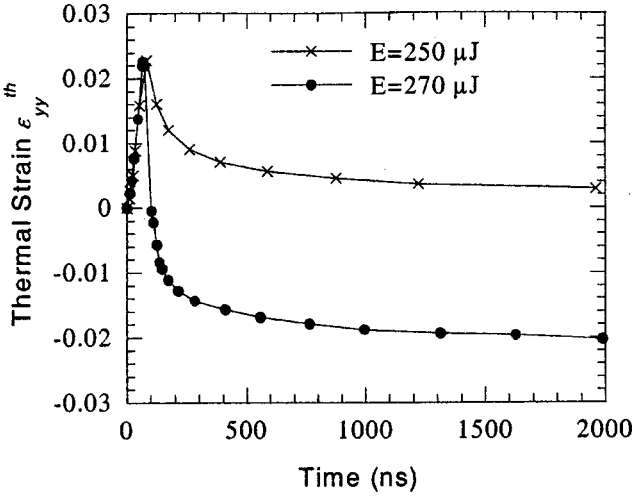

Fig. 7 Transient thermal strain at the center point on the top surface

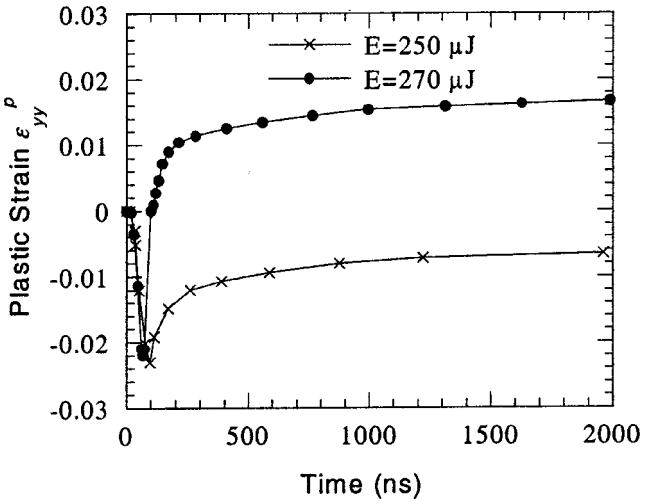

Fig. 8 Transient plastic strain at the center point on the top surface

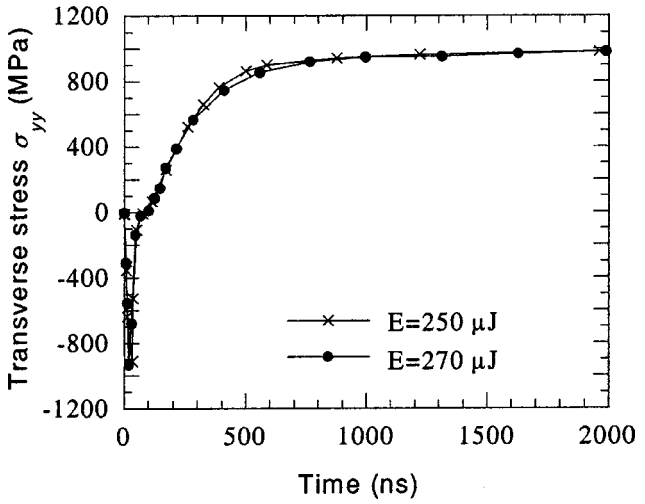

Fig. 10 Transient transverse stress σ_{yy} at the center point on the top surface

heating period since the thermal expansion of the heated area is constrained by the surrounding cooler materials. In the subsequent cooling period, the plastic strain decreases gradually, and is partially canceled with a residual value of −0.0047 for the case without melting. For bending involving melting, the compressive plastic strain is created during heating and it is released to zero during melting. This represents a significant difference between the two cases. Physically, the melted material can not support any strain due to the free surface while the material not melted can support a relatively large strain because of the surrounding cooler material, which is exactly what modeled here and shown in the results. After the melted element begins solidified, a tensile plastic strain develops, and a residual plastic strain of 0.0185 is obtained.

The history of the total transverse strain ε_{yy} up to 2000 ns is shown in Fig. 9. Despite the differences in the thermal and plastic strains, it can be seen that the total strains in both cases have a similar trend. The total strain increases and then decreases, and at about 100 ns it increases rapidly and reaches the maximum value at around 400 ns as the target bends away from the laser beam. After that, it decreases slowly and the residual value is about −0.0015 for bending without melting and −0.0017 for bending with melting (not shown in the figure). In both cases, the final bending angle is positive, meaning in the direction toward the laser beam.

Unlike strain, the overall trend of the stress development is not much affected by melting and solidification. As shown in Fig. 10, the development of the transverse stress follows a similar trend and a tensile residual stress of about 0.97 GPa is obtained in both cases. This is because the yield stress and the Young's modulus are reduced significantly at high temperature. Fort the case without melting, the stress is released to almost zero near the melting point, while the stress is reduced to zero for the case with melting.

Figure 11 shows the relation between the bending angle and the pulse energy. Bending angle increases almost linearly with the pulse energy. The dash line is the fitted line for laser bending without melting and is extracted to compare with the data with melting. There is no discontinuity or large change in the relation between the bending angle and the laser energy when the laser energy is increased across the melting threshold. This is in consistent with the results of total strain calculations since bending is

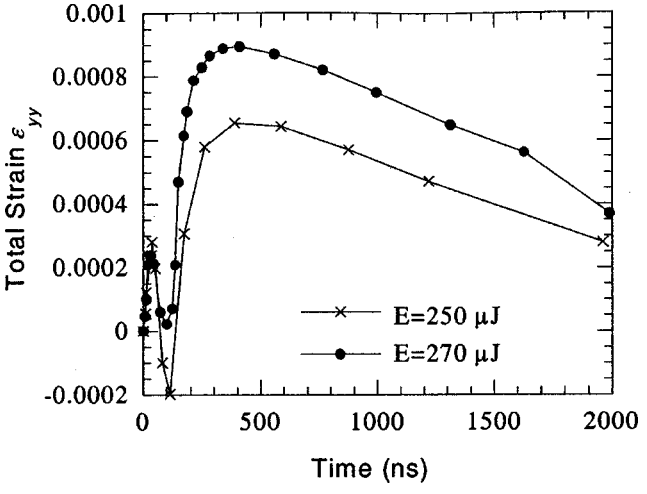

Fig. 9 Transient total strain ε_{yy} at the center point on the top surface

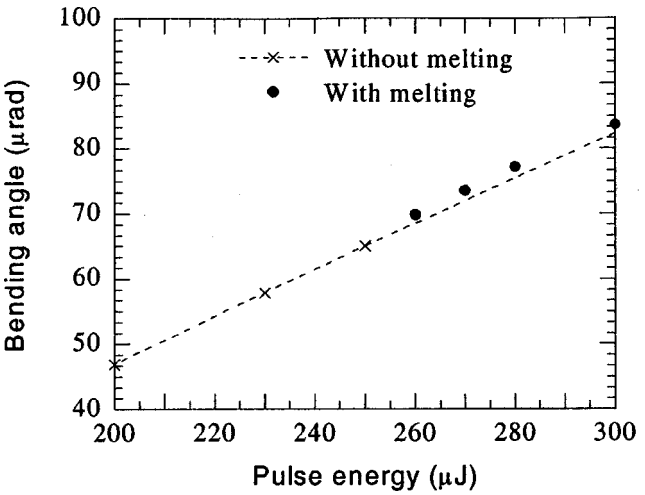

Fig. 11 Bending angle as a function of laser pulse energy

directly related to the total residual strain. As discussed previously, no large change of the total strain is found when the laser-energy is increased across the melting threshold.

4 Conclusion

A two-dimensional finite element model for calculating pulsed laser bending with melting and solidification is developed. The element removal and reactivation method is applied to each melted element to account for the stress and strain release in the melted material. A second initial temperature is necessary for the reactivated elements in order to compute the stress and strain development correctly. The bending angle and the residual stress and strain distribution of stainless steel irradiate by a laser pulse are obtained using this model. Results are also compared with those of laser bending without melting. No sudden change of the total residual strain, stress, and the bending angle is found when the laser energy is increased across the melting threshold.

Acknowledgment

Support of this work by the National Science Foundation (DMI-9908176) is gratefully acknowledged.

Nomenclature

E = laser pulse energy
I_0 = laser intensity at the center of the laser beam
I_s = laser flux
L = latent heat
$\dot{Q}_{ab}$ = volumetric heat source term induced by irradiation of a laser pulse
R_f = optical reflectivity
T = temperature
T_l = liquidus temperature
T_s = solidus temperature
$\tilde{c}$ = effective specific heat
c_p = specific heat
k = thermal conductivity
t = time
w = laser beam width
x, y, z = Cartesian coordinates
α = absorption coefficient
δ = position of solid-liquid interface
ε_{yy} = total strain along the y-direction
ε_{yy}^{p} = plastic strain along the y-direction
ε_{yy}^{th} = thermal strain along the y-direction
κ = imaginary part of the refractive index
λ = wavelength
ρ = density
σ_{yy} = stress along the y-direction

References

[1] Namba, Y., 1986, "Laser Forming in Space," *International Conference on Lasers*, C. P. Wang et al., eds., STS Press, Las Vegas, NV, pp. 403–407.
[2] Scully, K., 1987, "Laser Line Heating," J. Ship Prod., **3**, pp. 237–246.
[3] Arnet, H., and Vollertsen, F., 1995, "Extending Laser Bending for the Generation of Convex Shapes," Proc. Inst. Mech. Eng., **209**, pp. 433–442.
[4] Vollertsen, F., 1994, "Mechanisms and Models for Laser Forming," *Laser Assisted Net Shape Engineering, Proc. of the LANE*, M. Geiger et al., eds., Meisenbach, Bamburg, Germany, **1**, pp. 345–360.
[5] Geiger, M., and Vollertsen, F., 1993, "The Mechanisms of Laser Forming," Annals of the CIRP, **42**, pp. 301–304.
[6] Chen, G., Xu, X., Poon, C. C., and Tam, A. C., 1998, "Laser-Assisted Microscale Deformation of Stainless Steels and Ceramics," Opt. Eng., **37**, pp. 2837–2842.
[7] Chen, G., Xu, X., Poon, C. C., and Tam, A. C., 1999, "Experimental and Numerical Studies on Microscale Bending of Stainless Steel With Pulsed Laser," ASME J. Appl. Mech., **66**, pp. 772–779.
[8] Zhang, X., and Xu, X., 2001, "Fundamental and Applications of High Precision Laser Micro-Bending," IMECE, ASME, New York.
[9] Feng, Z., Zacharia, T., and David, S. A., 1997, "Thermal Stress Development in a Nickel Based Superalloy During Weldability Test," Weld. Res. Suppl., Nov., pp. 470–483.
[10] Lewis, R. W., and Ravindran, K., 1999, "Finite Element Simulation of Metal Casting," Int. J. Numer. Methods Eng., **47**, pp. 29–59.
[11] Taljat, B., Zacharia, T., and Wang, X., etc., 1998, "Numerical Analysis of Residual Stress Distribution in Tubes With Spiral Weld Cladding," Weld. Res. Suppl., Aug., pp. 328–335.
[12] Taljat, B., Radhakrishman, B., and Zacharia, T., 1998, "Numerical Analysis of GTA Welding Process With Emphasis on Post-Solidification Phase Transformation Effects on Residual Stresses," Mater. Sci. Eng., A, **246**, pp. 45–54.
[13] Maykuth, D. J., 1980, *Structural Alloys Handbook*, Metals and ceramics information center, Battelee Columbus Laboratories, Columbus, OH, **2**, pp. 1–61.
[14] Takeuti, Y., and Komori, S., 1979, "Thermal-Stress Problems in Industry 3: Temperature Dependency of Elastic Moduli for Several Metals at Temperatures From −196 to 1000°C," J. Therm. Stresses, **2**, pp. 233–250.
[15] *ABAQUS User's Manual*, Version 5.8, 1997, Hibbitt, Karlsson and Sorensen, Inc.
[16] Carslaw, H. S., and Jaeger, J. C., 1959, *Conduction of Heat in Solids*, 2nd Ed., Oxford University Press, Oxford, UK, Chap. XI, pp. 285–288.

B. L. Wang
Center for Advanced Materials Technology (CAMT),
School of Aerospace, Mechanical and Mechatronic Engineering J07,
University of Sydney,
Sydney NSW 2006, Australia
e-mail:
baolin.wang@aeromechanical.usyd.edu.au

X. H. Zhang
Center for Composite Materials,
Harbin Institute of Technology,
Harbin 150001, P. R. China

A Mode III Crack in a Functionally Graded Piezoelectric Material Strip

This paper considers a mode III crack problem for a functionally graded piezoelectric material strip. The mechanical and electrical properties of the strip are considered for a class of functional forms for which the equilibrium equation has an analytical solution. The problem is solved by means of singular integral equation technique. Both a single crack and two collinear cracks are investigated. The results are tabulated and plotted to show the effect of the material nonhomogeneity and crack location on the stress and electric displacement intensity factors. [DOI: 10.1115/1.1755692]

1 Introduction

In designing with piezoelectric materials, it is important to take into consideration imperfections, such as cracks, that are often pre-existing or are generated by external loads during the service life. The fracture of piezoelectric materials have received much attention. On the other hand, the development of functionally graded materials (FGMs) has demonstrated that they have the potential to reduce the stress concentration and increase the fracture toughness. Consequently, the concept of FGMs can be extended to the piezoelectric materials to improve its reliability. The fracture of functionally graded piezoelectric materials has been studied for the thermal loads, [1], and the antiplane mechanical and in-plane electric loads, [2].

Recently, Li and Weng [2] studied a mode III fracture problem for a functionally graded piezoelectric material (FGPM). The crack is located at the center of the strip. The material properties vary in the direction perpendicular to the crack, and they are also symmetric with respect to the cracked plane. Two important results were reported: (1) The crack tip singularity in a FGPM is of the same type as in the homogeneous piezoelectric materials; (2) The stress and the electric displacement intensity factors decrease with the increasing material gradient. In this paper, we present a more general solution to the mode III crack problem for a FGPM strip shown in Fig. 1. A class of functional forms for which the equilibrium equations have analytical solutions is studied. The influence of crack location (i.e., h_1/h) on the stress and electric displacement intensity factors is considered. The effect of interaction of more than one crack on SIFs is investigated by considering two collinear cracks in the strip. Different from the conclusion made in [2], we find that, for different material property distributions, the magnitudes of the stress and electric displacement intensity factors can increase or decrease with material gradient.

2 Formulation of the Crack Problem

Consider the crack geometry shown in Fig. 1. Assume that the medium is loaded away from the crack region. The problem in the absence of cracks has been solved, and the only applied are the antiplane shear stresses and the in-plane electric displacements on the crack surfaces.

Under antiplane deformation, the constitutive equations are

$$\tau_{xz}=c_{44}(y)\frac{\partial w}{\partial x}+e_{15}(y)\frac{\partial \phi}{\partial x}, \tag{1a}$$

$$\tau_{yz}=c_{44}(y)\frac{\partial w}{\partial y}+e_{15}(y)\frac{\partial \phi}{\partial y}, \tag{1b}$$

$$D_x=e_{15}(y)\frac{\partial w}{\partial x}-\in_{11}(y)\frac{\partial \phi}{\partial x}, \tag{1c}$$

$$D_y=e_{15}(y)\frac{\partial w}{\partial y}-\in_{11}(y)\frac{\partial \phi}{\partial y}, \tag{1d}$$

where $c_{44}(y)$, $e_{15}(y)$, and $\in_{11}(y)$ are the shear modulus, the piezoelectric constant, and the dielectric constant, respectively. The equilibrium equations are

$$\frac{\partial \tau_{xz}}{\partial x}+\frac{\partial \tau_{yz}}{\partial y}=0, \quad \frac{\partial D_x}{\partial x}+\frac{\partial D_y}{\partial y}=0. \tag{2}$$

In order to overcome the complexity of mathematics involved, we focus on a special class of FGPMs in which the variations of the properties are in the same proportion. Therefore, we assume

$$c_{44}(y)=c_0 f(y), \quad e_{15}(y)=e_0 f(y), \quad \in_{11}(y)=\in_0 f(y). \tag{3}$$

From Eqs. (1)–(3), we obtain

$$c_0\left(\frac{\partial^2 w}{\partial x^2}+\frac{\partial^2 w}{\partial y^2}\right)+e_0\left(\frac{\partial^2 \phi}{\partial x^2}+\frac{\partial^2 \phi}{\partial y^2}\right)+c_0 p(y)\frac{\partial w}{\partial y}+e_0 p(y)\frac{\partial \phi}{\partial y}=0, \tag{4a}$$

$$e_0\left(\frac{\partial^2 w}{\partial x^2}+\frac{\partial^2 w}{\partial y^2}\right)-\in_0\left(\frac{\partial^2 \phi}{\partial x^2}+\frac{\partial^2 \phi}{\partial y^2}\right)+e_0 p(y)\frac{\partial w}{\partial y}-\in_0 p(y)\frac{\partial \phi}{\partial y}=0, \tag{4b}$$

where

$$p(y)=\frac{1}{f(y)}\frac{\mathrm{d}f(y)}{\mathrm{d}y}. \tag{5}$$

Let the solution of (4) be given by

$$w(x,y)=\frac{1}{2\pi}\int_{-\infty}^{\infty}F_1(y,s)\mathrm{e}^{-\mathrm{i}sx}\mathrm{d}s, \tag{6a}$$

$$\phi(x,y)=\frac{e_0}{\in_0}w(x,y)+\frac{1}{2\pi}\int_{-\infty}^{\infty}F_2(y,s)\mathrm{e}^{-\mathrm{i}sx}\mathrm{d}s. \tag{6b}$$

From Eqs. (4) and (6) it follows that

Contributed by the Applied Mechanics Division of THE AMERICAN SOCIETY OF MECHANICAL ENGINEERS for publication in the ASME JOURNAL OF APPLIED MECHANICS. Manuscript received by the ASME Applied Mechanics Division, September 19, 2002; final revision, Oct. 13, 2003. Associate Editor: H. Gao. Discussion on the paper should be addressed to the Editor, Prof. Robert M. McMeeking, Journal of Applied Mechanics, Department of Mechanical and Environmental Engineering, University of California–Santa Barbara, Santa Barbara, CA 93106-5070, and will be accepted until four months after final publication of the paper itself in the ASME JOURNAL OF APPLIED MECHANICS.

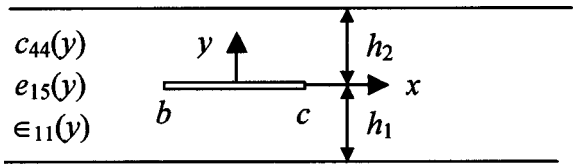

Fig. 1 Geometry of the crack problem

$$\frac{d^2F_1}{dy^2}+p(y)\frac{dF_1}{dy}-s^2F_1=0,\quad \frac{d^2F_2}{dy^2}+p(y)\frac{dF_2}{dy}-s^2F_2=0. \tag{7}$$

If we replace the unknown function F_1 by H_1 and F_2 by H_2 so that

$$F_1(y,s)=H_1(y,s)[f(y)]^{-1/2},\quad F_2(y,s)=H_2(y,s)[f(y)]^{-1/2}, \tag{8}$$

Eq. (7) would then become

$$\frac{d^2H_1}{dy^2}-\frac{1}{4}\left(p^2+2\frac{dp}{dy}+4s^2\right)H_1=0,$$

$$\frac{d^2H_2}{dy^2}-\frac{1}{4}\left(p^2+2\frac{dp}{dy}+4s^2\right)H_2=0. \tag{9}$$

We will now look for a particular class of functions for which (9) have analytical solutions. The simplest such classes of functions are obtained by assuming that

$$p^2+2\frac{dp}{dy}=4\ell_0, \tag{10}$$

where ℓ_0 is a constant. Three classes of functions satisfying (10) may thus be obtained as follows [3]:

(a) $\ell_0=\beta^2$:

$$p(y)=\mp 2\beta,\quad f(y)=\exp(\mp 2\beta y), \tag{11}$$

$$p(y)=2\beta\coth(\beta y+\delta),\quad f(y)=\sinh^2(\beta y+\delta), \tag{12}$$

$$p(y)=2\beta\tanh(\beta y+\delta),\quad f(y)=\cosh^2(\beta y+\delta), \tag{13}$$

(b) $\ell_0=-\beta^2$:

$$p(y)=2\beta\cot(\beta y+\delta),\quad f(y)=\sin^2(\beta y+\delta), \tag{14}$$

$$p(y)=-2\beta\tan(\beta y+\delta),\quad f(y)=\cos^2(\beta y+\delta), \tag{15}$$

(c) $\ell_0=0$:

$$p(y)=2\beta/(\beta y+1),\quad f(y)=(\beta y+1)^2, \tag{16}$$

$$p(y)=0,\quad f(y)=1, \tag{17}$$

where β and δ are arbitrary constants. Using the substitutions $\beta\to-\beta$ and $\delta\to\pi/2-\delta$, the property distribution (15) can be reduced to (14). Further, Eq. (17) describes a homogeneous material strip.

3 The Solution

Under conditions (11)–(17), the fundamental solution to Eqs. (9) can be obtained in analytical forms:

$$H_1=A(s)\exp(|s|\gamma y)+B(s)\exp(-|s|\gamma y),$$

$$H_2=C(s)\exp(|s|\gamma y)+D(s)\exp(-|s|\gamma y), \tag{18}$$

where

$$\gamma=\sqrt{1+\ell_0/s^2}. \tag{19}$$

From Eqs. (18), (8), and (6) it follows that

$$w(x,y)=\frac{1}{2\pi}\int_{-\infty}^{\infty}[f_a(y)A_1(s)+f_b(y)B_1(s)]e^{-isx}ds,\quad y<0, \tag{20a}$$

$$\phi(x,y)=\frac{e_0}{\in_0}w(x,y)+\frac{1}{2\pi}\int_{-\infty}^{\infty}[f_a(y)C_1(s)+f_b(y)D_1(s)]e^{-isx}ds,\quad y<0, \tag{20b}$$

and

$$w(x,y)=\frac{1}{2\pi}\int_{-\infty}^{\infty}[f_a(y)A_2(s)+f_b(y)B_2(s)]e^{-isx}ds,\quad y>0, \tag{21a}$$

$$\phi(x,y)=\frac{e_0}{\in_0}w(x,y)+\frac{1}{2\pi}\int_{-\infty}^{\infty}[f_a(y)C_2(s)+f_b(y)D_2(s)]e^{-isx}ds,\quad y>0, \tag{21b}$$

where $A_1(s)$, $B_1(s)$, $C_1(s)$, $D_1(s)$, $A_2(s)$, $B_2(s)$, $C_2(s)$ and $D_2(s)$ are unknown constants, and

$$f_a(y)=[f(y)]^{-1/2}e^{|s|\gamma y},\quad f_b(y)=[f(y)]^{-1/2}e^{-|s|\gamma y}. \tag{22}$$

Now consider the boundary and continuity conditions (see Fig. 1). Suppose that under antiplane deformation the upper and lower surfaces of the crack are contacted without friction. Hence, the crack can be treated as an electrically permeable one and there is no stress on its surfaces. This assumption is same as that in [2]. We shall treat the crack problem by means of the superposition technique. That is we first solved the problem without any cracks and then use the equal and opposite values of the stress as the tractions on the crack surfaces. Then the continuity and boundary conditions are as follows:

$$\tau_{yz}(x,-h_1)=0,\quad D_y(x,-h_1)=0,\quad x\in(-\infty,\infty), \tag{23}$$

$$\tau_{yz}(x,h_2)=0,\quad D_y(x,h_2)=0,\quad x\in(-\infty,\infty), \tag{24}$$

$$\tau_{yz}(x,+0)=\tau_{yz}(x,-0),\quad D_y(x,+0)=D_y(x,-0),\quad x\in(-\infty,\infty), \tag{25}$$

$$\phi(x,+0)=\phi(x,-0),\quad x\in(-\infty,\infty), \tag{26}$$

$$w(x,+0)=w(x,-0),\quad x\notin(b,c), \tag{27a}$$

$$\tau_{yz}(x,+0)=\tau_{yz}(x,-0)=\tau_0(x),\quad x\in(b,c). \tag{27b}$$

The seven homogeneous boundary conditions shown in Eqs. (23)–(26) may be used to eliminate seven of the eight unknowns, $A_1(s)$, $B_1(s)$, $C_1(s)$, $D_1(s)$, $A_2(s)$, $B_2(s)$, $C_2(s)$, and $D_2(s)$. The mixed boundary conditions (27) would then give a system of dual integral equations to determine the remaining one function. By defining a new unknown

$$g(x)=\frac{\partial w(x,+0)-\partial w(x,-0)}{\partial x}, \tag{28}$$

the problem may also be reduced to a singular integral equation in g. In this case it is seen that Eq. (27*a*) is equivalent to

$$g(x)=0\quad \text{for } x\notin(b,c),\qquad \text{and}\qquad \int_b^c g(x)dx=0, \tag{29}$$

and (27*b*) gives the desired integral equation.

By substituting now from Eqs. (20) and (21) through the Hook's law into boundary conditions (23) and (24), continuity conditions (25) and (26), and by using Eq. (28), $A_1(s)$, $B_1(s)$, $C_1(s)$, $D_1(s)$, $A_2(s)$, $B_2(s)$, $C_2(s)$, and $D_2(s)$ may be determined in terms of the Fourier transforms of g. Noting that g is zero for $x\notin(b,c)$, the following expressions are found:

$$A_1(s)=\frac{f_b'(-h_1)[f_a'(0)f_b'(h_2)-f_b'(0)f_a'(h_2)]}{[f_b'(0)-f_a'(0)][f_b'(-h_1)f_a'(h_2)-f_b'(h_2)f_a'(-h_1)]}\times\frac{\mathrm{i}[f(0)]^{1/2}}{s}\int_b^c g(t)\mathrm{e}^{\mathrm{i}st}\mathrm{d}t, \tag{30a}$$

$$A_2(s)=\frac{f_b'(h_2)[f_a'(0)f_b'(-h_1)-f_b'(0)f_a'(-h_1)]}{[f_b'(0)-f_a'(0)][f_b'(-h_1)f_a'(h_2)-f_b'(h_2)f_a'(-h_1)]}\times\frac{\mathrm{i}[f(0)]^{1/2}}{s}\int_b^c g(t)\mathrm{e}^{\mathrm{i}st}\mathrm{d}t, \tag{30b}$$

$$B_1(s)=-\frac{f_a'(-h_1)}{f_b'(-h_1)}A_1(s), \tag{30c}$$

$$B_2(s)=-\frac{f_a'(h_2)}{f_b'(h_2)}A_2(s), \tag{30d}$$

and

$$C_1(s)=-\frac{e_0}{\in_0}A_1(s), \tag{31a}$$

$$D_1(s)=-\frac{e_0}{\in_0}B_1(s), \tag{31b}$$

$$C_2(s)=-\frac{e_0}{\in_0}A_2(s), \tag{31c}$$

$$D_2(s)=-\frac{e_0}{\in_0}B_2(s), \tag{31d}$$

where

$$f_a'(y)=\partial f_a(y)/\partial y,\quad f_b'(y)=\partial f_b(y)/\partial y. \tag{32}$$

Substituting from Eqs. (1) and (20) into the boundary condition (27*b*), we obtain

$$\frac{1}{\pi}\int_b^c g(t)K(x,t)\mathrm{d}t=\tau_0(x)/c_0, \tag{33}$$

where

$$K(x,t)=\frac{\mathrm{i}}{2}\int_{-\infty}^{\infty}k(s)\mathrm{e}^{\mathrm{i}s(t-x)}\mathrm{d}s, \tag{34}$$

$$k(s)=[f(0)]^{3/2}\frac{[f_a'(0)f_b'(-h_1)-f_b'(0)f_a'(-h_1)][f_a'(0)f_b'(h_2)-f_b'(0)f_a'(h_2)]}{s[f_b'(0)-f_a'(0)][f_b'(-h_1)f_a'(h_2)-f_b'(h_2)f_a'(-h_1)]}. \tag{35}$$

Therefore, the integral kernel k can be obtained by inserting the property distributions (11)–(17) into Eqs. (22) and then into Eq. (35). In particular, if the material properties are described by Eq. (17), the explicit form for the kernel k can be obtained as follows:

$$k(s)=-\frac{\sinh(sh_1)\sinh(sh_2)}{\sinh(sh)}. \tag{36}$$

For other property distributions, k is a very complicated function of s.

4 The Singular Integral Equation

In order to determine the singular behavior of (33), the behavior of the kernel k needs to be examined. For this, it is sufficient to determine and separate those leading terms in the asymptotic expansion of k as $|s|\to\infty$ that would lead to unbounded integrals. From the expression of k given in (35) it can be shown that in the asymptotic expansions for $|s|\to\infty$ the only terms that would give unbounded integrals are

$$k(\pm\infty)=-\mathrm{sgn}(s)\frac{f(0)}{2}. \tag{37}$$

By adding and substituting the asymptotic value given by (37) to and from k in (34), and by evaluating the integrals involving the leading term, we obtain

$$K(x,t)=\frac{f(0)}{2}\frac{1}{t-x}+\frac{\mathrm{i}}{2}\int_{-\infty}^{\infty}\Lambda(s)\mathrm{e}^{\mathrm{i}s(t-x)}\mathrm{d}s, \tag{38}$$

where

$$\Lambda(s)=k(s)+\mathrm{sgn}(s)f(0)/2. \tag{39}$$

Thus, (33) may be modified as follows:

$$\frac{f(0)}{2}\frac{1}{\pi}\int_b^c\frac{1}{t-x}g(t)\mathrm{d}t+\frac{1}{\pi}\int_b^c K_1(x,t)g(t)\mathrm{d}t=\tau_0(x)/c_0, \tag{40}$$

where

$$K_1(x,t)=\frac{\mathrm{i}}{2}\int_{-\infty}^{\infty}\Lambda(s)\mathrm{e}^{\mathrm{i}s(t-x)}\mathrm{d}s=-\int_0^{\infty}\Lambda(s)\sin[s(t-x)]\mathrm{d}s, \tag{41}$$

is a known bounded function.

5 Crack Tip Field Intensity Factors

The singular integral Eq. (40) contains a Cauchy-type kernel. Consequently, the crack tip behavior can be characterized by a standard square-root singularity. This means that the forms of the singular stress and electric fields at the crack tips in a FGPM are same as those in a homogeneous piezoelectric material. The solution of the singular integral Eq. (40) has the following form:

$$g(x)=\frac{F(x)}{\sqrt{(x-b)(c-x)}}, \tag{42}$$

where F is a bounded function. After normalizing the interval (b,c) Eq. (40) may be solved numerically by using a Gaussian quadrature formula. The mode III stress intensity factor at, for example, the crack tip $x=b$ is defined by

$$k_3(b)=\lim_{x\to b-0}\sqrt{2(b-x)}\,\tau_{yz}(x,0). \tag{43}$$

Observing that Eq. (40) gives the stress component $\tau_{yz}(x,0)$ on the plane of the crack for $x\in(b,c)$ as well as $x\notin(b,c)$, substituting from Eq. (42) into Eq. (40) a simple asymptotic analysis would show that

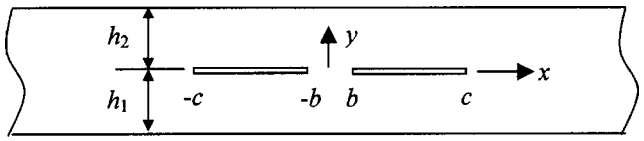

Fig. 2 Two symmetrically located collinear cracks

$$\tau_{yz}(x,0)=\frac{c_{44}(0)}{2}\left[\frac{F(b)}{\sqrt{(c-b)(b-x)}}-\frac{F(c)}{\sqrt{(c-b)(x-c)}}+O(\sqrt{(b-x)(x-c)})\right]. \quad (44)$$

Thus, from Eqs. (43) and (44) we obtain the stress intensity factors

$$k_3(b)=\frac{c_{44}(0)}{2}\frac{F(b)}{\sqrt{a}}, \quad k_3(c)=-\frac{c_{44}(0)}{2}\frac{F(c)}{\sqrt{a}}, \quad (45)$$

where a is the half-crack length (i.e., $a=(c-b)/2$). Since the crack is assumed to be electrically permeable. There is no electric potential discontinuity across the crack and the electric field E_y is finite at the crack tips. It can be shown from Eqs. (1) that the electric displacement $D_y(x,0)$ near the crack tip has the following form:

$$D_y(x,0)=[e_{15}(0)/c_{44}(0)]\tau(x,0), \quad x\to b-0 \text{ or } x\to c+0. \quad (46)$$

Therefore, the electric displacement shows singularity at the crack tips. The electric displacement intensity factor k_4 at, for example, the crack tip $x=b$ defined by

$$k_4(b)=\lim_{x\to b-0}\sqrt{2(b-x)}D_y(x,0), \quad (47)$$

can be obtained from

$$k_4=[e_{15}(0)/c_{44}(0)]k_3. \quad (48)$$

Since k_3 depends only on $\tau_0(x)$ (see Eqs. (40), (42), and (45)), the applied electric load would contribute nothing to the crack tip fields. Further, we note that the piezoelectric coefficient e_{15} and the dielectric coefficient $\in_{11}$ do not enter Eq. (40). This means that the piezoelectric effect has no effect on the stress intensity factor.

6 Collinear Cracks

In formulating the problem, no conditions of symmetry with respect to $x=0$ were assumed regarding to the crack geometry and the external load $\tau_0(x)$. Thus, the integral Eq. (40) derived in Section 4 is valid basically for any number of collinear cracks defined by $y=0$, $b_j<x<c_j$, $(j=1,\ldots,n)$ along the x-axis with the additional single-valuedness condition of the form (29) for each crack, namely

$$\int_{b_j}^{c_j} g_j(x)\mathrm{d}x=0, \quad (j=1,\ldots,n). \quad (49)$$

The only change in the integral equation would be in replacing the integral (b,c) by the sum of the integrals $L_i=(b_i,c_i)$ $(i=1,\ldots,n)$ corresponding to the collinear cracks.

As an example, we consider the case of two symmetrically located and symmetrically loaded collinear cracks (Fig. 2). That is, we assume that $b_1=b$, $c_1=c$, $b_2=-c$, $c_2=-b$, $\tau_{yz}(x,0)=\tau_{yz}(-x,0)=\tau_0(x)$, $b<x<c$. In this case, using the symmetry conditions, Eq. (40) may be expressed as

$$\frac{f(0)}{2}\frac{1}{\pi}\int_b^c\left[\frac{1}{t-x}+\frac{1}{t+x}\right]g(t)\mathrm{d}t+\frac{1}{\pi}\int_b^c K_2(x,t)g(t)\mathrm{d}t=\tau_0(x)/c_0, \quad (50)$$

where

$$K_2(x,t)=K_1(x,t)-K_1(x,-t). \quad (51)$$

The integral Eq. (50) is again solved under the following single-valuedness condition:

$$\int_b^c g(x)\mathrm{d}x=0. \quad (52)$$

To solve Eq. (50), the length parameters in it are normalized according to

$$x=\bar{x}(c-b)/2+(c+b)/2, \quad t=\bar{t}(c-b)/2+(c+b)/2. \quad (53)$$

Thus, the integral Eq. (50) can be reduced to the following standard form:

$$\frac{f(0)}{2}\frac{1}{\pi}\int_{-1}^{1}\left[\frac{1}{\bar{t}-\bar{x}}+\frac{1}{\bar{t}+x_1}\right]g(t)\mathrm{d}\bar{t}+\frac{c-b}{2}\frac{1}{\pi}\int_{-1}^{1}K_2(x,t)g(t)\mathrm{d}\bar{t}=\tau_0(x)/c_0, \quad (54)$$

where

$$x_1=\bar{x}+\frac{2(c+b)}{c-b}. \quad (55)$$

The solution of (54) has the same form as Eq. (42). It can also be expressed as

$$g(t)=\frac{F(t)}{\sqrt{1-t^2}}\sqrt{\frac{2}{c-b}}=\sum_{n=1}^{\infty}\frac{A_nT_n(\bar{t})}{\sqrt{1-t^2}}, \quad (56)$$

where T_n is the Chebyshev polynomial of the first kind. By substituting from Eq. (56) into Eq. (54) and by using the well-known orthogonality condition [4]:

$$\frac{1}{\pi}\int_{-1}^{1}\frac{T_n(\bar{t})}{(\bar{t}-\bar{x})\sqrt{1-t^2}}\mathrm{d}\bar{t}=\begin{cases}U_{n-1}(\bar{x}), & n\geq 1,\ |\bar{x}|<1\\ -\dfrac{\mathrm{sgn}(\bar{x})}{\sqrt{\bar{x}^2-1}}[\bar{x}-\mathrm{sgn}(\bar{x})\sqrt{\bar{x}^2-1}]^n, & n\geq 0,\ |\bar{x}|>1\\ 0, & n=0,\ |\bar{x}|<1\end{cases} \quad (57)$$

we find

$$\frac{f(0)}{2}\sum_{n=1}^{\infty}A_nU_{n-1}(\bar{r})+\frac{f(0)}{2}\sum_{n=1}^{\infty}A_n\frac{1}{\sqrt{x_1^2-1}}[\sqrt{x_1^2-1}-x_1]^n+\frac{c-b}{2}\frac{1}{\pi}\sum_{n=1}^{\infty}A_n\int_{-1}^{1}K_2(x,t)\frac{T_n(\bar{t})}{\sqrt{1-t^2}}\mathrm{d}\bar{t}=\tau_0(x)/c_0, \quad (58)$$

where U_{n-1} is the Chebyshev polynomial of the second kind. The simplest method for solving the functional Eq. (58) is truncating the series and using an appropriate collocation in x (see, for example, [5]). In this problem, the stress intensity factors can also be obtained from Eq. (45).

7 Results and Discussions

Since the applied electrical load does not influence the crack tip singularities, it is sufficient to consider a uniform shear loading τ_0. Five kinds of property distributions, namely, $f(y)=\exp(2\beta y)$, $f(y)=\sinh^2(\beta y+0.8814)$, $f(y)=\cosh^2(\beta y)$, $f(y)$

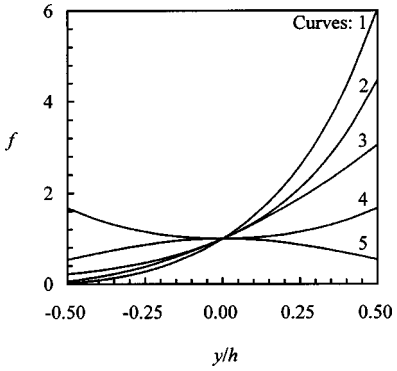

Fig. 3 Material properties distributions; $\beta h=1.5$, curve 1: $f=\sinh^2(\beta y+0.8814)$, curve 2: $f=\exp(2\beta y)$, curve 3: $f=(\beta y+1)^2$, curve 4: $f=\cosh^2(\beta y)$, curve 5: $f=\sin^2(\beta y+\pi/2)$

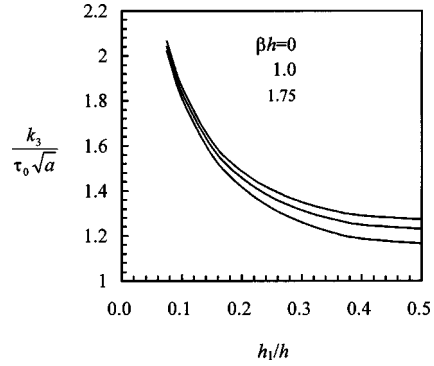

Fig. 6 The effect of the crack location on the stress intensity factors; $a=0.75h$, $\mu=\mu_0\cosh^2(\beta y)$

$=\sin^2(\beta y+\pi/2)$, and $f(y)=(\beta y+1)^2$ are investigated. The shapes of these property distributions are displayed in Fig. 3 for $\beta h=1.5$. These functions show a same value 1 at the cracked plane (i.e., $y=0$ plane).

The normalized values of the stress intensity factors for a single crack are given in Figs. 4–8 and Tables 1–6. The electric displacement intensity factors can be obtained directly from Eq. (48). Figures 4–8 show the effect of the crack location h_1/h on k_3 in a uniformly loaded FGPM strip. In these figures $a=(c-b)/2$ is the half-crack length. For comparison, the values of k_3 for a homogeneous medium ($\beta=0$) are also displayed in each figure. As expected, for $h_1/h\to 0$, k_3 become unbounded. A somewhat unexpected result is that in some cases, if the material nonhomogeneity parameter β is relatively large, as h_1/h decreases k_3 does not monotonously increase, it rather goes through a minimum before becoming unbounded (Figs. 5 and 8). From the results shown in Figs. 4–8, it is noted that the stress intensity factors can increase (Figs. 4, 5, 7, and 8) or decrease (Fig. 6) with increasing parameter β. The influence of β on k_3 becomes more significant when the crack approaches the center ($h_1=h/2$) of the strip.

Some examples for the stress intensity factors are shown in Tables 1–6 for different crack lengths. In these tables, again $a=(c-b)/2$ is the half-crack length. The crack is located symmetrically; that is, $h_1=h_2$. As expected, in all cases as crack length approaches zero we have $k_3\to\tau_0\sqrt{a}$. For reference, Table 1 also shows the results for the corresponding homogeneous layer (i.e., for $\beta=0$).

Tabulated in Table 3 are stress intensity factors against a/h for the property distribution $f(y)=\cosh^2(\beta y)$. From the results, it is

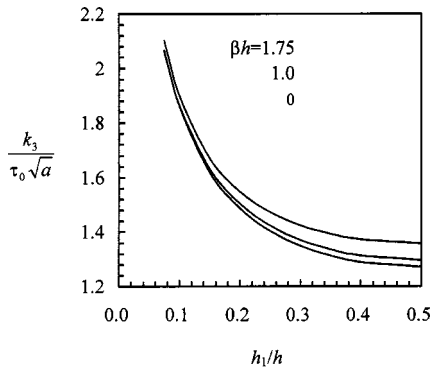

Fig. 4 The effect of the crack location on the stress intensity factors; $a=0.75h$, $f=\exp(2\beta y)$

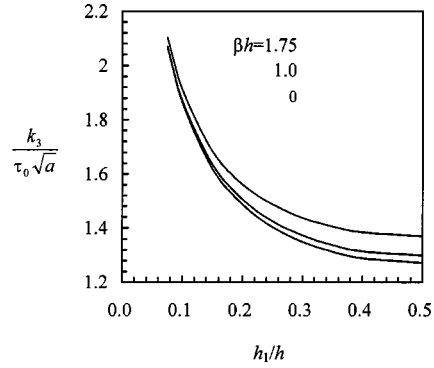

Fig. 7 The effect of the crack location on the stress intensity factors; $a=0.75h$, $f=\sin^2(\beta y+\pi/2)$ or $f=\cos^2(\beta y)$

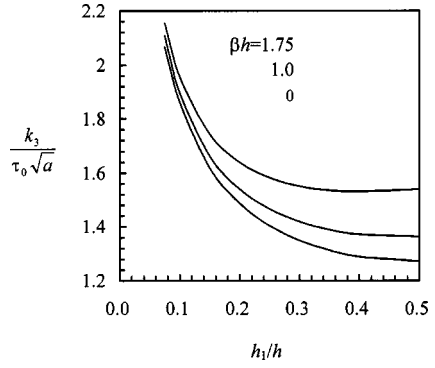

Fig. 5 The effect of the crack location on the stress intensity factors; $a=0.75h$, $f=\sinh^2(\beta y+0.8814)$

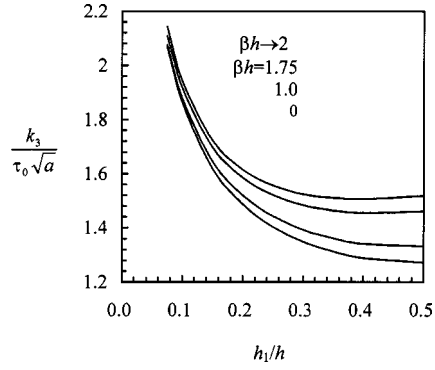

Fig. 8 The effect of the crack location on the stress intensity factors; $a=0.75h$, $f=(\beta y+1)^2$

Table 1 Stress intensity factors for property distribution $f=\exp(2\beta y)$; $h_1=h_2=0.5h$

	$k_3/\tau_0\sqrt{a}$					
a/h	$\beta h=0$	$\beta h=\pm0.5$	$\beta h=\pm1$	$\beta h=\pm1.25$	$\beta h=\pm1.5$	$\beta h=\pm1.75$
1.0	1.377	1.388	1.413	1.438	1.463	1.491
0.9	1.333	1.342	1.370	1.390	1.413	1.439
0.8	1.288	1.296	1.322	1.340	1.361	1.385
0.7	1.242	1.250	1.273	1.289	1.309	1.331
0.6	1.195	1.202	1.223	1.238	1.255	1.275
0.5	1.149	1.155	1.173	1.186	1.201	1.218
0.4	1.105	1.110	1.125	1.135	1.148	1.162
0.3	1.064	1.068	1.079	1.087	1.097	1.108
0.2	1.031	1.033	1.040	1.046	1.052	1.059
0.1	1.008	1.009	1.012	1.014	1.017	1.019

Table 2 Stress intensity factors for property distribution $f=\sinh^2(\beta y+\delta_0)$; $h_1=h_2=0.5h$, δ_0 is such that $\sinh\delta_0=1$

	$k_3/\tau_0\sqrt{a}$				
a/h	$\beta h=\pm0.5$	$\beta h=\pm1$	$\beta h=\pm1.25$	$\beta h=\pm1.5$	$\beta h=\pm1.75$
1.0	1.408	1.496	1.559	1.631	1.709
0.9	1.361	1.444	1.504	1.572	1.645
0.8	1.314	1.390	1.444	1.507	1.573
0.7	1.265	1.334	1.384	1.440	1.501
0.6	1.217	1.279	1.323	1.374	1.429
0.5	1.168	1.2	1.260	1.304	1.352
0.4	1.120	1.164	1.195	1.231	1.271
0.3	1.076	1.109	1.133	1.160	1.190
0.2	1.038	1.059	1.075	1.093	1.112
0.1	1.011	1.020	1.026	1.033	1.041

Table 3 Stress intensity factors for property distribution $f=\cosh^2(\beta y)$; $h_1=h_2=0.5h$

	$k_3/\tau_0\sqrt{a}$					
a/h	$\beta h=\pm0.5$	$\beta h=\pm1$	$\beta h=\pm1.25$	$\beta h=\pm1.5$	$\beta h=\pm1.75$	$\beta h=\pm2$
1.0	1.367	1.337	1.314	1.288	1.257	1.221
0.9	1.323	1.295	1.274	1.249	1.220	1.187
0.8	1.279	1.253	1.234	1.210	1.184	1.154
0.7	1.234	1.210	1.192	1.171	1.146	1.119
0.6	1.188	1.167	1.151	1.132	1.110	1.085
0.5	1.143	1.125	1.111	1.095	1.076	1.054
0.4	1.100	1.085	1.074	1.060	1.044	1.026
0.3	1.061	1.049	1.040	1.030	1.018	1.004
0.2	1.028	1.021	1.015	1.009	1.001	0.9918
0.1	1.008	1.004	1.002	0.999	0.996	0.9921

Table 4 Stress intensity factor for property distribution $f=\cosh^2(\beta y+1)$; $h_1=h_2=0.5h$

	$k_3/\tau_0\sqrt{a}$					
a/h	$\beta h=\pm0.5$	$\beta h=\pm1$	$\beta h=\pm1.25$	$\beta h=\pm1.5$	$\beta h=\pm1.75$	$\beta h=\pm2$
1.0	1.379	1.383	1.386	1.389	1.392	1.393
0.9	1.334	1.338	1.341	1.344	1.346	1.348
0.8	1.289	1.293	1.295	1.298	1.300	1.302
0.7	1.243	1.246	1.248	1.251	1.253	1.254
0.6	1.196	1.199	1.201	1.204	1.205	1.207
0.5	1.150	1.153	1.155	1.156	1.158	1.160
0.4	1.106	1.108	1.111	1.111	1.112	1.114
0.3	1.065	1.067	1.069	1.069	1.070	1.071
0.2	1.031	1.032	1.034	1.034	1.035	1.035
0.1	1.008	1.009	1.009	1.009	1.010	1.010

clear that as β increases k_3 decreases. The results clearly indicate that for a material with property distribution $f(y)=\cosh^2(\beta y)$ the stress intensity factor k_3 is smaller than the corresponding values for a homogeneous piezoelectric layer (i.e., for $\beta=0$). The same trend can be found in Fig. 6.

Table 6 shows the stress intensity factors for $f(y)=(\beta y+1)^2$. Since the material property must be positive defined, $\beta y+1$ should not equal zero in the entire region of y. This means that for $h_1=h_2=0.5h$, βh can approach but can not equal ±2.

Table 5 Stress intensity factors for property distribution $f=\sin^2(\beta y+\pi/2)$ or $f=\cos^2(\beta y)$; $h_1=h_2=0.5h$

	$k_3/\tau_0\sqrt{a}$					
a/h	$\beta h=\pm0.5$	$\beta h=\pm1$	$\beta h=\pm1.25$	$\beta h=\pm1.5$	$\beta h=\pm1.75$	$\beta h=\pm2$
1.0	1.388	1.419	1.443	1.472	1.506	1.547
0.9	1.342	1.372	1.394	1.421	1.453	1.490
0.8	1.296	1.323	1.343	1.368	1.398	1.432
0.7	1.250	1.274	1.293	1.315	1.342	1.374
0.6	1.202	1.224	1.241	1.261	1.285	1.313
0.5	1.156	1.174	1.188	1.206	1.227	1.250
0.4	1.110	1.125	1.137	1.151	1.168	1.188
0.3	1.068	1.080	1.089	1.100	1.112	1.127
0.2	1.033	1.041	1.046	1.053	1.061	1.071
0.1	1.009	1.012	1.014	1.017	1.020	1.024

Table 6 Stress intensity factors for property distribution $f=(\beta y+1)^2$; $h_1=h_2=0.5h$

	$k_3/\tau_0\sqrt{a}$					
a/h	$\beta h=\pm0.5$	$\beta h=\pm1$	$\beta h=\pm1.25$	$\beta h=\pm1.5$	$\beta h=\pm1.75$	$\beta h\rightarrow\pm2$
1.0	1.398	1.459	1.504	1.558	1.619	1.683
0.9	1.352	1.409	1.451	1.501	1.558	1.618
0.8	1.305	1.357	1.396	1.442	1.494	1.549
0.7	1.258	1.306	1.341	1.383	1.431	1.481
0.6	1.210	1.252	1.284	1.322	1.364	1.410
0.5	1.162	1.198	1.226	1.258	1.294	1.334
0.4	1.115	1.145	1.168	1.194	1.224	1.257
0.3	1.072	1.095	1.112	1.132	1.155	1.180
0.2	1.036	1.050	1.061	1.074	1.089	1.105
0.1	1.010	1.016	1.020	1.025	1.031	1.038

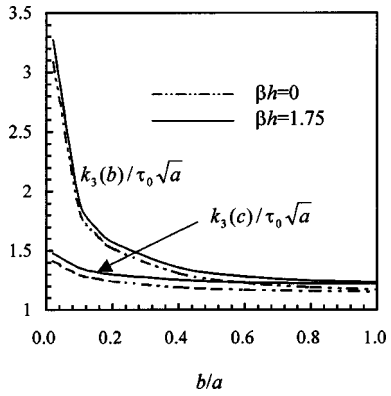

Fig. 9 Stress intensity factors for two collinear cracks in a FGPM strip; $a=(c-b)/2=0.5h$, $h_1=h_2$, $f=\exp(2\beta y)$

A sample result for two collinear cracks in a FGPM layer is shown in Fig. 9 which also show the stress intensity factors in the corresponding homogeneous layer (i.e., for $\beta=0$). Again, the electric displacement intensity factors can be obtained from Eq. (48). In this example the layer thickness is used as the normalized length parameter. The half-crack length is fixed as $a=0.5h$. $b/h=0$ and $b/h\rightarrow\infty$ correspond to two limiting cases of a single crack of length $2(c-b)$ and $c-b$, respectively. The figure shows that for $b\rightarrow0$ as expected $k_3(b)$ becomes unbounded, whereas $k_3(c)$ tends to the values corresponding to a single crack of length $2c$.

8 Conclusions

The fracture problem for a functionally graded piezoelectric material strip under antiplane shear is investigated for a class of

property distributions. Both a single crack and two collinear cracks are considered. The singular stress and electric fields at the crack tips in a functionally graded piezoelectric material have the same forms as those in a homogeneous piezoelectric material. It is found that the stress and electric displacement intensity factors do not depend on the applied electrical loads. The piezoelectric effect has no effect on the stress intensity factors. It is clear that the material nonhomogeneity has quite considerable influence on crack tip stress and electric displacement intensity factors: it can increase or decrease the magnitudes of the stresses and the electric displacements at the crack tips.

It should be pointed out that the results given in this paper are valid only for the special assumption where the variations of the material properties are in the same proportion. For more general case without such assumption, further research is required.

Acknowledgments

The authors would like to thank the NSFC (#10102004) and the Australia Research Council (Discovery Project Grant: DP0346037) for the support of this research. BLW is an ARC Australian Research Fellow funded by the Australian Research Council.

References

[1] Wang, B. L., and Noda, N., 2001, ''Thermally Induced Fracture of a Smart Functionally Graded Composite Structure,'' Theor. Appl. Fract. Mech., **35**(2), pp. 93–109.

[2] Li, C., and Weng, G. J., 2002, ''Antiplane Crack Problem in Functionally Graded Piezoelectric Materials,'' ASME J. Appl. Mech., **69**(4), pp. 481–488.

[3] Erdogan, F., and Ozturk, M., 1992, ''Diffusion Problems in Bonded Nonhomogeneous Materials With an Interface Cut,'' Int. J. Eng. Sci., **30**(10), pp. 1507–1523.

[4] Gradshteyn, I. S., and Ryzhik, I. M., 1965, *Tables of Integrals, Series and Products*, Academic Press, San Diego, CA.

[5] Erdogan, F., and Wu, B. H., 1996, ''Crack Problems in FGM Layers Under Thermal Stresses,'' J. Therm. Stresses, **19**, pp. 237–265.

M. Khurram Wadee
e-mail: m.k.wadee@ex.ac.uk
Department of Engineering,
School of Engineering,
Computer Science and Mathematics,
University of Exeter,
North Park Road,
Exeter EX4 4QF, UK

Ciprian D. Coman
Department of Mathematics,
University of Leicester,
University Road,
Leicester LE1 7RH, UK

Andrew P. Bassom
Department of Mathematical Sciences,
School of Engineering,
Computer Science and Mathematics,
University of Exeter,
North Park Road,
Exeter EX4 4QE, UK

Numerical Stability Criteria for Localized Post-buckling Solutions in a Strut-on-Foundation Model

Some stability results are established for localized buckling solutions of a strut-on-foundation model which has an initially unstable post-buckling path followed by a restabilizing property. These results are in stark contrast with those for models with non-restabilizing behavior for which all solutions are unstable under dead-loading conditions. By approximating solutions with a nonperiodic set of functions, the stability of these static solutions can be assessed by examining the nature of the equilibrium using total potential energy considerations. [DOI: 10.1115/1.1757486]

1 Introduction

Elastic stability theory is a well-worked subject in structural mechanics and has proved to be successful in describing complicated nonlinear phenomena through the application of appropriate mathematical techniques. There has naturally been a trend of analyzing questions of increasing sophistication as more and more analytical and computational tools have been brought to bear on the problems. Very often progress has been made by modeling real structures or structural elements with simplified representations made up of a few elements and assuming that loading is conservative. This is particularly true in the study of localized buckling, [1], and, recently, some of the methods developed have been applied directly to more realistic systems in terms of complicated (nonlinear) geometries or material properties, [2,3]. The pioneering work of Koiter [4] and, later, Thompson and Hunt [5] paved the way by identifying total potential energy of an elastic system as being fundamental to the study of equilibrium solutions and their stability. The latter work forwarded two axioms regarding the equilibrium of structural systems described by a finite set of generalized coordinates. The first of these states that an extremum with respect to all the generalized coordinates of the total potential energy represents an equilibrium solution whose stability is governed by the second axiom: this says that an equilibrium is stable only if given by a local minimum of the energy. These two axioms encapsulate the analysis of post-buckling of engineering structures as long as they remain within their elastic regimes and the loading is conservative, i.e., it maintains its magnitude and direction during any deformation.

In recent times attention has turned to the various forms of buckling which better reflect the forms attained by real structures. For example, periodic buckling is found in structures with stable post-buckling behavior such as plates under in-plane compression and is characterized by significant deformation throughout the structure. Localized buckling, on the other hand, can occur in shell-type structures where unstable post-buckling occurs. In localized buckling, although large deformations are limited to a small region, the location of the region is often uncertain and can potentially be at numerous points within the system. As shells are prominent structural elements, the study of their buckling behavior is of importance to engineers. Although localized post-buckling solutions have been identified, relatively little has been deduced concerning the stability of the solutions themselves and it is this we aim to examine here. There have been analyses conducted close to the critical buckling load and others which have examined the general problem but for a limited—one might argue not very realistic—range of nonlinearities (e.g., where only a destabilizing effect is present). Our intention is to relax some of these restrictions and the essence of our stability analysis is based on the classical notions of potential energy and the axioms above.

The total potential energy, V, of a structural system comprises two components viz. the strain energy stored in the structure due to deformations, U, and the work done by the loading P in moving a distance $\mathcal{E}$. This is written as

$$V = U - P\mathcal{E} \tag{1}$$

and if the energy can be written down in terms of a set of n generalized coordinates, Q_i, then equilibrium occurs when

$$\frac{\partial V}{\partial Q_i} = 0, \quad \text{for } i = 1,2,\ldots,n. \tag{2}$$

The most convenient form of the generalized coordinates depends on the context of the structure under consideration. If the post-buckling deflection is expected to be sinusoidal then it seems sensible to decompose deformations in terms of Fourier components. On the other hand, if a structure is long in the sense that the natural length scale of buckling phenomena is small relative to the entire length then some other form may be useful as we shall see below.

Contributed by the Applied Mechanics Division of THE AMERICAN SOCIETY OF MECHANICAL ENGINEERS for publication in the ASME JOURNAL OF APPLIED MECHANICS. Manuscript received by the ASME Applied Mechanics Division, September 25, 2002; final revision, September 22, 2003. Associate Editor: R. C. Benson. Discussion on the paper should be addressed to the Editor, Prof. Robert M. McMeeking, Journal of Applied Mechanics, Department of Mechanical and Environmental Engineering, University of California–Santa Barbara, Santa Barbara, CA 93106-5070, and will be accepted until four months after final publication of the paper itself in the ASME JOURNAL OF APPLIED MECHANICS.

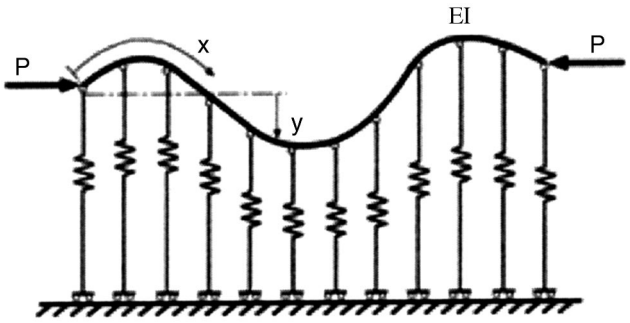

Fig. 1 An elastic strut resting on an elastic foundation acted on by a compressive axial load

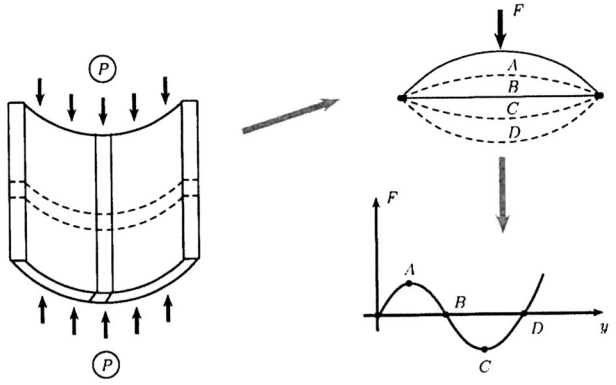

Fig. 2 The von Kármán analogy between the post-buckling response of a cylindrical shell element (panel) and the up-down-up response of a strut-on-foundation model. If the panel is thin, the rings have very little bending stiffness and act as thin arches for normal compressive loads (see the top right diagram). The load-deflection curve for such a structure has the well-known shape shown in the bottom graph.

2 Problem Formulation

We examine the stability of a continuous one-dimensional structure which is both long and admits localized solutions, [6]. Previous work on the stability of post-buckling solutions in this problem has concentrated mostly on analysis close to the bifurcation point but the stability of a post-buckling solution can vary significantly when higher-order nonlinearities modify the effects due to the one dominant at criticality. For the finite length version of our present example Lange and Newell [7] used a double-scale approach to demonstrate that close to criticality the solutions bifurcating from the fundamental state are unstable (see also Fu [8] and Calvo et al. [9] for extension to localized solutions in the infinite-length case). More general results were obtained by Sandstede [10] who examined this model but with only a destabilizing quadratic nonlinearity ($c_2=0$ in (3) below). He showed that such primary solutions are stable for a certain load range for rigid loading only—all solutions are unstable under dead loading. The term primary solution, the form which bifurcates from the critical point, is taken to mean a localized profile whose amplitude decays monotonically from the center of localization and is usually reminiscent of a hyperbolic secant function. With the addition of a restabilizing cubic nonlinearity, however, the situation becomes yet more involved and it is this that we wish to tackle, at least in part, here. This type of solution is known to bifurcate from the flat profile at the buckling load of the strut and, in fact, there are two such solutions which emerge at critical loading. In passing, we note that other forms of localization are possible which are essentially copies of the primary profile glued together, [11]. However, these forms do not emerge from the critical state and are strictly subcritical phenomena. We will focus our interest on primary solutions in the remainder of this study.

The structure to be studied is a long axially compressed strut resting on a nonlinear elastic (Winkler) foundation (see Fig. 1). Let x denote the axial coordinate and y the vertical deflection. The linear bending stiffness of the strut is taken to be EI and it is assumed that the strut rests on a nonlinear elastic foundation which provides a resistive vertical force F per unit length (see [5]). The structure is loaded by a parametric conservative compressive axial force P.

2.1 The Nonlinearities. When it comes to the choice of nonlinearities in our model we have several options. Firstly, if we wish to examine large deflections, then elastica nonlinearities ought to be included, [3,12], but it is then easy to lose sight of the important aspects of the analysis as they can be obscured by complicated algebra. On the other hand, without due care, important terms may be omitted leading to an over-simplified model. We therefore choose a model which is sophisticated enough to admit realistic behavior but also one where the analysis is not obfuscated by extraneous nonlinear terms which do not add to the physical relevance of the model to the order of approximation intended.

To ensure that the structural system undergoes a subcritical bifurcation, the nonlinearity which dominates in this region must have a negative coefficient. This choice means that the bifurcation point is unstable and localized buckling is then favored over its periodic counterpart as it requires less energy to be triggered, [1]. Higher-order positive terms are then required to cause the system to restabilize. In order to model these various features we choose to capture the restabilization phenomenon at the lowest possible orders so that in addition to the linear term in the foundation force a negative quadratic term and a positive cubic term are included. Thus we take

$$F = ky - c_1 y^2 + c_2 y^3 \tag{3}$$

where the foundation constants k, c_1, and c_2 are all positive. This choice of nonlinearity is reminiscent of the analogy used by von Kármán who proposed a similar model to describe the post-buckling response of circular cylindrical shells under axial loading (see Fig. 2). The radial displacement of the shell is asymmetric (i.e., there is more resistance to inward deflection than to outward deflection) and also exhibits the destabilizing-restabilizing behavior given by (3). Although the above choice may seem to be a crude model of the full shell problem, it does have the merit of exhibiting many of the essential features required while maintaining some simplicity. The strain energy of the system is the sum of bending energy, U_B, and energy stored in the foundation, U_F, where

$$U_B = \frac{1}{2} EI \int_{-\infty}^{\infty} y''^2 \mathrm{d}x,$$
$$U_F = \int_{-\infty}^{\infty} \left(\frac{1}{2} k y^2 - \frac{1}{3} c_1 y^3 + \frac{1}{4} c_2 y^4 \right) \mathrm{d}x \tag{4}$$

and a prime denotes differentiation with respect to x. End shortening, $\mathcal{E}$, is taken to be the standard form for a strut with only the leading-order term contributing, i.e.,

$$\mathcal{E} = \frac{1}{2} \int_{-\infty}^{\infty} y'^2 \mathrm{d}x \tag{5}$$

and, inserting all these quantities into the basic form for total potential energy (1), gives

$$V = \int_{-\infty}^{\infty} \left(\frac{1}{2} EI y''^2 - \frac{1}{2} P y'^2 + \frac{1}{2} k y^2 - \frac{1}{3} c_1 y^3 + \frac{1}{4} c_2 y^4 \right) \mathrm{d}x. \tag{6}$$

The governing differential equation is obtained by a straightforward application of the calculus of variations and the system can be readily nondimensionalized by the scalings

$$x \to x \sqrt[4]{\frac{k}{EI}}, \quad P \to \frac{P}{\sqrt{kEI}}, \quad y \to \frac{y}{|c_1|}, \tag{7}$$

to give the key ordinary differential equation for the model,

$$y'''' + Py'' + y - y^2 + c_2 y^3 = 0. \tag{8}$$

Then the only remaining parameters are the axial load, P, and the restabilizing cubic coefficient c_2.

3 Asymptotic Results for Stability

In this section we sketch results for the problem based on a double-scales asymptotic approach, [13]. It will be seen in due course that the theory predicts only unstable solutions and is incapable of capturing the behavior of the system far from the point of bifurcation. This deficiency will be subsequently rectified and a method developed which can track solutions much further into the post-buckling regime. Moreover, our strategy is capable of describing accurately both the buckled shapes and stability characteristics of the structure under the more general dead loading conditions.

3.1 Linear Eigenvalue Analysis and Basic Perturbation Results. To isolate the value of the parametric loading P at which the flat fundamental (unbuckled) state loses stability it suffices to examine the linearized form of (8) so that the quadratic and cubic terms are omitted. Then, for positive P, three regions with distinct behaviors can be identified. When $P > P^{\mathrm{C}} = 2$, the four eigenvalues of the truncated problem are purely imaginary and are symmetrically spaced about the real axis. The deflection in this case is thus expected to be periodic in x. As P is reduced, the pairs either side of the real axis coalesce when $P = P^{\mathrm{C}}$ and the system undergoes a Hamiltonian-Hopf bifurcation, [1]. Finally, once $P < P^{\mathrm{C}}$, the two pairs split symmetrically into the four quadrants of the complex plane with the forms $\pm\alpha \pm \mathrm{i}\omega$ where

$$\alpha = \sqrt{\frac{1}{2} - \frac{P}{4}}, \quad \omega = \sqrt{\frac{1}{2} + \frac{P}{4}}. \tag{9}$$

These parts of the eigenvalues of the linearized problem are important in motivating the perturbation expansion below and in particular, it is observed that the real part, α, is small when P is close to P^{C}.

In the vicinity of P^{C} a double-scale perturbation analysis reveals the behavior of the emergent primary solutions. To this end we define a small perturbation parameter, ε, which measures evolution from the critical state such that

$$\varepsilon^2 \equiv P^{\mathrm{C}} - P = 2 - P \tag{10}$$

whereupon the real and imaginary parts of the linear eigenvalues (9) become

$$\alpha = \frac{\varepsilon}{2}, \quad \omega = 1 - \frac{\varepsilon^2}{8} + \mathcal{O}(\varepsilon^4). \tag{11}$$

The amplitude of the solutions varies on a slower scale than the period of the deflection at $P = P^{\mathrm{C}}$ and so we define a slow space scale such that $X = \varepsilon x$. By expressing y as

$$y = \sum_{i=0}^{\infty} \{A_i(X)\cos i(\omega x + \phi_0) + B_i(X)\sin i(\omega x + \phi_0)\}, \tag{12}$$

where A_i and B_i are slowly varying amplitudes and ϕ_0 is a phase angle, the governing Eq. (8) is transformed into a partial differential equation, [6]. If each amplitude is also expressed as a power series in ε

$$A_i(X) = \sum_{j=1}^{\infty} \varepsilon^j A_i^{(j)}(X), \quad B_i(X) = \sum_{j=1}^{\infty} \varepsilon^j B_i^{(j)}(X) \tag{13}$$

and progressively higher-order coefficients of ε extracted, we derive a set of equations which reveal the behavior of the amplitudes in the formal expansions of each A_i and B_i. The first equation arising from the double-scale approach which gives non-trivial information concerns the amplitude of the fundamental mode at the first-order $A_1^{(1)}$ and is

$$4\frac{\mathrm{d}^2 A_1^{(1)}}{\mathrm{d}X^2} - A_1^{(1)} + \left(\frac{19}{18} - \frac{3}{4}c_2\right) A_1^{(1)3} = 0. \tag{14}$$

For bounded localized solutions the coefficient of the cubic term must be positive which yields the condition $c_2 < 38/27$, [14]. For larger c_2 the asymptotic theory predicts that localized solutions cannot exist and this result ties in with the study of Woods and Champneys [15] who used a normal forms type of analysis for the restabilizing strut problem. Apart from this condition on c_2, Eq. (14) is only expected to be valid very close to the critical point at $P = P^{\mathrm{C}}$ and gives no clue as to how the system may evolve when ε is not small.

The system we are studying is *reversible* which means that there is an involution which stems from invariance of solutions to the transformation $y(x) \to y(-x)$. Also, any solution can be freely translated along the x-axis and so we can seek solutions on the semi-infinite domain $0 \leqslant X < \infty$ with the imposition of the so-called symmetric section condition $y'(0) = y'''(0) = 0$. The slow-space analysis completely decouples the fast variation from the slow one, [13], and, in particular, suggests that the phase ϕ_0 in (12) is arbitrary. However, a more advanced analysis based upon the ideas of exponential asymptotics reveals that for primary localization ϕ_0 is not free but rather is restricted to the discrete values $\phi_0 = 0$ or π, [16,17]. This reinforces the importance of the symmetric section which means that all primary solutions to this system must be even functions about their own centers, [6], and

$$A_1^{(1)} = 6\left(19 - \frac{27}{2}c_2\right)^{-1/2} \operatorname{sech}\frac{X}{2} = 2\sqrt{\frac{2}{3}}\,\delta^{-1/2}\operatorname{sech}\frac{X}{2} \tag{15}$$

where, for later convenience, we adopt the definition $\delta \equiv 38/27 - c_2$.

The asymptotic form in ascending powers of ε to the formal double-scale approximation of the static system is, [17],

$$\begin{aligned} y = {} & \varepsilon a_1 \operatorname{sech}\frac{X}{2}\cos(\omega x + \phi_0) + \varepsilon^2\left(a_2 \operatorname{sech}\frac{X}{2}\tanh\frac{X}{2}\sin(\omega x + \phi_0)\right. \\ & \left. + \frac{1}{2}a_1^2\left(1 + \frac{1}{9}\cos 2(\omega x + \phi_0)\right)\operatorname{sech}^2\frac{X}{2}\right) \\ & + \varepsilon^3\left(a_3 \operatorname{sech}\frac{X}{2}\cos(\omega x + \phi_0) + a_4 \operatorname{sech}^3\frac{X}{2}\cos(\omega x + \phi_0)\right. \\ & + \frac{1}{27}a_1(4a_1 + 3a_2)\operatorname{sech}^2\frac{X}{2}\tanh\frac{X}{2}\sin 2(\omega x + \phi_0) \\ & \left. + \frac{(27\delta - 32)}{6912}a_1^3 \operatorname{sech}^3\frac{X}{2}\cos 3(\omega x + \phi_0)\right) + \mathcal{O}(\varepsilon^4), \end{aligned} \tag{16}$$

where the constants $a_1 - a_4$ are given by

$$a_1 = 2\sqrt{\frac{2}{3}}\,\delta^{-1/2},$$

$$a_2 = \delta^{-1/2}\left(\sqrt{\frac{3}{2}} + \frac{16}{81}\sqrt{\frac{2}{3}}\,\delta^{-1}\right),$$

$$a_3 = \delta^{-1/2}\left(-\frac{317}{72}\sqrt{\frac{1}{6}} - \frac{1252}{81}\sqrt{\frac{2}{3}}\,\delta^{-1} + \frac{10432}{729}\sqrt{\frac{2}{3}}\,\delta^{-2}\right),$$

$$a_4=\delta^{-1/2}\left(-\frac{307}{72}\sqrt{\frac{1}{6}}-\frac{2296}{243}\sqrt{\frac{2}{3}}\,\delta^{-1}-\frac{46912}{6561}\sqrt{\frac{2}{3}}\,\delta^{-2}\right).$$

It is fortunate that the solutions of higher-order equations arising in the perturbation expansion can also be found explicitly.

3.2 Analysis of Dynamical Stability. In order to assess asymptotic stability, particularly under dead loading conditions, it is necessary to add an acceleration term to the governing equation of the static model. We proceed as outlined in Calvo et al. [9] whereupon

$$m\ddot{y}+EIy''''+Py''+ky-c_1y^2+c_2y^3=0 \tag{17}$$

where m is the mass per unit length of the strut, a dot denotes partial differentiation with respect to time, and a prime is now a partial spatial derivative. A nondimensional version of this equation can be written as

$$\ddot{y}+y''''+Py''+y-y^2+c_2y^3=0. \tag{18}$$

To carry out a double-scale analysis on this equation, it is necessary to define a slow space scale $X=\varepsilon x$ as before and we also need to introduce a slow time scale such that $T=\varepsilon t$. The amplitudes of the Fourier modes in (12) and (13) are generalized to be functions of both X and T so that $A_i^{(j)}=A_i^{(j)}(X,T)$ and $B_i^{(j)}=B_i^{(j)}(X,T)$. Following the procedure described earlier, it is found that the lowest-order equation which governs the amplitudes is now

$$\frac{\partial^2A_1^{(1)}}{\partial T^2}=4\frac{\partial^2A_1^{(1)}}{\partial X^2}-A_1^{(1)}+\frac{3}{4}\delta A_1^{(1)3} \tag{19}$$

which encapsulates the static version of the equation when time derivatives are absent and so has the solution given in (15). In addition if a small dynamic disturbance is present such that

$$A_1^{(1)}(X,T)=A(X)+a(X)e^{\lambda T}, \tag{20}$$

where $A(X)$ is the function defined in (15) then substituting (20) in (19) and linearizing in $a(X)$ gives

$$4\frac{\mathrm{d}^2a}{\mathrm{d}X^2}+\left(6\,\mathrm{sech}^2\frac{X}{2}-1-\lambda^2\right)a=0. \tag{21}$$

The above equation has an unstable eigenfunction $a=\mathrm{sech}^2\,X/2$, which is still localized in space, with eigenvalue $\lambda=\sqrt{3}$. Thus the original solution will grow in time with exponential rate $\exp(\sqrt{3}\varepsilon t)$. It is important to note that the above analysis reveals that the instability is independent of the restabilization present in the structure (with the caveat that $c_2<38/27$).

This double-scale approach is unable to account for higher-order effects as it is restricted to the vicinity of $P=P^{\mathrm{C}}$ so that ε is small. It would be desirable to find some method which, although based on a simple mode-based approach, did have the added ability to describe phenomena further into the subcritical region.

4 Analysis Far From the Bifurcation Point

In order to analyze the behavior of the structural system "far" from the bifurcation point, an alternative strategy needs to be adopted. We necessarily need to turn to a numerical method. A suitable candidate which is capable of both determining approximate equilibrium solutions and their stability is a modified Rayleigh-Ritz procedure which can be motivated by the form of the solution garnered from the slow-space expansion. Conventional Rayleigh-Ritz analysis is suitable for periodic analysis which stems from the assumption that amplitudes of the constituent modes are constant in X. That Rayleigh-Ritz ideas can be adapted to the study of *localized* post-buckling phenomena was first demonstrated by Wadee et al. [13] for the case of quadratic nonlinearity ($c_2=0$). They showed that the procedure is able to track primary solutions from very close to P^{C} right down to zero load. Furthermore, for the case $c_2>0$, it is possible to follow accurately solutions into and beyond the first restabilizing region, [14].

The double-scale solutions, though not very accurate when examining the behavior of the structure other than very close to criticality, do nevertheless have some desirable properties. For example, they decay exponentially in both directions about an assumed center at a rate dictated by the real part of the linear eigenvalues, ($\pm\alpha$ in (9)). Any approximate localized solution, even away from the critical point, ought to incorporate such behavior. Thus we use a procedure involving two steps culminating in a hybrid technique. Firstly, we take the form of the double-scale solution but treat the amplitudes of each mode as unknown. Furthermore, the accuracy of the solutions is enhanced by allowing the shape factors α and ω to be variables as well. Thus our assumption is that the primary solution has the form

$$\begin{aligned}y=&A_1\,\mathrm{sech}\,A_7x\cos A_8x+A_2\,\mathrm{sech}^2\,A_7x+A_3\,\mathrm{sech}^2\,A_7x\cos 2A_8x\\&+A_4\,\mathrm{sech}\,A_7x\tanh A_7x\sin A_8x+A_5\,\mathrm{sech}^3\,A_7x\cos A_8x\\&+A_6\,\mathrm{sech}^3\,A_7x\tanh A_7x\sin A_8x\end{aligned} \tag{22}$$

for some constants A_1-A_8. The first five terms in (22) are immediately motivated by the double-scale solution (16). Most higher-order harmonic functions are not included in (22) as the amplitudes of such terms tend to remain small for a range of the post-buckling regime. One way of viewing this technique is to recognize that in many perturbation expansions the functional form of the higher-order terms can be well approximated by a combination of the lower-order terms. Thus, much of the effect of higher-order terms can be achieved by applying our hybrid Rayleigh-Ritz approach to a relatively small number of lower-order functions. However, one extra term (with coefficient A_6) has been included which would arise if the expansion in (16) were to be taken to higher order, [14]. In numerical terms, this coefficient is found to grow siginificantly far from criticality and so its inclusion seems appropriate.

Our experience has shown that (22) constitutes a reasonable compromise between the conflicting factors of accuracy and ease of computation. Application of a similar hybrid technique but using a Galerkin procedure to describe nonperiodic solutions has been reported by Geer and Andersen [18]. They were able to put the use of nonperiodic functions to span the solution space on a firm footing and it has been demonstrated that the Galerkin and Rayleigh-Ritz procedures give identical results in the present elastic strut model, [19].

By inserting (22) into the total potential energy functional (6), we deduce that $V=V(A_i)$, where $i=1,2,\ldots,8$. Naturally, finding an explicit form of the expression is a long-winded exercise so we turned to the software Mathematica [20]. The requisite integrals were calculated using contour integration in the complex plane around appropriate closed paths and exact expressions were obtained, [13]. Equilibrium is determined by the solution of $\partial V/\partial A_i=0$ for $i=1,2,\ldots,8$; an alternative view of this is the specification that the various modes should be mutually orthogonal. MATHEMATICA was used to evaluate these derivatives and the resulting set of nonlinear algebraic equations were then solved numerically using a multidimensional Newton-Raphson procedure, [21]. A requirement of the scheme, which turns out to be a bonus, is that second derivatives of V are required and this allows us easily to find out the nature of the equilibrium states (extrema of V).

In accordance with the theory of elastic stability, a stable equilibrium path is determined by a local minimum of the energy functional, [5]. With our modal description with the amplitudes now known, it is sufficient to show that the Hessian matrix of V is positive definite to ensure stability. Thus all eight eigenvalues of

this matrix must be greater than zero but, rather than showing these individually, we depict the determinant of the matrix where the criterion

$$\Delta = \det\left(\left[\frac{\partial^2 V}{\partial A_i \partial A_j}\right]\right) > 0, \quad \text{for } i,j = 1,2,\ldots,8 \tag{23}$$

is a *necessary* condition for stability.

The second derivatives of V with respect to the variables $A_1, \ldots, A_8$ are needed to find the numerical solutions to the equilibrium problem and thereby find Δ. As the positive definiteness condition is another way of expressing the second axiom of elastic stability, it is sufficient to demonstrate the stability or otherwise of primary localized solutions at least to the level of approximation assumed in the Rayleigh-Ritz procedure.

5 Numerical Comparisons

It has been noted earlier that two paths bifurcate at $P = P^C$ which correspond to the two permitted values of phase angle, $\phi_0 = 0$ or π between the center of the slowly varying amplitude and the sinusoidal oscillation, [17]. It turns out that both of these paths can be followed from close to criticality by the Rayleigh-Ritz procedure. Formerly, only the branch corresponding to $\phi_0 = 0$ has been tracked, [13,14], but in addition here we demonstrate that the other one can be followed with a similar degree of accuracy.

Our approximate solutions are compared directly against numerical solutions obtained using the boundary value solver AUTO97, [22]. It should be noted that whereas finding localized solutions to the strut model is straightforward using this program, it is nonetheless incapable of addressing the issue of stability. Thus a key attraction of our hybrid approach is that not only can it follow localized solutions but it can also furnish important information regarding the stability of these solutions.

5.1 Quadratic Nonlinearity Only: $c_2 = 0$. Before proceeding to the case of a restabilizing foundation, we present the stability calculation for the quadratic foundation case $F = y - y^2$ which is known to have unstable solutions under dead loading conditions, [10]. The procedure adopted to continue a numerical solution in P was as follows. An initial solution was found near criticality, typically at $P \approx 1.9$, using a shooting technique, [6]. This was then fed into AUTO97 as an initial solution which could be tracked either towards P^C or zero. In practical terms, numerical solutions very close the critical point do not converge very well and so they are only shown up to about $P = 1.96$. The Rayleigh-Ritz solver requires a good initial guess for convergence to be assured and then these solutions can be tracked in P. Around limit points, however, continuation in one of the amplitudes is possible as described in Wadee and Bassom [14] until the path on the other side of the fold is picked up.

As the solutions are supposedly unstable, we would expect the energy not to be a minimum throughout. Figure 3 shows that $\Delta < 0$ for the range of P shown although it approaches zero quite quickly. Thus we seem to have successfully established a quantitative criterion to judge the stability of primary localized solutions. Details of the post-buckling solutions referred to here can be found in Wadee et al. [13].

5.2 Restabilizing Case: $0 < c_2 < 38/27$. The Rayleigh-Ritz analysis was carried out for three positive values of c_2 which give rise to different behaviors of the foundation (see Fig. 4). The first, $c_2 = 0.24$, represents a case where the foundation force, F, becomes negative for a range of positive y before bottoming out. In the second case ($c_2 = 0.3$), the foundation response is always resistive but there is a negative stiffness region for positive y and finally, the last case ($c_2 = 0.4$) is one for which the foundation always resists deflection and its stiffness always remains positive.

The bifurcation diagram for a restabilizing model with c_2 is more complex than for the quadratic-only counterpart. Two paths still bifurcate from P^C but then both undergo an infinite number of oscillations between two limiting subcritical parameter values, [15]. This phenomenon is called *snaking* and the initially localized profiles eventually evolve into a periodic form.

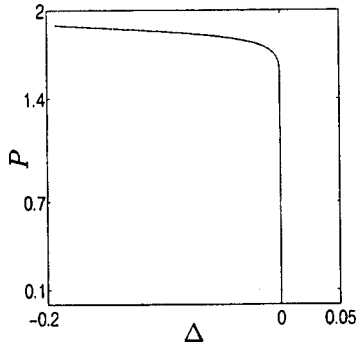

Fig. 3 Variation of Δ (Eq. (23)) with load P for the model with only a quadratic destabilizing nonlinearity ($c_2 = 0$). Sample values: $\Delta(1.0) = -9.6\times10^{-7}$ and $\Delta(0.0) = -7.5\times10^{-10}$.

The three restabilization values chosen give rise to qualitatively different behaviors from a physical perspective and we assess the accuracy of our approximate scheme against all three. The results are summarized in Figs. 5–7. The bifurcation diagrams show good agreement between numerics and the Rayleigh-Ritz procedure well into the first restabilization region as is confirmed by the selected eigensolutions on the branch corresponding to primary localized solutions centered at a trough (or $\phi_0 = \pi$) shown in Fig. 6 (see Wadee and Bassom [14] for eigensolutions on the other branch, $\phi_0 = 0$). For the smallest value of c_2, the range between the maxima and minima of the snaking curve shown in Fig. 5(*a*) is large. As c_2 is increased, the range decreases and both extrema also get progressively closer to $P = P^C$ (Fig. 5(*b*) and (*c*)). The determinant of the Hessian of V, Δ, for each branch in Fig. 5 is shown in Fig. 7. The points identified as O_p and O_t on the curves denote the positions on the branches $\phi_0 = 0$ and π, respectively, where Δ changes sign. These locations correspond precisely with the position of the folds where the solutions evolve from being unstable to stable.

In all three cases depicted the solutions are accurately tracked around the first limit point after which the solutions become stable. The change over from stability can readily be identified in Fig. 7 where Δ can be seen to change sign when it is plotted against end shortening although there are seemingly flat regions in the case of $c_2 = 0.24$ and 0.3. This backs up the observation of Maddocks [23] who has postulated that during evolution of static solutions under the variation of a parameter, their instability undergoes a transformation to stability (or vice versa) if the path encounters a limit point. The swapping from instability to stability

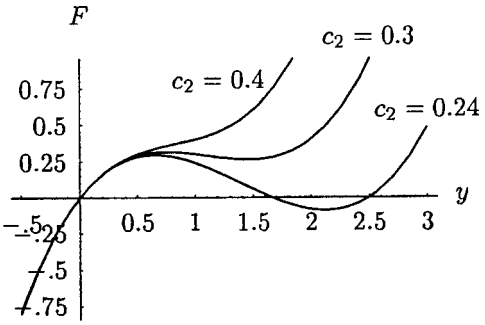

Fig. 4 The variation of foundation force $F = y - y^2 + c_2 y^3$ against lateral deflection y for various values of the coefficient c_2

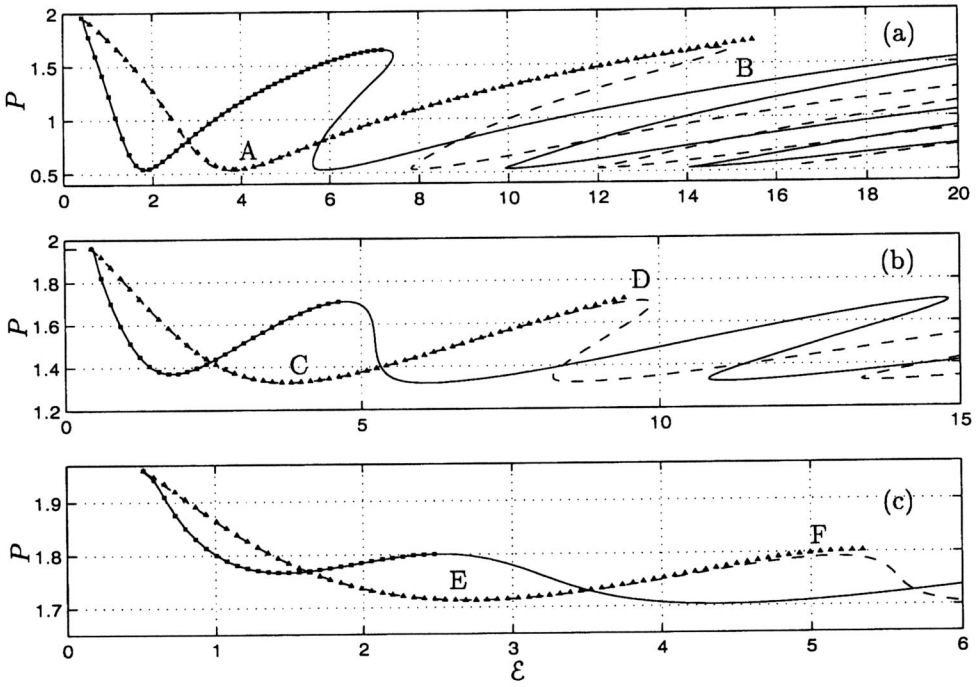

Fig. 5 Initial bifurcation diagrams depicting the post-buckling behavior of primary localized solutions of the restabilizing strut model with (*a*) $c_2=0.24$; (*b*) $c_2=0.3$, and (*c*) $c_2=0.4$. Numerical (AUTO97) solutions for peak-centred ($\phi_0=0$) and trough-centered ($\phi_0=\pi$) orbits are shown against end-shortening, $\mathcal{E}$, with solid and dashed lines, respectively. Discrete points show solutions obtained using the nonperiodic Rayleigh-Ritz procedure.

according to the classification of the extremum matches closely that expected for both forms of localized solutions which bifurcate from the critical point. (Of course, if pairs of negative eigenvalues existed this would also give a positive determinant but we have found only positive eigenvalues in that region.)

Further into the post-buckling regime the stable region is also accurately tracked in all the cases and the second fold is detected as is evidenced by Δ rapidly approaching zero again indicating the solution is once again becoming unstable. After this point, however, the accuracy of the solution diminishes rapidly and is not

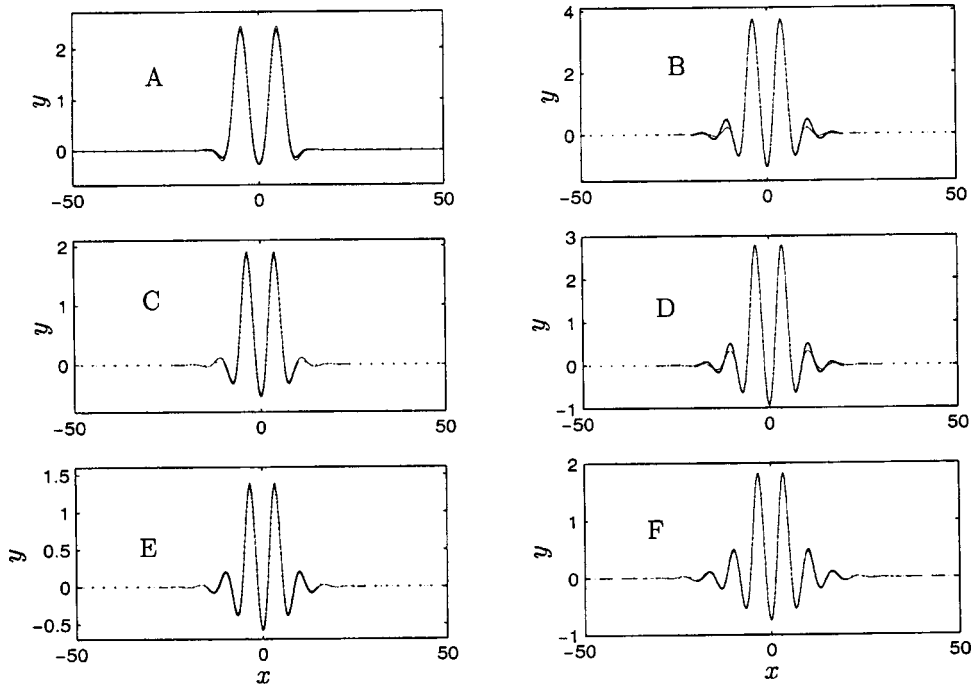

Fig. 6 Comparison of buckling solutions obtained using AUTO97 (solid line) and the Rayleigh-Ritz method (discrete points) for the fold points A–F identified on the $\phi_0=\pi$ branches in Fig. 5

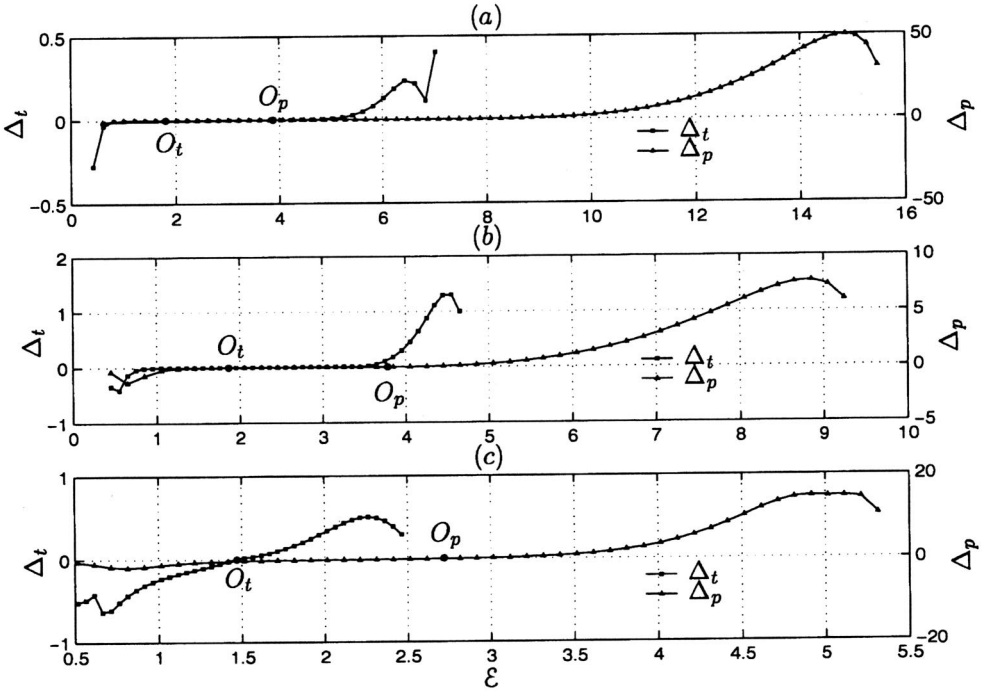

Fig. 7 Variation of the determinant of the Hessian of the energy function, Δ, with end-shortening for various values of c_2: (*a*) 0.24; (*b*) 0.3; (*c*) 0.4. The peak-centered branch is labeled Δ_p and the trough-centered branch is labeled Δ_t. The fold point on the corresponding bifurcation diagram in Fig. 5 is identified with a large dot.

shown here. The infinite snaking of the two branches eventually leads to a periodic solution—each turning point corresponds to the growth of the amplitude of another pair of sinusoidal oscillations either side of the center of localization eventually to the size of the central deflection, [15].

The nonperiodic Rayleigh-Ritz procedure is capable of detecting the early localized behavior of the system. On the other hand, an accurate representation of the limiting post-buckling behavior can be obtained by a straightforward application of conventional periodic Rayleigh-Ritz analysis. The key feature to note about the periodic solution evolving from the localized one is that they both have the same energy corresponding to the so-called *Maxwell criterion* in the sense described by Hunt et al. [24]. The mechanism of the transformation is understood and now some quantitative results about stability have also been established which confirm other studies, [25].

6 Conclusions

In this work we have established a numerical method to assess the stability of primary (single-humped) localized solutions which emerge from the critical state of a strut-on-foundation model. The technique has successfully predicted the stability (or otherwise) of such solutions both for a simple destabilizing nonlinearity and for the case in which the initially unstable path is restabilized by higher-order nonlinear effects. Whereas asymptotic analysis fails to pick up any change in stability due to restabilization, the method presented here has the attractive feature of not only representing the solutions accurately but is also able to track them around folds as the loading parameter is varied and to give a quantitative assessment of where their stability characteristics change. By using a solution of the form originating from a double-scale analysis, we have been able to continue accurately post-buckling solutions under conditions of dead loading far beyond the region in which the perturbation expansion is valid. Broadly speaking, the assessment of stability is based on writing the total potential energy in terms of a set of nonperiodic modes and then determining whether the equilibrium points (extrema) are maxima or minima of potential energy with respect to amplitudes of these functions. Agreement with independent numerical solutions and previously known theoretical results is excellent well into the post-buckling of the strut model.

The study of the stability of localized buckling is still in its relative infancy. An important case that would be of considerable interest is the stability of localized solutions in the elastoplastic model developed in [3]. By adopting an unstable elastoplastic constitutive law, our analysis has revealed that structural localization is, roughly speaking, a precursor of material instabilities via a bifurcating branch of unstable solutions for the particular model adopted therein.

The case highlighted here is that of dead loading where an applied force is the controlling parameter. The rigid loading case would be studied by taking U as in (4) and minimizing it subject to the integral constraint $\mathcal{E}=$const. (see (5)). This imposition restricts behavior of the structure such that some regimes in which solutions are unstable under dead loading are in fact stable under conditions of rigid loading, [10,25]. Fully numerical work shows that the solution paths extend further into the regime and that after a few oscillations of the snaking curve, the strut becomes unstable under rigid as well as dead loading—where the curve bends back on itself. Such behavior is reminiscent of the severe post-buckling of shells and equilibrium positions on these parts of the curve are not physically realizable. However, in the early post-buckling evolution a study of the subtly distinct problem of rigid loading may prove enlightening from the perspectives of engineering and applied mechanics.

Acknowledgment

CDC was supported by a UK Engineering and Physical Sciences Research Council Grant (No. GR/N05666/01).

We are grateful for the comments of the referees which have helped to improve the presentation of this paper.

References

[1] Hunt, G. W., Bolt, H. M., and Thompson, J. M. T., 1989, ''Structural Localization Phenomena and the Dynamical Phase-Space Analogy,'' Proc. R. Soc. London, Ser. A, **425**, pp. 245–267.

[2] Champneys, A. R., Hunt, G. W., and Thompson, J. M. T., eds., 1997, ''Localization and Solitary Waves in Solid Mechanics,'' Philos. Trans. R. Soc. London, Ser. A, **355**, pp. 2073–2213.

[3] Coman, C. D., Bassom, A. P., and Wadee, M. K., 2003, ''Elasto-Plastic Localized Responses in One-Dimensional Structural Models,'' J. Eng. Math., to appear.

[4] Koiter, W. T., 1967, ''On the Stability of Elastic Equilibrium,'' Ph.D. thesis, Technological University of Delft, Holland, 1945; English translation issued by NASA, Tech. Trans., **F10**, p. 833.

[5] Thompson, J. M. T., and Hunt, G. W., 1973, *A General Theory of Elastic Stability*, John Wiley and Sons, London.

[6] Hunt, G. W., and Wadee, M. K., 1991, ''Comparative Lagrangian Formulations for Localized Buckling,'' Proc. R. Soc. London, Ser. A, **434**, pp. 485–502.

[7] Lange, C. G., and Newell, A. C., 1971, ''The Post-Buckling Problem for Thin Elastic Shells,'' SIAM (Soc. Ind. Appl. Math.) J. Appl. Math., **21**(4), pp. 605–629.

[8] Fu, Y. B., 2001, ''Perturbation Methods and Nonlinear Stability Analysis,'' *Nonlinear Elasticity*, Y. B. Fu and R. W. Ogden, eds., Cambridge University Press, Cambridge, UK, pp. 345–391.

[9] Calvo, D. C., Yang, T.-S., and Akylas, T. R., 2000, ''On the Stability of Solitary Waves With Decaying Oscillatory Tails,'' Proc. R. Soc. London, Ser. A, **456**, pp. 469–487.

[10] Sandstede, B., 1997, ''Instability of Localized Buckling Modes in a One-Dimensional Strut Model,'' Philos. Trans. R. Soc. London, Ser. A, **355**, pp. 2083–2097.

[11] Wadee, M. K., and Bassom, A. P., 1999, ''Effects of Exponentially Small Terms in the Perturbation Approach to Localized Buckling,'' Proc. R. Soc. London, Ser. A, **455**, pp. 2351–2370.

[12] Hunt, G. W., Wadee, M. K., and Shiacolas, N., 1993, ''Localized Elasticæ for the Strut on the Linear Foundation,'' ASME J. Appl. Mech., **60**(4), pp. 1033–1038.

[13] Wadee, M. K., Hunt, G. W., and Whiting, A. I. M., 1997, ''Asymptotic and Rayleigh-Ritz Routes to Localized Buckling Solutions in an Elastic Instability Problem,'' Proc. R. Soc. London, Ser. A, **453**, pp. 2085–2107.

[14] Wadee, M. K., and Bassom, A. P., 2000, ''Restabilization in Structures Susceptible to Localized Buckling: An Approximate Method for the Extended Post-Buckling Regime,'' J. Eng. Math., **38**(1), pp. 77–90.

[15] Woods, P. D., and Champneys, A. R., 1999, ''Heteroclinic Tangles and Homoclinic Snaking in the Unfolding of a Degenerate Reversible Hamiltonian Hopf Bifurcation,'' Physica D, **129**, pp. 147–170.

[16] Yang, T.-S., and Akylas, T. R., 1997, ''On Asymmetric Gravity-Capillary Solitary Waves,'' J. Fluid Mech., **330**, pp. 215–232.

[17] Wadee, M. K., Coman, C. D., and Bassom, A. P., 2002, ''Solitary Wave Interaction Phenomena in a Strut Buckling Model Incorporating Restabilization,'' Physica D, **163**, pp. 26–48.

[18] Geer, J. F., and Andersen, C. M., 1989, ''A Hybrid Perturbation Galerkin Technique With Applications to Slender Body Theory,'' SIAM (Soc. Ind. Appl. Math.) J. Appl. Math., **49**(2), pp. 344–361.

[19] Wadee, M. K., Higuchi, Y., and Hunt, G. W., 2000, ''Galerkin Approximations to Static and Dynamic Localization Problems,'' Int. J. Solids Struct., **37**(22), pp. 3015–3029.

[20] Wolfram Research Inc., 1999, MATHEMATICA: *A System for Doing Mathematics by Computer*, Version 4, Wolfram Research, Champaign, IL.

[21] Press, W. H., Flannery, B. P., Teukolsky, S. A., and Vetterling, W. T., 1992, *Numerical Recipes in C. The Art of Scientific Programming*, 2nd Ed., Cambridge University Press, New York.

[22] Doedel, E. J., Champneys, A. R., Fairgrieve, T. F., Kuznetsov, Y. A., Sandstede, B., and Wang, X., 1997, AUTO97: Continuation and Bifurcation Software for Ordinary Differential Equations; available via anonymous ftp from ftp://ftp.cs.concordia.ca/pub/doede1/auto.

[23] Maddocks, J. H., 1987, ''Stability and Folds,'' Arch. Ration. Mech. Anal., **99**(4), pp. 301–328.

[24] Hunt, G. W., Peletier, M. A., Champneys, A. R., Woods, P. D., Wadee, M. A., Budd, C. J., and Lord, G. J., 2000, ''Cellular Buckling in Long Structures,'' Nonlinear Dyn., **21**(1), pp. 3–29.

[25] Peletier, M. A., 2001, ''Sequential Buckling: A Variational Analysis,'' SIAM J. Math. Anal., **32**, pp. 1142–1168.

F. Ma
Fellow ASME

H. Zhang

Department of Mechanical Engineering,
University of California,
Berkeley, CA 94720

A. Bockstedte
Mechanics and Ocean Engineering,
Technical University of Hamburg-Harburg,
D-21073 Hamburg, Germany

G. C. Foliente

P. Paevere

CSIRO Manufacturing and Infrastructure
Technology,
Highett,
Victoria 3190, Australia

Parameter Analysis of the Differential Model of Hysteresis

The extended Bouc-Wen differential model is one of the most widely accepted phenomenological models of hysteresis in mechanics. It is routinely used in the characterization of nonlinear damping and in system identification. In this paper, the differential model of hysteresis is carefully reexamined and two significant issues are uncovered. First, it is shown that the unspecified parameters of the model are functionally redundant. One of the parameters can be eliminated through suitable transformations in the parameter space. Second, local and global sensitivity analyses are conducted to assess the relative sensitivity of each model parameter. Through extensive Monte Carlo simulations, it is found that some parameters of the hysteretic model are rather insensitive. If the values of these insensitive parameters are fixed, a greatly simplified model is obtained.
[DOI: 10.1115/1.1668082]

1 Introduction

Structures exhibit inelastic behavior under severe cyclic loads associated with earthquakes, high winds, and recurrent waves. When the restoring force is plotted against the structural deformation, inelastic behavior often manifests itself in the form of hysteresis loops. The area enclosed by each loop is a measure of the energy dissipated over a complete cycle as the result of internal friction within the structure. In general terms, hysteresis refers to the hereditary and the memory nature of an inelastic system, in which the restoring force depends not only on the instantaneous deformation but also on the past history of deformation. Mechanical and structural systems capable of dissipating appreciable energy tend to possess large hysteresis loops. Hysteresis is thus particularly important in depicting the damping characteristics of inelastic systems. Yet, a fundamental and comprehensive theory of hysteresis has not been developed. In order to address practical problems in the contemporary design and analysis of structures, phenomenological models of hysteresis are often used.

In the past few decades, various phenomenological models of hysteresis have been proposed. One of the most widely accepted models is a differential model originally proposed by Bouc [1] and subsequently generalized by Wen [2] and other researchers. In this model the restoring force and deformation are connected through a nonlinear differential equation containing unspecified parameters. By choosing the parameters suitably, it is possible to generate a large variety of different shapes of the hysteresis loops. The classical Bouc-Wen model contains only five loop parameters. The generalized differential model in its present form contains 13 parameters; it can account for strength degradation, stiffness degradation, and even pinching characteristics of an inelastic structure. As the differential model becomes increasingly popular, questions concerning the complexity and consistency of the model are brought up more frequently.

The extended Bouc-Wen model of hysteresis is carefully reexamined in this paper. Two significant issues are uncovered. First, it is shown that the unspecified parameters of the model are functionally redundant. In either the classical or contemporary version, one of the model parameters can be eliminated through suitable transformations in the parameter space. The number of model parameters can thus be reduced without affecting the system response. Second, local and global sensitivity analyses are carried out on the differential model of hysteresis. The global analysis employed is a probabilistic method recently expounded by Sobol and it can account for the mutual interactions of the parameters. Through extensive Monte Carlo simulations, the relative sensitivity of each parameter is assessed. It is found that some parameters of the model are rather insensitive. These insensitive parameters should perhaps be set to constant values, thereby resulting in a greatly simplified hysteretic model.

The two issues discussed above are indeed significant in updating the differential model. In the literature, there are many deductions based upon the extended Bouc-Wen model of hysteresis. In light of this update, some of these deductions may no longer be valid unless modified. The organization of this paper is as follows. In Section 2, the differential model of hysteresis in both its classical and modern forms are reviewed. The reduction of unspecified parameters by transformation is then explained in Section 3. Sensitivity analysis of the differential model is reported in Section 4. Finally, a summary of findings is provided in Section 5. As the differential model of hysteresis becomes increasingly popular in theory and applications, it is hoped that the streamlining and reformulation reported in this paper will allow it to be used with added confidence in the years to come.

2 Differential Hysteresis

To describe the differential model of hysteresis, consider an inelastic system possessing a finite number of degrees-of-freedom. Suppose the equation of motion can be decoupled and, along the direction of the generalized coordinate u, the system is governed by

Contributed by the Applied Mechanics Division of THE AMERICAN SOCIETY OF MECHANICAL ENGINEERS for publication in the ASME JOURNAL OF APPLIED MECHANICS. Manuscript received by the ASME Applied Mechanics Division, Oct. 17, 2002; final revision, Sept. 19, 2003. Associate Editor: A. A. Ferri. Discussion on the paper should be addressed to the Editor, Prof. Robert M. McMeeking, Journal of Applied Mechanics, Department of Mechanical and Environmental Engineering University of California–Santa Barbara, Santa Barbara, CA 93106-5070, and will be accepted until four months after final publication of the paper itself in the ASME JOURNAL OF APPLIED MECHANICS.

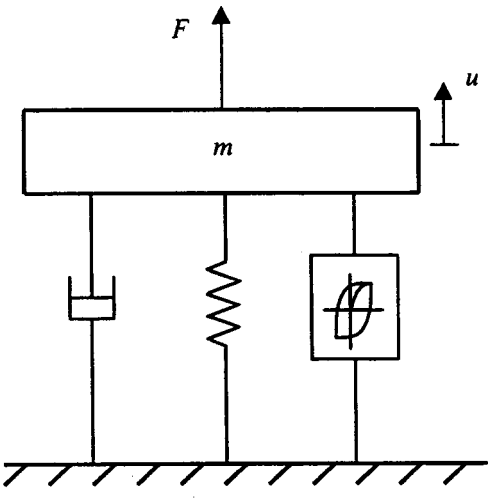

Fig. 1 Schematic diagram of an inelastic system

$$m\ddot{u}+c\dot{u}+R_T(u,z)=F(t) \tag{1}$$

where u is the system displacement, z is an imaginary hysteretic displacement, and m, c are, respectively, the mass and damping coefficients. It is assumed that the excitation $F(t)$ is cyclic. In the development of the differential model, the total restoring force $R_T(u,z)$ is separated into an elastic and a hysteretic component by

$$R_T(u,z)=\alpha ku+(1-\alpha)kz \tag{2}$$

where k is the stiffness coefficient and $0\leqslant\alpha\leqslant 1$ is a weighting parameter. Obviously, the restoring force is purely hysteretic if $\alpha=0$; it is purely elastic if $\alpha=1$. A diagrammatic representation of the system is given in Fig. 1.

Basic hystersis loops may be generated if the hysteretic displacement z and the total displacement u are connected by the nonlinear differential equation, [2],

$$\dot{z}=A\dot{u}-\beta|\dot{u}||z|^{n-1}z-\gamma\dot{u}|z|^n. \tag{3}$$

There are five unspecified loop parameters A, α, β, γ, n in Eqs. (1) and (3), which represent the classical Bouc-Wen model. Over the years, the original Bouc-Wen model has been extended several times. Many new parameters have been added to fit a variety of hysteretic shapes which include degradation and pinching. The result is a hysteresis model with 13 loop parameters given by

$$\dot{z}=h(z)\left\{\frac{A\dot{u}-\nu(\beta|\dot{u}||z|^{n-1}z+\gamma\dot{u}|z|^n)}{\eta}\right\}. \tag{4}$$

In the above expression, ν and η are degradation shape functions, [3], and $h(z)$ is a pinching shape function, [4]. In general, degradation depends on the response duration and severity. A convenient measure of the combined effect of duration and severity is the energy

$$E(t)=\int_0^t(1-\alpha)kz\dot{u}dt \tag{5}$$

dissipated through hysteresis from initial time $t=0$ to present time t. Since

$$\varepsilon(t)=\int_0^t z\dot{u}dt \tag{6}$$

is proportional to $E(t)$, it may also be used as a measure of response duration and severity. Many functional relations between ν, η, and ε are possible. From practical considerations, both ν and η are assumed to depend linearly on ε as the system evolves:

$$\nu(\varepsilon)=1+\delta_\nu\varepsilon \tag{7}$$

Table 1 Parameters of differential model of hysteresis

Parameter	Description
α	Ratio of linear to nonlinear response
A, β, γ	Basic hysteresis shape control
n	Sharpness of yield
δ_ν	Strength degradation
δ_η	Stiffness degradation
ζ_s	Measure of total slip
q	Pinching initiation
p	Pinching slope
ψ	Pinching magnitude
δ_ψ	Pinching rate
λ	Pinching severity/rate interaction

$$\eta(\varepsilon)=1+\delta_\eta\varepsilon. \tag{8}$$

Two unspecified degradation parameters δ_ν and δ_η are thereby introduced. The pinching function $h(z)$ takes the form, [5],

$$h(z)=1-\zeta_1 e^{-[z\ \mathrm{sgn}(\dot{u})-qz_u]^2/\zeta_2^2} \tag{9}$$

where $\mathrm{sgn}(\dot{u})$ is the signum function of $\dot{u}$ and z_u is the ultimate value of z given by

$$z_u=\left(\frac{A}{\nu(\beta+\gamma)}\right)^{1/n}. \tag{10}$$

The two functions $\zeta_1(\varepsilon)$ and $\zeta_2(\varepsilon)$ control the progress of pinching and are written as

$$\zeta_1(\varepsilon)=\zeta_s[1-e^{(-p\varepsilon)}] \tag{11}$$

$$\zeta_2(\varepsilon)=(\psi+\delta_\psi\varepsilon)(\lambda+\zeta_1). \tag{12}$$

Six unspecified pinching parameters ζ_s, q, p, ψ, δ_ψ, and λ are thus present. Altogether there are 13 loop parameters of hysteresis A, α, β, γ, n, δ_ν, δ_η, ζ_s, q, p, ψ, δ_ψ, and λ. This generalized model of hysteresis possesses all the important features observed in real structures, which include strength degradation, stiffness degradation, and pinching of the successive hysteresis loops. The probable role played by each of the thirteen loop parameters is summarized in Table 1. As an example of hysteresis loops generated by the differential model, consider a structure with natural frequency $f_n=2.8$ Hz and damping factor $\zeta=0.02$ driven by the scaled E-W component of the 1940 El Centro earthquake over a duration of 15 seconds. Put $A=1$, $\alpha=0.01$, $\beta=1.4$, $\gamma=0.2$, $n=1$, $\delta_\nu=0.002$, $\delta_\eta=0.001$, $\zeta_s=0.95$, $q=0.25$, $p=2$, $\psi=0.2$, $\delta_\psi=0.005$, and $\lambda=0.1$. When the restoring force $R_T(u,z)$ is plotted against the system displacement u in Fig. 2, the evolution of the hysteretic path is clearly shown.

A differential model of hysteresis has many advantages in analysis. Chief among them is its ability to generate a large variety of realistic hysteresis loops. Another advantage is the coupling of the equation of motion (1) to loop equation (3) or (4) to form an overall differential system. This greatly facilitates subsequent theoretical and numerical manipulations.

3 Elimination of a Redundant Parameter

Consider a nonlinear system governed by Eqs. (1) and (4). From a strict mathematical standpoint, either $[u,\dot{u},z]^T$ or $[u,\dot{u},R_T(u,z)]^T$ can be taken as a solution vector. Note that z is an imaginary displacement while $R_T(u,z)$ is a measurable force. The system response is usually chosen as $[u,\dot{u},R_T(u,z)]^T$ since it is directly connected to the hysteresis loops. Upon solution of Eqs. (1) and (4), a graph of $R_T(u,z)$ against u is often compared to experimental data from cyclic performance tests. A good fit would indicate that the loop parameters are specified properly. It must be remembered, however, that the thirteen loop parameters are empirical parameters; they are not derived from fundamental equations of mechanics. It has never been claimed that all 13 parameters are essential in producing the common features of hysteresis.

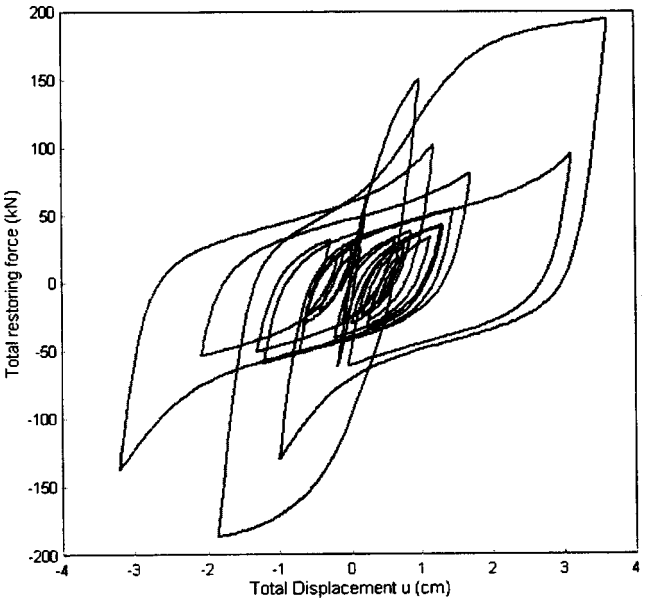

Fig. 2 Example of hysteresis loops generated by the differential model

After all, the physical meanings of many of these parameters have not been adequately clarified. A given set of loop parameters uniquely determines the system response, but a given response may not determine the parameters unambiguously. It would be very useful, particularly in system identification, if the number of unspecified parameters can be reduced.

It will be shown that a class of transformations in the parameter space can be devised to freeze one of the loop parameters without affecting the system response. The transformations always map one of the parameters to a constant in such a way that the system response, and hence the hysteretic trace, remains invariant. Since the hysteretic force $(1-\alpha)kz$ is proportional to k, the stiffness coefficient is used as an additional parameter to define the parameter set

$$P=\{A,k,\alpha,\beta,\gamma,n,\delta_\nu,\delta_\eta,\zeta_s,q,p,\psi,\delta_\psi,\lambda\}. \tag{13}$$

Define a transformation from P into

$$\overline{P}=\{\overline{A},\overline{k},\overline{\alpha},\overline{\beta},\overline{\gamma},\overline{n},\overline{\delta}_\nu,\overline{\delta}_\eta,\overline{\zeta}_s,\overline{q},\overline{p},\overline{\psi},\overline{\delta}_\psi,\overline{\lambda}\} \tag{14}$$

so that

$$\overline{A}=1 \tag{15a}$$

$$\overline{k}=(\alpha+A-\alpha A)k \tag{15b}$$

$$\overline{\alpha}=\frac{\alpha}{\alpha+A-\alpha A} \tag{15c}$$

$$\overline{\beta}=A^{n-1}\beta \tag{15d}$$

$$\overline{\gamma}=A^{n-1}\gamma \tag{15e}$$

$$\overline{n}=n \tag{15f}$$

$$\overline{\delta}_\nu=A\delta_\nu \tag{15g}$$

$$\overline{\delta}_\eta=A\delta_\eta \tag{15h}$$

$$\overline{\zeta}_s=\zeta_s \tag{15i}$$

$$\overline{q}=q \tag{15j}$$

$$\overline{p}=Ap \tag{15k}$$

$$\overline{\psi}=\frac{1}{A}\psi \tag{15l}$$

$$\overline{\delta}_\psi=\delta_\psi \tag{15m}$$

$$\overline{\lambda}=\lambda. \tag{15n}$$

As a consequence, the value of A is fixed at 1 under the above transformation. It will be proved that when the parameters in $\overline{P}$ are used in Eqs. (1) and (4), the same system response $[u,\dot{u},R_T(u,z)]^T$ is obtained. With $\overline{P}$, the system equations become

$$m\ddot{\overline{u}}+c\dot{\overline{u}}+\overline{R}_T(\overline{u},\overline{z})=F(t) \tag{16}$$

$$\dot{\overline{z}}=\overline{h}(\overline{z})\left\{\frac{\overline{A}\dot{\overline{u}}-\overline{\nu}(\overline{\beta}|\dot{\overline{u}}||\overline{z}|^{\overline{n}-1}\overline{z}+\overline{\gamma}\dot{\overline{u}}|\overline{z}|^{\overline{n}})}{\overline{\eta}}\right\}. \tag{17}$$

Note that both the excitation and initial conditions remain unaltered when the parameter set is changed from P to $\overline{P}$. Postulate that

$$\overline{u}(t)=u(t),\quad \dot{\overline{u}}(t)=\dot{u}(t),\quad \overline{z}(t)=\frac{1}{A}z(t) \tag{18}$$

where u, $\dot{u}$, z satisfy Eqs. (1) and (4) with parameters from P. Observe that the energy term

$$\dot{\overline{\varepsilon}}=\dot{\overline{u}}\overline{z}=\frac{1}{A}\dot{u}z=\frac{1}{A}\dot{\varepsilon}. \tag{19}$$

If there is no hysteretic energy dissipated at $t=0$, then upon integration

$$\overline{\varepsilon}(t)=\frac{1}{A}\varepsilon(t). \tag{20}$$

The transformation (15) implies that

$$\overline{\nu}=1+\overline{\delta}_\nu\overline{\varepsilon}=1+A\delta_\nu\frac{1}{A}\varepsilon=1+\delta_\nu\varepsilon=\nu \tag{21}$$

$$\overline{\eta}=1+\overline{\delta}_\eta\overline{\varepsilon}=1+A\delta_\eta\frac{1}{A}\varepsilon=1+\delta_\eta\varepsilon=\eta \tag{22}$$

$$\overline{\zeta}_1(\overline{\varepsilon})=\overline{\zeta}_s(1-e^{-\overline{p\varepsilon}})=\zeta_s(1-e^{-Ap\varepsilon/A})=\zeta_s(1-e^{-p\varepsilon})=\zeta_1(\varepsilon) \tag{23}$$

$$\overline{\zeta}_2(\overline{\varepsilon})=(\overline{\psi}+\overline{\delta}_\psi\overline{\varepsilon})(\overline{\lambda}+\overline{\zeta}_1)=\left(\frac{1}{A}\psi+\delta_\psi\frac{1}{A}\varepsilon\right)(\lambda+\zeta_1)=\frac{1}{A}\zeta_2(\varepsilon) \tag{24}$$

$$\overline{z}_u=\left(\frac{\overline{A}}{\overline{\nu}(\overline{\beta}+\overline{\gamma})}\right)^{1/\overline{n}}=\left(\frac{1}{\nu A^{n-1}(\beta+\gamma)}\right)^{1/n}$$
$$=\left(\frac{A}{\nu(\beta+\gamma)}\right)^{1/n}\frac{1}{A}=\frac{1}{A}z_u \tag{25}$$

and

$$\overline{h}(\overline{z})=1-\overline{\zeta}_1 e^{-(\overline{z}\,\mathrm{sgn}(\dot{\overline{u}})-\overline{q}\overline{z}_u)^2/\overline{\zeta}_2^2}$$
$$=1-\zeta_1 e^{-(z/A\mathrm{sgn}(\dot{u})-qz_u/A)^2/(\zeta_2^2/A^2)}=h(z). \tag{26}$$

It can now be verified by substitution that the postulated relations in (18) satisfy Eqs. (16) and (17). Moreover,

$$\overline{R}_T(\overline{u},\overline{z})=\overline{\alpha}\overline{k}\overline{u}+(1-\overline{\alpha})\overline{k}\overline{z}$$

$$=\frac{\alpha}{\alpha+A-\alpha A}(\alpha+A-\alpha A)ku$$

$$+\left(1-\frac{\alpha}{\alpha+A-\alpha A}\right)(\alpha+A-\alpha A)k\frac{1}{A}z$$

$$=R_T(u,z). \tag{27}$$

Thus $[u,\dot{u},R_T(u,z)]^T=[\overline{u},\dot{\overline{u}},\overline{R}_T(\overline{u},\overline{z})]^T$, and Eqs. (1) and (4) produce the same system response from either P or $\overline{P}$. In other words, the solution vector $[u,\dot{u},R_T(u,z)]^T$ is invariant under transformation of the parameter set from P to $\overline{P}$. The hysteretic traces associated with P and $\overline{P}$ are identical. The parameter A is redundant and can be eliminated from the differential model of hysteresis using transformation (15). The same can be said about the classical Bouc-Wen model (1) and (3), for which the number of parameters can be reduced from five to four.

Instead of the parameter A, one can choose to fix α, β, γ, δ_ν, δ_η, p, or ψ in the extended differential model, subject to certain restrictions. For example, the sign of γ cannot be changed and α cannot be fixed at 1. As an illustration, the following transformation will eliminate the parameter δ_ν:

$$\overline{\delta}_\nu=1 \tag{28a}$$

$$\overline{A}=\delta_\nu A \tag{28b}$$

$$\overline{k}=\left(\alpha+\frac{1}{\delta_\nu}-\frac{\alpha}{\delta_\nu}\right)k \tag{28c}$$

$$\overline{\alpha}=\frac{\alpha}{\alpha+\dfrac{1}{\delta_\nu}-\dfrac{\alpha}{\delta_\nu}} \tag{28d}$$

$$\overline{\beta}=\delta_\nu^{1-n}\beta \tag{28e}$$

$$\overline{\gamma}=\delta_\nu^{1-n}\gamma \tag{28f}$$

$$\overline{n}=n \tag{28g}$$

$$\overline{\delta}_\eta=\frac{1}{\delta_\nu}\delta_\eta \tag{28h}$$

$$\overline{\zeta}_s=\zeta_s \tag{28i}$$

$$\overline{q}=q \tag{28j}$$

$$\overline{p}=\frac{1}{\delta_\nu}p \tag{28k}$$

$$\overline{\psi}=\delta_\nu\psi \tag{28l}$$

$$\overline{\delta}_\psi=\delta_\psi \tag{28m}$$

$$\overline{\lambda}=\lambda. \tag{28n}$$

If the indices ν and η are interchanged, a corresponding set of transformation equations is obtained for mapping δ_η to 1. In system identification, the loop parameters are estimated from experimental data on hysteresis loops taken from cyclic performance tests, [6–8]. The values of δ_ν and δ_η estimated from wood structures are usually much less than 1. It therefore seems more convenient to map A to 1. This will be assumed in the next section. The differential model is streamlined whichever parameter one chooses to fix. In particular, elimination of one parameter will appreciably accelerate the convergence of numerical algorithms in system identification.

It must be pointed out that functional dependence of the loop parameters in the classical model (3) was discovered earlier by Ni et al. [9]. When applied directly to the extended model, the two transformations given by Ni et al. [9] will absorb either A or k but will not preserve the hysteretic trace unless the extended parameters are also transformed. The class of transformations devised in the present paper may be regarded as a generalization of this earlier investigation.

4 Parameter Sensitivity Analysis

Assume that transformation (15) has been applied to fix the value of A at 1. There remain 12 loop parameters in the extended Bouc-Wen differential model. Does every parameter contribute equally to the system response? Will variations in some parameters combine to annul the effect of each other? Attempts were made in the past to understand the influence of each parameter on the system response. For example, Baber and Noori [4] investigated the effect of variations of A, n, ν, η, ζ_1, and ζ_2 on the ratio between hysteretic and total displacement. Wong et al. [10] studied the steady-state response of structures with different values of the loop parameters β, γ, and n. Later on, a more organized study of local sensitivity was conducted by Ni et al. with the classical model (3) containing five parameters, [9]. Despite numerous applications of the extended Bouc-Wen model [11,12], there is hardly any systematic and comprehensive study of the influence of loop parameters on the system response. One basic objective of the current paper is to address this overlooked issue by conducting sensitivity analysis.

The sensitivity of a model with respect to an input parameter is the degree to which the parameter affects the model output. Sensitivity analysis is the study of how changes in the output of a model can be apportioned, qualitatively or quantitatively, to variations in different input parameters. There is a large class of techniques for parameter sensitivity analysis. A review of some of the popular methods is given by Hamby [13], and Iman and Helton [14]. In this paper, the one-factor-at-a-time method and the Sobol sensitivity indices are used.

4.1 Local Sensitivity Analysis. The simplest way to conduct sensitivity analysis is to repeatedly vary one parameter at a time while holding the others fixed at chosen nominal values. This is referred to as one-factor-at-a-time method. It is easy to implement, often computationally inexpensive, and useful in providing a graphical representation of sensitivity ranking. However, it is a local method in the sense that it only addresses sensitivity relative to the chosen base values and not for the entire parameter space. How the base values should be chosen is often an issue itself. In addition, interactions of parameters cannot be addressed by this local method.

As a typical example of local sensitivity analysis, a shear wall of the type described in [8] is used. The shear wall has a natural frequency $f_n=3.6$ Hz and damping factor $\zeta=0.02$. It is driven by the scaled E-W component of the 1940 El Centro earthquake over a duration of 10 seconds, as shown in Fig. 3. Select as base values $\alpha=0.05$, $\beta=1$, $\gamma=0.1$, $n=1.5$, $\delta_\nu=0.025$, $\delta_\eta=0.15$, $\zeta_s=0.85$, $q=0.15$, $p=2.5$, $\psi=0.1$, $\delta_\psi=0.005$, and $\lambda=0.5$. Each of these 12 parameters is then varied, one at a time, by up to 50% from its base value while holding all other parameters at the base position. The choice of the base values is such that the resulting range spanned by each parameter is well within the usual range for fitting the experimental hysteresis loops of wood structures. Denote the system response by $[x_1,x_2,x_3]^T=[u,\dot{u},R_T(u,z)]^T$ at the base values and by $[y_1,y_2,y_3]^T$ when one parameter, say w, is varied. Define the root-mean-square error

$$e_w=\left[\sum_{i=1}^{M}\{(x_{1i}-y_{1i})^2+(x_{2i}-y_{2i})^2+(x_{3i}-y_{3i})^2\}\right]^{1/2} \tag{29}$$

where M is the number of sampling points. Put $M=500$ in this example. A spider diagram is obtained when e_w is plotted against the varied parameter w, as shown in Fig. 4. As each w is varied over its range, the maximum error

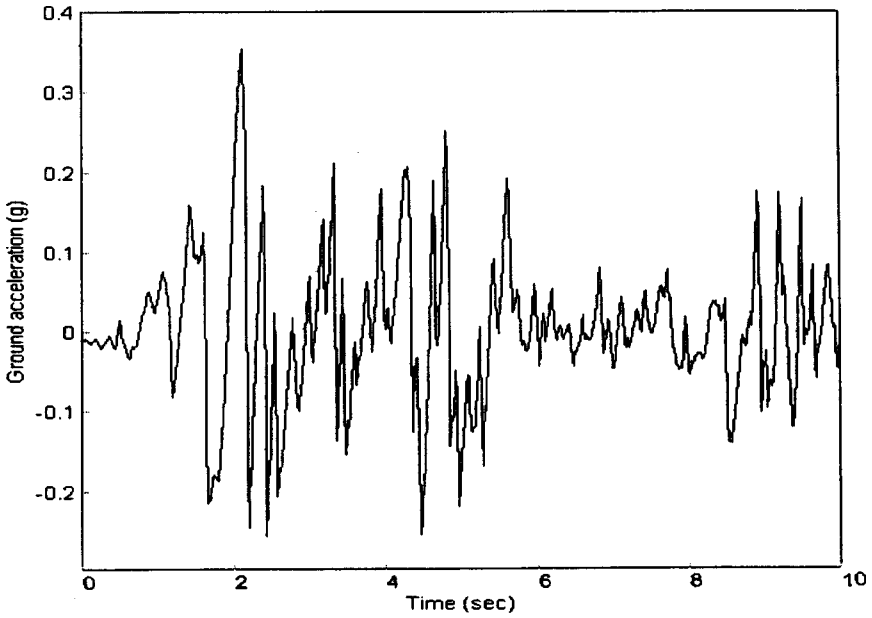

Fig. 3 Scaled east-west ground acceleration component of 1940 El Centro earthquake

$$\|e_w\| = \max(e_w) \tag{30}$$

is recorded. These maximum values may be used as a measure of sensitivity. Based upon $\|e_w\|$, the 12 loop parameters of hysteresis are ranked in order of decreasing sensitivity in Table 2. With two slightly different sets of base values, it is found that the sensitivity ranking given in Table 2 does not change. It must be emphasized that any conclusion reached through local sensitivity analysis is limited by the choice of base values. It is also limited by the excitation used. However, an inspection of Fig. 3 suggests clearly that the chosen excitation can only be synthesized by a large number of sinusoidal functions. That means its Fourier spectrum consists of many characteristic frequencies. Thus results obtained with the chosen excitation would be typical of a large class of cyclic excitation.

4.2 Global Sensitivity Analysis. Most techniques for global sensitivity analysis were developed fairly recently. In global sensitivity analysis, it is not necessary to choose any base values. Sensitivity with respect to a parameter is assessed when all model parameters vary simultaneously, instead of one at a time. Oftentimes the sensitivity with respect to a group of parameters can also be assessed. A sensitivity index is a number that gives quantitative information about the relative sensitivity of the model with respect to selected parameters. In this sense the number $\|e_w\|$ defined in Eq. (30) is a local sensitivity index. A set of powerful global sensitivity indices is the group of Sobol indices, [15].

Suppose $f(\mathbf{x}) = f(x_1, \cdots, x_n)$ is a real integrable function defined on the n-dimensional unit cube $I^n = \{\mathbf{x} | 0 \leqslant x_i \leqslant 1, i = 1, \cdots, n\}$. Let

$$f_0 = \int_{I^n} f(\mathbf{x}) d\mathbf{x} \tag{31}$$

$$f_i(x_i) = \int_{I^{n-1}} f(\mathbf{x}) d\mathbf{x}/dx_i - f_0 \tag{32}$$

where $d\mathbf{x}/dx_i$ denotes the product of all the dx_k except dx_i, and

$$f_{ij}(x_i, x_j) = \int_{I^{n-2}} f(\mathbf{x}) d\mathbf{x}/dx_i dx_j - f_0 - f_i(x_i) - f_j(x_j). \tag{33}$$

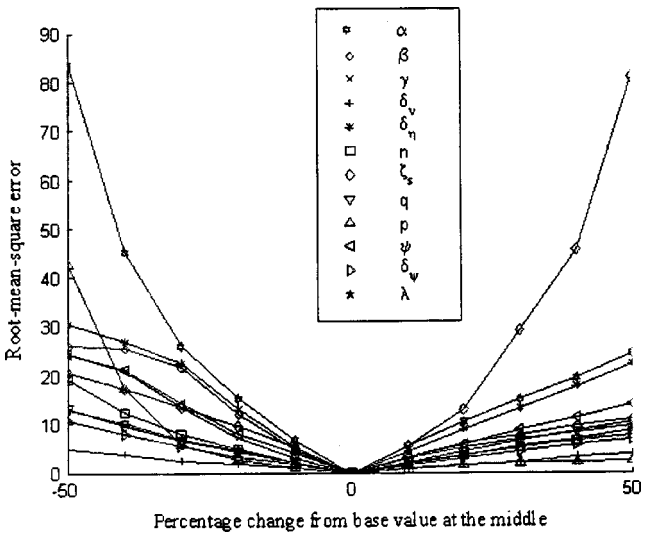

Fig. 4 Spider diagram generated by the one-factor-at-a-time method

Table 2 Parameter sensitivity ranking

Parameter w	Local Analysis		Global Analysis			
			Sobol Index		Total Effect Index	
	$\|e_w\|$	Rank	S_w	Rank	S_w^T	Rank
α	83.69	1	0.0894	2	0.2806	2
β	25.82	5	0.0410	4	0.1451	5
γ	24.31	6	0.0379	5	0.0962	7
n	19.10	8	0.0339	7	0.0930	8
δ_ν	4.78	12	0.0288	9	0.0151	12
δ_η	30.35	4	0.0308	8	0.2781	3
ζ_s	80.91	2	0.2803	1	0.6486	1
q	13.16	9	0.0377	6	0.0583	10
p	42.54	3	0.0255	10	0.0891	6
ψ	24.27	7	0.0449	3	0.1928	4
δ_ψ	10.49	11	0.0234	12	0.0574	11
λ	12.73	10	0.0238	11	0.0742	9

In this way one can define inductively all $f_{i_1,\cdots,i_s}(x_{i_1},\cdots,x_{i_s})$ for any subset of variables $x_{i_1},\cdots,x_{i_s}$ with indices $1\leqslant i_1<\cdots<i_s \leqslant n$. Furthermore, let

$$D=\int_{I^n} f^2(\mathbf{x})d\mathbf{x}-f_0^2 \tag{34}$$

$$D_{i_1,\cdots,i_s}=\int_{I^s}\cdots\int f^2_{i_1,\cdots,i_s}(x_{i_1},\cdots,x_{i_s})dx_{i_1}\cdots dx_{i_s}. \tag{35}$$

It has been established by Sobol that, under the assumption that $\mathbf{x}$ is uniformly distributed in I^n, the quantity

$$S_{i_1,\cdots,i_s}=D_{i_1,\cdots,i_s}/D \tag{36}$$

is a measure of the global sensitivity of the function $f(\mathbf{x})$ with respect to the group of variables $x_{i_1},\cdots,x_{i_s}$. The quantity $S_{i_1,\cdots,i_s}$ is termed a Sobol sensitivity index. It can be proved that

$$\sum S_{i_1,\cdots,i_s}=\sum_{i=1}^{n} S_i+\sum_{1\leqslant i<j\leqslant n} S_{ij}+\cdots+S_{1,2,\cdots,n}=1. \tag{37}$$

In other words, the sum over all the different groups of indices is one. There is a total 2^n-1 Sobol indices for $f(\mathbf{x})$. All the integrals in the Sobol indices can be evaluated by Monte Carlo simulations, [16]. The amount of computational effort can be substantial if n is large. To speed up the convergence of Monte Carlo integration, probably the most effective way is to use quasi-random numbers, [17], instead of pseudo-random numbers for choosing the samples. Other variance reduction schemes such as antithetic variates, [18], may also be employed. In this paper, Latin hypercube sampling, [19], is used instead of the crude Monte Carlo sampling. As a result, the sampling size is generally reduced to about one third of the original size.

Based upon the development of Sobol, Homma and Saltelli [20] have introduced another set of sensitivity indices to measure the mutual interactions of parameters. A given parameter x_j can interact with other parameters in groups of two, three, or more members. In view of Eq. (37), the ''total effect'' index with respect to x_j is defined as

$$S_j^T=1-\sum_{i_k\neq j} S_{i_1,\cdots,i_s} \tag{38}$$

where the sum is over all the different groups of indices that do not include j. The index S_j^T provides a measure of the total sensitivity with respect to x_j, which includes its interactions with other model parameters. A scheme has been developed, [20], for the calculation of the ''total effect'' indices that economizes on core memory and computing time. Both the Sobol index S_j and the total sensitivity index S_j^T will be computed in this paper.

There are, of course, other competing methods for global sensitivity analysis, [21,22]. These alternative methods are all based upon the conditional variances of model output. Among them, the Fourier amplitude sensitivity test (FAST) is considered the most elegant. However, it has been shown that FAST and Sobol indices generate nearly identical sensitivity ranking in a number of test cases, [23]. The Sobol sensitivity indices are generally superior to FAST and other global sensitivity indices in that the single-parameter indices S_i and multiparameter indices $S_{i_1,\cdots,i_s}$ can be represented by the same Eq. (36) and they can also be calculated in a similar fashion.

In reporting the results of global sensitivity analysis, the same shear wall described earlier will again be used. Recall that the shear wall has a natural frequency $f_n=3.6$ Hz, damping factor $\zeta=0.02$, and is driven by the scaled E-W component of the 1940 El Centro earthquake over a duration of 10 seconds. Recall that the value of A is fixed at 1 by transformation (15). After an examination of the large amount of experimental data on wood structures, it is decided that acceptable ranges for the remaining 12 parameters are $0\leqslant\alpha\leqslant0.1$, $0.5\leqslant\beta\leqslant1.5$, $-0.3\leqslant\gamma\leqslant0.5$, $0\leqslant n\leqslant3$, $0\leqslant\delta_\nu\leqslant0.05$, $0\leqslant\delta_\eta\leqslant0.3$, $0.7\leqslant\zeta_s\leqslant1$, $0\leqslant q\leqslant0.3$, $0\leqslant p\leqslant5$, $0\leqslant\psi\leqslant0.2$, $0\leqslant\delta_\psi\leqslant0.01$, and $0\leqslant\lambda\leqslant1$. The Sobol sensitivity index of the system response with respect to each of the parameter is evaluated through Monte Carlo simulations. In contrast to local analysis, no base values need to be specified. The ''total effect'' index associated with each parameter is also calculated. Even with a streamlined program, the computation of the total sensitivity indices often requires long run-time. The various indices are collected together in Table 2.

4.3 Discussion of Results. It is observed from Table 2 that the ranking generated by the local sensitivity analysis largely agrees with that by global analysis. In addition, the ranking generated by the Sobol indices S_w closely matches that by the total sensitivity indices S_w^T. This might suggest that interactions among various parameters are not significant over the range specified. Both the local and global methods indicate that α and ζ_s are the most sensitive parameters. On the other hand, δ_ν, δ_ψ, and λ are probably the least sensitive parameters. None of the unspecified parameters in the classical Bouc-Wen model are insensitive. The variation of an insensitive parameter would not appreciably change the system response. It would not appreciably alter the hysteresis loops. Perhaps the values of these insensitive parameter should be fixed, thereby simplifying the differential model of hysteresis.

As an illustration, consider the shear wall used previously in sensitivity analysis. With the exception of δ_ν, let all other parameters take the base values specified earlier in the one-factor-at-a-time analysis. Let δ_ν take the values 0, 0.05, and 0.1 successively. It is observed that the first two values are, respectively, the lower and upper limits of the range of δ_ν specified in global analysis. The third value is even outside the range. The system response corresponding to these three values of δ_ν is computed, and the displacement u of the shear wall is plotted in Fig. 5. The solid line is associated with $\delta_\nu=0$, the dashed line with $\delta_\nu=0.05$, and the dash-dotted with $\delta_\nu=0.1$. One can see that there is little difference in the three system displacements. It therefore seems feasible to fix δ_ν at, say, the midrange value of 0.025.

Information on parameter sensitivity is particularly valuable in system identification and system optimization. In these areas certain error functional is minimized. A sensitive parameter far away from its sought-after value will generally cause an appreciable increase in the error functional. As a result, convergence can be accelerated with various numerical schemes. On the other hand, an insensitive parameter tends to drift around its sought-after value since changes in its value contribute little to the error functional. This could cause many problems in convergence. Clearly, great simplification results if the insensitive parameters can be fixed. It must be emphasized that global sensitivity ranking relies appreciably on the range of variation of each parameter. Over the range specified, δ_ν, δ_ψ, and λ are rather insensitive parameters. This observation should be reassessed for a different range of variation.

5 Conclusions

The extended Bouc-Wen differential model is one of the most widely accepted phenomenological models of hysteresis in mechanics. It is routinely used in the characterization of nonlinear damping and in system identification. In this model the restoring force and system displacement are connected through a nonlinear differential equation containing unspecified parameters. By choosing the parameters suitably, it is possible to generate a large variety of different shapes of the hysteresis loops. The classical Bouc-Wen model contains only five control parameters. The generalized differential model in its present form contains 13 parameters; it can account for strength degradation, stiffness degradation, and even pinching characteristics of an inelastic structure. In this pa-

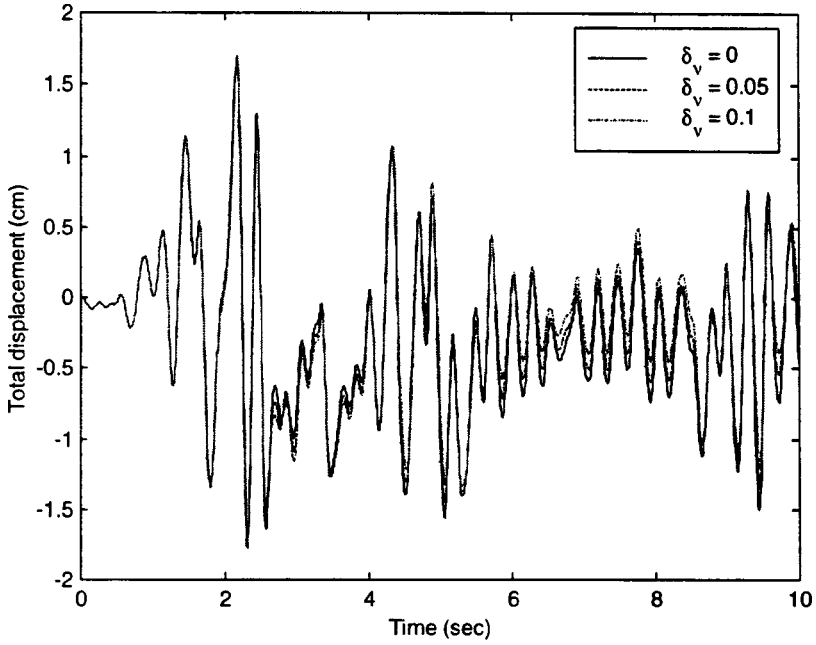

Fig. 5 Effect of varying the insensitive parameter δ_ν

per, the differential model of hysteresis has been carefully reexamined. Mathematical transformations have been devised to freeze one of the unspecified parameters without affecting the system response. Local and global sensitivity analyses have been conducted to assess the relative sensitivity of each control parameter. The various parameters have been ranked in order of decreasing sensitivity with three different methods. Although a limited set of data is presented, extensive numerical calculations have been performed by the authors to support any qualitative results herein. For example, in global analysis sensitivity indices with respect to a group of two or more parameters are not reported because there are $2^{12}-1-12=4083$ such indices. Major findings are summarized in the following statements.

1. The unspecified parameters of the differential model are functionally redundant. One of the parameters can be eliminated through suitable transformations in the parameter space. This is true for both the classical and the extended differential models of hysteresis.
2. In the extended differential model, there are three or four unspecified parameters that have been consistently ranked at or near the bottom of the sensitivity scale. If the values of these insensitive parameters can be fixed, a greatly simplified model is obtained. None of the unspecified parameters in the classical Bouc-Wen model are insensitive. Any statement made through local sensitivity analysis is limited by the choice of base values, while global sensitivity analysis is limited by the choice of the range of variation of the parameters.
3. Over a practical range, it appears that interactions among various unspecified parameters in the extended differential model are not significant. It is not claimed that the range of variation selected for global sensitivity analysis in this paper covers all applications. The total sensitivity indices should be re-evaluated for each application that involves a range of variation not covered by the selected range.

As explained earlier, the cyclic excitation $F(t)$ chosen for sensitivity analysis possesses a rich spectrum. Thus the above statements on sensitivity are applicable for a large class of cyclic excitation. However, these statements on sensitivity may not be valid for an excitation whose spectrum has little overlap with that of the chosen excitation. Among other things, it is hoped that the present paper would point to directions along which further research efforts to refine the differential model can be profitably made. It appears feasible, for example, to determine if energy dissipation should indeed be separated additively into an elastic and hysteretic component. Perhaps there is an even closer representation of reality if the total energy is divided according to a power law. As the differential model of hysteresis becomes increasingly popular in theory and applications, the update reported in this paper will hopefully allow it to be used with added confidence in the years to come.

Acknowledgments

We would like to thank Mr. Chinghang Ng for assistance in the preparation of the manuscript. This research has been supported in part by the National Science Foundation under Grant No. CMS-9908194. Opinions, findings, and conclusions expressed in this paper are those of the authors and do not necessarily reflect the views of the sponsor.

References

[1] Bouc, R., 1967, "Forced Vibration of Mechanical Systems With Hysteresis," *Proceedings of the 4th Conference on Nonlinear Oscillations*, Prague, Czechoslovakia, p. 315.
[2] Wen, Y. K., 1976, "Method for Random Vibration of Hysteretic Systems," J. Eng. Mech., **102**, pp. 249–263.
[3] Baber, T. T., and Wen, Y. K., 1981, "Random Vibration of Hysteretic Degrading Systems," J. Eng. Mech., **107**, pp. 1069–1087.
[4] Baber, T. T., and Noori, M. N., 1986, "Modeling General Hysteresis Behavior and Random Vibration Application," ASME J. Vib., Acoust., Stress, Reliab. Des., **108**, pp. 411–420.
[5] Foliente, G. C., 1995, "Hysteretic Modeling of Wood Joints and Structural Systems," J. Struct. Div. ASCE, **121**, pp. 1013–1022.
[6] Loh, C. H., and Chung, S. T., 1993, "A Three-Stage Identification Approach for Hysteretic Systems," Earthquake Eng. Struct. Dyn., **22**, pp. 129–150.
[7] Kyprianou, A., Worden, K., and Panet, M., 2001, "Identification of Hysteretic Systems Using the Differential Evolution Algorithm," J. Sound Vib., **248**, pp. 289–314.
[8] Zhang, H., Foliente, G. C., Yang, Y., and Ma, F., 2002, "Parameter Identification of Inelastic Structures Under Dynamic Loads," Earthquake Eng. Struct. Dyn., **31**, pp. 1113–1130.
[9] Ni, Y. Q., Ko, J. M., and Wong, C. W., 1998, "Identification of Nonlinear Hysteretic Isolators From Periodic Vibration Tests," J. Sound Vib., **217**, pp. 737–756.

[10] Wong, C. W., Ni, Y. Q., and Lau, S. L., 1992, ''Steady-State Oscillation of Hysteretic Differential Model II: Performance Analysis,'' J. Eng. Mech., **120**, pp. 2299–2325.
[11] Wen, Y. K., 1980, ''Equivalent Linearization for Hysteretic Systems Under Random Excitation,'' ASME J. Appl. Mech., **47**, pp. 150–154.
[12] Roberts, J. B., and Spanos, P. D., 1990, *Random Vibration and Statistical Linearization*, John Wiley and Sons, New York, pp. 257–284.
[13] Hamby, D. M., 1994, ''A Review of Techniques for Parameter Sensitivity Analysis of Environmental Models,'' Environ. Monitor. Assess., **32**, pp. 135–154.
[14] Iman, R. L., and Helton, J. C., 1991, ''The Repeatability of Uncertainty and Sensitivity Analyses for Complex Probabilistic Risk Assessments,'' Risk Anal, **11**, pp. 591–606.
[15] Sobol, I. M., 1993, ''Sensitivity Estimates for Nonlinear Mathematical Model,'' Mathematical Modeling and Computational Experiment, **1**, pp. 407–414.
[16] Press, W. H., Flannery, B. P., Teukolsky, S. A., and Vetterling, W. T., 1988, *Numerical Recipes in C: The Art of Scientific Computing*, Cambridge University Press, Cambridge, UK, pp. 237–241.
[17] Sobol, I. M., 1990, ''Quasi-Monte-Carlo Methods,'' Prog. Nucl. Energy, **24**, pp. 55–61.
[18] Hammersley, J. M., and Morton, K. W., 1956, ''A New Monte Carlo Technique: Antithetic Variates,'' Proc. Cambridge Philos. Soc., **52**, pp. 449–475.
[19] McKay, M. D., Beckman, R. J., and Conover, W. J., 1979, ''A Comparison of Three Methods for Selecting Values of Input Variables in the Analysis of Output From a Computer Code,'' Technometrics, **21**, pp. 239–245.
[20] Homma, T., and Saltelli, A., 1996, ''Importance Measures in Global Sensitivity Analysis of Nonlinear Models,'' Reliability Eng. Sys. Safety, **52**, pp. 1–17.
[21] Iman, R. L., and Hora, S. C., 1990, ''A Robust Measure of Uncertainty Importance for Use in Fault Tree System Analysis,'' Risk Anal, **10**, pp. 401–406.
[22] Chan, K., Tarantola, S., Saltelli A., and Sobol, I. M., 2000, ''Variance-Based Methods,'' *Sensitivity Analysis*, A. Saltelli, K. Chan, and E. M. Scott, eds., John Wiley and Sons, New York, pp. 167–197.
[23] Saltelli, A., and Bolado, R., 1998, ''An Alternative Way to Compute Fourier Amplitude Sensitivity Test (FAST),'' Comput. Stat. Data Anal., **26**, pp. 445–460.

Akke S. J. Suiker
Koiter Institute Delft,
Faculty of Aerospace Engineering,
Delft University of Technology,
P.O. Box 5058,
2600 GB Delft, The Netherlands

Norman A. Fleck
Cambridge Center for Micromechanics,
Department of Engineering,
Cambridge University,
Trumpington Street,
Cambridge CB2 1PZ, UK

Frictional Collapse of Granular Assemblies

The frictional collapse of an assembly of equisized spheres is studied by a discrete element model. The macroscopic constitutive response is determined as a function of the level of Coulomb friction between particles. It is found that the level of Coulomb friction has a strong effect upon the relative proportion of sliding and rolling between particles, and consequently upon the macroscopic strength of the granular assembly. The discrete element predictions are shown to be in good agreement with experimental results obtained from triaxial tests on an aggregate of steel spheres. It is demonstrated that the shape of the collapse surface can be adequately represented by the Lade-Duncan continuum model. [DOI: 10.1115/1.1753266]

1 Introduction

Since the pioneering work of Cundall and Strack [1], discrete element models (DEM) have been popular for analyzing the mechanical characteristics of granular materials; see, for example, [2–9]. Most studies focus on two-dimensional particle configurations, where the particles are represented by circular disks. Although two-dimensional discrete element analyses have provided insight into the mechanical response of particle assemblies, they are of limited value in simulating the behavior of advanced laboratory experiments. The response to complicated loading paths, such as those applied to a granular material in a true triaxial apparatus, [10,11], can only be adequately simulated by means of three-dimensional numerical analyses.

Apart from the direct simulation of laboratory tests, three-dimensional discrete element analyses are useful for the development and verification of continuum models of granular compaction and flow. The use of macroscopic stress and strain measures to characterize the deformation state of a granular assembly is valid provided the representative volume element contains a sufficiently large number of particles; under such conditions, the use of average macroscopic variables with a continuum constitutive law leads to major advantages in computational economy compared with the discrete element method.

Various micromechanical models have been derived by homogenisation of microstructural particle interactions, [12–19], although checks on their accuracy by comparison with experiments and with discrete element simulations are lacking. Typically, the micromechanical descriptions are based on upper and lower bounds of the true response. For example, the assumption of ''affine deformation'' gives an approximation for the deformation at the particle contact level in terms of the imposed macroscopic strain field over the particle assembly. This kinematic assumption is often made in the homogenization of granular materials, [12–16,20,21], and commonly results in an overprediction of the macroscopic strength and stiffness, [22–24].

In this paper the discrete element method is used to study the frictional behavior of three-dimensional particle assemblies. The macroscopic constitutive response under axisymmetric stress conditions is determined as a function of the level of Coulomb friction between particles. These predictions are compared to experimental results obtained from triaxial tests on an aggregate of steel spheres. Furthermore, to reveal the degree of local particle rearrangement by sliding and rotation, the assembly of discrete particles is subjected to three different kinematic conditions: (1) both particle sliding and particle rotation are allowed to occur, (2) particle sliding is permitted, but particle rotation is prevented, and (3) particle sliding is allowed to occur in accordance with an affine deformation field, while particle rotation is prevented. Finally, the collapse surface is computed in the deviatoric plane of principal stress space by subjecting the three-dimensional granular assembly to a set of proportional stress paths.

2 Particle Assembly Simulated by Discrete Element Model

The mechanical behavior of a three-dimensional assembly of elastic-frictional particles is studied by employing the discrete element program Particle Flow Code (PFC).[1] In this discrete element program, the system of equations describing the dynamic interaction of an assembly of spherical particles is solved by using an explicit time-stepping scheme; at each time step the change in the interparticle forces is computed from the relative velocities at the particle contacts via the incremental force-displacement relation for each contact. After updating the interparticle forces, the new out-of-balance force at each particle contact is determined and used to calculate the new translational and rotational particle accelerations from Newton's law of motion. Integration of the particle accelerations provides the particle velocities and thereby the particle displacements. The particle displacements give the new particle positions, after which, by using the updated velocities at the particle contacts, the procedure is repeated. Checks are carried out to determine if contacts have become established or have ceased to exist. The normal force versus overlap contact law obeys the well-known Hertzian theory; see, for example, [25]. The contact is either fully sticking (with the tangential stiffness set by the contact area) or undergoes full slip in accordance with the Coulomb friction criterion

$$|f_d^c| \leqslant -f_n^c \tan \phi^c \tag{1}$$

where f_n^c is the normal contact force, f_d^c is the shear contact force, and ϕ^c is the friction angle at the particle contact c. Since the particle contacts are supposed to have no resistance against tension, the normal and shear contact forces are set to zero if the overlap between two particles becomes less than zero. For a more detailed description of the above method, see [1,26].

The geometry used in the computations consists of a cuboidal volume that is randomly filled with spherical particles, see Fig. 1. The particles of the granular assembly are allowed to rotate, un-

Contributed by the Applied Mechanics Division of THE AMERICAN SOCIETY OF MECHANICAL ENGINEERS for publication in the ASME JOURNAL OF APPLIED MECHANICS. Manuscript received by the ASME Applied Mechanics Division, October 22, 2002; final revision, October 9, 2003. Editor: R. M. McMeeking. Discussion on the paper should be addressed to the Editor, Prof. Robert M. McMeeking, Journal of Applied Mechanics, Department of Mechanical and Environmental Engineering, University of California–Santa Barbara, Santa Barbara, CA 93106-5070, and will be accepted until four months after final publication of the paper itself in the ASME JOURNAL OF APPLIED MECHANICS.

[1]Itasca Consulting Group, Inc., Minneapolis, MN, U.S.A.

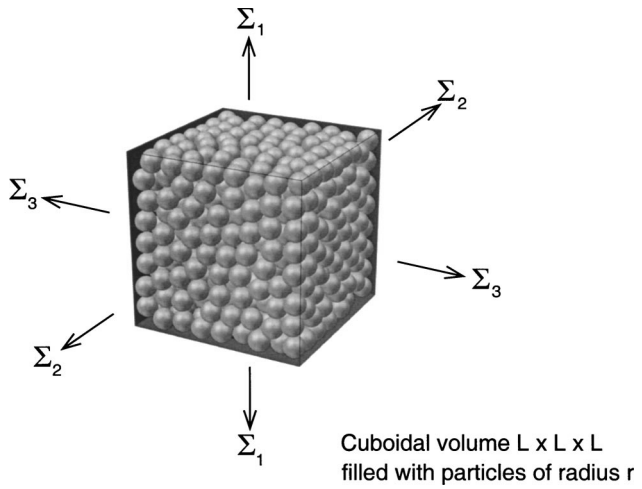

Fig. 1 Cuboidal volume $L\times L\times L$ of equi-sized spheres with radius r, subjected to principal stresses Σ_1, Σ_2, and Σ_3

less otherwise stated. A *strain-controlled* loading path is prescribed by moving the outer walls of the cube towards each other, where the relative wall velocity $\dot{u}_i^{\text{wall}}$ is related to the average macroscopic deformation rate of the assembly, $\dot{E}_{ij}$, by

$$\dot{u}_i^{\text{wall}}=\dot{E}_{ij}L_j \tag{2}$$

with L_j the relative position between points on two opposite faces of the cube. The normal contact stiffness at the walls is chosen to be sufficiently high, such that the walls act as "rigid" objects. The tangential contact stiffness at the walls is set to zero, i.e., the boundary particles may freely slide along the walls.

In order to minimize the inertia forces in a quasi-static analysis, the wall velocity needs to be relatively small. Accordingly, the number of discrete time steps required for reaching a macroscopic deviatoric strain of 5% is specified to lay between 1.0×10^5 and 1.6×10^5. Additional checks have shown that for a selected particle density of 2650 kg/m^3 this number of time-steps leads to negligibly small inertia forces. A *stress-controlled* loading path is prescribed by means of a servo-control algorithm, which adjusts the wall velocities $\dot{u}_i^{\text{wall}}$ to reduce the error between the measured stress Σ_{ij} and the desired stress Σ_{ij}^{des}. This servo-control algorithm has the form

$$\dot{u}_i^{\text{wall}}=g_j(\Sigma_{ij}-\Sigma_{ij}^{\text{des}}) \tag{3}$$

where g_j is the gain, whose appropriate values have been determined by trial and error. The Cauchy stress Σ_{ij} represents the spatial average over a so-called "measurement sphere," and is determined by using the well-known expression [12,17,18,27]

$$\Sigma_{ij}=\frac{1}{2V}\sum_{c=1}^{C}(f_j^c l_i^c+f_i^c l_j^c) \tag{4}$$

where V is the volume of the measurement sphere, C is the total number of particle contacts in the measurement sphere, l_i^c is the branch vector that connects the centers of two neighboring particles in contact, and f_j^c is the contact force at contact "c." The center of the measurement sphere corresponds to the center of the cuboidal volume, and the diameter of the measurement sphere equals the width of the cuboidal volume.

2.1 Convergence Study for Effective Medium Calculation In the discrete element model, a sufficiently large number of particles needs to be determined for mimicking the response of a continuum. This is done by analyzing the response of a cuboidal volume of *equi-sized spherical particles* (often called a "monodisperse packing," [28]), loaded in *axisymmetric compression*, $\Sigma_1<\Sigma_2=\Sigma_3\leqslant 0$. Here, Σ_1, Σ_2, and Σ_3 denote the principal stresses in the longitudinal direction, x_1, and the transverse directions of the specimen, x_2 and x_3, respectively. Stress measures that are commonly employed for describing the mechanical behavior of isotropic particle assemblies are the deviatoric stress (invariant) Σ^{dev} (also known as the "von Mises stress") and the hydrostatic stress (invariant) Σ^{hydr}, given by

$$\Sigma^{\text{dev}}=\sqrt{\frac{3}{2}\Sigma'_{ij}\Sigma'_{ij}}$$
$$\Sigma^{\text{hydr}}=\frac{1}{3}\Sigma_{kk}. \tag{5}$$

Here and below, a repeated suffix denotes summation and Σ'_{ij} is the deviatoric stress tensor according to $\Sigma'_{ij}=\Sigma_{ij}-\Sigma^{\text{hydr}}\delta_{ij}$, with δ_{ij} the well-known Kronecker delta symbol. The stress measures Σ^{dev} and Σ^{hydr} are work conjugates to the deviatoric strain rate $\dot{E}^{\text{dev}}$ and volumetric strain rate $\dot{E}^{\text{vol}}$, respectively, where

$$\dot{E}^{\text{dev}}=\sqrt{\frac{2}{3}\dot{E}'_{ij}\dot{E}'_{ij}}$$
$$\dot{E}^{\text{vol}}=\dot{E}_{kk} \tag{6}$$

and $\dot{E}'_{ij}$ is the deviatoric strain rate tensor given by $\dot{E}'_{ij}=\dot{E}_{ij}-1/3\dot{E}^{\text{vol}}\delta_{ij}$. For an axisymmetric stress configuration, Eq. (5) simplifies to

$$\Sigma^{\text{dev}}=|\Sigma_1-\Sigma_3|$$
$$\Sigma^{\text{hydr}}=\frac{1}{3}(\Sigma_1+2\Sigma_3) \tag{7}$$

and the corresponding strain rates, Eq. (6), simplify to

$$\dot{E}^{\text{dev}}=\frac{2}{3}|\dot{E}_1-\dot{E}_3|$$
$$\dot{E}^{\text{vol}}=\dot{E}_1+2\dot{E}_3 \tag{8}$$

where $\dot{E}_1$ is the longitudinal strain rate, and $\dot{E}_3(=\dot{E}_2)$ is the transverse strain rate.

Two different particle sizes are considered; particles with a radius $r=0.05L$ (cuboidal volume of 1145 particles), and particles with a radius $r=0.025L$ (cuboidal volume of 9167 particles), where L is the length of the sides of the cuboidal volume, see also Fig. 1. After generation of the discrete particle assembly, a confining pressure Σ^{conf} is applied onto the outer walls of the cuboidal volume, thereby invoking the servo-control algorithm, Eq. (3). During application of the confining pressure, a small amount of interparticle friction is introduced ($\phi^c=14$ deg) in order to reduce the time necessary to satisfy the convergence criterion

$$\frac{\Sigma_i-\Sigma_i^{\text{des}}}{\Sigma_i^{\text{des}}}<\beta \quad \text{with} \quad i\in\{1,2,3\} \tag{9}$$

where the tolerance β is set to 5.0×10^{-3}. Note that the convergence criterion includes all three principal stresses.

Three different confining pressures are considered, which in terms of the particle shear modulus G^{part} are: $\Sigma^{\text{conf}}/G^{\text{part}}=-2.5\times10^{-6}$, -5.0×10^{-6} and -7.5×10^{-6}. These ratios reflect a particle system that is close to the *rigid-sphere limit* ($\Sigma^{\text{conf}}/G^{\text{part}}=0$). The porosity p of the granular specimen after application of the confining pressure $\Sigma^{\text{conf}}/G^{\text{part}}=-5.0\times10^{-6}$ is 0.382. For the confining pressures $\Sigma^{\text{conf}}/G^{\text{part}}=-2.5\times10^{-6}$ and -7.5×10^{-6} the initial porosity is slightly higher and lower, respectively. The particle shear modulus and Poisson's ratio are taken as $G^{\text{part}}=20$ GPA and $\nu^{\text{part}}=0.20$, respectively. When the particle system has achieved equilibrium with the confining pressure (i.e. Eq. (9)

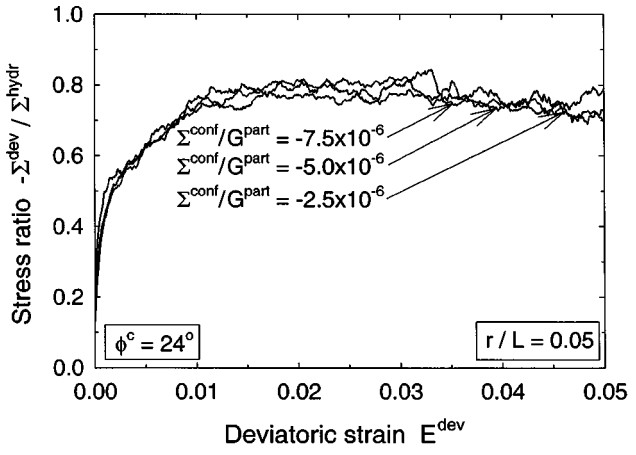

(*a*)

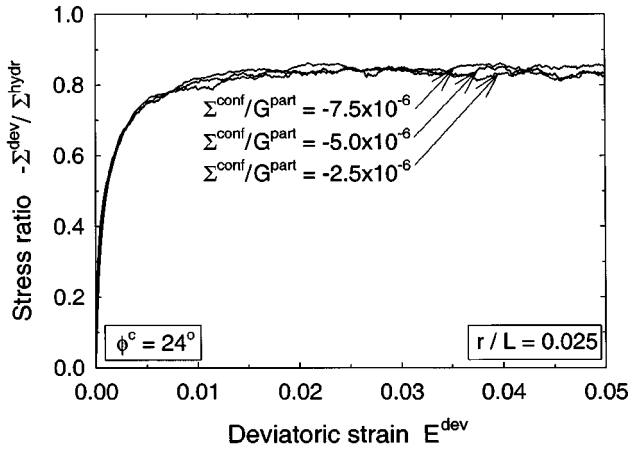

(*b*)

Fig. 2 Stress-strain response under axisymmetric compression; three confining pressures: $\Sigma^{conf}/G^{part}=-2.5\times10^{-6}$, -5.0×10^{-6} and -7.5×10^{-6} (contact friction angle $\phi^c=24$ deg). (*a*) Particle radius $r=0.05L$. (*b*) Particle radius $r=0.025L$.

is satisfied), the initial contact friction angle is incremented to the actual contact friction angle, which here equals $\phi^c=24$ deg. Subsequently, strain-controlled axial shortening is applied (in correspondence with Eq. (2)) at fixed confining pressure. Loading is terminated when the deviatoric strain has attained the value $E^{dev}=5\%$: this value is considered to be the limit of applicability of small strain theory.

In Figs. 2(*a*) and 2(*b*) the evolution of the stress ratio $-\Sigma^{dev}/\Sigma^{hydr}$ is plotted against the deviatoric strain E^{dev}, for the particle radii $r/L=0.05$ and $r/L=0.025$, respectively. The maximum stress level is reached at a deviatoric strain of approximately 2%, and shows only a mild difference in magnitude for the two cases considered. After reaching the maximum stress level, the stress remains almost constant under increasing deformation, i.e., steady-state collapse occurs. In both figures, the normalized stress-strain relations are independent of the level of confining pressure, implying that the collapse value of macroscopic deviatoric stress increases in proportion to the macroscopic hydrostatic pressure. The small differences between the individual stress-strain curves are driven by bifurcations of particle equilibrium states. If, for two granular samples, the initial characteristics at the particle level differ only slightly, (associated with different initial confining pressures), the equilibrium path to be followed will be different; this effect is more pronounced at the macroscopic level when the representative volume contains a smaller number of particles, see Figs. 2(*a*) and 2(*b*). Similar bifurcations are observed in

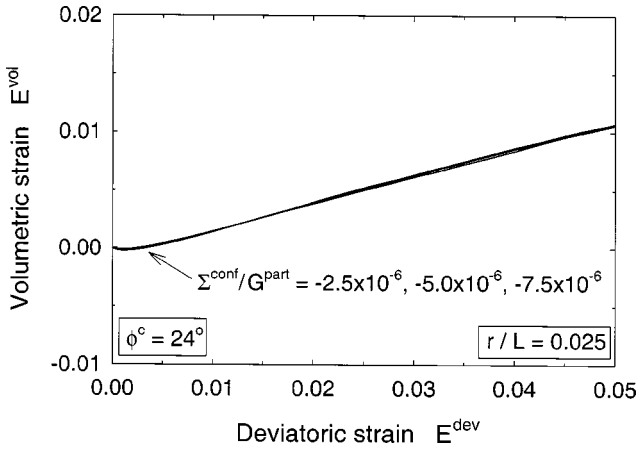

Fig. 3 Deformation characteristics under axisymmetric compression; three confining pressures: $\Sigma^{conf}/G^{part}=-2.5\times10^{-6}$, -5.0×10^{-6} and -7.5×10^{-6} (contact friction angle $\phi^c=24$ deg, particle radius $r=0.025L$)

laboratory tests on relatively coarse, noncohesive granular materials, [29], with the actual sequence of local stick-slip events between particles depending upon the initial compaction level of the material. The smoothness of the individual curves depicted in Fig. 2(*b*) indicate that the discrete system with $r/L=0.025$ responds like a continuum.

The strain response (measured after the initial confining pressure was applied) is shown in Fig. 3 for the aggregate of small particles ($r/L=0.025$). It can be seen that the response is identical for the three confining pressures considered and that proportional straining is achieved when the deviatoric strain exceeds 2%.

2.2 Influence of Contact Friction Angle Upon Macroscopic Response. The influence of the contact friction angle ϕ^c on the response is examined by simulating an axisymmetric compression test on a cuboidal volume of small particles, $r/L=0.025$. Four sets of simulations were performed, with $\phi^c=4$ deg, $\phi^c=14$ deg, $\phi^c=24$ deg, and $\phi^c=34$ deg. The specimen preparation and loading procedure are similar to those outlined in the previous section. In each simulation the confining pressure was set at $\Sigma^{conf}/G^{part}=-5.0\times10^{-6}$, corresponding to an initial porosity of $p=0.382$. Figure 4 depicts the macroscopic stress-strain curves

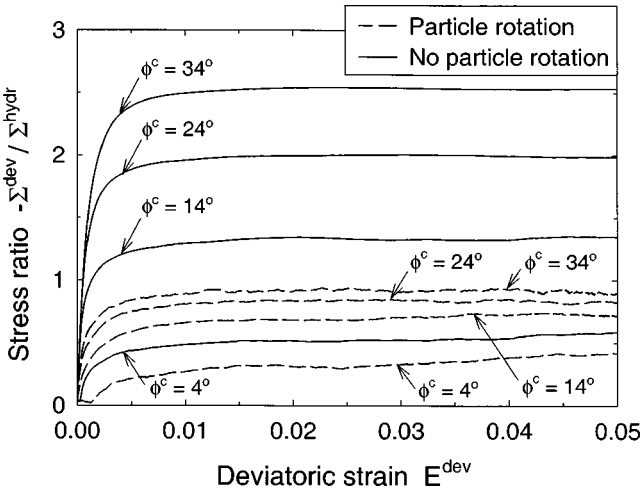

Fig. 4 Stress-strain response under axisymmetric compression; the contact friction angles are: $\phi^c=4$ deg, 14 deg, 24 deg, and 34 deg. Unconstrained and constrained particle rotation.

for the various contact friction angles considered. The ultimate collapse level increases for an increasing contact friction angle. The results of simulations with particle rotation prevented are included in the figure, and will be discussed in more detail in the subsequent section.

In order to elaborate upon the macroscopic collapse behavior, it is instructive to introduce the following set of internal state variables for the particle assembly: the *sliding contact fraction* s_f, defined by the ratio of the number of sliding contacts to the total number of contacts in the particle assembly, the *coordination number* $\bar{n}$, which is the *average* number of contacts per particle, and the *porosity* p, which equals the ratio of the void volume to the total volume occupied by the particle assembly. The steady-state values of the parameters (i.e., the values at $E^{\text{dev}}=5\%$) are plotted in Figs. 5(*a*) to 5(*c*) as a function of the contact friction angle ϕ^c. The initial value of p (after the confining pressure has been applied but with $E^{\text{dev}}=0\%$) is included in Fig. 5(*c*), and is represented by the dashed line. The plots contain results for unconstrained particle rotation and for full constraint against particle rotation; in each case the relative sliding of particles can occur in accordance with the Coulomb friction law, Eq. (1).

Consider first the sliding contact fraction s_f, as shown in Fig. 5(*a*). At steady-state collapse the number of sliding contacts decreases with increasing contact friction angle, which reflects an increase of the macroscopic strength. At the highest contact friction angle considered, $\phi^c=34$ deg, only about 10% of the total number of particle contacts is sliding, indicating that rolling of particles dominates. Both for constrained and unconstrained particle rotations the sliding contact fraction approaches zero in the limit of infinite contact friction; i.e., $s_f\rightarrow 0$ when $\phi^c\rightarrow 90$ deg. In the limit of frictionless particles, $\phi^c\rightarrow 0$ deg, the sliding contact fraction for constrained and unconstrained particle rotations should also be identical, since the deformation mechanism by particle rolling becomes inactive for particles with ideally smooth contact surfaces. The sliding contact fraction s_f is expected to approach 1.0 when $\phi^c\rightarrow 0$ deg, and the anticipated trends towards this limit have been indicated in Fig. 5(*a*) by the dashed lines. The limiting value of unity can be explained by recalling that the sliding contact fractions plotted in Fig. 5(*a*) reflect systems of nearly rigid particles that are in *neutral mechanical equilibrium* (i.e., a particle system that is on the verge of instability, as indicated in Fig. 4 by the horizontal tangential slope of the stress-strain curves at $E^{\text{dev}}=5\%$). For a system of rigid frictionless particles, a state of neutral mechanical equilibrium can be reached under isotropic loading conditions, where a network of normal contact forces is established that keeps the particle assembly just stable. When the particle system is subsequently subjected to a small deviatoric loading perturbation, all particle chains inside the contacts network will immediately collapse since the tangential resistance at every particle contact is equal to zero. Hence, all particle contacts will be subjected to sliding, and thus $s_f=1.0$. Since this collapse mechanism corresponds to zero macroscopic shear strength, it is difficult, if not impossible, to adequately simulate it by means of a discrete element analysis.

As pointed out in [30], a *minimum* average coordination number is geometrically required in order to construct a system of rigid spherical particles that is in a state of neutral equilibrium. Packing structures corresponding to a minimum average coordination number are sometimes called *isostatic packings*, [31]. For a three-dimensional isostatic packing of rigid, equi-sized *frictionless* spheres, the (minimum) coordination number is equal to 6, [30]. This value is recovered by extrapolating the curves for unconstrained and constrained particle rotation in Fig. 5(*b*) towards $\phi^c=0$ deg. For a three-dimensional isostatic packing of rigid, equi-sized *frictional* spheres which undergo no relative slip, the (minimum) coordination number is equal to 4, [32]. Again, in Fig. 5(*b*) this appears to be the asymptotic limit to which the curve for the unconstrained particle rotation decreases under increasing contact friction. In contrast, the curve for constrained particle

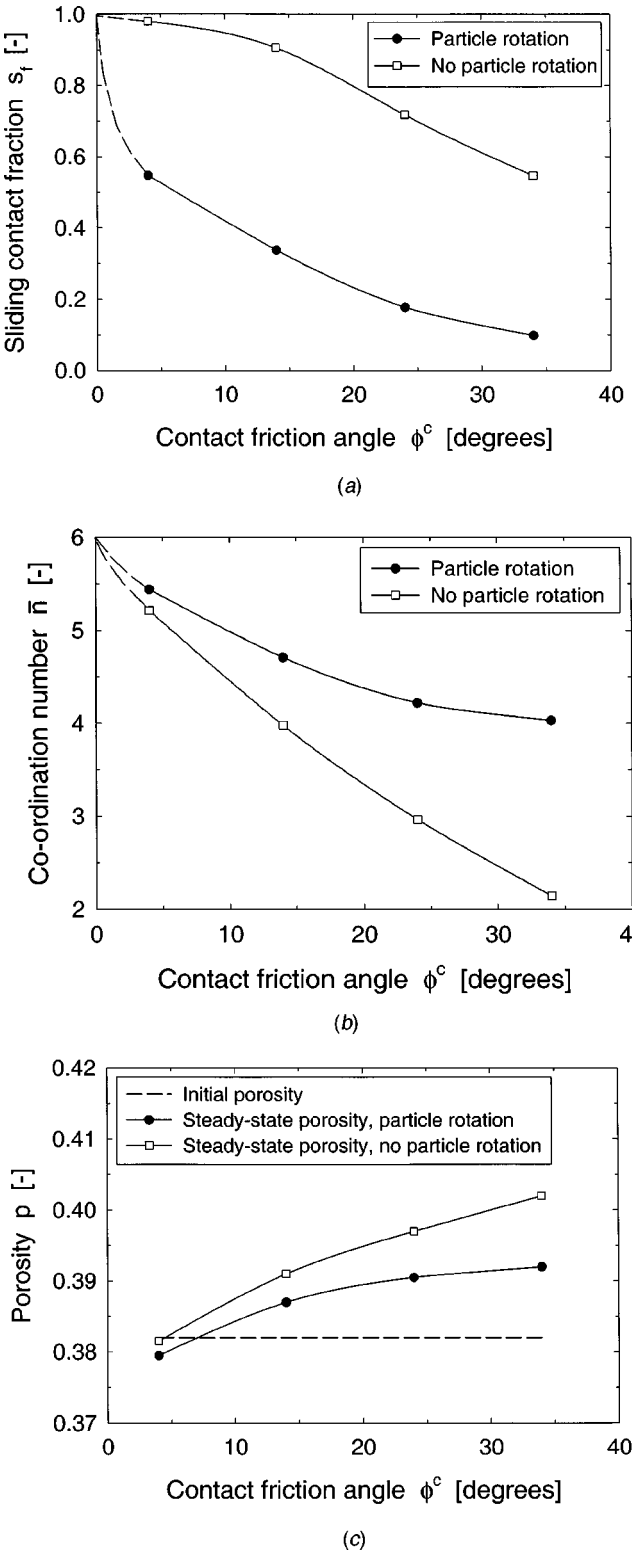

Fig. 5 Influence of contact friction angle ϕ^c on macroscopic internal state variables (for unconstrained and constrained particle rotation). (*a*) Sliding contact fraction s_f at steady-state collapse ($E^{\text{dev}}=5\%$). (*b*) Coordination number $\bar{n}$ at steady-state collapse. (*c*) Porosity p at initial state (dashed line) and at steady-state collapse (solid line).

rotation is expected to approach zero in the limit of infinite contact friction. This can be explained as follows. As discussed in [30], the minimum coordination number necessary for geometrical stability of a particle structure is directly related to the number

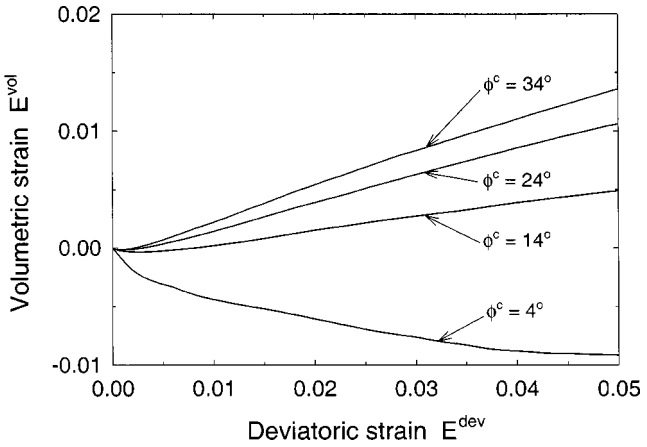

Fig. 6 Deformation characteristics under axisymmetric compression; the contact friction angles are: ϕ^c=4 deg, 14 deg, 24 deg, and 34 deg

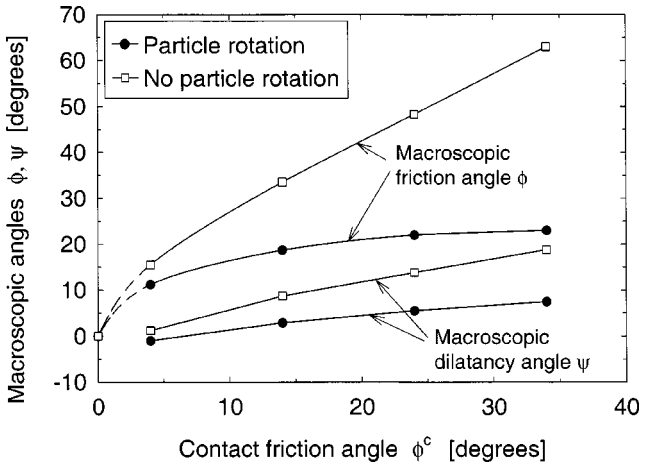

Fig. 7 Contact friction angle ϕ^c versus macroscopic friction angle ϕ and dilatancy angle ψ at steady-state collapse (E^{dev} =5%)

of internal degrees of freedom of the particle structure. An increase in contact friction leads to an increasing constraint on inter-particle sliding, whereby in the limit of infinite contact friction the internal degrees-of-freedom related to inter-particle sliding become fully constrained. The prevention of both inter-particle sliding and rolling turns the granular assembly into a rigid body with infinite shear strength and shear stiffness. Towards this limit case, the sliding contact fraction approaches zero, $s_f \rightarrow 0$; thus, most of the particles in the system will be "floating" (i.e., these particles do not transmit quasi-static forces to neighboring particles). The minimum coordination number then approaches zero because the infinite sample strength will be determined by a stable, rigid network of only a small number of contacting particles.

For the case of unconstrained particle rotation, curves with a trend similar to that in Fig. 5(*b*) were reported in [31]. Nevertheless, the particle systems of equi-sized spheres studied in [31] were obtained directly after particle deposition, which resulted in moderately stable packings with coordination numbers that are somewhat higher (between 4.5 and 6.2) than the coordination numbers for isostatic packings of rigid spheres, [30,32].

When considering the dependence of the porosity p at E^{dev} =5% upon the contact friction angle ϕ^c, see Fig. 5(*c*), it appears that p increases slightly under increasing ϕ^c. Combining this curve with the initial porosity $p=0.382$, it follows that for the lowest friction angle, $\phi^c=4$ deg, the granular assembly with unconstrained particle rotation compacts, and for greater friction angles it dilates. This is also evident from the deformation characteristics plotted in Fig. 6, where the compactive and dilative behaviors are illustrated by a monotonically decreasing volumetric strain ($\dot{E}^{vol}<0$) and a monotonically rising volumetric strain ($\dot{E}^{vol}>0$), respectively. A trend similar to that in Fig. 6 has been reported in [4] for the case of two-dimensional discrete element computations on an aggregate of circular discs under bi-axial loading. The results shown in Figs. 5 and 6 taken together have the following physical interpretation: as ϕ^c increases, the aggregate deformation at steady-state collapse becomes predominated by the rolling of particles past each other, and this results in a dilated structure with a co-ordination number approaching the minimum co-ordination number for a frictional isostatic packing.

2.3 Influence of Particle Rotation Upon Macroscopic Response. In order to explore the influence of particle rotation upon the macroscopic collapse response, the stress-strain curves for the cases where particle rotation is prevented are now compared to those where particle rotation is permitted, see Fig. 4. It can be seen that the deviatoric strength increases by a factor of two to three when particle rotation is prevented. Also, prevention of particle rotation causes steady-state collapse to be attained at a smaller strain level, and the overall response becomes smoother.

The prevention of particle rotation can be interpreted as a kinematic constraint that increases the shear strength of the granular assembly, [3,6,33]. In support of this line of reasoning, granular materials comprising angular-shaped particles (which experience restricted particle rotation due to interparticle locking) usually have a higher macroscopic shear strength at a given confining pressure than granular materials comprising round particles, [34].

Figure 7 shows the relation between the contact friction angle ϕ^c and the macroscopic friction angle ϕ, as computed by mapping the responses in Fig. 4 at E^{dev}=5% (=steady-state collapse) onto the Drucker-Prager criterion

$$F = \Sigma^{dev} + \frac{6\sin\phi}{3-\sin\phi}\Sigma^{hydr} = 0. \tag{10}$$

Under axisymmetric compression, the Drucker-Prager criterion reflects the same macroscopic friction angle as the Mohr-Coulomb hexagonal surface,

$$F = \Sigma^{hydr}\sin\phi + \frac{\sqrt{3}}{3}\Sigma^{dev}\sin\left(\theta+\frac{\pi}{3}\right) + \frac{\Sigma^{dev}}{3}\cos\left(\theta+\frac{\pi}{3}\right)\sin\phi = 0 \tag{11}$$

where θ is the angle of similarity,

$$\cos 3\theta = \frac{27}{2}\frac{J_3}{(\Sigma^{dev})^3} \quad \text{with} \quad 0 \leqslant \theta \leqslant \frac{\pi}{3}. \tag{12}$$

Here, J_3 is the third deviatoric stress invariant given by $J_3 = \Sigma'_{ik}\Sigma'_{kj}\Sigma'_{ji}/3$. Under axisymmetric compression, $\theta=\pi/3$ and Eq. (11) reduces to Eq. (10). Figure 7 clearly shows that for a higher contact friction angle the difference in macroscopic strength for unconstrained and constrained particle rotation becomes larger, indicating that the mechanism of particle rolling becomes increasingly important. As discussed in Section 2.2., the macroscopic shear strength for the assembly with constrained particle rotation is expected to become infinitely large when the contact friction approaches infinity. In contrast, for the case of unconstrained particle rotation, the macroscopic friction angle for the assembly with unconstrained particle rotation asymptotes to $\phi \approx 24°$ with increasing contact friction. In the no-sliding limit the particles are still able to roll, and therefore the macroscopic friction angle remains finite. It has already been suggested above that the macroscopic

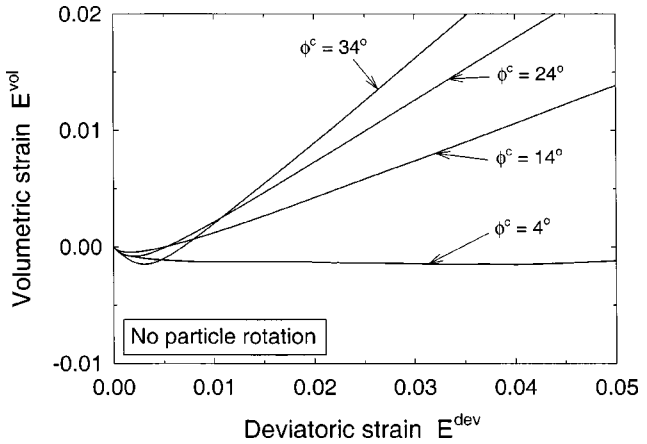

Fig. 8 Deformation characteristics under axisymmetric compression; the contact friction angles are: ϕ^c=4 deg, 14 deg, 24 deg, and 34 deg. Constrained particle rotation.

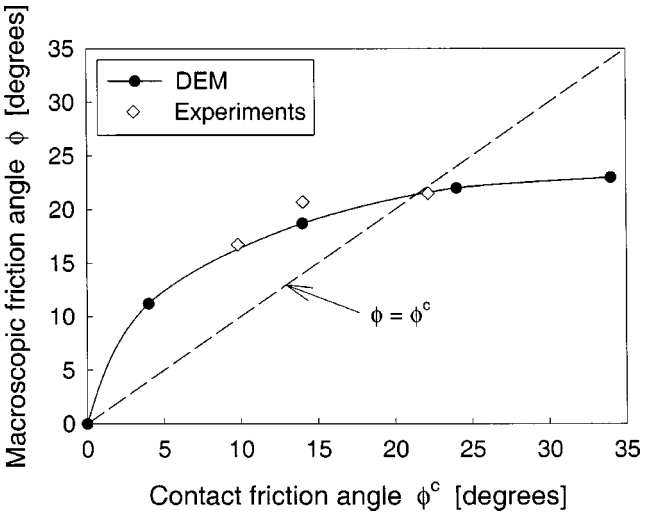

Fig. 9 Contact friction angle ϕ^c versus macroscopic friction angle ϕ. DEM versus experimental results (triaxial tests on an aggregate of steel spheres).

shear strength is zero in the limit of vanishing contact friction angle. This anticipated trend at vanishing contact friction is designated in Fig. 7 by the dashed lines.

The prevention of particle rotation also leads to an increase of the sliding contact fraction at collapse, see Fig. 5(*a*). This can be explained by the fact that prevention of particle rolling requires more particle contacts to slide in order to attain the same level of macroscopic deformation. Additionally, the prevention of particle rotation yields a lower coordination number (Fig. 5(*b*)) and a higher porosity (Fig. 5(*c*)) at steady-state collapse. Thus, the prevention of particle rotation leads to a strongly dilatant material behavior, as depicted in Fig. 8. In Figs. 6 and 8, the ratio of volumetric strain rate $\dot{E}^{\mathrm{vol}}$ to deviatoric strain rate $\dot{E}^{\mathrm{dev}}$ at $E^{\mathrm{dev}}=5\%$ defines the steady-state macroscopic dilatancy angle ψ associated with the flow potential G, where[2]

$$G=\Sigma^{\mathrm{dev}}+\frac{6\sin\psi}{3-\sin\psi}\Sigma^{\mathrm{hydr}}. \tag{13}$$

Note that the above Drucker-Prager flow potential in stress space equals the Drucker-Prager collapse criterion given by Eq. (10) when the dilatancy angle ψ is replaced by the friction angle ϕ. As usual, the direction of plastic flow is obtained by taking the stress derivative of the flow potential G. The dependence of the macroscopic dilatancy ψ upon the contact friction angle ϕ^c has been included in Fig. 7. It is clear that the macroscopic dilatancy angle is consistently less than the macroscopic friction angle, implying "nonassociated plastic flow."

2.4 Comparison of Discrete Element Simulations With Triaxial Tests on an Aggregate of Steel Spheres. A set of triaxial tests on an aggregate of steel spheres has been performed recently by Davy and Fleck (private communication) in order to explore experimentally the dependence of the steady-state macroscopic friction angle upon the contact friction angle of the spheres. A circular cylindrical sample of 50 mm diameter by 50 mm height was constructed, using spheres of approximately 4.5 mm in diameter. The aspect ratio of the granular specimen thus equals 1, and is equal to that of the discrete element model. The ratio of the sphere radius to the specimen diameter is 0.045. Although this relative particle size is somewhat bigger than that used in the discrete element simulations ($r/L=0.025$), from Figs. 2(*a*) and (*b*) it is expected that in the range $0.025<r/L<0.05$ the effect of particle size on steady-state sample strength (or steady-state macroscopic friction angle) will be very small. The sample of steel spheres was subjected to triaxial compression in three states to investigate the influence of particle contact friction: copper-coated spheres (as-received state), spheres lubricated with PTFE (polytetrafluorethylene) spray, and braze-coated spheres. The initial porosity of the samples was between 0.388 and 0.402, which is close to the initial porosity of the discrete element model (0.382). The tests involved a measurement of the steady-state macroscopic friction angle ϕ by fitting the Mohr-Coulomb collapse law, Eq. (11), to the triaxial data, and a direct measurement of the inter-particle friction between two steel spheres (which provides the contact friction angle ϕ^c). The triaxial tests follow the method described in [35], and were performed at a relatively low confining pressure (at about 0.1 MPa) in order to obtain a particle system that is close to the rigid-sphere limit.

The measured macroscopic and microscopic friction angles are plotted in Fig. 9, and are compared with the discrete element predictions where particle rotation is permitted, taken from Fig. 7. The predicted response is in excellent agreement with the experimental results. Both the discrete element method and the experiments reveal that the macroscopic friction angle ϕ exceeds the contact friction angle ϕ^c for ϕ^c less than about 21°. As ϕ^c increases, the relative proportion of inter-particle rolling to sliding increases, and ϕ levels off in value.

2.5 Influence of Particle Redistribution Upon Macroscopic Response. The effect of particle redistribution upon the macroscopic stress level can be elucidated by successively subjecting the discrete granular assembly in Fig. 1 to three different kinematic conditions: (1) particle sliding and particle rotation are allowed to occur, (2) particle sliding is allowed to occur, but particle rotation is prevented, (3) particle sliding is allowed to occur in accordance with an affine deformation field, and particle rotation is prevented. For the cases (1) and (2), the essential boundary conditions are imposed onto the outer walls of the particle assembly, see Eq. (2). In contrast, case (3) requires the translational velocity $\dot{u}_i$ of *all* particles to be prescribed, according to

$$\dot{u}_i=\dot{E}_{ij}x_j \tag{14}$$

where $\dot{E}_{ij}$ is the uniform, macroscopic strain rate and x_j are the coordinates of the particle center.

In the discrete element simulations, the contact friction angle equals $\phi^c=24$ deg, the initial confining pressure is $\Sigma^{\mathrm{conf}}=-2.5\times10^{-6}G^{\mathrm{part}}$ and the particle radius is $r=0.025L$. Two extremes of

[2]Although in the discrete element model the macroscopic strain rate is composed of elastic and permanent components, at 5% deviatoric strain the elastic strain rate is much smaller than the total strain rate. Hence, it is expected that the flow direction is not greatly in error when computed by using the values for the total strain rate.

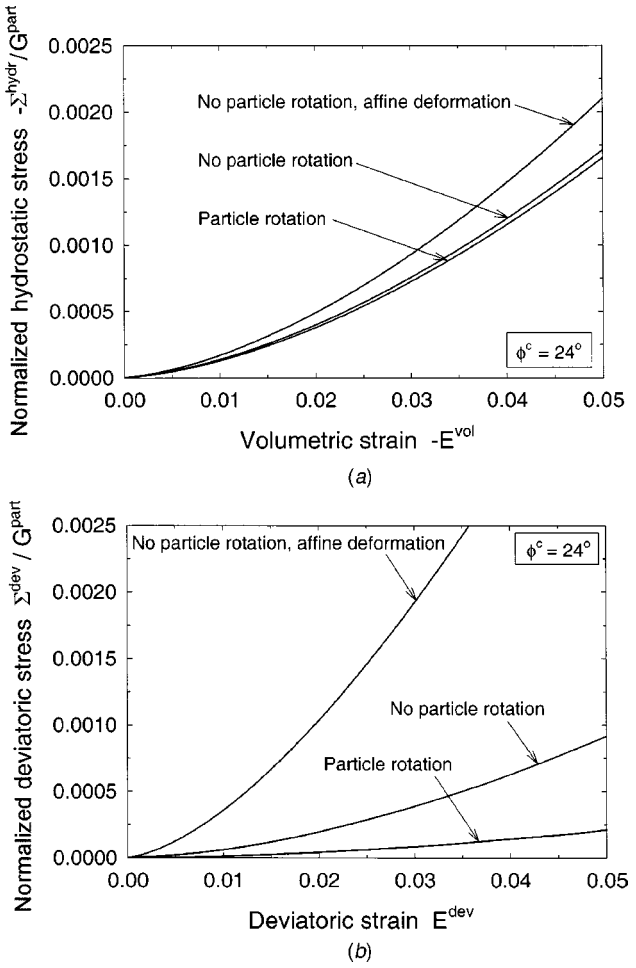

Fig. 10 Influence of particle rotation and particle rearrangement (ϕ^c=24 deg) for prescribed deformation paths. (*a*) Volumetric deformation ($\dot{E}_{11}=\dot{E}_{22}=\dot{E}_{33}$). (*b*) Deviatoric deformation ($\dot{E}_{11}=-1/2\dot{E}_{22}=-1/2\dot{E}_{33}$).

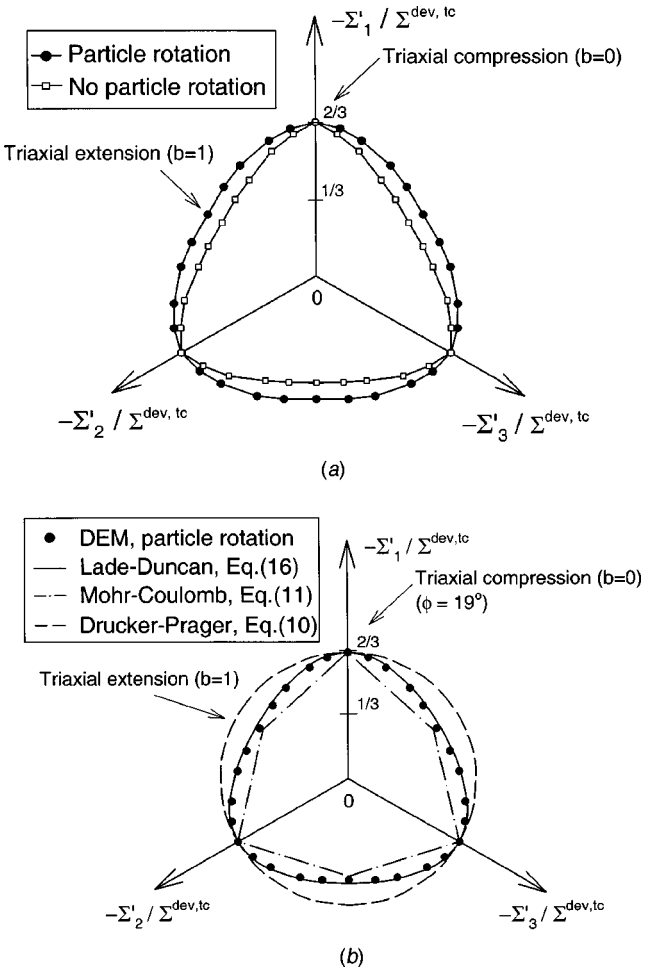

Fig. 11 Collapse contour in deviatoric plane (contact friction angle ϕ^c=24 deg). (*a*) DEM with unconstrained and constrained particle rotation. (*b*) DEM versus Lade-Duncan model, Mohr-Coulomb model and Drucker-Prager model (macroscopic friction angle ϕ=19 deg).

deformation path have been explored: *volumetric deformation*, where $\dot{E}_{11}=\dot{E}_{22}=\dot{E}_{33}$ (and $\dot{E}_{12}=\dot{E}_{23}=\dot{E}_{31}=0$) and *deviatoric deformation*, where $\dot{E}_{11}=-1/2\dot{E}_{22}=-1/2\dot{E}_{33}$ (and $\dot{E}_{12}=\dot{E}_{23}=\dot{E}_{31}=0$). For the volumetric deformation path, Fig. 10(*a*) sketches the volumetric strain versus the normalized hydrostatic stress. It is clear that the suppression of particle rotation hardly alters the macroscopic stress-strain curve. However, the introduction of an affine deformation field gives rise to noticeable stiffening. For the deviatoric deformation path, the effects of particle rotation and particle rearrangement upon the macroscopic stress level are more pronounced, see Fig. 10(*b*). The effect of particle rotation appears to strongly influence the stress magnitude, which is consistent with the result in Fig. 4. Also, the large stress increase induced by the affine deformation field suggests that substantial particle rearrangements occur when particle rotation is permitted.

For the deviatoric deformation path, at $E^{\text{dev}}=5\%$ steady-state collapse has been reached, and the macroscopic strengths are $-\Sigma^{\text{dev}}/\Sigma^{\text{hydr}}=0.94$, 1.99, and 2.74 for the cases where particle rotation is permitted, particle rotation is prevented, and affine deformation is applied, respectively. Hence, the assumption of "affine deformation," also known as the *Voigt approximation*, is not very realistic when homogenizing the mechanical behavior of an assembly of rotating particles; it would lead here to an overestimation of the macroscopic strength by a factor of 2.74/0.94=2.9.

2.6 Collapse Contour in Deviatoric Plane. The collapse contour in the deviatoric plane of the principal stress space is computed by means of *true triaxial tests*, wherein the three principal stresses depicted in Fig. 1 are varied independently. By keeping the hydrostatic pressure, Eq. (5(b)), at a constant value, a full range of radial deviatoric stress paths is imposed, as parameterized by the ratio

$$b=\frac{\Sigma_2-\Sigma_3}{\Sigma_1-\Sigma_3} \quad \text{with} \quad 0<b<1. \tag{15}$$

In Eq. (15), $b=0$ corresponds to triaxial compression (as discussed in the previous sections), while $b=1$ corresponds to triaxial extension. In the discrete element simulations, the stress-controlled loading paths, Eq. (15), are traced by invoking the servo-control algorithm, Eq. (3). Again, a cuboidal volume is randomly filled with 9167 spherical particles each of radius $r=0.025L$. The contact friction angle is assigned the value $\phi^c=24$ deg and the confining pressure equals $\Sigma^{\text{conf}}=-2.5\times10^{-6}G^{\text{part}}$.

The DEM collapse contours depicted in Fig. 11 have been composed by computing the stress states that correspond to a deviatoric strain $E^{\text{dev}}=1\%$. The axes $\Sigma_1'/\Sigma^{\text{dev},tc}$, $\Sigma_2'/\Sigma^{\text{dev},tc}$ and $\Sigma_3'/\Sigma^{\text{dev},tc}$ represent the three principal deviatoric stresses normalized by the von Mises stress under triaxial compression, $\Sigma^{\text{dev},tc}$, taken at $E^{\text{dev}}=1\%$. Figure 11(*a*) illustrates that the prevention of particle rotation provides the collapse contour with somewhat sharper corners. Further, both for constrained and unconstrained particle rotation the shear strength in triaxial compression is higher than in triaxial extension. This behavior is typical for non-

cohesive granular materials such as sand, as observed experimentally, [10,11]. In order to specify the collapse characteristics of sand in the deviatoric plane, Lade and Duncan have proposed the following phenomenological collapse criterion, [36],

$$F = I_1^3 - k_1 I_3 = 0 \tag{16}$$

where I_1, I_3 are the stress invariants

$$I_1 = 3\Sigma^{\text{hydr}} = \Sigma_{kk}$$
$$I_3 = \frac{1}{3}\Sigma_{ij}\Sigma_{jk}\Sigma_{ki} - \frac{1}{2}\Sigma_{kk}\Sigma_{ij}\Sigma_{ji} + \frac{1}{6}(\Sigma_{kk})^3 \tag{17}$$

and k_1 is a dimensionless strength parameter, which, for a cohesionless granular material, can be explicitly formulated as, [37],

$$k_1 = \frac{[\alpha(1+b)+(2-b)]^3}{b\alpha^2+(1-b)\alpha}. \tag{18}$$

In the above expression, the material parameter α is related to the macroscopic friction angle ϕ in axisymmetric compression

$$\alpha = \frac{1+\sin\phi}{1-\sin\phi} \tag{19}$$

and b characterizes the radial stress path applied, see Eq. (15). Thornton [8] has recently demonstrated close agreement between the Lade-Duncan model and a collapse contour computed by a discrete element model for a polydisperse packing of spheres (i.e., a packing of spheres with various sizes). This finding is supported by the result in Fig. 11(*b*), which depicts the collapse contour for the monodisperse packing with unconstrained particle rotation, taken from Fig. 11(*a*), together with the collapse contours of Lade-Duncan, Eq. (16), Mohr-Coulomb, Eq. (11), and Drucker-Prager, Eq. (10). It is noted that for $b=0$ Eqs. (16) and (10) are reduced to Eq. (11) for any choice of ϕ. Here, the macroscopic friction angle is prescribed as $\phi=19$ deg, in order to reproduce the DEM simulations at triaxial compression. This value is a little lower than the steady-state friction angle at triaxial compression, $\phi=22$ deg (see Fig. 7), indicating that at $E^{\text{dev}}=1\%$ the granular sample is close to steady-state collapse. As shown in Fig. 11(*b*), for stress paths other than axisymmetric compression, the Lade-Duncan model is in much better agreement with the discrete element results than the Mohr-Coulomb and Drucker-Prager models.

3 Concluding Remarks

The three-dimensional discrete element simulations discussed in this paper reveal the effect of the particle contact friction angle upon the degree of local particle rearrangement and upon the macroscopic strength. During collapse, the effect of particle rearrangement on the stress level is substantial, especially when the granular system suffers deviatoric deformations. When the collapse mechanism has reached a steady-state, the coordination number of the particle structure closely corresponds to the minimum coordination number of an isostatic packing. When the particles in the granular assembly are subjected to an affine deformation field in combination with constrained particle rotation, the mechanism of particle rearrangement is fully suppressed, leading to a considerable increase of the macroscopic stress. Accordingly, the assumption of ''affine deformation'' (the Voigt approximation), which is often adopted in the homogenization of granular materials, is far from realistic when deriving continuum models for granular assemblies with rotating particles. When only particle rotation is prevented in the discrete model, the stress level at a specific strain may still be considerably higher than for the case of unconstrained particle rotation, with the difference depending strongly on the magnitude of the particle contact friction. Preventing particle rotation also endows the collapse contour with sharper corners, implying an increase in the ratio of the shear strength under triaxial compression to the shear strength under triaxial extension.

Acknowledgments

A.S.J.S. is grateful for the hospitality offered by the Cambridge Center for Micromechanics at the Cambridge University, Cambridge, U. K., during an eight-month leave from the Delft University of Technology, Delft, The Netherlands. The authors are grateful to Dr. Catherine Davy for the provision of triaxial test data for an aggregate of steel spheres. Both authors acknowledge the EU support in the form of TMR and RTN grants ERB-4061-PL-95-0988 and HPRN-CT-2002-00198.

References

[1] Cundall, P. A., and Strack, O. D. L., 1979, ''A Discrete Numerical Model for Granular Assemblies,'' Geotechnique, **1**, pp. 47–65.
[2] Thornton, C., and Barnes, D. J., 1986, ''Computer Simulated Deformation of Compact Granular Assemblies,'' Acta Mech., **64**, pp. 45–61.
[3] Ting, J. M., Corkum, B. T., Kauffmann, C. R., and Greco, C., 1989, ''Discrete Numerical Model for Soil Mechanics,'' J. Geotech. Eng., **115**, pp. 379–398.
[4] Bathurst, R. J., and Rothenburg, L., 1990, ''Observations on Stress-Force Fabric Relationships in Idealized Granular Materials,'' Mech. Mater., **9**, pp. 65–80.
[5] Bardet, J. P., and Proubet, J., 1992, ''Shear-Band Analysis in Idealized Granular Material,'' J. Eng. Mech., **118**, pp. 397–415.
[6] Oda, M., Iwashita, K., and Kazama, H., 1997, ''Micro-Structure Developed in Shear Bands of Dense Granular Soils and Its Computer Simulation. Mechanism of Dilatancy and Failure,'' *IUTAM Symposium on Mechanics of Granular and Porous Materials*, N. A. Fleck and A. C. F. Cocks, eds., Kluwer, Dordrecht, The Netherlands, pp. 353–364.
[7] Thomas, P. A., and Bray, J. D., 1999, ''Capturing Nonspherical Shape of Granular Media With Disk Clusters,'' J. Geotech. Geoenvir. Eng., **125**, pp. 169–178.
[8] Thornton, C., 2000, ''Numerical Simulations of Deviatoric Shear Deformation of Granular Media,'' Geotechnique, **50**, pp. 43–53.
[9] Kruyt, N. P., and Rothenburg, L., 2002, ''Probability Density Functions of Contact Forces for Cohesionless Frictional Granular Materials,'' Int. J. Solids Struct., **39**, pp. 571–583.
[10] Goldscheider, M., 1976, ''Grenzbedingung und Fliessregel von Sand,'' Mech. Res. Commun., **3**, pp. 463–468.
[11] Lade, P. V., and Kim, M. K., 1988, ''Single Hardening Constitutive Model for Frictional Materials: III. Comparison With Experimental Data,'' Comput. Geotech., **6**, pp. 31–47.
[12] Christofferson, J., Mehrabadi, M. M., and Nemat-Nasser, S., 1981, ''A Micromechanical Description of Granular Material Behavior,'' ASME J. Appl. Mech., **48**, pp. 339–344.
[13] Walton, K., 1987, ''The Effective Elastic Moduli of a Random Packing of Spheres,'' J. Mech. Phys. Solids, **35**, pp. 213–226.
[14] Jenkins, J. T., 1988, ''Volume Change in Small Strain Axisymmetric Deformations of Granular Material,'' *Micromechanics of Granular Materials*, M. Satake and J. T. Jenkins, ed., Elsevier, Amsterdam, pp. 143–152.
[15] Fleck, N. A., Kuhn, L. T., and McMeeking, R. M., 1992, ''Yielding of Metal Powder Bonded by Isolated Contacts,'' J. Mech. Phys. Solids, **40**, pp. 1139–1162.
[16] Storåkers, B., Fleck, N. A., and McMeeking, R. M., 1999, ''The Viscoplastic Compaction of Composite Powders,'' J. Mech. Phys. Solids, **47**, pp. 785–815.
[17] Liao, C. L., Chan, T. C., Suiker, A. S. J., and Chang, C. S., 2000, ''Pressure-Dependent Elastic Moduli of Granular Assemblies,'' Int. J. Numer. Analyt. Meth. Geomech., **24**, pp. 265–279.
[18] Suiker, A. S. J., de Borst, R., and Chang, C. S., 2001, ''Micro-Mechanical Modelling of Granular Material—Part 1: Derivation of a Second-Gradient Micro-Polar Constitutive Theory,'' Acta Mech., **149**, pp. 161–180.
[19] Suiker, A. S. J., de Borst, R., and Chang, C. S., 2001, ''Micro-Mechanical Modelling of Granular Material—Part 2: Plane Wave Propagation in Infinite Media,'' Acta Mech., **149**, pp. 181–200.
[20] Digby, P. J., 1981, ''The Effective Elastic Moduli of Porous Granular Rock,'' ASME J. Appl. Mech., **48**, pp. 803–808.
[21] Chang, C. S., Sundaram, S. S., and Misra, A., 1989, ''Initial Moduli of Particulated Mass With Frictional Contacts,'' Int. J. Numer. Analyt. Meth. Geomech., **13**, pp. 629–644.
[22] Liao, C. L., Chang, T. P., Young, D. H., and Chang, C. S., 1997, ''Stress-Strain Relationships for Granular Materials Based on the Hypothesis of Best-Fit,'' Int. J. Solids Struct., **34**, pp. 4087–4100.
[23] Heyliger, P. R., and McMeeking, R. M., 2001, ''Cold Plastic Compaction of Powders by a Network Model,'' J. Mech. Phys. Solids, **49**, pp. 2031–2054.
[24] Redanz, P., and Fleck, N. A., 2001, ''The Compaction of a Random Distribution of Metal Cylinders by the Discrete Element Method,'' Acta Mater., **49**, pp. 4325–4335.
[25] Johnson, K. L., 1985, *Contact Mechanics*, Cambridge University Press, London, UK.
[26] Cundall, P. A., 1988, ''Computer Simulations of Dense Sphere Assemblies,'' *Micromechanics of Granular Materials*, M. Satake and J. T. Jenkins, ed., Elsevier, Amsterdam, pp. 113–123.
[27] Bathurst, R. J., and Rothenburg, L., 1988, ''Micromechanical Aspects of Isotropic Granular Assemblies With Linear Contact Interactions,'' ASME J. Appl. Mech., **55**, pp. 17–23.

[28] Torquato, S., 2002, *Random Heterogeneous Materials, Microstructure and Macroscopic Properties*, Springer-Verlag, New York.
[29] Suiker, A. S. J., 2002, *The Mechanical Behavior of Ballasted Railway Tracks*, dissertation, Delft University Press, Delft, The Netherlands (pdf-format available at http://www.library.tudelft.nl/dissertations/).
[30] Alexander, S., 1998, ''Amorphous Solids: Their Structure, Lattice Dynamics and Elasticity,'' Phys. Rep., **296**, pp. 65–236.
[31] Silbert, L. E., Ertaş, D., Grest, G. S., Halsey, T. C., and Levine, D., 2002, ''Geometry of Frictionless and Frictional Sphere Packings,'' Phys. Rev. E, **65**(031304), pp. 1–6.
[32] Edwards, S. F., 1998, ''The Equations of Stress in a Granular Material,'' Physica A, **249**, pp. 226–231.
[33] Ng, T. T., and Dobry, R., 1994, ''A Non-linear Numerical Model for Soil Mechanics,'' J. Geotech. Eng., **120**, pp. 388–403.
[34] Lambe, T. W., and Whitman, R. V., 1969, *Soil Mechanics*, John Wiley and Sons, New York.
[35] Davy, C. A., Fleck, N. A., and Bolton, M. D., 2004, ''The Collapse Behavior of a Sugar Aggregate,'' submitted, for publication.
[36] Lade, P. V., and Duncan, J. M., 1975, ''Elastoplastic Stress-Strain Theory for Cohesionless Soil,'' J. Geotech. Eng., **101**, pp. 1037–1053.
[37] Chen, W. F., and Saleeb, A. F., 1982, *Constitutive Equations for Engineering Materials*, John Wiley and Sons, New York.

On Timoshenko Beams of Rectangular Cross-Section

James R. Hutchinson
Professor Emeritus
Department of Civil and Environmental Engineering,
University of California,
Davis, CA 95616
Life Mem. ASME

It was recently shown that the shear coefficient for a rectangular Timoshenko beam is highly dependent on the aspect ratio of the beam. This research investigates the reasons for that behavior by comparison of the Timoshenko beam solution with a new three-dimensional solution for a simply supported beam. The new solution is a series solution that converges to any desired accuracy. Comparisons are also made to both elementary and Mindlin plates. The Mindlin plate solution is in excellent agreement with the three-dimensional solution for the simply supported case, and is used as a basis of comparison for a free-free beam. It is found that a shear coefficient which would cause matching of the three-dimensional and Mindlin solutions would have to be a function of the wave length as well as the aspect ratio. Physical explanations are given for the high dependence on aspect ratio and for the dependence on wave length. [DOI: 10.1115/1.1751186]

Introduction

In a recent paper, Hutchinson [1] derived a general expression for the shear coefficient in Timoshenko beams. In a discussion of that paper Stephen [2] pointed out that he had derived the same expression for the shear coefficient in an entirely different way in 1980, [3]. This particular shear coefficient will be referred to as the S-H coefficient in this paper. In his discussion Stephen noted, ''A further very interesting feature of [1], Figs. 3 and 4, is the possibility of the S-H coefficient taking on negative value for combination of large width-to-depth ratios and for large Poisson's ratio. The effect of a negative coefficient would be to stiffen the structure, leading to a natural frequency higher than that predicted by Euler-Bernoulli theory. Nevertheless, the physical implication of a possible negative coefficient requires further consideration.'' The purpose of this paper is to further investigate this interesting phenomenon.

In Ref. [1], Timoshenko beam theory, using the S-H coefficient, was compared to a three-dimensional series solution of the governing equations for the completely free beam. The three-dimensional solution was described in Hutchinson and Zillmer [4,5]. Because of limitations on the number of terms required in the series, the convergence was not assured for the range of cases needed for meaningful comparison. The limitation was caused by the size of the characteristic matrix. The order of the characteristic matrix for the three-dimensional problem was $N_xN_y+N_yN_z+N_zN_x$, where N_x, N_y, and N_z are the number of terms in the x, y, and z directions. The number of terms in each direction must be kept approximately proportional to the dimensions in the corresponding directions. For a compact body, however, convergence is no problem. A convergent three-dimensional solution for a $1\times1\times2$ rectangular parallelepiped is used in this paper for comparison.

One of the comparisons in Ref. [1] was to the work of Armenàkas et al. [6] for the vibration of infinitely long circular cylindrical shells. Their $n=1$ case corresponds to the beam vibrations of simply supported beams. The frequencies from that work correspond almost exactly with the frequencies found using Timoshenko beam theory and the S-H coefficient. Because of that close correspondence, it was decided to look at the simply supported rectangular beam.

The only easy three-dimensional solution for the simply supported rectangular beam is for the plane stress case developed in Ref. [5]. It was found, however, that a new series solution could be developed for the simply supported case for which the order of the matrix would be N_x+N_y. This solution could then be easily made to converge to any required accuracy and provides an excellent basis of comparison. Both the elementary plate and the Mindlin plate solutions were evaluated for the case of simple supports on the ends and free along the sides and compared with the three-dimensional solution and the Timoshenko beam solution. It was found that the Mindlin and three-dimensional solution agreed very well so that the Mindlin plate solution could be used as a basis of comparison for beams with other end support conditions.

The case of a beam with free ends was also investigated and compared to the elementary and Mindlin plate solutions. The elementary and Mindlin plate solutions for the completely free plate are more complicated than that of the plate simply supported on two opposite edges. A solution for the completely free Mindlin plate was presented by Gorman and Ding [7] in 1996. They used the method of superposition. Rather than try to duplicate their solution process I decided to develop a new series solution. The superposition method and the series solution method are basically the same. They both satisfy the differential equations identically, some of the boundary conditions identically and the remaining boundary conditions approximately. The approximation of the boundary conditions becomes better as more terms are chosen in the series. The differences between the superposition and series method is more in the derivation process than in the final results.

In all comparisons it was found that the Timoshenko beam solution with the S-H coefficient gave good results only over limited ranges. An S-H coefficient for which the beam would provide a good match with the more accurate solutions would have to be a function of the wave length as well as the aspect ratio. To study this phenomenon, both displacement and stress resultant mode shapes were investigated for the simply supported beam.

Beam Solutions

The Timoshenko beam equations and solutions, as well as the elementary Euler-Bernoulli beam equations and their solutions are well known. One concise reference which gives the characteristic equations for a number of boundary conditions is Flügge [8]. The S-H coefficient, k, for a beam of rectangular cross-section is

Contributed by the Applied Mechanics Division of THE AMERICAN SOCIETY OF MECHANICAL ENGINEERS for publication in the ASME JOURNAL OF APPLIED MECHANICS. Manuscript received by the ASME Applied Mechanics Division, August 6, 2002; final revision, August 6, 2003. Associate Editor: R. C. Benson. Discussion on the paper should be addressed to the Editor, Prof. Robert M. McMeeking, Journal of Applied Mechanics, Department of Mechanical and Environmental Engineering, University of California–Santa Barbara, Santa Barbara, CA 93106-5070, and will be accepted until four months after final publication of the paper itself in the ASME JOURNAL OF APPLIED MECHANICS.

$$k = -\frac{2(1+\nu)}{C+\nu(1-W^2)} \tag{1}$$

where ν is Poisson's ratio, W is the width-to-depth ratio of the beam, and C is

$$C = -2.4 - 3\nu + \nu W^2 + \sum_{n=1}^{\infty} \frac{36\nu^2 W^4[n\pi - W\tanh(n\pi/W)]}{(n\pi)^5(1+\nu)}. \tag{2}$$

The Timoshenko beam equations solved with the above S-H coefficient is referred to as the Timoshenko solution in this paper.

Three-Dimensional Solution

Table 1 is a subset of the solution forms derived in Ref. [4]. Sinusoidal motion is assumed so that each term is considered as multiplied by $\sin \omega t$. In the table the *s* and *c* in parentheses refer to the sine and cosine, respectively, with the argument αx for the first set in parentheses in column 1, βy for the second set in column 1, and δz for the third set in column 1, $\overline{\alpha} x$ for the first set in columns 2, 3, and 4, $\overline{\beta} y$ for the second set in columns 2, 3, and 4, and $\overline{\delta} z$ for the third set in columns 2, 3, and 4. The relations between the wave numbers are

$$\alpha^2 + \beta^2 + \delta^2 = \omega^2/c_1^2 \tag{3}$$

$$\overline{\alpha}^2 + \overline{\beta}^2 + \overline{\delta}^2 = \omega^2/c_2^2 \tag{4}$$

where ω is the natural frequency, and c_1 and c_2 are the dilatational and shear wave velocities, respectively. The constant K appearing in Table 1 is $\omega^2\lambda/c_1^2$. The constants λ and μ are Lame's constants.

The physical dimensions and coordinate system used in this section is shown in Fig. 1. The width of the beam is $2a$. The depth of the beam is $2b$, and the length of the beam is $2c$. To satisfy simply supported boundary conditions at the ends $z = \pm c$ set,

$$\delta = \overline{\delta} = \pi/2c. \tag{5}$$

Note that $\pi/2c$ could be multiplied by an integer, but it is equally valid to consider $2c$ as the wave length L. The boundary conditions on the sides of the beam are

$$\tau_{xy}(a,y,z) = 0 \tag{6}$$

$$\tau_{xz}(a,y,z) = 0 \tag{7}$$

$$\tau_{xy}(x,b,z) = 0 \tag{8}$$

$$\tau_{yz}(x,b,z) = 0 \tag{9}$$

Table 1 Solution forms for the three-dimensional elasticity equations in Cartesian coordinates

	1	2	3	4
u	$-\alpha(s)(s)(c)$	$-\overline{\beta}(s)(s)(c)$	$-\overline{\delta}(s)(s)(c)$	0
v	$\beta(c)(c)(c)$	$-\overline{\alpha}(c)(c)(c)$	0	$\overline{\delta}(c)(c)(c)$
w	$-\delta(c)(s)(s)$	0	$\overline{\alpha}(c)(s)(s)$	$\overline{\beta}(c)(s)(s)$
σ_x	$-(K+2\mu\alpha^2)$ $(c)(s)(c)$	$-2\mu\overline{\alpha}\overline{\beta}$ $(c)(s)(c)$	$-2\mu\overline{\alpha}\overline{\delta}$ $(c)(s)(c)$	0
σ_y	$-(K+2\mu\beta^2)$ $(c)(s)(c)$	$2\mu\overline{\alpha}\overline{\beta}$ $(c)(s)(c)$	0	$-2\mu\overline{\beta}\overline{\delta}$ $(c)(s)(c)$
σ_z	$-(K+2\mu\delta^2)$ $(c)(s)(c)$	0	$2\mu\overline{\alpha}\overline{\delta}$ $(c)(s)(c)$	$2\mu\beta\delta$ $(c)(s)(c)$
τ_{xy}	$-2\mu\alpha\beta$ $(s)(c)(c)$	$\mu(\overline{\alpha}^2-\overline{\beta}^2)$ $(s)(c)(c)$	$-\mu\beta\delta$ $(s)(c)(c)$	$-\mu\overline{\alpha}\delta$ $(s)(c)(c)$
τ_{yz}	$-2\mu\beta\delta$ $(c)(c)(s)$	$\mu\overline{\alpha}\delta$ $(c)(c)(s)$	$\mu\overline{\alpha}\beta$ $(c)(c)(s)$	$\mu(\beta^2-\delta^2)$ $(c)(c)(s)$
τ_{zx}	$2\mu\alpha\delta$ $(s)(s)(s)$	$\mu\beta\delta$ $(s)(s)(s)$	$\mu(\delta^2-\overline{\alpha}^2)$ $(s)(s)(s)$	$\mu\overline{\alpha}\beta$ $(s)(s)(s)$

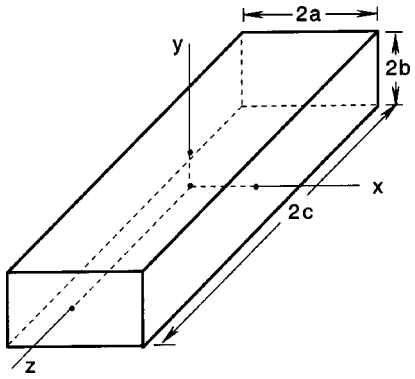

Fig. 1 Coordinates and dimensions for the beam

$$\sigma_x(a,y,z) = 0 \tag{10}$$

$$\sigma_y(x,b,z) = 0. \tag{11}$$

Two series are formed from linear combinations of the four solution forms in Table 1. For example,

$$\sigma_x = \sum_{n=1}^{N_y} A_n[a_1C_1 + a_2C_2 + a_3C_3 + a_4C_4] + \sum_{n=1}^{N_x} B_n[b_1C_1 + b_2C_2 + b_3C_3 + b_4C_4] \tag{12}$$

where C_1, C_2, C_3, and C_4 refer to the expressions in columns 1, 2, 3, and 4 of Table 1, respectively. The *a*'s and *b*'s are chosen so as to partially satisfy the boundary conditions. N_x and N_y refer to the number of terms in the x and y directions, respectively. With exception of the *C*'s, expressions for all displacements and stresses are identical to Eq. (12). For the *A* series choose

$$\beta = \overline{\beta} = \frac{(2n-1)\pi}{2b} \quad n = 1,2,3 \ldots N_y. \tag{13}$$

This choice makes the *A* series satisfy boundary conditions (8) and (9). For the *B* series choose,

$$\alpha = \overline{\alpha} = \frac{(n-1)\pi}{a} \quad n = 1,2,3 \ldots N_x. \tag{14}$$

This choice makes the *B* series satisfy boundary conditions (6) and (7). Choosing the *a*'s and *b*'s as follows, completes identical satisfaction of boundary conditions (6), (7), (8), and (9).

$$a_1 = (\beta^2 + \delta^2 - \overline{\alpha}^2)/\alpha \sin \alpha a \tag{15}$$

$$a_2 = -2\beta/\sin \overline{\alpha} a \tag{16}$$

$$a_3 = -2\delta/\sin \overline{\alpha} a \tag{17}$$

$$a_4 = 0 \tag{18}$$

$$b_1 = (\delta^2 + \alpha^2 - \overline{\beta}^2)/\beta \cos \beta b \tag{19}$$

$$b_2 = 2\alpha/\cos \overline{\beta} b \tag{20}$$

$$b_3 = 0 \tag{21}$$

$$b_4 = -2\delta/\cos \overline{\beta} b \tag{22}$$

To keep track of the wave numbers, the β's in Eq. (13) will be subscripted with an *A* and the α's in Eq. (14) will be subscripted with a *B*. Similarly the α's and β's in Eqs. (15) to (18) will be subscripted with an *A* and the α's and β's in Eqs. (19) to (22) will be subscripted with a *B*. Boundary condition (10) is satisfied by setting

$$\int_0^b \sigma_x(a,y) \sin \beta_{An} y \, dy = 0. \tag{23}$$

Evaluation of this integral gives

$$[M_{11}]\{A\}+[M_{12}]\{B\}=0 \tag{24}$$

where M_{11} is a diagonal matrix of order n_y. The coefficients on the diagonal are

$$M_{11nn}=\frac{b}{2}[-(K+2\mu\alpha_{An}^2)(\beta_{An}^2+\delta^2-\overline{\alpha}_{An}^2)/\alpha_{An}\tan\alpha_{An}a + 4\mu\overline{\alpha}_{An}^2(\beta_{An}^2+\delta^2)/\overline{\alpha}_{An}\tan\overline{\alpha}_{An}a] \quad \text{where } n=1,2,3\ldots N_y. \tag{25}$$

The matrix M_{12} has the following coefficients:

$$M_{12nm}=[-(K-2\mu\alpha_{Bm}^2)(\delta^2+\alpha_{Bm}^2-\overline{\beta}_{Bm}^2)/(\beta_{An}^2-\beta_{Bm}^2) - 4\mu\alpha_{Bm}^2\overline{\beta}_{Bm}^2/(\beta_{An}^2-\overline{\beta}_{Bm}^2)]\cos\alpha_{Bm}a\sin\beta_{An}b \quad \text{where } n=1,2,3,\ldots N_y \quad \text{and} \quad m=1,2,3,\ldots N_x. \tag{26}$$

Boundary condition (11) is satisfied by setting

$$\int_0^a \sigma_y(x,b)\cos\alpha_{Bn}x\,dx=0. \tag{27}$$

Evaluation of this integral gives

$$[M_{21}]\{A\}+[M_{22}]\{B\}=0 \tag{28}$$

where M_{22} is a diagonal matrix of order N_x. The coefficients on the diagonal are

$$M_{22mm}=\left(\frac{a}{2}\right)^*[-(K+2\mu\beta_{Bm}^2)\beta_{Bm}\tan\beta_{Bm}b(\delta^2+\alpha_{Bm}^2-\beta_{Bm}^2)/ \beta_{Bm}^2+4\mu(a_{Bm}^2+\delta^2)\overline{\beta}_{Bm}\tan\overline{\beta}_{Bm}b] \quad \text{where } m=1,2,3\ldots N_x. \tag{29}$$

The asterisk on $a/2$ means that for m greater than 1 the quantity is $a/2$, whereas, $m=1$ is a special case and for that case a must be substituted for $a/2$. The matrix M_{21} has the following coefficients:

$$M_{21mn}=[(K-2\mu\beta_{An}^2)(\delta^2+\beta_{An}^2-\overline{\alpha}_{An}^2)/(\alpha_{Bm}^2-\alpha_{An}^2) + 4\mu\beta_{An}^2\overline{\alpha}_{An}^2/(\alpha_{Bm}^2-\overline{\alpha}_{An}^2)]\cos\alpha_{Bm}a\sin\beta_{An}b \quad \text{where } n=1,2,3,\ldots N_y \quad \text{and} \quad m=1,2,3,\ldots N_x. \tag{30}$$

Equations (24) and (28) can be written as a single matrix equation as follows:

$$\begin{bmatrix} M_{11} & M_{12} \\ M_{21} & M_{22} \end{bmatrix}\begin{Bmatrix} A \\ B \end{Bmatrix}=\begin{Bmatrix} 0 \\ 0 \end{Bmatrix}. \tag{31}$$

It can be seen from Eqs. (3) and (4) that α^2, β^2, $\overline{\alpha}^2$, and $\overline{\beta}^2$ have the possibility of taking on negative values. For the A series β and $\overline{\beta}$ are positive so α_A^2 and $\overline{\alpha}_A^2$ can be negative, likewise, for the B series α and $\overline{\alpha}$ are positive so β_B^2 and $\overline{\beta}_B^2$ can be negative. In Eqs. (25), (26), (29), and (30) the only place where any of the values α_A, $\overline{\alpha}_A$, β_B, or $\overline{\beta}_B$ occur in the nonsquared form, they are in the form $\alpha_{An}\tan\alpha_{An}a$ which is real and is computed as $-|\alpha_{An}|\tanh(|\alpha_{An}|a)$.

A dimensionless frequency parameter is introduced as the frequency divided by the shear velocity times the depth of the beam $(2b)$. This frequency parameter will be referred to as the frequency in the remainder of this paper. The only parameters of the problem are the width-to-depth ratio, the length-to-depth ratio and Poisson's ratio. To solve Eq. (31), values of the width-to-depth ratio, the length-to-depth ratio, and Poisson's ratio are assumed. A starting value of the frequency is assumed and frequency values are stepped along until a sign change in the determinant of the matrix $[M]$ is found. The interval is then halved repeatedly until the desired accuracy is obtained.

Plate Solutions

The elementary plate has been treated in a number of books and papers. The most extensive compendium of solutions is in the monograph by Leissa [9]. The elementary SS-F-SS-F plate is treated by Leissa starting on p. 53. Because of the completeness of that work it is not necessary to repeat the equations here. Leissa also treats the SS-F-SS-F Mindlin Plate starting on p. 318 using the 1956 work of Mindlin et al. [10]. There is a drawback with the equation development in the 1956 Mindlin et al. paper. In that paper, the authors assume a shear coefficient of $\pi^2/12$ and build that into their Eqs. (3), [10]. The use of any other shear coefficient in Eqs. (3), [10], will produce incorrect results. This drawback is easily remedied by going back to Mindlin's 1951 paper, [11]. Using the expressions for δ_1^2 and δ_2^2 from Mindlin's Eq. (59), [11], and σ_1 and σ_2 from Eq. (60), [11], and ω^2 from Eq. (54), [11], will clear up the problem. The remainder of the Mindlin et al. 1956 paper clearly shows how the solution is accomplished and will not be repeated here.

The choice of a best shear coefficient in the Mindlin theory has also received some attention. In his 1951 paper Mindlin [11] determined the shear coefficient in two different ways. One way was matching the thickness shear modes, which led to the coefficient $\pi^2/12$. The other way was matching the three-dimensional solution for straight crested flexural waves at short wave lengths, resulting in a shear coefficient that is a function of Poisson's ratio and is found by solving a cubic equation. In a 1984 paper, Hutchinson [12] found that by matching the solution for straight crested flexural waves at long wave lengths a shear coefficient of $5/(6-\nu)$ could be found. In Ref. [12] this shear coefficient was found best for the lower frequency modes and so is the one used in this paper. A brief numerical check also showed that this coefficient provided the closest match to the three-dimensional theory developed in this paper. This coefficient was also suggested in the work of Witrick [13] in 1986 and Stephen [14] in 1997. Both Mindlin [11] and Stephen [14] pointed out that for thickness shear modes a coefficient of $\pi^2/12$ provides accurate results, but for the modes considered in this paper the coefficient of $5/(6-\nu)$ was clearly best. There is an interesting connection between the plate coefficient $5/(6-\nu)$ and the S-H coefficient given in Eq. (1). If one considers the value of W in Eqs. (1) and (2) approaching zero, one gets $k=5(1+\nu)/(6+5\nu)$. This is the plane stress solution. If one considers the conversion to plane strain by the appropriate substitution of Poisson's ratio one gets $5/(6-\nu)$.

For the completely free Mindlin plate solution a new series solution was developed. This series solution is very similar to the method used by Gorman and Ding [7]. It uses solutions of the governing equations. It satisfies some of the boundary conditions exactly and approximates the rest. The superposition method of Gorman and Ding accomplishes the same thing but in a different manner. For the plate solutions it was decided to use the same coordinate system as Mindlin rather than the beam coordinate system shown in Fig. 1. In the Mindlin coordinate system x and y are in the plane of the plate and z is out of the plate forming a right handed orthogonal coordinate system. In this coordinate system x is the width y is the length and z is the depth of the corresponding beam.

To carry out the series solution, solutions of the differential equation are found. The three types of solution forms are tabulated in Table 2. In this table only solution forms which are symmetric in both the length-y and width-x coordinates are shown. To match beam solutions, only the solutions which are symmetric in the width coordinate are needed. Solutions symmetric in y account for

Table 2 Solution forms for Mindlin plates in Cartesian coordinates

	Form 1	Form 2	Form 3	Multiplier
w	1	1	0	$\cos(\xi x)\cos(\eta y)$
ψ_x	$-(\sigma_1-1)\xi_1$	$-(\sigma_2-1)\xi_2$	$1/\xi_3$	$\sin(\xi x)\cos(\eta y)$
ψ_y	$-(\sigma_1-1)\eta_1$	$-(\sigma_2-1)\eta_2$	$-1/n_3$	$\cos(\xi x)\sin(\eta y)$
M_x/D	$-(\sigma_1-1)(\xi_1^2-\nu\eta_1^2)$	$-(\sigma_2-1)(\eta_2^2-\nu\xi_2^2)$	$1-\nu$	$\cos(\xi x)\cos(\eta y)$
M_y/D	$-(\sigma_1-1)(\eta_1^2-\nu\xi_1^2)$	$(\sigma_2-1)(\eta_2^2-\nu\xi_2^2)$	$-(1-\nu)$	$\cos(\xi x)\cos(\eta y)$
$M_{yx}/D(1-\nu)$	$(\sigma_1-1)\xi_1\eta_1$	$(\sigma_2-1)\xi_2\eta_2$	$(\xi_3^2-\eta_3^2)/2\xi_3\eta_3$	$\sin(\xi x)\sin(\eta y)$
Q_x/κ^2Gh	$-\sigma_1\xi_1$	$-\sigma_2\xi_2$	$1/\xi_3$	$\sin(\xi x)\cos(\eta y)$
Q_y/κ^2Gh	$-\sigma_1\eta_1$	$-\sigma_2\eta_2$	$-1/\eta_3$	$\cos(\xi x)\sin(\eta y)$

modes 1, 3, 5 . . . . For modes 2, 4, 6 . . . slight modifications must be made to the table. The multiplier in the last column of the table applies to all three forms, thus for example, the displacement w for Form 2 is $\cos(\xi_2 x)\cos(\eta_2 y)$. Other notation follows that of Mindlin [8] with one exception—what Mindlin calls ω, I will call δ_3^2, and I will introduce a dimensionless frequency ω. The notation is as follows:

G-shear modulus

h-plate thickness

ν=Poisson's ratio

D-plate stiffness $\quad D=Gh^3/6(1-\upsilon)$

κ^2-Shear coefficient

ρ-density

p-natural frequency

ω-dimensionless frequency $\quad \omega=\rho p^2 h/D$

Mindlin's values δ_1^2, δ_2^2, δ_3^2, σ_1, and σ_2 can be expressed in terms of the dimensionless frequency as

$$\delta_1^2=\frac{3\omega^2(1-\nu)}{h^2}\left[\frac{1}{12}+\frac{1}{6(1-\nu)\kappa^2}+\sqrt{\left(\frac{1}{12}-\frac{1}{6(1-\nu)\kappa^2}\right)^2+\frac{4}{6(1-\nu)\omega^2}}\right] \tag{32}$$

$$\delta_2^2=\frac{3\omega^2(1-\nu)}{h^2}\left[\frac{1}{12}+\frac{1}{6(1-\nu)\kappa^2}-\sqrt{\left(\frac{1}{12}-\frac{1}{6(1-\nu)\kappa^2}\right)^2+\frac{4}{6(1-\nu)\omega^2}}\right] \tag{33}$$

$$\delta_3^2=\frac{\omega^2-12\kappa^2}{h^2} \tag{34}$$

$$\sigma_1=\frac{2\delta_2^2h^2}{(1-\nu)(\omega^2-12\kappa^2)} \tag{35}$$

$$\sigma_2=\frac{2\delta_1^2h^2}{(1-\nu)(\omega^2-12\kappa^2)}. \tag{36}$$

The relationship between ξ, η and δ is

$$\xi_1^2+\eta_1^2=\delta_1^2 \tag{37}$$

$$\xi_2^2+\eta_2^2=\delta_2^2 \tag{38}$$

$$\xi_3^2+\eta_3^2=\delta_3^2. \tag{39}$$

Use is made of the symmetry and antisymmetry in the problem so the boundary conditions only need to be considered at positive x and positive y. The boundary conditions which must be satisfied are

$$M_x(a,y)=0 \quad M_y(x,b)=0 \tag{40}$$

$$M_{yx}(a,y)=0 \quad M_{yx}(x,b)=0 \tag{41}$$

$$Q_x(a,y)=0 \quad Q_y(x,b)=0. \tag{42}$$

Solutions are formed in two series which are called the A series and the B series. The general form of these series is

$$f(x,y)=\sum_{n=1}^{N_x}A_n[a_{1n}g_{1n}+a_{2n}g_{2n}+a_{3n}g_{3n}]+\sum_{n=1}^{N_y}B_n[b_{1n}g_{1n}+b_{2n}g_{2n}+b_{3n}g_{3n}] \tag{43}$$

where N_x and N_y are the number of terms in the x and y directions respectively. A, B, a, and b are arbitrary constants. The function f represents any of the functions in the left column of Table 1 (i.e., displacement, slopes, moments, or shears). The g_1, g_2, g_3, represent the functions listed in the columns 1, 2, and 3 with their appropriate multipliers. Thus, for the displacement w, g_1 would be $\cos(\xi_{1n}x)\cos(n_{1n}x)$, for the slope ψ_x, g_1 would be $-(\sigma_1-1)\xi_{1n}\sin(\xi_{1n}x)\cos(\eta_{1n}y)$ etc.

Choosing

$$\xi_{An}=\xi_{1An}=\xi_{2An}=\xi_{3An}=\frac{(n-1)\pi}{a} \quad n=1,2,3\ldots N_x \tag{44}$$

makes the A series satisfy the boundary conditions $M_{yx}(a,y)=0$ and $Q_x(a,y)=0$. Choosing

$$\eta_{Bn}=\eta_{1Bn}=\eta_{2Bn}=\eta_{3Bn}=\frac{(n-1)\pi}{b} \quad n=1,2,3\ldots N_y \tag{45}$$

makes the B series satisfy the boundary conditions $M_{yx}(x,b)=0$ and $Q_y(x,b)=0$. The coefficients can now be adjusted to satisfy $M_{yx}(a,y)=0$ and $Q_x(a,y)=0$ in the B series and $M_{yx}(x,b)=0$ and $Q_y(x,b)=0$ in the A series. The A series representation of the twisting moment is

$$M_{yx}(x,b)=\sum_{1}^{N_x}A_n[a_{1n}T_{1n}+a_{2n}T_{2n}+a_{3n}T_{3n}]\frac{1}{\xi_n}\sin\xi_n x \tag{46}$$

where

$$T_1=(1-\nu)(\sigma_1-1)\xi_A^2\eta_{A1}\sin(\eta_{A1}b) \tag{47}$$

$$T_2=(1-\nu)(\sigma_2-1)\xi_A^2\eta_{A2}\sin(\eta_{A2}b) \tag{48}$$

$$T_3=(1-\nu)(\xi_A^2-\eta_{A3}^2)\eta_{A3}\sin(\eta_{A3}b)/2\eta_{A3}^2. \tag{49}$$

The A series representation of the shear Q is

$$Q_y(x,b)=\sum_{1}^{N_x} A_n[a_{1n}V_{1n}+a_{2n}V_{2n}+a_{3n}V_{3n}]\cos\xi_n x \quad (50)$$

where

$$V_1=-\sigma_1\eta_{A1}\sin(\eta_{A1}b) \quad (51)$$

$$V_2=-\sigma_2\eta_{A2}\sin(\eta_{A2}b) \quad (52)$$

$$V_3=-\eta_{A3}\sin(\eta_{A3}b)/\eta_{A3}^2. \quad (53)$$

The quantities in brackets in Eqs. (46) and (50) must be zero. This is accomplished by letting

$$a_1=T_2V_3-T_3V_2 \quad (54)$$

$$a_2=T_3V_1-T_1V_3 \quad (55)$$

$$a_3=T_1V_2-T_2V_1. \quad (56)$$

The same process is carried out to determine the values b_1, b_2, and b_3 so that $M_{yx}(a,y)=0$ and $Q_x(a,y)=0$. The only remaining boundary conditions are on the bending moments and those will be satisfied by orthogonality. That is by setting

$$\int_0^a M_y(x,b)\cos\left(\frac{(m-1)\pi x}{a}\right)dx=0 \quad m=1,2,3\ldots N_x \quad (57)$$

$$\int_0^b M_x(a,y)\cos\left(\frac{(m-1)\pi y}{b}\right)dy=0 \quad m=1,2,3\ldots N_y. \quad (58)$$

Evaluation of the integral in Eq. (57) leads to the matrix equation

$$[C_{11}]\{A\}+[C_{12}]\{B\}=\{0\} \quad (59)$$

where the matrix $[C_{11}]$ is a diagonal matrix whose terms are

$$C_{11n}=(a/2)^*[-a_{1n}(\sigma_1-1)(\eta_{A1n}^2+\nu\xi_{An}^2)\cos(\eta_{A1n}b) -a_{2n}(\sigma_2-1)(\eta_{A2n}^2+\nu\xi_{An}^2)\cos(\eta_{A2n}b) -a_{3n}(1-\nu)\cos(\eta_{A3n}b)] \quad (60)$$

where $(a/2)^*$ equals a for $n=1$ and $a/2$ for $n>1$ and $n=1,2,3\ldots N_x$. The matrix $[C_{12}]$ is a full matrix whose coefficients are

$$C_{12mn}=[-b_{1n}(\sigma_1-1)(\eta_{Bn}^2+\nu\xi_{B1n}^2)\xi_{B1n}\sin(\xi_{B1n}a)/ (\xi_{B1n}^2-\xi_{Am}^2)-b_{2n}(\sigma_2-1)(\eta_{Bn}^2+\nu\xi_{B2n}^2)\xi_{B2n}\sin(\xi_{B2n}a)/ (\xi_{B2n}^2-\xi_{Am}^2)-b_{3n}(1-\nu)\xi_{B3n}\sin(\xi_{B3n}a)/ (\xi_{B3n}^2-\xi_{Am}^2)]\cos(\xi_{Am}a)\cos(\eta_{Bn}b) \quad (61)$$

where $m=1,2,3\ldots N_x$ $n=1,2,3\ldots N_y$.

Evaluation of the integral in Eq. (58) leads to the matrix equation

$$[C_{21}]\{A\}+[C_{22}]\{B\}=\{0\} \quad (62)$$

where the matrix $[C_{22}]$ is a diagonal matrix whose terms are

$$C_{22n}=(b/2)^*[-b_{1n}(\sigma_1-1)(\xi_{B1n}^2+\nu\eta_{Bn}^2)\cos(\xi_{B1n}a) -b_{2n}(\sigma_2-1)(\xi_{B2n}^2+\nu\eta_{Bn}^2)\cos(\xi_{B2n}a) -b_{3n}(1-\nu)\cos(\xi_{B3n}a)] \quad (62)$$

where $(b/2)^*$ equals b for $n=1$ and $b/2$ for $n>1$ and $n=1,2,3\ldots N_x$. The matrix $[C_{12}]$ is a full matrix whose coefficients are

$$C_{21mn}=[-a_{1n}(\sigma_1-1)(\xi_{An}^2+\nu\eta_{A1n}^2)\eta_{A1n}\sin(\eta_{A1n}a)/ (\eta_{A1n}^2-\eta_{Bm}^2)-a_{2n}(\sigma_2-1) \times(\xi_{An}^2+\nu\eta_{A2n}^2)\eta_{A2n}\sin(\eta_{A2n}a)/ (\eta_{A2n}^2-\eta_{Bm}^2)-a_{3n}(1-\nu)\eta_{A3n}\sin(\eta_{A3n}b)/ (\eta_{A3n}^2-\eta_{Bm}^2)]\cos(\xi_{An}a)\cos(\eta_{Bn}b) \quad (64)$$

where $m=1,2,3\ldots N_y$ $n=1,2,3\ldots N_x$.

Combining Eqs. (30) and (33) gives

$$\begin{bmatrix}C_{11} & C_{12}\\ C_{21} & C_{22}\end{bmatrix}\begin{Bmatrix}A\\ B\end{Bmatrix}=\begin{Bmatrix}0\\ 0\end{Bmatrix}. \quad (65)$$

The matrix C is a square matrix of order N_x+N_y. The entire problem can be made dimensionless just by setting the thickness $h=1$. The lengths a and b are then the ratios of a and b to h. The only parameters in the problem are a, b, ν, κ^2 and ω. Natural frequencies are found by assuming values of a, b, ν, and κ^2 then searching for the values of ω which make the determinant of C go to zero. Mode shapes are found by solving for the relative values of A and B after the natural frequency is established.

It should be noted from Eqs. (37)–(39) that ξ^2 and η^2 can be negative. Some authors (e.g., Refs. [7] and [10]) talk about dividing into regions because of this, however, the problem can be handled more simply. It can be seen that the only places ξ and η appear in a nonsquared form in any of the foregoing equations, they appear in the form $\cos(\xi a)$ or in the form $\xi\sin(\xi a)$ where ξ can stand for either ξ or η and a can stand for either a or b. Both of these forms are real. If ξ^2 is positive they are calculated as $\cos(\xi a)$ and $\xi\sin(\xi a)$. If ξ^2 is negative they are calculated as $\cosh(|\xi|a)$ and $-|\xi|\sinh(|\xi|a)$, respectively. It also is desirable to divide the hyperbolic functions by $\exp(\xi a)$ to prevent computer overflow.

The elementary plate solutions were found by simply letting the thickness of the plate go very small compared with the other dimensions, solving using the above Mindlin plate formulation and then using an appropriate scaling factor on the frequency. The accuracy of this approximation was checked by comparing the solutions in Gorman and Ding [7] and in Leissa [9].

Results for Simply Supported Comparison

Convergence checks were made on the three-dimensional solution. For a square beam, it was found that by using five terms in each series, the frequency was good to about four significant figures. By using 100 terms in each series the frequency was good to about eight significant figures. As in my previous experience with these series solutions, it was found best to choose a number of terms in each of the series roughly proportional to the dimensions in those directions. In keeping with this concept, for all numerical results reported, I choose 100 terms in the shortest direction and a correspondingly larger number of terms in the long direction. For example, for a beam with a width-to-depth ratio of 10, I took 100 terms in the y (depth) direction and 1000 terms in the x (width) direction.

In Fig. 2, the values of a shear coefficient reciprocal, which would make the Timoshenko beam theory match the three-dimensional solution, are shown as dashed lines. The solid line is the S-H coefficient reciprocal plotted as a function of the width-to-depth ratio. The numbers on the dashed lines indicate the length-to-depth ratio. It can be seen that when the width-to-depth ratio is less than 2 the match between the required coefficient and the S-H coefficient is very good for any wave length. The match for greater values of width-to-depth ratios is only good for long wave lengths. If the length-to-width ratio is greater than 5 the required coefficient matches the S-H coefficient relatively well.

A perhaps better comparison is made with the natural frequencies in Figs. 3 through 5. These figures show the variation of frequency with the width-to-depth ratio for length-to-depth ratios of 10, 20, and 40, respectively. The figures show the frequencies as determined by the three-dimensional solution (3D), the Mindlin plate solution (M), the Timoshenko beam solution (TB), the elementary plate solution (EP), and the elementary beam solution (EB). The three-dimensional and Mindlin solution plotted as es-

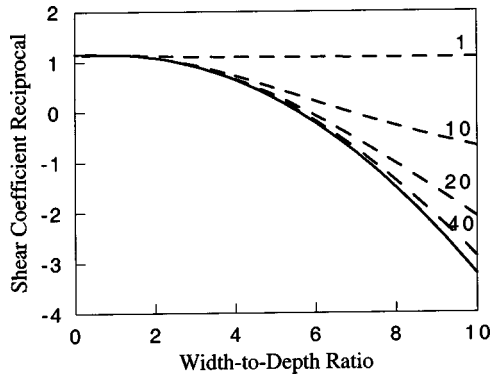

Fig. 2 Shear coefficient reciprocal versus width-to-depth ratio. ——S-H coefficient. — — —Coefficients which match three-dimensional solutions for length-to-depth ratios of 1, 10, 20, and 40. For a simply supported beam.

sentially the same curve and are labeled (3D-M). Tabulated results are also given for selected values in Table 3. By comparing Fig. 2 to Figs. 3 through 5 it can be seen that in the regions where the required shear coefficient matches the S-H coefficient, the frequencies for the Timoshenko beam match that of the three-dimensional solution and the Mindlin plate solution. In Figs. 3 through 5 it can be seen that the frequency does in fact become higher than the frequency predicted by the Euler-Bernoulli beam theory as the width-to-depth ratio increases. These results are all for a Poisson's ratio of 0.3. For a higher Poisson's ratio the

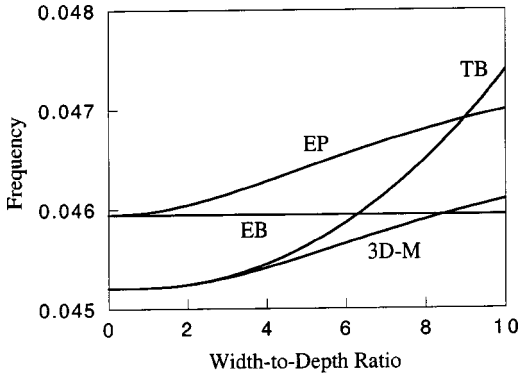

Fig. 3 Frequency versus width-to-depth ratio, for a length-to-depth ratio of 10 and Poisson's ratio of 0.3, for the five solution methods considered. For a simply supported beam.

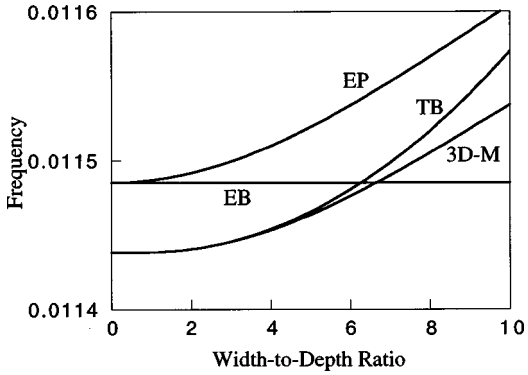

Fig. 4 Frequency versus width-to-depth ratio, for a length-to-depth ratio of 20 and Poisson's ratio of 0.3, for the five solution methods considered. For a simply supported beam.

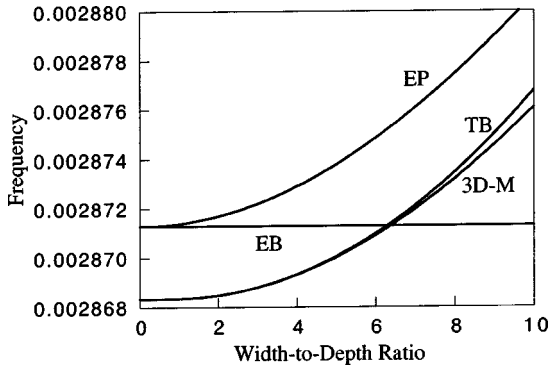

Fig. 5 Frequency versus width-to-depth ratio, for a length-to-depth ratio of 40 and Poisson's ratio of 0.3, for the five solution methods considered. For a simply supported beam.

changes in Figs. 2 through 5 would all be greater, and conversely as Poisson's ratio approaches zero all changes disappear.

One very interesting result which is evident in Figs. 3 through 5 is that the elementary plate solution shows a frequency variation with the width-to-depth ratio that mimics the frequency variation for the three-dimensional solution. The elementary plate formulation does not allow for any shear deformation or rotary inertia. This leads to the conclusion that the large variation of frequency with the width-to depth ratio is not brought about by the presence of shear deformation and rotary inertia, but rather by plate action. There are several things occurring in the plate that aren't usually accounted for in beam theory. One, is the effect of the variation of the displacement v (y direction) as a function of the width coordinate x on the inertia. This effect was accounted for in Ref. [1] by assuming full anticlastic curvature and leads to increased inertia and hence a lowering effect on the frequency. Another plate effect is the twisting effect which produces the twisting moment. This effect was accounted for in Ref. [1] by the assumption of the shear stress distribution found from the three-dimensional solution of the tip loaded cantilever. This assumption gave shear stresses τ_{xz} as well as τ_{yz}. It is the τ_{xz} stresses that produce the resultant twisting moment in the plate. This twisting produces a stiffening effect and hence increases the frequency. The combination of these plate effects leads to a rise in the frequency with an increase in the width-to-depth ratio. The plate effects are the main cause of the frequency variation with the width-to-depth ratio. The derivation of the S-H coefficient by Stephen [3] is based on a three-dimensional solution and, so, also contains the plate effects.

The plate effects also lead to an understanding of the reasons for the divergence of the Timoshenko beam equations from the three-dimensional solution for large width-to-depth ratios and short wave lengths. Both Refs. [1] and [3] made use of three-dimensional static solutions which were applicable to long beams.

Table 3 Frequencies for the simply supported beam for selected length-to-depth (L/D) and width-to-depth (W) ratios computed by the methods listed below. For the Mindlin plate a shear coefficient of $5/(6\text{-}\nu)$ was used. For the Timoshenko beam the S-H coefficient was used. Poisson's ratio was 0.3.

L/D	W	3-D Solution	Mindlin Plate	Timoshenko. Beam	Elementary Beam	Elementary Plate
1	2	2.3925141	2.3926823	2.4201901	4.5940508	4.7507985
1	10	2.4195486	2.4153869	4.7318781	4.5940508	4.7990391
10	2	0.0452410	0.0452478	0.0452420	0.0459405	0.0460392
10	10	0.0460918	0.0460982	0.0473894	0.0459405	0.0469963
20	2	0.0114405	0.0114410	0.0114405	0.0114851	0.0114916
20	10	0.0115377	0.0115384	0.0115732	0.0114851	0.0116040
40	2	0.0028685	0.0028685	0.0028685	0.0028713	0.0028717
40	10	0.0028761	0.0028761	0.0028768	0.0028713	0.0028806

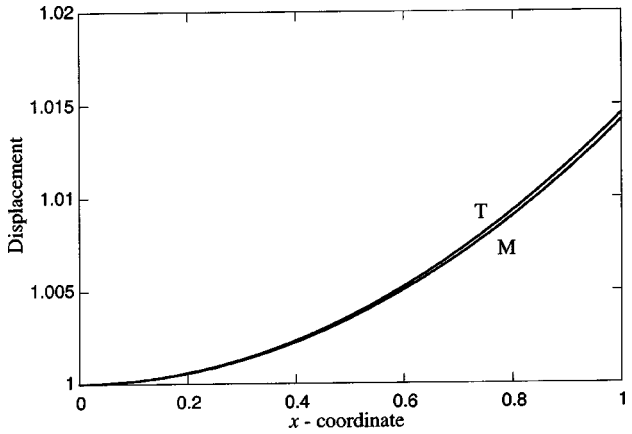

Fig. 6 Displacement versus x at $y=z=0$, for a length-to-depth ratio of 10 and width-to-depth ratio of 2. For a simply supported beam.

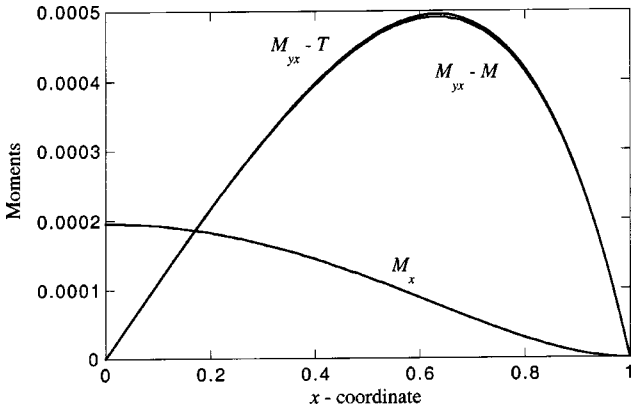

Fig. 8 Twisting moment M_{yx} versus x at $y=L/2$, $z=0$ and bending moment M_x versus x at $y=z=0$, for a length-to-depth ratio of 10 and width-to-depth ratio of 2. For a simply supported beam.

For a short wide beam, the end effects are significant. In the central portion of the beam, the variation of the displacement with x will be greatly suppressed and the plate will be flatter in that region. To better understand this phenomenon, mode shapes were investigated. Both displacement and stress resultant mode shapes were found for the Timoshenko beam theory and the Mindlin plate theory. To show the anticlastic behavior, plots were made of the displacement at $z=0$ and $y=0$ as a function of x. All modes were normalized to unit displacement at $x=y=z=0$. Figure 6 shows the Timoshenko and Mindlin solutions (labeled T and M) for a length-to-depth ratio of 10 and width-to-depth ratio of 2. It can be seen in this figure that the two solutions almost coincide. By looking at Figs. 2 and 3 it can be seen that this is also where the frequencies are reasonably close together. Figure 7 on the other hand is for a length-to-depth ratio of 10 and width-to-depth ratio of 10 for which the frequencies do not match. The Timoshenko and Mindlin solutions do not match for this case. The displacement is much flatter for the Mindlin plate solution than for the beam solution. Displacement modes shapes were also found for length-to-depth ratios of 20 and 40 for several values of the width-to-depth ratio. In all cases the same behavior was noticed. That is, if the frequencies agreed the mode shapes did also, and if the frequencies didn't agree the Mindlin plate displacement modes were much flatter.

Looking at the stress resultants also proved valuable. For the Timoshenko beam solution the twisting moment resultant was found by integrating $y\tau_{xy}$ across the thickness of the beam, where x and y refer to the beam coordinates shown in Fig. 1. Figures 8 and 9 show some of the modal resultant moments in the body. The coordinate system and notation used for these figures is Mindlin's coordinate system and notation. Figures 8 and 9 show the twisting moment M_{yx} at $y=L/2$ and $z=0$ for both the Timoshenko and Mindlin solutions. Also shown is the plot is the bending moment M_x at $y=z=0$. This is the bending moment in the thickness direction and is neglected (assumed zero) in the Timoshenko beam formulation. The moments are in dimensionless form. They are made dimensionless by dividing by the shear modulus and the depth squared. In Fig. 8 a length-to-depth ratio of 10 and width-to-depth ratio of 2 was used. It can be seen that the twisting moments for both the Timoshenko and Mindlin formulations are a very good match. The bending moment M_y which was not shown was 0.021 or approximately 40 times the maximum twisting moment and 100 times the thickness bending moment M_x. Figure 9 is for a length-to-depth ratio of 10 and width-to-depth ratio of 10. It can be seen that there is no match between the two twisting moments, and the moment M_x is larger than the twisting moment found using the Mindlin method. The bending moment M_y for this example is 0.023 or roughly seven times the maximum twisting moment and five times the bending moment M_x. Other com-

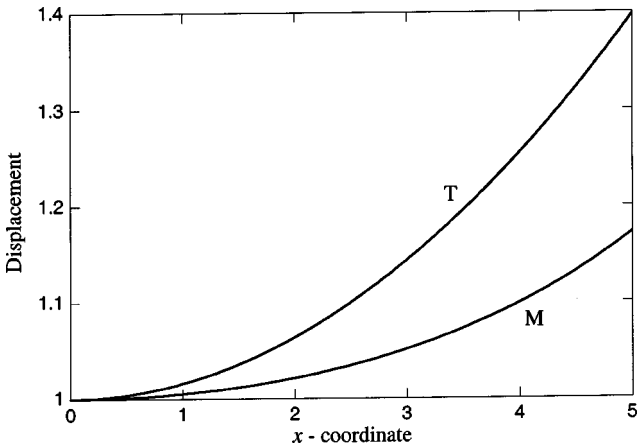

Fig. 7 Displacement versus x at $y=z=0$, for a length-to-depth ratio of 10 and width-to-depth ratio of 10. For a simply supported beam.

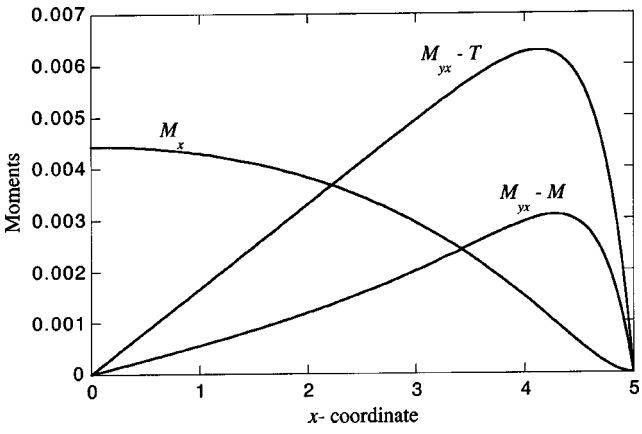

Fig. 9 Twisting moment M_{yx} versus x at $y=L/2$, $z=0$ and bending moment M_x versus x at $y=z=0$, for a length-to-depth ratio of 10 and width-to-depth ratio of 10. For a simply supported beam.

parisons of the twisting moment show similar results, that is, when the frequencies for the two solutions match the twisting moments match, but when they aren't reasonably close the twisting moments also differ. Also when there is no match the thickness bending moment is not negligible.

Results for Free-Free Comparison

Solutions for the Mindlin plate were checked against the work of Gorman and Ding [7]. Of the 360 frequencies for thick plates there was lack of agreement in only ten values. In private correspondence with Professor Gorman it was determined that 6 of those disagreements were typographical and four were due to false roots which sometimes occur in these types of formulations. There were also some minor disagreements in mode identification, however overall the agreement between the two was excellent. The results of the thin plate values in Gorman and Ding were compared with the Mindlin series solution using a thickness-to-width ratio of 0.0001. The results agreed to the same degree of accuracy as for the thick plate. Because of this agreement, the elementary plate solution plots, shown in this paper, are actually the results for a thickness-to-width ratio of 0.0001 using the thick plate formulation.

Solutions for the Mindlin plate were checked against the three-dimensional solution of Hutchinson and Zillmer [5,6]. To get convergence in the three-dimensional solution a $1\times1\times2$ parallelepiped was chosen and $20\times20\times40$ terms were used in the solution. The three-dimensional fundamental frequency was 1.64723 for a Poisson's ratio of 0.300. Mindlin plate theory yielded a frequency of 1.64725 for a shear coefficient of $5/(6-\nu)$. Timoshenko beam theory yielded a frequency of 1.65066 using the S-H coefficient. It is remarkable that both of these simple theories yielded good results for a shape that could neither be considered a beam nor a plate.

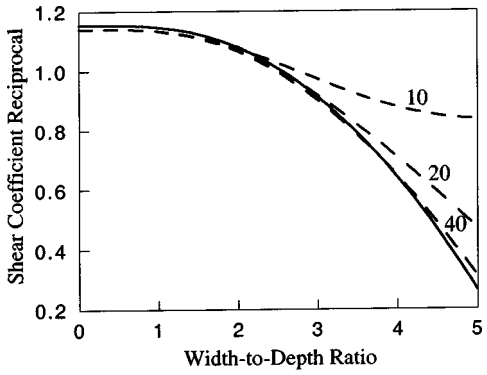

Fig. 10 Shear coefficient reciprocal versus width-to-depth ratio. ——S-H coefficient. — — —Coefficients which match Mindlin plate solutions for the first mode for length-to-depth ratios 10, 20, and 40. For a free-free beam.

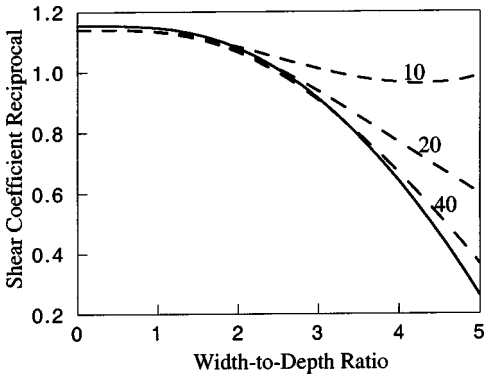

Fig. 11 Shear coefficient reciprocal versus width-to-depth ratio. ——S-H coefficient. — — —Coefficients which match Mindlin plate solutions for the second mode for length-to-depth ratios 10, 20, and 40. For a free-free beam.

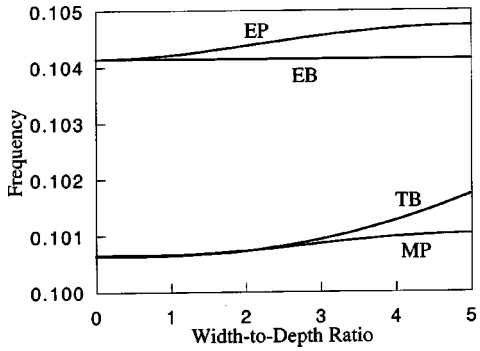

Fig. 12 First mode frequency versus width-to-depth ratio, for a length-to-depth ratio of 10, for the four solutions considered. For a free-free beam.

Plots were made comparing the S-H coefficient reciprocal with the beam shear coefficient reciprocal required to make the Mindlin solution match the beam solution. A Poisson's ratio of 0.3 and a Mindlin plate coefficient of $5/(6-\nu)$ was used for all plots. Unlike the simply supported case, where one can simply refer to a wave length, for the free-free beam different modes must be considered separately. Figures 10 and 11 show the S-H coefficient reciprocal vs. the width-to-depth ratio for the first two modes, respectively. The length-to-depth ratio is a parameter in these plots and is numbered on the plots. It can be seen that the behavior is very similar to simply supported case shown in Fig. 2. Plots were also made for the third and fourth modes but they were so similar to those shown in Figs. 10 and 11 that they are not shown. Figures 12 through 15 show the frequency versus width-to-depth ratio for beams of a fixed length. In these figures EP refers to the elementary plate solution, EB refers to the elementary beam solution, TB refers to the Timoshenko beam solution and MP refers to the Mindlin plate solution. Figures 12 through 14 are for the first mode for length-to-depth ratios of 10, 20 and 40, respectively. Figure 15 is for the second mode with a length-to-depth ratio of 20. It can be seen in all these plots that the change of frequency of the elementary plate mimics that of the frequency change of the Mindlin plate. This is the same behavior that was found for the simply supported case. The change in frequency with the beam aspect ratio can be attributed to plate action and not to the shear stress distribution. It can also be seen by comparing Fig. 10 with

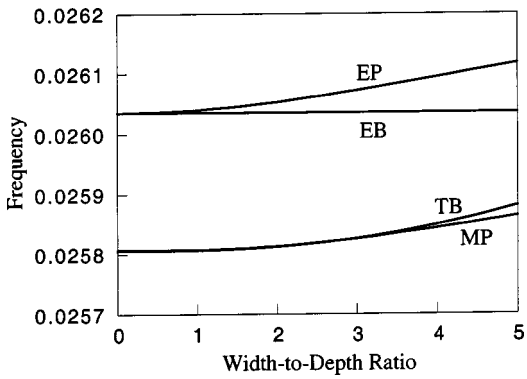

Fig. 13 First mode frequency versus width-to-depth ratio, for a length-to-depth ratio of 20, for the four solutions considered. For a free-free beam.

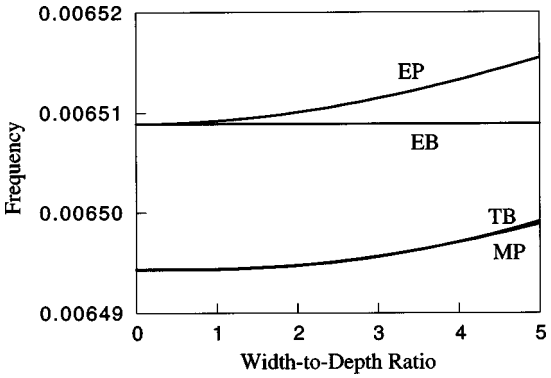

Fig. 14 First mode frequency versus width-to-depth ratio, for a length-to-depth ratio of 40, for the four solutions considered. For a free-free beam.

Figs. 12 through 14 and Fig. 11 with Fig. 15 that in regions where the required shear coefficient matches the S-H coefficient that the frequencies for the Timoshenko and Mindlin solutions also match.

Finally it should be noted that all results reported in this paper were for a Poisson's ratio of 0.3. This was not meant to imply that the solution was not highly dependent on Poisson's ratio. On the contrary, the solution is highly dependent on Poisson's ratio. In fact Poisson's ratio is the cause of the dependence of the frequencies on the width of the beam. For a Poisson's ratio higher than the value of 0.3 all changes with the width-to-depth ratio in Figs.

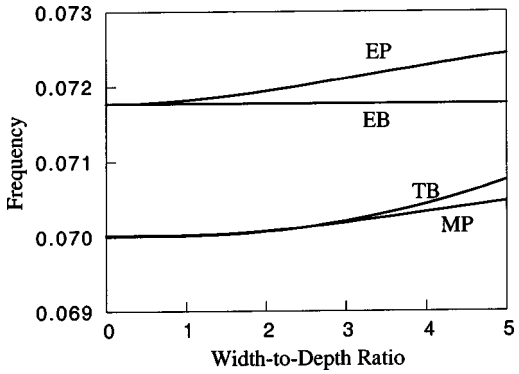

Fig. 15 Second mode frequency versus width-to-depth ratio, for a length-to-depth ratio of 20, for the four solutions considered. For a free-free beam.

2 through 15 would be greater. For a Poisson's ratio of zero all changes in those figures would disappear and they would simply become horizontal lines.

Conclusions

- The new three-dimensional solution provides an excellent basis of comparison for the Timoshenko beam and Mindlin plate approximations.
- The Timoshenko beam solution using the S-H coefficient gives good results only for a width-to-depth ratio of 2 or less, or a length-to-width ratio of 5 or greater.
- The Mindlin plate theory provides excellent results over the entire range considered.
- The S-H coefficient is not just a function of the shear stress distribution, but also includes the plate effects of the anticlastic inertia and twisting.
- The S-H coefficient, while including some of the plate effects, does not include all the effects when the wave length is short.
- A wide rectangular beam may have a frequency which exceeds the frequency predicted by the Euler-Bernoulli beam theory.

Dedication

This paper is dedicated to the memory of Scott D. Zillmer, 1956–2002.

References

[1] Hutchinson, J. R., 2001, "Shear Coefficients for Timoshenko Beam Theory," ASME J. Appl. Mech., **68**, pp. 87–92.
[2] Stephen, N. G., 2001, "Discussion: 'Shear Coefficients for Timoshenko Beam Theory' (Hutchinson, J. R., ASME J. Appl. Mech., **68**, pp. 87–92)," ASME J. Appl. Mech., **68**, pp. 959–961.
[3] Stephen, N. G., 1980, "Timoshenko Shear Coefficient From a Beam Subjected to a Gravity Loading," ASME J. Appl. Mech., **47**, pp. 87–92.
[4] Hutchinson, J. R., and Zillmer, S. D., 1983, "Vibration of a Free Rectangular Parallelepiped," ASME J. Appl. Mech., **50**, pp. 123–130.
[5] Hutchinson, J. R., and Zillmer, S. D., 1986, "On the Transverse Vibration of Beams of Rectangular Cross-Section," ASME J. Appl. Mech., **53**, pp. 39–44.
[6] Armenàkas, A. E., Gazis, D. C., and Herrmann, G., 1969, *Free Vibrations of Circular Cylindrical Shells*, Pergamon Press, Oxford, UK.
[7] Gorman, D. J., and Ding, Wei, 1996, "Accurate Free Vibration Analysis of the Completely Free Rectangular Mindlin Plate," J. Sound Vib., **189**, pp. 341–353.
[8] Flügge, W., 1962, *Handbook of Engineering Mechanics*, McGraw-Hill, New York, pp. 61-14–61-16.
[9] Leissa, A. W., 1969, "Vibration of Plates," NASA SP-160.
[10] Mindlin, R. D., Schacknow, A., and Deresiewicz, H., 1956, "Flexural Vibrations of Rectangular Plates," ASME J. Appl. Mech., **23**, pp. 430–436.
[11] Mindlin, R. D., 1951, "Influence of Rotatory Inertia and Shear on Flexural Motions of Isotropic, Elastic Plates," ASME J. Appl. Mech., **18**, pp. 31–38.
[12] Hutchinson, J. R., 1984, "Vibrations of Thick Free Circular Plates, Exact Versus Approximate Solutions," ASME J. Appl. Mech., **51**, pp. 581–585.
[13] Witrick, W. H., 1987, "Analytical, Three-Dimensional Elasticity Solutions to Some Plate Problems, and Some Observations on Mindlin's Plate Theory," Int. J. Solids Struct., **23**, pp. 441–464.
[14] Stephen, N. G., 1997, "Mindlin Plate Theory—Best Shear Coefficient and Higher Spectra Validity," J. Sound Vib., **202**, pp. 539–553.

H. J. Rathbun
Mem. ASME
e-mail: palmtree@engineering.ucsb.edu

Z. Wei

M. Y. He

F. W. Zok

A. G. Evans
Mem. ASME

Materials and Mechanical Engineering Departments,
University of California,
Santa Barbara, CA 93106

D. J. Sypeck
Mem. ASME
Aerospace Engineering Department,
Embry-Riddle Aeronautical University,
Daytona Beach, FL 32114

H. N. G. Wadley
Department of Materials Science and Engineering,
University of Virginia,
Charlottesville, VA 22903-2442

Measurement and Simulation of the Performance of a Lightweight Metallic Sandwich Structure With a Tetrahedral Truss Core

Metallic sandwich panels with tetrahedral truss cores have been fabricated and their structural performance evaluated. A fabrication technique involving deformation-shaping and brazing has been used. The responses of the structure in core shear and panel bending have been measured. The results demonstrate robust behavior beyond the limit load. A finite element simulation of the core shear response duplicates the features found experimentally. When combined with the constitutive properties of the face sheet material, these shear characteristics have been shown to predict, with good fidelity, the limit load for panels in bending. [DOI: 10.1115/1.1757487]

1 Introduction

The attainment of minimum weight structures has a long history, [1–8]. Three technical factors are involved in achieving this goal: (i) materials selection, [1], (ii) topology optimization, [9–17], and (iii) multifunctionality, [12,16]. Topologies that can be used to achieve high load capacity at low weight are exemplified by truss structures that stretch or compress without bending and honeycomb core panels, [11–20]. The truss topology has the benefit that the open spaces can be used to impart functionalities in addition to load bearing, such as active cooling [1,12,16], whereupon, the extra weight of an additional component normally needed to imbue that extra function can be saved.

Performance indices are needed to ascertain minimum weight configurations and to compare designs. The indices are based on overall structural weight, W (per unit area), load, P (per unit width), stiffness, and yield strain, ε_Y. When the faces and the core are made from the same alloy, the weight index is, [1,6,11]:

$$\Psi = \frac{W}{\rho L} \tag{1}$$

where L is the length of the panel/beam and ρ the density of the solid material.

For designs based on *strength*, the loads supported in *compression* can be compared using the load index, [6]:

$$\Pi = \frac{P}{EL} \tag{2a}$$

where E is the Young's modulus. For *bending* over a span S, it is more convenient to express the load index through a combination of the maximum bending moment, M, and maximum transverse shear, V (both per unit width), [11]:

$$\Pi_b = \frac{V}{\sqrt{EM}}. \tag{2b}$$

The ratio of the maximum M and V defines a characteristic length scale, $\ell \equiv M/V$, [11]. For example, in three-point bending, $\ell = S/2$, [11,17]. When this index is used, the weight index (1) is redefined with ℓ replacing L.

Comparative indices exist for *stiffness* but they are configuration-dependent, [1,2,7,9]. Stiffness governs the weight at smaller loads, while strength is performance limiting at higher loads, [1], exemplified by Fig. 1. The present assessment is restricted to strength-limited designs, pertinent to high loads.

Strength-limited minimum weight designs are found by *identifying the failure modes*, specifying the load capacity and then varying the dimensions to determine the lowest weight for each mode, [1,11]. The benchmark configurations against which competing technologies should be compared are summarized on Fig. 2, [12,15].

For flat panels, sandwich designs with honeycomb cores represent the performance benchmark in bending [11] (Fig. 2(*a*)), while hat-stiffened panels define the benchmark in compression, [6], (Fig. 2(*b*)). For curved configurations, the reference system is comprised of distributed axial and circumferential stiffeners, [1,12,21], (Fig. 2(*c*)). Alternative topologies need not structurally outperform these benchmarks, provided that they exploit other attributes such as cost, durability, strength retention after impact, [1,22,23], and multifunctionality, [1,12,16].

Contributed by the Applied Mechanics Division of THE AMERICAN SOCIETY OF MECHANICAL ENGINEERS for publication in the ASME JOURNAL OF APPLIED MECHANICS. Manuscript received by the ASME Applied Mechanics Division, December 2, 2002; final revision, December 29, 2003. Associate Editor: E. Arruda. Discussion on the paper should be addressed to the Editor, Prof. Robert M. McMeeking, Journal of Applied Mechanics, Department of Mechanical and Environmental Engineering, University of California–Santa Barbara, Santa Barbara, CA 93106-5070, and will be accepted until four months after final publication of the paper itself in the ASME JOURNAL OF APPLIED MECHANICS.

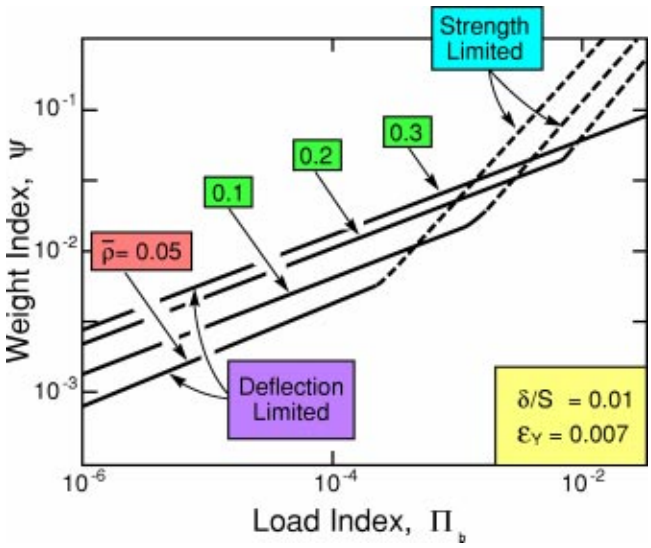

Fig. 1 The minimum weight as a function of load for a simply supported panel subject to a uniformly distributed pressure, evaluated for a material with yield strain, $\varepsilon_Y = 0.007$, and maximum allowable center displacement, $\delta/S = 0.1$. Results are presented for several values of the relative density of the core. In all cases, at large loads, the panels become strength-limited.

Panels with open truss cores offer one such alternative, [11,18]. They are more amenable to forming into complex shapes than honeycomb cores, [19], and they allow fluids to readily pass through, [16], rendering them less susceptible to internal corrosion. They are also attractive for cross flow heat exchange, [7]. In flat panels, when optimized, such cores are as light as the benchmark designs in both bending, [11], (Fig. 2(*a*)) and compression, [1,21], (Fig. 2(*b*)). Moreover, in curved panels, they are much more structurally efficient than stiffened designs, [1,21], (Fig. 2(c)). At loads relevant to aerospace applications, [6], the minimum weight occurs at a core relative density in the range 2–3%, with thin faces (thickness to load span of order 3×10^{-3}), [11]. The failure mechanisms operating at the optimum depend on the yield strain of the alloy being used, [11]. At the high yield strains pertinent to aerospace grade Al alloys, failure occurs by concurrent face yielding, face buckling and elastic buckling of the compressed truss core members, [11]. For the lower yield strains relevant to stainless steels, the failure modes are concurrent face yielding, face buckling and core member yielding, [11].

Experimental assessments of these predictions have been made in panels fabricated by an investment casting process, [18], using materials having yield strains in the range where the core response is yield (rather than elastic buckling) dominated. These investigations had two primary limitations: (i) due to the constraints on aspect ratio imposed by investment casting, the core members were less slender than that at the optimum, (ii) the casting introduced defects that limited the ductility, inhibiting the ability to probe the performance envelope. Other limitations included the relatively high manufacturing cost associated with investment casting, as well as the limited property range that can be accessed (relative to wrought material).

These issues are addressed in the present study by applying a manufacturing procedure for open cell tetrahedral truss core structures (Fig. 3) applicable to wrought metals, [19]. The cores are made using metal perforation and deformation-shaping processes. They are bonded to thin metal face sheets using a brazing approach. The specific objectives of this article are as follows: (i) manufacture wrought panels with core densities in the range found for fully optimized panels (about 2%), [11]; (ii) measure the performance of these panels subject to overall bending loads, as-

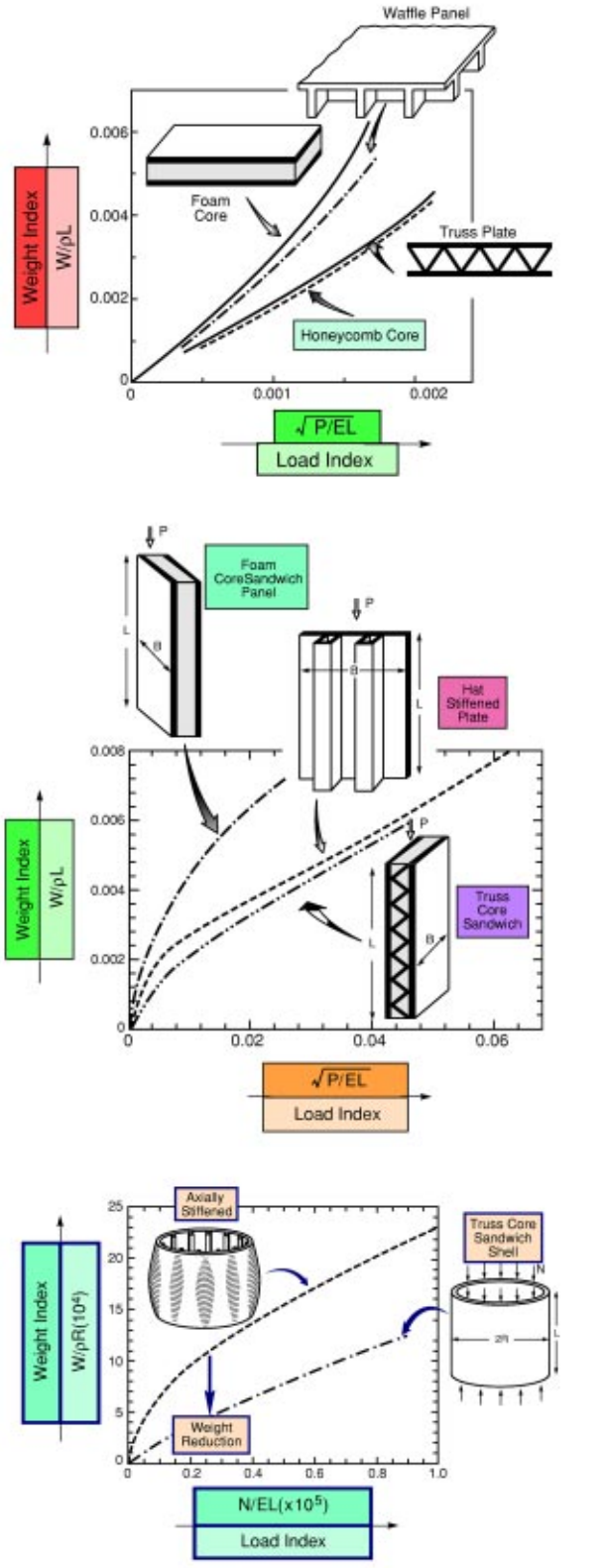

Fig. 2 (*a*) The minimum weight as a function of load capacity for various panels under shear and bending load. (*b*) Weight index versus load index for axially compressed flat panels, [1,10,18,22]. (*c*) The minimum weight as a function of load for axially compressed curved panels. *N* is the load per unit length of the periphery, [12].

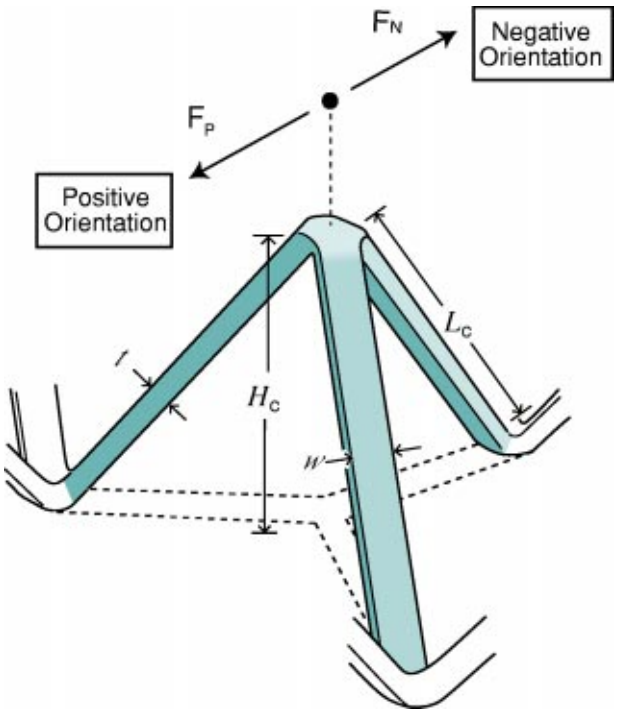

Fig. 3 Tetrahedral unit with ligaments having rectangular cross-section. The directions of positive and negative shear are indicated.

sess their robustness, and compare the load capacity with predictions, [11]; (iii) perform independent core shear measurements and simulations to facilitate model validation.

2 Basic Mechanics

The four possible failure modes for the tetrahedral truss core sandwich structure with solid face sheets are face sheet yielding, face sheet buckling, core member yielding and core member buckling, [11]. The face sheet failure modes are dictated by the bending moment per unit width, M. The associated constraints are, [11]:

$$\frac{M}{t_f H_c} \leq \sigma_y \quad \text{(face sheet yielding)} \tag{3a}$$

$$\frac{M}{t_f H_c} \leq \frac{49\pi^2 E}{432(1-\nu^2)}\left(\frac{t_f}{d}\right)^2 \quad \text{(face sheet buckling)} \tag{3b}$$

where H_c is the core height, t_f is the face sheet thickness, L_c is the truss member length, $d \equiv \sqrt{L_c^2 - H_c^2}$, σ_y is the yield strength, and ν is Poisson's ratio. The core failure modes are dictated by the shear force per unit width, V, [11]. For truss members with rectangular cross-section (width, w and thickness, t), the constraints are

$$\frac{\sqrt{3}VdL_c}{H_c wt} \leq \sigma_y \quad \text{(core member yielding)} \tag{3c}$$

$$\frac{\sqrt{3}VdL_c}{H_c wt} \leq \frac{k\pi^2 E}{12}\left(\frac{t}{L_c}\right)^2 \quad \text{(core member buckling)} \tag{3d}$$

where k depends on the end conditions of the truss members. For conservatism, we assume that the nodal connections between the core members and the face sheets are pin-jointed ($k=1$), [11]. For convenience, each geometric parameter is normalized by ℓ, allowing the constraint functions to be rewritten in the nondimensional forms:

$$\left(\frac{V}{\sqrt{EM}}\right)^2 \frac{E}{\sigma_y}\frac{\ell^2}{t_f H_c} \leq 1 \quad \text{(face sheet yielding)} \tag{4a}$$

$$\left(\frac{V}{\sqrt{EM}}\right)^2 \frac{432(1-\nu^2)}{49\pi^2}\frac{d^2\ell^2}{t_f^3 H_c} \leq 1 \quad \text{(face sheet buckling)} \tag{4b}$$

$$\left(\frac{V}{\sqrt{EM}}\right)^2 \frac{E}{\sigma_y}\frac{\sqrt{3}dL_c\ell}{H_c wt} \leq 1 \quad \text{(core member yielding)} \tag{4c}$$

$$\left(\frac{V}{\sqrt{EM}}\right)^2 \frac{12\sqrt{3}}{k\pi^2}\frac{dL_c^3\ell}{H_c wt^3} \leq 1 \quad \text{(core member buckling)} \tag{4d}$$

A failure mode is considered active when the associated constraint function reaches unity. As discussed below (Section 6), this approach can be used to predict the load at failure initiation during panel bending.

3 Sandwich Panel Construction

Truss cores can be fabricated from wrought metals by starting with perforated metal sheets and bending along diagonal nodes, [19]. To illustrate the fabrication, commercially available 304 stainless steel (Fe-18Cr-8Ni) with hexagonal perforations was obtained from Woven Metal Products, Inc. (Alvin, TX). The truss members had width $w=1.26$ mm and thickness, $t=0.59$ mm. The rectangular cross sections (which have lower core performance than square sections) were convenient for manufacturing, [19]. After bending (Fig. 4(*a*)), the core height was, $H_c=10$ mm, such

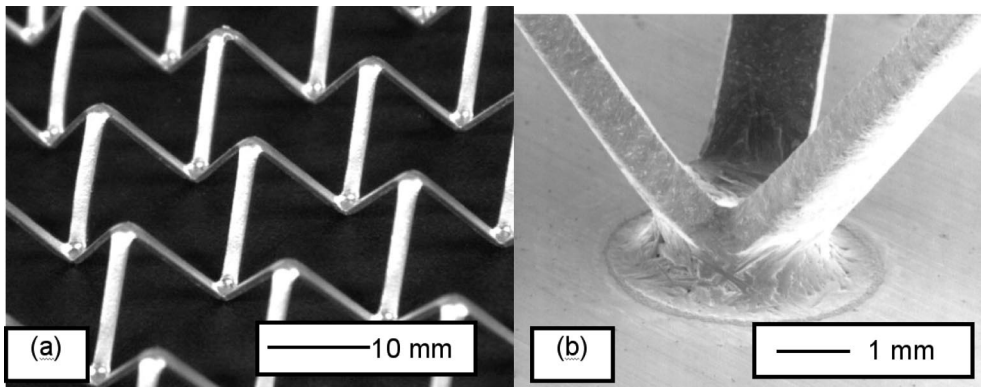

Fig. 4 (*a*) Tetrahedral truss core after shaping, (*b*) typical core/face sheet bond

Table 1 Geometric parameters for three point bending panels

Parameter	Dimension (mm)
Core height, H_c	9.8
Face sheet thickness, t_f	0.75
Truss member length, L_c	12.2
Truss member width, w	1.26
Truss member thickness, t	0.59
Span length, S	202
Panel width, B	66

that the relative density was, $\bar{\rho} \equiv \rho_c/\rho = 1.7\%$, (where ρ_c is the density of the core and ρ is the density of the solid material).

A brazing approach was used for attaching the face-sheets to the cores. The cores were lightly sprayed with a powder comprising a mix of a polymer (Nicrobraz® 520) and 140 mesh Ni-25Cr-10P alloy (Nicrobraz® 51), both supplied by Wal Colmonoy Corp. (Madison Heights, MI). The solidus and liquidus of this alloy are 880 and 950°C, respectively, whereas the solidus of 304 stainless steel is approximately 1400°C. The coated cores were placed between solid 304 stainless steel face sheets and a small compressive pressure was applied. The panel assemblies were heated in vacuum ($<10^{-2}$ torr) to 550°C for 1h to volatilize the polymer[1]. The system was evacuated to less than 10^{-3} torr, and the temperature increased to 1100°C and held for 1 h. At temperature, the alloy melts and is drawn into the core/face sheet contacts by capillarity. Bonding then occurs as interdiffusion changes the local composition, causing it to solidify. Robust joints with desirable nodes ensue (Fig. 4(*b*)). Upon bonding, the core height diminishes slightly, to $H_c = 9.8$ mm, increasing the core relative density to $\bar{\rho} = 1.8\%$. This density is very close to that found for fully optimized panels, [11].

For the panel bending assessment, a face sheet thickness, $t_f = 0.75$ mm, was chosen, exceeding that for the optimum structure, [11]. For the core shear tests, much thicker face sheets were used ($t_f = 3$ mm) to prevent distortions during the measurements.

4 Test Design

After cooling to ambient, the panels were machined for testing. The flexure panels had span length, $S = 202$ mm, width $B = 66$ mm, and mass 0.22 kg (Table 1). They were tested in three-point loading by using a procedure similar to that described elsewhere, [19,22]. Flat-faced loading platens 16 mm thick were adhesively bonded to the faces of the panels. The loads were applied through lubricated rollers inset into the platens that allowed the specimen to rotate upon bending, with minimal friction. The tests were performed in a servo-electric test frame. The load and load-point displacements were measured simultaneously.

The shear test assembly comprised two L-shaped platens that rigidly held each of the two face sheets of the panel (Fig. 5). The assembly was placed between flat loading surfaces connected to the load cell and actuator of a servo-hydraulic load frame. Imposing a compressive load to the assembly created a condition of nearly pure shear at the truss core. The tests were performed at a load point displacement rate of 0.1 mm/min. Displacements were measured by a laser extensometer. Tests were performed in the negative and positive orientations shown in Fig. 3, [18,20]. In the positive orientation, one truss member is in tension and the other two in compression and vice versa for the negative orientation.

A high resolution digital camera was connected to the testing frame in order to capture side-view images of the core. These images were used to identify the failure mechanisms.

The constitutive properties of the 304 stainless steel used in the face sheets were measured after exposure to a simulated bonding cycle (1100°C for one hour). Flat dog-bone-shaped tensile specimens were tested at a strain rate of $10^{-4}\,s^{-1}$.

[1]Note that the alloy powder remains adhered to the structure after volatilization.

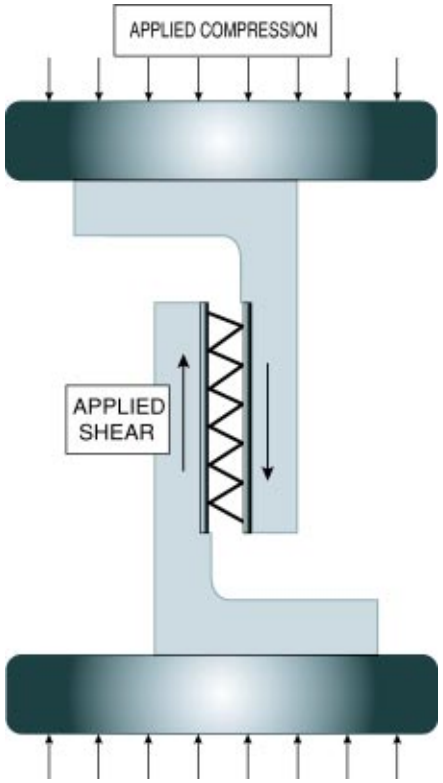

Fig. 5 Shear test fixture assembly

5 Measurements and Observations

Figure 6 shows the true stress-strain response of the 304 stainless steel. The material exhibits a 0.2% offset yield strength, $\sigma_y = 217$ MPa. The hardening rate beyond yield is almost linear up to a strain of 10% and can be characterized by a hardening modulus, $H \equiv d\sigma/d\varepsilon = 2.5$ GPa.

The shear stress/strain responses measured in the positive and negative orientations (Fig. 7) demonstrate the asymmetry of the tetrahedral truss core. In the negative orientation, the limit load is

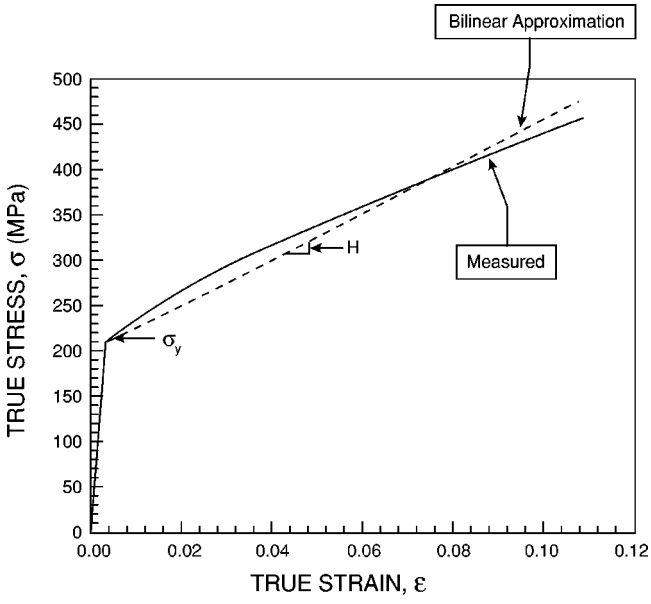

Fig. 6 True stress-strain response for 304 stainless steel following annealing at 1100°C for 1 hour

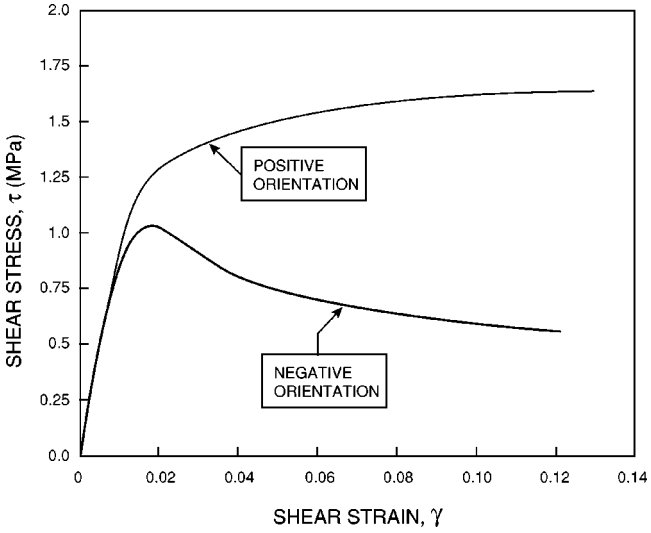

Fig. 7 Shear stress/strain response of tetrahedral truss core panels in the negative and positive orientations

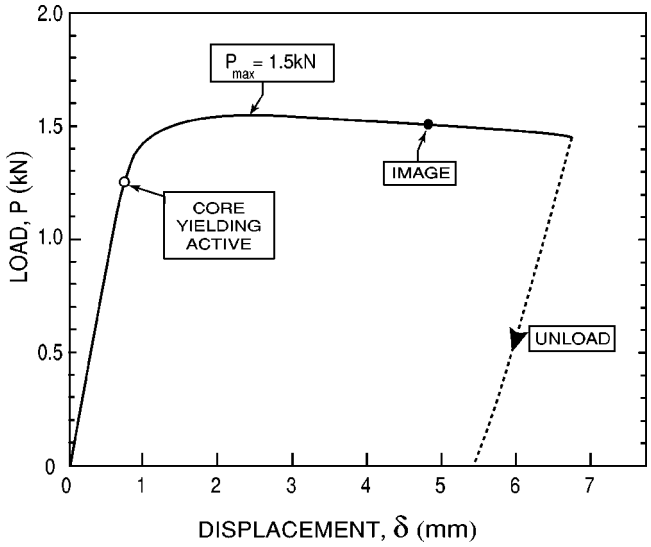

Fig. 8 Load-deflection response during panel bending. The open symbol represents the predicted load from Eq. (5) at which yielding occurs.

appreciably lower than in the positive orientation because the most heavily stressed trusses are in compression and susceptible to plastic buckling, [18,20]. The maximum shear stress in this orientation, $\tau_{max}=1.0$ MPa, occurs at a shear strain of 1.4%, observed to be coincident with plastic buckling of the compressed members. In the positive orientation, the corresponding maximum is $\tau_{max}=1.7$ MPa, occurring at a shear strain of 13%. In this orientation, the most highly stressed trusses are in tension. They stretch and transfer load onto the compressed trusses, eventually causing them to buckle plastically.

A load/displacement curve measured in bending is summarized in Fig. 8. An approximately steady-state load, $P_{ss}=1.5$ kN is attained at displacements between 2 mm$<\delta_{ss}<$5 mm, followed by gradual softening beyond 5 mm. An image obtained at the limit load (Fig. 9) indicates that the response is asymmetric and that the panel fails by core shear. That is, since the truss assemblies on the left experience shear in the negative orientation, [18], failure occurs through plastic buckling of the compressed members. The buckling induces large strains that cause face sheet yielding and result in the formation of a macroscopic plastic hinge at the outer loading platen, [1,20,22]. In contrast, the right side experiences positive shear. Consequently, the trusses stretch with relatively small ensuing strain levels, inhibiting both face yielding and hinging. After unloading, all of the core/face-sheet bonds were intact with no visible cracking.

6 Finite Element Simulation of the Shear Response

The finite element simulation approach is similar to that described by Hyun et al. [20]. The exact rectangular geometry of the truss members has been used, as well as the measured stress/strain curve for the faces (Fig. 6). The truss assembly and the finite element mesh are shown in Fig. 10. The finite element code ABAQUS has been used. The base of the truss assembly is fixed. The top, where the assembly is bonded to the upper face, is displaced parallel to the face, without rotation. The deformations of the core that occur in the negative and positive orientations at large displacements are shown in Fig. 10. They demonstrate the plastic buckling of the compressed member in the negative orientation and the stretching of the tensile member in the positive orientation.

The shear stress/plastic strain relations calculated for the two orientations are superposed on the experimental measurements in Fig. 11. The similarity between the curves in both orientations affirms the self-consistency of the present measurement and simulation protocols and provides confidence in the scaling relations (with relative density and core member aspect ratio) elaborated elsewhere, [11,13,20]. There are two minor discrepancies. The simulations generally underestimate the flow strength by a few percent. Since the simulations use the stiffest possible boundary

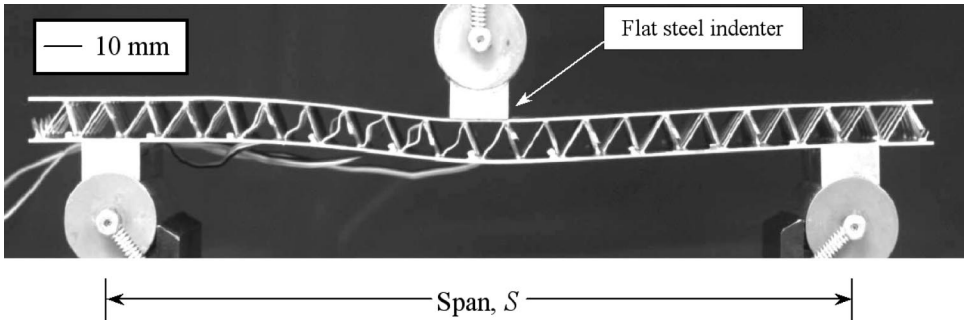

Fig. 9 Image of the panel obtained at the displacement indicated in Fig. 8. Note the plastic buckling of the compressed truss core members on the left side and the associated plastic hinge. The span was $S=202$ mm, the flat steel indenters were 16.0 mm wide and the overhang, $h_{over}=22.5$ mm.

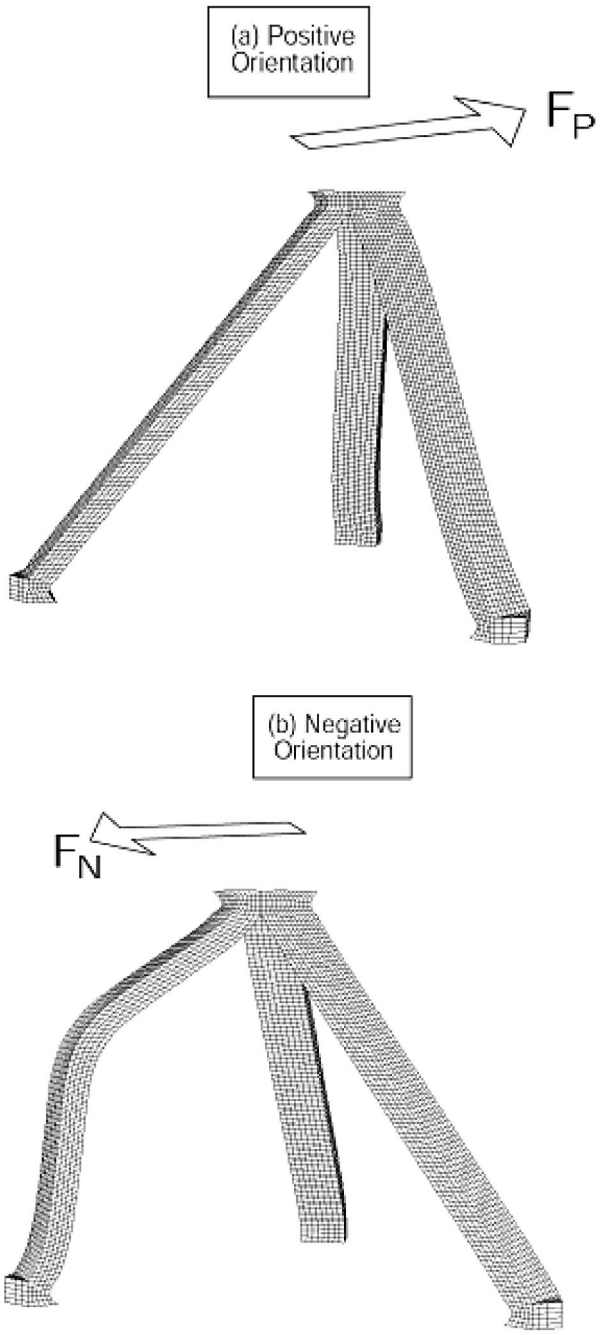

Fig. 10 Finite element simulations showing the deformation after shearing in (*a*) the positive orientation at $\gamma_{pl}=0.14$ and (*b*) the negative orientation at $\gamma_{pl}=0.10$. Note the plastic buckling of the compressed member in the latter.

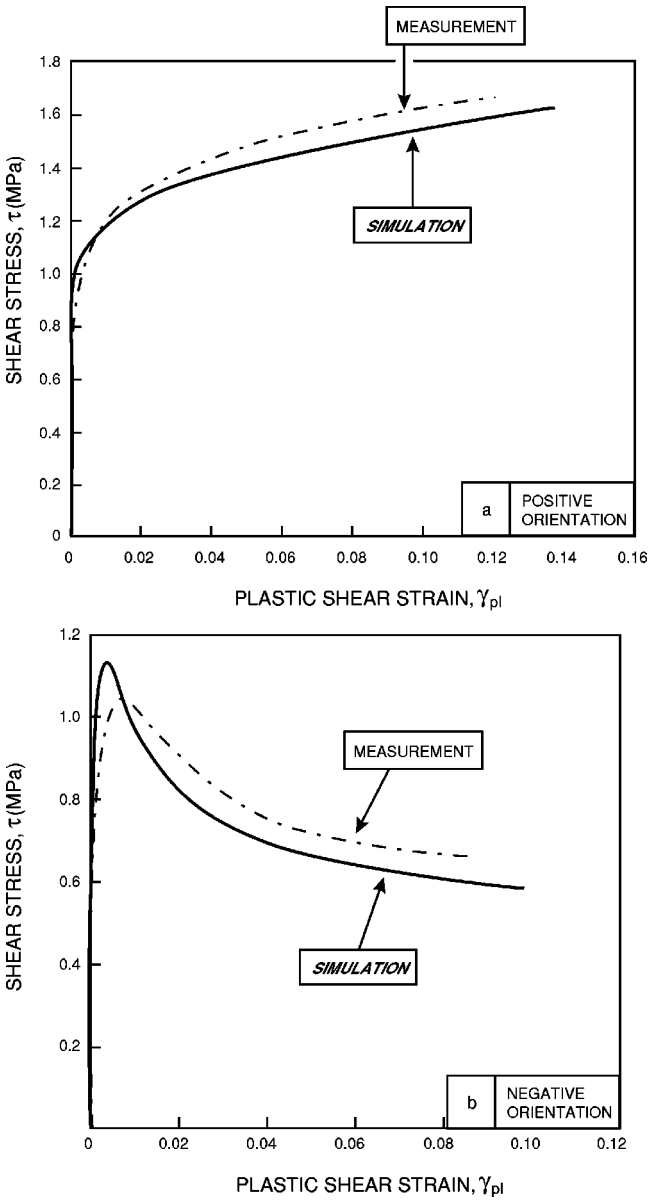

Fig. 11 Simulations of the shear stress as a function of plastic strain in (*a*) the positive orientation and (*b*) the negative orientation. The experimental measurements have been superposed.

conditions, this difference implies that the material comprising the truss members has higher strain hardening than that measured for the faces. This may be attributable to chemical interactions between the braze alloy and the steel. The second discrepancy relates to the onset of plastic buckling in the negative orientation. The simulation overestimates the stress at which this occurs by about 10%. This difference is associated with the imperfection sensitivity of the buckling condition.

7 The Bending Response

Initial Failure Load. By inserting the geometric parameters for the panel (Table 1) into equation (4),[2] core member yielding is found to become active at the lowest load, when $\Pi_b \equiv V/\sqrt{EM} = 6.8\times10^{-4}$. The corresponding absolute yield load is

$$P_y = \Pi_b^2 BES. \tag{5}$$

Inserting the panel dimensions (Table 1) into (5), the predicted yield load becomes $P_y = 1.25$ kN. This value corresponds closely to that measured at the onset of nonlinearity (Fig. 8), affirming that failure initiates in the core.

Limit Load. The beam theory solution for the collapse load of a sandwich panel in three-point bending with small overhang, h_{over}, is given by, [1,22],

[2]The analysis assumes $\sigma_y/E = 0.001$ and $\nu = 0.33$. Further, for three point bending, $\ell = S/2 = 101$ mm.

$$P_A = \frac{2Bt_f^2}{S}\sigma_y + 2BH_c\tau_{\max}\left(1+\frac{2h}{S}\right). \quad (6a)$$

The corresponding result for a panel with large overhang is, [1,22],

$$P_B = \frac{2Bt_f^2}{S}\sigma_y + 2BH_c\tau_{\max}. \quad (6b)$$

Here, the pertinent value of $\tau_{\max}$ is that corresponding to the softer, negative orientation. The lower of the two loads, P_A and P_B, dictates panel bending strength.

Upon incorporating into (6) the measured shear strength in the negative orientation, $\tau_{\max}=1.0$ MPa, the face sheet yield strength, $\sigma_Y=217$ MPa, and the panel dimensions (Table 1), the peak loads are predicted to be $P_A=1.7$ kN and $P_B=1.5$ kN. The lower value is virtually identical to the measured collapse load. The quality of the agreement suggests that simple beam theory models can adequately account for measured limit loads, provided that independent information about the core shear strength and face strength is available.

8 Summary

Metallic sandwich panels with tetrahedral truss cores have been fabricated by deformation shaping and brazing. The responses in core shear and panel bending have been measured. The results demonstrate a robustness attributed to the wrought nature of the material. Finite element models of the shear response duplicate the essential features found experimentally. A small (few percent) discrepancy is attributed to incomplete understanding of the stress/strain characteristics of the material state in the truss members.

When combined with the constitutive properties of the face sheet material, the core shear characteristics have been used to predict the limit load for panels in bending by beam theory. The closeness of the agreement indicates that such models are capable of adequately predicting limit loads, given independent information about the core shear strength.

Acknowledgments

We are grateful to DARPA/ONR for the support of this work through research grants N00014-96-1-1028 (program manager, S. Fishman) and N00014-01-1-0517 (program managers, L. Christodoulou and S. Fishman). Also, we would like to thank S. Chiras for performing the three-point bending experiment, and A. Jamieson for assistance in preparation of the figures.

Nomenclature

B = beam width
d = base leg of tetrahedral truss assembly ($\equiv\sqrt{L_c^2-H_c^2}$)
E = Young's modulus
F_N = shear force in negative orientation
F_P = shear force in positive orientation
h_{over} = overhang in three-point bend experiment
H = hardening modulus
H_c = core height
k = buckling constant ($k=1$ for pinned ends, 4 for built-in ends)
L = length of panel/beam
L_c = truss member length
M = moment per unit width
N = load per unit peripheral length for axially compressed curved panels
P = load per unit width
P_A, P_B = collapse loads in bending for small and large overhangs, respectively
P_{ss} = steady-state load in three-point bending
P_y = yield load in three-point bending
S = three-point bend span length
t = truss core member thickness
t_f = face sheet thickness
V = shear per unit width
w = truss core member width
W = weight per unit area
δ = displacement in three point bending
δ_{ss} = deflection range for P_{ss}
ϵ_y = yield strain
γ, γ_{pl} = shear strain and plastic shear strain, respectively
ℓ = characteristic length scale ($\equiv M/V$)
Ψ = nondimensional weight index
Π, Π_b = load indices
ρ = density of solid material
$\underline{\rho}$ = relative core density ($\equiv\rho_c/\rho$)
ρ_c = density of core
σ_y = 0.2% offset yield strength
τ = shear stress
$\tau_{\max}$ = maximum shear stress
ν = Poisson's ratio

References

[1] Ashby, M. F., Evans, A. G., Fleck, N. A., Gibson, L. J., Hutchinson, J. W., and Wadley, H. N. G., 2000, *Metal Foams: A Design Guide*, Butterworth-Heinemann, Boston, MA.
[2] Clark, J. P., Roth, R., and Field, F. R., 1997, *Techno-Economic Issues in Material Science* (ASM Handbook Vol. 20, Materials Science and Design), ASM International, Materials Park, OH.
[3] Allen, H. G., 1969, *Analysis and Design of Structural Sandwich Panels*, Pergamon Press, Oxford, UK.
[4] Koiter, W. T., 1963, Koninkl. Nederl. Akademie van Wetenschappen, Ser. B, **66**, pp. 265–279.
[5] Hutchinson, J. W., "Plastic Buckling," 1974, Adv. Appl. Mech., **14**, pp. 67–144.
[6] Budiansky, B., 1999, "On The Minimum Weights of Compression Structures," Int. J. Solids Struct., **36**, pp. 3677–3708.
[7] Gerard, G., 1956, *Minimum Weight Analysis of Compression Structures*, New York University Press, New York.
[8] Tvergaard, V., 1973, "Imperfection-Sensitivity of a Wide Integrally Stiffened Panel Under Compression," Int. J. Solids Struct., **9**, pp. 177–192.
[9] Weaver, P. M., and Ashby, M. F., 1997, "Material Limits For Shape Efficiency," Prog. Mater. Sci., **41**, pp. 61–128.
[10] Parkhouse, J. G., 1984, *Structuring: A Process of Material Distribution, Proc. 3rd Int. Conf. On Space Structures*, H. Nooschin, ed., Elsevier, London, pp. 367–374.
[11] Wicks, N., and Hutchinson, J. W., 2001, "Optimal Truss Plates," Int. J. Solids Struct., **38**, pp. 5165–5183.
[12] Evans, A. G., Hutchinson, J. W., Fleck, N. A., Ashby, M. F., and Wadley, H. N. G., 2001, "The Topological Design of Multifunctional Cellular Materials," Prog. Mater. Sci., **46**, pp. 309–327.
[13] Deshpande, V. S., and Fleck, N. A., 2001, "Collapse of Truss Core Sandwich Beams in 3-Point Bending," Int. J. Solids Struct., **38**, p. 6275–6305.
[14] Fuller, R. B., 1961, "Synergetic Building Construction," U.S. Patent, 2,986,241, 30.
[15] Evans, A. G., 2001, "Lightweight Materials and Structures," MRS Bull., **26**, p. 790.
[16] Gu, S., Lu, T. J., and Evans, A. G., 2001, "On The Design of Two-Dimensional Cellular Metals For Combined Heat Dissipation and Structural Load Capacity," Int. J. Heat Mass Transfer, **44**, pp. 2163–2175.
[17] Zok, F. W., Rathbun, H. J., Wei, Z., and Evans, A. G., 2003, "Design of Metallic Textile Core Sandwich Panels," Int. J. Solids Struct., **40**, pp. 5707–5722.
[18] Chiras, S., Mumm, D. R., Evans, A. G., Wicks, N., Hutchinson, J. W., Dharmasena, K., Wadley, H. N. G., and Fichter, S., 2002, "The Structural Performance of Near-Optimized Truss Core Panels," Int. J. Solids Struct., **39**, pp. 4093–4115.
[19] Sypeck, D. J., and Wadley, H. N. G., 2002, "Cellular Metal Truss Core Sandwich Structures," Advanced Engineering Materials, **4**(10), pp. 759–764.
[20] Hyun, S., Karlsson, A. M., Torquato, S., and Evans, A. G., 2003, "Simulated Properties of Kagomé and Tetragonal Truss Core Panels," Int. J. Solids Struct., **40**(25), pp. 6989–6998.
[21] Hutchinson, J. W., and He, M. Y., 2000, "Buckling of Cylindrical Sandwich Shells With Metal Foam Cores," Int. J. Solids Struct., **37**, pp. 6777–6794.
[22] Bart-Smith, H., Hutchinson, J. W., and Evans, A. G., 2001, "Measurement and Analysis of the Structural Performance of Cellular Metal Sandwich Contruction," Int. J. Mech. Sci., **43**, pp. 1945–1963.
[23] Fleck, N. A., and Deshpande, V. S., 2004, "Blast Resistance of Clamped Sandwich Beams," J. Appl. Mech., (in press).

Experimental Investigation on the Plasticity of Hexagonal Aluminum Honeycomb Under Multiaxial Loading

Dirk Mohr
Mem. ASME

Mulalo Doyoyo
Mem. ASME

Impact and Crashworthiness Laboratory,
Massachusetts Institute of Technology,
Cambridge, MA 02139

A new custom-built universal biaxial testing device (UBTD) is introduced and successfully used to investigate the response of aluminum honeycomb under various combinations of large shear and compressive strains in its tubular direction. At the macroscopic level, different characteristic regimes are identified in the measured shear and normal stress-strain curves: elastic I, elastic II, nucleation, softening, and crushing. The first elastic regime shows a conventional linear elastic response, whereas the second elastic regime is nonlinear due to the generation of elastic buckles in the honeycomb microstructure. Nucleation is the point at which the cellular structure loses its load carrying capacity as a result of plastic collapse. It precedes a rapid drop of stress levels in the softening regime as pronounced plastic collapse bands emerge in the microstructure. Formation and growth of plastic folds dominate the microstructural response in the crushing phase. The mechanical features of this phase are long stress plateaus for both the corresponding shear and compressive stress-strain curves. Based on these observations, honeycomb plasticity is established by making analogies of plastic hinge lines and folding systems in the cellular microstructure with dislocations and slip line systems in a solid lattice, respectively. The initial yield surface is found to take the form of an ellipse in stress space, while the crushing behavior is described by a linear envelope along with a nonassociated flow rule based on total strain increments. [DOI: 10.1115/1.1683715]

1 Introduction

The cellular microstructure of a honeycomb is composed of a network of joined, parallel, thin-walled tubes. As a result, honeycombs are strongly orthotropic, thereby providing high mechanical performance per unit weight under shear and normal loading in the tubular direction. Among the three orthotropy axes of the honeycomb microstructure the tubular or T-direction is the strongest direction. As compared to loading in the weaker in-plane directions (W and L), the variation in internal energy is typically by one to two orders of magnitude as high upon loading in the T-direction. Combined out-of-plane loading, i.e., combinations of normal and shear stresses in the T-W and T-L–planes, is a characteristic of most engineering applications of honeycombs. In particular, the mechanical response of honeycombs to plastic out-of-plane deformations is of growing interest for industrial applications. Traditionally, sandwich structures are designed for elastic loading scenarios (e.g., Allen [1]), but recent studies on the crushing of sandwich profiles have shown the merits of thin sandwich sheets in crashworthiness applications (e.g., Mohr and Wierzbicki [2]). Other industrial applications include the forming of sandwich floor panels for passenger cars or the use of honeycombs sandwich structures for the hood of a car, where the design for the accidental impact of a pedestrian requires in-depth knowledge of the plasticity of metallic honeycombs.

A summary on various honeycomb properties is given in the textbook *Cellular Solids: Structure and Properties* by Gibson and Ashby [3]. The in-plane behavior of honeycombs can be studied on the basis of two-dimensional beam models. Thus, besides analytical expressions for elastic properties, closed-form solutions for the macroscopic yield loci for in-plane loading could be derived (Klintworth and Stronge [4]). Papka and Kyriakides [5] used a two-dimensional beam model for the cell walls of the microstructure to reproduce the complex deformation modes of polymeric honeycombs under biaxial in-plane loading. The response of a metallic honeycomb to uniaxial compressive loading in the T-direction was studied in detail by various authors and an analytical expression for the mean crushing stress was presented by McFarland [6] and Wierzbicki [7].

However, little is known on the mechanical behavior of metallic honeycombs under combined out-of-plane loading. Standard testing techniques such as the combined compression-torsion Taylor-Quiney tests on cylindrical specimens are not suitable for honeycombs, where the orthotropy axes are aligned with the Cartesian coordinate system. Other experimentalists report premature failure of the bond between the honeycomb and loading platens when performing shear tests according to the ASTM Standard C273 (Hexcel [8]). Uncontrolled localization of deformation in double shear lap honeycomb specimens subjected to combined shear and normal loading generated unacceptable noise in the corresponding force displacement curves (Wierzbicki [9]).

Recent findings indicate that the use of the Arcan apparatus in the clamped configuration allows for the biaxial testing of honeycombs (Petras and Sutcliffe [10]). Based on the detailed analysis of this testing configuration (Mohr and Doyoyo [11]), the enhanced arcan apparatus (EAA) was developed for the biaxial testing of cellular materials (Mohr and Doyoyo [12]). The underlying concept is to perform fully displacement-controlled tests, thereby bypassing problems due to the localization of deformation in honeycombs. The EAA has been successfully used to measure the initial failure envelope of aluminum honeycomb subjected to combined out-of-plane loading (Doyoyo and Mohr [13]).

Contributed by the Applied Mechanics Division of THE AMERICAN SOCIETY OF MECHANICAL ENGINEERS for publication in the ASME JOURNAL OF APPLIED MECHANICS. Manuscript received by the Applied Mechanics Division, Mar. 25, 2003; final revision, July 23, 2003. Associate Editor: M.-J. Pindera. Discussion on the paper should be addressed to the Editor, Prof. Robert M. McMeeking, Journal of Applied Mechanics, Department of Mechanical and Environmental Engineering, University of California–Santa Barbara, Santa Barbara, CA 93106-5070, and will be accepted until four months after final publication in the paper itself in the ASME JOURNAL OF APPLIED MECHANICS.

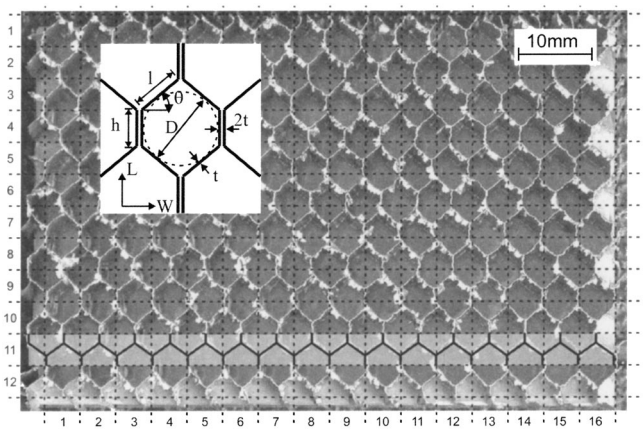

Fig. 1 Top view of the sandwich specimen before being bonded to the second grip plate. The insert shows a schematic of a single honeycomb cell. The shaded rectangle highlights the nature of the microstructure.

Following the concept of the EAA, we present a new testing device called the universal biaxial testing device (UBTD) to study the post-yield behavior of aluminum honeycomb under combined out-of-plane loading. Two force components are measured to determine the macroscopic stresses in the sandwich specimen. An in-depth discussion of experimental observations discloses the nature of microstructural deformation mechanisms that determine the mechanical behavior. It is found that a folding system composed of plastic hinge lines and compatibility zones determines the plasticity of a metallic honeycomb under quasi-static loading. At the same time, the following observations are made on the macroscopic level: (1) an elliptical yield envelope defines the onset of microstructural collapse, (2) a linear inner envelope describes the stress level under large deformations, and (3) a nonassociated flow rule characterizes the relationship between strain increments and the stress state.

2 Specimen and Homogenization

2.1 Material. Aluminum 5056-H39 foil is the base material for the cellular structure of the tested honeycomb. The foil thickness is $t=33\,\mu$m. The hexagonal microstructure is produced in the expansion process. Cell walls initially aligned with the L-direction (ribbon direction) are bonded together and thus are of double thickness (inset in Fig. 1). Their width is $h=2.4$ mm, whereas the width of the single-thickness walls is $l=3.1$ mm. The cell wall expansion angle as defined in Fig. 1 is $\theta=40°$. The initial density is $\rho_0=46.5\,\mathrm{kg/m^3}$, which corresponds to a relative density of 1.8% (with respect to the density of solid aluminum).

2.2 Specimen. For the present study, we perform combined compression and shear tests on sandwich specimens. In this configuration, a honeycomb core of constant height is sandwiched between two faceplates (Fig. 2). The faceplates serve as grips to mount the specimen onto the testing device. An epoxy adhesive (Lord 310A/B) was used to bond the honeycomb onto roughened aluminum grip plates. The specimen width of $l_W=80$ mm was predefined by the size of the biaxial testing device. This corresponds to 16.5 honeycomb cells along the W-direction. The width along the ribbon direction, $l_L=52.8$ mm, was chosen according to the recommendation of ASTM C273. Two opposite aspects had to be taken into account for the choice of the specimen height: As a result of the bonding technique employed, the cell walls are embedded into an adhesive layer; thus, to minimize the influence of the adhesive layer on the test results, the specimen height should be large as compared to the up to 1 mm thick bond line. On the other hand, under shear loading, a large width to height ratio l_W/C (i.e., a small specimen height) is desirable to guarantee a homogeneous stress field along the W-direction. Here, a height of $C=15$ mm is chosen for the sandwich specimen.

We will test the specimens under combinations of normal and shear loading in the T-W−plane. Alternatively, the specimens could have been prepared for testing in the T-L−plane. Note that when calibrating transverse isotropic constitutive models from experimental data, the use of the normal-shear interaction curves found from experiments in the TW-plane results in an underestimation of the energy absorption of honeycombs, while models calibrated from T-L data will rather overestimate the energy absorption. In practical applications, the underestimation of the energy absorption is preferred, and thus, as a first step, we limit our attention to the T-W−plane.

2.3 Homogenization. We discuss the mechanical response of metallic honeycomb on two scales: On the macroscopic level, honeycomb is described as a homogeneous material, whereas on the microstructural level the cellular microstructure and individual cell walls are considered.

The honeycomb microstructure is periodic along the in-plane directions W and L. The characteristic length of the periodicity is the honeycomb cell size D (see Fig. 1). Thus, successful modeling of the honeycomb by its homogeneous equivalent requires the macroscopic (structural) scales λ_W, λ_L along the in-plane directions to be large as compared to the cell size, i.e., $\lambda_W/D\gg 1$ and $\lambda_L/D\gg 1$. For example, for the present specimen, we have $\lambda_W=80$ mm, $\lambda_L=52.8$ mm, and $D\cong 5$ mm and thus $\lambda_W/D\cong 16$ and $\lambda_L/D\cong 10$. Experimental results described below reveal that this morphological in-plane periodicity is preserved under inelastic out-of-plane loading. In other words, on the macroscopic scale, both the undeformed and deformed configurations of the honeycomb microstructure are statistically homogenous in the W-L−plane.

In contrast, significant morphological changes occur along the T-direction when the microstructure is subjected to combined out-of-plane loading. Note that in sandwich applications, the macroscopic scale along the T-direction, λ_T, is given by the core height, $\lambda_T=C$. Initially, the cell walls are straight along the T-direction. However, in particular under compressive loading, localization of deformation and plastic collapse bands dominate the microstructural response (Mohr and Doyoyo [14]). The microstructure loses

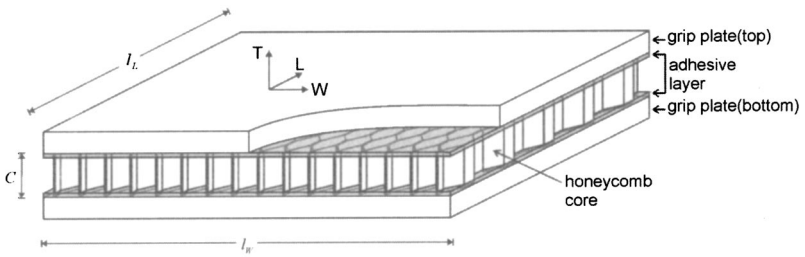

Fig. 2 Schematic of the sandwich specimen

its statistical homogeneity along the T-direction and becomes *heterogeneous on the macroscopic scale*. Thus, size effects may arise according to the representative volume element (RVE) chosen to characterize the macroscopic behavior (see, e.g., François et al. [15]).

The macroscopic (engineering) strain tensor $\mathbf{E}$ is introduced as the spatial mean of the local strains in the RVE. Under combined out-of-plane loading, we assume the following form of the strain tensor:

$$\mathbf{E}=\varepsilon(\mathbf{e}_T\otimes\mathbf{e}_T)+\frac{1}{2}\gamma_{TL}(\mathbf{e}_T\otimes\mathbf{e}_L+\mathbf{e}_L\otimes\mathbf{e}_T)+\frac{1}{2}\gamma_{TW}(\mathbf{e}_T\otimes\mathbf{e}_W+\mathbf{e}_W\otimes\mathbf{e}_T) \tag{1}$$

where $(\mathbf{e}_T,\mathbf{e}_L,\mathbf{e}_W)$ is an orthogonal unit vector basis aligned with the initial orthotropy axes of the honeycomb. Equation (1) implies that the elastic and plastic Poisson's effects are neglected. Here, we assume the sandwich specimen height as a characteristic length of the RVE along the T-direction. Thus, the macroscopic strains are directly given by the displacement field (u_T,u_W) applied to the top boundaries of the specimen. The normal strain reads

$$\varepsilon=\frac{u_T}{C}. \tag{2}$$

Under combined loading in the T-W–plane, we have $\gamma_{TL}=0$ and $\gamma_{TW}=\gamma$, where

$$\gamma=\frac{u_W}{C}. \tag{3}$$

It follows from the loss of statistical homogeneity along the T-direction that the choice of the specimen height C might affect the observed macroscopic response. A detailed study of this potential size effect is left to future research.

The energy conjugate stress tensor $\mathbf{\Sigma}$ reads:

$$\mathbf{\Sigma}=\sigma(\mathbf{e}_T\otimes\mathbf{e}_T)+\tau_{TL}(\mathbf{e}_T\otimes\mathbf{e}_L+\mathbf{e}_L\otimes\mathbf{e}_T)+\tau_{TW}(\mathbf{e}_T\otimes\mathbf{e}_W+\mathbf{e}_W\otimes\mathbf{e}_T). \tag{4}$$

Note that due to the significant orthotropy of the honeycomb, in-plane stress components are typically about two orders of magnitude smaller than out-of-plane components σ, τ_{TL} and τ_{TW}, and thus are neglected in our discussion. In the present experiments, we have $\tau_{TL}=0$ and

$$\sigma=\frac{F_T}{A_0} \tag{5}$$

and

$$\tau=\frac{F_W}{A_0} \tag{6}$$

where $\tau:=\tau_{TW}$. $A_0=l_W\times l_L$ is the cross-sectional area of the sandwich specimen. F_T and F_W are the normal and shear forces acting on the specimen.

3 Experimental Procedure

Previous work demonstrated that displacement-controlled testing procedures are most suitable to investigate the mechanical behavior of honeycombs (Petras and Sutcliffe [10] and Doyoyo and Mohr [13]). The control of all displacements during testing avoids undesirable deformation modes due to localization in cellular solids (Mohr and Doyoyo [12]). Here, the universal biaxial testing device (UBTD) is used to apply combinations of large compressive and shear displacements to the boundaries of a honeycomb specimen. All tests are performed under quasi-static loading conditions.

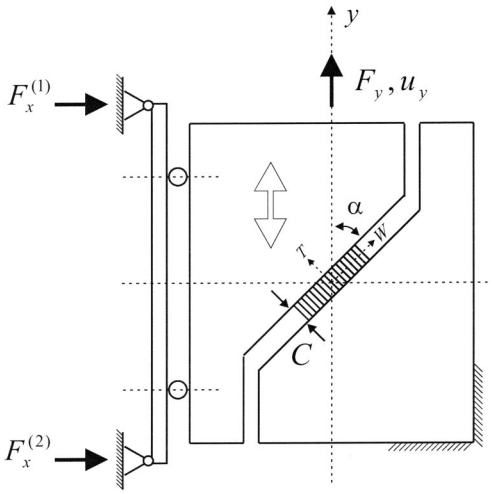

Fig. 3 Schematic of the universal biaxial testing device (UBTD)

3.1 Mechanical Details. The design of the UBTD is based on the concept of the enhanced arcan apparatus (see Mohr and Doyoyo [12]). A schematic of the UBTD is given in Fig. 3. The specimen is placed between the fixed and movable parts of the apparatus. The movable part is allowed to slide along the vertical direction (*y*-axis) only. All other degrees of freedom of the movable part including rotations are restricted. The inclination of the specimen with respect to the loading axis (*y*-direction) determines the combination of applied shear and normal displacements. This inclination is measured by the biaxial loading angle α (angle between the *W*-axis and *y*-axis in Fig. 3). The corresponding normal and shear displacements are

$$u_T=u_y\sin\alpha \tag{7}$$

$$u_W=u_y\cos\alpha \tag{8}$$

where u_y denotes the vertical displacement. In other words, the biaxial displacement field on the top boundary of the specimen is uniquely characterized by the biaxial loading angle and the resultant displacement. Note that the biaxial testing angle is fixed throughout testing, whereas the resultant displacement is prescribed, which limits the experimental capabilities to linear loading paths in terms of displacements. As shown in detail by Mohr and Doyoyo [11], reliable testing requires the measurement of at least two force components in the testing plane. The UBTD monitors three force components throughout testing: the horizontal forces $F_x^{(1)}$ and $F_x^{(2)}$, and the vertical force F_y (Fig. 3). From static equilibrium, we find the normal and shear force components, F_T and F_W, acting on the sandwich specimen:

$$F_T=F_y\sin\alpha-(F_x^{(1)}+F_x^{(2)})\cos\alpha \tag{9}$$

$$F_W=F_y\cos\alpha+(F_x^{(1)}+F_x^{(2)})\sin\alpha \tag{10}$$

3.2 Technical Details. A picture of the UBTD is shown in Fig. 4. Within this section, we denote the part numbers according to Fig. 4 in parentheses. The UBTD is designed as an integral testing frame that provides the function described above. The movable part of the device (1 to 5) slides vertically on four ball bearings (5) along two fixed guidance rods (8). Parts (7) to (13) belong to the fixed portion of the device. The bottom plate (12) is rigidly connected to the table of a universal testing machine (MTS, Model G45, Eden-Prarie, MN). A universal joint (2) connects the movable grip (1) to the screw-driven crosshead of the universal testing machine. A set of removable clamps (4,10) positioned the specimen in the center between the movable and fixed part of the device. Four screws on either side provided sufficient

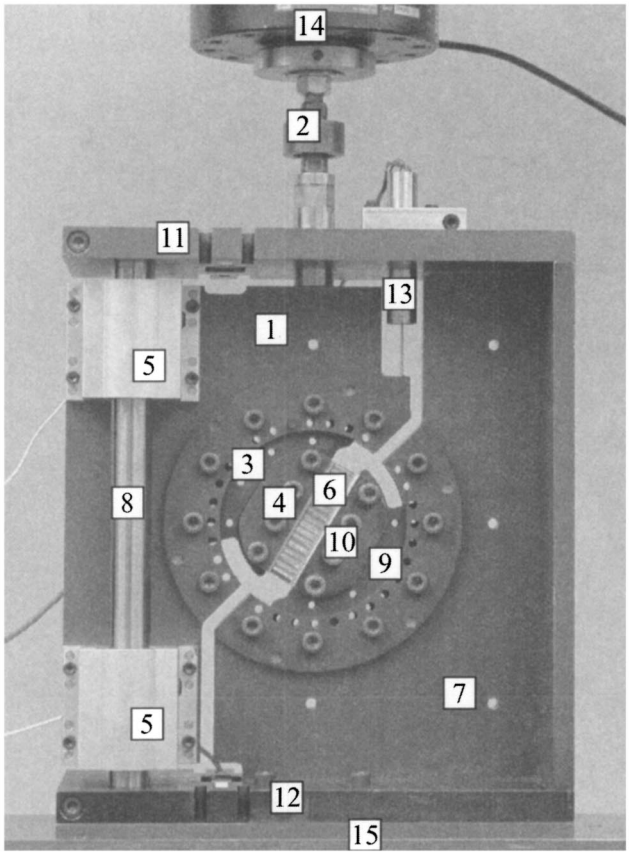

Fig. 4 Photograph of the UBTD (front view): 1-movable grip plate, 2-universal joint, 3-rotating specimen holder (top), 4-positioning clamp (top), 5-roller bearing, 6-sandwich specimen, 7-fixed grip plate, 8-vertical guidance rod, 9-rotating specimen holder (bottom), 10-positioning clamp (bottom), 11-top plate, 12-bottom plate, 13-LVDT, 14-vertical load cell (movable crosshead), and 15-table of fixed cross-head

clamping pressure. The inclination of the specimen (6) is set prior to testing by rotating the specimen holders (3,9). Tests can be performed at any biaxial loading angle between 0 and 90°, with an increment of 1 deg.

A linear variable differential transformer (13) built into the UBTD measures the relative displacement between the movable and fixed portion of the device. This measurement provides the resultant displacement acting on the specimen, u_y, assuming the UBTD to be rigid as compared to the honeycomb specimen. Displacements ranging from -10 mm to $+10$ mm are allowed by the current design. The vertical force F_y is recorded by the standard load cell (14) of the universal testing machine (200 kN MTS load cell). The horizontal forces are measured by two DC-DC load cells (Sensotec, Model 31) integrated into the top (11) and bottom plates (12) of the fixed portion of the UBTD. Figure 5 shows details of the integrated horizontal load cell. The load cells have been calibrated as built in for a total horizontal load of up to 3 kN. The accuracy of the horizontal load measurement at room temperature is $\pm 2\%$.

3.3 Sample Tests. We present the results from tests at 60deg to illustrate the testing procedure. Recordings of the vertical force and the two horizontal forces are shown in Figs. 6 and 7. All force readings are set to zero before the sandwich specimen is placed between the adjusted rotating specimen holders. Compressive stresses arise (predominantly) along the T-direction as the clamping pressure is applied to the short sides of the specimen grip plates. This may be explained by constrained Poisson's deformation in the grip plates (Henn [16]). After clamping, the crosshead was adjusted such that the vertical load was zero (Fig. 6). However, from the nature of the testing method, an initial offset in the horizontal force measurement is inevitable. For the present 60 deg tests, the horizontal preload load ranges from 170 to 300 N (see the encircled region in Fig. 7). All tests are performed at a constant crosshead velocity of 1 mm/min. Pictures are taken at different stages during the test. The tests were paused for image acquisition, which generated small relaxation drops in the load (Fig. 6). Furthermore, two unloading/reloading cycles are typically performed at large strains.

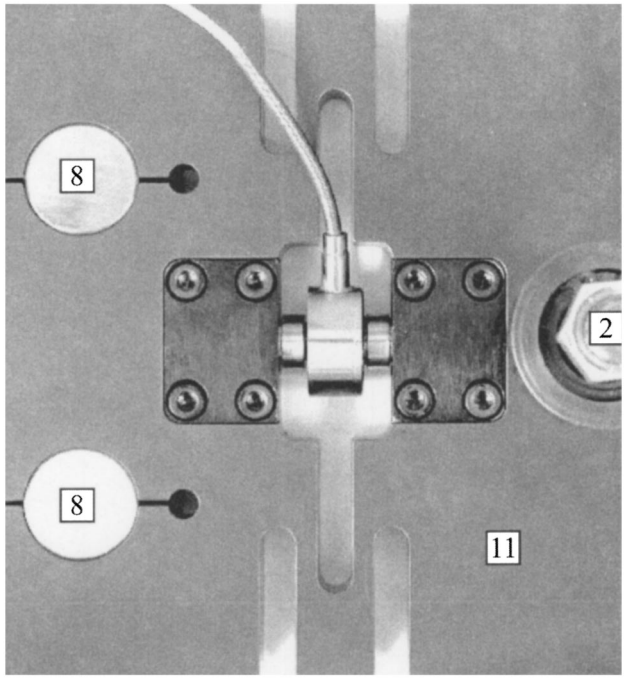

Fig. 5 Detail of how the horizontal load cell is integrated into the top plate (labels are consistent with the captions of Fig. 4)

Comparison of the horizontal force measurements reveals that, after the vertical load is applied, a difference develops between the two horizontal force components. Under compressive loading, the force acting on the bottom load cell is higher than the force

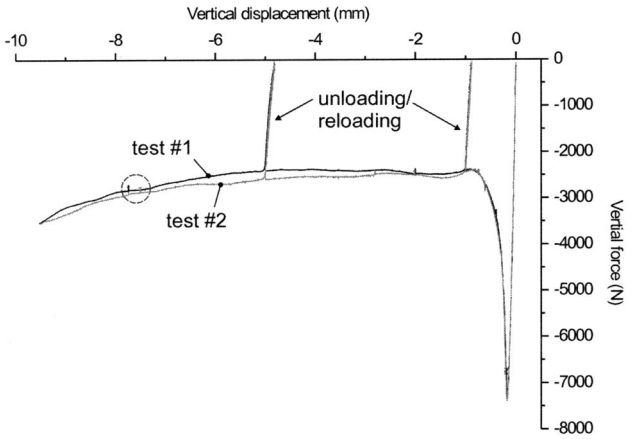

Fig. 6 Vertical force (MTS load cell) versus vertical displacement (LVDT) for tests under 60 deg loading. The encircled region highlights an example for minor drops in the load curve while the test was paused for image acquisition.

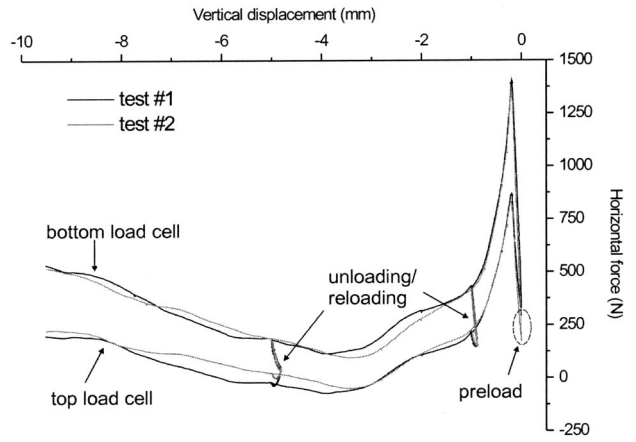

Fig. 7 Plots of the horizontal forces measured during tests under 60 deg loading. Note the two groups of curves: The upper and lower groups represent the recording of the horizontal force in the bottom plate and top plate, respectively.

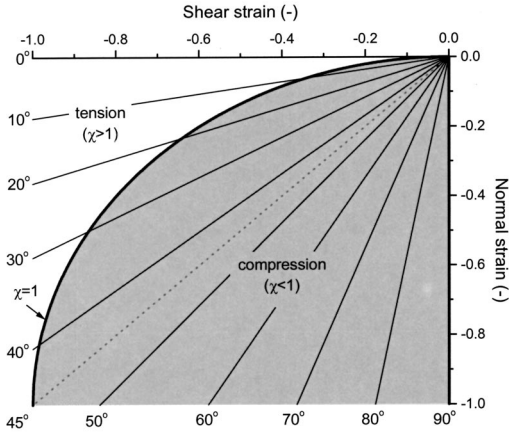

Fig. 8 Linear strain paths for various biaxial loading angles. The transition curve labeled $\chi=1$ cuts the domain into the expected compression and tension regimes.

acting on the top load cell. This observation is explained as follows: Suppose that the resultant reaction force in the deforming specimen acts at the geometric center of the specimen. At the same time, note that, throughout testing, the geometric center of the specimen moves with respect to the mechanical center of the testing device. The latter is defined by the intersection of the testing axis (y-axis) with the centerline between the horizontal load cells (dashed horizontal line in Fig. 3). Thus, due to this motion, an eccentricity of the resultant force with respect to the load cells emerges. As a result, a torsion moment acts on the horizontal bearings, which is counterbalanced by a pair of horizontal forces, reducing the load on the top load cell and increasing the load on the bottom load cell. Also heterogeneity of deformation inside the specimen is expected to contribute to the torsion moment. However, this effect has no influence on the total horizontal force $F_x^{(1)}+F_x^{(2)}$, which appears in the expressions for the average shear and normal stresses (see Eqs. (9) and (10)).

It must be noted that the present experiments are highly repeatable, irrespective of the biaxial loading angle. Very little scatter is observed in the force-displacement curves in Figs. 6 and 7. Characteristic features of those curves including force extrema or local changes in slope are almost identical for different specimens. This consistency emphasizes the overall reliability of the present experimental procedure including specimen dimensions and preparation.

4 Experimental Observations

Tests are performed on the honeycomb with the UBTD at 0, 10, 30, 40, 50, 60, 70, 80, and 90 deg loading. Large displacements are applied in the negative y-direction. Recall that from the nature of the experimental setup, strain paths remain constant throughout each test. In other words, the normal strain is proportional to the shear strain, and the proportionality factor is determined by the biaxial loading angle from the relation $\varepsilon=\gamma\tan\alpha$. All macroscopic strain paths are in the quadrant of negative normal strains and negative shear strains. Consequently, all elastic stress states are in the compression-shear quadrant of the stress space. However, under large (compressive) strains, tensile stresses develop for small loading angles. The generation of tensile stresses at small testing angles may be explained as follows. Consider the total stretch $\chi=\sqrt{(1+\varepsilon)^2+\gamma^2}$ that expresses the ratio of current to initial length of a fiber initially aligned with the T-direction. We anticipate that tensile stresses occur if $\chi>1$, and analogously, compressive stresses occur if $\chi<1$. The transition curve $\chi=1$ along with the various strain paths is plotted in Fig. 8. According to this consideration, tests at loading angles above 45 deg should only generate compressive stresses whereas tests at lower loading angles should exhibit compressive stresses first before tensile stresses build up. We therefore split our upcoming discussion into two parts: The first part focuses on the observations made for tests at large biaxial loading angles where the stress state is exclusively in the compression-shear quadrant, while the second part describes the observations for tests at small loading angles where tensile stresses emerge at large displacements.

4.1 Compression-Dominated Crushing. Figures 9–11 show the mechanical response curves for large biaxial loading angles. We discuss the results from tests under 60 deg and 80 deg loading as examples of crushing under compression and shear stresses. A sequence of photographs taken during both tests is shown in Figs. 12 and 13. In the mechanical response curves, the corresponding picture points are denoted by symbols labeled by small roman letters. The undeformed specimen configuration is denoted as *a*, while successive deforming configurations are denoted as *b*, *c*, *d*, *e*, and *f*, respectively.

First, consider the normal stress-strain curves in Fig. 9. Initially, the compressive stress rises linearly with strain (labeled as elastic I), until the response becomes slightly nonlinear as it can be seen from a continuous decrease in slope in the regime labeled as elastic II. Pictures taken at point *b* show a pattern of shallow buckles

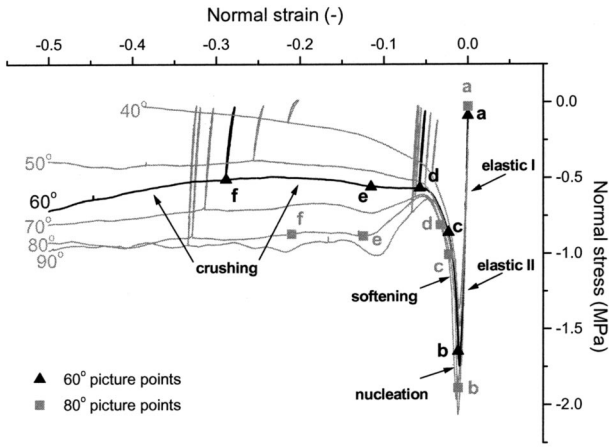

Fig. 9 Normal stress-strain curve for large biaxial loading angles. The corresponding pictures for 60 and 80deg are shown in Fig. 12 and Fig. 13, respectively.

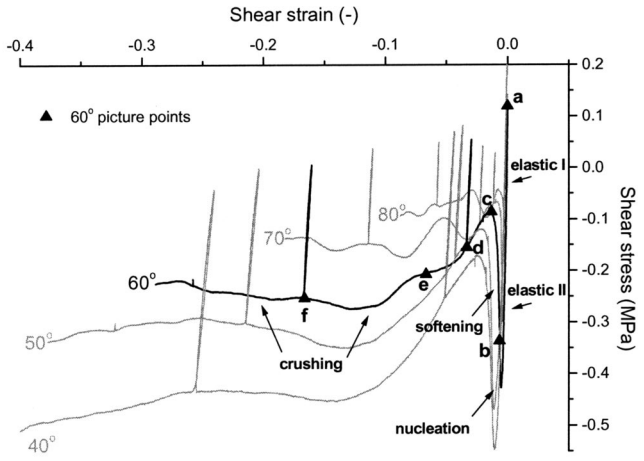

Fig. 10 Shear stress-strain curve for large biaxial loading angles. The corresponding pictures for 60 deg are shown in Fig. 12.

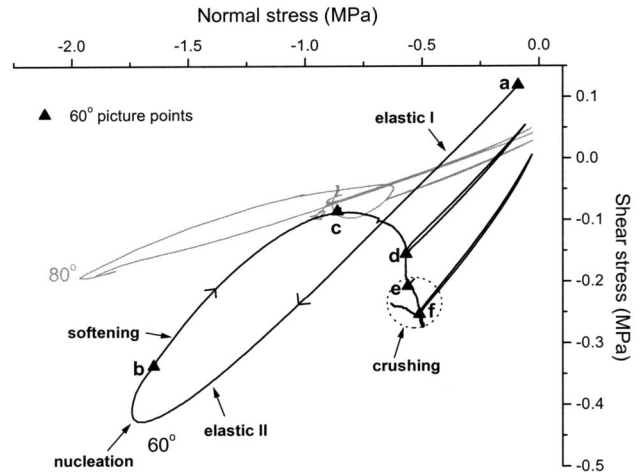

Fig. 11 Shear stress versus normal stress curve for selected large biaxial loading angles (60,80 deg)

that developed in the elastic II regime (Figs. 12(*b*), 13(*b*)). As the peak stress is overcome (labeled as nucleation), the compressive stress steadily drops with strain. This phase denoted as softening is associated with the stable plastic collapse of the cellular microstructure under compressive loading. We emphasize that plastic collapse is a stable event as confirmed by the photographs in Fig. 18 (to be discussed in detail later). Mechanically, this stability is manifested by the small scatter on the measured nucleation stresses and the maintaining of a constant stress level when the tests were paused for image acquisition in the softening phase (see points "*c*" in Fig. 9). Observe from the acquired photographs (Figs. 12(*d*) and 13(*d*)) that a characteristic collapse band becomes visible in the honeycomb microstructure throughout the softening phase. Consequently, we refer to the peak stress as a nucleation stress for collapse bands in the microstructure. For loading angles 60, 70, 80, and 90 deg, the compressive stress reaches a local minimum at $\varepsilon^* = -0.05 \pm .005$ and $\sigma^* = -0.6 \pm .05$ MPa. Then the compressive stress remains either constant (for 60 deg) or increases to attain a constant plateau level, which is a property of the *crushing regime*. The plateau level is initiated at a normal strain of approximately $2\varepsilon^*$.

The shear stress-strain curves show similar characteristics (Fig. 10). Both the elastic I and elastic II regimes are identifiable before a peak shear stress is reached. Furthermore, all the shear stress-strain curves exhibit significant softening between the nucleation point and the local minimum before a stable crushing regime is reached at a more or less constant stress level. However, in contrast to the nature of the compressive stress-strain curves, the minimum shear stress reached at the end of the softening regime varies significantly with the loading angle.

Figure 11 shows the correlation between the normal and shear responses in stress space. Consider the plots for 60 and 80 deg that describe the mechanical response at large loading angles. The sharp turning point in Fig. 11 shows that both the compressive and shear stresses decease almost simultaneously. To be exact, note that the loop turns clockwise, which implies that the shear stress decreases before the compressive stress reaches its maximum magnitude. The same conclusion is drawn for the next turning point: The shear stress reaches its minimum (point "*c*") ahead of the compressive stress (point "*d*"). The shaded circle at the end of the 60 deg curve in Fig. 11 highlights the crushing regime. Specifically, the center of the shaded circle corresponds to the mean crushing stresses whereas the diameter can be interpreted as the maximum amplitude of fluctuations in stress relative to the mean value in the crushing regime.

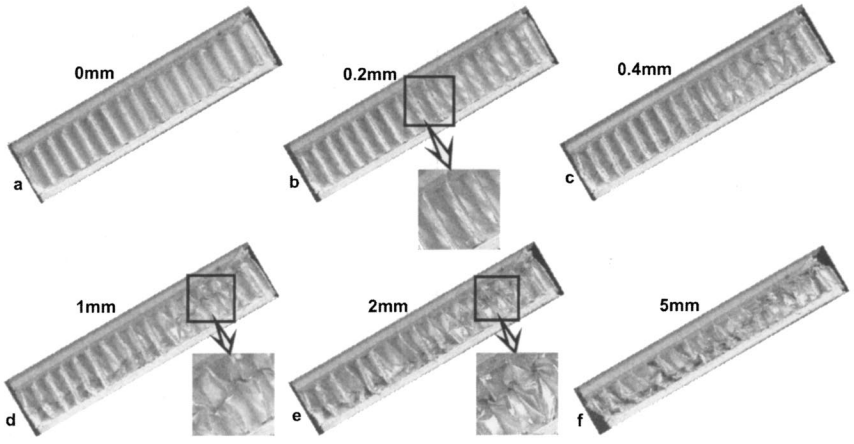

Fig. 12 A sequence of photographs of hexagonal aluminum honeycomb during biaxial loading at 60 deg angle at different resultant displacements. Note the development of collapse bands into plastic folds under load. The measurements next to each figure represent the magnitudes of the resultant displacement at each picture point.

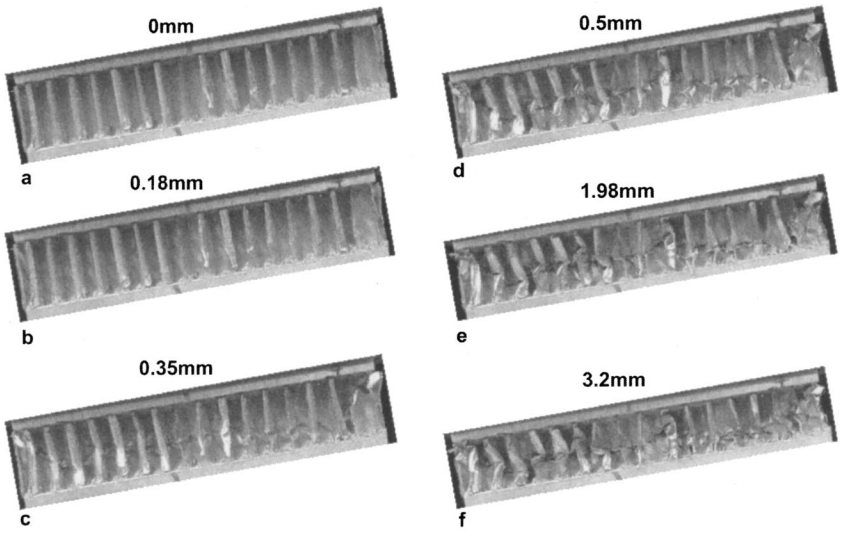

Fig. 13 A sequence of photographs of hexagonal aluminum honeycomb during biaxial loading at 80 deg angle at different resultant displacements. Note the development of collapse bands into plastic folds under load. The measurements next to each figure represent the magnitudes of the resultant displacement at each picture point.

4.2 Tension-Dominated Crushing. The mechanical response curves for low biaxial loading angles (0, 10, and 30 deg) are shown in Figs. 14 and 15. The normal stress-strain curve (Fig. 14) clearly shows that the normal stress changes from the state of being compressive to that of being tensile at large strains. This compressive-to-tensile stress transition occurs right from the beginning of the test under 0 deg loading (note that point "*b*" lies above point "*a*" in Fig. 14). For 10 and 30 deg loading, the compressive stress initially increases to a peak value and then decreases with strain as the transition to tensile stressing takes place at larger strains. The increase of the compressive stress to a peak value is analogous to the mechanical response at large loading angles. However, the subsequent softening phase is not bounded by some local minimum because the compressive stress continues to decrease until the normal stress becomes tensile. Thus, the normal stress-strain curves cross the abscissa axis denoting that the tensile stress is generated during crushing at small loading angles.

Now consider the shear stress-strain curves for small testing angles (Fig. 15). Again, we distinguish between the elastic I and elastic II regimes as the initial response becomes nonlinear. In contrast to all the other tests, the shear stress-strain curve for 0deg loading does not exhibit a softening regime, but instead it remains constant first and then increases monotonically until fracture limits the load carrying capacity of the specimen. At point "*b*" shear buckles have formed in the microstructure (Fig. 16(*b*)). However, for $\chi>1$ the cell walls aligned in the L-direction are stretched rather than folded, thereby providing a significant contribution to the shear strength of the microstructure. Fracture of the cell walls occurs in the vicinity of the bond line between the specimen and the grip (see ellipse in Fig. 16(*f*)).

The shear stress-strain curve under 30 deg loading is similar to

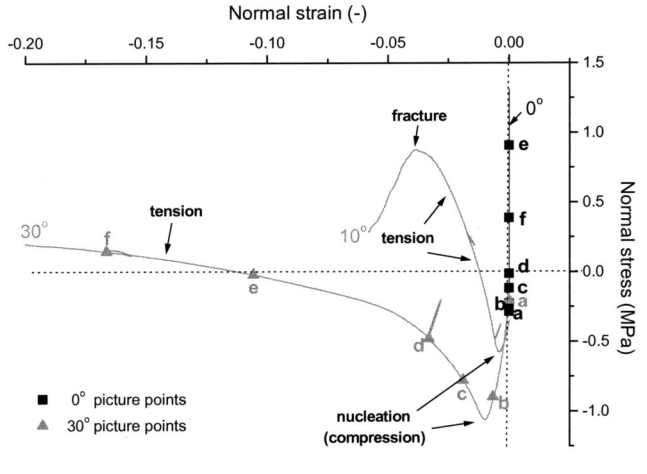

Fig. 14 Normal stress-strain curve for low biaxial loading angles. Note that all data points 0 deg lie on the ordinate axis. The corresponding pictures for 0deg and 30 deg are shown in Fig. 16 and Fig. 17, respectively.

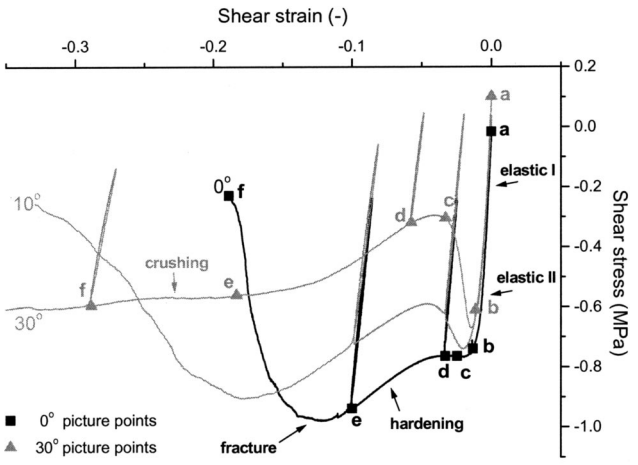

Fig. 15 Shear stress-strain curve for low biaxial loading angles. The corresponding pictures for 0 and 30 deg are shown in Fig. 16 and Fig. 17, respectively.

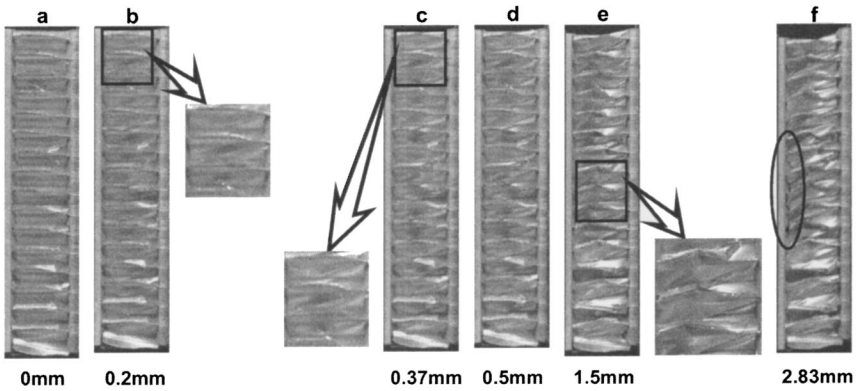

Fig. 16 A sequence of photographs of hexagonal aluminum honeycomb during biaxial loading at 0 deg angle at different resultant displacements. The measurements next to each figure represent the magnitudes of the resultant displacement at each picture point.

the response for large loading angles (Fig. 15). A pronounced peak stress is observed before a collapse band forms in the softening regime (Fig. 17(*c*)) and the shear stress level remains approximately constant in the crushing regime (Fig. 15). The shear response to 10deg loading show combined features of the responses at small and large loading angles: The shear stress curve shows a peak value and a softening phase similar to large angle testing, but it gradually increases without ever reaching a plateau value until fracture occurs just like during the 0deg testing (Fig. 15).

5 Honeycomb Plasticity

Here, we propose that the honeycomb equivalence to dislocation motions in metals is plastic hinge lines. Under combined compression and shear loading, plastic hinge lines nucleate, move, and pile up in the cellular honeycomb microstructure. The mechanisms postulated below apply to the compression-dominated behavior and are supported by the representative photographs acquired from a test performed at 60 deg loading (Figs. 18(*a*)–(*d*)).

Under out-of-plane loading, the elastic membrane stress state in the initially flat cell walls is that of combined shear and compression (Kelsey [17]). The driving force of buckling at the microstructural level is the principal compressive stress in the thin cell walls. Thus, as the local, principal compressive stresses exceed a threshold value, elastic buckling of the cell walls occurs (at the macro level, this is denoted by the transition from elastic I to elastic II regime). The load distribution within the microstructure

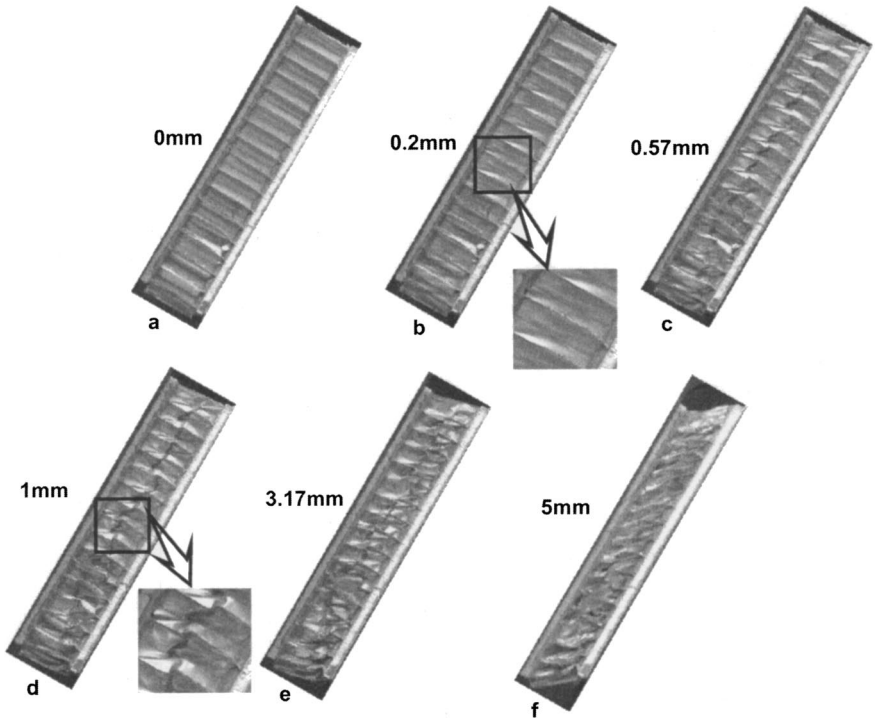

Fig. 17 A sequence of photographs of hexagonal aluminum honeycomb during biaxial loading at 30 deg angle at different resultant displacements. The measurements next to each figure represent the magnitudes of the resultant displacement at each picture point.

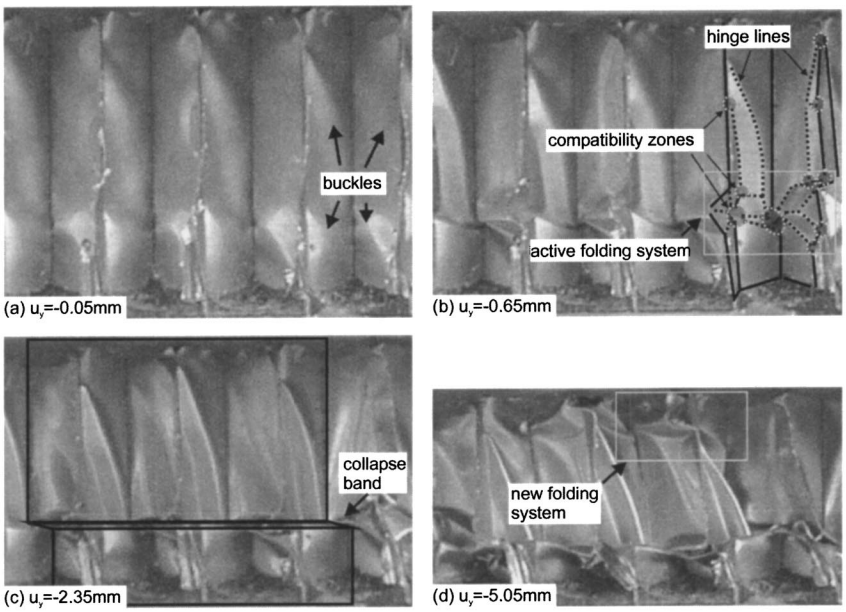

Fig. 18 Representative photographs of collapse mechanisms of the compression-dominated crushing illustrated with the observations made at 60 deg loading

changes dramatically. With the formation of buckles, the stress state changes in the affected/deflected regions from the membrane stretching-dominated state to the bending-dominated state (Fig. 18(*a*)). As a result, the honeycomb loses stiffness at the macroscopic level, which explains the convex nature of the macroscopic stress-strain curves in the elastic II regime. However, at the same time, the membrane stresses increase in the immediate vicinity of the intersection line between neighboring cell walls, where deflections are prohibited. The macroscopic peak load is reached (nucleation) when the membrane stresses at the intersection lines satisfy the yield condition of the cell wall material (von Kármán et al. [18]). Beyond this point, the buckles no longer disappear upon unloading. Instead, they are ''frozen'' by the surrounding plastically deformed undeflected regions.

Subsequently, the depth of the buckles increases further with loading while the bending deformation becomes plastic and focuses along the *plastic hinge lines* within the microstructure. At this stage, the buckles become clearly visible without magnification. However, the formation of plastic hinge lines is prohibited at the cell wall intersections. We call these intersections *compatibility zones* and they are regions where bending is restricted by the requirement of compatibility between the deformation fields of the adjacent cell walls (Fig. 18(*b*)). At large macroscopic deformations, the microstructure locally folds along plastic hinge lines, whereas compatibility between neighboring cell walls is achieved at the expense of plastic membrane deformation in the compatibility zones. We refer to a system of plastic hinge lines and compatibility zones that allow for the folding of the microstructure as a *folding system*. Note that among all the evolving plastic hinge lines, only a few contribute to the active folding system (Fig. 18(*b*)). A *collapse band* may be seen as a series of active folding systems. Figure 18(*c*) illustrates the localization of microstructural deformation within collapse bands while the microstructure above and below undergoes a rigid body translation. New folding systems are set in motion as the cell walls of the active folding systems contact each other, thereby raising their crushing resistance beyond the activation threshold for a new collapse band (Fig. 18(*d*)).

Previous work on the crashworthiness of thin-walled structures (e.g., Wierzbicki and Abramowicz [19]) suggests that the energy dissipations due to bending along plastic hinge lines and due to stretching in the compatibility zones are two competing mechanisms that determine the kinematics of a folding system. From Alexander's postulate (Alexander [20]), it follows that the plastic hinge lines naturally change orientation and move such as to minimize the overall plastic dissipation in a folding system.

The compatibility zones in the honeycomb microstructure act as ''grain boundaries of a honeycomb.'' Hinge lines typically end in the compatibility zones (pile up). At the same time, new hinge lines are generated in this critical region, thereby activating other folding systems. This may be viewed as a reflection of a hinge line. Also note that the compatibility zones are crucial for the strength of a honeycomb: The bending process along a plastic hinge line alone is almost catastrophic, i.e., the plastic dissipation per unit displacement decreases dramatically during bending (e.g., Wierzbicki and Abramowicz [19]). However, the compatibility zones typically exhibit the opposite behavior: the plastic dissipation per unit displacement increases as folding proceeds, until necking, brittle fracture or intracellular delamination limit the load carrying capacity of the compatibility zones.

Although the analogy between the folding system in a honeycomb and the slip line system in metals can be made, one fundamental difference shall be emphasized: The slip line systems in metallic crystals are predefined in the undeformed lattice, whereas the folding systems in metallic honeycombs are deformation induced. In other words, hinge lines nucleate and folding systems form according to the applied macroscopic deformation field. This difference is crucial with respect to constitutive modeling, and poses an exciting challenge for future research. At the same time, it should be noted that the nucleation of folding systems relies on the local plastic collapse of the microstructure and thus, based on von Kármán's model for the collapse of thin plates (von Kármán et al. [18]), it is expected that folding system characteristics such as the plastic hinge line orientation can be controlled by the choice of the microstructural properties such as the ratio of cell wall width to cell wall thickness.

6 Phenomenological Modeling

The focus in this section is on the phenomenological analysis of compression-dominated crushing. This choice is made with practical applications in mind: one would expect the honeycomb core

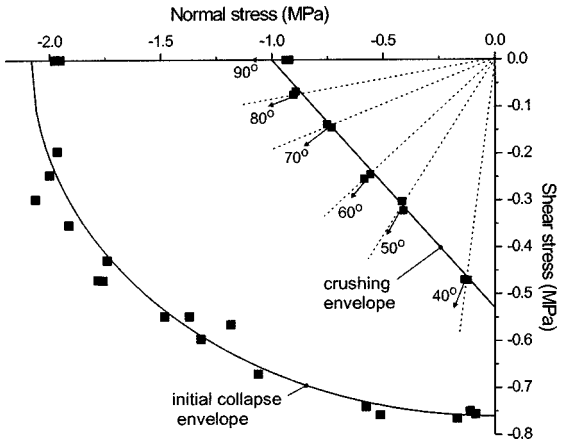

Fig. 19 Initial collapse and crushing envelopes in stress space. The square dots are experimental data points. The vectors indicate the direction of plastic flow during crushing, whereas the dashed straight lines starting from the origin prescribe the direction of plastic flow according to the simplified flow rule given by Eq. (15).

in a sandwich panel to experience largely a combination of compressive and shear stresses rather than that of tensile and shear stresses. The initial yield envelope defining the onset of plastic collapse in terms of macroscopic stresses is presented. To describe the mechanical response in the crushing regime, we introduce a crushing envelope along with a flow rule.

Honeycomb elasticity as well as the transition from initial collapse to the crushing regime (that is, softening) are not addressed from a phenomenological point of view. We refer to the textbook by Gibson and Ashby [3] for a description of orthotropic elasticity of the statistically homogeneous honeycomb microstructure. Under large deformations, however, the elastic moduli evolve (Mohr and Doyoyo [14]) and most importantly, the elastic material behavior changes from transverse-orthotropic to full-anisotropic elasticity. In other words, coupling effects between elastic shear strains and normal stresses and vice versa come into play and require special attention. At the same time, most engineering applications of honeycomb either exploit its orthotropic elastic behavior or its crushing behavior, where elastic strains are small as compared to the total strains and thus negligible. The later argument also partially justifies why the phenomenological description below does not include the transition from the nucleation envelope to the crushing envelope. The other argument for omitting a discussion of this transition phase is the lack of experimental evidence. Based on the results from numerical simulations of the honeycomb microstructure under multiaxial loading (Mohr and Doyoyo [21]) and the honeycomb plasticity presented above, the authors believe that loading path dependency might play a key role on the shape of post-yield envelopes in this transition regime, a property that could not be studied with the present testing method. This concern also applies to the crushing envelope, but must be tempered since the crushing envelope represents the mean over a wide range of individual envelopes in the crushing phase.

6.1 Initial Yield Envelope. We ignore irreversible deformation in the honeycomb microstructure prior to collapse and define the initial yield envelope by the onset of plastic collapse of the honeycomb microstructure. The corresponding collapse stresses are defined by the initial peak stresses of the macroscopic stress-strain curves. A plot of the data points found from the present experiments is shown in Fig. 19. It appears that an elliptical yield envelope provides the best description for the onset of plastic collapse:

$$f_0(\sigma,\tau)=\left(\frac{\sigma}{\sigma_0}\right)^2+\left(\frac{\tau}{\tau_0}\right)^2-1=0. \tag{11}$$

From a fit of Eq. (11) to the data, we find the yield stress under uniaxial compression $\sigma_0=-2.08$ MPa and the shear yield stress under pure shear $\tau_0=0.76$ MPa. It follows from the morphological orthotropy of the undeformed microstructure that the initial yield envelope must be symmetric with respect to shear. However, Eq. (11) is only valid for compressive stresses ($\sigma\leqslant 0$). Under tensile stresses, the microstructural deformation mode is expected to change, which might require a different phenomenological description on the macroscopic level.

6.2 Crushing Behavior. In our discussion of the experimental observations, the crushing phase is characterized by more or less constant normal and shear stress levels. We define the crushing stresses $\bar{\sigma}$ and $\bar{\tau}$ as means over the respective energy conjugate strains:

$$\bar{\sigma}=\frac{1}{\varepsilon_{\max}-2\varepsilon^*}\int_{2\varepsilon^*}^{\varepsilon_{\max}}\sigma\,\mathrm{d}\varepsilon \tag{12}$$

and

$$\bar{\tau}=\frac{1}{\gamma_{\max}-2\gamma^*}\int_{2\gamma^*}^{\gamma_{\max}}\tau\,\mathrm{d}\gamma. \tag{13}$$

The characteristic interval $[2\varepsilon^*,\varepsilon_{\max}]$ determines the length of the crushing phase. Based on the experimental results, we suggest $2\varepsilon^*=-0.1$ and $\varepsilon_{\max}=-0.5$. The corresponding shear strain interval $[2\gamma^*,\gamma_{\max}]$ is found from the relation $\gamma=\varepsilon/\tan\alpha$. A plot of the data points $(\bar{\sigma},\bar{\tau})$ is presented in Fig. 19. It appears that under monotonic loading along a linear strain path the corresponding ''crushing envelope'' is a linear function in the shear stress–normal stress plane:

$$f_c(\bar{\sigma},\bar{\tau})=\frac{\bar{\sigma}}{\bar{\sigma}_0}+\left|\frac{\bar{\tau}}{\bar{\tau}_0}\right|-1=0. \tag{14}$$

The mean stress under uniaxial compression (so-called ''plateau stress'') found from a fit to the experimental data is $\bar{\sigma}_0=-1.0$ MPa. Again, we restrict the validity of the yield envelope to compressive stresses only, i.e., $\bar{\sigma}\leqslant 0$. Recall that tests at small biaxial loading angles developed tensile stresses under large strains and are thus not considered for the evaluation of the compression-dominated crushing behavior. For instance the mean shear stress, $\bar{\tau}_0=0.53$ MPa, is determined from the extrapolation of the data in Fig. 19, instead of using the results from the tension-dominated 0 deg tests.

Further analysis of the data (Fig. 19) suggests that the relationship between the direction of the inelastic deformation and the location on the crushing envelope may be expressed as follows (flow rule equivalent):

$$\frac{d\varepsilon}{d\gamma}\cong\frac{\bar{\sigma}}{\bar{\tau}}. \tag{15}$$

Note that for the present experiments along linear strain paths, the left-hand side corresponds to the tangent of the biaxial loading angle, i.e., it represents the direction of the strain resultant in the T-W plane. The right-hand side represents the direction of the corresponding stress resultant. According to Eq. (15), the strain and stress resultants are parallel in the crushing regime.

7 Conclusions

A custom-built universal biaxial testing device (UTBD) was successfully used to perform reliable tests on hexagonal aluminum honeycomb relative to its tubular direction. Based on the experimental results, the mechanical response of a honeycomb sandwich specimen to combined compressive and shear loading was analyzed in depth, both at the microstructural and the macroscopic levels. It appeared that deformation-induced folding systems de-

termine the plasticity of the aluminum honeycomb. Folding systems nucleate after plastic collapse of the microstructure. They are composed of plastic hinge lines and compatibility zones along the intersection of neighboring cell walls. On the macroscopic level, an elliptic envelope was suggested to describe the nucleation process in the (compressive) normal-shear stress plane. Furthermore, a linear envelope along with a nonassociated flow rule was identified in the same plane to define the relationship among the mean normal stress, the mean shear stress and the direction of the macroscopic strain increment.

Acknowledgments

We thank Prof. Tomasz Wierzbicki for valuable discussions. Thanks are due to Stephen Rudolph for his outstanding contribution to the design and precision machining of the UBTD. Discussions with Stefan Henn and Mark Jeunnette from BMW R&D at Munich on the testing technique were highly appreciated. Financial support of the Joint MIT/Industry Ultralight Consortium is also acknowledged. Hexcel Corporation is thanked for supplying the aluminum alloy honeycomb tested in this study.

References

[1] Allen, H. G., 1969, *Analysis and Design of Structural Sandwich Panels*, Pergamon Press, Oxford, UK.
[2] Mohr, D., and Wierzbicki, T., 2003, ''Shear Folding of Soft-Core Sandwich Profiles,'' Int. J. Mech. Sci., **45**(2), pp. 253–271.
[3] Gibson, L. J., and Ashby, M. F., 1997, *Cellular Solids: Structure and Properties*, 2nd Ed., Cambridge University Press, Cambridge, UK.
[4] Klintworth, J. W., and Stronge, W. J., 1988, ''Elasto-Plastic Yield Limits and Deformation Laws for Transversely Crushed Honeycombs,'' Int. J. Mech. Sci., **30**, pp. 273–292.
[5] Papka, S. D., and Kyriakides, S., 1999, ''Biaxial Crushing of Honeycombs—Part II: Analysis,'' Int. J. Solids Struct., **36**(29), pp. 4397–4423.
[6] McFarland, R. K., 1963, ''Hexagonal Cell Structure Under Post-Buckling Axial Load,'' AIAA J., **1**, pp. 1380–1385.
[7] Wierzbicki, T., 1983, ''A Crushing Analysis of Metal Honeycomb,'' Int. J. Impact Eng., **1**, pp. 157–174.
[8] Hexcel, 1997, private communication.
[9] Wierzbicki, T., 1997, ''Experimental, Numerical, and Analytical Study of Honeycomb Material,'' Report No. 1, Impact and Crashworthiness Laboratory, MIT.
[10] Petras, A., and Sutcliffe, M. P. F., 2000, ''Indentation Failure Analysis of Sandwich Beams,'' Composite Structures, **50**(3), pp. 311–318.
[11] Mohr, D., and Doyoyo, M., 2002, ''Analysis of the Arcan Apparatus in the Clamped Configuration,'' J. Compos. Mater., **36**(22), pp. 2583–2594.
[12] Mohr, D., and Doyoyo, M., 2003, ''A New Method for the Biaxial Testing of Cellular Solids,'' Exp. Mech., **43**(2), pp. 173–182.
[13] Doyoyo, M., and Mohr, D., 2003, ''Microstructural Response of Aluminum Honeycomb to Combined Out-of-Plane Loading,'' Mech. Mater., **35**(9), pp. 865–876.
[14] Mohr, D., and Doyoyo, M., 2003, ''Nucleation and Propagation of Plastic Collapse Bands in Aluminum Honeycomb,'' J. Appl. Phys., **94**(4), pp. 2262–2270.
[15] François, D., Pineau, A., and Zaoui, A., 1998, *Mechanical Behavior of Materials, Volume I: Elasticity and Plasticity*, Kluwer, Dordrechet, The Netherlands.
[16] Henn, S., 2004, ''Development of a Material Model for the Crack Inititation in Cast Aluminum Alloys Under Monotonic Loading,'' Ph.D. thesis, BMW Munich, in prepartation.
[17] Kelsey, S., Gellatly, R. A., and Clark, B. W., 1958, ''The Shear Modulus of Foil Honeycomb Cores,'' Aircr. Eng., **30**, pp. 294–302.
[18] von Kármán, T., Sechler, E. E., and Donnell, L. H., 1932, ''The Strength of Thin Plates in Compression,'' Trans. ASME, **54**, pp. 53–63.
[19] Wierzbicki, T., and Abramowicz, W., 1983, ''On the Crushing Mechanics of Thin-Walled Structures,'' ASME J. Appl. Mech., **50**, pp. 727–739.
[20] Alexander, J. M., 1960, ''An Approximative Analysis of the Collapse of Thin Cylindrical Shell Under Axial Loading,'' Q. J. Mech. Appl. Math., **13**(1), pp. 10–15.
[21] Mohr, D., and Doyoyo, M., 2004, ''Deformation-Induced Folding Systmes in Thin-Walled Monolithic Hexagonal Metallic Honeycomb Under Multi-axial Loading,'' Int. J. Solids Struct., in press.
[22] Arcan, M., Hashin, Z., and Voloshin, A., 1978, ''A Method to Produce Uniform Plane-Stress States With Applications to Fiber-Reinforced Materials,'' Exp. Mech., **18**, pp. 141–146.
[23] ASTM C273, 1994, ''Standard Test Method for Shear Properties of Sandwich Core Materials,'' *Annual Book of ASTM Standards*.

The Resistance of Clamped Sandwich Beams to Shock Loading

N. A. Fleck[1]
e-mail: naf1@eng.cam.ac.uk

V. S. Deshpande

Engineering Department,
Cambridge University,
Trumpington Street,
Cambridge, CB2 1PZ, UK

A systematic design procedure has been developed for analyzing the blast resistance of clamped sandwich beams. The structural response of the sandwich beam is split into three sequential steps: stage I is the one-dimensional fluid-structure interaction problem during the blast loading event, and results in a uniform velocity of the outer face sheet; during stage II the core crushes and the velocities of the faces and core become equalized by momentum sharing; stage III is the retardation phase over which the beam is brought to rest by plastic bending and stretching. The third-stage analytical procedure is used to obtain the dynamic response of a clamped sandwich beam to an imposed impulse. Performance charts for a wide range of sandwich core topologies are constructed for both air and water blast, with the monolithic beam taken as the reference case. These performance charts are used to determine the optimal geometry to maximize blast resistance for a given mass of sandwich beam. For the case of water blast, an order of magnitude improvement in blast resistance is achieved by employing sandwich construction, with the diamond-celled core providing the best blast performance. However, in air blast, sandwich construction gives only a moderate gain in blast resistance compared to monolithic construction. [DOI: 10.1115/1.1629109]

1 Introduction

A major consideration in the design of military vehicles (such as ships and aircraft) is their resistance to air and water blast. Early work (at the time of World War II) focused on monolithic plates, and involved measurement of blast resistance by full scale testing for a limited range of materials and geometries. Simple analytical models were also developed, such as the one-dimensional fluid-structure interaction model of Taylor [1].

Over the last decade a number of new core topologies for sandwich panels have emerged, showing structural advantage over monolithic construction for quasi-static loadings. These include metallic foams, [2], lattice materials of pyramidal and tetrahedral arrangement, [3], woven material, [4], and egg-box, [5]. The current study is an attempt to extend and to synthesize analytical models for the dynamic response of clamped beams in order to optimize the blast resistance of clamped sandwich beams. Explicit comparisons are made between the performance of competing core concepts.

The clamped sandwich beams, as sketched in Fig. 1, is representative of that used in the design of commercial and military vehicles: For example, the outermost structure on a ship comprizes plates welded to an array of stiffeners. While it is appreciated that the precise dynamic response of plates is different from that explored here for beams, the qualitative details will be similar, and major simplifications arise from the fact that simple analytical formulas can be derived for the beam.

In a parallel study, Xue and Hutchinson [6] have compared the blast resistance of clamped sandwich beams to that of monolithic beams of the same mass via three-dimensional finite element (FE) simulations. In these FE calculations, Xue and Hutchinson [6] modeled the core topologies explicitly but ignored the fluid-structure interaction; a prescribed impulse was applied to the outer face of the sandwich beam and was applied uniformly to the monolithic beam. A limited number of FE calculations were performed to identify near-optimal sandwich configurations, and the superior blast resistance of sandwich beams compared to that of monolithic beams was demonstrated.

Review of the Characteristics of a Water Blast. The main characteristics of a shock wave resulting from an underwater explosion are well established due to a combination of detailed large-scale experiments and modeling over the past 60 years. Useful summaries of the main phenomena are provided by Cole [7] and Swisdak [8], and are repeated briefly here in order to underpin the current study.

The underwater detonation of a high explosive charge converts the solid explosive material into gaseous reaction products (on a time scale, t, of microseconds). The reaction products are at an enormous pressure (on the order of GPa), and this pressure is transmitted to the surrounding water by the propagation of a spherical shock wave at approximately sonic speed. Consider the response of a representative fluid element at a radial distance r from the explosion. Upon arrival of the primary shock wave, the pressure rises to a peak value p_o almost instantaneously. Subsequently, the pressure decreases at a nearly exponential rate, with a time constant θ on the order of milliseconds, and is given by $p(t)=p_o \exp(-t/\theta)$. The magnitude of the shock wave peak pressure and decay constant depend upon the mass and type of explosive material and the distance r. After the primary shock wave has passed, subsequent secondary shocks are experienced, due to the damped oscillation of the gas bubble which contains the explosive reaction products. However, these secondary shock waves have much smaller peak pressures, and are usually much less damaging than the primary shock to a structure in the vicinity of the explosion than the primary shock.

Experimental data (and physical models) support the use of simple power-law scaling relations between the mass m of explosive, the separation r between explosion and point of observation,

[1]To whom correspondence should be addressed.

Contributed by the Applied Mechanics Division of THE AMERICAN SOCIETY OF MECHANICAL ENGINEERS for publication in the ASME JOURNAL OF APPLIED MECHANICS. Manuscript received by the ASME Applied Mechanics Division, May 19, 2002; final revision, July 10, 2003. Associate Editor: R. M. McMeeking, Discussion on the paper should be addressed to the Editor, Prof. Robert M. McMeeking, Department of Mechanical and Environmental Engineering University of California—Santa Barbara, Santa Barbara, CA 93106-5070, and will be accepted until four months after final publication of the paper itself in the ASME JOURNAL OF APPLIED MECHANICS.

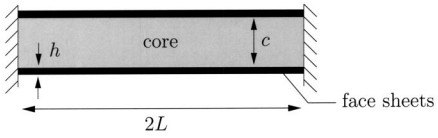

Fig. 1 Geometry of the sandwich beam

and the resulting shock wave characteristics, p_o and θ. For example, for an underwater TNT explosion, the peak pressure is taken from Table 2 of Swisdak [8] as

$$p_o = 52.4\left(\frac{m^{1/3}}{r}\right)^{1.13} \quad \text{MPa}, \tag{1}$$

where m is in kilograms and r is in meters. Also, the time constant θ is

$$\theta = 0.084 m^{1/3}\left(\frac{m^{1/3}}{r}\right)^{-0.23} \quad \text{ms}. \tag{2}$$

These relations have been validated for the domain of m and r such that p_o lies in the range 3–140 MPa, see Swisdak [8] for further details. Similar scaling relations have been obtained for other high explosives, and the coefficients in the above relations hold to reasonable accuracy for them also.

Next consider the case of a blast wave in air due to the detonation of a high explosive. Again, a primary shock wave travels at near sonic speed, with an exponential pressure-time history at any fixed location from the explosive. The time constant for the pulse θ is similar in magnitude to that in water, but the peak pressure is an order of magnitude lower (see Ashby et al. [2] for a recent discussion, building upon the work of Smith and Hetherington [9]).

Scope and Motivation of the Study. The main objective of this study is to develop analytical formulas for characterizing the structural response of a sandwich beam subjected to blast loading in water or in air. These formulas are of direct practical use for designing laboratory-scale and industrial-scale blast-resistant sandwich beams, including the choice of face sheet and core.

First, the relevant mechanical response of candidate core topologies is reviewed. Second, the dynamic structural response of a clamped sandwich beam is analyzed; it is argued that the response can be separated into three distinct stages. Stage I is the response of the front face sheet to the primary shock wave, including the effects of fluid-structure interaction. Crushing of the core occurs in stage II. And in stage III the sandwich beam is brought to rest by plastic bending and stretching. Third, performance charts for a wide range of sandwich core topologies are constructed for both air and water blast, with the monolithic beam taken as the reference case. These performance charts are used to determine the optimal geometry to maximize blast resistance for a given mass of sandwich beam.

2 Review of Core Topologies

In recent years a number of micro-architectured materials have been developed for use as the cores of sandwich beams and panels. Here we briefly review the properties of the following candidate cores for application in blast-resistant construction: pyramidal cores, diamond-celled lattice materials, metal foams, hexagonal-honeycombs and square-honeycombs.

Pyramidal cores, as shown schematically in Fig. 2(*a*), are fabricated from sheet-metal by punching a square pattern and then by alternately folding the sheet to produce a corrugated pattern. The core is then bonded to the solid faces by brazing. The pyramidal core has an out-of-plane effective modulus (and longitudinal shear modulus) which scale linearly with the relative density $\bar{\rho}$ of the core. Provided the struts are sufficiently stocky for the elastic buckling strength of the struts to exceed their yield strength, the out-of-plane compressive strength of the pyramidal core also scales linearly with $\bar{\rho}$. A detailed discussion on the mechanical properties of lattice materials such as pyramidal cores has been given previously by Deshpande and Fleck [3]. For example, the normal compressive strength σ_{nY} of the pyramidal core with the struts making an angle $\omega = 45°$ with the face sheets is

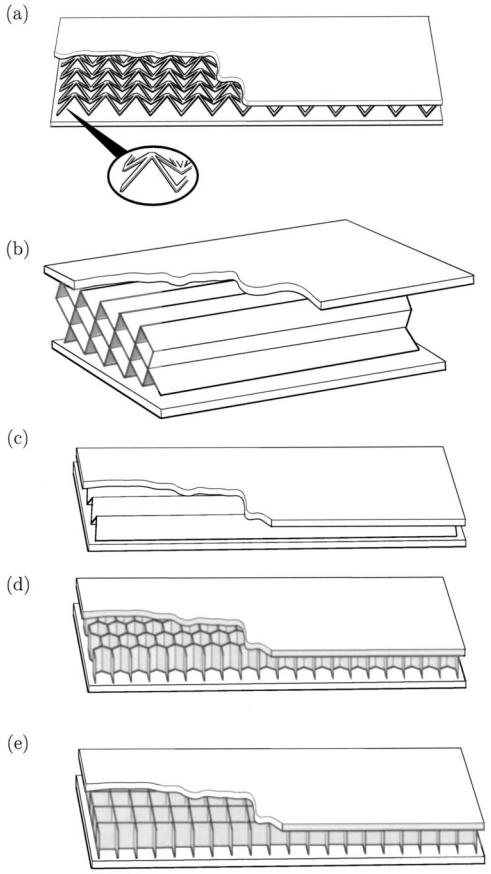

Fig. 2 Sketches of the sandwich core topologies; (*a*) pyramidal core, (*b*) diamond-celled core, (*c*) corrugated core, (*d*) hexagonal-honeycomb core, and (*e*) square-honeycomb core

$$\frac{\sigma_{nY}}{\sigma_Y} = \begin{cases} 0.5\bar{\rho} & \text{set by yield, if } \bar{\rho} > \dfrac{96\sqrt{2}\epsilon_Y}{\pi^2} \\ \dfrac{\pi^2}{96\sqrt{2}\epsilon_Y}\bar{\rho}^2, & \text{set by elastic buckling, otherwise,} \end{cases} \tag{3}$$

where σ_Y and ϵ_Y are the uniaxial yield strength and strain of the solid material from which the pyramidal core is made. Here we have assumed that the core struts are pin-jointed to the face sheets in order to get a conservative estimate of the elastic buckling strength. The in-plane strength of the pyramidal core in the length direction of the sandwich beam is governed by the bending strength of the nodes. Consequently, the in-plane strength scales as $\bar{\rho}^{3/2}$ and at the low relative densities for which these pyramidal cores find application, this strength is negligible, $\sigma_{lY} = 0$.

Diamond-celled lattice materials have the geometry shown in Fig. 2(*b*), and have recently been proposed as cores of sandwich beams. These lattice materials can be manufactured either by brazing together wire meshes, [4], or slotting together sheet metal. With the diamond-like cells aligned along the longitudinal axis of the beam as shown in Fig. 2(*b*), these materials provide high

strengths in both the normal and longitudinal directions of the beam. Typically diamond-cells have a semi-angle $\omega = 45°$ and the core has a normal compressive strength

$$\frac{\sigma_{nY}}{\sigma_Y} = \begin{cases} 0.5\bar{\rho}, & \text{set by yield, if } \bar{\rho} > \dfrac{4\sqrt{3\epsilon_Y}}{\pi}; \\ \dfrac{\pi^2}{96\epsilon_Y}\bar{\rho}^3, & \text{set by elastic buckling, otherwise,} \end{cases} \tag{4a}$$

while the longitudinal strength is given by

$$\frac{\sigma_{lY}}{\sigma_Y} = \bar{\rho}. \tag{4b}$$

Note that the diamond-celled core has identical strength-density relations to the single layered corrugated core shown in Fig. 2(*c*). However, unlike in a corrugated core, the size of the diamond-cells can be varied independently from the sandwich beam core thickness and hence made as small as required to prevent wrinkling of the sandwich face sheets.

Metal foams are random cellular solids with a highly imperfect microstructure. In most cases they are close to isotropic in elasto-plastic properties. The connectivity of neighboring cell edges is sufficiently small for the cell walls to bend under all macroscopic stress states, Ashby et al. [2]. Consequently, the modulus scales quadratically with relative density $\bar{\rho}$, while the macroscopic yield strength scales with $\bar{\rho}^{3/2}$ according to, [2],

$$\frac{\sigma_{nY}}{\sigma_Y} = \frac{\sigma_{lY}}{\sigma_Y} = 0.3\bar{\rho}^{3/2}. \tag{5}$$

Hexagonal-honeycombs are extensively used as cores of sandwich beams in the configuration sketched in Fig. 2(*d*), i.e., with the out-of-plane direction of the honeycomb aligned along the transverse direction of the beam. Thus, neglecting the elastic buckling of the cell walls we take

$$\frac{\sigma_{nY}}{\sigma_Y} = \bar{\rho}. \tag{6}$$

On the other hand, in the longitudinal direction of the beam, hexagonal-honeycomb cores deform by the formation of plastic hinges at the nodes which results in a negligible strength. Thus, in practical applications it is reasonable to assume $\sigma_{lY} = 0$ for these honeycombs.

Square-honeycombs as sketched in Fig. 2(*e*) can be manufactured by slotting together sheet metal. With the square cells aligned parallel to the longitudinal axis of the beam as sketched in Fig. 2(*e*), the square-honeycomb core provides high strength in both the normal and longitudinal directions. Neglecting elastic buckling of the cell walls in the normal direction, the normal and longitudinal strength of the square-honeycomb are given by

$$\frac{\sigma_{nY}}{\sigma_Y} = \bar{\rho}, \quad \text{and,} \tag{7a}$$

$$\frac{\sigma_{lY}}{\sigma_Y} = 0.5\bar{\rho}, \tag{7b}$$

respectively.

All the cores discussed above have their relative advantages and disadvantages with regards to properties, ease of manufacture and cost. For the purposes of judging the relative performance of the cores described above we define an ''ideal'' core. The ''ideal'' core has optimal strengths in the normal and longitudinal directions given by

$$\frac{\sigma_{nY}}{\sigma_Y} = \frac{\sigma_{lY}}{\sigma_Y} = \bar{\rho}. \tag{8}$$

This core is 100% efficient in carrying load in both these directions. It is not clear whether such a core is physically realizable: The diamond-celled core with the diamond cells aligned along the longitudinal axis of the beam or a square-honeycomb come closest to this ''ideal'' performance.

3 Analytical Models for the Structural Response of a Clamped Sandwich Beam to Blast Loading

For the sandwich beam, the structural response is split into a sequence of three stages: stage I is the one-dimensional fluid-structure interaction problem during the blast event, and results in a uniform velocity being imposed on the outer face sheet; stage II is the phase of core crush, during which the velocities of the faces and core equalize by momentum transfer; stage III is the retardation phase during which the beam is brought to rest by plastic bending and stretching. This analysis is used to calculate the transverse displacement (and longitudinal tensile strain accumulated) of selected sandwich beams as a function of the magnitude of blast loading.

3.1 Order-of-Magnitude Estimate for the Time Scale of Each Stage of the Dynamic Response. The justification for splitting the analysis into three distinct stages is the observation that the time periods for the three phases differ significantly. The duration of the primary shock for a typical blast wave in air or water due to the detonation of an explosive is of the order of 0.1 ms. In contrast, the period for core crush is approximately 0.4 ms, argued as follows. Suppose that a blast wave in water provides an impulse of 10^4 Nsm^{-2} to a steel sandwich structure, with a 10 mm thick face sheet. Then, the front face acquires an initial velocity v_o of 127 ms^{-1}. On taking the core to have a thickness of $c = 100$ mm and a densification strain $\epsilon_D = 0.5$, the compression phase lasts for $\epsilon_D c/v_o = 0.39$ ms. In contrast, the structural response time is on the order of 25 ms: this can be demonstrated by considering the dynamic response of a stretched rigid-ideally plastic string. Consider a string of length $2L$, gripped at each end, made from a material of density ρ_f and uniaxial yield strength σ_{fY}. Then, the transverse equation of motion for the membrane state is

$$\rho_f \ddot{w} - \sigma_{fY}\frac{\partial^2 w}{\partial x^2} = 0, \tag{9}$$

where $w(x,t)$ is the transverse displacement, the overdot denotes differentiation with respect to time t, and x is the axial coordinate from one end of the string. For illustrative purposes, assume the string is given an initial velocity profile $\dot{w}(t=0) = \dot{w}_o \sin(\pi x/2L)$. Then, the solution of (9) is

$$w = \frac{2\dot{w}_o L}{\pi}\sqrt{\frac{\rho_f}{\sigma_{fY}}}\sin\left(\frac{\pi}{2L}\sqrt{\frac{\sigma_{fY}}{\rho_f}}t\right)\sin\frac{\pi x}{2L}. \tag{10}$$

The string attains its maximum displacement and comes to rest after a time

$$T = L\sqrt{\frac{\rho_f}{\sigma_{fY}}}. \tag{11}$$

Now substitute representative values for the case of a steel ship hull: $L = 5$ m, $\rho_f = 7850$ kgm^{-3}, and $\sigma_{fY} = 300$ MPa, gives $T = 25$ ms, as used above.

3.2 Stage I: One-Dimensional Fluid-Structure Interaction Model. Consider the simplified but conservative idealisation of a plane wave impinging normally and uniformly upon an infinite sandwich plate. For most practical geometries and blast events, the time scale of the blast is sufficiently brief for the front face of a sandwich panel to behave as a rigid plate of mass per unit area m_f. We adopt the one-dimensional analysis of Taylor [1], and consider an incoming wave in the fluid of density ρ_w, traveling with a constant velocity c_w in the direction of increasing x mea-

sured perpendicular to the sandwich panel. The origin is taken at the front face of the sandwich panel, and the transverse deflection of the face is written as $w(t)$ in terms of time, t. Then, the pressure profile for the incoming wave can be taken as

$$p_I(x,t)=p_o e^{-(t-x/c_w)/\theta}, \tag{12}$$

upon making the usual assumption of a blast wave of exponential shape and time constant θ (on the order of 0.1 ms, as discussed above). The magnitude of the peak pressure p_o is typically in the range 10–100 MPa, and far exceeds the static collapse pressure for the sandwich plate (typically on the order of 1 MPa).

If the front face were rigid and fixed in space, the reflected wave would read

$$p_{r1}(x,t)=p_o e^{-(t+x/c_w)/\theta}, \tag{13}$$

corresponding to perfect reflection of the wave, traveling in the $-x$ direction. But the front face sheet is not fixed: it accelerates as a rigid body with a mass per unit area m_f, and moves with a velocity $\dot{w}(t)$. Consequently, the fluid elements adjacent to the front face possess the common velocity $\dot{w}(t)$, and a rarefaction wave p_{r2}, of magnitude

$$p_{r2}(x,t)=-\rho_w c_w \dot{w}\left(t+\frac{x}{c_w}\right), \tag{14}$$

is radiated from the front face. Thus, the net water pressure $p(x,t)$ due to the incoming and reflected waves is

$$p(x,t)=p_I+p_{r1}+p_{r2}=p_o[e^{-(t-x/c_w)/\theta}+e^{-(t+x/c_w)/\theta}] - \rho_w c_w \dot{w}\left(t+\frac{x}{c_w}\right). \tag{15}$$

The front face of the sandwich panel (at $x=0$) is accelerated by the net pressure acting on it, giving the governing ordinary differential equation for face motion as

$$m_f \ddot{w}+\rho_w c_w \dot{w}=2p_o e^{-t/\theta}. \tag{16}$$

Upon imposing the initial conditions $w(0)=\dot{w}(0)=0$, and defining the nondimensional measure $\psi \equiv \rho_w c_w \theta/m_f$, the solution of (16) is

$$w(t)=\frac{2p_o\theta^2}{m_f(\psi-1)\psi}[(\psi-1)+e^{-\psi t/\theta}-\psi e^{-t/\theta}], \tag{17}$$

and the pressure distribution follows immediately via (15). In particular, the pressure on the front face is

$$p(t,x=0)=2p_o e^{-t/\theta}-\frac{2p_o\psi}{\psi-1}[e^{-t/\theta}-e^{-\psi t/\theta}]. \tag{18}$$

For the case of a liquid containing dissolved gases, the pressure loading on the front face ceases and the liquid cavitates when $p(t,x=0)\to 0$, thereby defining the cavitation time τ_c. Substitution of this condition into (18) provides the simple relation

$$\frac{\tau_c}{\theta}=\frac{1}{\psi-1}\ln\psi, \tag{19}$$

and the impulse conveyed to the face follows from (17) as

$$I_{\text{trans}}=\zeta I \tag{20a}$$

where

$$\zeta \equiv \psi^{-\psi/\psi-1}, \tag{20b}$$

and I is the maximum achievable impulse given by

$$I=\int_0^\infty 2p_o e^{-t/\theta}dt=2p_o\theta. \tag{21}$$

This maximum impulse is only realized for the case of a stationary rigid front face. The ratio I_{trans}/I is plotted as a function of the fluid-structure interaction parameter ψ in Fig. 3; the transmitted

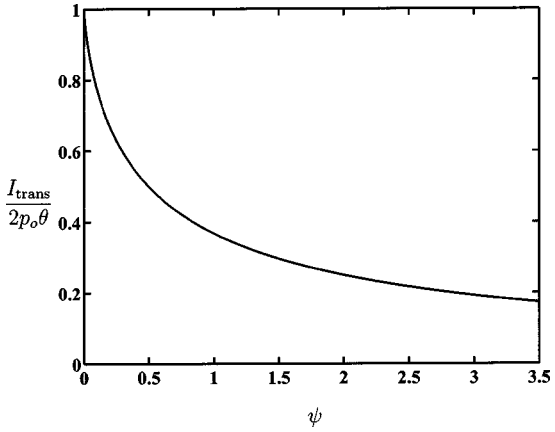

Fig. 3 The ratio of the impulse transmitted to the structure I_{trans}, and the impulse transmitted to a fixed rigid structure $2p_o\theta$, as a function of the fluid-structure interaction parameter ψ

impulse decreases substantially with increasing ψ. It is instructive to substitute some typical values for air and water blast into relations (19) and (20*b*) in order to assess the knock down in transmitted impulse and the magnitude of the cavitation time in relation to the blast time constant θ due to the fluid-structure interaction. For the case of an air blast, we take $\rho_w=1.24\ \text{kgm}^{-3}$, $c_w=330\ \text{ms}^{-1}$, $\theta=0.1$ ms, and $m_f=78\ \text{kgm}^{-2}$ for a 10 mm thick steel plate. Hence, we find that $\psi=0.052$, $\tau_c/\theta=3.1$ and $I_{\text{trans}}/I\approx 0.85$. In contrast, a water blast, we take $\rho_w=1000\ \text{kgm}^{-3}$, $c_w=1400\ \text{ms}^{-1}$, $\theta=0.1$ ms, $m_f=78\ \text{kgm}^{-2}$; this implies the values $\psi=1.79$, $\tau_c/\theta=0.74$ and $I_{\text{trans}}/I=0.267$. We conclude that a significant reduction in transferred impulse can be achieved by employing a light face sheet for the case of water blast, while for air blast the large jump in acoustic impedance between air and the solid face sheet implies that all practical designs of solid face sheet behave essentially as a fixed, rigid face with full transmission of the blast impulse. We anticipate that sandwich panels with light faces can be designed to ensure the reduced transmission of impulse from an incoming water blast wave.

In summary, the first phase of the analysis comprises the acceleration of the front face to a velocity v_o by the incoming (and reflected) primary shock wave. The core and back face of the sandwich beam remain stationary during this initial stage. It is instructive to obtain order of magnitude estimates for the initial velocity of the front face, and its deflection at time $t=\tau_c$. For an impulse of magnitude $10^3\ \text{Nsm}^{-2}$ in air, and $10^4\ \text{Nsm}^{-2}$ in water, the acquired velocity of the front face is approximately $13\ \text{ms}^{-1}$ for the air blast, and $34\ \text{ms}^{-1}$ for the water blast (steel face sheet, of thickness 10mm). Relation (17) reveals that the lateral deflection of the front face is 2.5 mm for the air blast and 1.83 mm for the water blast. It is expected that sandwich beams for ship application will be of core thickness c of order 0.1–1.0 m, and so the degree of core compression during the initial phase of blast loading is negligible.

Taylor [1] has modeled the influence of structural support to the dynamic response of the face sheet by adding the term kw to (16), corresponding to a uniformly distributed restraining force of magnitude kw giving

$$m_f \ddot{w}+\rho_w c_w \dot{w}+kw=2p_o e^{-t/\theta}. \tag{22}$$

The physical interpretation is that k denotes the structural stiffness due to an array of supports between the face sheet and the underlying, motionless structure. By solving (22), and considering representative values for k for the case of a steel plate on a ship

superstructure, Taylor demonstrated that the stiffness term can be neglected with little attendant loss of accuracy. The main objective of the current study is to compare the relative performance of various sandwich panel configurations, and so the simplified analysis is adequate for our purposes.

3.3 Stage II: One-Dimensional Model of Core Compression Phase. In the second phase of motion it is envisaged that the core is crushed by the advancing outer face sheet, and consequently the outer face sheet is decelerated by the core while the core and the rear face of the sandwich beam are accelerated. For simplicity, we consider a one-dimensional slice through the thickness of the sandwich beam and neglect the reduction in momentum due to the impulse provided by the supports. This approximation is motivated by noting that the time period of this phase is much smaller than the overall structural response time of the structure. Subsequent retardation of the sandwich beam is due to plastic bending and stretching in Stage III of the motion. Detailed finite element calculations carried out recently by Qiu et al. [10] support this assertion. The core is treated as a rigid, ideally plastic crushable solid with a nominal crush strength σ_{nY} up to a nominal densification strain ϵ_D. After densification has been achieved, it is assumed that the core is rigid.

Overall considerations of energy and momentum conservation can be used to determine the final value of core compressive strain $\epsilon_c(\leqslant \epsilon_D)$ and the final common velocity v_f of faces and core at the end of the core crush stage. The quantities ϵ_c and v_f suffice to proceed with the third stage of analysis to calculate the beam deflection. However, if additional information on the core crush phase is to be obtained, such as the time for core crush T_c, a one-dimensional plastic shock wave analysis is required. First, we present the immediate results for ϵ_c and v_f, and then we outline the shock wave analysis in order to obtain T_c.

Momentum conservation during core crush dictates that

$$(2m_f+\rho_c c)v_f = m_f v_o, \tag{23}$$

and so a direct relation exists between the common velocity of the sandwich beam v_f after core crush and the initial velocity of the outer face, v_o. The ratio of the energy lost U_{lost} in this phase to the initial kinetic energy of the outer face sheet is then given by

$$\frac{U_{\text{lost}}}{m_f v_o^2/2} = \frac{1+\hat{\rho}}{2+\hat{\rho}} \tag{24}$$

where $\hat{\rho}=\rho_c c/m_f$. This loss in energy is dissipated by plastic dissipation in compressing the core and thus we equate

$$U_{\text{lost}} = \sigma_{nY}\epsilon_c c, \tag{25}$$

where ϵ_c is the average compressive strain in the core. Combining the two above relation, the core compression strain ϵ_c is given by

$$\epsilon_c = \frac{\epsilon_D}{2}\frac{\hat{\rho}+1}{\hat{\rho}+2}\hat{I}^2, \tag{26}$$

in terms of the dimensionless parameter $\hat{I}=I_{\text{trans}}/\sqrt{m_f c\sigma_{nY}\epsilon_D}$. However, if U_{lost} is too high such that ϵ_c as given by (26) exceeds the densification strain ϵ_D, then ϵ_c is set to the value ϵ_D and additional dissipation mechanisms must occur for energy conservation. The above analysis neglects any such additional mechanisms. FE calculations by Xue and Hutchinson [6] and Qiu et al. [10] reveal that the additional mechanism are tensile stretching of the outer face near the supports together with additional crushing of the core under sharply increasing stress.

Now a word of warning. The Stage II analysis neglects the impulse provided by the support reactions during the core compression phase. This assumption breaks down for stubby beams subjected to large impulses; the quality of the approximation is analyzed in detail by Qiu et al. [10] via a set of dynamic finite element calculations.

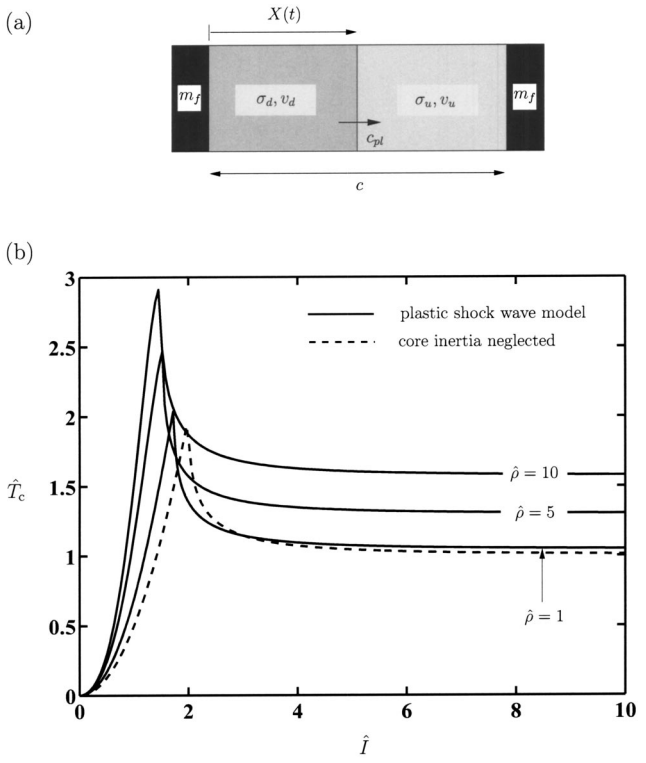

Fig. 4 (*a*) Sketch of the propagation of a one-dimensional shock in the sandwich core, (*b*) the nondimensional core compression time $\hat{T}_c$ as a function of the nondimensional impulse $\hat{I}$ transmitted to the structure

Plastic Shock-Wave Analysis. The above analysis assumes that the core compresses uniformly through its thickness at constant stress. In reality, the core can compress nonuniformly due to buckling of strut elements within the core and due to inertial effects. Here, we consider the case of a core which contains a sufficiently large number of microstructural units (the cells of a metal foam, or the units of a diamond-celled core) for it to be represented by a porous solid. However, the role of inertia is included, and a plastic shock wave analysis is performed in order to deduce the spatial and temporal evolution of strain within the core.

Consider a sandwich structure, with face sheets of mass per unit area m_f, and a core of initial thickness c and relative density ρ_c. The front face sheet has an initial velocity v_o, while the core and inner face sheet are initially at rest. As assumed above, we consider a one-dimensional problem as sketched in Fig. 4(*a*) with the core treated as a rigid, ideally plastic solid with a nominal crush strength σ_{nY} up to a nominal densification strain ϵ_D; at densification the core locks up and becomes rigid. After impact of the front face sheet upon the core, a plastic shock wave moves through the core at a velocity c_{pl}. Suppose that the shock wave has advanced by a distance X after a time t has elapsed, as sketched in Fig. 4(*a*). Upstream of the shock wave, the undeformed core and rear face of sandwich beam have a velocity v_u, whilst downstream of the shock wave the core has compacted to the densification strain ϵ_D and shares the velocity v_d with the front face. The propagation behavior of the shock wave can be determined by numerical integration as follows.

Conservation of momentum dictates

$$[m_f+\rho_c(c-X)]v_u+[m_f+\rho_c X]v_d = m_f v_o, \tag{27}$$

while energy conservation states

$$\frac{1}{2}m_f v_o^2=\frac{1}{2}[m_f+\rho_c(c-X)]v_u^2+\frac{1}{2}[m_f+\rho_c X]v_d^2+\sigma_{nY}\epsilon_D X, \tag{28}$$

and mass conservation across the shock wave provides

$$c_{pl}\epsilon_D=v_d-v_u. \tag{29}$$

Now the compressive stress on the upstream face of the shock wave is related directly to the mass and acceleration of upstream material, giving

$$\sigma_u=[m_f+\rho_c(c-X)]\dot{v}_u, \tag{30}$$

and a similar relation holds for the compressive stress on the downstream face of the shock wave,

$$\sigma_d=-[m_f+\rho_c X]\dot{v}_d. \tag{31}$$

Time differentiation of (27) and the elimination of $(\dot{v}_u,\dot{v}_d)$ from the resulting expression via (30) and (31) leads to the well-known statement of momentum conservation across the shock wave,

$$\sigma_u-\sigma_d=\rho_c c_{pl}(v_u-v_d). \tag{32}$$

As the shock wave progresses through the core it slows down, and, for a sufficiently low initial value of front face velocity v_o, the shock wave arrests at a travel X_c less than the core thickness c. Upon noting that $\dot{X}=c_{pl}$ the crush time T_c is calculated via (29) to give

$$T_c=\int_0^{X_c}\frac{dX}{c_{pl}}=\int_0^{X_c}\frac{\epsilon_D}{v_d-v_u}dX. \tag{33}$$

Now (v_d-v_u) can be expressed as a function of X via (27) and (28), and (33) thereby integrated numerically in order to obtain the core crush time, T_c. The integral reads in nondimensional form,

$$\hat{T}_c=\frac{T_c v_o}{\epsilon_D c}=\int_0^{\overline{X}_c}\frac{1}{\overline{v}_d-\overline{v}_u}d\overline{X}, \tag{34}$$

where $\overline{X}\equiv X/c$, $\overline{X}_c\equiv X_c/c=\epsilon_c/\epsilon_D$, as specified by (26), $\overline{v}_d\equiv v_d/v_o$ and $\overline{v}_u\equiv v_u/v_o$. In the above relation $\overline{v}_d-\overline{v}_u$ depends upon $\overline{X}$ according to

$$(\overline{v}_d-\overline{v}_u)^2=\frac{1+\hat{\rho}(2-\overline{X})+\hat{\rho}^2(1-\overline{X})}{[1+\hat{\rho}(1-\overline{X})]^2(1+\hat{\rho}\overline{X})}-\frac{2(2+\hat{\rho})\hat{\rho}\overline{X}}{[1+\hat{\rho}(1-\overline{X})](1+\hat{\rho}\overline{X})\hat{I}^2}. \tag{35}$$

For the case $\overline{X}\equiv X/c<1$, $\hat{T}_c$ is calculated as a function of $\hat{I}$ by evaluating (34), with $(\overline{v}_d-\overline{v}_u)$ expressed by (35), and the upper limit of integration $\overline{X}_c=\epsilon_c/\epsilon_D$ expressed in terms of $\hat{I}$ via (26). However, at sufficiently high values of impulse $\hat{I}$, the plastic shock wave traverses the thickness of the core c without arrest. The period of core compression is again specified by (34), with $(\overline{v}_d-\overline{v}_u)$ expressed by (35), and the upper limit of integration $\overline{X}_c=1$.[1] At the transition value $\hat{I}_t$, the shock wave arrests at the same instant that it traverses the core thickness; $\hat{I}_t$ is obtained by equating ϵ_c to ϵ_D in (26), to give

$$\hat{I}_t^2=\frac{2(\hat{\rho}+2)}{\hat{\rho}+1}. \tag{36}$$

It is noted in passing that $\hat{I}_t$ is only mildly sensitive to the magnitude of the mass ratio $\hat{\rho}$: as $\hat{\rho}$ is increased from zero (negligible core mass) to infinity (negligible face sheet mass), $\hat{I}$ decreases from 2 to $\sqrt{2}$. Thus, it is predicted that the plastic shock wave will arrest before it traverses the core provided $\hat{I}$ is less than $\sqrt{2}$ for all ratios of core to face sheet mass.

The dependence of $\hat{T}_c=T_c v_o/\epsilon_D c$ on $\hat{I}$ is shown in Fig. 4(*b*) for selected values of $\hat{\rho}$. It is clear from the figure that $\hat{T}_c$ increases from zero to a peak value as $\hat{I}$ increases from zero to the transition value $\hat{I}_t$. At higher values of $\hat{I}$, $\hat{T}_c$ decreases: at very large values of $\hat{I}$, $\hat{T}_c$ approached a finite asymptote which equals unity for the case $\hat{\rho}=0$. It is assumed that the core becomes rigid after it has densified, and the core and face sheet velocities instantaneously jump in value to v_f at $\hat{T}=\hat{T}_c$.

Simple analytical expressions for the dependence of $\hat{T}_c$ upon $\hat{I}$ can be obtained in the limiting case of a negligible core mass, $\hat{\rho}\rightarrow 0$. Consider first the case where the impulse is sufficiently small for the core to compress by a strain ϵ_c less than the densification value ϵ_D. Then, the core provides a constant compression stress σ_{nY} upon the front and back face sheets, so that the front face has the velocity

$$v_d=v_o-\frac{\sigma_{nY}t}{m_f}, \tag{37}$$

while the rear face has the velocity

$$v_u=\frac{\sigma_{nY}t}{m_f}. \tag{38}$$

The core compression time T_c is obtained by equating v_d and v_u, to obtain

$$\hat{T}_c=\frac{\hat{I}^2}{2}. \tag{39}$$

Continuing with the choice $\hat{\rho}\rightarrow 0$, now address the case where the impulse exceeds the transition value $\hat{I}_t=2$, so that the core densifies before the front and rear-face sheet velocities have equalized to $v_o/2$, as demanded by momentum conservation. The core compression time is set by the time for the face sheets to undergo a relative approach of $\epsilon_D c$. Upon noting that the front face sheet displaces by

$$s_d=v_o t-\frac{\sigma_{nY}}{2m_f}t^2, \tag{40}$$

while the back face sheet displaces by

$$s_u=\frac{\sigma_{nY}}{2m_f}t^2, \tag{41}$$

the core compression time T_c is determined by the condition

$$s_d-s_u=v_o T_c-\frac{\sigma_{nY}}{m_f}T_c^2=\epsilon_D c. \tag{42}$$

with solution

$$\hat{T}_c\equiv\frac{T_c v_o}{\epsilon_D c}=\frac{\hat{I}}{2}[\hat{I}-\sqrt{\hat{I}^2-4}]. \tag{43}$$

3.4 Stage III: Dynamic Structural Response of Clamped Sandwich Beam. At the end of stage II the core and face sheets have a uniform velocity v_f as dictated by (23). The final stage of sandwich response comprises the dissipation of the kinetic energy acquired by the beam during stages I and II by a combination of beam bending and longitudinal stretching. The problem under consideration is a classical one: what is the dynamic response of a clamped beam of length $2L$ made from a rigid ideally-plastic material with mass per unit length m subjected to an initial uniform transverse velocity v_f? This problem has been investigated by a number of researchers. In particular, Symmonds [11] developed analytical solutions based on a small displacement analysis while Jones [12] developed an approximate method for large dis-

[1]Note that in such cases the above analysis conserves momentum but does not account for the additional dissipation mechanisms required to conserve energy.

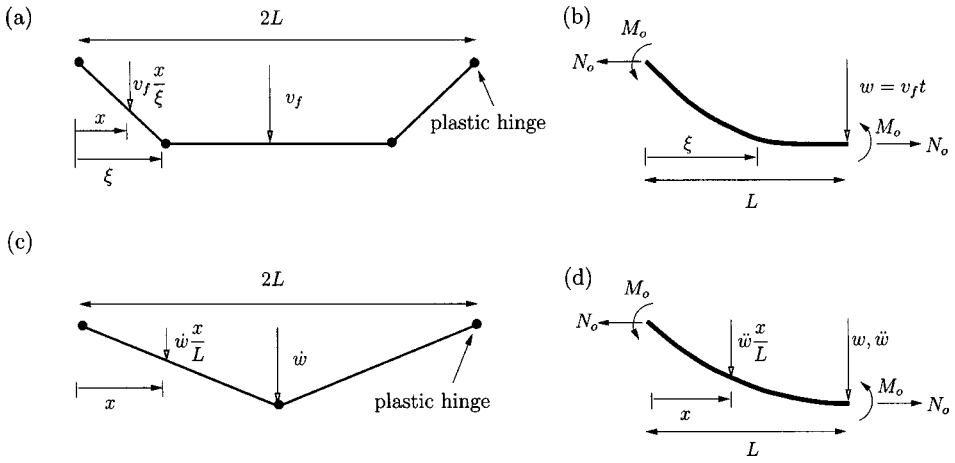

Fig. 5 Analysis of stage III of the blast response. (*a*) Velocity profile in phase I, (*b*) a free-body diagram of the half-beam in phase I, with the deflected shape sketched approximately, (*c*) velocity profile in phase II, and (*d*) a free-body diagram of the half-beam in phase II, with the deflected shape sketched approximately. The accelerations of the beam are shown in (*d*).

placements using an energy balance method. These methods are summarized in Jones [13]. Here we present an approximate solution that is valid in both the small and large displacement regime: it reduces to the exact small displacement solution of Symmonds [11] for small v_f and is nearly equal to the approximate large deflection solution of Jones [13] for large v_f.

Active plastic straining in the beam is by a combination of plastic bending and longitudinal stretching with shear yielding neglected: An evaluation of the magnitude of the transient shear force within the face sheet in the dynamic clamped beam calculation of Jones [13] reveals that shear yielding is expected only for unrealistic blast pressures as discussed above. We assume that yield of an beam element is described by the resultant longitudinal force N and the bending moment M. The shape of the yield surface in (N,M) space for a sandwich beam depends on the shape of the cross section and the relative strength and thickness of the faces and the core. A yield locus described by

$$\frac{|M|}{M_o}+\frac{|N|}{N_o}=1, \tag{44}$$

where N_o and M_o are the plastic values of the longitudinal force and bending moment, respectively, is highly accurate for a sandwich beam with thin, strong faces and a thick, weak core. It becomes less accurate as the beam section approached the monolithic limit. It is difficult to obtain a simple closed-form analytical solution for the dynamic beam response with this choice of yield surface. Here, we approximate this yield locus to be a circumscribing square such that

$$|N|=N_o \tag{45a}$$

$$|M|=M_o, \tag{45b}$$

with yield achieved when one or both of these relations are satisfied. We could equally well approximate the yield locus to be an inscribing square such that

$$|N|=0.5N_o \tag{46a}$$

$$|M|=0.5M_o, \tag{46b}$$

with again at yield one or both of these relations satisfied. Jones [13] has explored the choice of circumscribing and inscribing yield surfaces for a monolithic beam and shown that the resulting solutions bound the exact response. We proceed to develop the analysis for the circumscribing yield locus: the corresponding formulas for the inscribed locus may be obtained by replacing M_o by $0.5M_o$ and N_o by $0.5N_o$.

In the dynamic analysis we shall assume that displacements occur only in a direction transverse to the original axis of the beam and thus stretching is a result of only transverse displacements. Moderate transverse deflections are considered, such that the deflection w at the mid-span of the beam is assumed to be small compared to the beam length $2L$ and the longitudinal force $N=N_o$ can be assumed to be constant along the beam. The motion of the beam can be separated into two phases as in the small displacement analysis of Symmonds [11]. In phase I, the central portion of the beam translates at the initial velocity v_f while segments of length ξ at each end rotate about the supports. The bending moment is taken to vary from $-M_o$ at the outer stationary plastic hinges at the supports to $+M_o$ at ends of the segments of length ξ with the bending moment constant in the central flat portion. Thus, time increments in curvature occur only at the ends of the rotating segments while axial straining is distributed over the length of the rotating segments. A free-body diagram for half of the clamped beam is shown in Fig. 5(*b*); conservation of the moment of momentum about a fixed end after a time t gives

$$(mLv_f)\frac{L}{2}=m(L-\xi)v_f\left(\xi+\frac{L-\xi}{2}\right)+2M_o t+\frac{1}{2}N_o v_f t^2 + \int_0^{\xi}\frac{mv_f x^2}{\xi}dx, \tag{47}$$

where x is the axial coordinate from one end of the beam, as shown in Fig. 5(*b*). This equation gives ξ as a function of time t

$$\xi=\sqrt{\frac{3t(v_f N_o t+4M_o)}{mv_f}}. \tag{48}$$

Phase I continues until the traveling hinges at the inner ends of the segments of length ξ coalesce at the midspan, i.e., $\xi=L$. Thus, from (48), phase I ends at a time T_1

$$T_1=\frac{M_o}{N_o v_f}\left[\sqrt{4+\frac{mL^2 v_f^2 N_o}{3M_o^2}}-2\right], \tag{49}$$

and the displacement of the mid-span w_1 at this time is given by

$$w_1=v_f T_1=\frac{M_o}{N_o}\left[\sqrt{4+\frac{mL^2 v_f^2 N_o}{3M_o^2}}-2\right]. \tag{50}$$

In phase II of the motion, stationary plastic hinges exist at the midspan and at the ends of the beam, with the moment varying between $-M_o$ at the beam end to $+M_o$ at the midspan. The

velocity profile is triangular, as sketched in Fig. 5(*c*). The equation of motion of the half-beam in phase II follows from the free-body diagram sketched in Fig. 5(*d*) as

$$2M_o + N_o w = -\frac{\ddot{w}}{L}\int_0^L mx^2 dx = -\frac{mL^2}{3}\ddot{w}, \tag{51}$$

where x is the axial coordinate from one end of the beam as shown in Fig. 5(*d*). With initial conditions $w(T_1)=w_1$ and $\dot{w}(T_1)=v_f$, this differential equation admits a solution of the form

$$w(t)=\frac{v_f}{\omega}\sin[\omega(t-T_1)]+\left(\frac{2M_o}{N_o}+w_1\right)\cos[\omega(t-T_1)]-\frac{2M_o}{N_o}, \tag{52a}$$

where

$$\omega=\frac{1}{L}\sqrt{\frac{3N_o}{m}}. \tag{52b}$$

The maximum deflection w of the midspan of the beam occurs at a time T when $\dot{w}(T)=0$. Upon substituting this termination condition in the velocity equation, as given by the time derivative of (52*a*), the response time T is obtained as

$$T=T_1+\frac{1}{\omega}\tan^{-1}\left[\frac{N_o v_f}{\omega(2M_o+w_1N_o)}\right], \tag{53}$$

and the corresponding maximum deflection of the midspan of the beam is

$$w=\sqrt{\frac{v_f^2}{\omega^2}+\left(\frac{2M_o}{N_o}+w_1\right)^2}-\frac{2M_o}{N_o}. \tag{54}$$

The deflected shape of the beam can be obtained using the procedure detailed on p. 81 of Jones [13] but the derivation and result are omitted here as they are not central to the present discussion.

We specialize this analysis to the case of sandwich beams. Recall that we are considering clamped sandwich beams of span $2L$ with identical face sheets of thickness h and a core of thickness c, as shown in Fig. 1. The face sheets are made from a rigid ideally plastic material of yield strength σ_{fY} and density ρ_f, while the core of density ρ_c has a normal compressive strength σ_{nY} and a longitudinal strength σ_{lY}. The plastic bending moment of the sandwich beam with the compressed core is given by

$$M_o=\sigma_{lY}\frac{(1-\epsilon_c)c^2}{4}+\sigma_{fY}h[(1-\epsilon_c)c+h], \tag{55}$$

while the plastic membrane force N_o is given by

$$N_o=2\sigma_{fY}h+\sigma_{lY}c. \tag{56}$$

For simplicity we assume that the plastic membrane force N_o due to the core is unaffected by the degree of core compression; while this assumption is thought to be reasonable for all the cores considered, it requires experimental verification. We now introduce the nondimensional geometric variables of the sandwich beam

$$\overline{c}\equiv\frac{c}{L},\quad \overline{h}\equiv\frac{h}{c},\quad \hat{c}\equiv\overline{c}(1-\epsilon_c),\ \text{and}\ \hat{h}\equiv\frac{\overline{h}}{1-\epsilon_c}, \tag{57}$$

and the nondimensional core properties

$$\overline{\rho}\equiv\frac{\rho_c}{\rho_f},\quad \overline{\sigma_l}\equiv\frac{\sigma_{lY}}{\sigma_{fY}}\quad\text{and}\quad \overline{\sigma_n}\equiv\frac{\sigma_{nY}}{\sigma_{fY}}. \tag{58}$$

The nondimensional structural response time $\overline{T}$ and blast impulse $\overline{I}$ are

$$\overline{T}\equiv\frac{T}{L}\sqrt{\frac{\sigma_{fY}}{\rho_f}},\quad \overline{I}\equiv\frac{I}{L\sqrt{\rho_f\sigma_{fY}}}\equiv\frac{\hat{I}\overline{c}\sqrt{\overline{\sigma_n}\epsilon_D\overline{h}}}{\zeta}, \tag{59}$$

where ζI is the blast impulse transmitted to the structure by the fluid. Consequently, the response time T, as given by (53), can be rewritten in the nondimensional form as

$$\overline{T}=\frac{\alpha_2}{2}\frac{\overline{c}(2\overline{h}+\overline{\rho})}{\overline{I}\zeta}\left[\sqrt{1+\frac{4\overline{I}^2\zeta^2\alpha_3}{3\alpha_1\alpha_2}}-1\right] + \sqrt{\frac{\overline{c}(2\overline{h}+\overline{\rho})}{3\hat{c}(2\hat{h}+\overline{\sigma_l}\overline{c}/\hat{c})}}\tan^{-1}\left[4\overline{I}\zeta\sqrt{\frac{\alpha_3}{3\alpha_1\alpha_2+4\overline{I}^2\zeta^2\alpha_3}}\right], \tag{60}$$

where

$$\alpha_1=\hat{c}^3[(1+2\hat{h})^2-1+\overline{\sigma_l}\overline{c}/\hat{c}](1+2\hat{h})\overline{c}(\overline{\rho}+2\overline{h}), \tag{61a}$$

$$\alpha_2=\frac{\hat{c}[(1+2\hat{h})^2-1+\overline{\sigma_l}\overline{c}/\hat{c}]}{2\hat{h}+\overline{\sigma_l}\overline{c}/\hat{c}},\quad\text{and} \tag{61b}$$

$$\alpha_3=\hat{c}(1+2\hat{h}). \tag{61c}$$

The maximum defection (54) of the inner and outer faces at the midspan can be written nondimensionally as

$$\overline{w}\equiv\frac{w}{L}=\frac{\alpha_2}{2}\left[\sqrt{1+\frac{8\overline{I}^2\zeta^2\alpha_3}{3\alpha_1\alpha_2}}-1\right], \tag{62a}$$

and

$$\overline{w}_o=\overline{w}+\epsilon_c\overline{c}, \tag{62b}$$

respectively. It is emphasized that the deflection of the inner face of the sandwich beam is due to only stage III of the deformation history, while the deflection of the outer face is the sum of the deflections in stage III and the deflection due to core compression in stage II.

It is difficult to give a precise failure criterion for the beam as it is anticipated that the blast impulse for incipient failure is sensitive to the details of the built-in end conditions of the clamped beams. Here, we state a failure criterion based on an estimate of the tensile strain in the face sheets due to stretching of the beam and neglect the tensile strains due to bending at the plastic hinges. The tensile strain ϵ_m in the face sheets due to stretching is approximately equal to

$$\epsilon_m=\frac{1}{2}\left(\frac{w}{L}\right)^2. \tag{63}$$

By setting this strain ϵ_m to equal the tensile ductility ϵ_f of the face sheet material, an expression is obtained for the maximum nondimensional impulse $\overline{I}_c$ that the sandwich beam can sustain without tensile failure of the face sheets; substitution of (63) into (62*a*), with the choice $\epsilon_m=\epsilon_f$, gives

$$\overline{I}_c=\frac{1}{\zeta}\sqrt{\frac{3\alpha_1\alpha_2}{8\alpha_3}\left[\left(\frac{2\sqrt{2\epsilon_f}}{\alpha_2}+1\right)^2-1\right]}. \tag{64}$$

The above analysis, comprising stages I, II, and III for the response of a clamped sandwich beam to blast loading, gives the deflection $\overline{w}$, response time $\overline{T}$, the core compression ϵ_c and the maximum tensile strain ϵ_m in the sandwich beam in terms of

i. the loading parameters as specified by the blast impulse $\overline{I}$, and the fluid-structure interaction parameter ψ,
ii. the beam geometry $\overline{c}$ and $\overline{h}$, and
iii. the core properties as given by the core relative density $\overline{\rho}$, its longitudinal tensile strength $\overline{\sigma_l}$, compressive strength $\overline{\sigma_n}$ and its densification strain ϵ_D.

We proceed to illustrate graphically the functional dependence of $\overline{w}$, $\overline{T}$, ϵ_c, and ϵ_m on the blast impulse $\overline{I}$. Consider a represen-

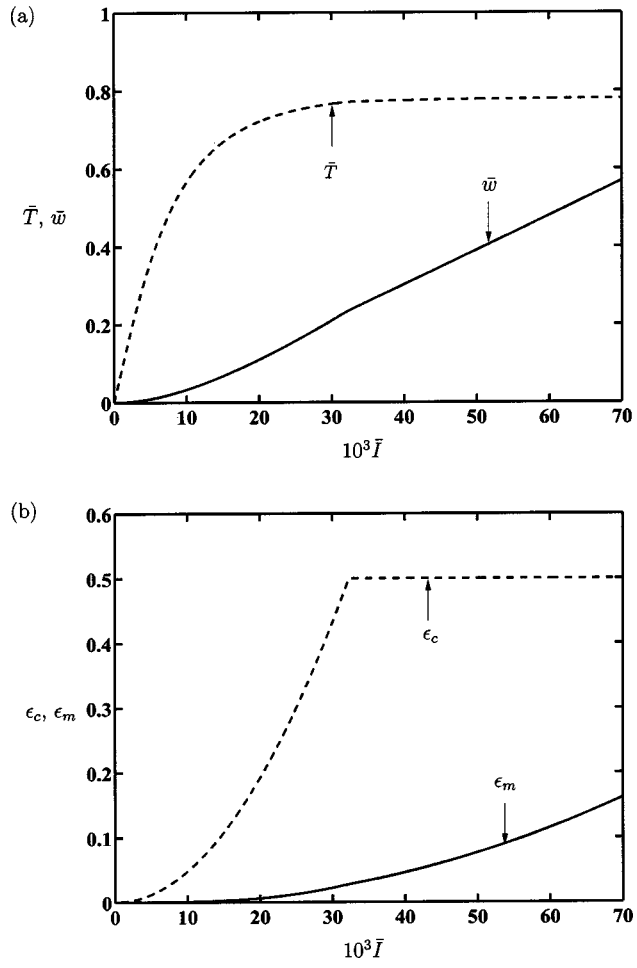

Fig. 6 Response of a clamped sandwich beam ($\bar{c}=0.1, \bar{h}=0.1$) with a pyramidal core ($\bar{\rho}=0.1, \epsilon_Y=0.002, \epsilon_D=0.5$) for an assumed $\psi=1.78$; (*a*) the normalized response time $\bar{T}$ and deflection $\bar{w}$ and (*b*) core compression ϵ_c, and tensile strain in beam ϵ_m, as a function of the normalized blast impulse $\bar{I}$

tative sandwich beam with $\bar{c}=\bar{h}=0.1$ and comprising a pyramidal core of relative density $\bar{\rho}=0.1$ made from the same solid material as the face sheets (with $\epsilon_Y=0.2\%$). As specified in Section 2, the core yields rather than elastically buckles, and the normal and longitudinal strengths of this pyramidal core are $\bar{\sigma}_n=0.05$ and $\bar{\sigma}_l=0$, respectively. The densification strain of the core is taken as $\epsilon_D=0.5$. To complete the specification, we assume a fluid-structure interaction parameter $\psi=1.79$ which is representative of an underwater blast with a time constant $\theta=0.1$ ms and 10 mm thick steel faces as discussed in Section 3.1. The normalized deflection $\bar{w}$ of the inner face of the sandwich beam and response time $\bar{T}$ are plotted in Fig. 6(*a*) as a function of the normalized blast impulse while the compression ϵ_c and tensile stretch ϵ_m are plotted in Fig. 6(*b*). For $\bar{I}<0.03$, the compressive strain ϵ_c induced in the core in Stage II is less than ϵ_D and $\bar{w}$ increases approximately quadratically with $\bar{I}$. At higher impulses the core compression is fixed at the densification limit ϵ_D and $\bar{w}$ scales approximately linearly with $\bar{I}$. On the other hand, the structural response time initially increases linearly with $\bar{I}$, but at high impulses the beam behaves as a stretched plastic string and $\bar{T}$ is almost independent of the magnitude of $\bar{I}$.

4 Performance Charts for Water Blast Resistance

The analysis detailed above is now used to investigate the relative response of monolithic and sandwich beams to blast loading. In a typical design scenario, the solid material and length of the structural element are dictated by design constraints such as corrosion resistance and bulkhead spacing, thus leaving the sandwich panel geometry, viz. the face sheet and core thickness, and core relative density and topology, as the free design variables. Two design problems will be addressed:

1. For a given material combination, beam length and blast impulse, what is the relation between sandwich geometry and the inner face sheet deflection?
2. For a given material combination, beam length and allowable inner face sheet deflection, what is the relation between the required sandwich geometry and the level of blast impulse?

4.1 Monolithic Beams. As a reference case we first present the response of a monolithic beam subjected to a water blast. Consider a monolithic beam of thickness h and length $2L$ made from a rigid-ideally plastic solid material of density ρ_f and yield strength σ_{fY} subjected to a blast impulse I.

We define a fluid-structure interaction parameter $\bar{\psi}$

$$\bar{\psi}=\psi\frac{h}{L}=\frac{\rho_w c_w \theta}{\rho_f L}, \tag{65}$$

which is closely related to the Taylor [1] fluid-structure interaction parameter ψ but written in terms of the specified beam length. The impulse I_{trans} transmitted to the beam is given by (20*b*) for a specified value of $\bar{\psi}$ and a known beam geometry h/L.

First, we specialize the analysis of Section 3.4 to the case of a monolithic beam with plastic moment $M_o=N_o h/4$, where $N_o=h\sigma_{fY}$ is the plastic membrane force. The nondimensional maximum deflection of the midspan of the beam $\bar{w}=w/L$ and normalized structural response time $\bar{T}\equiv T/L\sqrt{\rho_f/\sigma_{fY}}$ follow from (54) and (53), respectively, as

$$\bar{w}=\frac{h}{2L}\left[\sqrt{1+\frac{8\bar{I}^2\zeta^2}{3}\left(\frac{L}{h}\right)^4}-1\right] \quad \text{and} \tag{66a}$$

$$\bar{T}=\frac{1}{2\bar{I}\zeta}\left(\frac{h}{L}\right)^2\left[\sqrt{1+\frac{4}{3}\bar{I}^2\zeta^2\left(\frac{L}{h}\right)^4}-1\right] + \frac{1}{\sqrt{3}}\tan^{-1}\left[\frac{2\bar{I}\zeta(L/h)^2}{\sqrt{3+4\bar{I}^2\zeta^2(L/h)^4}}\right], \tag{66b}$$

where ζI is the impulse transmitted into the structure. For $\zeta\bar{I}\ll 1$, the above relations reduce to

$$\bar{w}=\frac{2}{3}\bar{I}^2\zeta^2\left(\frac{L}{h}\right)^3 \tag{67}$$

$$\bar{T}=\bar{I}\zeta\left(\frac{L}{h}\right)^2, \tag{68}$$

which are identical to the small deflection predictions of Symmonds [11].

With the tensile strain in the beam given by (63), the maximum impulse $\bar{I}_c$ sustained by a monolithic beam made from material of tensile ductility ϵ_f is

$$\bar{I}_c=\frac{1}{\zeta}\sqrt{\frac{3}{8}\left(\frac{h}{L}\right)^2\left[\left(2\sqrt{2\epsilon_f}\left(\frac{L}{h}\right)+1\right)^2-1\right]}. \tag{69}$$

A representative design chart is now constructed for a monolithic beam subjected to a water blast. Consider a steel beam of length $2L=10$ m subjected to a blast with a decay time $\theta=0.12$ ms. The

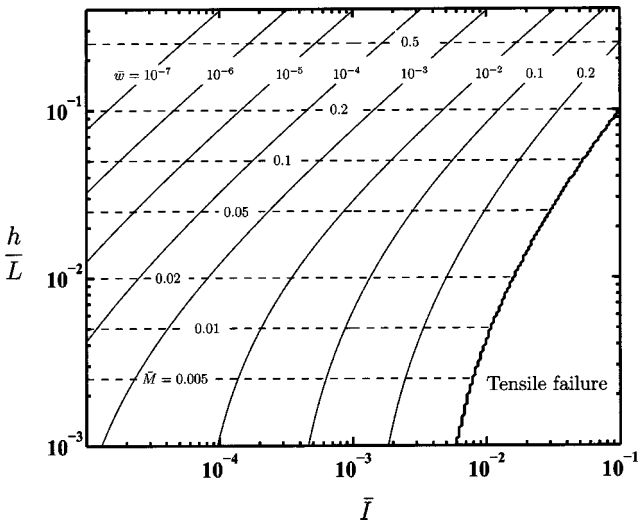

Fig. 7 Design chart for a monolithic beam of tensile ductility $\epsilon_f = 0.2$, subjected to a water blast with $\bar{\psi} = 5 \times 10^{-3}$. Contours of the midspan displacement $\bar{w}$ are given as solid lines and contours of dimensionless mass $\bar{M}$ are shown as dotted lines.

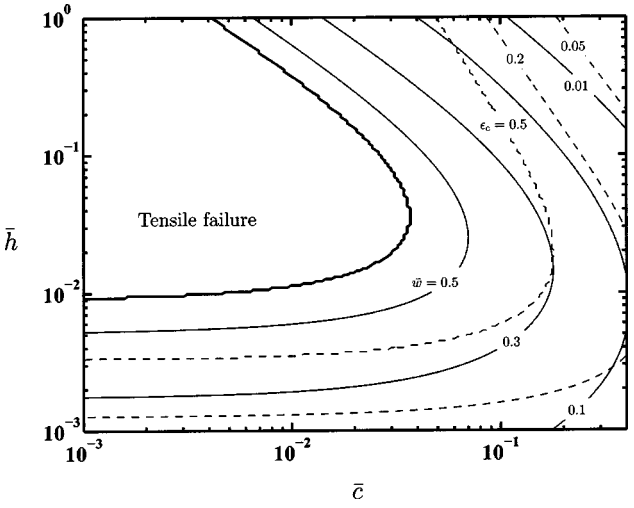

Fig. 8 Design chart for a sandwich beam, with a pyramidal core ($\bar{\rho} = 0.1, \epsilon_Y = 0.002, \epsilon_D = 0.5$), subjected to a water blast. The nondimensional impulse is $\bar{I} = 10^{-2}$, and the fluid-structure interaction parameter is taken as $\bar{\psi} = 5 \times 10^{-3}$. The regime of tensile failure is shown for an assumed tensile ductility of face sheets of $\epsilon_f = 0.2$. Contours of $\bar{w}$ and ϵ_c are included.

fluid-structure interaction parameter $\bar{\psi}$ then takes the value $\bar{\psi} = 5 \times 10^{-3}$. Contours of nondimensional deflection $\bar{w}$ are plotted in Fig. 7 as a function of the normalized blast impulse $\bar{I}$ and beam geometry, h/L, for $\bar{\psi} = 5 \times 10^{-3}$. Note that the contours of the $\bar{w}$ have been truncated at high impulses due to tensile tearing as dictated by (69), with the choice $\epsilon_f = 0.2$. Contours of nondimensional mass $\bar{M} = M/(L^2 \rho_f) = 2h/L$, where M is the mass per unit width of the beam, have also been added to the figure. As expected, the beam deflection increases increasing with blast impulse, for a beam of given mass.

4.2 Sandwich Beams. The blast response of clamped sandwich beams, comprising solid faces and the five types of cores discussed in Section 2, will be analyzed in this section. We restrict attention to cores made from the same solid material as the solid face sheets in order to reduce the number of independent nondimensional groups by one. With the sandwich beam length and material combination specified, the design variables in the problem are the nondimensional core thickness $\bar{c} \equiv c/L$ and face sheet thickness $\bar{h} \equiv h/c$.

Figure 8 shows a design chart with axes $\bar{c}$ and $\bar{h}$ for a clamped sandwich beam with a pyramidal core ($\bar{\rho} = 0.1$, $\epsilon_Y = 0.002$) and subjected to a normalized blast impulse $\bar{I} = 10^{-2}$. The fluid-structure interaction parameter is again taken as $\bar{\psi} = 5 \times 10^{-3}$; this is representative for steel sandwich beams of length $2L = 10$ m subject to a water blast with a decay constant $\theta = 0.12$ ms. Further, the densification strain ϵ_D of the core is assumed to be 0.5 and the tensile ductility of the solid steel is taken as $\epsilon_f = 0.2$. Contours of nondimensional maximum deflection of the mid-span of the inner face of the beam and contours of the compressive strain ϵ_c in the core have been added to the chart: both $\bar{w}$ and ϵ_c increase with decreasing $\bar{c}$ and beam failure by tensile tearing of the face sheets is evident at the top left-hand corner of the chart.

The effect of the fluid-structure interaction parameter $\bar{\psi}$ upon the likelihood of tensile failure of the above sandwich beam is shown in Fig. 9. The figure shows the regime of tensile failure of the face sheets on a design chart with axes $(\bar{c}, \bar{h})$. Apart from the choice of $\bar{\psi}$, the nondimensional parameters are the same as those used to construct Fig. 8: $\bar{\rho} = 0.1$ and $\epsilon_D = 0.5$ for the pyramidal core, $\epsilon_f = 0.2$ for the faces and $\bar{I} = 10^{-2}$. With increasing values of $\bar{\psi}$ (associated with shorter spans, $2L$, and with longer values of the decay constant θ), tensile failure is less likely. Thus, tensile failure is unlikely to occur for sandwich beams provided $\bar{\psi}$ exceeds approximately 0.02.

The inverse design problem of the relation between the pyramidal core ($\bar{\rho} = 0.1$, $\epsilon_Y = 0.002$, $\epsilon_D = 0.5$) sandwich beam geometry and the blast impulse for a specified deflection $\bar{w} = 0.1$ and for $\bar{\psi} = 5 \times 10^{-3}$ is addressed in Fig. 10. Tensile failure of the steel faces ($\epsilon_f = 0.2$) is inactive for the choice $\bar{w} = 0.1$. For the purposes of selecting sandwich beam geometries that maximise the blast impulse at a given mass subject to the constraint of a maximum allowable inner face deflection $\bar{w}$, contours of non-dimensional mass $\bar{M}$ have been added to Fig. 10, where

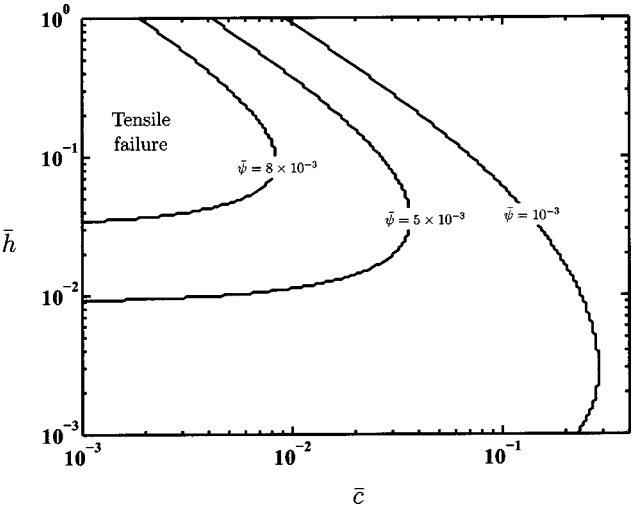

Fig. 9 The effect of $\bar{\psi}$ upon the magnitude of the tensile failure regime within the design chart, for face sheets of ductility $\epsilon_f = 0.2$. The sandwich beam has a pyramidal core ($\bar{\rho} = 0.1, \epsilon_Y = 0.002, \epsilon_D = 0.5$) and the nondimensional impulse is taken as $\bar{I} = 10^{-2}$.

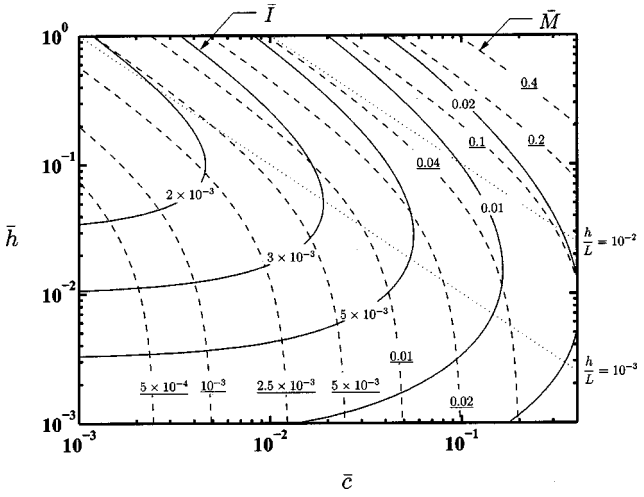

Fig. 10 Design chart for a sandwich beam, with a pyramidal core ($\bar{\rho}=0.1, \epsilon_Y=0.002, \epsilon_D=0.5$), subjected to a water blast. The beam deflection is $\bar{w}=0.1$ and the fluid-structure interaction parameter is taken as $\bar{\psi}=5\times10^{-3}$. Contours of $\bar{I}$ and $\bar{M}$ are displayed. The dotted lines trace the paths of selected values of h/L.

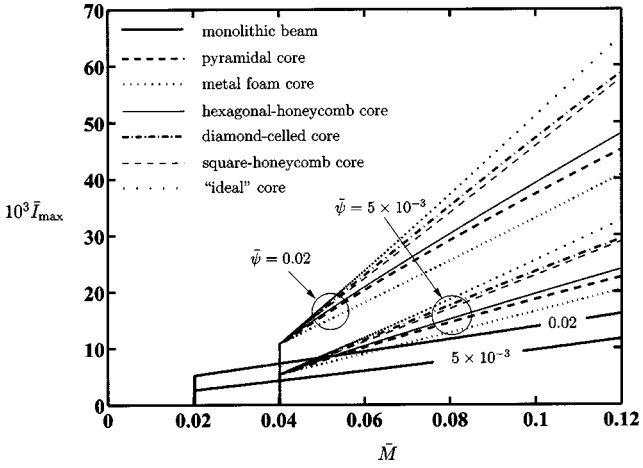

Fig. 11 A comparison of the maximum blast impulse sustained by monolithic beams and by optimal designs of sandwich beams, subjected to the constraints $\bar{w}\leq0.1$ and $h/L\geq10^{-2}$. Results are presented for $\bar{\psi}=5\times10^{-3}$ and 0.02. The core relative density is $\bar{\rho}=0.1$ and densification strain is $\epsilon_D=0.5$.

$$\bar{M}=\frac{M}{\rho_f L^2}=2(2\bar{h}\bar{c}+\bar{c}\bar{\rho}), \tag{70}$$

and M is the mass per unit width of the sandwich beam. The figure reveals that geometries that maximize the blast impulse $\bar{I}$ for a given mass $\bar{M}$ have $\bar{h}\to0$ at almost constant $\bar{c}$, implying that $h/L\to0$. The physical interpretation is as follows. With decreasing face sheet thickness (or face sheet mass) the blast impulse transmitted to the structure reduces: The Taylor analysis gives $\bar{I}_{\text{trans}}\to0$ as $h\to0$. This limit is practically unrealistic as a minimum face sheet thickness is required for other reasons, for example to withstand wave loading, quasi-static indentation by foreign objects such as rocks and other vessels and fragment capture in a blast event. Consequently, we add the additional constraint of a minimum normalized face sheet thickness h/L into the analysis. Contours of h/L for two selected values of h/L have been added to Fig. 10. These lines represent limits on acceptable sandwich beam designs, with designs lying above these lines satisfying the constraint on h/L: designs that maximize blast impulse for a given mass then lie along the lines of constant h/L.

The maximum blast impulse sustained by the sandwich beams with the five different topologies of the core (but $\bar{\rho}=0.1$, $\epsilon_Y=0.002$ and $\epsilon_D=0.5$ in all cases), subject to the constraints $h/L>10^{-2}$ and the inner face deflection $\bar{w}\leq0.1$ are plotted in Fig. 11 as a function of the nondimensional mass $\bar{M}$ for the choice $\bar{\psi}=5\times10^{-3}$. For comparison purposes, the blast impulse sustained by a monolithic beam subjected to the same constraints is also included in Fig. 11. It is evident that sandwich beams all perform considerably better than the monolithic beam. This is mainly due to the fact that the sandwich beams have a thin outer face sheet which results in a small impulse transmitted into the structure whereas the relatively thick beams in monolithic design absorb a larger fraction of the blast impulse. A comparison of the various sandwich cores shows that sandwich beams with a metal foam and pyramidal core almost attain the performance of the hexagonal-honeycomb core. However, the diamond-celled and square-honeycomb core beams, which have high strength in both the through-thickness and longitudinal directions, out perform the other sandwich beams. The performance of the diamond-celled core approaches that of the ''ideal'' sandwich core. It is noted that $\bar{M}$ has minimum achievable values. This is explained as follows. Since $h/L\equiv\bar{h}\bar{c}$, the expression (70) for $\bar{M}$ can be rewritten as

$$\bar{M}=4\frac{h}{L}+2\bar{c}\bar{\rho}. \tag{71}$$

The above constraint on the minimum h/L implies a minimum value for $\bar{M}$ of $4h/L$. Thus, for the constraint $h/L\geq10^{-2}$, $\bar{M}$ has the minimum value of 0.04 as evident in Fig. 11. Similarly, for a monolithic beam of thickness h, $\bar{M}$ is given by $\bar{M}=2h/L$ and so a constraint on the minimum value of h/L gives directly a minimum acceptable mass $\bar{M}$. With increasing values of the $\bar{\psi}$, the fraction of the blast impulse transmitted into the structure decreases and thus all the beams sustain higher blast. However, the relative performance of the various beam configurations remains unchanged.

The effect of the constraint on h/L on the performance of the above sandwich beams is illustrated in Fig. 12 for the choice $\bar{\psi}=5\times10^{-3}$. As the allowable minimum value of h/L decreases from 10^{-2} to 10^{-3}, the blast impulses sustained by the sandwich beams increase. Further, the rankings of the cores change slightly: while the diamond-celled core still performs the best followed by the square-honeycomb core, the metal foam core is now seen to out perform the pyramidal and hexagonal-honeycomb cores at higher masses. This can be rationalized as follows. Upon imposing the constraint $h/L\geq10^{-3}$, a large fraction of the mass of the sandwich beam is in the core. Recall that the pyramidal and hexagonal-honeycomb cores have no longitudinal strength while the metal foam core gives some additional longitudinal stretching resistance to the sandwich beam, and this results in its superior performance.

So far we have determined the optimal designs of sandwich beams for a midspan deflection of $\bar{w}\leq0.1$. But how does the relative performance depend upon the allowable value of $\bar{w}$? The performance of the sandwich beams with constraints $h/L\geq10^{-2}$ and $\bar{\psi}=5\times10^{-3}$ is illustrated in Fig. 13 for $\bar{w}\leq0.1$ and $\bar{w}\leq0.4$. As expected, the beams can sustain higher impulses when the constraint on $\bar{w}$ is relaxed to $\bar{w}\leq0.4$. However, the rankings change for the two levels of $\bar{w}$ considered in Fig. 13. With the higher allowable deflections, the longitudinal stretching of the core becomes increasingly important and the metal foam core out performs the pyramidal or hexagonal-honeycomb cores. The

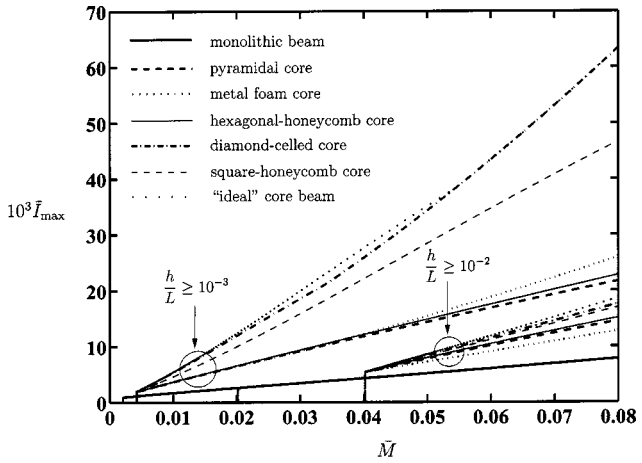

Fig. 12 A comparison of the maximum blast impulse sustained by monolithic beams and by optimal designs of sandwich beams, subjected to the constraint $\bar{w} \leq 0.1$ with $\bar{\psi} = 5 \times 10^{-3}$. Results are presented for constraints $h/L \geq 10^{-2}$ and 10^{-3}. The core relative density is $\bar{\rho} = 0.1$, $\epsilon_Y = 0.002$ and densification strain is $\epsilon_D = 0.5$.

diamond-celled core has a high compressive and an ideal longitudinal strength, and has a blast performance which is nearly indistinguishable from that of the "ideal" core under the constraint $\bar{w} \leq 0.4$.

In the above analysis the relative density of the core has been taken to be $\bar{\rho} = 0.1$, and the yield strain of the core material taken to be representative of that for structural steels, $\epsilon_Y = 0.002$. Consequently, the individual struts of the pyramidal and diamond-celled cores deform by plastic yield. We proceed to investigate the blast performance of the pyramidal and diamond-celled core sandwich beams at relative densities $\bar{\rho}$ such that elastic buckling of the core members can intervene. The optimal performance of diamond-celled core sandwich beams with the constraints $h/L \geq 10^{-2}$ and $\bar{w} \leq 0.1$ is plotted in Fig. 14(*a*) for selected values of core relative density $\bar{\rho} = 0.02$, 0.05, 0.1 and 0.2. The core is assumed to be made from a solid of yield strain $\epsilon_Y = 0.002$ and consequently cores of density $\bar{\rho} = 0.02$ and 0.05 deform by elastic buckling. While the performance of the low core density beams is slightly superior to the $\bar{\rho} = 0.1$ beams, these beams of low core density have stubby designs with high values of $c/2L$. Thus, these optimal designs become impractical for high blast impulses and the curves in Fig. 14(*a*) have been truncated at $c/2L = 0.2$. A similar analysis was performed for the pyramidal core; these cores deform by elastic buckling at $\bar{\rho} \leq 0.015$. The results for the optimal blast performance of these beams are summarized in Fig. 14(*b*); again the low density cores provide superior performance but the beams are stubby (high $c/2L$) and hence practical designs of these beams are unable to sustain high blast impulses. A comparison of Figs. 14(*a*) and 14(*b*) reveals that over the entire range of relative densities investigated, the diamond-celled core beams always out perform the pyramidal core beams.

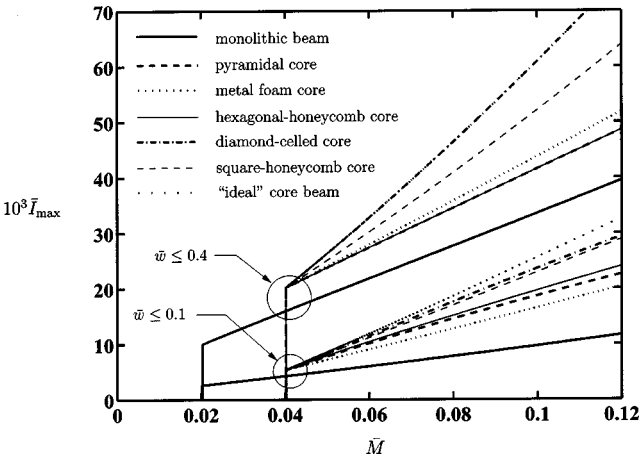

Fig. 13 A comparison of the maximum blast impulse sustained by monolithic beams and by optimal designs of sandwich beams, subjected to the constraint $h/L \geq 10^{-2}$ with $\bar{\psi} = 5 \times 10^{-3}$. Results are presented for constraints $\bar{w} \leq 0.1$ and 0.4. The core relative density is $\bar{\rho} = 0.1$, $\epsilon_Y = 0.002$ and densification strain is $\epsilon_D = 0.5$.

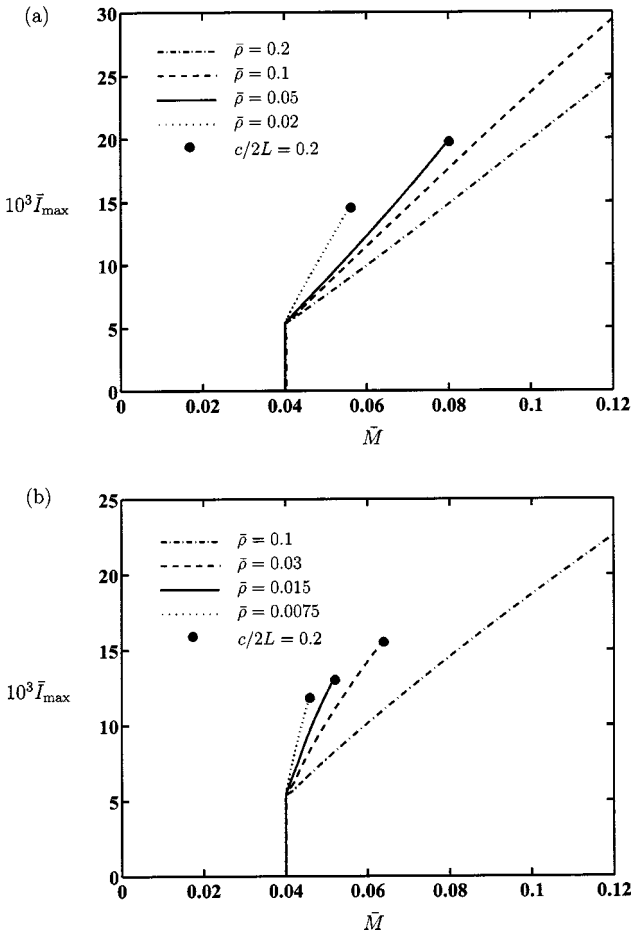

Fig. 14 Comparison of the maximum blast impulse sustained by optimal (*a*) diamond-celled and (*b*) pyramidal core sandwich beams for selected core densities, with $\bar{\psi} = 5 \times 10^{-3}$ and $h/L \geq 10^{-2}$, $\bar{w} \leq 0.1$. The yield strain of the core parent material is assumed to be $\epsilon_Y = 0.002$ and densification strain of the core is taken as $\epsilon_D = 0.5$.

5 A Comparison of Structural Performance Under Air and Water Blast Loading

Due to the low acoustic impedance of air, the Taylor fluid-structure interaction parameter $\psi \approx 0$ for an air blast, as discussed in Section 3.2. In this section we discuss blast loading in air by assuming $\psi \equiv \psi h/L = 0$: The entire blast impulse is transmitted to the sandwich structure.

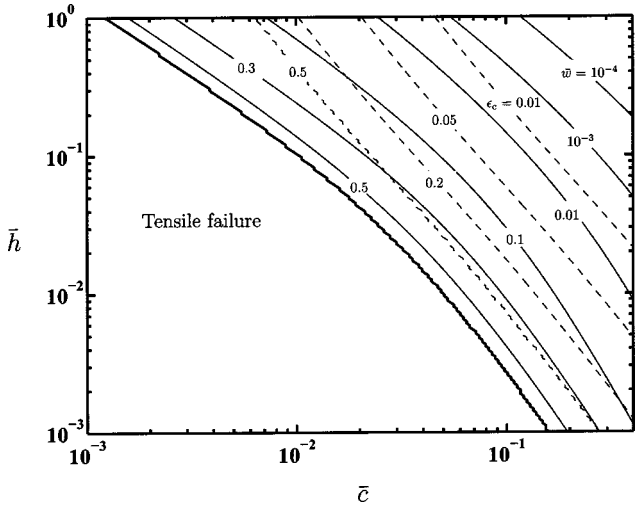

Fig. 15 Design chart for a sandwich beam, with a pyramidal core ($\bar{\rho}=0.1, \epsilon_Y=0.002, \epsilon_D=0.5$), subjected to an air blast. The nondimensional impulse is $\bar{I}=10^{-3}$. The regime of tensile failure is shown for an assumed tensile ductility of face sheets of $\epsilon_f=0.2$. Contours of $\bar{w}$ and ϵ_c are included.

Consider the representative case of a sandwich beam with a pyramidal core ($\bar{\rho}=0.1, \epsilon_D=0.5, \epsilon_Y=0.002$), subjected to an air blast of magnitude $\bar{I}=10^{-3}$. The design chart is given in Fig. 15, with axes of $\bar{c}$ and $\bar{h}$, and with contours displayed for the midspan deflection $\bar{w}$ of the inner face and through-thickness core compression ϵ_c. The tensile ductility of the face sheet material is taken to be $\epsilon_f=0.2$ representative of structural steels; despite this moderately high value of ϵ_f, tensile failure of the face sheets dominates the chart with less than half the design space of Fig. 15 resulting in acceptable designs. In contrast, for water blast (Fig. 8), tensile failure is of less concern even for a higher blast impulse of $\bar{I}=10^{-2}$; the underlying explanation is that only a small fraction of the impulse is transmitted into the sandwich structure for water blast loading.

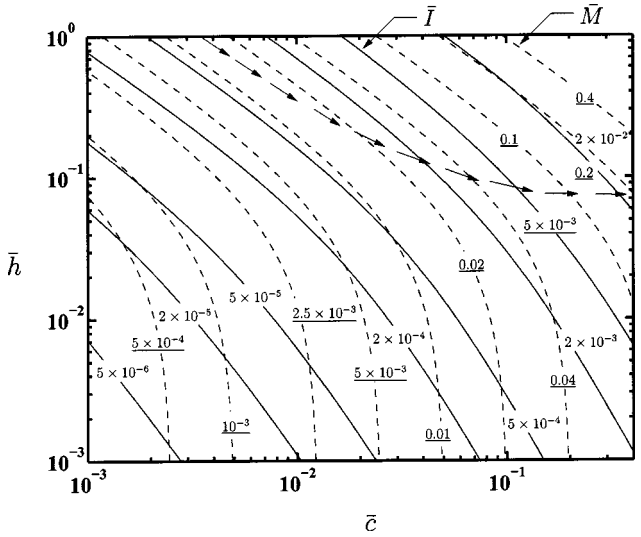

Fig. 16 Design chart for a sandwich beam, with a pyramidal core ($\bar{\rho}=0.1, \epsilon_Y=0.002, \epsilon_D=0.5$), subjected to an air blast. The beam deflection is $\bar{w}=0.1$. Contours of $\bar{I}$ and $\bar{M}$ are displayed. The arrows trace the path of designs which maximize the impulsive resistance with increasing mass.

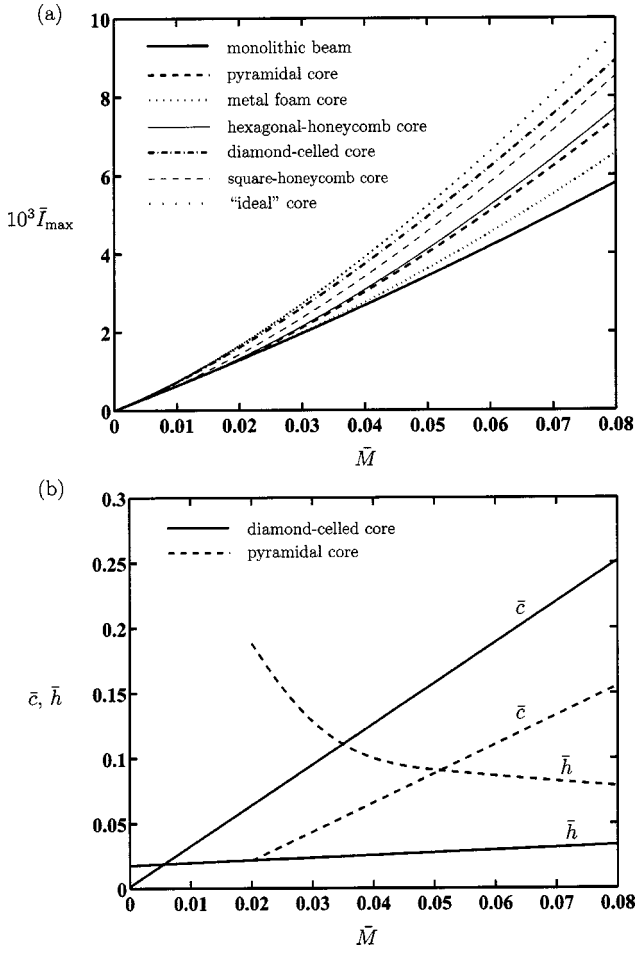

Fig. 17 (*a*) Comparison of the maximum impulse sustained by monolithic and sandwich beams for an air blast with the constraint $\bar{w}\leq 0.1$. The core relative density and densification strain are, $\bar{\rho}=0.1$ and $\epsilon_D=0.5$, respectively, and $\epsilon_Y=0.002$. (*b*) The optimal designs of sandwich beams with pyramidal and diamond-celled core.

A design map for air blast loading of the above pyramidal core sandwich beam is given in Fig. 16, with contours of $\bar{I}$ required to produce a mid-span deflection of $\bar{w}=0.1$. The figure should be contrasted with the water blast map shown in Fig. 10, again for $\bar{w}=0.1$; the only difference in the assumed values of the plots is that $\bar{\psi}=0$ in Fig. 16 and $\bar{\psi}=5\times10^{-3}$ in Fig. 10. While the contours of $\bar{M}$ are identical in the two figures, the contours of $\bar{I}$ are of markedly different shape. For the case of air blast (Fig. 16) there is no need to impose a constraint on the minimum value for h/L: The trajectory of $(\bar{c},\bar{h})$ which maximizes $\bar{I}$ for a given $\bar{M}$ no longer lies along a line of constant h/L and is associated with $h/L\equiv\bar{h}\bar{c}$ values in the range 0.003 to 0.032. The arrows shown in Fig. 16 trace the optimum designs with increasing mass. This can be contrasted with the water blast problem where the optimum designs lay along the specified minimum value of h/L.

The air blast performance of the optimized sandwich beams is compared to that of the monolithic beam in Fig. 17(*a*). Specifically, the maximum sustainable impulse is plotted against the nondimensional mass $\bar{M}$, with the deflection constraint $\bar{w}\leq 0.1$ imposed. In contrast to the case of water blast, the performance gain upon employing sandwich construction instead of monolithic beams is relatively small; at best the diamond-celled core sustains

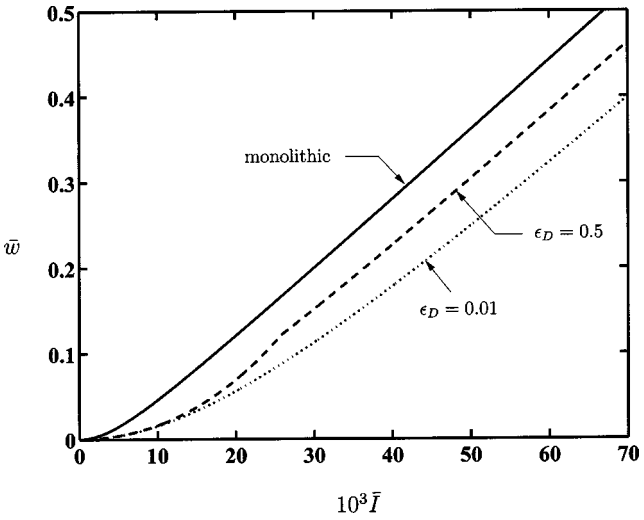

Fig. 18 The normalized deflection of the bottom face of a diamond-celled core ($\bar{\rho}=0.1, \epsilon_Y=0.002$) sandwich beam with $\bar{c}=\bar{h}=0.2$ as a function of the normalized impulse, for two selected values of the core densification strain ϵ_D. The response of a monolithic beam of the same mass $\bar{M}=0.2$ is included.

an impulse about 45% greater than a monolithic beam of equal mass. The geometry of the optimal pyramidal and diamond-celled sandwich core beams of Fig. 17(*a*) are plotted in Fig. 17(*b*). For both configurations, $\bar{c}$ increases with increasing mass, with the optimal pyramidal core beams having a lower $\bar{c}$ (and a higher $\bar{h}$) as compared to the optimal diamond-celled core beams.

In water blast, the sandwich beam out performs the monolithic beam mainly due to the fact that the thin (and therefore light) outer face of the sandwich beam acquires a smaller fraction of the blast impulse compared to the relatively thick monolithic beam. However, in the case of air blast, the full blast impulse is transmitted to the structure for both the sandwich and monolithic beams. The superior air blast resistance of sandwich beams to monolithic beams, as seen in Fig. 17(*a*) is attributed solely to the shape factor effect of the sandwich construction. To clarify this point, the deflection of a sandwich beam with a diamond-celled core ($\bar{\rho}=0.1, \bar{c}=\bar{h}=0.2$) is plotted in Fig. 18 as a function of the air impulse for two assumed values of core densification strain $\epsilon_D=0.01$ and $\epsilon_D=0.5$ along with the response of a monolithic beam of equal mass $M=0.2$. Figure 18 reveals that the beam with the core densification strain $\epsilon_D=0.01$ which maintains the separation of the face sheets and is the strongest while the monolithic beam is the weakest: it is the shape factor effect that gives the sandwich construction structural advantage in air blast.

6 Comparison With Three-Dimensional Finite Element Simulations

Xue and Hutchinson [6] conducted three-dimensional finite element (FE) simulations of the dynamic response of clamped sandwich beams with the corrugated, square-honeycomb, and pyramidal core geometries. In these FE simulations, Xue and Hutchinson [6] modelled the core members explicitly including the development of contact between the core members and the face sheets under increasing through-thickness compressive strain. An impulse was applied to the front face of the sandwich beam and thus their numerical results can be compared directly to our analytical predictions for air blast, with $\bar{\psi}=0$.

Xue and Hutchinson [6] modeled sandwich beams made from 304 stainless steel and assumed an elastic, power-law hardening stress versus strain response for the solid steel with a yield strain $\epsilon_Y=0.2\%$ and a power law hardening exponent $N=0.17$. In the analytic predictions given below we assume a rigid, ideally plastic

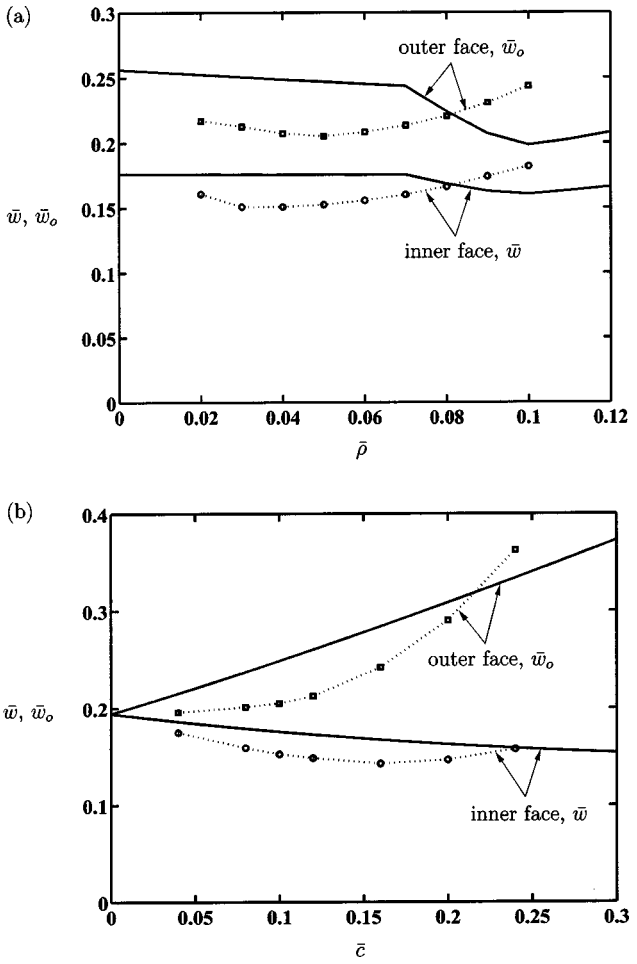

Fig. 19 Comparison of the analytical predictions and the three-dimensional FE predictions of Xue and Hutchinson [6] for the deflection of sandwich beams with a corrugated core. The beams have a mass $\bar{M}=0.04$ and are subjected to an impulse $\bar{I}=5\times10^{-3}$. The effect upon $\bar{w}$ and $\bar{w}_o$ of (*a*) core relative density $\bar{\rho}$ for $\bar{c}=0.1$ and (*b*) $\bar{c}$ with the core relative density held fixed at $\bar{\rho}=0.04$. The solid lines give the analytic solutions and the dotted lines (with symbols) give the FE results.

solid material response, and include elastic buckling of the core members by assuming a solid material yield strain $\epsilon_Y=0.2\%$. In line with experimental data for metal foams, we take the densification strain ϵ_D of the core to be related to the relative density $\bar{\rho}$ through, [2],

$$\epsilon_D = 0.8 - 1.75\bar{\rho}. \tag{72}$$

Xue and Hutchinson [6] investigated the effects of core relative density and core thickness for sandwich beams of total mass $\bar{M}=0.04$ and considered an impulse $\bar{I}=5\times10^{-3}$. Comparisons between the FE and analytical predictions of the maximum face sheet displacements of the corrugated core sandwich beams are shown in Fig. 19: In Fig. 19(*a*) the effect of core relative density is investigated with $\bar{c}=0.1$, while in Fig. 19(*b*) the effect of $\bar{c}$ is studied for a core of relative density $\bar{\rho}=0.04$. While the analytical predictions are within 15% of the FE calculations in all cases, the analytical model does not capture the qualitative form of the variations as predicted by the FE analysis. A careful comparison with the FE results indicates that this is mainly due to the fact that for $\bar{I}=5\times10^{-3}$, the analytical solutions predict full densification

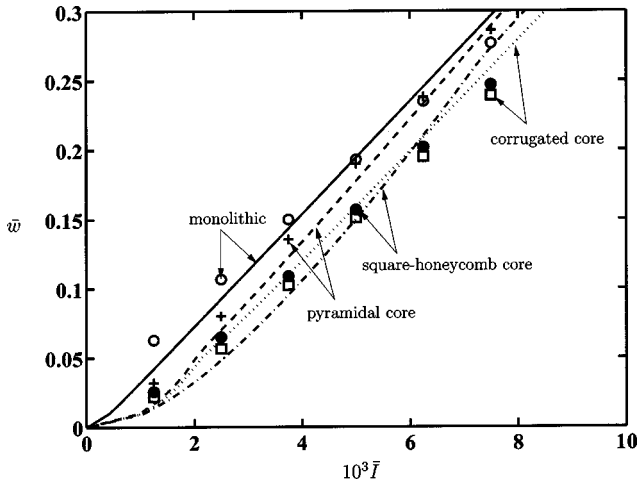

Fig. 20 Comparison of the analytical predictions and the three-dimensional FE predictions of Xue and Hutchinson [6] for the deflection $\bar{w}$ of monolithic beams and sandwich beams with corrugated, square-honeycomb, and pyramidal cores. The beams have a fixed mass $\bar{M}=0.04$ and the sandwich beams have a core of relative density $\bar{\rho}=0.04$ and aspect ratio $\bar{c}=0.1$. The symbols denote the FE results while the lines are the analytical predictions.

in nearly all cases while in the FE simulations no distinct densification limit exits; rather, continued core compression occurs at increasing stress level after contact has begun between the core members and the face sheets. An improved core constitutive model with continued hardening rather than lockup after some critical strain ϵ_D may be able to address this deficiency; this is however beyond the scope of the present study.

Xue and Hutchinson [6] employed a series of FE calculations to identify a ''near-optimal'' sandwich configurations with mass $\bar{M}=0.04$. They concluded that a sandwich beam with a core of relative density $\bar{\rho}=0.04$ and $\bar{c}=0.1$ (giving $\bar{h}=0.08$) is an optimal configuration for a moderately large blast. Comparisons between the FE and analytical predictions (with the choice $\epsilon_D=0.5$) of the deflections of the inner face sheet of these ''optimum'' sandwich beams as a function of blast impulse are shown in Fig. 20. Over the range of impulses considered, the analytical predictions are within 10% of the three-dimensional FE calculations for the pyramidal, corrugated and square-honeycomb core sandwich beams as well as for the monolithic beams. Note that the FE calculations predict that the monolithic beam out performs the pyramidal core sandwich beam (i.e., smaller deflections at the same impulse) for impulses $\bar{I}>5\times10^{-3}$. This is due to the wrinkling of the face sheets between the nodes of the pyramidal truss. While this effect is not included in the current analysis, the analytical model too will predict that the monolithic beam out performs the pyramidal core beam at large deflections: at large deflections the degree of axial stretching becomes significant, yet the pyramidal core provides no longitudinal strength.

7 Discussion

An approximate analytical methodology has been presented to predict the dynamic response of sandwich beams to blast loadings in air and water. A number of approximations have been made to make the problem tractable to an analytical solution. Principally, these are (i) the one-dimensional approximation of the blast event, (ii) separation of the stages of the response into three sequential phases, (iii) neglect of the support reaction during the blast event and during the core compression phases, and (iv) a highly simplified core constitutive model wherein the core is assumed to behave as a ideally plastic locking solid. The effects of strain hardening and rate sensitivity of the solid material has also been neglected. Despite these approximations, the analysis has been shown to compare well with three-dimensional FE calculations. Thus, the analysis presented here is not only adequate to explore trends and scaling relations but is also expected to suffice to make approximate predictions for the purposes of selecting core topologies and sandwich beam geometries. The nondimensional formulas presented here bring out the stages of the response clearly and hence aid the interpretation of more accurate numerical calculations such as the recent dynamic finite element analysis of Xue and Hutchinson [6].

Two notes of caution on the model presented here must be mentioned. Recent numerical fluid-structure interaction calculations on similar sandwich structures performed by Belytschko[14] indicate that the one-dimensional Taylor analysis underestimates the impulse transmitted into the sandwich structure and thus the performance gains due to sandwich constructions indicated here may be somewhat optimistic. Second, the failure of the face sheets near the supports by dynamic necking have not been addressed here. Additional investigations are required to establish an appropriate failure criterion under dynamic conditions.

8 Concluding Remarks

An analytical methodology has been developed to analyze the dynamic response of metallic sandwich beams subject to both air and water blasts. The response of the sandwich beams is separated into three sequential stages: Stage I is the fluid-structure interaction problem, stage II is the phase of core compression, and in stage III the clamped beam is brought to rest by plastic stretching and bending. The simple analytical formulas presented above are in good agreement with more accurate three-dimensional FE calculations given in a parallel study of Xue and Hutchinson [6].

The analysis has been used to construct performance charts for the response of both monolithic and sandwich beams subject to both air and water borne blasts. For the case of water blast, an order of magnitude improvement in blast resistance is achieved by employing sandwich construction. This is mainly due to fluid-structure interaction: The reduced mass of the sandwich outer face leads to a reduction in the impulse transmitted to the structure from the water. In air, the impedance mismatch between air and the face sheet is comparable to that between air and a monolithic beam; consequently, the use of sandwich construction gives a more moderate gain in blast resistance compared to monolithic construction. For both air and water blast the diamond-celled core sandwich beam gives the best performance due to the longitudinal strength provided by the core. Comparisons of the predictions presented here with three-dimensional coupled fluid-structure numerical calculations and blast experiments need to be performed to validate and extend this analysis.

Acknowledgments

The authors are grateful to ONR for their financial support through US-ONR IFO grant number N00014-03-1-0283 on the The Science and Design of Blast Resistant Sandwich Structures. We are pleased to acknowledge Profs. M. F. Ashby, T. Belytschko, A. G. Evans, J. W. Hutchinson, R. M. McMeeking, and F. Zok for many insightful discussions during the course of this work.

References

[1] Taylor, G. I., 1963, ''The Pressure and Impulse of Submarine Explosion Waves on Plates,'' *The Scientific Papers of G. I. Taylor, Vol III*, Cambridge Univ. Press, Cambridge, UK pp. 287–303.
[2] Ashby, M. F., Evans, A. G., Fleck, N. A., Gibson, L. J., Hutchinson, J. W., and Wadley, H. N. G., 2000, *Metal Foams: A Design Guide*, Butterworth Heinemann, London.
[3] Deshpande, V. S., and Fleck, N. A., 2001, ''Collapse of Truss Core Sandwich Beams in 3-Point Bending,'' Int. J. Solids Struct., **38**(36–37), pp. 6275–6305.
[4] Sypeck, D. J., and Wadley, H. N. G., 2001, ''Multifunctional Microtruss Laminates: Textile Synthesis and Properties,'' J. Mater. Res., **16**(3), pp. 890–897.

[5] Deshpande, V. S., and Fleck, N. A., 2003, ''Energy Absorption of an Egg-Box Material,'' J. Mech. Phys. Solids, **51**(1), p. 187.
[6] Xue, Z., and Hutchinson, J. W., 2003, ''A Comparative Study of Blast-Resistant Metal Sandwich Plates,'' Int. J. Impact Eng., to appear.
[7] Cole, R. H., 1948, *Underwater Explosions*, Princeton University Press, Princeton, NJ.
[8] Swisdak, M. M., 1978, ''Explosion Effects and Properties—Part II: Explosion Effects in Water,'' Technical Report, Naval Surface Weapons Center, Dahlgren, VA.
[9] Smith, P. D., and Hetherington, J. G., 1994, *Blast and Ballistic Loading of Structures*, Butterworth Heinemann, London.
[10] Qiu, X., Deshpande, V. S., and Fleck, N. A., 2003, ''Finite Element Analysis of the Dynamic Response of Clamped Sandwich Beams,'' Eur. J. Mech. A/Solids, **22**, pp. 801–814.
[11] Symmonds, P. S., 1954, ''Large Plastic Deformations of Beams Under Blast Type Loading,'' *Proceedings of the Second U.S. National Congress of Applied Mechanics*, pp. 505–515.
[12] Jones, N., 1971, ''A Theoretical Study of the Dynamic Plastic Behavior of Beams and Plates With Finite Deflections,'' Int. J. Solids Struct., **7**, p. 1007.
[13] Jones, N., 1989, *Structural Impact*, Cambridge University Press, Cambridge, UK.
[14] Belytschko, T., 2003, private communication.

Chandra S. Yerramalli[1]
Anthony M. Waas[2]
Professor,
e-mail: dcw@umich.edu

Aerospace Engineering Department,
University of Michigan,
1320 Beal Avenue,
Ann Arbor, MI 48109-2140

A Nondimensional Number to Classify Composite Compressive Failure

A new nondimensional number (η) to predict the dominant failure mechanism of fiber reinforced composites under compression loading is presented. Results from previous experimental investigations on the failure of glass fiber reinforced and carbon fiber reinforced vinylester matrix composites, respectively, were used to motivate and develop η. Experimental results available in the open literature are used to compare the predictions of η. This number can be used as a design tool to develop new composite materials with a preferred failure mode. The exercise of developing such a number provides insight into parameters that control the compressive strength of fiber reinforced composite materials. [DOI: 10.1115/1.1756923]

1 Introduction

Mechanism based compressive failure strength prediction models provide a better understanding of the failure behavior of composites. However, these models require that the failure mechanism of the composite under the given loading and constituent material properties be known beforehand. Thus, a method to predict the failure mechanism is very useful not only from the view point of predicting the failure mechanism a priori but also in understanding the various factors that affect the failure mechanism of composites under compression. Initial work on understanding compressive strength behavior of fiber reinforced polymer matrix composites (FRPC) was based on an elastic micro-buckling analysis by Rosen [1]. Later, Argon [2], Budiansky [3], and Budiansky and Fleck [4], realized that misalignments in fiber reinforcement cause the development of local shear stresses which coupled with matrix inelasticity lead to buckling of fibers locally. The failure mode resulting from this mechanism is called kinking. Compared to kinking failure, composites with brittle matrices or with fibers of relatively large diameter tend to fail by fracture along the fiber matrix interface, when subjected to axial compression. This mechanism, which is governed by transverse stresses and the fiber-matrix interfacial fracture energy is referred to as splitting. Experimental evidence for splitting failure is provided in Schutz [5], Lee and Waas [6], Piggott and Harris [7], and Drzal et al. [8]. Experiments conducted by Lee and Waas [6], Piggott and Harris [7], Oguni and Ravichandran [9], and Piggott [10] on glass and carbon fiber reinforced polymer matrix composites under pure compression provided insight into parameters affecting the splitting compressive strength of polymer matrix composites. Recent work by Yerramalli and Waas [11], have high lighted the effect of combined loading on failure mechanisms while work by Oguni et al. [12], has shown the effect of multiaxial compression on failure mode transition in E-glass/vinylester composites.

Splitting failure models for fiber reinforced polymer matrix composites under pure compression loading using classical linear elastic fracture mechanics and energy considerations are presented in Lee and Waas [6], Lee [13], and Lee et al. [14]. Independently, Oguni and Ravichandran [9], obtained expressions for splitting compressive strength of fiber reinforced polymer matrix composites in the presence of lateral confining pressure.

Details of the kink band failure mode under pure compression and under combined compression and shear have been extensively studied by Kyriakides et al. [15]; Vogler and Kyriakides [16] and Hsu et al. [17], who have used the AS4/PEEK material system at a fixed fiber volume fraction in their experiments. The effect of fiber mechanical properties and fiber volume fraction on the compression response of fiber composites has been studied by Yerramalli and Waas [11]. Other practical and relevant considerations of kinking, such as the effect of adjacent plies (Drapier et al. [18]), the effect of stress gradients (Jelf and Fleck [19]; Berbinau et al. [20]; Khamseh and Waas [21]; Ahn and Waas [22]; Drapier et al. [23]; Wisnom and Atkinson [24]; Wisnom [25]), and size effects (Bazant et al. [26]), have also received attention. Compared to the focus on kinking failure, relatively little attention has been paid to splitting failure.

The present paper examines the previous experimental data on compressive failure reported in the literature, with a focus on understanding the effect of three different parameters viz. fiber geometry (i.e., diameter), matrix mechanical properties and type of loading (uniaxial or axial-shear loading) on compressive failure. These experimental data are then examined in the light of a new non-dimensional number that is used to classify the failure mechanism.

The paper is organized as follows: First the results of previous experimental studies on glass fiber and carbon fiber/vinyl ester composites are summarized. This is followed by a discussion of failure mechanisms and their dependence on fiber geometry, matrix properties, and interfacial fracture energy captured through simple analytical models developed earlier. The development of η and a discussion on how η can be used to predict and demarcate compressive failure mode and thus compressive strength, using available experimental results are presented next. Finally, concluding remarks are offered.

2 Experimental Results on Glass Fiber and Carbon Fiber Vinyl Ester Composites

Cylindrical specimens of 6.8 mm diameter and 12.5 mm gage length were used to study the compression behavior of glass fiber and carbon fiber composites to understand the effect of fiber diameter, matrix material properties, and interfacial fracture energy on compressive failure mechanism and compressive strength. Two different glass fiber diamaters (13.5 μm and 24 μm) were studied.

[1]Currently Post-doctoral Research Fellow, McKay Orthopaedic Research Laboratory, University of Pennsylvania.
[2]To whom correspondence should be addressed.

Contributed by the Applied Mechanics Division of THE AMERICAN SOCIETY OF MECHANICAL ENGINEERS for publication in the ASME JOURNAL OF APPLIED MECHANICS. Manuscript received by the Applied Mechanics Division, June 5, 2003; final revision; November 4, 2003. Associate Editor: M.-J. Pindera. Discussion on the paper should be addressed to the Editor, Prof. Robert M. McMeeking, Journal of Applied Mechanics, Department of Mechanical and Environmental Engineering, University of California–Santa Barbara, Santa Barbara, CA 93106-5070, and will be accepted until four months after final publication in the paper itself in the ASME JOURNAL OF APPLIED MECHANICS.

Table 1 Relevant mechanical properties of various fibers and matrices

	E (MPa)	G (MPa)	r_0 (mm)
Glass fiber	72,000	29,508	0.012
Carbon fiber	276,000	8960	0.0025
Silicon carbide		80,000	0.008
Vinylester	3585	1318	
Lithium Aluminum Silicate		3585	

The diameters were selected based on availability. Carbon fibers of 5 μm diameters were studied. The material properties of glass fiber and the carbon fiber (assumed isotropic) and that of vinylester resin are given in Table 1. This table also shows the properties of other fiber and matrix systems, taken from the literature (Budiansky et al. [27]). The E-glass fibers were obtained from Vetrotex Certainteed and the carbon fibers from Hexcel corporation. Vinylester (Dow Derakane 411-C50) resin was used as the matrix material for both type of reinforcing fibers. For the pure compression tests, a special test fixture made of hardened steel with four guide rods and a thick base was used. The four guide rods and the thick base was needed to prevent any macroscopic buckling of the specimens. A schematic of the test fixture is shown in Fig. 1. To investigate the effect of matrix properties, the specimens were subjected to compression-torsion loading using a servo-hydraulic tension-torsion loading frame. For this purpose, collet grips were used to grip the specimens since they can provide resistance to slipping of the specimen in torsion and also in compression loading. Specific details of this experimental setup and the experimental investigation are provided in Yerramalli and Waas [28]. Torsion loading subjects the matrix to shear, thereby changing the effective inelastic reponse of the matrix. As a result, the same matrix material, under different loading states provides a means to study the axial compression reponse in the presence of an effective matrix material that has different quantifiable properties. This aspect is further discussed later.

3 Failure Mechanisms

Failure mechanisms that dominate the compressive behavior of polymer matrix composites are kinking and splitting. However, the factors triggering these failure mechanisms are entirely different. Kinking is generally assumed to be a geometric instability induced failure mechanism whereas splitting is governed by the propensity to fracture, where crack growth is initiated from preexisting flaws. Splitting in FRPC is dictated by the balance between the magnitude of the fiber/matrix interfacial fracture energy and the available stored strain energy. Thus, a mechanism based approach to studying failure should ideally include the effect of each of the important parameters like fiber diameter, fiber misalignment, fiber and matrix properties and type of loading on the resulting analysis.

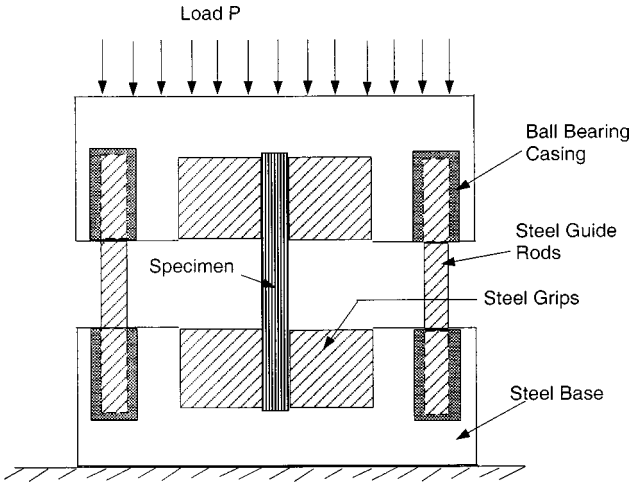

Fig. 1 A cross-sectional view of pure compression grips

Table 2 Comparison of splitting and kinking failure stress for glass/vinylester (dia. 24 μm) composite with misalignment angle, ϕ=2.5° and γ_f=0.1224 KJ/m^2

V_f	A	n	$G_c^{\text{experiment}}$ (MPa)	τ_y (MPa)	Eq. (2) (MPa)	Eq. (1) (MPa)	Fail. Mechanism Lee and Waas [6]
0.1	77.3	6.15	1800	35.6	495	270	Splitting
0.2	101.15	5.8	2400	43.8	629	389	Splitting
0.3	88.6	5.25	2750	32.35	536	505	Splitting
0.4	158	3	3140	23.2	428	619	Split/Kink
0.5	68.68	12.44	3260	45.4	718	732	Split/Kink
0.6	78.71	7.25	3630	37.23	639	845	Split/Kink

The expression for splitting compressive stress, σ_{cr}^{sp} as derived in Lee [13], Lee and Waas [6] and given in Yerramalli and Waas [11] is as follows:

$$\sigma_{cr}^{sp} = \sqrt{\frac{8V_f^2\gamma_f}{r_0(1/\delta-\beta)}}, \tag{1}$$

where V_f is fiber volume fraction, γ_f is interfacial fracture energy, r_0 is fiber radius, δ and β are constants dependent on the elastic properties of the matrix and the fiber. In terms of engineering constants, δ and β can be expressed as

$$\delta = E_f + E_m\left(\frac{1}{V_f}-1\right)$$

$$\alpha = \left[\frac{2(1+\nu_f)(1-2\nu_f)}{E_f}(V_f^{-1}-1) + \frac{2(1+\nu_m)(1-2\nu_m+V_f^{-1})}{E_m}\right]^{-1}$$

$$\beta = [E_f + (V_f^{-1}-1)\{E_m + 4\alpha(\nu_f-\nu_m)^2\}]^{-1}$$

where a subscript m refers to matrix properties and a subscript f refers to fiber properties. The symbols E and ν denote the axial modulus and the poisson's ratio of fiber or matrix depending on the subscript. For a unidirectional composite with initial misalignment ϕ, the kinking compressive stress, σ_{cr}^{k} as given by the Argon-Budianksy-Fleck prediction (see Budiansky and Fleck [4]), is

$$\sigma_{cr}^{k} = \frac{\tau_y}{\phi+\gamma_y}, \tag{2}$$

where τ_y is the composite shear yield stress and γ_y is the corresponding composite shear strain. A comparison of the predictions from Eq. (1) and Eq. (2) along with relevant mechanical properties (shear modulus, G_c, shear yield stress, τ_y, calculated based on the $0.7G_c$ criterion, Jelf and Fleck [19], and the Ramberg-Osgood fit parameters, A and n, as described in Jelf and Fleck [19]) are presented in Table 2 and Table 3. The rightmost column indicates the failure mechanism observed during experiments. It is clear that in case of glass composites, Eq. (2) tends to overestimate the failure stress as compared to the predictions of Eq. (1) at low volume fractions, where the failure mechanism is splitting. In case of carbon composites, where the observed failure mechanism is kinking, the splitting model predictions are high compared to the predictions from the kinking model of Eq. (2). From the above equations it is evident that fiber diameter, interfacial fracture energy—influenced by the type of fiber, and the effective shear properties at failure—influenced by the nature of loading, (e.g., combined compression-torsion) are three important parameters

Table 3 Comparison of splitting and kinking failure stress for carbon/vinylester (dia. 5 μm) composite with misalignment angle, ϕ=2.5° and γ_f=0.06 KJ/m^2

V_f	A	n	$G_c^{experiment}$ (MPa)	τ_y (MPa)	Eq. (2) (MPa)	Eq. (1) (MPa)	Fail. Mechanism Lee and Waas [6]
0.1	67	6.62	1600	38.6	420	508	Kinking
0.2	55.9	10.75	1800	58.8	400	886	Kinking
0.3	160	3	2400	48.9	371	1263	Kinking
0.4	100	5.3	3000	43.3	579	1639	Kinking
0.5	159	3.48	3316	41	648	2014	Kinking
0.6	98.44	3.25	3750	36.4	233	2390	Kinking

that control the failure mechanism and thus the failure strength of fiber reinforced composites. In the following sections, a discussion of these three important parameters is presented.

Effect of Fiber Diameter. As can be seen from Eq. (1), the compressive splitting stress is inversely proportional to the fiber radius and directly proportional to the fracture energy γ_f. Thus, one would expect that, if the fracture energy γ_f, fiber volume fraction, V_f, and the elastic properties of fiber and matrix are kept the same, reducing the fiber diameter should result in an increase in compressive splitting strength. Based on the above model, it was decided to examine the results of previous experiments on pure compression response of glass fiber composites reinforced with glass fibers of 13.5 μm and 24 μm diameter, as a function of fiber volume fraction, Yerramalli [29]. Under pure compression loading, it was observed that instead of an increase in failure strength with decreasing fiber diameter for a given fiber volume fraction (as predicted by the splitting compressive strength prediction (see Eq. (1)), the compressive strength assumed a fairly constant value associated with a *change* in the failure mechanism from splitting to kinking with increasing fiber volume fraction. The change from splitting to kinking occurs at around V_f =40%. Even at a low fiber volume fraction of 10%, where splitting was observed in case of glass composites reinforced with 24 μm diameter specimens, the composite specimens reinforced with glass fibers of 13.5 μm diameter failed by kinking for all the fiber volume fractions tested.

At higher volume fractions (60%), the glass fiber composite with a larger diameter clearly exhibits a higher compressive strength than the lower diameter glass composite with both exhibiting failure by kinking. This clearly shows the importance of fiber diameter on kinking compressive strength. A three-dimensional finite element model developed by the authors (Yerramalli [29] and Yerramalli and Waas [30]) has been able to capture and provide an explanation for this result. It is noted that the Argon-Budiansky-Fleck prediction of compressive strength does not display a direct dependency on fiber diameter. Instead, the effect of diameter indirectly enters through the dependency on shear yield strength of the composite. However, there are no known available results for the effect of fiber diameter on the shear yield strength of a composite.

The various failure mechanism observed in glass composites of 24 μm and 13.5 μm specimens are shown in Figs. 2 through 4. A plot of the failure compressive strength as a function of fiber volume fraction, V_f, for both glass composites (reinforced with two different fiber diameters) is presented in Fig. 5. Note that carbon fiber composites (fiber diameter of (5 μm)) in the same matrix material failed by kinking throughout the range of fiber volume fractions studied.

Effect of Fiber Properties. The effect of fiber properties can be inferred from previous experimental results and the predictive formulas presented before. With different types of fibers viz. glass and carbon, it was found that the compressive strength as well as the failure mechanism changed. A comparison of the compressive failure strengths as observed in the experiments by Lee and Waas [6] for carbon and glass fiber reinforced composites are shown in Fig. 6. The variation of compressive strength as a function of fiber volume fraction, V_f, shows that both glass and carbon fiber reinforced composites have a similar trend. However, in interpreting the results of this plot, care must be taken to associate the various data points with the different failure mechanisms for the purpose of using a mechanism based strength prediction.

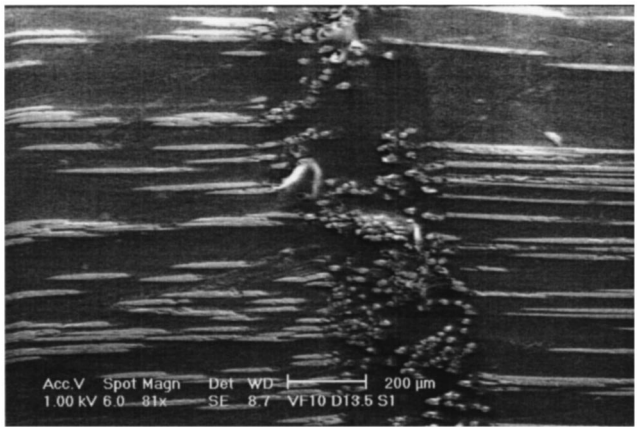

Fig. 2 Kink band in glass composites of fiber diameter 13.5 μm and V_f=10%

Effect of Loading. Research into the compressive strength behavior of fiber reinforced composites has shown that fiber misalignments cause a reduction in failure stress of the composites under pure compressive loading. In case of multiaxial loading (compression-compression or compression-torsion) the compressive failure strength and the failure mechanism are both affected. Oguni et al. [12] studied the failure mode transition due to confining pressure in E-glass/vinylester composites (with reinforcing fiber diameter of 24 μm). In the present paper, previous experimental results obtained from compression-torsion loading of cylindrical specimens of glass/vinylester composites (fiber diameters of 24 μm) and shown in Fig. 7, will be used for discussion (see Yerramalli and Waas [11]). The failure mechanism observed in glass composite specimens under compression-torsion loading is shown in Figs. 4 through 8. It was observed that at high compression to low rotation loading ratios, the specimens were failing in a combined splitting-kinking failure mode. On the other hand, at high rotation loading, e.g., pure torsion, the failure was dominated by matrix cracking due to twisting of fibers. At intermediate loading ratios, kinking was observed to be the failure mechanism. In

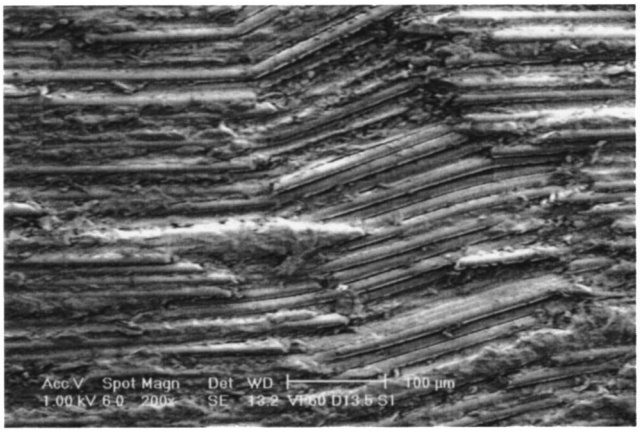

Fig. 3 Kink bands in glass composites of fiber diameter 13.5 μm and V_f=60%

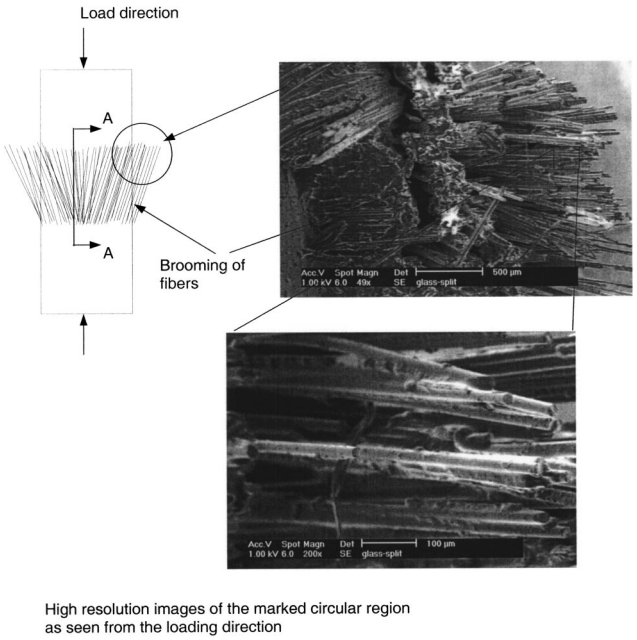

Fig. 4 Splitting failure zone in glass composites with brooming of fibers, 24 μm and V_f=50%

case of carbon/vinylester composites, the failure mechanism was observed to be kinking throughout the range of loading ratios examined. An interesting observation is that the same type of composite changes it's failure mode when stressed under different loading ratios. This observation was also made by Piggott [10] who found that the failure mode changed when the composites were tested under pure compression with partially cured matrix. The reason for the change in failure mechanism can be attributed to the magnitude of the shear modulus of the matrix and hence the composite. As evident from Eq. (2), the kinking stress is dependent on the shear properties of the composite. Hence, when the torsional load is sufficiently high, beyond the magnitude required

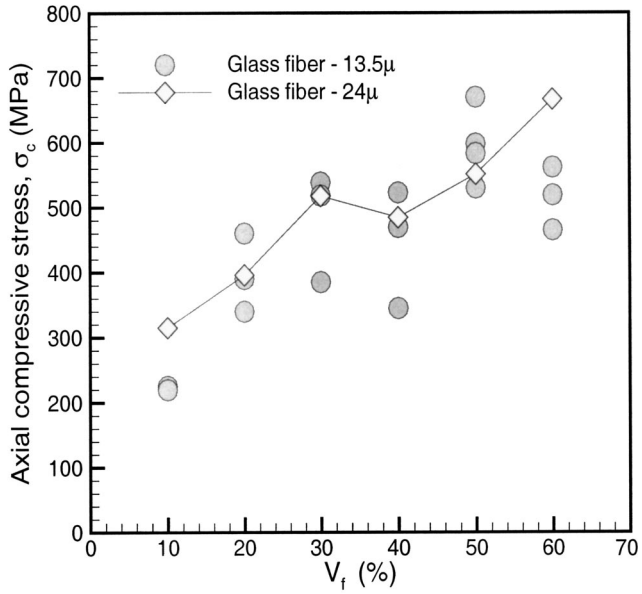

Fig. 5 Comparison of compressive strengths between glass 24 μm and 13.5 μm diameter specimens

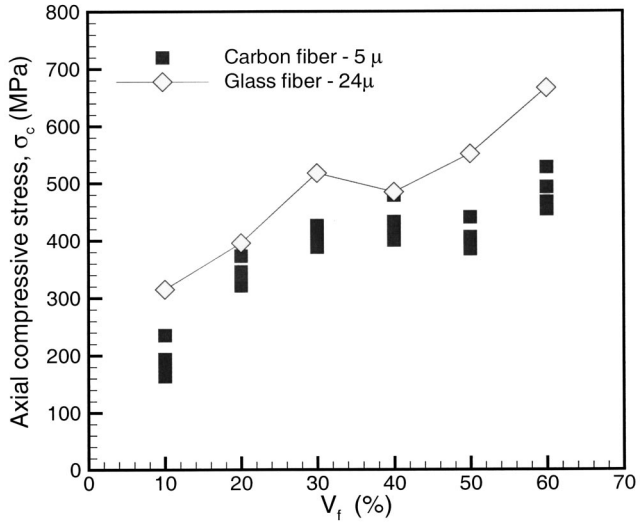

Fig. 6 Comparison of compressive stress of glass and carbon composites as function of V_f

to cause shear yielding of the composite and the matrix, glass composites tend to fail by kinking instead of splitting. Similarly, when a resin is partially cured (as was the case with the experiments conducted by Piggott [10]), it results in a matrix with a lower shear yield stress, inducing the glass fiber reinforced composites to fail by kinking instead of splitting, since, splitting would have required higher compressive stresses to cause failure.

4 Dimensional Analysis

The experimental results, as outlined in the previous sections, have revealed that the geometric (fiber diameter, V_f, misalignment angle, ϕ) parameters and the fiber and matrix mechanical and fracture properties (E_f, E_m, G_m, and γ_f) are the most important parameters controlling the failure mechanisms in fiber reinforced composites. Based on this observation, a suitable dimensionless number emerges that can be used to classify fiber reinforced composites based on their failure mechanism.

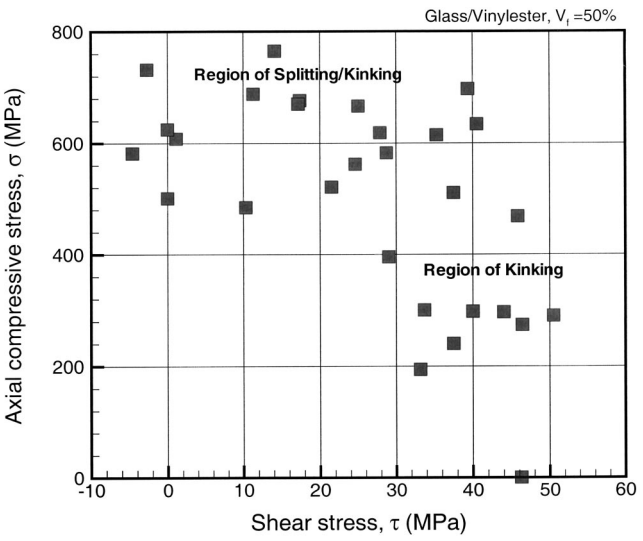

Fig. 7 Comparison of compressive stress of glass and carbon composites as function of V_f

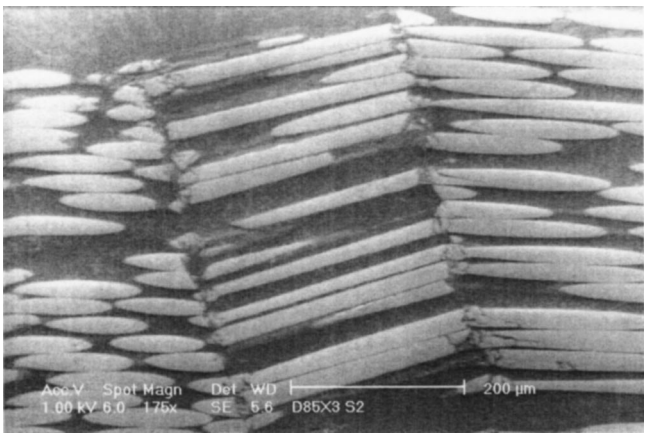

Fig. 8 Kink band in glass composite reinforced with 24 μm fiber diameter at $\Delta/R\theta=0.52$

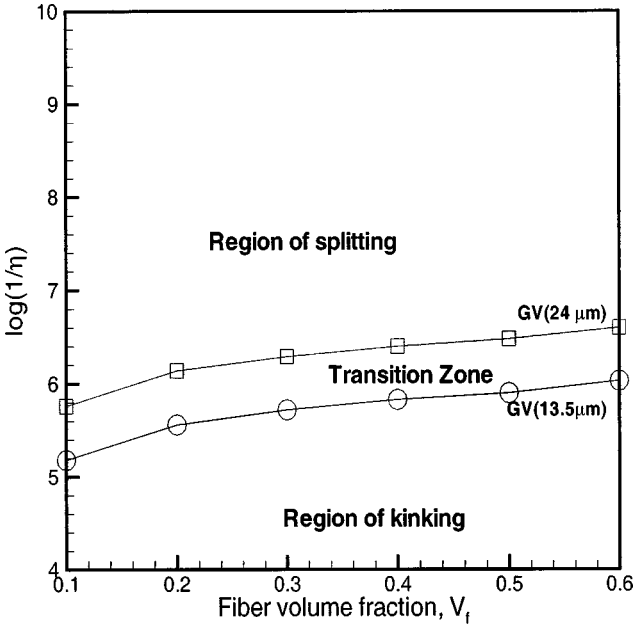

Fig. 9 Classification of failure zones based on η

The first step in determining this nondimensional number is to write a general functional relationship including all the terms relevant to the physical phenonmenon, which in this case is the failure mechanism in the composite.

$$f(\gamma_f, 2r_0, G_c, \phi_0)$$

Here, we consider only the basic material and geometric parameters affecting the failure mechanism. γ_f represents the interfacial fracture energy, G_c is the shear modulus of the composite which can be calculated from the matrix (G_m) and fiber (G_f) shear modulus values and the fiber volume fraction, V_f or determined experimentally. $2r_0$ is the fiber diameter which represents fiber geometry and ϕ_0 is a representation of initial fiber misalignment. These parameters can be written down in terms of their fundamental dimensions (M,L,T). The units of γ_f are J/m^2 which is $M^1L^0T^{-2}$. Similarly, the variables r_0, G_c, and ϕ_0 can be expressed as $M^0L^1T^0$, $M^1L^{-1}T^{-2}$, and radians, respectively. Thus, the following nondimensional number η now emerges

$$\eta = \frac{\gamma_f}{G_c 2r_0}. \tag{3}$$

This number can be interpreted as a ratio of surface modulus ($\gamma_f/r_0 \rightarrow$units of N/m^2) to composite shear modulus. It can be seen that this nondimensional number incorporates V_f and ϕ_0 implicitly since the effective value of composite shear modulus G_c is dependent on the fiber volume fraction, V_f, and the initial fiber misalignment, ϕ_0.

4.1 Usefulness of η. A progressive reduction in η indicates that the shear modulus is increasing relative to the interfacial fracture energy, γ_f. A higher shear modulus will make it less conducive to fail by kinking and causes the composite to split. Similarly, a large η implies that it is less likely for the composite to split and hence fail by kinking. Thus, using η, an a priori prediction of the failure mechanism can be made for a given fiber and matrix combination the variation of $\log(1/\eta)$ against fiber volume fraction, V_f, is shown in Fig. 9 for a glass/vinylester composite with $r_0 = 6.75\,\mu$m and $r_0 = 12\,\mu$m and $\gamma_f = 0.1224$ KJ/m^2. The shear modulus of the composite, G_C depends on fiber and matrix properties and the fiber volume fraction, V_f and is given in Table 2 and Table 3. Since, it was observed in the experiments that the glass composites of fiber diameter (13.5 μm) failed by kinking for all V_f, it is logical to assume the curve for 13.5 μm as a boundary for kinking and the curve corresponding to 24 μm glass composite as a boundary for splitting and the zone in between can be defined as a transition zone. It should be noted that the shear modulus for glass fiber (24 μm) and glass fiber (13.5 μm) reinforced composites are taken to be the same for the calculation of η. Thus, this universal band splits the plot in Fig. 9 into two regions. Points located in the splitting zone correspond to composites that fail by splitting. Points located in the bottom half (kinking zone) correspond to kinking failure. Points located in the band correspond to transition between kinking and splitting, and the co-existence of both failure mechanisms as has been reported by Piggott [10], Oguni et al. [12], and Yerramalli [29]; Yerramalli and Waas [30]. Thus, once η is calculated, Fig. 9 can be used to a priori establish what compressive failure mechanism is operative and thus an appropriate mechanism based compressive strength model can be used to predict the compressive failure strength. The width of the transition zone and the limits of the splitting zone at high V_f can be further refined with more experimental data. However, the current plot, based on available experimental data, could be a useful stepping stone for further classification and refinement of failure zones. If for *any material* the value of η is lying between these two bounds, then based on the V_f value, the failure mechanism could be kinking, splitting or a combination of both.

Calculating the value of η for carbon fiber composites, we see that the curve of $\log(1/\eta)$ lies in the bottom half below the 13.5 μm glass curve as shown in Fig. 10. This is the kinking region and is consistent with the experimental observation that carbon composites fail by kinking for all the fiber volume fractions tested. Further, for comparison, the value of η has been calculated for a ceramic matrix composite and it is found that the curve of $\log(1/\eta)$ lies in the top part of the plot. This indicates that the ceramic matrix composite fails by splitting, and this is exactly what was observed in the experimental results reported by Budiansky et al. [27].

5 Discussion

As seen in Fig. 10, η has been calculated as a function of V_f for different composite material systems. The values of γ_f chosen for glass fiber is 0.1224 KJ/m^2 and for carbon fibers it was taken as 0.06 KJ/m^2. In case of Silicon carbide fibers (diameter is 16 μm) the value of $\gamma_f = 0.022$ KJ/m^2 was taken from the paper by Budiansky et al. [27] and the composite shear modulus was calculated using micromechanical formulas. Using these values, it has been shown in the previous section that the curves of carbon/vinylester (CV) and sic/lialsi lie in two extreme corners of the plot, while, the curves for glass/vinylester (GV) composites lie in the center of the plot. It can therefore be inferred that the glass composites

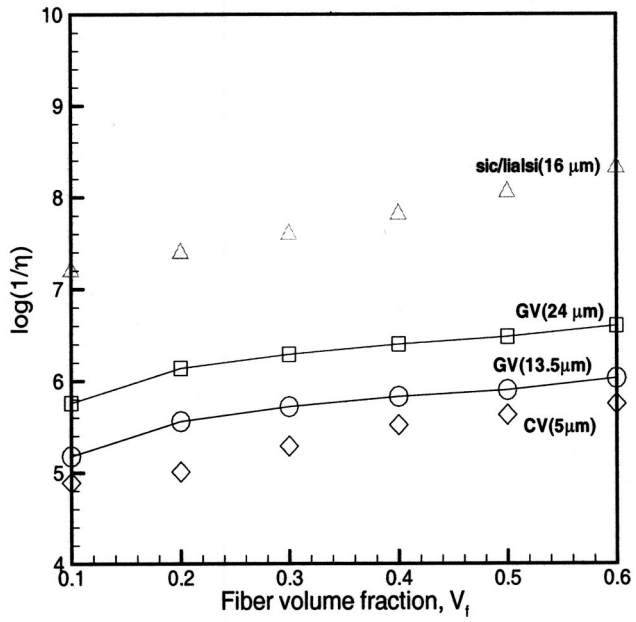

Fig. 10 Variation of the nondimensional number η for different material systems

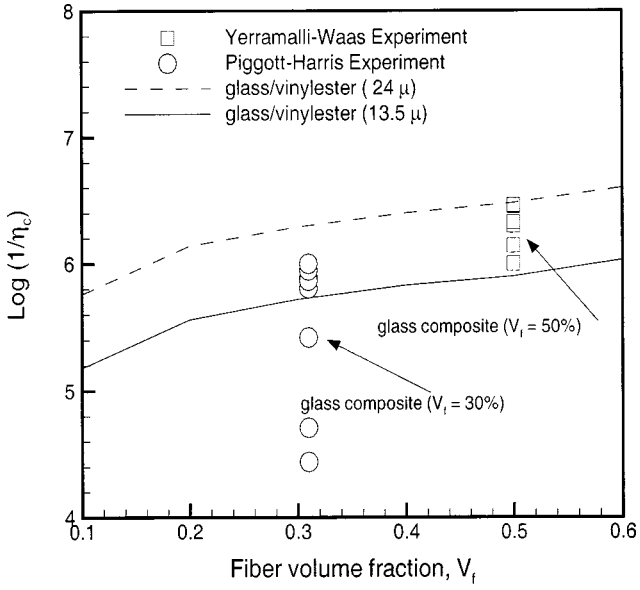

Fig. 11 Variation of nondimensional number for glass composites as a function of shear modulus at fixed V_f

tested lie in a transition zone where the failure mechanism changes from kinking to splitting or vice versa. This shows the importance of η. Based on the magnitude of η, a suitable fiber-matrix combination could be chosen so as to have a particular failure mechanism. Based on this number, one can explain the reason why a glass composite of smaller diameter fails by kinking while a glass composite reinforced with larger diameter fibers (24 μm) fails by splitting. With the reduction in the fiber diameter the value of surface modulus ($\gamma_f/2r_0$) increases for the same material system. This makes the splitting failure stress larger causing the composite to fail by kinking. Similarly, when the glass composites of 24 μm diameter fibers are subjected to compression-torsion loading they tend to have a failure mode transition from splitting to kinking. This can be explained by looking at the value of η as a function of applied shear stress. Once the value of remotely applied shear stress exceeds the value of shear yield stress, τ_y then the instantaneous shear modulus of the composite starts to reduce and leads to a higher value of η. A higher value of η indicates that the shear modulus is very low which makes it easier for the composite to fail by local buckling of fibers leading to kinking. The nondimensional number, η was calculated for the experimental data given in Piggott [10] and Yerramalli and Waas [11] and is presented in Fig. 11. The data obtained from Piggott [10] was for a $V_f=30\%$ glass composite with a partially cured matrix. The test data from Yerramalli and Waas [11] was obtained from testing glass composites ($V_f=50\%$) under combined compression-torsion loading. As can be seen, at a given fiber volume fraction, as the shear modulus decreased, $\log(1/\eta)$ decreases. Once this number approaches the threshold for kinking, which is defined by the curve corresponding to the 13.5 μm glass fiber composites, the specimens start to fail by kinking. This corroborates with the experimental observations made by Piggott [10] and Yerramalli and Waas [11].

As mentioned in the previous section, the accuracy of the transition zone width is dependent on the experimental data available in the literature. Therefore, a sensitivity analysis of η is in order to understand the influence of each parameter. Since $\eta=\gamma_f/G_c 2r_0$ it follows that

$$d\eta=\frac{d\gamma_f}{G_c r_0}-\frac{-\gamma_f dG_c}{G_c^2 r_0}-\frac{-\gamma_f dr_0}{G_c r_0^2}. \tag{4}$$

Thus, for fixed G_c and r_0, $d\eta=d\gamma_f/G_c r_0$. Consequently, a 10% uncertainity in γ_f, translates to a 10% uncertainity in η. Similarly, the uncertainities in G_c and r_0 can be used to calculate the uncertainities in η. It can be seen from Eq. (4), that the $d\eta/dG_c$ is inversely proportional to the square of G_c and r_0. Thus, indicating that the failure mechanism is highly sensitive to the geometric properties of fiber and the shear modulus of the composite.

The implications of η for the design of composites is now evident. As shown through the experimental results, carbon composites failed by kinking throughout the V_f examined. Yet, as indicated by Eq. (1), the splitting compressive strength of carbon composites is several times larger than the kinking strength (Eq. (2)). Thus it is desirable to *design* composites such that they will fail by splitting. This implies a need to reduce η for carbon composites. A reduction is possible by either increasing the value of G_c or reducing the value of surface modulus γ_f/r_0. Experimental results with Boron fiber composites, as described in Schutz [5] and Reed and Golda [31], show an elevated compressive strength when compared to similar composites with smaller fiber diameter. Similarly, as shown in Fig. 5, at $V_f=60\%$, the larger diameter glass composites failed at a higher compressive stress than the smaller diameter glass composites (at the same fiber volume fraction). Thus, carbon fibers with a larger diameter will exhibit a higher compressive strength than their smaller (5 μm) diameter counterparts. One cannot keep increasing the fiber diameter indefinitely, however, without considering other strength limiting mechanisms such as interior fiber defects which will increase statistically with an increase in material volume.

6 Conclusions

A new nondimensional number η has been presented to classify the compression failure mechanism of continuous fiber reinforced composites. This number was used to explain the causes for the different failure mechanisms observed during compression testing of polymer matrix composites. Results from the open literature, and from an experimental program that studied the effect of fiber diameter, fiber properties and the type of loading were used to verify the predictions made by using η. It can be concluded from

this study that the fiber diameter, the matrix (and hence the composite) shear response (which is influenced by initial fiber misalignment) and the fiber-matrix interface fracture energy all play an important role in influencing the failure mechanism and hence the compressive strength. For the same material system (fiber matrix) a change in failure mode can be obtained, for example, by changing the fiber diameter or the interface fracture energy. In a similar vein, the matrix shear properties are also significant in controlling the failure mechanism, and thus the composite compressive strength.

Acknowledgment

The authors are grateful for the financial sponsorship of the Army Research Office with Dr. Bruce LaMattina as the Scientific Monitor.

References

[1] Rosen, B. W., 1965, ''Mechanics of Composite Strengthening,'' *Composite Materials*, S. H. Bush, ed., American Society of Metals, Metals Park, OH, pp. 37–75.
[2] Argon, A. S., 1972, ''Fracture of Composites,'' *Treatise on Materials Science and Technology*, H. Herman, ed., Academic Press, New York, **1**, pp. 79–114.
[3] Budiansky, B., 1983, ''Micromechanics,'' Comput. Struct., **16**, pp. 3–12.
[4] Budiansky, B., and Fleck, N. A., 1993, ''Compressive Failure of Fibre Composites,'' J. Mech. Phys. Solids, **41**(1), pp. 183–211.
[5] Schutz, J. B., 1998, ''Properties of Composite Materials for Cryogenic Applications,'' Cryogenics, **38**(1), pp. 3–11.
[6] Lee, S. H., and Waas, A. M., 1999, ''Compressive Response and Failure of Fiber Reinforced Unidirectional Composites,'' Int. J. Fract., **100**, pp. 275–306.
[7] Piggott, M. R., and Harris, B., 1980, ''Compression Strength of Carbon, Glass and Kevlar-49 Fibre Reinforced Polyester Resins,'' J. Mater. Sci., **15**, pp. 2523–2538.
[8] Drzal, L. T., Rich, M. J., and Llyod, P. M., 1982, ''Adhesion of Graphite Fibers to Epoxy Matrices: I. The Role of Fiber Surface Treatment,'' J. Adhes., **16**, pp. 1–30.
[9] Oguni, K., and Ravichandran, G., 2000, ''An Energy-Based Model of Longitudinal Splitting in Unidirectional Fiber-Reinforced Composites,'' ASME J. Appl. Mech., **67**, pp. 437–443.
[10] Piggott, M. R., 1981, ''A Theoretical Framework for the Compressive Properties of Aligned Fibre Composites,'' J. Mater. Sci., **16**, pp. 2837–2845.
[11] Yerramalli, Chandra S., and Waas, A. M., 2003, ''A New Failure Criterion for Fiber Reinforced Polymer Composites Under Combined Compression-Torsion Loading,'' Int. J. Solids Struct., **40**, pp. 1139–1164.
[12] Oguni, K., Tan, C. Y., and Ravichandran, G., 2000, ''Failure Mode Transition in Unidirectional E-Glass/Vinylester Composites Under Multiaxial Compression,'' J. Compos. Mater., **34**(24), pp. 2081–2097.
[13] Lee, S. H., 1998, ''Compressive Behavior of Fiber Reinforced Unidirectional Composites,'' Ph.D. thesis, Aerospace Engineering Department, University of Michigan, Ann Arbor, MI.
[14] Lee, S. H., Yerramalli, C. S., and Waas, A. M., 2000, ''Compressive Splitting Response of Glass-Fiber Reinforced Unidirectional Composites,'' Compos. Sci. Technol., **60**, pp. 2957–2966.
[15] Kyriakides, S., Arseculeratne, R., Perry, E. J., and Liechti, K. M., 1995, ''On the Compressive Failure of Fiber Reinforced Composites'' (Proceedings of the Sixtieth Birthday Celebration of Prof. W. G. Knauss), *International Journal of Solids and Structures*, **32**, pp. 689–738.
[16] Vogler, T. J., and Kyriakides, S., 1999, ''Inelastic Behavior of an AS4/PEEK Composite Under Combined Transverse Compression and Shear. Part I: Experiments,'' J. Color Soc., **15**, pp. 783–806.
[17] Hsu, S. Y., Vogler, T. J., and Kyriakides, S., 1999, ''Inelastic Behavior of an AS4/PEEK Composite Under Combined Transverse Compression and Shear. Part II: Modeling,'' J. Color Soc., **15**, pp. 807–836.
[18] Drapier, S., Grandidier, J.-C., and Potier-Ferry, M., 1999, ''Towards a Numerical Model of the Compressive Strength for Long Fiber Composites,'' Eur. J. Mech. A/Solids, **18**(1), pp. 69–92.
[19] Jelf, P. M., and Fleck, N. A., 1994, ''The Failure of Composite Tubes due to Combined Compression and Torsion,'' J. Mater. Sci., **29**, pp. 3080–3084.
[20] Berbinau, P., Soutis, C., Goutas, P., and Curtis, P. T., 1999, ''Effect of Off-Axis Ply Orientation on 0°-Fibre Microbuckling,'' Composites, **30**, pp. 1197–1207.
[21] Khamseh, A., and Waas, A. M., 1992, ''Failure of Uniply Model Composites Under Compression,'' ASME J. Eng. Mater. Technol., **114**, pp. 304–310.
[22] Ahn, J. H., and Waas, A. M., 1999, ''A Micromechanics-Based Finite Element Model for Compressive Failure of Notched Uniply Composite Laminates Under Remote Biaxial Loads,'' ASME J. Eng. Mater. Technol., **121**, pp. 360–366.
[23] Drapier, S., Grandidier, J.-C., and Potier-Ferry, M., 1998, ''Non-Linear Numerical Approach to the Analysis of Microbuckling,'' Compos. Sci. Technol., **58**(5), pp. 785–790.
[24] Wisnom, M. R., and Atkinson, J. W., 1997, ''Constrained Buckling Tests Show Increasing Compressive Strain to Failure With Increasing Strain Gradient,'' Composites, Part A: Applied Science and Manufacturing, **28**(11), pp. 959–964.
[25] Wisnom, M. R., 1999, ''Size Effects in the Testing of Fibre-Composite Materials,'' Compos. Sci. Technol., **59**(13), pp. 1937–1957.
[26] Bazant, Z. P., Kim, J. H., Daniel, I. M., Becq-Giraudon, E., and Zi, G., 1999, ''Size Effect on Compression Strength of Fiber Composites Failing by Kink Band Propagation,'' Int. J. Fract., **95**, pp. 103–141.
[27] Budiansky, B., Hutchinson, J. W., and Evans, A. G., 1986, ''Matrix Fracture in Fiber-Reinforced Ceramics,'' J. Mech. Phys. Solids, **34**(2), pp. 167–189.
[28] Yerramalli, Chandra S., and Waas, A. M., 2001, ''Failure of Composites Under Combined Loading,'' *Proceedings of 2001 ASME International Mechanical Engineering Congress and Exposition*, New York, Nov. 11–16, ASME, New York, **66**, pp. 31–40.
[29] Yerramalli, Chandra S., 2003, ''A Mechanism Based Modeling Approach to Failure in Fiber Reinforced Composites,'' PhD thesis, Aerospace Engineering Department, University of Michigan, Ann Arbor, 2003.
[30] Yerramalli, Chandra S., and Waas, A. M., 2003, ''The Effect of Fiber Diamter on the Compressive Strength of Composites: a 3D Finite Element Based Study,'' Comput. Mech. Eng. Sci., in press.
[31] Reed, R. P., and Golda, M., 1997, ''Cryogenic Composite Supports: A Review of Strap and Struct Properties,'' Cryogenics, **37**, pp. 233–250.

Virtual Circular Dislocation-Disclination Loop Technique in Boundary Value Problems in the Theory of Defects

A. I. Kolesnikova
Institute of Problems of Mechanical Engineering,
Russian Academy of Sciences,
Bolshoj 61, Vas. Ostrov,
St. Petersburg 199178, Russia
e-mail: ankolesnikova@yandex.ru

A. E. Romanov
Ioffe Physico-Technical Institute,
Russian Academy of Sciences,
Polytechnicheskaya 26,
St. Petersburg, 194021, Russia
e-mail: aer@mail.ioffe.ru

A technique for elastic boundary value problem solutions for defects in solids is developed. The method is based on the introduction of virtual circular dislocation-disclination loops distributed continuously for satisfying the prescribed boundary conditions at free surfaces and interfaces. The set of dislocation-disclination loops which may be used as virtual ones is considered. The elastic fields and energies of the selected dislocation and disclination loops are presented. The method of the virtual circular dislocation-disclination loops is then applied to obtain the elastic fields and energies of a spherical dilatating inclusion in a plate and a half-space, of a prismatic dislocation loop parallel to free surfaces of a plate and a half-space, and the elastic fields of a twist disclination loop coaxial to a cylinder. [DOI: 10.1115/1.1757488]

1 Introduction

At present the technique of surface virtual defects to solve boundary problems in the theory of defects in solids is well known. It was originally formulated by Louat [1] and then developed by Marcinkowski in the case of surface dislocations, [2]. The generalization of this method for surface disclinations and for surface flux lines in type II superconductors was given by Romanov and Vladimirov [3] and Vladimirov et al. [4], respectively.

The technique proceeds as follows: the field (e.g., elastic or magnetic) of the real defect in the medium with internal and external boundaries can be found as sum of the field of the defect in an infinite medium and a field of surface (virtual) defects. Naturally this method can be used for the evaluation of elastic fields of a nonsingular nature, e.g., for a prescribed distribution of surface loads or displacements.

The appropriate virtual defects have field components, which contribute to the boundary conditions. They are distributed continuously with an unknown distribution. In terms of these distribution functions, the boundary conditions are expressed as integral equations. The singular lines of the virtual defects are external to the considered medium (in the case of free surfaces they can be placed on the surfaces, so these defects are named *surface* defects). The integral equations can be solved for virtual defect distributions, and therefore their fields can be found. Finally, the fields of the real crystal lattice defects may be found.

The method of surface straight defects was successfully applied to find the elastic and magnetic fields of real defects, i.e., dislocations, disclinations, flux lines in type II superconductors parallel to free surfaces and interfaces, [4–7]. The method was used by Belov, Chamrov, Indenbom, and Lothe [8] in the cases of straight dislocations emerging at planar boundaries by applying the technique involving surface dislocation segments. In our previous work, we proposed to explore virtual surface circular dislocation-disclination loops in the solution of boundary problems for straight-line defects in solids, [9–11], e.g., the elastic field of edge dislocations and wedge disclinations normal to the surfaces of a plate were determined for the first time. Louat and Sadananda used surface dislocation loops to solve the problem of a spherical inclusion in a half-space, [12].

The present work deals with the development of a technique using virtual dislocation-disclination loops along with a demonstration of new solutions. In the first part of this paper, we calculate the elastic fields of particular dislocation-disclination loops in infinite media by the Mura method (see Section 2) and determine the type of the boundary value problems which may be solved with the help of circular dislocation-disclination loops. In the second part, we demonstrate the applications of this method for determining the elastic fields and energies of a dilatating spherical inclusion in a plate and a half-space, of a prismatic dislocation loop parallel to the free surfaces of a plate and a half-space, and the elastic fields of a twist disclination loop coaxial to a cylinder.

The technique developed here and the associated results have a variety of possible applications in solid state mechanics and physics. The elastic fields and energy of a dilatating inclusion in a plate are useful for the analysis of the elastic behavior of nanoparticles in thin films. The displacements can be explored to determine the corrugation of film surfaces due to embedded nanoparticles. The associated elastic strains modify the physical properties of the material both inside and outside the inclusion. For example, the electronic properties, such as the band gap, can be substantially changed in the case of quantum dots, which from a mechanical point of view are nanosize dilatating inclusions. The elastic displacements of the circular prismatic dislocation loop in thin films are necessary for correct identification of such defects. Modern transmission electron microscopy (TEM) permits precise experimental determination of the TEM contrast (image) related to the presence of the defect in a thin film. For a detailed understanding of the TEM contrast, the defect displacement field must be known. Therefore the elastic fields for a prismatic a dislocation loop in a plate can be utilized for modeling the TEM contrast and the following comparison with experimental observations. In addition, the elastic stresses and energy of the prismatic dislocation loop can be applied effectively for analyses of relaxation processes near nanosize clusters in semiconductor thin films. Finally, the solution of the twist disclination loop in a cylinder can be applied when considering the twist of polymer macro-molecules in mesosize fibrils.

Contributed by the Applied Mechanics Division of THE AMERICAN SOCIETY OF MECHANICAL ENGINEERS for publication in the ASME JOURNAL OF APPLIED MECHANICS. Manuscript received by the ASME Applied Mechanics Division, September 11, 2003; final revision, December 30, 2003. Editor: R. M. McMeeking. Discussion on the paper should be addressed to the Editor, Prof. Robert M. McMeeking, Journal of Applied Mechanics, Department of Mechanical and Environmental Engineering University of California–Santa Barbara, Santa Barbara, CA 93106-5070, and will be accepted until four months after final publication of the paper itself in the ASME JOURNAL OF APPLIED MECHANICS.

All of our results for dislocation-disclination loops are derived in the framework of isotropic linear elasticity. The compact forms for the elastic fields of the dislocation-disclination loops involve the Lipschitz-Hankel integrals, [13–17]. The properties of integrals of this type were investigated by Eason, Noble, and Sneddon [18]. Their utility in writing the elastic fields of circular dislocation loops was first carried out by Salamon and Dundurs [13].

2 Circular Dislocation-Disclination Loops as Virtual Defects: Classification and Elastic Fields of the Loops

2.1 Plastic Distortion and the Mura Method. Toshio Mura defined the plastic distortion β_{ij}^* for dislocations and disclinations in the following form, [19]:

$$\beta_{ij}^* = \delta_i(S)[-b_j - e_{jpq}\omega_p(x_q - x_q^0)], \tag{1}$$

where $\delta_i(S) = \int_{S_i}\delta(\mathbf{r}-\mathbf{r}')dS_i'$, $\delta(\mathbf{r}-\mathbf{r}')$ is the three-dimensional delta-function, S_i is the cut-surface with normal $\mathbf{n}_i$, b_j is the Burgers vector of a dislocation, ω_p is the Frank vector of a disclination, x_q^0 is the coordinate of the rotation axis, and e_{jpq} is the permutation tensor. In Eq. (1), the term in the rectangular brackets represents the jump of displacements $[u_j]$ at the cut-surface S_i related to the defect. In [19], the jump of displacements has the opposite sense; this is due to the definition of upper and low faces of the cut-surface (compare [19] and [9]). In general, the appearance of a defect in a continuum can be decomposed into the four following steps: (i) make a cut along S_i; (ii) displace the upper face S_i^+ relative to the low face S_i^- by value $[u_j]$; (iii) insert (or remove) the material into the holes which arise (or from the areas of overlap); and (iv) "glue" the material at S_i^+ and S_i^-. As a result of this procedure, a defect with plastic distortion β_{ij}^* is generated.

The plastic distortion β_{ij}^* allows one to obtain the total displacement field u_m, [19]:

$$u_m(r') = -i\int_{-\infty}^{\infty}\int\int \xi_l C_{jikl} L_{mk}\overline{\beta}_{ij}^* \exp(i\boldsymbol{\xi}\cdot\mathbf{r})d\xi_x d\xi_y d\xi_z, \tag{2}$$

where C_{jikl} are the elastic constants; L_{mk} and $\overline{\beta}_{ij}^*$ are Fourier transforms of the Green's function G_{km} and plastic distortion β_{ij}^*, respectively, and $\boldsymbol{\xi}\cdot\mathbf{r} = \xi_x x + \xi_y y + \xi_z z$. For an isotropic medium we have

$$C_{jikl} = \frac{2G\nu}{1-2\nu}\delta_{ji}\delta_{kl} + G(\delta_{ik}\delta_{jl} + \delta_{il}\delta_{jk});$$

$$L_{mk} = \frac{1}{(2\pi)^{3/2}}\frac{2(1-\nu)\xi^2\delta_{mk} - \xi_m\xi_k}{2(1-\nu)G\xi^4}, \tag{3}$$

where G is shear modulus, ν is Poisson ratio, δ_{km} is the Kroneker delta, and $\xi^2 = \xi_x^2 + \xi_y^2 + \xi_z^2$. Equations (2) and (3) can be then used to obtain the elastic fields of dislocations, disclinations, and Somigliana dislocations of arbitrary configuration in an infinite isotropic medium, and in particular, circular defect loops.

2.2 Elastic Fields of Circular Loops. In Fig. 1 we present some examples of circular defect loops. The loops have plastic distortions depending linearly on the radial coordinate r and have trigonometric multipliers $\cos\varphi$ and $\sin\varphi$ in Cartesian (x,y,z) and cylindrical (r,φ,z) coordinate systems. In fact, the plastic distortions for these loops are initial terms of the Fourier expansion are written as

$$\beta_{zj}^* = A_0 + A_1\cos\varphi + B_1\sin\varphi, \quad j = x,y,z \quad or \quad j = r,\varphi,z$$

$$A_0 = A_1 = B_1 = (b+\omega r)H\left(1-\frac{r}{a}\right)\delta(z), \tag{4}$$

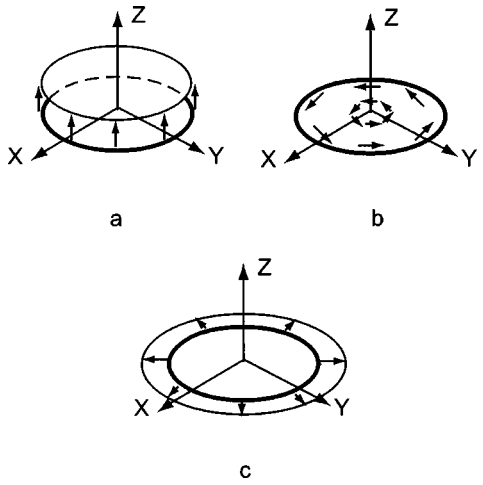

Fig. 1 Dislocation-disclination loops being used as virtual defects in solutions of elastic boundary value problems. (*a*) Prismatic dislocation loop. (*b*) Twist disclination loop. (*c*) Radial disclination loop (Somigliana dislocation). The displacement jumps at the cut-surfaces are shown schematically.

where b is a magnitude of the Burgers vector, ω is a value of the Frank vector, $H(1-r/a)$ is the Heaviside step function, $\delta(z)$ is the one-dimensional delta-function, and a is the loop radius. In the framework of the chosen coordinate system (Cartesian or cylindrical), the plastic distortions given by Eqs. (4) are linearly independent. Some of the loops associated with these distortions are ordinary dislocation and disclination loops, as shown in Figs. 1(*a*) and (*b*), respectively; others are Somigliana dislocation loops (see, for example, Fig. 1(*c*)). The elastic fields and energies for other defect loops not shown in Fig. 1 can be found in earlier work, [9,11].

For the purpose of the present research, we consider only the prismatic dislocation loop, the twist disclination loop, and the radial disclination (Somigliana dislocation) loop. These loops are used as real loops and as virtual defect loops in the solution of axisymmetric boundary value problems.

2.2.1 Prismatic Dislocation Loop. The plastic distortion of the interstitial prismatic dislocation loop (Fig. 1(*a*)) is

$$\beta_{zz}^* = bH\left(1-\frac{r}{a}\right)\delta(z). \tag{5}$$

With the help of the Mura technique we find the total displacement field:

$$u_r = \frac{b}{4(1-\nu)}\left[(2\nu-1)J(1,1;0) + \frac{|z|}{a}J(1,1;1)\right];$$

$$u_\varphi = 0;$$

$$u_z = \frac{b\,\mathrm{sgn}(z)}{4(1-\nu)}\left[2(1-\nu)J(1,0;0) + \frac{|z|}{a}J(1,0;1)\right]. \tag{6}$$

Here

$$\mathrm{sgn}(z) = \begin{cases} -1, & z<0, \\ +1, & z>0, \end{cases} \qquad J(m,n;p)$$

are Lipschitz-Hankel integrals, [18], given by $J(m,n;p) = \int_0^\infty J_m(\kappa)J_n(\kappa r/a)\exp(-\kappa|z|/a)\kappa^p d\kappa$, and $J_m(\kappa)$ is the Bessel function.

In the framework of linear elasticity and applying Hooke's law for isotropic materials we find the elastic strains ε_{ij} and stresses σ_{ij}. The stresses are

$$\sigma_{rr}=\frac{Gb}{2(1-\nu)}\left[\frac{1-2\nu}{r}J(1,1;0)+\frac{|z|}{a^2}J(1,0;2)-\frac{1}{a}J(1,0;1)-\frac{|z|}{ar}J(1,1;1)\right];$$

$$\sigma_{\varphi\varphi}=\frac{Gb}{2(1-\nu)}\left[\frac{2\nu-1}{r}J(1,1;0)-\frac{2\nu}{a}J(1,0;1)+\frac{|z|}{ar}J(1,1;1)\right];$$

$$\sigma_{zz}=-\frac{Gb}{2(1-\nu)}\left[\frac{1}{a}J(1,0;1)+\frac{|z|}{a^2}J(1,0;2)\right]; \tag{7}$$

$$\sigma_{rz}=-\frac{Gb}{2(1-\nu)}\frac{z}{a^2}J(1,1;2);$$

$$\sigma_{z\varphi}=\sigma_{r\varphi}=0.$$

The stresses given by Eqs. (7) satisfy the equations of equilibrium. Note that Eqs. (6) and (7) are equivalent to the formulas obtained by Dundurs and Salamon [13,14] and Salamon and Comninou [15] for a prismatic dislocation loop in two-phase material when the phases possess identical elastic properties.

2.2.2 Twist Disclination Loop. The twist disclination loop shown in Fig. 1(*b*) has the plastic distortion:

$$\beta^*_{z\varphi}=\omega r H\left(1-\frac{r}{a}\right)\delta(z). \tag{8}$$

In this case the total displacements have the following simple form:

$$u_\varphi=\frac{\omega a}{2}\,\mathrm{sgn}(z)J(2,1;0);$$

$$u_r=u_z=0, \tag{9}$$

and the stresses are

$$\sigma_{r\varphi}=-\frac{G\omega}{2}\,\mathrm{sgn}(z)J(2,2;1);$$

$$\sigma_{z\varphi}=-\frac{G\omega}{2}J(2,1;1);$$

$$\sigma_{rr}=\sigma_{\varphi\varphi}=\sigma_{zz}=\sigma_{rz}=0. \tag{10}$$

2.2.3 Radial Disclination Loop. Consider the radial disclination loop (Somigliana dislocation), which can be defined by the procedure depicted in Fig. 1(*c*). The plastic distortion of this loop defect is

$$\beta^*_{zr}=\omega r H\left(1-\frac{r}{a}\right)\delta(z). \tag{11}$$

The total displacements of the radial disclination loop are given by

$$u_r=\frac{\omega a\,\mathrm{sgn}(z)}{4(1-\nu)}\left[2(1-\nu)J(2,1;0)-\frac{|z|}{a}J(2,1;1)\right];$$

$$u_\varphi=0;$$

$$u_z=\frac{\omega a}{4(1-\nu)}\left[(2\nu-1)J(2,0;0)-\frac{|z|}{a}J(2,0;1)\right]. \tag{12}$$

The stress field is

$$\sigma_{rr}=\frac{G\omega\,\mathrm{sgn}(z)}{2(1-\nu)}\left[2(\nu-1)\frac{a}{r}J(2,1;0)-\frac{|z|}{a}J(2,0;2)+2J(2,0;1)+\frac{|z|}{r}J(2,1;1)\right];$$

$$\sigma_{\varphi\varphi}=\frac{G\omega\,\mathrm{sgn}(z)}{2(1-\nu)}\left[2(1-\nu)\frac{a}{r}J(2,1;0)-\frac{|z|}{r}J(2,1;1)+2\nu J(2,0;1)\right];$$

$$\sigma_{zz}=\frac{G\omega}{2(1-\nu)}\frac{z}{a}J(2,0;2); \tag{13}$$

$$\sigma_{rz}=\frac{G\omega}{2(1-\nu)}\left[\frac{|z|}{a}J(2,1;2)-J(2,1;1)\right];$$

$$\sigma_{r\varphi}=\sigma_{z\varphi}=0.$$

3. The Virtual Circular Dislocation-Disclination Loop Method

In the framework of the virtual defect method the elastic field p_{ij} (displacements, distortions, strains, and stresses) of the real defect placed in the medium with free surfaces and interfaces is presented as

$$p_{ij}={}^{\infty}p_{ij}+{}^{i}p_{ij}, \tag{14}$$

where ${}^{\infty}p_{ij}$ is the field of the real defect in an infinite medium without interfaces and ${}^{i}p_{ij}$ is the additional field, due to ensembles of virtual defects distributed continuously with unknown distribution functions ${}^{k}f$ (index k is a counter for virtual defect ensembles). The boundary conditions at the free surfaces and interfaces $p_{ij}|_S=\alpha$ are then rewritten with respect to Eqs. (14), and become integral equations for the unknown distribution functions. Virtual defects are placed outside the medium in which their elastic fields act. In the limit case, they can be placed directly on free surfaces. The problem exists of how to choose the appropriate defects as virtual ones.

For cylindrical symmetry problems the external and internal surfaces can be planar, cylindrical, spherical; and the real defects can be point defects, straight linear and circular loop defects, volumetric cylindrical, spheroidal, and two-axes ellipsoidal defects. In the case when the combination of the boundaries and real defects have cylindrical symmetry we arrive at a problem of cylindrical symmetry. For point and volume defects we have additional requirements concerning their plastic distortions. These distortions must admit their representations via distortions of circular defect loops distributed continuously while retaining cylindrically symmetric geometry.

In solving boundary value problems with cylindrical symmetry, we introduce dislocation-disclination loops as virtual defects. In this article we consider two possibilities: (i) the distribution functions ${}^{k}f$ depend on the loop radius and (ii) the distribution functions ${}^{k}f$ depend on the position of the virtual loop.

For planar boundaries, ensembles of virtual circular loops are placed either on free surfaces or at some distance from the interfaces, [12–14]. Then the boundary conditions lead to integral equations for unknown radius-dependent distribution functions ${}^{k}f$:

$${}^{\infty}p_{ij}|_S+\sum_k\int_0^\infty {}^{k}f(a)\,{}^{k}p_{ij}|_S\,da=\alpha, \tag{15}$$

where a is the loop radius, and ${}^{k}p_{ij}$ is a field due to the virtual loop from the kth ensemble. It is necessary that the angular dependence of the elastic field components of the virtual defects corresponds to the angular dependence of the elastic field components of the real defect. Since the elastic fields of the circular

loops have the Lipshitz-Hankel integral representation, it is efficient to apply the Hankel-Bessel transformation to Eqs. (15). The direct and reverse Hankel-Bessel transformations are defined as, e.g., [20]:

$$H_\nu(\lambda)=\int_0^\infty \psi(r)J_\nu(r\lambda)rdr, \tag{16}$$

$$\psi(r)=\int_0^\infty H_\nu(\lambda)J_\nu(r\lambda)\lambda d\lambda, \tag{17}$$

where $H_\nu(\lambda)$ is Hankel-transform of the function $\psi(r)$. The index ν indicates the kind of Bessel function $J_v(\lambda r)$ used in the core of the transformation.

In the case of cylindrical surfaces, ensembles of the virtual circular loops are placed on cylindrical surfaces and transform the boundary conditions to integral equations for unknown coordinate-dependent distribution functions:

$$^\infty p_{ij}|_S+\sum_k \int_{-\infty}^{\infty} {}^k f(z_0)\,{}^k p_{ij}(z-z_0)|_S dz_0=\alpha. \tag{18}$$

Equation (18) are solved with the help of the Fourier transformation.

The boundary conditions on the interfaces are usually given in terms of displacements or tractions. The number of necessary loop families corresponds to the number of the boundary conditions on the surface. For instance, in the case of an internal phase boundary between medium I and II there are six sets of boundary conditions: three conditions for displacements and three conditions for stress components. Therefore, the number of virtual loop families is six, but it is enough to use only three types of virtual loops. Three loop distributions are located in medium I and influence medium II and three loop distributions are located in medium II and influence medium I. In the case of a free surface there are three conditions for the components of the traction vector. Therefore the maximum number of virtual loop families is three. In general, the number of boundaries does not influence the number of virtual defect types. As a result, prismatic dislocation loops, twist disclination loops, and radial disclination (Somigliana dislocation) loops may be used as virtual defects in polar angle independent elastic problems of cylindrical symmetry. For defects with angle-dependent elastic fields, e.g., edge dislocations, one can utilize another set of virtual loops having the same angle dependence, e.g., glide dislocation loops, [9,11].

4 Elastic Fields and Energies of Defects in Axisymmetrical Problems

4.1 Spherical Inclusion in a Plate and a Half-Space. Consider a spherical dilatating inclusion located in a plate of thickness t as shown in Fig. 2. The plastic distortion of the inclusion is $\beta^*_{xx}=\beta^*_{yy}=\beta^*_{zz}=\varepsilon^*\delta(\Omega_{\rm sph})$, where $\delta(\Omega_{\rm sph})=\{^{1,\mathbf{r}\in\Omega_{\rm sph}}_{0,\mathbf{r}\notin\Omega_{\rm sph}}\}$, $\Omega_{\rm sph}$ is the area of the inclusion; and $\varepsilon^*=\Delta R/R$ characterizes the relative change of the inclusion radius. The latter may also be interpreted as the misfit strain characterizing crystal lattice mismatch between the inclusion and the surrounding matrix. Referring to the geometry and coordinate system shown in Fig. 2 and assuming that the elastic properties of the inclusion and surrounding matrix are the same, the total displacements $^\infty u_j$ and elastic stresses $^\infty\sigma_{ij}$ of an inclusion in infinite media are, [21]:

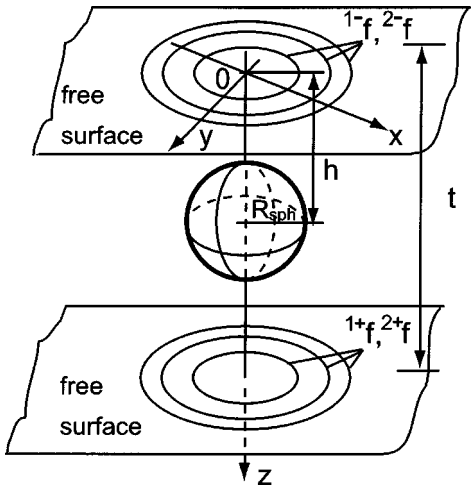

Fig. 2 Spherical inclusion in a plate. Distributions of virtual loop defects are shown on the plate surfaces.

$$
\begin{aligned}
{}^\infty u_r^{(\rm in)}&=\frac{\varepsilon^*(1+\nu)R_{\rm sph}}{3(1-\nu)}\cdot\tilde r;\\
{}^\infty u_\varphi^{(\rm in)}&=0;\\
{}^\infty u_z^{(\rm in)}&=\frac{\varepsilon^*(1+\nu)R_{\rm sph}}{3(1-\nu)}\cdot(\tilde z-\tilde h);\\
{}^\infty u_r^{(\rm out)}&=\frac{\varepsilon^*(1+\nu)R_{\rm sph}}{3(1-\nu)}\cdot\frac{\tilde r}{(\tilde r^2+(\tilde z-\tilde h)^2)^{3/2}};\\
{}^\infty u_\varphi^{(\rm out)}&=0;\\
{}^\infty u_z^{(\rm out)}&=\frac{\varepsilon^*(1+\nu)R_{\rm sph}}{3(1-\nu)}\cdot\frac{\tilde z-\tilde h}{(\tilde r^2+(\tilde z-\tilde h)^2)^{3/2}}\cdot\\
{}^\infty\sigma_{rr}^{(\rm in)}&={}^\infty\sigma_{\varphi\varphi}^{(\rm in)}={}^\infty\sigma_{zz}^{(\rm in)}=-\frac{4G\varepsilon^*(1+\nu)}{3(1-\nu)};\\
{}^\infty\sigma_{rz}^{(\rm in)}&={}^\infty\sigma_{r\varphi}^{(\rm in)}={}^\infty\sigma_{z\varphi}^{(\rm in)}=0;\\
{}^\infty\sigma_{rr}^{(\rm out)}&=\frac{2G\varepsilon^*(1+\nu)}{3(1-\nu)}\left(-\frac{2}{(\tilde r^2+(\tilde z-\tilde h)^2)^{3/2}}+\frac{3(\tilde z-\tilde h)^2}{(\tilde r^2+(\tilde z-\tilde h)^2)^{5/2}}\right);\\
{}^\infty\sigma_{\varphi\varphi}^{(\rm out)}&=\frac{2G\varepsilon^*(1+\nu)}{3(1-\nu)}\cdot\frac{1}{(\tilde r^2+(\tilde z-\tilde h)^2)^{3/2}};\\
{}^\infty\sigma_{zz}^{(\rm out)}&=\frac{2G\varepsilon^*(1+\nu)}{3(1-\nu)}\left(\frac{1}{(\tilde r^2+(\tilde z-\tilde h)^2)^{3/2}}-\frac{3(\tilde z-\tilde h)^2}{(\tilde r^2+(\tilde z-\tilde h)^2)^{5/2}}\right);\\
{}^\infty\sigma_{rz}^{(\rm out)}&=\frac{2G\varepsilon^*(1+\nu)}{3(1-\nu)}\left(\frac{-3\tilde r(\tilde z-\tilde h)}{(\tilde r^2+(\tilde z-\tilde h)^2)^{5/2}}\right);\\
{}^\infty\sigma_{r\varphi}^{(\rm out)}&={}^\infty\sigma_{z\varphi}^{(\rm out)}=0.
\end{aligned}
\tag{19, 20}
$$

Here superscripts (in) and (out) designate the solutions inside and outside the inclusion, respectively. We use normalized variables $\tilde r=r/R_{\rm sph}$, $\tilde z=z/R_{\rm sph}$, $\tilde h=h/R_{\rm sph}$, and $R_{\rm sph}$ is the radius of the spheroid. We work in a cylindrical coordinate system, with coordinates r, φ, and z.

On the free surface of the plate the following boundary conditions for the total stress field $\sigma_{ij}={}^\infty\sigma_{ij}+{}^i\sigma_{ij}$ must hold:

$$\sigma_{jz}|_{\{^{z=t}_{z=0}\}}=0,\quad j=r,\varphi,z. \tag{21}$$

The inclusion stresses ${}^{\infty}\sigma_{zz}$ and ${}^{\infty}\sigma_{rz}$ given by Eqs. (20) contribute to the boundary conditions given in Eqs. (21). To satisfy the boundary conditions we assume that an additional field ${}^{i}\sigma_{ij}$ is generated by the distributions of circular prismatic dislocation loops (ensemble 1) and radial disclination loops (ensemble 2), placed on the free surfaces of the plate (see Fig. 2). These virtual defects possess stress components σ_{zz} and σ_{rz} and a component $\sigma_{\varphi z}$ vanishes. Rewriting Eqs. (21) with the help of the fields of the virtual loops we obtain the integral equations with respect to unknown functions of loop distributions ${}^{1-}f(a)$, ${}^{2-}f(a)$ placed on the surface $z=0$ and ${}^{1+}f(a)$, ${}^{2+}f(a)$ placed on the surface $z=t$:

$$
\begin{aligned}
&{}^{\infty}\sigma_{zz}^{(\mathrm{out})}|_{z=0}+\int_0^{\infty}{}^{1-}f(a)\cdot{}^{1-}\sigma_{zz}|_{z=0}da+\int_0^{\infty}{}^{1+}f(a)\cdot{}^{1+}\sigma_{zz}|_{z=0}da+\int_0^{\infty}{}^{2-}f(a)\cdot{}^{2-}\sigma_{zz}|_{z=0}da+\int_0^{\infty}{}^{2+}f(a)\cdot{}^{2+}\sigma_{zz}|_{z=0}da=0;\\
&{}^{\infty}\sigma_{zz}^{(\mathrm{out})}|_{z=t}+\int_0^{\infty}{}^{1-}f(a)\cdot{}^{1-}\sigma_{zz}|_{z=t}da+\int_0^{\infty}{}^{1+}f(a)\cdot{}^{1+}\sigma_{zz}|_{z=t}da+\int_0^{\infty}{}^{2-}f(a)\cdot{}^{2-}\sigma_{zz}|_{z=t}da+\int_0^{\infty}{}^{2+}f(a)\cdot{}^{2+}\sigma_{zz}|_{z=t}da=0;\\
&{}^{\infty}\sigma_{rz}^{(\mathrm{out})}|_{z=0}+\int_0^{\infty}{}^{1-}f(a)\cdot{}^{1-}\sigma_{rz}|_{z=0}da+\int_0^{\infty}{}^{1+}f(a)\cdot{}^{1+}\sigma_{rz}|_{z=0}da+\int_0^{\infty}{}^{2-}f(a)\cdot{}^{2-}\sigma_{rz}|_{z=0}da+\int_0^{\infty}{}^{2+}f(a)\cdot{}^{2+}\sigma_{rz}|_{z=0}da=0;\\
&{}^{\infty}\sigma_{rz}^{(\mathrm{out})}|_{z=t}+\int_0^{\infty}{}^{1-}f(a)\cdot{}^{1-}\sigma_{rz}|_{z=t}da+\int_0^{\infty}{}^{1+}f(a)\cdot{}^{1+}\sigma_{rz}|_{z=t}da+\int_0^{\infty}{}^{2-}f(a)\cdot{}^{2-}\sigma_{rz}|_{z=t}da+\int_0^{\infty}{}^{2+}f(a)\cdot{}^{2+}\sigma_{rz}|_{z=t}da=0,
\end{aligned}
\tag{22}
$$

where ${}^{k}\sigma_{jz}|_{z=0}$ and ${}^{k}\sigma_{jz}|_{z=t}$ $(k=1+,\ 1-,\ 2+,\ 2-;\ j=z,r)$ are stresses of the virtual loops from ensembles 1 (index 1) and 2 (index 2) on the surfaces $z=0$ (index $-$) and $z=t$ (index $+$).

To proceed further we substitute Eqs. (7), (13) into Eqs. (22), introduce a new variable $\beta=\kappa/a$, change the order of the integration, and transform Eqs. (22) with the help of Hankel-Bessel transformation Eq. (16) with the core $J_0(r\beta)$ for the first pair of equations and $J_1(r\beta)$ for the second pair. Finally, we obtain a system of algebraic equations for functions ${}^{1-}H$, ${}^{1+}H$, ${}^{2-}H$, ${}^{2+}H$, with ${}^{1-,1+}H=\int_0^{\infty}{}^{1-,1+}f(a)J_1(a\beta)ada$ and ${}^{2-,2+}H=\int_0^{\infty}{}^{2-,2+}f(a)J_2(a\beta)a^2da$:

$$
\begin{aligned}
&-\frac{2G\varepsilon^*(1+\nu)R_{\mathrm{sph}}^3}{3(1-\nu)}\beta E_1-\frac{Gb}{2(1-\nu)}\cdot{}^{1-}H-\frac{Gb}{2(1-\nu)}(1+t\beta)E_0\cdot{}^{1+}H-\frac{G\omega}{2(1-\nu)}t\beta E_0\cdot{}^{2+}H=0;\\
&-\frac{2G\varepsilon^*(1+\nu)R_{\mathrm{sph}}^3}{3(1-\nu)}\beta\frac{E_0}{E_1}-\frac{Gb}{2(1-\nu)}(1+t\beta)E_0\cdot{}^{1-}H-\frac{Gb}{2(1-\nu)}\cdot{}^{1+}H+\frac{G\omega}{2(1-\nu)}t\beta E_0\cdot{}^{2-}H=0;\\
&\frac{2G\varepsilon^*(1+\nu)R_{\mathrm{sph}}^3}{3(1-\nu)}\beta E_1+\frac{Gb}{2(1-\nu)}t\beta E_0\cdot{}^{1+}H-\frac{G\omega}{2(1-\nu)}\cdot{}^{2-}H-\frac{G\omega}{2(1-\nu)}(1-t\beta)E_0\cdot{}^{2+}H=0;\\
&-\frac{2G\varepsilon^*(1+\nu)R_{\mathrm{sph}}^3}{3(1-\nu)}\beta\frac{E_0}{E_1}-\frac{Gb}{2(1-\nu)}t\beta E_0\cdot{}^{1-}H-\frac{G\omega}{2(1-\nu)}(1-t\beta)E_0\cdot{}^{2-}H-\frac{G\omega}{2(1-\nu)}{}^{2+}H=0,
\end{aligned}
\tag{23}
$$

where $E_0=\exp[-t\beta]$ and $E_1=\exp[-h\beta]$.

Solving this system we find

$$
\begin{aligned}
{}^{1-}H&=\frac{4\varepsilon^*(1+\nu)R_{\mathrm{sph}}^3}{3b}\cdot\frac{E_1\beta[-1+E_0^2E_1^{-2}(1+2t\beta)-E_0^4E_1^{-2}+E_0^2(1-2t\beta)]}{(1-E_0^2)^2-4E_0^2t^2\beta^2};\\
{}^{1+}H&=\frac{4\varepsilon^*(1+\nu)R_{\mathrm{sph}}^3}{3b}\cdot\frac{E_0^{-1}E_1\beta[-E_0^4-E_0^2E_1^{-2}+E_0^4E_1^{-2}(1-2t\beta)+E_0^2(1+2t\beta)]}{(1-E_0^2)^2-4E_0^2t^2\beta^2};\\
{}^{2-}H&=\frac{4\varepsilon^*(1+\nu)R_{\mathrm{sph}}^3}{3\omega}\cdot\frac{E_1\beta[1+E_0^2E_1^{-2}(1-2t\beta)-E_0^4E_1^{-2}-E_0^2(1+2t\beta)]}{(1-E_0^2)^2-4E_0^2t^2\beta^2};\\
{}^{2+}H&=\frac{4\varepsilon^*(1+\nu)R_{\mathrm{sph}}^3}{3\omega}\cdot\frac{E_0^{-1}E_1\beta[E_0^4-E_0^2E_1^{-2}+E_0^4E_1^{-2}(1+2t\beta)-E_0^2(1-2t\beta)]}{(1-E_0^2)^2-4E_0^2t^2\beta^2}.
\end{aligned}
\tag{24}
$$

Equations (23) can be considered a general system for a problem of cylindrical symmetry for defects in a plate for which ${}^{\infty}\sigma_{zz}$ and ${}^{\infty}\sigma_{rz}$ are the relevant stress components in boundary conditions given by Eqs. (21). To treat the other defect one should rewrite the free terms, which are the Hankel-Bessel transforms of the stresses, i.e., $\int_0^{\infty}J_0(r\beta){}^{\infty}\sigma_{zz}|_{z=0}rdr$, $\int_0^{\infty}J_0(r\beta){}^{\infty}\sigma_{zz}|_{z=t}rdr$, $\int_0^{\infty}J_1(r\beta){}^{\infty}\sigma_{rz}|_{z=0}rdr$, $\int_0^{\infty}J_1(r\beta){}^{\infty}\sigma_{rz}|_{z=t}rdr$, of the considered real defect.

Using the normalized Hankel-Bessel transforms of the distribution functions ${}^{1-}\tilde{H}$, ${}^{1+}\tilde{H}$, ${}^{2-}\tilde{H}$, ${}^{2+}\tilde{H}$, i.e., the second multipliers in the right hand side of Eqs. (24), and the elastic fields of the prismatic dislocation loop given by Eqs. (6) and (7) and radial disclination loop given by Eqs. (12) and (13), one can easily find the additional fields of the displacements ${}^{i}u_j$ and stresses ${}^{i}\sigma_{jk}$ of the virtual surface loops. Finally, the displacements for the dilatating inclusion in the plate are

$$u_r = {}^{\infty}u_r + \frac{\varepsilon^*(1+\nu)R_{\rm sph}^3}{3(1-\nu)}\Bigg[(2\nu-1)\int_0^\infty J_1(r\beta)\Big({}^{1-}\tilde{H}E_2 + {}^{1+}\tilde{H}\frac{E_0}{E_2}\Big)d\beta + \int_0^\infty J_1(r\beta)\Big({}^{1-}\tilde{H}z\beta E_2 + {}^{1+}\tilde{H}(t-z)\beta\frac{E_0}{E_2}\Big)d\beta + 2(1-\nu)\int_0^\infty J_1(r\beta)\Big({}^{2-}\tilde{H}E_2 - {}^{2+}\tilde{H}\frac{E_0}{E_2}\Big)d\beta + \int_0^\infty J_1(r\beta)\Big(-{}^{2-}\tilde{H}z\beta E_2 + {}^{2+}\tilde{H}(t-z)\beta\frac{E_0}{E_2}\Big)d\beta\Bigg];$$

$$u_\varphi = 0;$$

$$u_z = {}^{\infty}u_z + \frac{\varepsilon^*(1+\nu)R_{\rm sph}^3}{3(1-\nu)}\Bigg[2(1-\nu)\int_0^\infty J_0(r\beta)\Big({}^{1-}\tilde{H}E_2 - {}^{1+}\tilde{H}\frac{E_0}{E_2}\Big)d\beta + \int_0^\infty J_0(r\beta)\Big({}^{1-}\tilde{H}z\beta E_2 - {}^{1+}\tilde{H}(t-z)\beta\frac{E_0}{E_2}\Big)d\beta + (2\nu-1)\int_0^\infty J_0(r\beta)\Big({}^{2-}\tilde{H}E_2 + {}^{2+}\tilde{H}\frac{E_0}{E_2}\Big)d\beta + \int_0^\infty J_0(r\beta)\Big(-{}^{2-}\tilde{H}z\beta E_2 - {}^{2+}\tilde{H}(t-z)\beta\frac{E_0}{E_2}\Big)d\beta\Bigg], \tag{25}$$

$$0\leqslant z\leqslant t, \quad R_{\rm sph}\leqslant h\leqslant t-R_{\rm sph},$$

where $E_2=\exp[-z\beta]$. Inside and outside the inclusion ${}^{\infty}u_j = {}^{\infty}u_j^{(in)}$ or ${}^{\infty}u_j = {}^{\infty}u_j^{(\rm out)}$, correspondently.

The corresponding stress field has the following form:

$$\sigma_{rr} = {}^{\infty}\sigma_{rr} + \frac{2G\varepsilon^*(1+\nu)R_{\rm sph}^3}{3(1-\nu)}\Bigg[\frac{1-2\nu}{r}\int_0^\infty J_1(r\beta)\Big({}^{1-}\tilde{H}E_2 + {}^{1+}\tilde{H}\frac{E_0}{E_2}\Big)d\beta + \int_0^\infty J_0(r\beta)\Big({}^{1-}\tilde{H}z\beta E_2 + {}^{1+}\tilde{H}(t-z)\beta\frac{E_0}{E_2}\Big)\beta d\beta - \int_0^\infty J_0(r\beta)\Big({}^{1-}\tilde{H}E_2 + {}^{1+}\tilde{H}\frac{E_0}{E_2}\Big)\beta d\beta - \frac{1}{r}\int_0^\infty J_1(r\beta)\Big({}^{1-}\tilde{H}z\beta E_2 + {}^{1+}\tilde{H}(t-z)\beta\frac{E_0}{E_2}\Big)d\beta + \frac{2(\nu-1)}{r}\int_0^\infty J_1(r\beta)\Big({}^{2-}\tilde{H}E_2 - {}^{2+}\tilde{H}\frac{E_0}{E_2}\Big)d\beta - \int_0^\infty J_0(r\beta)\times\Big({}^{2-}\tilde{H}z\beta E_2 - {}^{2+}\tilde{H}(t-z)\beta\frac{E_0}{E_2}\Big)\beta d\beta + 2\int_0^\infty J_0(r\beta)\times\Big({}^{2-}\tilde{H}E_2 - {}^{2+}\tilde{H}\frac{E_0}{E_2}\Big)\beta d\beta + \frac{1}{r}\int_0^\infty J_1(r\beta)\Big({}^{2-}\tilde{H}z\beta E_2 - {}^{2+}\tilde{H}(t-z)\beta\frac{E_0}{E_2}\Big)d\beta\Bigg];$$

$$\sigma_{\varphi\varphi} = {}^{\infty}\sigma_{\varphi\varphi} + \frac{2G\varepsilon^*(1+\nu)R_{sph}^3}{3(1-\nu)}\Bigg[\frac{2\nu-1}{r}\int_0^\infty J_1(r\beta)\Big({}^{1-}\tilde{H}E_2 + {}^{1+}\tilde{H}\frac{E_0}{E_2}\Big)d\beta - 2\nu\int_0^\infty J_0(r\beta)\Big({}^{1-}\tilde{H}E_2 + {}^{1+}\tilde{H}\frac{E_0}{E_2}\Big)\beta d\beta + \frac{1}{r}\int_0^\infty J_1(r\beta)\Big({}^{1-}\tilde{H}z\beta E_2 + {}^{1+}\tilde{H}(t-z)\beta\frac{E_0}{E_2}\Big)d\beta + \frac{2(1-\nu)}{r}\int_0^\infty J_1(r\beta)\Big({}^{2-}\tilde{H}E_2 - {}^{2+}\tilde{H}\frac{E_0}{E_2}\Big)d\beta + 2\nu\int_0^\infty J_0(r\beta)\Big({}^{2-}\tilde{H}E_2 - {}^{2+}\tilde{H}\frac{E_0}{E_2}\Big)\beta d\beta - \frac{1}{r}\int_0^\infty J_1(r\beta)\times\Big({}^{2-}\tilde{H}z\beta E_2 - {}^{2+}\tilde{H}(t-z)\beta\frac{E_0}{E_2}\Big)\beta d\beta\Bigg];$$

$$\sigma_{zz} = {}^{\infty}\sigma_{zz} - \frac{2G\varepsilon^*(1+\nu)R_{sph}^3}{3(1-\nu)}\Bigg[\int_0^\infty J_0(r\beta)\Big({}^{1-}\tilde{H}E_2 + {}^{1+}\tilde{H}\frac{E_0}{E_2}\Big)\beta d\beta + \int_0^\infty J_0(r\beta)\Big({}^{1-}\tilde{H}z\beta E_2 + {}^{1+}\tilde{H}(t-z)\beta\frac{E_0}{E_2}\Big)\beta d\beta - \int_0^\infty J_0(r\beta)\Big({}^{2-}\tilde{H}z\beta E_2 - {}^{2+}\tilde{H}(t-z)\beta\frac{E_0}{E_2}\Big)\beta d\beta\Bigg]; \tag{26}$$

$$\sigma_{rz} = {}^{\infty}\sigma_{rz} - \frac{2G\varepsilon^*(1+\nu)R_{\rm sph}^3}{3(1-\nu)}\Bigg[\int_0^\infty J_1(r\beta)\Big({}^{1-}\tilde{H}z\beta E_2 - {}^{1+}\tilde{H}(t-z)\beta\frac{E_0}{E_2}\Big)\beta d\beta - \int_0^\infty J_1(r\beta)\Big({}^{2-}\tilde{H}z\beta E_2 + {}^{2+}\tilde{H}(t-z)\beta\frac{E_0}{E_2}\Big)\beta d\beta + \int_0^\infty J_1(r\beta)\Big({}^{2-}\tilde{H}E_2 + {}^{2+}\tilde{H}\frac{E_0}{E_2}\Big)\beta d\beta\Bigg];$$

$$\sigma_{z\varphi} = \sigma_{r\varphi} = 0, \quad 0\leqslant z\leqslant t, \quad R_{\rm sph}\leqslant h\leqslant t-R_{\rm sph}.$$

The stresses given by Eqs. (26) satisfy boundary conditions expressed in Eqs. (21) and the equilibrium equations.

In the limit case when the plate thickness $t\to\infty$ we find the displacements and the stresses of the inclusion in a half-space:

$$u_r = {}^{\infty}u_r + \frac{\varepsilon^*(1+\nu)R_{\rm sph}}{3(1-\nu)}\Bigg[\frac{(3-4\nu)\tilde{r}}{[\tilde{r}^2+(\tilde{z}+\tilde{h})^2]^{3/2}} - \frac{6\tilde{r}\tilde{z}(\tilde{z}+\tilde{h})}{[\tilde{r}^2+(\tilde{z}+\tilde{h})^2]^{5/2}}\Bigg];$$

$$u_\varphi = 0; \tag{27}$$

$$u_z = {}^{\infty}u_z + \frac{\varepsilon^*(1+\nu)R_{\rm sph}}{3(1-\nu)}\Bigg[\frac{(4\nu-3)(\tilde{z}+\tilde{h})}{[\tilde{r}^2+(\tilde{z}+\tilde{h})^2]^{3/2}} - \frac{2\tilde{z}[2(\tilde{z}+\tilde{h})^2-\tilde{r}^2]}{[\tilde{r}^2+(\tilde{z}+\tilde{h})^2]^{5/2}}\Bigg];$$

$$\sigma_{rr} = {}^{\infty}\sigma_{rr} + \frac{2G\varepsilon^*(1+\nu)}{3(1-\nu)}\Bigg[\frac{2(2\nu-3)}{[\tilde{r}^2+(\tilde{z}+\tilde{h})^2]^{3/2}} - \frac{3(\tilde{z}+\tilde{h})^2-12(\tilde{z}+\tilde{h})(3\tilde{z}+\tilde{h})}{[\tilde{r}^2+(\tilde{z}+\tilde{h})^2]^{5/2}} - \frac{30\tilde{z}(\tilde{z}+\tilde{h})^3}{[\tilde{r}^2+(\tilde{z}+\tilde{h})^2]^{7/2}}\Bigg]$$

$$\sigma_{\varphi\varphi} = {}^{\infty}\sigma_{\varphi\varphi} + \frac{2G\varepsilon^*(1+\nu)}{3(1-\nu)}\Bigg[\frac{(3-8\nu)}{[\tilde{r}^2+(\tilde{z}+\tilde{h})^2]^{3/2}} - \frac{6(\tilde{z}+\tilde{h})[(1-2\nu)(\tilde{z}+\tilde{h})-\tilde{h}]}{[\tilde{r}^2+(\tilde{z}+\tilde{h})^2]^{5/2}}\Bigg];$$

$$\sigma_{zz} = {}^{\infty}\sigma_{zz} - \frac{2G\varepsilon^*(1+\nu)}{3(1-\nu)}\Bigg[\frac{1}{[\tilde{r}^2+(\tilde{z}+\tilde{h})^2]^{3/2}} - \frac{3(\tilde{z}+\tilde{h})^2-18\tilde{z}(\tilde{z}+\tilde{h})}{[\tilde{r}^2+(\tilde{z}+\tilde{h})^2]^{5/2}} - \frac{30\tilde{z}(\tilde{z}+\tilde{h})^3}{[\tilde{r}^2+(\tilde{z}+\tilde{h})^2]^{7/2}}\Bigg]; \tag{28}$$

$$\sigma_{rz}={}^{\infty}\sigma_{rz}-\frac{2G\varepsilon^{*}(1+\nu)}{3(1-\nu)}\left[\frac{3\tilde{r}(\tilde{z}+\tilde{h})}{[\tilde{r}^2+(\tilde{z}+\tilde{h})^2]^{5/2}}-\frac{6\tilde{r}\tilde{z}[4(\tilde{z}+\tilde{h})^2-r^2]}{[\tilde{r}^2+(\tilde{z}+\tilde{h})^2]^{7/2}}\right];$$

$$\sigma_{z\varphi}=\sigma_{r\varphi}=0;$$

$$Tr\boldsymbol{\sigma}=\mathrm{Tr}^{\infty}\boldsymbol{\sigma}+\frac{8G\varepsilon^{*}(1+\nu)^2}{3(1-\nu)}\cdot\frac{2(\tilde{z}+\tilde{h})^2-\tilde{r}^2}{[\tilde{r}^2+(\tilde{z}+\tilde{h})^2]^{5/2}},$$

$$0\leqslant z,\quad R_{\mathrm{sph}}\leqslant h.$$

The results of Eqs. (27) and Eqs. (28) can be compared with the general results obtained by Seo and Mura for an ellipsoidal inclusion, [22].

The elastic energy of an arbitrary defect is defined as, [19]

$$E=-\frac{1}{2}\int_V\sigma_{ij}\beta_{ij}^{*}dV', \tag{29}$$

where V is the entire volume of the medium.

Utilizing Eqs. (26) or Eqs. (28) we find the energy of the dilatating inclusion in a plate or in a half-space. The energy of the inclusion in a half-space is

$$E=\frac{8\pi G\varepsilon^{*2}(1+\nu)R_{\mathrm{sph}}^3}{3(1-\nu)}-\frac{4\pi G\varepsilon^{*2}(1+\nu)^2R_{\mathrm{sph}}^3}{9(1-\nu)}\cdot\frac{1}{\tilde{h}^3},$$

$$R_{\mathrm{sph}}\leqslant h. \tag{30}$$

Here the first term is the energy of inclusion in infinite medium and the second term is the interaction energy between inclusion and the free surface.

4.2 Prismatic Dislocation Loop in a Plate and in a Half-Space. Consider an interstitial prismatic dislocation circular loop with radius a_0 that is parallel to the free surfaces of a plate of thickness t (Fig. 3). The center of the loop has coordinates $(0,0,h)$. The plastic distortion of the loop, its total displacements ${}^{\infty}u_i$, and elastic stresses ${}^{\infty}\sigma_{ij}$ in an infinite medium are given by Eqs. (5)–(7) by replacing z with $z-h$. For satisfying the boundary conditions Eqs. (21) we again represent the resulting elastic field as a sum of the loop field in an infinite medium and an additional field due to the distributions of virtual loops. In this problem we use prismatic dislocation loops and radial disclination loops as virtual defects. The solution of this boundary problem is similar to that of the spherical inclusion.

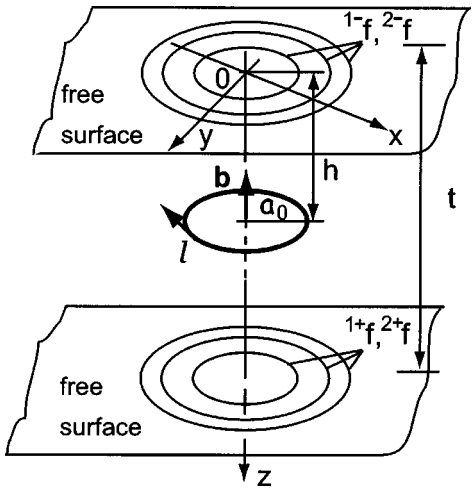

Fig. 3 Prismatic dislocation loop in a plate. Distributions of virtual loop defects are shown on the plate surfaces.

Substituting the free terms in Eqs. (23) for $-(Gb/2(1-\nu))a_0J_1(a_0\beta)(1+h\beta)E_1$, $-(Gb/2(1-\nu))a_0J_1(a_0\beta)(1+(t-h)\beta)E_0/E_1$, $+(Gb/2(1-\nu))a_0J_1(a_0\beta)h\beta E_1$, and $-(Gb/2(1-\nu))a_0J_1(a_0\beta)(t-h)\beta E_0/E_1$ and solving the resulting system we find ${}^{1-}H$, ${}^{1+}H$, ${}^{2-}H$, ${}^{2+}H$ for the case of prismatic loop in a plate. The normalized functions ${}^{1-}\tilde{H}$, ${}^{1+}\tilde{H}$, ${}^{2-}\tilde{H}$, ${}^{2+}\tilde{H}$ appearing in expressions for the displacements given by Eqs. (25) and stresses Eqs. (26) are

$${}^{1-}\tilde{H}=a_0J_1(a_0\beta)E_1\left[\frac{-(1+h\beta)+E_0^2E_1^{-2}(1+2t\beta-h\beta+2t^2\beta^2-2th\beta^2)}{(1-E_0^2)^2-4E_0^2t^2\beta^2}+\frac{E_0^4E_1^{-2}(-1+h\beta)+E_0^2(1-2t\beta+h\beta+2t^2\beta^2-2th\beta^2)}{(1-E_0^2)^2-4E_0^2t^2\beta^2}\right];$$

$${}^{1+}\tilde{H}=-a_0J_1(a_0\beta)\frac{E_1}{E_0}\left[\frac{E_0^4(1+h\beta-t\beta)+E_0^2E_1^{-2}(1+t\beta-h\beta)}{(1-E_0^2)^2-4E_0^2t^2\beta^2}+\frac{E_0^4E_1^{-2}(-1+t\beta+h\beta-2th\beta^2)+E_0^2(1+t\beta+h\beta+2th\beta^2)}{(1-E_0^2)^2-4E_0^2t^2\beta^2}\right]; \tag{31}$$

$${}^{2-}\tilde{H}=a_0J_1(a_0\beta)E_1\left[\frac{h\beta+E_0^2E_1^{-2}(-h\beta-2t^2\beta^2+2th\beta^2)}{(1-E_0^2)^2-4E_0^2t^2\beta^2}+\frac{E_0^4E_1^{-2}h\beta+E_0^2(-h\beta+2t^2\beta^2-2th\beta^2)}{(1-E_0^2)^2-4E_0^2t^2\beta^2}\right];$$

$${}^{2+}\tilde{H}=-a_0J_1(a_0\beta)\frac{E_1}{E_0}\left[\frac{E_0^4(t\beta-h\beta)-E_0^2E_1^{-2}(t\beta-h\beta)}{(1-E_0^2)^2-4E_0^2t^2\beta^2}+\frac{E_0^4E_1^{-2}(-t\beta+h\beta+2th\beta^2)+E_0^2(-t\beta+h\beta-2th\beta^2)}{(1-E_0^2)^2-4E_0^2t^2\beta^2}\right].$$

Finally, the displacements of the interstitial prismatic loop in the plate u_j acquire the form of Eqs. (25) with ${}^{\infty}u_j$ taken from Eqs. (6) and replacing the coefficient $\varepsilon^{*}(1+\nu)R_{\mathrm{sph}}^3/3(1-\nu)$ by $b/4(1-\nu)$.

The stresses due to the prismatic loop in the plate may be found in a similar manner.

In the limit when the plate thickness $t\to\infty$, we obtain the displacements and elastic stresses of the prismatic loop in a half-space:

$$u_r=\frac{b}{4(1-\nu)}\Bigg[(2\nu-1)J^*(1,1;0)+\frac{|z-h|}{a_0}J^*(1,1;1)-(2\nu-1)J^{**}(1,1;0)-\frac{z+h}{a_0}J^{**}(1,1;1)+\frac{4(1-\nu)h}{a_0}J^{**}(1,1;1)-\frac{2zh}{a_0^2}J^{**}(1,1;2)\Bigg];$$

$$u_\varphi=0; \tag{32}$$

$$u_z=\frac{b}{4(1-\nu)}\Bigg[2\,\mathrm{sgn}(z-h)(1-\nu)J^*(1,0;0)+\frac{z-h}{a_0}J^*(1,0;1)-2(1-\nu)J^{**}(1,0;0)-\frac{z+h}{a_0}J^{**}(1,0;1)+\frac{2(2\nu-1)h}{a_0}J^{**}(1,0;1)-\frac{2zh}{a_0^2}J^{**}(1,0;2)\Bigg].$$

$$\sigma_{rr}=\frac{Gb}{2(1-\nu)}\Bigg[\frac{1-2\nu}{r}J^*(1,1;0)+\frac{|z-h|}{a_0^2}J^*(1,0;2)-\frac{1}{a_0}J^*(1,0;1)-\frac{|z-h|}{a_0 r}J^*(1,1;1)-\frac{1-2\nu}{r}J^{**}(1,1;0)-\frac{z-3h}{a_0^2}J^{**}(1,0;2)+\frac{1}{a_0}J^{**}(1,0;1)+\frac{z+h}{a_0 r}J^{**}(1,1;1)-\frac{4(1-\nu)h}{a_0 r}J^{**}(1,1;1)+\frac{2zh}{a_0^2 r}J^{**}(1,1;2)-\frac{2zh}{a_0^3}J^{**}(1,0;3)\Bigg];$$

$$\sigma_{\varphi\varphi}=\frac{Gb}{2(1-\nu)}\Bigg[\frac{2\nu-1}{r}J^*(1,1;0)-\frac{2\nu}{a_0}J^*(1,0;1)+\frac{|z-h|}{a_0 r}J^*(1,1;1)-\frac{2\nu-1}{r}J^{**}(1,1;0)+\frac{2\nu}{a_0}J^{**}(1,0;1)-\frac{z+h}{a_0 r}J^{**}(1,1;1)+\frac{4(1-\nu)h}{a_0 r}J^{**}(1,1;1)+\frac{4\nu h}{a_0^2}J^{**}(1,0;2)-\frac{2zh}{a_0^2 r}J^{**}(1,1;2)\Bigg];$$

$$\sigma_{zz}=\frac{Gb}{2(1-\nu)}\Bigg[-\frac{1}{a_0}J^*(1,0;1)-\frac{|z-h|}{a_0^2}J^*(1,0;2)+\frac{1}{a_0}J^{**}(1,0;1)+\frac{z+h}{a_0^2}J^{**}(1,0;2)+\frac{2zh}{a_0^3}J^{**}(1,0;3)\Bigg]; \tag{33}$$

$$\sigma_{rz}=\frac{Gb}{2(1-\nu)}\Bigg[-\frac{z-h}{a_0^2}J^*(1,1;2)+\frac{z-h}{a_0^2}J^{**}(1,1;2)+\frac{2zh}{a_0^3}J^{**}(1,1;3)\Bigg];$$

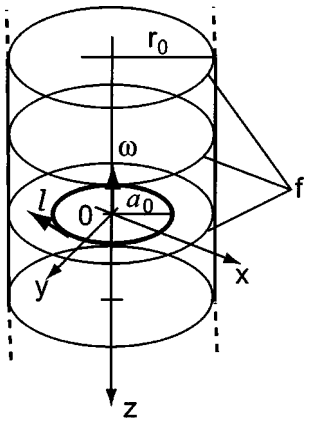

Fig. 4 Twist disclination loop of radius a_0 coaxial to a cylinder. Distribution of virtual twist disclination loops is shown on cylinder surface.

$$\sigma_{z\varphi}=\sigma_{r\varphi}=0,\quad 0\leqslant z.$$

Here $J^*(m,n;p)=\int_0^\infty J_m(\kappa)J_n(\kappa r/a_0)\exp(-\kappa|z-h|/a_0)\kappa^p d\kappa$ and

$$J^{**}(m,n;p)=\int_0^\infty J_m(\kappa)J_n\left(\kappa\frac{r}{a_0}\right)\exp\left(-\kappa\frac{|z+h|}{a_0}\right)\kappa^p d\kappa.$$

The solutions expressed in Eqs. (32) and Eqs. (33) are compact; they satisfy the boundary conditions Eqs. (21) and the equilibrium equations. They may be compared with expressions given by Dundurs, and Salamon [14].

The energy of the prismatic loop in a half-space has the following form:

$$E\cong\frac{Gb^2a_0}{2(1-\nu)}\Bigg[\left(\ln\frac{8a_0}{r_{\mathrm{core}}}-2\right)-\pi\Bigg(J^{**}(1,1;0)\Big|_{r=a_0}^{z=h}+\frac{2h}{a_0}J^{**}(1,1;1)\Big|_{r=a_0}^{z=h}+\frac{2h^2}{a_0^2}J^{**}(1,1;2)\Big|_{r=a_0}^{z=h}\Bigg)\Bigg], \tag{34}$$

where r_{core} is the core cutoff radius of the loop.

The first term in Eq. (34) is the energy of the prismatic dislocation loop in an infinite medium and the second term is the interaction energy between the prismatic loop and the free surface.

4.3 Twist Disclination Loop Coaxial to a Circular Cylinder. Consider a twist disclination loop of radius a_0 placed coaxially in an infinitely long elastic circular cylinder of radius r_0 as shown in Fig. 4; the coordinates of the loop center are (0,0,0). On the free surface of the cylinder, the following boundary conditions for the stress field must be fulfilled:

$$\sigma_{rj}|_{r=r_0}=0,\quad j=r,\varphi,z. \tag{35}$$

The twist disclination loop has the stress component $\sigma_{r\varphi}$ (see Eqs. (10)) contributing to the conditions Eqs. (35). We present the resulting field of the twist disclination loop in the cylinder in the form of Eqs. (15). The additional field ${}^{i}p_{ij}$ is produced by the virtual twist loops distributed in the manner shown in Fig. 4. All virtual loops have the same radius r_0. Then the boundary conditions Eqs. (35) can be rewritten in terms of the distribution function $f(z_0)$ of the virtual twist disclination loops:

$$-\frac{G\omega}{2}\operatorname{sgn}(z)J(2,2;1)\big|_{r=r_0}+\int_{-\infty}^{\infty}f(z_0)\left[-\frac{G\omega}{2}\operatorname{sgn}(z-z_0)\int_0^{\infty}J_2(\kappa)J_2(\kappa)\exp\left[-\frac{|z-z_0|}{r_0}\kappa\right]\kappa d\kappa\right]dz_0=0. \tag{36}$$

Applying the Fourier transformation to Eq. (36), one can find the Fourier transform of the distribution function $\hat{f}$. The Fourier transforms of the elastic fields (i.e., displacements, distortions, strains, and stresses) due to virtual loop distributions are written as

$$^{i}\hat{p}_{ij}(r,s)=\sqrt{2\pi}\hat{f}(s)\hat{p}_{ij}(r,s). \tag{37}$$

Here $\hat{p}_{ij}(r,s)$ are Fourier transforms of the elastic fields of the single virtual twist disclination loop.

Finally, the stresses of the twist disclination loop are

$$\begin{aligned}\sigma_{r\varphi}&=-\frac{G\omega}{2}\operatorname{sgn}(z)\left(J(2,2;1)-\int_0^{\infty}J_2\left(\kappa\frac{r_0}{a_0}\right)J_2\left(\kappa\frac{r}{r_0}\right)\times\exp\left[-\kappa\frac{|z|}{a_0}\right]\kappa d\kappa\right);\\ \sigma_{z\varphi}&=-\frac{G\omega}{2}\left(J(2,1;1)-\frac{a_0}{r_0}\int_0^{\infty}J_2\left(\kappa\frac{r_0}{a_0}\right)J_1\left(\kappa\frac{r}{r_0}\right)\times\exp\left[-\kappa\frac{|z|}{a_0}\right]\kappa d\kappa\right);\\ \sigma_{rr}&=\sigma_{\varphi\varphi}=\sigma_{zz}=\sigma_{rz}=0.\end{aligned} \tag{38}$$

On the basis of Eqs. (29), (8), and (38), the energy of the twist disclination loop in a cylinder can be calculated.

If we take $a_0 \gg r_{core}$ as an approximation, the energy is

$$E=\frac{G\omega^2a_0^3}{2}\left[\left(\ln\frac{8a_0}{r_{\text{core}}}-\frac{8}{3}\right)-\pi\int_0^{\infty}J_2\left(\kappa\frac{r_0}{a_0}\right)J_2\left(\kappa\frac{a_0}{r_0}\right)d\kappa\right]. \tag{39}$$

Here the term in circular brackets is the energy of the twist loop in an infinite medium, and the integral term is the energy of interaction between the loop and cylindrical free surface.

5 Concluding Remarks

The virtual circular loop technique is an effective tool for the solution of the boundary value problems of cylindrical symmetry in the theory of defects. The technique is based on the introduction of virtual circular dislocation-disclination loop distributions for satisfying the boundary conditions on free surfaces and interfaces. The distributions of virtual defects are placed on the planes (in the case of plane free surfaces and interfaces) and on cylindrical surfaces (in the case of cylindrical free surfaces and interfaces). The boundary conditions written in terms of virtual dislocation-disclination loops distributions give integral equations for distribution functions depending on the loop radius (in the case of plane surfaces and interfaces) and for distribution functions depending on the loop coordinate (in the case of cylindrical free surfaces and interfaces). In this work, a prismatic dislocation loop, a twist disclination loop, and a radial disclination loop (Somigliana dislocation) have been used as virtual defects for obtaining the elastic fields of a spherical inclusion and a prismatic dislocation loop in a plate and a half-space, and the elastic fields a twist disclination loop in an elastic cylinder.

In conclusion, we have developed the general technique of circular virtual dislocation-disclination loops for the solution of the axisymmetrical elasticity boundary value problems.

Acknowledgments

This work was supported by the Physics of Solid State Nanostructures Program of the Ministry of Industry and Sciences of Russia.

References

[1] Louat, N., 1962, "Solution of Boundary Problems in Plane Strain," Nature (London), **196**(4859), pp. 1081–1082.
[2] Marcinkowski, M. J., 1979, *Unified Theory of the Mechanical Behavior of Matter*, John Wiley and Sons, New York.
[3] Romanov, A. E., and Vladimirov, V. I., 1981, "Straight Disclinations Near a Free Surface. I. Stress Fields," Phys. Status Solidi A, **63**(1), pp. 109–118.
[4] Vladimirov, V. I., Kolesnikova, A. L., and Romanov, A. E., 1985, "Wedge Disclinations in an Elastic Plate," Phys. Met. Metall., **60**(6), pp. 58–67 (translated from Russian).
[5] Vladimirov, V. I., Romanov, A. E., and Kolesnikova, A. L., 1984, "Flux Line Near Surface of Superconductor," *Physics and Technology of the Treatment of Metal Surface*, Physico-Technical Institute, Leningrad, Russia, pp. 33–38 (in Russian).
[6] Jagannadham, K., and Marcinkowski, M. J., 1980, "Surface Dislocation Model of a Dislocation in a Two Phase Medium," J. Mater. Sci., **15**(2), pp. 709–726.
[7] Gutkin, M. Yu., and Romanov, A. E., 1991, "Straight Edge Dislocation in a Thin Two-Phase Plate. I. Elastic Stress Fields," Phys. Status Solidi A, **125**(1), pp. 107–125.
[8] Belov, A. J., Chamrov, V. A., Indenbom, V. L., and Lothe, J., 1983, "Elastic Fields of Dislocations Piercing the Interface of an Anisotropic Bicrystal," Phys. Status Solidi B, **119**(2), pp. 565–578.
[9] Kolesnikova, A. L., and Romanov, A. E., 1986, "Circular Dislocation-Disclination Loops and Their Application to Boundary Problem Solution in the Theory of Defects," preprint of Physico-Technical Institute, No. 1019, Leningrad, Russia (in Russian).
[10] Kolesnikova, A. L., and Romanov, A. E., 1987, "Edge Dislocation Perpendicular to the Surface of a Plate," Sov. Tech. Phys. Lett., **13**(6), pp. 272–274 (translated from Russian).
[11] Kolesnikova, A. L., and Romanov, A. E., 2003, "Dislocation and Disclination Loops in the Virtual-Defect Method," Phys. Solid State, **45**(9), pp. 1706–1728 (translated from Russian).
[12] Louat, N., and Sadananda, K., 1991, "Some Consequences of the Elastic Interaction of Particles and Free Surfaces," Philos. Mag. A, **64**(1), pp. 213–221.
[13] Salamon, N. J., and Dundurs, J., 1971, "Dislocation Loops in Inhomogeneous Materials," J. Elast., **1**(2), pp. 153–160.
[14] Dundurs, J., and Salamon, N. J., 1972, "Circular Prismatic Dislocation Loop in Two-Phase Material," Phys. Status Solidi B, **50**(1), pp. 125–133.
[15] Salamon, N. J., and Comninou, M., 1979, "The Circular Prismatic Dislocation Loop in an Interface," Philos. Mag. A, **39**(5), pp. 685–691.
[16] Kuo, H. H., and Mura, T., 1972, "Circular Disclinations and Interface Effect," J. Appl. Phys., **43**(10), pp. 3936–3943.
[17] Kuo, H. H., Mura, T., and Dundurs, J., 1973, "Moving Circular Twist Disclination Loop in Inhomogeneous and Two-Phase Materials," Int. J. Eng. Sci., **11**(1), pp. 193–201.
[18] Eason, G., Noble, B., and Sneddon, I. N., 1955, "On Certan Integrals of Lipschitz-Hankel Type Involving Products of Bessel Functions," Philos. Trans. R. Soc. London, Ser. A, **247**(935), pp. 529–551.
[19] Mura, T., 1987, *Micromechanics of Defects in Solids*, Martinus Nijhoff, Boston.
[20] Ufliand, Ya. S., 1967, *Integral Transformations in Problems of Theory of Elasticity*, Nauka, Leningrad, Russia (in Russian).
[21] Theodosiu, C., 1982, *Elastic Models of Crystal Defects*, Springer-Verlag, Berlin.
[22] Seo, K., and Mura, T., 1979, "Elastic Field in a Half-Space due to Ellipsoidal Inclusions With Uniform Dilatation Eigenstrains," ASME J. Appl. Mech., **46**(3), pp. 568–572.

Journal of Applied Mechanics

Brief Notes

A Brief Note is a short paper that presents a specific solution of technical interest in mechanics but which does not necessarily contain new general methods or results. A Brief Note should not exceed 2500 words *or equivalent* (a typical one-column figure or table is equivalent to 250 words; a one line equation to 30 words). Brief Notes will be subject to the usual review procedures prior to publication. After approval such Notes will be published as soon as possible. The Notes should be submitted to the Editor of the JOURNAL OF APPLIED MECHANICS. Discussions on the Brief Notes should be addressed to the Editorial Department, ASME International, Three Park Avenue, New York, NY 10016-5990, or to the Editor of the JOURNAL OF APPLIED MECHANICS. Discussions on Brief Notes appearing in this issue will be accepted until two months after publication. Readers who need more time to prepare a Discussion should request an extension of the deadline from the Editorial Department.

Discontinuities in the Sensitivity Curves of Laminated Cylindrical Shells

Yiska Goldfeld
Research Scientist

Izhak Sheinman
Professor Faculty of Civil Engineering, Technion–Israel Institute of Technology, 32000 Haifa, Israel

The discontinuity in the sensitivity of laminated cylindrical shells is investigated via the initial post-buckling analysis. A general procedure for sensitivity, based on Koiter's parameters and using the Donnell and Sanders shell theories, is developed and used for parametric study of the discontinuity phenomenon. It was found that the discontinuity occurs at points of change of the circumferential wave number. [DOI: 10.1115/1.1748341]

Introduction

Shell-like structures are very sensitive to initial geometry imperfections. One of the main goals, in this field, is to find the various parameters that influence the shell's sensitivity, thereby improving the behavior of the whole structure.

In the present note the characteristic behavior of the imperfection sensitivity is investigated on the aid of Koiter's asymptotic theory, [1]. Koiter showed that the imperfection sensitivity of a structure is related to its initial post-buckling behavior, In other words, it is governed by the immediate slope at the bifurcation point: if the latter is negative, the real buckling load will be less than the theoretical one and the shell is sensitive. Accordingly, fewer parameters are needed for characterizing the sensitivity behavior.

Here, the sensitivity curves of an isotropic and laminated cylindrical shell are studied in terms of the circumferential wave number (CWN). It was found, [2,3], that discontinuities always occur at points where the CWN is changed, and in the present note these points are sought.

Contributed by the Applied Mechanics Division of THE AMERICAN SOCIETY OF MECHANICAL ENGINEERS for publication in the ASME JOURNAL OF APPLIED MECHANICS. Manuscript received by the ASME Applied Mechanics Division, August 12, 2002; final revision, October 25, 2003. Associate Editor: T. E. Triantifyllides.

Governing Equations

The governing equations are derived for the Donnell, [4], and Sanders, [5], kinematic relations, [6]. They are obtained via the variational principle for laminated cylindrical shell. Formulation of the two approaches is based on the displacement components in the axial (u), circumferential (v), and normal (w) directions.

The equilibrium equations read:

$$N_{xx,x}+\frac{N_{x\theta,\theta}}{R}=0$$

$$N_{x\theta,x}+\frac{N_{\theta\theta,\theta}}{R}+\delta\left[\frac{M_{\theta\theta,\theta}}{R^2}+\frac{M_{x\theta,x}}{R}+\frac{N_{\theta\theta}}{R^2}(w_{,\theta}-v)-\zeta\frac{N_{\theta\theta}}{R^2}(w_{,\theta}-v)+\frac{N_{x\theta}}{R}w_{,x}\right]=0$$

$$M_{xx,xx}+\frac{2M_{x\theta,x\theta}}{R}+\frac{M_{\theta\theta,\theta\theta}}{R^2}-\frac{N_{\theta\theta}}{R}+(N_{xx}w_{,x})_{,x}+\frac{(N_{\theta\theta}w_{,\theta})_{,\theta}}{R^2}+\frac{(N_{x\theta}w_{,x})_{,\theta}}{R}+\frac{(N_{x\theta}w_{,\theta})_{,x}}{R}-\delta\left[\frac{(N_{\theta\theta}v)_{,\theta}}{R^2}+\frac{(N_{x\theta}v)_{,x}}{R}\right]+q_{zz}=0 \quad (1)$$

with the following boundary conditions:

$$u \quad \text{or} \quad N_{xx}$$

$$v \quad \text{or} \quad N_{x\theta}+\delta\frac{M_{x\theta}}{R}$$

$$w \quad \text{or} \quad M_{xx,x}+\frac{2M_{x\theta,\theta}}{R}+N_{xx}w_{,x}+\frac{N_{x\theta}w_{,\theta}}{R}-\delta\frac{N_{x\theta}v}{R}$$

$$w_{,x} \quad \text{or} \quad M_{xx} \quad (2)$$

where

$\delta=0$ for Donnell's kinematic relations

$\delta=1$ for Sanders' kinematic relations.

ζ is a correction factor for the second theory ($\delta=1$) in the hydrostatic load case, [7,8]: $\zeta=0$ when the load remains parallel to its original, and $\zeta=1$ when the load remains normal to the deflected reference axis. The difference between the two versions is most pronounced for thin rings.

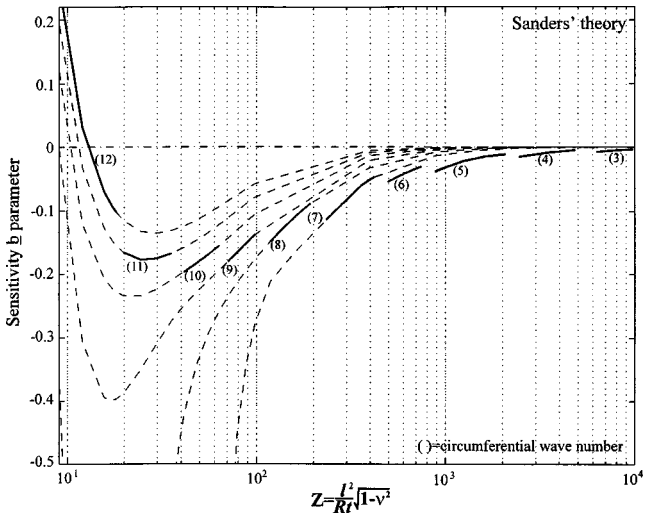

Fig. 1 Sensitivity b parameter versus Batdorf *Z*-parameter for simply supported ($N_{xx}=N_{x\theta}=0$) cylindrical shell under hydrostatic pressure

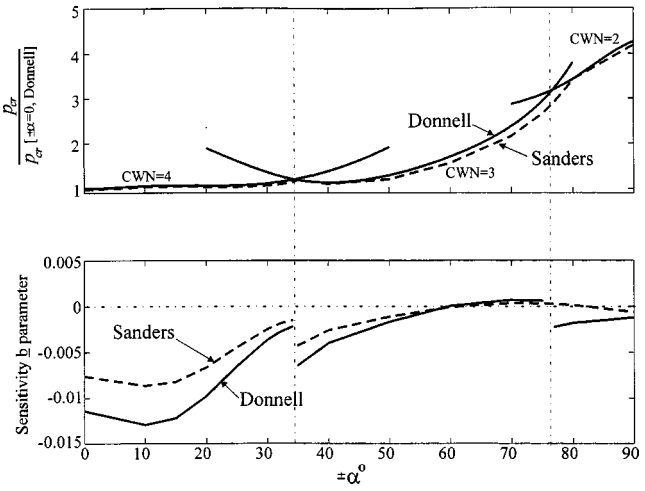

Fig. 3 Hydrostatic buckling load and sensitivity b parameter versus angle ply for simply supported ($N_{xx}=v=0$) cylindrical shell with $l/R=10$

Initial Post-buckling

The imperfection sensitivity parameters determine whether the load increases or decreases after buckling. Accordingly, the displacement, strain and stress vectors are expanded according to the following scheme:

$$\begin{Bmatrix} u \\ v \\ w \end{Bmatrix} = \lambda \begin{Bmatrix} u^{(0)} \\ v^{(0)} \\ w^{(0)} \end{Bmatrix} + \xi \begin{Bmatrix} u^{(1)} \\ v^{(1)} \\ w^{(1)} \end{Bmatrix} + \xi^2 \begin{Bmatrix} u^{(2)} \\ v^{(2)} \\ w^{(2)} \end{Bmatrix} + \ldots . \qquad (3)$$

The load parameter λ representing the deviation from the classical buckling load λ_c, and ξ being the perturbation parameter. The superscripts $^{(0)}$, $^{(1)}$ and $^{(2)}$ denote the prebuckling, buckling, and initial post-buckling states, respectively.

Applying the variational principle following Budiansky and Hutchinson, [9,10], the load parameter is obtained as

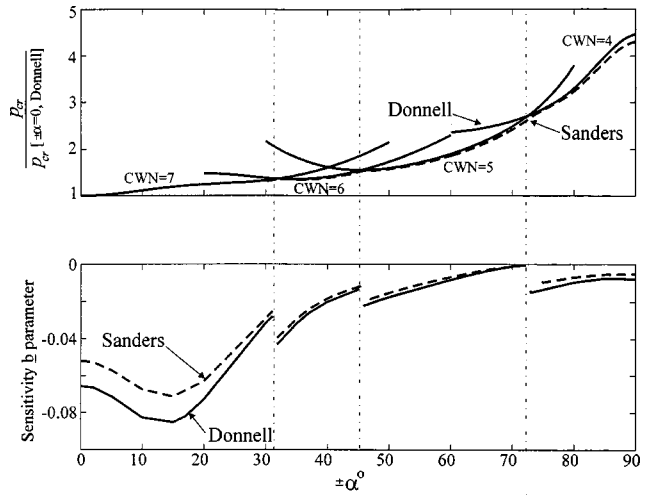

Fig. 2 Hydrostatic buckling load and sensitivity b parameter versus angle ply for simply supported ($N_{xx}=v=0$) cylindrical shell with $l/R=3$

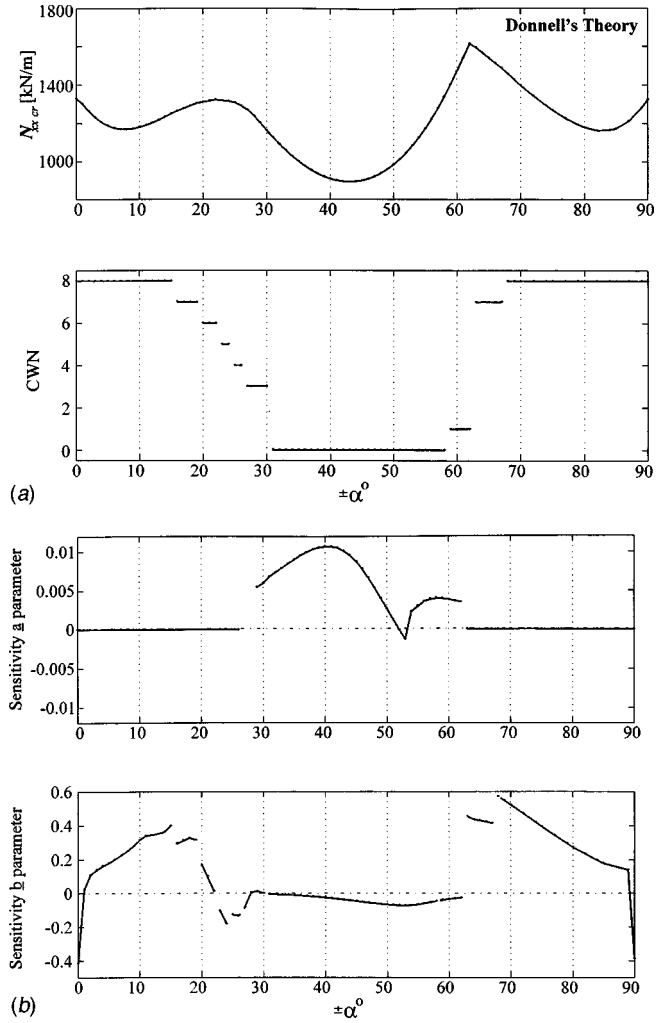

Fig. 4 (*a*) Axial buckling load and circumferential wave number versus angle ply for simply supported ($v=0$) cylindrical shell with $l/R=3$ (*b*) Sensitivity a and b parameters versus angle ply for simply supported ($v=0$) cylindrical shell with $l/R=3$

$$\frac{\lambda}{\lambda_c} = 1 + a\xi + b\xi^2 + \cdots \tag{4}$$

where a and b are known as the Koiter parameters. For isotropic cylindrical shells the coefficient a vanishes due to the periodicity of the buckling mode in the circumferential direction, but for a laminated cylindrical shell under axial compression it was found that it does not. As for the coefficient b a positive value indicates that the shell is insensitive, a negative value measures the level of sensitivity. For the linear prebuckling state Budiansky and Hutchinson derived the well-known formulas:

$$a = -\frac{3\sigma_1 \cdot L_2(u_1)}{2\lambda_c \sigma_0 \cdot L_2(u_1)} \tag{5}$$

$$b = -\frac{\sigma_2 \cdot L_2(u_1) + 2\sigma_1 \cdot L_{11}(u_1, u_2)}{\lambda_c \sigma_0 \cdot L_2(u_1)}. \tag{6}$$

In terms of the displacement components the operator is written as

$$\begin{aligned}\sigma_i \cdot L_{11}(u_j, u_k) = \int_a^b \int_0^{2\pi} \Bigg\{ & N_{xx}^{(i)}[w_{,x}^{(j)} w_{,x}^{(k)}] + N_{\theta\theta}^{(i)} \Bigg[\frac{w_{,\theta}^{(j)} w_{,\theta}^{(k)}}{R^2} \\ & - \frac{\delta}{R^2}(v^{(j)} w_{,\theta}^{(k)} + v^{(k)} w_{,\theta}^{(j)}) \Bigg] \\ & + 2N_{x\theta}^{(i)} \Bigg[\frac{w_{,x}^{(j)} w_{,\theta}^{(k)}}{2R} + \frac{w_{,x}^{(k)} w_{,\theta}^{(j)}}{2R} - \frac{\delta}{2R}(v^{(j)} w_{,x}^{(k)} \\ & + v^{(k)} w_{,x}^{(j)}) \Bigg] \Bigg\} d\theta dx \quad i,j,k \\ = 0,1,2 \end{aligned} \tag{7}$$

The superscripts (i), (j), and (k) denote the relevant state as above.

These equations are solved through expansion of the dependent variables in Fourier series in the circumferential direction and in finite differences in the axial direction. Afterwards the Galerkin procedure is used to minimize the error due to the truncated form of the series.

Parametric Study

In order to locate the discontinuities in the sensitivity curves, one must first find the critical CWN which yields the minimum buckling load; a change in the wave number causes a discontinuity in the slope of the buckling curve. After that, one must calculate Koiter's sensitivity parameters (Eqs. (5) and (6)), using the critical buckling load and its associated wave number, here again, the sensitivity curve is characterized by a discontinuity, but unlike the buckling curves the discontinuity occurs in the curve itself.

For this purpose isotropic cylindrical shells and laminated two-ply ($\pm\alpha$) angle-ply cylindrical shells under hydrostatic and axial loading are considered, reproduced from Sheinman and Goldfeld [6].

Hydrostatic Pressure. In the first case Budiansky and Amazigo's, [11], simply supported isotropic cylindrical shell was reproduced here. At their work there was no consideration to the varying CWN and the sensitivity curve was continuous. Here, see Fig. 1, it is seen that the b parameter is highly dependent on the CWN and acquires a discontinuity on a change in the latter. Thus not only the critical buckling load characterized by transaction of the CWN is dependent on the Batdorf Z-parameter, but the b parameter (Eq. 6) as well. It is worth noting that in this example Donnell's and Sanders' theories yield the same values.

In the second case (laminated cylindrical shell) the buckling load and the b are plotted against the angle-ply ($\pm\alpha$) in Figs. 2 and 3 for $l/R = 3$ and 10, respectively. It is seen that both of them likewise highly dependent on the CWN, and the b parameter acquires a discontinuity as in the first case. It is found that the initial circumferential internal force, $N_{\theta\theta}$ affects it most.

Furthermore, it is seen that the buckling load and the sensitivity are also highly dependent on the angle ply. Regarding the sensitivity level, it is seen that the angle ply has the same effect as a stringer, namely, as it increases so does the buckling load while the sensitivity decreases.

The different between Sanders' and Donnell's shell theories is insignificant for buckling load but still Sanders' yield lower values, and quite pronounced for the b parameter; the more accurate the theory (Sanders), the lower the sensitivity and the buckling load.

Axial Compression. The axial buckling load (applied by setting $N_{xx} = \overline{N}_{xx}$ at one edge), the CWN, the a and b parameters are plotted againset the angle ply ($\pm\alpha$) in Fig. 4 according to Donnell's theory. Here, again, the discontinuities occur at points where the CWN changes, both in the b parameter and in the slope of the buckling-load curve (at $\pm\alpha = 62°$ the transition is most pronounced, from CWN=1 to CWN=7).

Unlike its isotropic counter part, for the laminated cylindrical shell the a parameter does not necessarily vanish: for CWN=0 (axisymmetric buckling mode), the sensitivity is characterized by the asymmetric a parameter and while for CWN≠0 it is characterized by the b parameter.

Conclusions

From the results the following conclusions can be drawn:

- Discontinuities in the b parameter always occur at points where the critical circumferential wave number changes.
- Where the sensitivity a parameter is not zero, the sensitivity b parameter vanishes, and vice versa.
- The angle ply has, in some cases, the same effect as a stringer configuration: as it increases does the buckling load, while the sensitivity decreases.

References

[1] Koiter, W. T., 1945, thesis, Delft, Amsterdam, H. J. Paris; Technical Report AFFDL-TR-70-25, Air Force Flight Dynamics Laboratory, Air Force Systems Command, Wright-Patterson Air Force Base, OH, Feb. 1970 (translated edition).

[2] Arbocz, J., and Hol, J. M. A. M., 1989, "ANILISA—Computational Modules for Koiter's Imperfection Sensitivity Theory," Report LR-582, Faculty of Aerospace Engineering, Delft University of Technology.

[3] Arbocz, J., and Hol, J. M. A. M., 1990, "Koiter's Stability Theory in a Computer-Aided Engineering (CAE) Environment," Int. J. Solids Struct., **26**(9/10), pp. 945–973.

[4] Donnell, L. H., 1933, "Stability of Thin-Walled Tubes Under Torsion," NACA TR-479.

[5] Sanders, J. L., 1963, "Nonlinear Theories for Thin Shells," Quar. J. Appl. Math., **21**(1), pp. 21–36.

[6] Sheinman, I., and Goldfeld, Y., 2001, "Buckling of Laminated Cylindrical Shells in Terms of Different Shell Theories and Formulations," AIAA J., **39**(9), pp. 1773–1781.

[7] Simitses, G. J., 1986, *An Introduction to the Elastic Stability of Structures*, Robert E. Krieger, Malabar, FL.

[8] Sheinman, I., and Tene, Y., 1973, "Potential Energy of a Normal Pressure Field Acting on an Arbitrary Shell," AIAA J., **11**(8), p. 1216.

[9] Budiansky, B., and Hutchinson, J. W., 1964, "Dynamic Buckling of Imperfection Sensitive Structures," *Proceedings XI International Congress on Applied Mechanics*, Munich, pp. 83–106.

[10] Hutchinson, J. W., and Budiansky, B., 1966, "Dynamic Buckling Estimates," AIAA J., **4**(3), pp. 525–530.

[11] Budiansky, B., and Amazigo, J. C., 1968, "Initial Post-buckling of Cylindrical Shells Under Hydrostatic Pressure," J. Math. Phys., **47**, pp. 223–235.

A Combined Fourier Series–Galerkin Method for the Analysis of Functionally Graded Beams

H. Zhu
Graduate Student

B. V. Sankar
Professor,
Fellow ASME

Department of Mechanical and Aerospace Engineering,
University of Florida, Gainesville, FL 32611-6250

The method of Fourier analysis is combined with the Galerkin method for solving the two-dimensional elasticity equations for a functionally graded beam subjected to transverse loads. The variation of the Young's modulus through the thickness is given by a polynomial in the thickness coordinate and the Poisson's ratio is assumed to be constant. The Fourier series method is used to reduce the partial differential equations to a pair of ordinary differential equations, which are solved using the Galerkin method. Results for bending stresses and transverse shear stresses in various beams show excellent agreement with available exact solutions. The method will be useful in analyzing functionally graded structures with arbitrary variation of properties.
[DOI: 10.1115/1.1751184]

Introduction

Functionally graded materials (FGMs) possess properties that vary gradually with location within the material. FGMs differ from composites wherein the volume fraction of the inclusion is uniform throughout the composite. The closest analogies of FGMs are laminated composites, but the latter possess distinct interfaces across which properties change abruptly. Suresh and Mortensen [1] provide an excellent introduction to the fundamentals of FGMs. As the use of FGMs increases, for example, in aerospace, automotive, and biomedical applications, new methodologies have to be developed to characterize FGMs, and also to design and analyze structural components made of these materials. For example, Pindera and Dunn [2] developed a higher order micromechanical theory for FGMs (HOTFGM) that explicitly couples the local and global effects. Delale and Erdogan [3] derived the crack-tip stress fields for an inhomogeneous cracked body with constant Poisson ratio and with a shear modulus variation given by $\mu = \mu_0 e^{(\alpha x + \beta y)}$. In general the analytical methods should be such that they can be incorporated into available methods with the least amount of modifications, if any. One such problem is that of response of FGMs to thermomechanical loads. Although FGMs are highly heterogeneous, it will be useful to idealize them as continua with properties changing smoothly with respect to the spatial coordinates. This will enable obtaining closed-form solutions to some fundamental solid mechanics problems, and also will help in developing finite element models of the structures made of FGMs.

In a series of papers Sankar and his co-workers, [4–7], reported analytical methods for the thermomechanical and contact analysis of FGM beams and also for sandwich beams with FG cores. In these studies the thermomechanical properties of the FGM were assumed to vary through the thickness in an exponential fashion, e.g., $E(z)=E_0 e^{\lambda z}$. The material was assumed to be isotropic at every point and the Poisson's ratio was assumed to be constant everywhere. This assumption enabled them to obtain analytical solutions using Fourier expansion methods. However, in practice the properties of FGM will vary in an arbitrary fashion and the aforementioned solution technique may not be useful. In the present paper we assume that the property variation through the thickness can be expressed in the form of a polynomial in the z coordinate. We demonstrate the application of both Fourier series and Galerkin methods for obtaining an approximate solution for displacements and stresses in a FG beam. The solutions are compared with available exact solutions and the agreement is found to be very good.

Contributed by the Applied Mechanics Division of THE AMERICAN SOCIETY OF MECHANICAL ENGINEERS for publication in the ASME JOURNAL OF APPLIED MECHANICS. Manuscript received by the ASME Applied Mechanics Division, July 1, 2002, final revision, December 5, 2003. Associate Editor: R. R. C. Benson.

Analysis

Consider a functionally graded (FG) beam of height h and length L as shown in Fig. 1. The beam and the loading are symmetric about the center line $x=L/2$. The beam is assumed to be in a state of plane strain normal to the x-z plane.

The transverse load $p_z(x)$ acting on the beam can be represented by a Fourier series as

$$\sigma_{zz}(x,0) = -p_z(x) = -p_n \sin \xi x \tag{1a}$$

where $\xi = n\pi/L$, $n=1,3,5\ldots$ and Fourier coefficients p_n are given by

$$p_n = \frac{2}{L}\int_0^L p_z(x)\sin \xi x dx. \tag{1b}$$

We will demonstrate the solution method for the load $p_n \sin \xi x$ in this note. Then the traction boundary condition on the bottom surface of the beam is given by

$$\sigma_{zz}(x,0) = -p_n \sin \xi x, \quad \tau_{xz} = 0. \tag{1c}$$

Since n is odd, the load is also symmetric about the centerline. The boundary conditions are similar to that of a simply supported beam, but the actual boundary conditions will become clear later.

We assume that the FGM is isotropic at every point and the Poisson's ratio v is a constant through the thickness. The variation of Young's modulus E in the thickness direction is given by a polynomial in z as

$$E(z) = E_0\left(a_1 + a_2\left(\frac{z}{h}\right) + a_3\left(\frac{z}{h}\right)^2 + a_4\left(\frac{z}{h}\right)^3\right) \tag{2}$$

where E_0 is the Young's modulus at $z=0$, and a_1, a_2, a_3, and a_4 are material constants.

The differential equations of equilibrium are

$$\frac{\partial \sigma_{xx}}{\partial x} + \frac{\partial \tau_{xz}}{\partial z} = 0$$
$$\frac{\partial \tau_{xz}}{\partial x} + \frac{\partial \sigma_{zz}}{\partial z} = 0. \tag{3}$$

Assuming that the principal material directions coincide with the x and z-axes, the constitutive equations are

$$\begin{Bmatrix} \sigma_{xx} \\ \sigma_{zz} \\ \tau_{xz} \end{Bmatrix} = \begin{bmatrix} c_{11} & c_{13} & 0 \\ c_{13} & c_{33} & 0 \\ 0 & 0 & c_{55} \end{bmatrix} \begin{Bmatrix} \varepsilon_{xx} \\ \varepsilon_{zz} \\ \gamma_{xz} \end{Bmatrix} \tag{4}$$

or

$$\sigma = C\varepsilon.$$

The elasticity matrix $[C]$ is related to material constants by

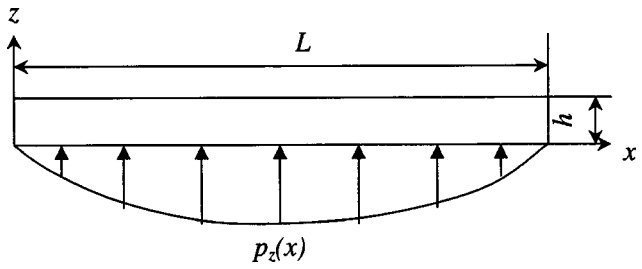

Fig. 1 A FGM beam subjected to symmetric transverse loading

$$C^{-1}=\begin{pmatrix} \frac{1}{E_{11}} & \frac{-\nu_{13}}{E_{11}} & 0 \\ \frac{-\nu_{13}}{E_{11}} & \frac{1}{E_{33}} & 0 \\ 0 & 0 & \frac{1}{G_{13}} \end{pmatrix}. \tag{5}$$

We assume the solution for displacements as

$$\begin{aligned} u(x,z)&=U(z)\cos\xi x \\ w(x,z)&=W(z)\sin\xi x \end{aligned} \tag{6}$$

Substituting Eq. (6) into (4), we obtain

$$\begin{pmatrix} \sigma_{xx} \\ \sigma_{zz} \\ \tau_{xz} \end{pmatrix}=\begin{pmatrix} c_{11} & c_{13} & 0 \\ c_{13} & c_{33} & 0 \\ 0 & 0 & G \end{pmatrix}\begin{pmatrix} -\xi U\sin\xi x \\ W'\sin\xi x \\ (U'+\xi W)\cos\xi x \end{pmatrix}. \tag{7}$$

The prime ($'$) after a variable denotes differentiation with respect to z. With Eqs. (6) and (7), one can state that the boundary conditions of the beam at $x=0$ and $x=L$ are $w(0,z)=w(L,z)=0$ and $\sigma_{xx}(0,z)=\sigma_{xx}(L,z)=0$, which corresponds to simply support conditions in the context of beam theory. Equations (7) can be written as

$$\begin{aligned} \begin{pmatrix} \sigma_{xx} \\ \sigma_{zz} \end{pmatrix}&=\begin{pmatrix} S_x \\ S_z \end{pmatrix}\sin\xi x \\ \tau_{xz}&=T_z\cos\xi x \end{aligned} \tag{8}$$

where

$$\begin{aligned} \begin{pmatrix} S_x \\ S_z \end{pmatrix}&=\begin{pmatrix} c_{11} & c_{13} \\ c_{13} & c_{33} \end{pmatrix}\begin{pmatrix} -\xi U \\ W' \end{pmatrix} \\ T_z&=G(U'+\xi W). \end{aligned} \tag{9}$$

Substituting for σ_{xx}, σ_{zz}, τ_{xz} from Eqs. (7) into equilibrium Eqs. (3), we obtain a set of ordinary differential equations in $U(z)$ and $W(z)$:

$$\begin{aligned} \xi S_x+T_z'&=0 \\ S_z'-T_z\xi&=0. \end{aligned} \tag{10}$$

In order to solve Eqs. (10) we employ the Galerkin method. We assume solutions of the form

$$\begin{aligned} U(z)&=c_1\phi_1(z)+c_2\phi_2(z)+c_3\phi_3(z)+c_4\phi_4(z) \\ W(z)&=b_1\phi_1(z)+b_2\phi_2(z)+b_3\phi_3(z)+b_4\phi_4(z) \end{aligned} \tag{11}$$

where ϕ_s are basis functions, and b_s and c_s are coefficients to be determined. For simplicity we choose 1, z, z^2, z^3 as basis functions. That is,

$$\phi_1(z)=1; \quad \phi_2(z)=z; \quad \phi_3(z)=z^2; \quad \phi_4(z)=z^3. \tag{12}$$

Substituting the approximate solution in the governing differential equations, we obtain the residuals. The residuals are minimized by equating their weighted averages to zero:

$$\begin{aligned} \int_0^h(\xi S_x+T_z')\phi_i(z)dz=0, \quad i=1,4 \\ \int_0^h(S_z'-T_z\xi)\phi_i(z)dz=0, \quad i=1,4. \end{aligned} \tag{13}$$

Using integration by parts we can rewrite Eqs. (13) as

$$\begin{aligned} &\int_0^h\phi_i\xi S_x dz+T_z(h)\phi_i(h)-T_z(0)\phi_i(0)-\int_0^h T_z\phi_i'dz=0 \\ &\qquad i=1,4 \\ &\int_0^h S_z\phi_i'dz+\int_0^h T_z\xi\phi_i dz-(S_z(h)\phi_i(h)-S_z(0)\phi_i(0))=0 \\ &\qquad i=1,4. \end{aligned} \tag{14}$$

Substituting for $S_x(z)$, $S_z(z)$, and $T_z(z)$ from Eqs. (9) into (14) and using the approximate solution for $U(z)$ and $W(z)$ in (11) we obtain

$$\begin{pmatrix} K_{ij}^{(1)} & K_{ij}^{(2)} \\ K_{ij}^{(3)} & K_{ij}^{(4)} \end{pmatrix}\begin{pmatrix} b \\ c \end{pmatrix}=\begin{pmatrix} f_i^{(1)} \\ f_i^{(2)} \end{pmatrix} \tag{15}$$

where

$$\begin{aligned} K_{ij}^{(1)}&=\xi\int_0^h c_{13}\phi_i\phi_j'dz-\xi\int_0^h G\phi_i'\phi_j dz \\ K_{ij}^{(2)}&=-\int_0^h G\phi_i'\phi_j'dz-\xi^2\int_0^h c_{11}\phi_i\phi_j dz \\ K_{ij}^{(3)}&=-\xi^2\int_0^h G\phi_i\phi_j dz-\int_0^h c_{33}\phi_i'\phi_j'dz \\ K_{ij}^{(4)}&=\xi\int_0^h c_{13}\phi_i'\phi_j dz-\xi\int_0^h G\phi_i\phi_j'dz \\ f_i^{(1)}&=\phi_i(0)T_z(0)-\phi_i(h)T_z(h) \\ f_i^{(2)}&=\phi_i(0)S_z(0)-\phi_i(h)S_z(h) \\ \begin{pmatrix} b \\ c \end{pmatrix}^T&=(b_1\ b_2\ b_3\ b_4\ c_1\ c_2\ c_3\ c_4). \end{aligned} \tag{16}$$

Traction boundary conditions on the top and bottom surfaces of beam are

$$\begin{aligned} \tau_{xz}(x,0)&=0 \\ \tau_{xz}(x,h)&=0 \\ \sigma_{zz}(x,0)&=-p_n\sin\xi x \\ \sigma_{zz}(x,h)&=0. \end{aligned} \tag{17}$$

In terms of S_z and T_z, the boundary conditions take the form

$$\begin{aligned} T_z(0)=T_z(h)&=0 \\ S_z(0)&=-p_n \\ S_z(h)&=0. \end{aligned} \tag{18}$$

Equations (18) can be used to evaluate $f_i^{(1)}$ and $f_i^{(2)}$ in (16) which are the right-hand side of Eq. (15). Solving Eq. (15), we obtain the solutions for the coefficients b_i and c_i, which yield the approximate solutions for $U(z)$ and $W(z)$ in (11). Once $U(z)$ and $W(z)$ are determined, stress at any point can be computed using Eqs. (8) and (9).

Table 1 The coefficients of the cubic polynomial for $E(z)$. $E_0 = 10$ GPa and beam thickness $h = 10$ mm.

E_h/E_0	a_1	a_2	a_3	a_4
10	1	2.9577	−0.7889	6.7982
0.1	1	−2.1845	1.9844	−0.6996

Results and Discussion

In order to verify the present method examples from [1] are used. In these examples the variation of Young's modulus is assumed to be of the form $E = E_0 e^{\lambda z/h}$. The same variation can be approximated by the polynomial form given in Eq. (2). The coefficients of the polynomial, $a_1, \ldots a_4$ were determined by using the least squares curve fitting. Two types of beams were considered, and the variation of Young's modulus in these beams are given by $E_h/E_0 = 10$ and $E_h/E_0 = 0.1$, respectively. In the first beam the load is applied on the softer face of the beam and in the second on the harder side. In both cases E_0 was taken as 1 GPa and $\nu = 0.25$. The thickness of the beam is $h = 10$ mm. The coefficients of the cubic polynomial for $E(z)$ are given in Table 1.

The results for the normalized bending stress for various values of $\xi h = n\pi/L$ are presented in Figs. 2 and 3. It should be noted that smaller values of ξh represent slender beams or beams subjected to more uniformly distributed loads, whereas larger values of ξh indicate short stubby beams or beams subjected to concentrated loads. From Figs. 2 and 3 it can be noted that the results of the Galerkin method agree very well with the exact solution, [1]. The difference of two solutions is imperceptible. The normalized stresses are less than 1 when the loads are applied to the softer face (Fig. 2, $E_h/E_0 = 10$). On the other hand, the normalized stresses are much greater than 1 when the loads are applied to the harder face (Fig. 3, $E_h/E_0 = 0.1$). One can also note the approximate location of the neutral axis for the two beams in these figures.

The transverse shear stresses are plotted in Figs. 4 and 5. The approximate solution also agrees well with exact solitions. The shear stresses attain the maximum value at the neutral axis. The normalized maximum shear stress values are above the conventional 1.5, when the loads are applied on the harder surface of the beam (Fig. 5), but fall below 1.5, in some cases when the loads are applied to the soft side (Fig. 4).

The present method can be applied to functionally graded structures with arbitrary variation of properties and also can be extended to platelike structures and sandwich construction wherein the core material and/or the face sheets are functionally graded.

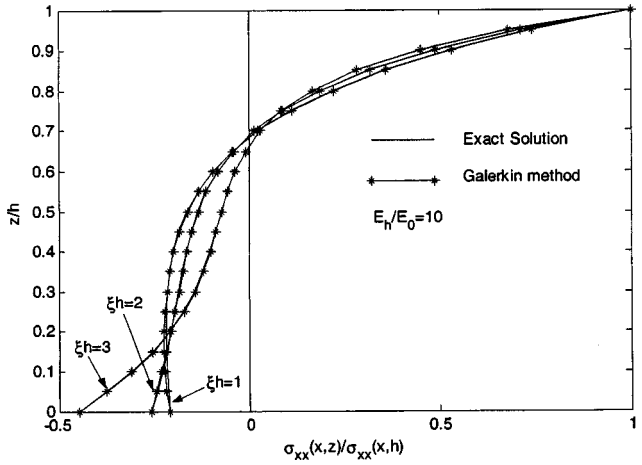

Fig. 2 Normalized axial stress σ_{xx} through the thickness of FGM beam for $E_h = 10\,E_0$. The exact solution and that of Galerkin method are indistinguishable.

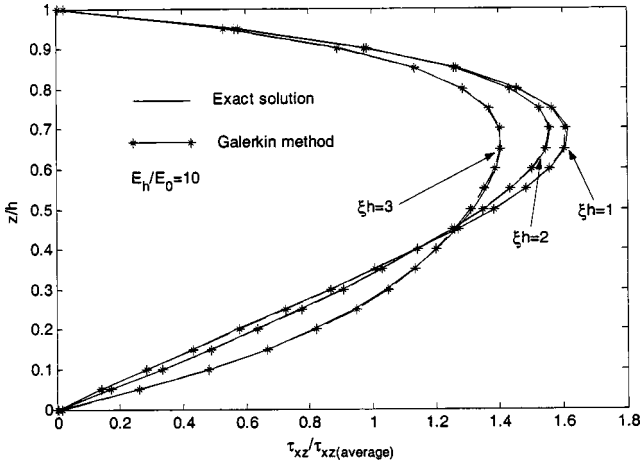

Fig. 4 Transverse shear stress through the thickness of FGM beam for $E_h = 10\,E_0$. The exact solution and that of Galerkin method are indistinguishable.

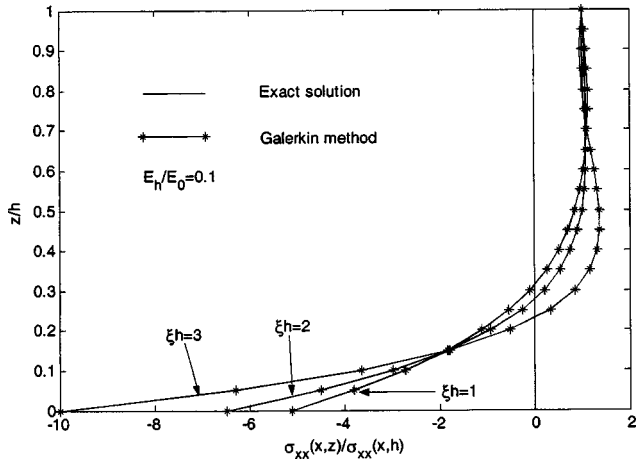

Fig. 3 Normalized axial stress σ_{xx} through the thickness of FGM beam for $E_h = 0.1\,E_0$. The exact solution and that of Galerkin method are indistinguishable.

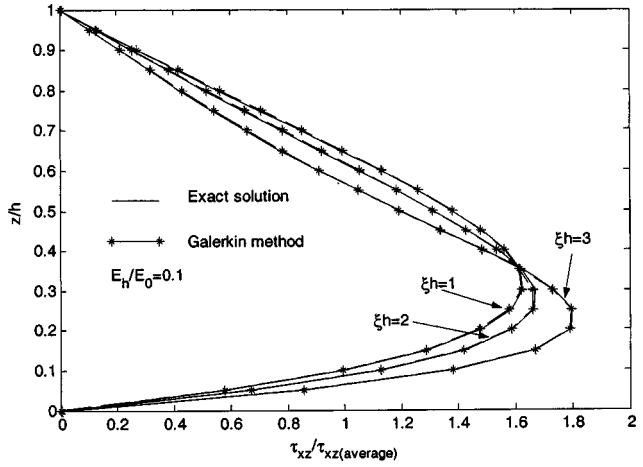

Fig. 5 Transverse shear stress through the thickness of FGM beam for $E_h = 0.1\,E_0$. The exact solution and that of Galerkin method are indistinguishable.

Acknowledgment

This research has been supported by the NASA Langley Research Center Grant NAG-1-1887. The authors are thankful to Dr. D. R. Ambur, Head, Mechanics & Durability Branch, for many suggestions and constant encouragement.

References

[1] Suresh, S., and Mortensen, A., 1998, *Fundamentals of Functionally Graded Materials*, IOM Communications Ltd., London.
[2] Pindera, M.-J., and Dunn, P., 1995, "An Evaluation of Coupled Microstructural Approach for the Analysis of Functionally Graded Composites via the Finite Element Method," NASA CR 195455, Lewis Research Center, Cleveland, OH.
[3] Delale, F., and Erdogan, F., 1983, "The Crack Problem for a Nonhomogeneous Plane," ASME J. Appl. Mech., **50**, pp. 609–614.
[4] Sankar, B. V., 2001, "An Elasticity Solution for Functionally Graded Beams," Compos. Sci. Technol., **61**, pp. 689–696.
[5] Sankar, B. V., and Tzeng, J. T., 2002, "Thermal Stresses in Functionally Graded Beams," AIAA J., **40**(6), pp. 1228–1232.
[6] Venkataraman, S., and Sankar, B. V., 2001, "Analysis of Sandwich Beams With Functionally Graded Core," AIAA Paper 2001-1281.
[7] Apetre, N. A., Sankar, B. V., and Venkataraman, S., 2002, "Indentation of a Sandwich Beam With Functionally Graded Core," AIAA Paper 2002-1683.

Fracture of Brittle Microbeams

M. Ostoja-Starzewski
Department of Mechanical Engineering, McGill University, 817 Sherbrooke Street West Montreal, PQ H3A 2K6, Canada
e-mail: martin.ostoja@mcgill.ca
Fellow ASME

The random polycrystalline microstructure of microbeams necessitates a reexamination of the crack driving force G stemming from the Griffith fracture criterion. It is found that, in the case of dead-load conditions, G computed by straightforward averaging of the spatially random elastic modulus E is lower than that obtained by correct ensemble averaging of the stored elastic energy. This result holds for both Euler-Bernoulli and Timoshenko models of micro-beams. However, under fixed-grip conditions G is to be computed by a direct ensemble averaging of E. It turns out that these two cases provide bounds on G under mixed loading. Furthermore, crack stability is shown to involve a stochastic competition between potential and surface energies, whose weak randomness leads to a relatively stronger randomness of the critical crack length. [DOI: 10.1115/1.1651091]

Background

According to Griffith's theory, [1], of elastic-brittle solids, the strain energy release rate G is given by

$$G=\frac{\partial W}{\partial A}-\frac{\partial U}{\partial A}=2\gamma \tag{1}$$

where A is the crack surface area formed, W is the work performed by the applied loads, U is the elastic strain energy, and γ is the energy required to form a unit of new material surface (e.g., [2]). The material parameter γ is conventionally taken as constant, but, given the presence of a randomly microheterogeneous material structure, its random field nature is sometimes considered explicitly (e.g., [3,4]). If one recognizes, however, that the random material structure also affects the elastic moduli, the computation of the left-hand side of (1) needs to be reexamined as well. Furthermore, randomness of both potential and surface energies will result in a stochastic, rather than deterministic, crack stability criterion. These issues are studied here in the case of cracking involving a beam-type configuration.

Dead-Load Conditions

This case of constant load implies that the force is nonrandom, but the kinematic variable is random. Now, only the second term in (1) remains, and, assuming an Euler-Bernoulli beam, the strain energy is

$$U(a)=\int_0^a \frac{M^2}{2IE}\,dx, \tag{2}$$

where a is crack length, M is bending moment, I is beam's moment of inertia, and E is elastic modulus. Henceforth, we simply work with $a=A/B$, where B is the constant beam (and crack) width. In view of Clapeyron's theorem, the strain energy release rate may be written as

$$G=\frac{\partial U}{B\partial a}. \tag{3}$$

Now, if the beam's material is random, E is a random field parametrized by x, which we can write as a sum of a constant mean $\langle E\rangle$ and a zero-mean fluctuation $E'(x)$

$$E(\omega,x)=\langle E\rangle+E'(\omega,x)\qquad \omega\in\Omega, \tag{4}$$

where Ω is a sample space. Take $E'(x,\omega)$ as a wide-sense stationary random field. A random material is thus defined as an ensemble $\mathcal{B}=\{B(\omega);\omega\in\Omega\}=\{E(\omega,x);\omega\in\Omega,x\in[0,a]\}$. Here, and in the following, we explicitly show the dependence on ω, whenever we wish to indicate the random nature of a given quantity prior to ensemble averaging.

On the physical side, the need to consider randomness of E arises when the representative volume element (RVE) of continuum mechanics cannot be safely applied to the actual beam. Among others, problems of this type are driven by the challenges of micro and nanotechnology; see, e.g., ([5,6]). Such a case is shown in Fig. 1, where a so-called *microbeam* is so thin that its lateral dimension L—i.e., the very one defining its Young's modulus—begins to be comparable to the crystal size d. The "comparable" aspect is described by a mesoscale L/d, and the RVE is to be replaced by a statistical volume element (SVE). The finite-size scaling laws of the SVE—i.e., its approach to the RVE with $L/d\to\infty$—were recently reviewed in [7].

It follows from (1) that U is a random integral, such that, for each and every realization $\omega\in\Omega$, we should consider

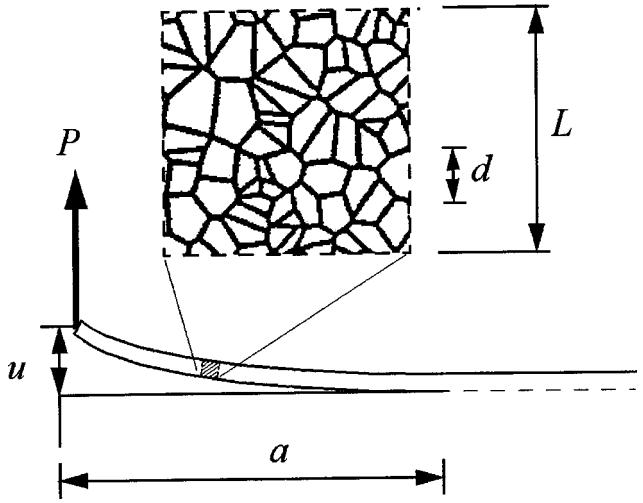

Fig. 1 Fracture of a microbeam of thickness *L* off a substrate. A statistical volume element (SVE) imposed by the random microheterogeneous structure characterized by scale *d* is shown.

Contributed by the Applied Mechanics Division of THE AMERICAN SOCIETY OF MECHANICAL ENGINEERS for publication in the ASME JOURNAL OF APPLIED MECHANICS. Manuscript received by the ASME Applied Mechanics Division, Dec. 16, 2002; final revision, Aug. 1, 2003. Associate Editor: M.-J. Pindera.

$$U(a,E(\omega))=\int_0^a \frac{M^2dx}{2IE(\omega,x)}. \tag{5}$$

Upon ensemble averaging, this leads to an average energy

$$\langle U(a,E)\rangle=\left\langle \int_0^a \frac{M^2dx}{2I[\langle E\rangle+E'(\omega,x)]}\right\rangle. \tag{6}$$

In the conventional formulation of deterministic fracture mechanics, random microscale heterogeneities $E'(x,\omega)$ are disregarded, and (5) is evaluated by simply replacing the denominator by $\langle E\rangle$, so that

$$U(a,\langle E\rangle)=\int_0^a \frac{M^2dx}{2I\langle E\rangle}. \tag{7}$$

Clearly, this amounts to postulating that the response of an idealized homogeneous material is equal to that of a random one on average. Therefore, we are interested in making a statement about $\langle U(a,E)\rangle$ versus $U(a,\langle E\rangle)$, and about $\langle G(E)\rangle$ versus $G(\langle E\rangle)$.

First, note that, since the random process E is positive-valued almost surely (i.e., with probability one), Jensen's inequality, [8], yields an inequality between harmonic and arithmetic averages of the random variable $E(\omega)$

$$\frac{1}{\langle E\rangle}\leqslant\left\langle\frac{1}{E}\right\rangle, \tag{8}$$

whereby the x-dependence is immaterial in view of the assumed wide-sense stationarity of field E. With (6) and (7), this implies that

$$U(a,\langle E\rangle)=\int_0^a \frac{M^2dx}{2I\langle E\rangle}\leqslant\int_0^a \frac{M^2}{2I}\left\langle\frac{1}{E}\right\rangle dx$$

$$=\left\langle \int_0^a \frac{M^2dx}{2IE(\omega,x)}\right\rangle=\langle U(a,E)\rangle, \tag{9}$$

since the conditions required by Fubini's theorem, [8] are met.

Now, if we define the strain energy release rate $G(a,\langle E\rangle)$ in a hypothetical material specified by $\langle E\rangle$, and the strain energy release rate $\langle G(a,E)\rangle$ properly ensemble averaged in the random material $\{E(\omega,x);\omega\in\Omega,x\in[0,a]\}$

$$G(a,\langle E\rangle)=\frac{\partial U(a,\langle E\rangle)}{B\partial a}\quad \langle G(a,E)\rangle=\frac{\partial\langle U(a,E)\rangle}{B\partial a}, \tag{10}$$

and note that the side condition is the same in both cases

$$U(a,\langle E\rangle)|_{a=0}=0\quad \langle U(a,E)\rangle|_{a=0}=0, \tag{11}$$

we obtain

$$G(a,\langle E\rangle)\leqslant\langle G(a,E)\rangle. \tag{12}$$

This provides a formula for the ensemble average G under dead-load conditions using deterministic fracture mechanics for Euler-Bernoulli beams made of random materials.

Another derivation of this is obtained by first introducing a complementary energy through an application of a *random Legendre transformation*, [9],

$$U^*(a,E(\omega))=M\cdot\theta-U(a,E(\omega))\quad \omega\in\Omega, \tag{13}$$

where θ is the angle of twist conjugate to M, such that

$$U^*(a,E(\omega))=\int_0^a \frac{IE(\omega)}{2}\theta^2dx. \tag{14}$$

It then follows from (8) that

$$U^*(a,\langle E(\omega)\rangle)=\int_0^a \frac{I\langle E(\omega)\rangle}{2}\theta^2dx\geqslant\int_0^a \frac{I\langle E^{-1}(\omega)\rangle^{-1}}{2}\theta^2dx$$

$$=U^*(a,\langle E^{-1}(\omega)\rangle^{-1}), \tag{15}$$

which, with the side condition

$$U^*(a,\langle E\rangle)|_{a=0}=0\quad U^*(a,\langle E^{-1}\rangle^{-1})|_{a=0}=0, \tag{16}$$

and the definitions

$$G^*(a,\langle E\rangle)=\frac{\partial U(a,\langle E\rangle)}{B\partial a}\quad G^*(a,\langle E^{-1}\rangle^{-1})=\frac{\partial U(a,\langle E^{-1}\rangle^{-1}}{B\partial a}, \tag{17}$$

yields

$$G^*(a,\langle E\rangle)\geqslant G^*(a,\langle E^{-1}\rangle^{-1}). \tag{18}$$

Since $G(a,\langle E\rangle)=G^*(a,\langle E\rangle)$ in a linear elastic material, we obtain (12).

Inequality (12) shows that G computed under the assumption that the random material is directly replaced by a homogeneous material ($E(x,\omega)=\langle E\rangle$), is lower than G computed with E taken explicitly as a spatially varying material property. Clearly, $\langle G(a,E)\rangle$ is the correct quantity to be used under dead loading.

Remark 1. With the beam thickness L increasing, the mesoscale L/d grows, so that $E'\to 0$. Thus, $\langle E^{-1}\rangle^{-1}\to\langle E\rangle$, and (12) turns into an equality, whereby the deterministic fracture mechanics is recovered.

Remark 2. These results carry over to a Timoshenko beam. In that case, strain energy is defined by

$$U(a)=\int_0^a \frac{M^2}{2IE}dx+\int_0^a \frac{V^2}{2A\mu}dx, \tag{19}$$

where V is shear force, A is beam's moment of inertia, and μ is shear modulus. The random material is now defined as a vector random field $\mathcal{B}=\{C(\omega,x);\omega\in\Omega,x\in[0,a]\}$, where the stiffness $C=[E,\mu]$. With the strain energy release rate defined by (3), we now derive

$$G(a,\langle E\rangle,\langle\mu\rangle)\leqslant\langle G(a,E,\mu)\rangle=G^*(a,\langle E^{-1}\rangle^{-1},\langle\mu^{-1}\rangle^{-1}). \tag{20}$$

The equality in (20) follows from the random Legendre transformation.

Fixed-Grip Conditions

In this case the displacement is constant (i.e., nonrandom), and the load is random. Now, only the first term in (1) remains so that

$$G=-\frac{\partial U^e(a)}{B\partial a}. \tag{21}$$

Suppose now that there is loading by a force P at the tip, so that we have

$$G=-\frac{u}{2B}\frac{\partial P}{\partial a}. \tag{22}$$

Take now a cantilever beam problem implying $P=3uEI/a^3$. Then, we find

$$\langle G\rangle=-\frac{u}{2B}\left\langle\frac{\partial P}{\partial a}\right\rangle=-\frac{u}{2B}\frac{\partial\langle P\rangle}{\partial a}=\frac{9u^2I\langle E\rangle}{2Ba^4}. \tag{23}$$

Since the load—be it a force and/or a moment—is always proportional to E, this indicates that G can be computed by a direct ensemble averaging of E under fixed-grip loading, and, indeed, the same conclusion carries over to Timoshenko beams.

Mixed-Loading Conditions

In general, both load and displacement vary during crack growth, and there is no explicit relation between the crack driving force and the change in elastic strain energy. However, we can bound G under mixed loading (G_{mixed}) by G under dead load (G_P) and G under fixed grip (G_u), providing we note the following facts:

(i) Observe that $G_P=\langle G(a,E)\rangle$, while $G_u=G(a,\langle E\rangle)$. Clearly, in view of (18), the ensemble averages satisfy

$$G_u \leqslant G_P . \tag{24}$$

(ii) Any (dP,du) change in the P, u-plane, corresponding to G_{mixed} due to an extension of the crack by da, may be split into two parts: $(0,du)$ and $(dP,0)$. The first part, involving an extension of the crack by $(da)_1$, is computed as $G_P=\langle G(a+(da)_1,E)\rangle$. The second part, involving an extension of the crack by $(da)_2$, is computed as $G_u=G(a+(da)_2,\langle E\rangle)$.

(iii) Observe that

$$G_{\text{mixed}}(a+da)=G_u(a+(da)_2)+G_P(a+(da)_1)\leqslant G_P(a+da) \tag{25}$$

because $G_u(a+(da)_2)\leqslant G_P(a+(da)_2)$ by (24), while

$$G_{\text{mixed}}(a+da)=G_u(a+(da)_1)+G_P(a+(da)_2)\geqslant G_u(a+da) \tag{26}$$

because $G_P(a+(da)_1)\geqslant G_u(a+(da)_1)$ again by (24).

It follows that G_{mixed} due to $da=(da)_1+(da)_2$ is bounded by the G's computed under dead-load and fixed-grip conditions, from above and below, respectively:

$$G_u \leqslant G_{\text{mixed}} \leqslant G_P . \tag{27}$$

Note that, interestingly, in mechanics of random media, the energy-type inequalites are usually ordered in an inverse fashion: kinematic (resp. force) conditions provide upper (resp. lower) bounds.

Moving on to the case of Timoshenko beam loaded at the tip, we have four particular possibilities:

(i) P and M fixed: G_{P-M},
(ii) P and θ fixed: $G_{P-\theta}$,
(iii) u and M fixed: G_{u-M},
(iv) u and θ fixed: $G_{u-\theta}$,

wherein $G_{P-\theta}$ and G_{u-M} are G's under mixed conditions. Now, in place of (24) we have

$$G_{u-\theta}\leqslant G_{P-\theta}\leqslant G_{P-M} \quad G_{u-\theta}\leqslant G_{u-M}\leqslant G_{P-M} . \tag{28}$$

Stochastic Crack Stability

Recalling the fracture criterion (1), we observe that cracking along the x axis is governed by an interplay of two random fields (parametrized by x): the elastic property E and the surface energy density γ. In view of the scaling arguments concerning the SVE versus the RVE in the paragraph following Eq. (4), the first one is a function of the beam thickness L, but the second one is not. Thus, for statistically stationary and ergodic materials, the randomness of E decreases to zero as the mesoscale $L/d\to\infty$, but the randomness of γ remains constant. To sum up, cracking of microbeams is more sensitive to the material randomness of elastic moduli than cracking of, say, large plates.

Crack stability in any particular micro-beam ($\omega\in\Omega$), in a general loading situation, is governed by the condition of the same form as that in deterministic fracture mechanics, [2],

$$\frac{\partial^2(\Pi(\omega)+\Gamma(\omega))}{\partial a^2}\begin{cases}<0: & \text{unstable equilibrium}\\ =0: & \text{neutral equilibrium}\\ >0: & \text{stable equilibrium.}\end{cases} \tag{29}$$

Here both, the total potential energy $\Pi(\omega)$ and the surface energy $\Gamma(\omega)$ are random. Now, under dead-load conditions, the correctly averaged $\langle\Pi\rangle$ (shown by a solid line) is bounded from above by the deterministic Π estimated by a straightforward averaging of E

$$\Pi(\langle 1/E\rangle)=\langle\Pi\rangle\leqslant\Pi(\langle E\rangle). \tag{30}$$

The above follows again from (8). Typically, the energy Π goes like $-a^3$. Thus, in Fig. 2, we use a wedge of two parabolas to indicate scatter associated with the mean

$$\Pi(\langle 1/E\rangle)=\langle\Pi\rangle. \tag{31}$$

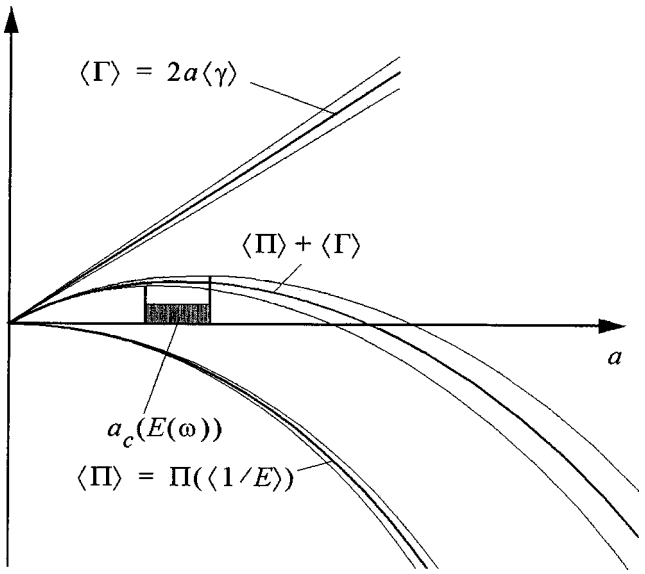

Fig. 2 Potential energy $\Pi(\langle 1/E\rangle)$ (thick line) and its scatter shown by a parabolic wedge (thin lines), summed with the surface energy $\langle\Gamma\rangle=2a\langle\gamma\rangle$ (thick line) and its scatter shown by a straight wedge (thin lines), results in $\Pi(\langle 1/E\rangle)+\langle\Gamma\rangle$ (thick line) and having scatter shown by a wider parabolic wedge (thin lines). Dashed region indicates the range of a critical crack length $a_c(E(\omega))$, a random variable.

Next, if we take, in analogy to (4), the surface energy density as a random field made up of a constant mean $\langle\gamma\rangle$ and a zero-mean fluctuation $\gamma'(x)$

$$\gamma(\omega,x)=\langle\gamma\rangle+\gamma'(\omega,x) \quad \omega\in\Omega, \tag{32}$$

then the surface energy $\Gamma(\omega)=2a[\langle\gamma\rangle+\gamma'(\omega)]$. Thus, using two straight lines, we indicate scatter about $\langle\Gamma\rangle=2a\langle\gamma\rangle$. Consequently, the scatter about the mean of $\Pi(\omega)+\Gamma(\omega)$ is larger than that of $\Pi(\omega)$ or $\Gamma(\omega)$ alone, and at the maximum of their sum we have a stochastic competition between both contributions. Evidently, according to (29), the critical crack length a_c becomes a random variable—i.e., $a_c(E(\omega))$—and we show its range by a dashed region in Fig. 2. In view of (30), there is an inequality between the average a_c properly calculated from $\Pi(\langle 1/E\rangle)$

$$\frac{\partial^2[\Pi(\langle 1/E\rangle)+\langle\Gamma\rangle]}{\partial a^2}=0\Rightarrow a_c(\langle 1/E\rangle)=\langle a_c(E)\rangle \tag{33}$$

and the deterministic a_c simplistically calculated from $\Pi(\langle E\rangle)$ is

$$\frac{\partial^2[\Pi(\langle E\rangle)+\langle\Gamma\rangle]}{\partial a^2}=0\Rightarrow a_c(\langle E\rangle). \tag{34}$$

The said inequality is

$$a_c(\langle 1/E\rangle)\leqslant a_c(\langle E\rangle). \tag{35}$$

Note that the equality $a_c(\langle 1/E\rangle)=\langle a_c(E)\rangle$ in (33) follows from (31). Finally, Fig. 2 shows that small random fluctuations in E and γ (i.e., scatter about the maximum of $\Pi(\langle 1/E\rangle)+\langle\Gamma\rangle$) lead to relatively much stronger (!) fluctuations in a_c.

Acknowledgment

Constructive comments of two anonymous reviewers helped in this work. The author also gratefully acknowledges the support of this research by the NSERC and the Canada Research Chairs Program.

References

[1] Griffith, A. A., 1921, "The Phenomena of Rupture and Flow in Solids," Philos. Trans. R. Soc. London, Ser. A, **221**, pp. 163–198.
[2] Gdoutos, E. E., 1993, *Fracture Mechanics: An Introduction*, Kluwer, Dordrecht, The Netherlands.
[3] Chudnovsky, A., and Kunin, B., 1987, "A Probabilistic Model of Brittle Crack Formation," J. Appl. Phys., **62**(10), pp. 4124–4129.
[4] Kunin, B., 1994, "A Stochastic Model for Slow Crack Growth in Brittle Materials," Appl. Mech. Rev., **47**, pp. 175–183.
[5] Altus, E., 2001, "Statistical Modeling of Heterogeneous Micro-Beams," Int. J. Solids Struct., **38**(34–35), pp. 5915–5934.
[6] Beran, M. J., 1998, "The Use of Classical Beam Theory for Micro-Beams Composed of Crystals," Int. J. Solids Struct., **35**(19), pp. 2407–2412.
[7] Ostoja-Starzewski, M., 2001, "Mechanics of Random Materials: Stochastics, Scale Effects, and Computation," *Mechanics of Random and Multiscale Microstructures*, D. Jeulin and M. Ostoja-Starzewski, eds., CISM Courses and Lectures **430**, Springer, Wien, pp. 93–161.
[8] Rudin, W., 1974, *Real and Complex Analysis*, McGraw-Hill, New York.
[9] Ostoja-Starzewski, M., 2002, "Microstructural Randomness Versus Representative Volume Element in Thermomechanics," ASME J. Appl. Mech., **69**, pp. 25–35.

Elastic-Plastic Stress Distribution in a Plastically Anisotropic Rotating Disk

N. Alexandrova
Department of Civil Engineering, University of Aveiro, 3810-193 Aveiro, Portugal
e-mail: nalexandrova@civil.ua.pt

S. Alexandrov
Institute for Problems in Mechanics, Russian Academy of Sciences, 101-1 Prospect Vernadskogo, 119526 Moscow, Russia
e-mail: sergei_alexandrov@yahoo.com

The plane state of stress in an elastic-plastic rotating anisotropic annular disk is studied. To incorporate the effect of anisotropy on the plastic flow, Hill's quadratic orthotropic yield criterion and its associated flow rule are adopted. A semi-analytical solution is obtained. The solution is illustrated by numerical calculations showing various aspects of the influence of plastic anisotropy on the stress distribution in the rotating disk.

[DOI: 10.1115/1.1751183]

1 Introduction

The dependence of stress distribution on the angular velocity in rotating disks is of significant importance due to a large number of applications. The majority of the work in this area is based on the assumption that the material is isotropic and obeys Tresca yield criterion with its associated flow rule (see [1] and a review in this paper). A comparison of the solutions for elastic-plastic rotating solid and annular disks based on Tresca and Mises yield criteria was given in [2]. In particular, the difference in stress distribution calculated with those two criteria was discussed. The effect of yield criteria on the stress distribution and limit angular velocity of a rotating disk with variable thickness was also investigated in [3]. In [4,5], the influence of temperature fields on the development of plastic zones in nonrotating thin disks was demonstrated. In particular, it appeared that the rise in temperature at which the entire plate became plastic was very small for various plate geometries. Summarizing the results obtained in [2–5] one may expect that deviations from isotropic material response can have a significant effect on the development of plastic zones in thin rotating disks. Elastic solutions for solid and annular rotating anisotropic disks were found in [6,7]. Plastic solutions for such disks are not available, to the best of our knowledge. Among the various theories of anisotropic plasticity, the one based on Hill's yield criterion and its associated flow rule, [8], is simplest and most popular. This yield criterion is adopted in the present paper. An axisymmetric problem is formulated assuming that the principal axes of anisotropy coincide with the radial and circumferential directions in plane of a thin disk rotating about its axis. The edges of the disk are stress free, and stresses are continuous across the elastic-plastic boundary. A semi-analytical solution is found under plane stress conditions.

Contributed by the Applied Mechanics Division of THE AMERICAN SOCIETY OF MECHANICAL ENGINEERS for publication in the ASME JOURNAL OF APPLIED MECHANICS. Manuscript received by the ASME Applied Mechanics Division, January 3, 2003, final revision, October 17, 2003. Associate Editor: M.-J. Pindera.

2 Solution

Consider a circular disk of outer radius b and inner radius a rotating with an angular velocity ω about its axis. The thickness of the disk is assumed to be small such that the plane state of stress can be adopted. In a cylindrical coordinate system $r\theta z$ with its z-axis coinciding with the axis of rotation, there are only two nonzero components of the stress tensor, σ_r and σ_θ. The elastic properties of the material are assumed to be isotropic, and the elastic portion of the strain tensor obeys Hooke's law. In the cylindrical coordinates chosen, Hill's yield criterion has the form

$$(G+H)\sigma_r^2-2H\sigma_r\sigma_\theta+(H+F)\sigma_\theta^2=1 \tag{1}$$

where G, H, F are constants which characterize the current state of material anisotropy. It is convenient to rewrite (1) as

$$\sigma_r^2+p_\theta^2-\eta\sigma_r p_\theta=\sigma_0^2 \tag{2}$$

where

$$\eta=2H/\sqrt{(G+H)(H+F)},\quad \eta_1=\sqrt{G+H}/\sqrt{H+F},$$
$$\sigma_0=1/(G+H),\quad p_\theta=\sigma_\theta/\eta_1. \tag{3}$$

The only nontrivial equation of motion is

$$\frac{\partial\sigma_r}{\partial r}+\frac{\sigma_r-\sigma_\theta}{r}=-\rho\omega^2 r, \tag{4}$$

where ρ the density of the material. The boundary conditions are

$$\sigma_r=0 \quad \text{at } r=a \quad \text{and} \quad r=b. \tag{5}$$

At small ω the entire disk is elastic. Since the elastic properties are assumed to be isotropic, the general solution for stresses is well known (see, for example, [9]). Using (5) the distribution of stresses can be found in the following form:

$$\sigma_r=\frac{3+\nu}{8}\rho\omega^2\left(a^2+b^2-\frac{a^2b^2}{r^2}-r^2\right),$$
$$\sigma_\theta=\frac{3+\nu}{8}\rho\omega^2\left(a^2+b^2+\frac{a^2b^2}{r^2}-\frac{1+3\nu}{3+\nu}r^2\right) \tag{6}$$

where ν is Poisson's ratio. Assume that yielding begins at the inner radius of the disk (it will be verified a posteriori). Then, using (3) and taking into account that $\sigma_\theta>0$, the angular velocity at the initial yielding, ω_e, is obtained by substitution of (6) into (2)

$$\frac{\rho\omega_e^2b^2}{\sigma_0}=\frac{4\eta_1}{(3+\nu)+(1-\nu)(a^2/b^2)}. \tag{7}$$

If ω is higher than ω_e, a plastic zone appears in the disk. The angular velocity at which the entire disk becomes plastic will be denoted by ω_p. In the range $\omega_e<\omega<\omega_p$ the disk consists of an inner plastic zone surrounded by an outer elastic zone. To find the distribution of stresses in the plastic zone, it is convenient to introduce the following nondimensional quantities:

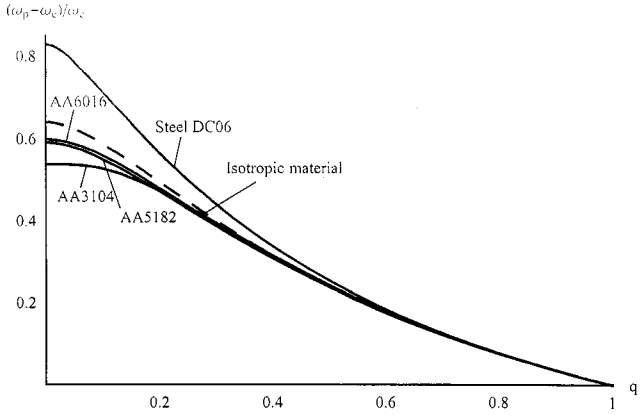

Fig. 1 Variation of the nondimensional quantity $(\omega_p-\omega_e)/\omega_e$ with q

$$\Omega=\rho\omega^2b^2/\sigma_0,\quad q=a/b,\quad \beta=r/b,\quad \gamma=c/b \tag{8}$$

where c is the radius of the elastic-plastic boundary. Equation (2) is satisfied automatically by the substitution

$$\sigma_r/\sigma_0=2\cos\varphi/\sqrt{4-\eta^2},\quad p_\theta/\sigma_0=\eta\cos\varphi/\sqrt{4-\eta^2}+\sin\varphi \tag{9}$$

where φ is a function of β. Substituting (9) into (4), with the use of (3), leads to the following ordinary differential equation for φ:

$$\frac{2\sin\varphi}{\sqrt{4-\eta^2}}\frac{d\varphi}{d\beta}-\left(\frac{2F\cos\varphi}{(H+F)\sqrt{4-\eta^2}}-\eta_1\sin\varphi\right)\frac{1}{\beta}-\Omega\beta=0. \tag{10}$$

The boundary condition to this equation follows from (5) at $r=a$ and (9) in the form

$$\varphi=\pi/2 \tag{11}$$

at $\beta=q$. The solution to (10) satisfying the boundary condition (11) can be obtained numerically and gives φ as a function of β. This function is not monotonic, φ attains its maximum at some value of β and, then, decreases. If the entire disk is plastic, then $\varphi=\pi/2$ at $\beta=1$, as follows from (5) at $r=b$ and (9). For a given value of q, it is clear from (10) that φ depends on β and Ω, $\varphi=\varphi(\beta,\Omega)$. Therefore, the solution to the equation $\varphi(1,\Omega_p)=\pi/2$, if it exists, gives the value of Ω_p corresponding to ω_p. The variation of the nondimensional quantity $(\omega_p-\omega_e)/\omega_e$ with q is shown in Fig. 1.

Once the solution to (10) has been found, the distribution of stresses in the plastic zone $q\leqslant\beta\leqslant\gamma$ is given by (9) with the use of (3). The general stress solution given in [9] is valid in the elastic region $\gamma\leqslant\beta\leqslant1$. Using the boundary condition (5) at $r=b$ and notation (8) it may be rewritten as

$$\frac{\sigma_r}{\sigma_0}=\frac{B}{\sigma_0}\left(\frac{1}{\beta^2}-1\right)+\frac{3+\nu}{8}\Omega(1-\beta^2),$$
$$\frac{\sigma_\theta}{\sigma_0}=-\frac{B}{\sigma_0}\left(\frac{1}{\beta^2}+1\right)+\frac{1+3\nu}{8}\Omega\left(\frac{3+\nu}{1+3\nu}-\beta^2\right) \tag{12}$$

where B is an arbitrary constant. For a given angular velocity in the range $\omega_e<\omega<\omega_p$ the magnitudes of γ and B can be determined from the condition of continuity of the stresses across the elastic-plastic boundary. At $\beta=\gamma$, it follows from (3), (9), and (12),

$$\frac{B}{\sigma_0}=\frac{1}{(1/\gamma^2-1)}\left[\frac{2}{\sqrt{4-\eta^2}}\cos\varphi_\gamma-\frac{3+\nu}{8}\Omega(1-\gamma^2)\right] \tag{13}$$

$$\frac{1}{4}[3+\nu+\gamma^2(1-\nu)]\Omega=\frac{\cos\varphi_\gamma}{\sqrt{4-\eta^2}}\left(\eta\eta_1+2\frac{1+\gamma^2}{1-\gamma^2}\right)+\eta_1\sin\varphi_\gamma \tag{14}$$

where φ_γ is the value of φ at $\beta=\gamma$ and is a function of γ since the solution to (10) gives φ as a function of β. Equation (14) should be solved numerically to obtain γ as a function of Ω. Then, B can be found as a function of Ω with the use of (13).

3 Numerical Results and Discussion

To illustrate the effect of plastic anisotropy on the development of the plastic zone some numerical results are presented in this section. In all cases, $\nu=1/3$. The solution for the isotropic material is obtained as a particular case of the general solution found at $F=G=H$. In Figs. 1–4, the corresponding calculations are illustrated by dashed lines. Four sets of anisotropic coefficients are considered ([10,11]):

$F/(G+H)=0.243$, $H/(G+H)=0.703$ for steel DC06;

$F/(G+H)=0.587$,

$H/(G+H)=0.410$ for aluminum alloy AA6016;

$F/(G+H)=0.498$,

$H/(G+H)=0.419$ for aluminum alloy AA5182;

$F/(G+H)=0.239$,

$H/(G+H)=0.301$ for aluminum alloy AA3104.

Note that the coefficients were measured for rolled sheets with straight principal axes of anisotropy. It is clear that the disk under consideration cannot be made of such sheets. However, for illus-

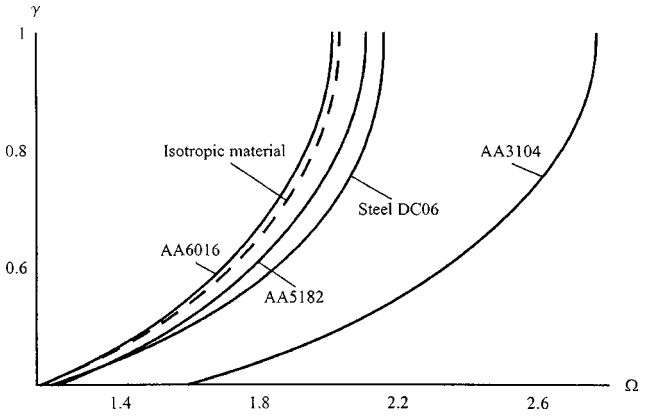

Fig. 2 Variation of the nondimensional radius of elastic-plastic boundary, γ, with Ω at $q=0.4$

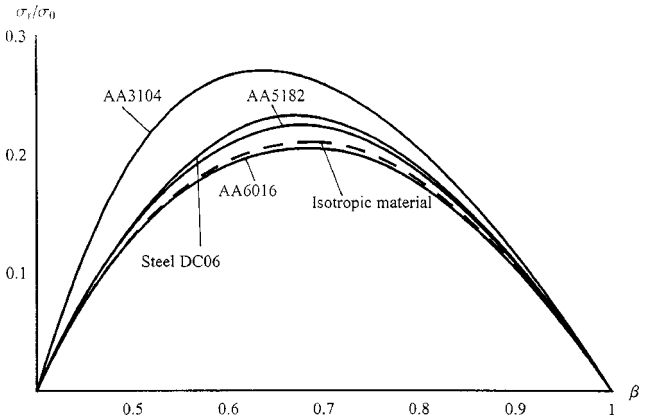

Fig. 3 Radial stress distribution at $\Omega=1.85$ and $q=0.4$

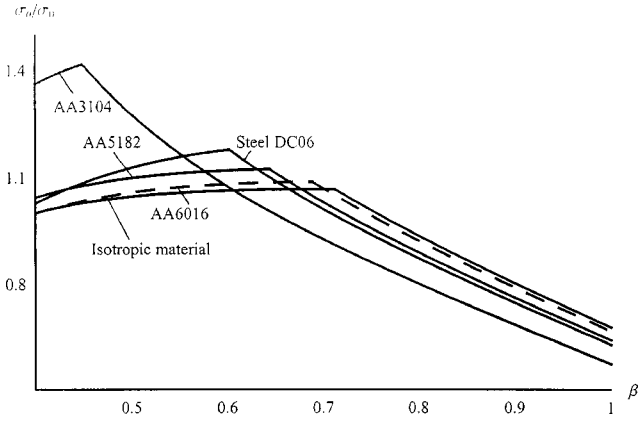

Fig. 4 Circumferential stress distribution at $\Omega=1.85$ and $q=0.4$

trative purposes it is possible to use the aforementioned coefficients for characterizing the level of anisotropy at each point. Figure 2 shows the variation of the radius of elastic-plastic boundary, γ, with Ω at $q=0.4$. Figures 3 and 4 illustrate typical radial and circumferential stress distributions at $\Omega=1.85$ and $q=0.4$, respectively.

There are two main conclusions to be made. First, the qualitative behavior of all curves is the same for anisotropic and isotropic materials: the increase in the angular velocity from ω_e to ω_p is relatively small (Fig. 1), and it tends to be smaller for the aluminum alloys of lower series. This is also illustrated in Fig. 2. Second, the anisotropic plastic properties have a significant effect on the size of the plastic zone and the stress distributions (Figs. 3 and 4). It is expected that this effect may have an influence on residual stress distributions, fatigue crack growth and other properties.

Acknowledgments

N.A. gratefully acknowledges support from the Foundation for Science and Technology (Portugal) under grant SFRH/BPD/6549/2001.

Nomenclature

a, b = inner and outer radii of the disk, respectively
c = elastic-plastic boundary
p_0 = modified tangential stress
q = ratio of the inner to outer radius of the disk
$r\theta z$ = cylindrical coordinate system
β = nondimensional polar radius
γ = nondimensional radius of the elastic-plastic boundary
η, η_1 = plastic anisotropic parameters
ν = Poisson's ratio
ρ = density of the material
σ_r, σ_θ = components of the stress tensor in the cylindrical coordinate system
φ = function of r
φ_γ = value of φ at $\beta=\gamma$
Ω = nondimensional parameter
ω = angular velocity
ω_e = angular velocity at the initial yielding
ω_p = angular velocity at which the entire disk becomes plastic

References

[1] Eraslan, A. N., and Orcan, Y., 2002, "Elastic-Plastic Deformation of a Rotating Solid Disk of Exponentially Varying Thickness," Mech. Mater., **34**, pp. 423–432.
[2] Rees, D. W. A., 1999, "Elastic-Plastic Stresses in Rotating Discs by von Mises and Tresca," Z. Angew. Math. Mech., **79**(4), pp. 281–288.
[3] Ma, G., Hao, H., and Miyamoto, Y., 2001, "Limit Angular Velocity of Rotating Disc With Unified Yield Criterion," Int. J. Mech. Sci., **43**, pp. 1137–1153.
[4] Alexandrov, S. E., and Chikanova, N. N., 2000, "Elastic-Plastic Stress-Strain State of a Plate With a Pressed-in Inclusion in Thermal Field," Mech. Solids, **35**(4), pp. 125–132.
[5] Alexandrov, S., and Alexandrova, N., 2001, "Thermal Effects on the Development of Plastic Zones in Thin Axisymmetric Plates," J. Strain Anal., **36**, pp. 169–176.
[6] Reddy, T. Y., and Srinath, H., 1974, "Elastic Stresses in a Rotating Anisotropic Annular Disk of Variable Thickness and Variable Density," Int. J. Mech. Sci., **16**, pp. 85–89.
[7] Zhou, F., and Ogawa, A., 2002, "Elastic Solutions for a Solid Rotating Disk With Cubic Anisotropy," ASME J. Appl. Mech., **69**, pp. 81–83.
[8] Hill, R., 1950, *Mathematical Theory of Plasticity*, Oxford University Press, London.
[9] Timoshenko, S. P., and Goodier, J. N., 1970, *Theory of Elasticity*, 3rd Ed., McGraw-Hill, New York.
[10] Bouvier, S., Teodosiu, C., Haddadi, H., and Tabacaru, V., 2002, "Anisotropic Work-Hardening Behavior of Structural Steels and Aluminium Alloys at Large Strains," *Proc. Sixth European Mechanics of Materials Conference*, S. Cescotto, ed., University of Liege-Belgium, EMAS, pp. 329–336.
[11] Wu, P. D., Jain, M., Savoie, J., MacEwen, S. R., Tugcu, P., and Neale, K. W., 2003, "Evaluation of Anisotropic Yield Functions for Aluminum Sheets," Int. J. Plasticity, **19**, pp. 121–138.

Saint-Venant Decay Rates for the Rectangular Cross Section Rod

N. G. Stephen
School of Engineering Sciences, Mechanical Engineering, The University of Southampton, Highfield, Southampton SO17 1BJ, UK

P. J. Wang
School of Mechanical, Materials, Manufacturing Engineering and Management, The University of Nottingham, University Park, Nottingham NG7 2RD, UK

A finite element-transfer matrix procedure developed for determination of Saint-Venant decay rates of self-equilibrated loading at one end of a semi-infinite prismatic elastic rod of general cross section, which are the eigenvalues of a single repeating cell transfer matrix, is applied to the case of a rectangular cross section. First, a characteristic length of the rod is modelled within a finite element code; a superelement stiffness matrix relating force and displacement components at the master nodes at the ends of the length is then constructed, and its manipulation provides the transfer matrix, from which the eigenvalues and eigenvectors are determined. Over the range from plane stress to plane strain, which are the extremes of aspect ratio, there are always eigenmodes which decay slower than the generalized Papkovitch-Fadle modes, the latter being largely insensitive to aspect ratio. For compact cross sections, close to square, the slowest decay is for a mode having a distribution of axial displacement reminiscent of that associated with warping during torsion; for less compact cross sections, slowest decay is for a mode characterized by cross-sectional bending, caused by self-equilibrated twisting moment.

[DOI: 10.1115/1.1687794]

1 Introduction

For a one-dimensional, beam-like structure, Saint-Venant's principle (SVP) allows one to replace a known load system on one end by a statically equivalent load distributed in a particular way demanded by the elastostatic solution, known as the relaxed end

Contributed by the Applied Mechanics Division of THE AMERICAN SOCIETY OF MECHANICAL ENGINEERS for publication in the ASME JOURNAL OF APPLIED MECHANICS. Manuscript received by the ASME Applied Mechanics Division, Jan. 22, 2003; final revision, Oct. 28, 2003. Associate Editor: K. R. Rajagopal.

condition. Statically equivalent implies that the resultant force and moment are unchanged; the difference between the two load distributions is termed self-equilibrating and since it has no resultant force or couple that requires reaction at some other locations on the structure, there is no reason why the associated stress and strain field should penetrate any great distance into the structure. That is the self-equilibrating load should produce only a local effect, which decays as one moves away from the beam end. On the other hand, more often than not, the exact distribution is not known, only the magnitude of the end load; either way, SVP is rarely invoked consciously, yet it underpins the day-to-day application of the discipline of strength of materials.

Exact elasticity solutions for these end effects are available when the rod has a mathematically amenable boundary, such as the solid and hollow circular cross section, [1,2]; however, for the important case of a rod of rectangular cross section, the well-known Papkovitch-Fadle (P-F) modes (see, for example, [3]), apply only to the extremes of aspect ratio which are plane strain and plane stress, and are subject to their inherent stress and displacement assumptions, while an antiplane solution, [4], assumes infinite width.

Toupin [5] provided the first proof of SVP in 1965, and there has been extensive research since that time, with reviews having been provided by Horgan and Knowles, [6–8]. Toupin argued that attempts to calculate decay rates are not "*consistent with the spirit of the principle, and the way it is used. After all, if one can construct, or is willing to construct solutions, there is no need for the principle.*" A counter view is that a knowledge of the minimum decay rate for a particular structure defines the extent of the region where a calculated stress may be in error. In a recent paper, [9], the present authors described a numerical procedure which allowed the determination of the Saint-Venant decay rates for a semi-infinite elastic rod of arbitrary cross section subjected to self-equilibrated loading at one end. This procedure is, in turn, a development of a transfer matrix method, [10], in which the decay rates and equivalent continuum beam properties of a repetitive pin-jointed framework, consisting of a series of identical cells, can be calculated. Nodal displacements and forces on either side of the generic cell form state vectors which are related by means of a transfer matrix, the latter being determined from a knowledge of the cell stiffness matrix; on account of translational symmetry, consecutive state vectors are related by a constant multiple λ, the decay factor, which leads directly to a standard eigenvalue problem. For the continuum elastic beam of arbitrary cross section, the beam is first regarded as a series of identical cells of a characteristic length, related to some cross-sectional dimension; the stiffness matrix of one such cell is constructed using a finite element code, such as ANSYS. Since displacement and force components are required only for master nodes at the ends of the cell, all others are treated as slave nodes. This condensation creates a superelement stiffness matrix, which is imported into a MATLAB environment where the manipulations to form the transfer matrix and determination of the eigenvalues are readily accomplished. Accuracy of the method was established in [9] by comparison with the decay rate predictions from a selection of the stock of exact elasticity solutions, and found to be excellent. The theory behind the method was described fully in [9], and is not repeated here.

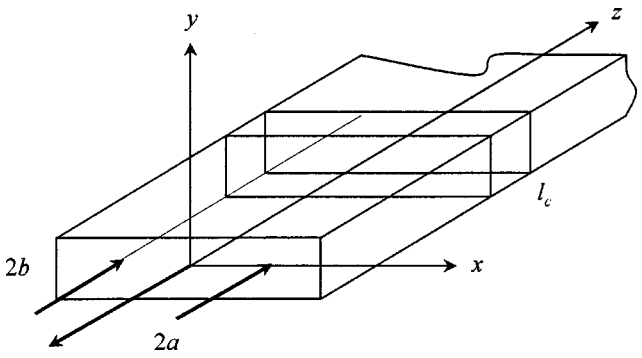

Fig. 1 Semi-infinite elastic rod of rectangular cross section subject to self-equilibrated load on the end $z=0$, and repeating cell of length l_c

2 Finite Element Modelling of the Cell

Figure 1 shows a typical repeating cell of the rod having width $2a$, depth $2b$ and length l_c. For numerical purposes we take b and l_c as equal to unity, when the calculated decay rates, over the range of aspect ratios $a/b=1/20\rightarrow 40$, are a multiple of the rod semi-depth b. The modelling data are given in Table 1; in all cases 20-node isoperimetric elements were used and Poisson's ratio was taken to be 0.25. The large dimension of the transfer matrix, for example 576×576 in the case of the square cross section, in turn leads to a large number of possible decay modes; 12 of the eigenvalues are equal to unity and these pertain to the six rigid body displacements, and the six transmission modes of tension, torsion, and shear and bending in two planes. The remaining eigenvalues occur as reciprocal pairs (the transfer matrix being symplectic) according to whether decay is from left to right, or vice versa, which leads to the prediction of 282 distinct left to right decay modes. Of these, the most important (and the most accurate) are those which provide the slowest (spatially) rates of decay; thus for the square cross section, only the first ten decay rates are presented, allowing some classification into families of decay modes.

Table 1 Finite element modeling data of rectangular crosssection of characteristic length, l_c

Aspect ratio a/b	Division of $2a\times2b$	Division of length, l_c	Number of elements	Nodes in cross-section	Size of transer matrix
1/20	4×8	10	320	121	726×726
1/10	4×8	10	320	121	726×726
1/4	3×8	5	120	95	570×570
1/2	3×8	5	120	95	570×570
2/3	4×6	5	120	93	558×558
4/5	4×6	5	120	93	558×558
1	5×5	5	125	96	576×576
5/4	6×4	5	120	93	558×558
3/2	6×4	5	120	93	558×558
2	8×3	5	120	95	570×570
4	8×3	5	120	95	570×570
10	8×4	5	160	121	726×726
20	8×4	5	160	121	726×726
40	8×4	5	160	121	726×726

Table 2 Slowest decay rates (kb) for various aspect ratios a/b. Shaded entries are those closest to the plane stress/strain Papkovitch-Fadle (P-F) and antiplane shear modes.

Aspect Ratio a/b	1/20	1/10	1/4	1/2	2/3	4/5	1	5/4	3/2	2	4	10	20	40
Exact	1.2985	1.3424	1.4996	1.7999	2.0420	1.8672± 0.6101*i*	1.6639± 0.5717*i*	1.4938± 0.4881*i*	1.3613	0.9000	0.3749	0.1345	0.0648	0.0319
2.1061± 1.1254*i*	2.1065± 1.1256*i*	2.1066± 1.1257*i*	2.1069± 1.1258*i*	2.1077± 1.1295*i*	2.0602± 0.5897*i*	2.0959± 1.1513*i*	1.9917± 1.1546*i*	1.6767± 0.9210*i*	1.3735± 0.3932*i*	1.0538± 0.5648*i*	0.5267± 0.2815*i*	0.2107± 0.1126*i*	0.1053± 0.0563*i*	0.0527± 0.0281*i*
	2.2884± 0.0534*i*	2.1514	2.1207	2.3902± 0.3650*i*	2.1060± 1.1386*i*	2.2734	2.2391± 1.1072*i*	1.8188	1.4040± 0.7591*i*	1.1951± 0.1826*i*	0.5302	0.2154	0.1146± 0.0022*i*	0.0573± 0.0031*i*
3.7488± 1.3843*i*	3.7538± 1.3848*i*	2.5242	2.8533	3.5074± 1.0764*i*	3.1086± 0.9965*i*	2.6663± 1.3941*i*	2.5474± 0.9238*i*	2.1330± 1.1154*i*	2.0723± 0.6645*i*	1.7535± 0.5385*i*	0.7133	0.2523	0.1877± 0.0692*i*	0.0938± 0.0346*i*
	3.9203± 0.6011*i*	3.7535± 1.3849*i*	3.7568± 1.3851*i*	3.7660± 1.4250*i*	3.1825± 1.6861*i*	2.8570± 0.9283*i*	2.5474± 0.9238*i*	2.2855± 0.7427*i*	2.1216± 1.1243*i*	1.8826± 0.7128*i*	0.9390± 0.3464*i*	0.3754± 0.1385*i*	0.1968± 0.0301*i*	0.0986± 0.0159*i*
5.3563± 1.5516*i*	5.3843± 1.5475*i*	4.0050± 0.5656*i*	4.1868± 0.6795*i*	3.9704	3.3620± 1.5510*i*	2.9431± 1.2492*i*	2.6221	2.3545± 0.9996*i*	2.2412± 1.0343*i*	1.9856	1.0468± 0.1701*i*	0.3997± 0.0567*i*	0.2693± 0.0773*i*	0.1346± 0.0387*i*
	5.6001± 0.9056*i*	5.3853± 1.5467*i*	5.3926± 1.5473*i*	4.2459± 2.2807*i*	3.8533± 1.3859*i*	3.1661	2.6672± 1.0872*i*	2.5329	2.5692± 0.9242*i*	2.1238± 1.1439*i*	1.3486± 0.3874*i*	0.5386± 0.1546*i*	↓	↓
6.9500± 1.6761*i*	7.0457± 1.6458*i*	5.6602± 0.8421*i*	5.7122± 1.2234*i*	4.4496± 2.1304*i*	3.8786	3.4276	2.6882	2.7421	2.5858	2.2264± 1.0688*i*	1.4284± 0.3071*i*	↓	↓	↓
$\pi/2 = 1.5708$		7.0696± 1.6502*i*	6.5369	4.7288± 1.3045*i*	4.0178	3.7984± 1.3745*i*	3.7970± 1.3876*i*	3.0389± 1.0999*i*	2.6787	2.3636± 0.6534*i*	1.6368	1.5795	1.5735	1.5718
					4.3477± 1.2607*i*		3.7970± 1.3876*i*	↓	↓	↓	↓	↓	↓	↓
								3.8331± 1.4297*i*	3.8309± 1.4160*i*	3.7496± 1.6404*i*	2.1239± 1.1439*i*	2.1133± 1.1293*i*	2.1133± 1.1304*i*	2.1130± 1.1308*i*
								4.0006± 1.3390*i*	3.9427± 1.3754*i*	3.8124± 1.6022*i*	2.1488± 1.1244*i*	2.1188± 1.1249*i*	2.1150± 1.1289*i*	2.1136± 1.1305*i*
											↓	↓	↓	↓
											3.7481± 1.6425*i*	3.8378± 1.4283*i*	3.8374± 1.4297*i*	3.8370± 1.4298*i*
											3.7655± 1.6320*i*	3.8412± 1.4255*i*	3.8392± 1.4295*i*	3.8376± 1.4302*i*

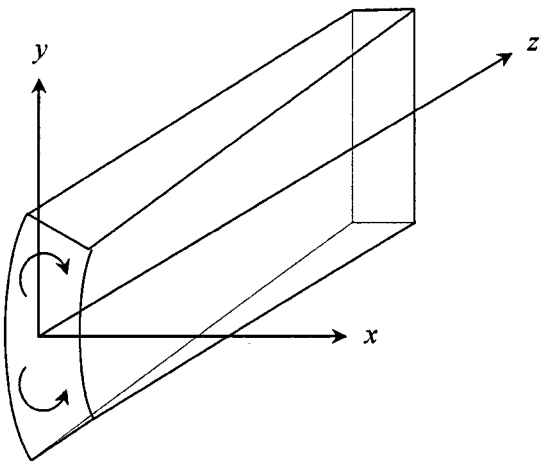

Fig. 2 Self-equilibrated twisting moment on the end $z=0$; aspect ratio $a/b<1$

3 Results and Discussion

The slowest decay rate predictions are shown in Table 2, in ascending magnitude of the real part which governs the rate of decay; thus the first row pertains to self-equilibrated loading that will penetrate the greatest distance into the structure. Exact decay rates are available only at the extremes of aspect ratio, for generalized plane stress ($a/b\rightarrow 0$) and plane strain ($a/b\rightarrow\infty$) when stress decays exponentially from one end as $\exp(-kz)$, where k are the roots of the well-known Papkovitch-Fadle (P-F) eigenequation (see [3], article 26)

$$\sin 2kb \pm 2kb = 0; \tag{1}$$

the two smallest roots are $kb=2.1062\pm 1.1254i$, $kb=5.3563\pm 1.5516i$ for the positive sign in Eq. (1), which is the symmetric case, and $kb=3.7488\pm 1.3843i$, $kb=6.9500\pm 1.6761i$ for the negative sign, the asymmetric case. In the case of antiplane strain, [4], decay from the loaded edge is as $\exp(-n\pi z/2b)$, where n is an integer, implying a slowest decay given by the root $kb=\pi/2$; these exact decay rates are shown in the first column The shaded entries in Table 2 are those that, by virtue of similarity of the displacement field, are closest to these known exact solutions, and are here regarded as generalized P-F or generalized shear modes.

First, it is noted that the decay rates of the generalized P-F modes appear largely insensitive to aspect ratio; thus for the cases $a/b\leqslant 2/3$, the real part of the slowest generalized symmetric P-F mode exceeds that of the exact plane stress value (2.1062) by less than 0.1%, and for $a/b=4/5$ it is less than the plane stress value by 0.5%. The maximum deviation occurs for the square cross section, $a/b=1$, at less than $+7\%$. For the slowest asymmetric generalized P-F mode, the real part exceeds the plane stress value (3.7488) by less than 3% for $a/b\leqslant 1$.

For all aspect ratios considered, there is at least one mode that decays slower than the generalized P-F modes. For $a/b\leqslant 1$, the mode associated with the real root is characterized by a bending of the cross section due to self-equilibrated twisting moment in the xy-plane, as depicted in Fig. 2. The mode associated with the complex root is characterized by an axial warping displacement field reminiscent of Saint-Venant torsion, and hence a stress field associated with the restraint of torsional warping (here referred to as the bi-moment mode).

For the cases $a/b>5/4$, Table 2, there are an increasing number of modes which decay slower than the slowest P-F modes; again the smallest of these modes is characterized by cross-sectional bending, but in fact they are physically the same modes of decay as those which provide the smallest decay rates for $a/b<4/5$; thus consider the dual relationship between the decay rates for the two cases $a/b=2/3$ and $a/b=3/2$; physically the bars are identical, the difference being an interchange of the coordinate axes and, by implication, the dimensions a and b. The slowest decay rate for $a/b=2/3$ is $kb=2.0420$, when stress decays as $\exp(-2.0420z/b)=\exp(-1.3613z/a)$, which is the smallest decay rate for $a/b=3/2$, albeit with a and b reversed; generalization of this result is straightforward for other aspect ratios. For any particular aspect ratio $a/b<1$, a dual decay rate may be found by simply multiplying by the aspect ratio: thus an entry for $a/b=4$ can be found from the decay rate for $a/b=1/4$, and multiplying by 1/4; for example, $1.4996\times 1/4=0.3749$. Indeed, in Table 2, with the exception of those entries below the symbol $\downarrow$, which denotes that some decay rates have not been entered, every decay mode for $a/b<1$ has a dual for $a/b>1$ on the same row.

Compared to the general rectangle, which is symmetric about the coordinate axes, the square cross section is, in addition, symmetric about the two diagonals; in turn the decay rates can occur as single eigenvalues, or as pairs, according to the (a)symmetry of the displacement field. For the slowest bi-moment mode ($kb=1.6639\pm 0.5717i$) both the axial displacement, w, and the cross-sectional displacements, u and v, are symmetric with respect to the diagonals, and asymmetric with respect to the x and y-axes; in consequence a single root, and a single eigenvector (decay mode), suffices. On the other hand, repeated decay rates occur for symmetric cross-sectional bending ($2.5474\pm 0.9238i$) and the asymmetric P-F mode ($3.7970\pm 1.3876i$), but not for the asymmetric cross-sectional bending, or symmetric P-F modes. The single roots at $a/b=1$ show (a)symmetries, as follows:

$(1.6639\pm 0.5717i)$	u, v and w are symmetric about both diagonals, asymmetric about both coordinate axes
$(3.8804\pm 1.3623i)$	u, v and w are asymmetric about both diagonals and coordinate axes
4.0408	u, v and w are asymmetric about both diagonals and coordinate axes
$(2.2391\pm 1.1072i)$	u, v and w are symmetric about both diagonals and coordinate axes
$(1.9917\pm 1.1546i)$	u, v and w are symmetric about both coordinate axes, asymmetric about the diagonals

In each case, there are (a)symmetries for each of the three displacement components.

In contrast the modes pertaining to the double roots show a less developed pattern of (a)symmetry; for example,

$(2.5474\pm 0.9238i)$	one mode has u and v symmetric about the y-axis, asymmetric about the x-axis, no (a)symmetries about diagonal; w no (a)symmetries; the other mode has w symmetric about the x-axis, asymmetric about the y-axis, no (a)symmetries about diagonals; u and v show no (a)symmetries
$3.7970\pm 1.3876i$	one mode has w symmetric about one diagonal, asymmetric about the other; u and v show no (a)symmetries; the other mode has u and v asymmetric about the x-axis, symmetric about the y-axis; w shows no (a)symmetries.

Now there is planar (a)symmetry in respect of u and v, or (a)symmetries for the axial displacement w, but not both. Thus it appears that the occurrence, or otherwise, of a double decay mode depends on the degree of (a)symmetry in the displacement field.

Finally, we note in Table 2 a decay rate which approaches the slowest antiplane strain shear decay rate of $kb=\pi/2$, with an error of less than 0.6% when $a/b \geqslant 10$.

4 Concluding Remarks

For the rectangular cross section, there are always eigenmodes that decay slower than the Papkovitch-Fadle (P-F) modes; typically these are modes characterized by a bending of the cross section, which would be precluded by plane stress/plane strain assumptions. The exception is for a compact cross section, that is, close to being square, when slowest decay is for a mode associated with a bi-moment. However, the P-F modes remain important as a means of classification of the various decay modes.

In discussing the decay rates, attention has focused on the slowest, as it is these which validate Saint-Venant's principle; for the square cross section, the slowest Saint-Venant decay is as $\exp(-1.6639z/b)=\exp(-4.7062z/d)$ where $d=2\sqrt{2}b$ is the section diagonal, which is the greatest linear dimension of the cross-section; this implies that stress level reduces to less than 1% of free end value at distance $z=d$ from the free end, indicating that SVP is clearly applicable. On the other hand, at first sight a very small decay rate, such as $kb=0.0648$ for aspect ratio $a/b=20$, Table 2, might suggest that SVP is inapplicable; indeed the stress level only reduces to 87.8% of its free end value at distance $z=2b$ (that is, distance 1×plate thickness) from the free end. However, if the decay characteristic is expressed in terms of multiples of the diagonal $d=2\sqrt{401}b$, decay is as $\exp(-2.5952z/d)$. This implies stress reduction to less than 7.5% at distance $z=d$ from the free end, and to less than 0.6% at twice that distance; thus SVP is still clearly applicable so long as the decay characteristic and, more importantly, the sense in which SVP is understood, is in terms of multiples of the cross section greatest linear dimension which is dominated by plate width $2a$ for this aspect ratio.

Nomenclature

- a, b = semi-width and semi-depth of rectangular cross section
- d = greatest linear dimension of cross section ($d=2\sqrt{a^2+b^2}$)
- i = $(-1)^{1/2}$
- k = decay rate ($k=\ln\lambda$)
- l_c = characteristic length
- u, v, w = displacement components in the x, y, and z-directions
- x, y, z = Cartesian coordinates
- λ = decay factor, eigenvalue of transfer matrix

References

[1] Klemm, R. L., and Little, R. W., 1970, "The Semi-Infinite Elastic Cylinder Under Self-Equilibrated End Loading," SIAM (Soc. Ind. Appl. Math.) J. Appl. Math., **19**, pp. 712–719.

[2] Stephen, N. G., and Wang, M. Z., 1992, "Decay Rates for the Hollow Circular Cylinder," ASME J. Appl. Mech., **59**, pp. 747–753.

[3] Timoshenko, S. P., and Goodier, J. N., 1970, *Theory of Elasticity*, Third Ed., McGraw-Hill, New York, Art. 26.

[4] Shun, Cheng, 1979, "Elasticity Theory of Plates and a Refined Theory," ASME J. Appl. Mech., **46**, pp. 644–650.

[5] Toupin, R. A., 1965, "Saint-Venant's Principle," Arch. Ration. Mech. Anal., **18**, pp. 83–96.

[6] Horgan, C. O., and Knowles, J. K., 1983, "Recent Developments Concerning Saint-Venant's Principle," Adv. Appl. Mech., **23**, pp. 179–269.

[7] Horgan, C. O., 1989, "Recent Developments Concerning Saint-Venant's Principle: An Update," Appl. Mech. Rev., **42**, pp. 295–303.

[8] Horgan, C. O., 1996, "Recent Developments Concerning Saint-Venant's Principle: A Second Update," Appl. Mech. Rev., **49**, pp. 101–111.

[9] Stephen, N. G., and Wang, P. J., 1996, "Saint-Venant Decay Rates: A Procedure for the Prism of General Cross-Section," Comput. Struct., **58**, pp. 1059–1066.

[10] Stephen, N. G., and Wang, P. J., 1996, "On Saint-Venant's Principle for the Pin-Jointed Framework," Int. J. Solids Struct., **33**, pp. 79–97.

On Source-Limited Dislocations in Nanoindentation

M. X. Shi
Department of Theoretical and Applied Mechanics,
University of Illinois at Urbana-Champaign,
Urbana, IL 61801

Y. Huang[1]
Department of Mechanical and Industrial Engineering,
University of Illinois at Urbana-Champaign,
Urbana, IL 61801
e-mail: huang9@uiuc.edu

M. Li
Alcoa Technical Center, Alcoa Center, PA 15069

K. C. Hwang
Department of Engineering Mechanics,
Tsinghua University, Beijing 100084, P.R. China

The discrete dislocation model is used in this note to investigate the source-limited dislocation generation and glide in nanoindentation. It is shown that once there are enough sources for dislocation generation, the material behavior becomes independent of the dislocation source distribution. [DOI: 10.1115/1.1751185]

1 Introduction

Nanoindentation has become a major experimental technique to probe the mechanical properties of materials at the nanoscale, [1,2]. Dislocation glide underneath the nanoindenter is identified as the key mechanism of plastic deformation in nanoindentation, [3,4]. Dislocation loops are observed near the edge of the nanoindenter, [4]. The quasi-continuum analysis, [5], shows that dislocations are indeed generated right underneath the corner of the rectangular indenter and then moved into the bulk material. In this note we present a discrete dislocation analysis to investigate the effect of dislocation source distribution in nanoindentation, particularly the source-limited dislocation generation and glide (i.e., very few sources for dislocation generation). Following Shi et al. [6], we modify the two-dimensional discrete dislocation model of van der Giessen, Needleman and co-workers, [7,8], for the equilibrium dislocation analysis by requiring that the glide component of the Peach-Koehler force on each dislocation vanishes at each time step.

2 Equilibrium Analysis of Discrete Dislocations

We study a region of 4 μm×2 μm subject to pressure on the top surface over a zone of 0.8 μm. The Young's modulus is 70 GPa, and Poisson's ratio is 0.33. Figure 1 shows the symmetric, right-half region (2 μm×2 μm). The symmetry or traction-free conditions give that the shear stress tractions vanish on all boundaries. In addition, the left boundary is subject to the symmetry condition $u_x=0$. The right surface is traction free, so is the top surface except over the loading region where the pressure is applied (over the region of 0.4 μm). Here for simplicity we use the

[1]Two whom correspondence should be addressed.

Contributed by the Applied Mechanics Division of THE AMERICAN SOCIETY OF MECHANICAL ENGINEERS for publication in the ASME JOURNAL OF APPLIED MECHANICS. Manuscript received by the ASME Applied Mechanics Division, Aug. 12, 2002; final revision, Oct. 25, 2003. Associate Editor: T. E. Triantifyllides.

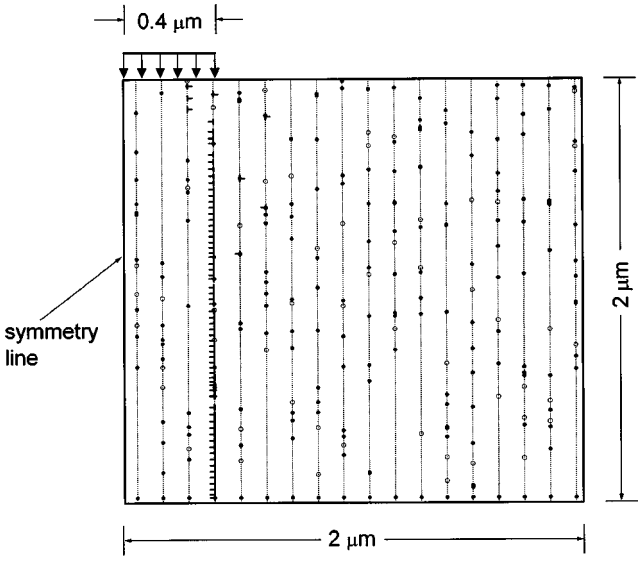

Fig. 1 Random distribution of dislocation sources (open circles) and obstacles (solid circles) on slip planes (dashed lines). There are 18 slip planes in the 2 μm×2 μm region, with 3 dislocation sources and 11 obstacles on each slip plane. The pressure is applied over a region of 0.4 μm on the top surface.

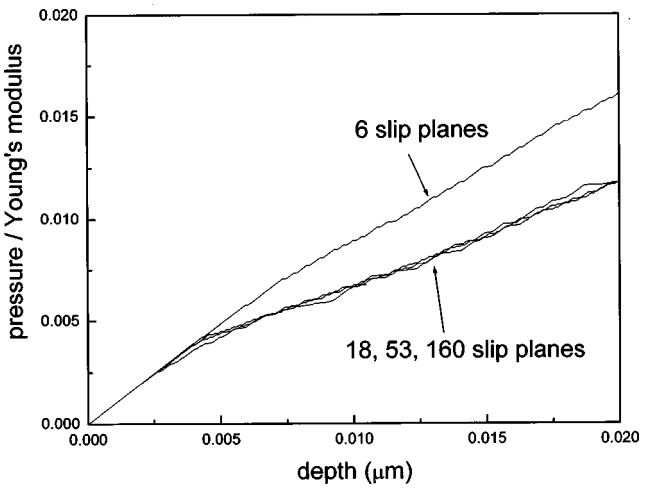

Fig. 2 The applied pressure (normalized by the Young's modulus) versus the indentation depth for the 2 μm×2 μm region in Fig. 1 with 6, 18, 53, and 160 slip planes

pressure in the finite loading region (0.4 μm) to represent the indentation. The bottom surface is also subject to boundary condition $u_y = 0$.

The right-half region in Fig. 1 contains 18 slip planes with the slip plane spacing 112.5 nm. We have chosen the slip planes parallel to the direction of pressure (on the top surface) since these slip planes allow dislocations to move downward, which is consistent with that observed by Tadmor et al. [5]. Initially, the solid is assumed to be free of mobile dislocations, but to contain a random distribution of dislocation sources and point obstacles. The sources mimic Frank-Read sources and generate a dislocation dipole when the Peach-Koehler force exceeds a critical value, [6–8]. The obstacles, which could be small precipitates or forest of dislocations, pin dislocations and will release them once the Peach-Koehler force attains the obstacle strength, [6–8].

There are three sources for dislocation generation (marked by open circles) randomly distributed on each slip plane, and their strength follows a normal distribution with the mean strength $\overline{\tau}_{\mathrm{NUC}} = 50$ MPa and standard deviation $0.2\overline{\tau}_{\mathrm{NUC}} = 10$ MPa. Once the glide component of the Peach-Koehler force exceeds $\tau_{\mathrm{NUC}} b$ over time $t_{\mathrm{NUC}} = 0.01$ μs, a dislocation dipole is generated, [6–8]. Here $b = 0.25$ nm is the length of the Burgers vector, and the glide component of the Peach-Koehler force on the Kth dislocation is given by

$$f^K = \mathbf{n}^{\mathbf{K}} \cdot \sigma \cdot \mathbf{b}^{\mathbf{K}}, \tag{1}$$

where $\mathbf{n}^{\mathbf{K}}$ is the slip plane normal, $\mathbf{b}^{\mathbf{K}}$ is the Burgers vector of the Kth dislocation and σ is the stress field excluding the contribution from the Kth dislocation itself.

There are ten obstacles (marked by solid circles) randomly distributed on each slip plane, with the obstacle strength $\tau_{\mathrm{OBS}} = 150$ MPa. When a dislocation meets an obstacle, it is pinned to this obstacle until the glide component of the Peach-Koehler force given in (1) exceeds $\tau_{\mathrm{OBS}} b$. On each slip plane there is an additional obstacle very close to the bottom surface with very large obstacle strength in order to prevent dislocations from exiting the bottom surface. This represents (or mimics) the effect of a hard substrate that blocks dislocations at the film/substrate interface. Dislocation annihilation is also accounted for. Two dislocations with opposite Burgers vectors on the same slip plane annihilate when their spacing is less than $6b$.

The same approach of van der Giessen, Needleman, and coworkers, [7,8], is used to decompose the problem into (1) an analytic solution for dislocations in an infinite solid, and (2) a finite element solution for a dislocation-free solid with finite boundaries. The finite element method can handle the second problem very effectively since it does not involve any singularities, [7,8]. However, Our analysis is different in that all dislocations reach equilibrium within each time increment, though they may exit the solid (from the top surface), or be pinned at obstacles. The dislocation positions are solved iteratively within each time increment until the glide component of the Peach-Koehler force vanishes for every dislocation, [6].

3 Results

Figure 1 also shows the dislocation distribution on all 18 slip planes in the solid at the pressure $0.012E$, where E is the Young's modulus. The distance between the end of loading region and the nearest slip plane is 6.25 nm. It is clearly observed that most dislocations are generated on the slip plane closest to the end of loading region. This is due to the high stress concentration at the end of loading region, [9]. In fact, the normal stress in the direction perpendicular to the applied pressure is even singular at the end of loading region, [9]. The pattern of dislocation distribution shown in Fig. 1 is similar to the patterns observed in the quasicontinuum analysis, [5], and experiments, [3,4].

In order to examine the effect of dislocation source distribution in nanoindentation, we have also studied the same region (2 μm×2 μm) with 6, 53, and 160 slip planes. The slip plane spacings are 337.5 nm, 37.5 nm, and 12.5 nm, respectively. The size of loading region remains the same (0.4 μm). The number of dislocation sources and obstacles also remain the same on each slip plane (3 and 10, respectively), but the total number of dislocation sources and obstacles for 6, 53, and 160 slip planes are approximately 1/3, 3, and 9 times of those shown in Fig. 1 for 18 slip planes. The distance between the end of loading region and the nearest slip plane is 106.25 nm for the solid with 6 slip planes, and this distance becomes 6.25 nm for 18, 53, and 160 slip planes. Figure 2 shows the applied pressure normalized by the Young's modulus versus the indentation depth for above four sets of slip planes, where the indentation depth is the maximum normal displacement (under the pressure) at the symmetry line. It is clearly observed that the curves for 18, 53, and 160 slip planes are essen-

tially the same, but the curve for 6 slip planes shows a much stiffer material response. The latter is therefore called the source-limited dislocation generation.

4 Concluding Remarks

The present note shows that, for source-limited dislocation generation (e.g., 6 slip planes with 18 dislocation sources), the material may display a stiff response. Once there are enough dislocation sources (e.g., 18, 53, or 160 slip planes with 54, 159, and 480 dislocation sources, respectively), the overall plastic response of the solid becomes independent of the dislocation source distribution. The present model oversimplifies dislocation activities (e.g., two-dimensional analysis, one set of slip planes, dislocation sources), but the above conclusion on source-limited dislocations in nanoindentation should hold qualitatively.

Acknowledgments

Y. H. acknowledges the support from NSF through grants 0084980 and 0103257, and NSFC. K. C. H. acknowledges the support from the Ministry of Education and NSFC.

References

[1] Nix, W. D., 1997, ''Elastic and Plastic Properties of Thin Films on Substrates: Nanoindentation Techniques,'' Mater. Sci. Eng., A, **234**, pp. 37–44.
[2] Gouldstone, A., Koh, H.-J., Zeng, K.-Y., Giannakopoulos, A. E., and Suresh, S., 2000, ''Discrete and Continuous Deformation During Nanoindentation of Thin Films,'' Acta Mater., **48**, pp. 2277–2295.
[3] Zielinski, W., Huang, H., Venkataraman, S., and Gerberich, W. W., 1995, ''Dislocation Distribution Under a Microindentation Into an Iron-Silicon Single Crystal,'' Philos. Mag. A, **72**, pp. 1221–1237.
[4] Gerberich, W. W., Nelson, J. C., Lilleodden, E. T., Anderson, P., and Wyrobek, J. T., 1996, ''Indentation Induced Dislocation Nucleation: The Initial Yield Point,'' Acta Mater., **44**, pp. 3585–3598.
[5] Tadmor, E. B., Miller, R., and Phillips, R., 1999, ''Nanoindentation and Incipient Plasticity,'' J. Mater. Res., **14**, pp. 2233–2250.
[6] Shi, M., Huang, Y., and Gao, H., 2003, ''The J-Integral and Geometrically Necessary Dislocations in Nonuniform Plastic Deformation,'' Int. J. Plasticity, in press.
[7] Needleman, A., and van der Giessen, E., 2001, ''Discrete Dislocation and Continuum Descriptions of Plastic Flow,'' Mater. Sci. Eng., A, **309**, pp. 1–13.
[8] van der Giessen, E., Deshpande, V. S., Cleveringa, H. H. M., and Needleman, A., 2001, ''Discrete Dislocation Plasticity and Crack Tip Fields in Single Crystals,'' J. Mech. Phys. Solids, **49**, pp. 2133–2153.
[9] Hills, D. A., and Nowell, D., 1994, *Mechanics of Fretting Fatigure*, Kluwer Academic Publishers, Boston.